Award Number: W81XWH-09-1-0391

TITLE:
Host Genes and Resistance/Sensitivity to Military Priority Pathogens

PRINCIPAL INVESTIGATOR:
Gerald I. Byrne, PhD

CONTRACTING ORGANIZATION:
University of Tennessee Health Science Center
Memphis, Tennessee 38163-1201

REPORT DATE:
June 2013

TYPE OF REPORT:
Final

PREPARED FOR: U.S. Army Medical Research and Materiel Command
Fort Detrick, Maryland 21702-5012

DISTRIBUTION STATEMENT: Approved for Public Release;
Distribution Unlimited

REPORT DOCUMENTATION PAGE

Form Approved
OMB No. 0704-0188

1. REPORT DATE *(DD-MM-YYYY)*	2. REPORT TYPE	3. DATES COVERED *(From - To)*
June 2013	Final	01 June 2009 – 31 May 2013

4. TITLE AND SUBTITLE

Host Genes and Resistance/Sensitivity to Military Priority Pathogens

5a. CONTRACT NUMBER
W81XWH-09-1-0391

5b. GRANT NUMBER
W81XWH-09-1-0391

5c. PROGRAM ELEMENT NUMBER

6. AUTHOR(S)

Byrne, Gerald, I; Cui, Yan; Li, Kui; Lu, Lu; Miller, Mark, A; Williams, Robert W.; Boon, Adranius; Bix, Mark; Marion, Tony.

5e. TASK NUMBER

5f. WORK UNIT NUMBER

7. PERFORMING ORGANIZATION NAME(S) AND ADDRESS(ES)

University of Tennessee Health Science Center
65 S. Dunlap
Memphis TN 38163-1201

8. PERFORMING ORGANIZATION REPORT NUMBER

9. SPONSORING / MONITORING AGENCY NAME(S) AND ADDRESS(ES)
U.S. Army Medical Research and Material Command
Fort Detrick, MD 21702-5012

10. SPONSOR/MONITOR'S ACRONYM(S)

11. SPONSOR/MONITOR'S REPORT NUMBER(S)

12. DISTRIBUTION / AVAILABILITY STATEMENT
Approved for public release; distribution unlimited

13. SUPPLEMENTARY NOTES

14. ABSTRACT

This report provides data from our study of differential susceptibility to DoD priority pathogens (*Francisella tularensis* (FT), *Burkholderia pseudomallei* (Bp), *Acinetobacter baumannii* (Ab), *Leishmania major* (Lm), SARS, H5N1 avian influenza) using BXD recombinant inbred mice. The FT project identified phenotypes that correlate with differential immune response to pneumonic infections. The Ab project has identified clear phenotypic differences between the innate immune responsiveness of B6 and D2 mice to pulmonary infection. The Bp project has identified QTLs linked with differential susceptibility to pneumonic Bp infection. The SARS project found difference in susceptibility to MA15 virus infection between B6 and D2 mouse strains. The influenza project has identified a significant QTL associated with early production of proinflammatory cytokines on Chr 6. The Lm project has identified two suggestive loci on Chr 12 and 15 regulating parasite burden. The mouse genomics core generated datasets for different mouse strains (available on www.genenetwork.org). The Bioinformatics (Modeling core) analyzed biological data from projects using Bayesian network analysis and created a Bayesian Network Webserver. The Chlamydia genetic studies in BXD mice was used as the prototype model. The bioinformatics core used this model to develop and integrate the algorithms for testing pathways underlying host responses to pathogen infections.

15. SUBJECT TERMS
Host genetics, Pathogens, Biodefense, Disease susceptibility, Humanized mice

16. SECURITY CLASSIFICATION OF:			17. LIMITATION OF ABSTRACT	18. NUMBER OF PAGES	19a. NAME OF RESPONSIBLE PERSON
a. REPORT	b. ABSTRACT	c. THIS PAGE			USAMRMC
U	U	U	UU	254	19b. TELEPHONE NUMBER *(include area code)*

Standard Form 298 (Rev. 8-98)
Prescribed by ANSI Std. Z39.18

Table of Contents

Introduction

This is our final progress report from a program studying Department of Defense priority Pathogens. We were allowed a one-year "no-cost-extension" to continue working on our projects. The grant supported the work of several investigators at the University of Tennessee Health Science Center and St. Jude Children's Research Hospital. Dr. Miller (*F. tularensis, Burkholderia, Acinetobacter*), Li (SARS Co-V), Dr. Bix (*Leishmania* major). The projects were supported by a modeling core (Dr. Cui) and a mouse genomic core (Drs Williams and Lu). Dr. Tony Marion joined the team during the third year to work on Francisella. Four of the original co-Investigators moved to other institutions during the funding period: Dr Adranius Boon to Washington University, MO; Dr James Bina to University of Pittsburgh, PA; Dr Fabio Re to Rosalin Franklin University, Il; Dr Isao Miyairi to Japan.

Our study hypothesis is that differential susceptibility to DoD-priority pathogens is the result of host genetic variability, and that these discrete loci and/or gene pathways can be identified using BXD recombinant inbred mice. The pathogens in our study are naturally occurring endemic diseases, emerging infections diseases and biowarfare agents: multidrug resistant *Acinetobacter baumannii*, *Burkholderia pseudomallei*, *Francisella tularensis*, *Leishmania major*, Severe Acute Respiratory Syndrome (SARS Co-V), highly pathogenic H5N1 Avian Influenza virus.
The use of advanced recombinant inbred mice (ARI) has been useful tools to discover host genes that contribute to disease phenotypes ranging from differences in pathogen burden, differences in disease severity and differences in disease outcome. We have an ARI strain set (BXD) comprising 157 well-characterized distinct strains expressing a high degree of genetic variability (> 5 million SNPs) that have enabled us to use forward genetic approaches. This approach that has successfully yielded highly specific host genetic information based on collecting easily measured phenotypes that can be then analyzed using our software tools (WEB QTL and the gene network). Many such studies have been previously reported in the context of this award and have been the subject of a number of published studies on *Chlamydia*, influenza, *Francisella* and *Burkholderia*. We have found that once host genes are identified to be statistically linked to disease status, application of a variety of experimental methods can then be exploited to provide definitive mechanistic data. We have also found that linking host disease phenotypes, genotypes with 'omics' data sets provides appropriate types of information for computational biology evaluations. These studies then provide systems information that link signaling to the metabolome and thus ensure the most comprehensive work-up of host-elicited changes in response to any pathogen that is being investigated.

Our study had three main objectives:

- To identify specific phenotypic differences in the response of BXD parental strains following infection with each of the DoD-priority pathogens
- To identify host genetic loci and pathways that correlate with differential susceptibility/resistance phenotype(s) of the parental mouse strains to the DoD-priority pathogen.
- To define and validate candidate genes and gene networks responsible for differential susceptibility/resistance phenotype(s) of the parental mouse strains for each DoD-priority pathogen.

In our final report, we present our findings for each pathogen in relation to the study objectives. We have fulfilled each of the study objectives to different extents for the different pathogens because we were not able to develop the infection models for the pathogens at the same rate. For example, the *Francisella*, *Burkholderia* and *Acinetobacter* models are more advanced that

the SARS and Leishmania models. Work on the influenza model stopped shortly after Dr Boon transferred to Washington University. We also present an update from the cores. The mouse genomics core generated datasets for different mouse strains, which are available on www.genenetwork.org. The Bioinformatics (Modeling core) analyzed biological data (response to infection by a pathogen) from projects using Bayesian network analysis and created a Bayesian Network Webserver (BNW - http://compbio.uthsc.edu/BNW).

We have obtained significant results for all projects supported by this grant funding. We are therefore very enthusiastic to follow up on the data we have obtained. We are applying for funding from different sources to continue these studies either as separate projects for the different DoD priority pathogens, or as a big program project that will involve pathogens and supporting cores to do “omics” studies.

Francisella tularensis (FT) project

Francisella tularensis Schu S4 is an extremely virulent bacterial pathogen in humans (LD_{50}<10 CFU) and in all mouse strains that have been studied (LD_{50}<10). In our hands, there is very little difference in the ultimate outcome of infection of the two parental mouse strains (B6 and D2); the mice all die and at very similar rates. However, we and others have observed differences in the bacterial burdens that are observed in B6 vs. D2 mice. It is known that B6 mice typically carry 5-10 fold higher FT burdens than D2 mice during acute infection. It stands to reason that these two mouse strains produce distinct innate immune responses that are responsible for this difference in bacterial burdens.

In an effort to identify phenotypes of differential innate immune responsiveness of B6 vs. D2 mice to pneumonic *Francisella tularensis* Schu S4 (FT) infection, we performed a timecourse study of disease-state lung parameters following pneumonic infection. Mice were challenged with 250 CFU of FT via intranasal instillation. At each of the following timepoints (12, 18, 24, 48, 72, 96, and 120 hours) post-infection, 5 mice/group were subjected to submandibular puncture for blood collection and were then sacrificed. Immediately after sacrifice, brochoalveolar lavage was performed using 1 ml of sterile PBS, cells were pelleted via centrifugation, BAL cells were enumerated using a Millipore Sceptor automatic cell counter, and BALF fluids were stored at 80˚C until use. Cytokine/chemokine quantitation in each BAL fluid was then performed via Luminex-based multiplex analysis (32-plex Millipore kit).

We found that on day 3 post-infection (72 hrs), cells numbers recruited to the lungs of D2 mice were significantly higher than observed in B6 mice (**Figure 1**). Interestingly, this difference in BAL cell numbers was transient.

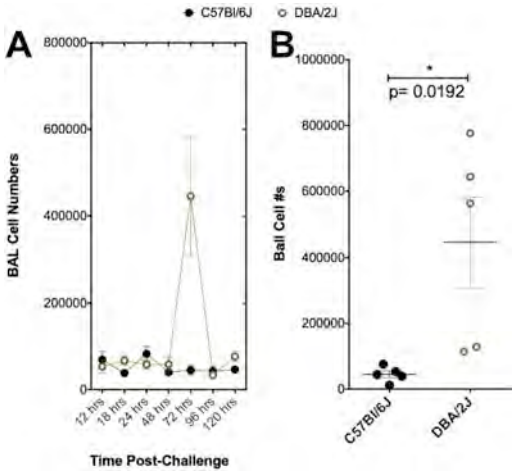

Figure 1. Differential expression of cytokines in the lung compartment of *Francisella tularensis* Schu S4-infected B6 and D2 mice. B6 and D2 mice (35/group were challenged via intranasal instillation with 250 CFU FT Schu S4. On day three (72 hrs) post-infection, 5 mice/group were sacrificed and bronchoalveolar lavage (BAL) was performed. Cells recruited to the lungs were enumerated using Millipore Scepter cell counter. Statistical analyses were performed using student-t tests and p values are indicated.

Multiplex cytokine analysis of BALF revealed that most of the cytokine and chemokine levels remained relatively flat in the lungs of both B6 and D2 mice for the first two days of acute infection. However, on day three significant increases in levels of several cytokines were observed in the lungs of either B6, D2, or both strains. Differential expression of 10 analytes (M-CSF, G-CSF, IL-1alpha, IL-6, IL-12p40, IL-17, LIF, RANTES, KC, and VEGF) was observed on day 3 post-infection (also see **Figure 2 and Figure 3**). On day 4 post-infection there were 11 analytes that appear to differentially expressed in B6 vs. D2 mice (M-CSF, G-CSF, IL-6, IL-12p70, IL-17, LIF, KC, VEGF, MIP-2, MCP-1, and MIG) and on day 5 post infection 10 of the analytes were differentially expressed by B6 vs. D2 mice (M-CSF, G-CSF, IL-1alpha, KC, VEGF, MIP-2, MIG, Eotaxin, MIP-1alpha, and MIP-1beta).

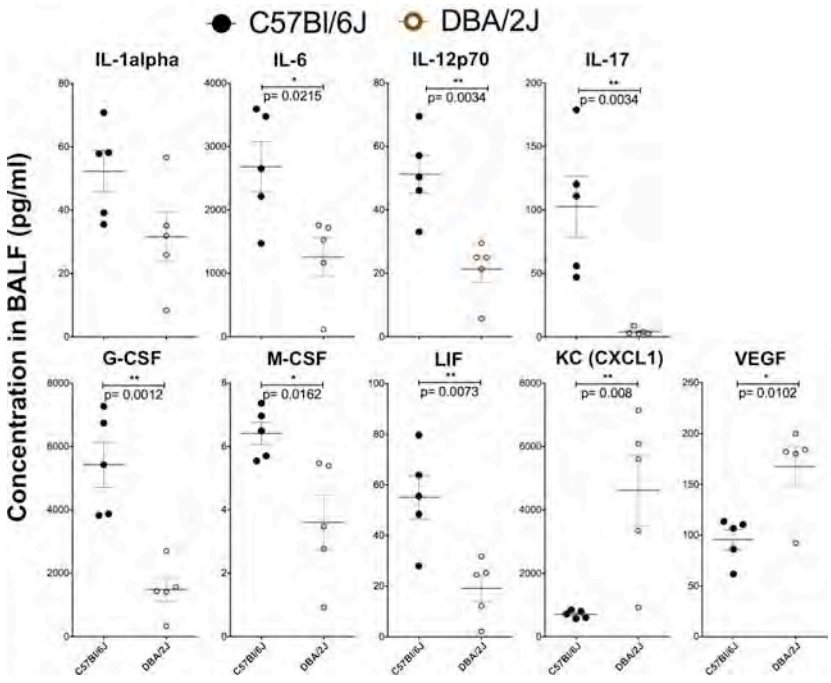

Figure 2. Differential expression of cytokines in the lung compartment of *Francisella tularensis* Schu S4-infected B6 and D2 mice. B6 and D2 mice (35/group were challenged via intranasal instillation with 250 CFU FT Schu S4. On day three (72 hrs) post-infection, 5 mice/group were sacrificed and bronchoalveolar lavage (BAL) was performed. Cytokine/chemokine quantitations in BAL fluids were performed via Luminex-based multiplex analysis (32-plex Millipore kit). Statistical analyses were performed using student-t tests and p values are indicated.

We also analyzed serum samples via Luminex-based cytokine/chemokine multiplex analysis (32-plex Millipore kit). Similar to our findings with the BALF, most of the cytokine levels remained fairly flat until three days post infection. At this timepoint, a significant elevation in concentration of many of the cytokines was apparent in serum of either B6, D2, or both strains (**Figure 4**). However, in contrast to what was observed in the BALF, there were only six analytes that appeared to be differentially expressed (IL-1beta, IL-6, IL-12p70, IL-17, MIP-1alpha, and IL-10), and only 4 of those were statistically relevant differences (**Figure 5**). Interestingly, only three of the six analytes that were differentially expressed in the serum were found to be differentially expressed in the lung compartment. On day 4 post-infection, 19 of the analytes (**Figure 4**) appeared to be differentially expressed by B6 vs. D2 mice (M-CSF, IL-1beta, IL-2, IL-5, IL-6, IL-10, IL-12p70, IL-13, RANTES, KC, MIP-2, MCP-1, MIG, Eotaxin, MIP-1alpha, MIP-1beta, TNF-alpha, IP-10, and IFN-gamma). On day 5, only IL-12p40 appeared to be differentially expressed by B6 vs. D2 mice.

These studies have identified a large number of potential disease-state phenotypes that could be useful for QTL analysis and gene network modeling studies. Choosing the most appropriate timepoint for collecting the data will be a critical decision. Clearly, days 3 and 4 post-infection offer the most distinct phenotypes for QTL analysis, and the day 4 timepoint offers the largest number of phenotypes. However, day 3 post-infection may be the more relevant timepoint for evaluating the effect of disease-state cytokine/chemokine expression on the developing innate immune response to FT.

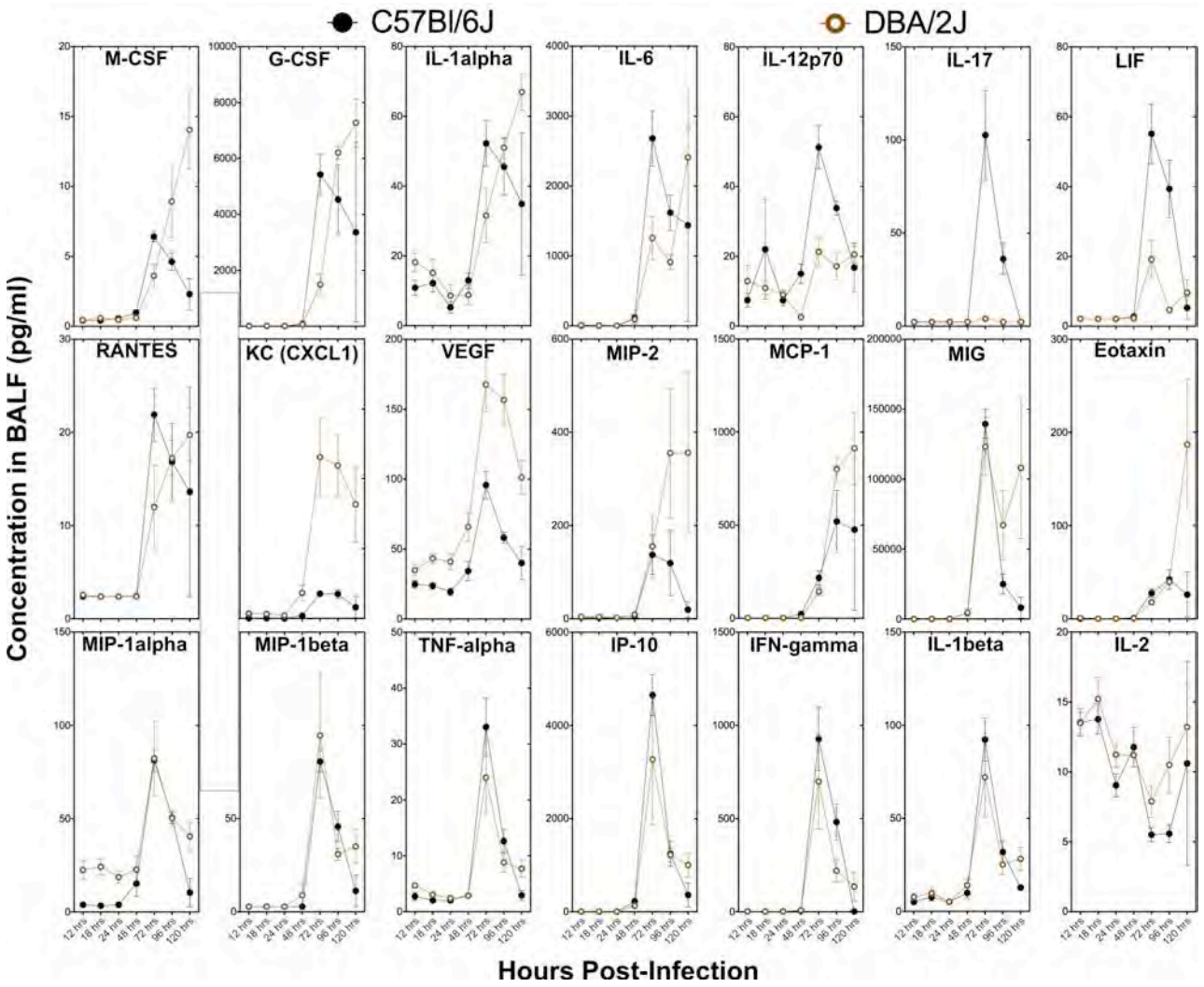

Figure 3. Kinetic monitoring of cytokine/chemokine production in the lung compartment of B6 and D2 mice following pneumonic challenge with *Francisella tularensis* Schu S4. B6 and D2 mice (35/group) were challenged via intranasal instillation with 250 CFU FT Schu S4. At the indicated time points (12, 18, 24, 48, 72, 96, and 120 hrs post-infection), mice were sacrificed and bronchoalveolar lavage was performed. Quantitation of cytokine/chemokine levels in the BAL fluids was performed via Luminex-based multiplex analysis (32-plex Millipore kit).

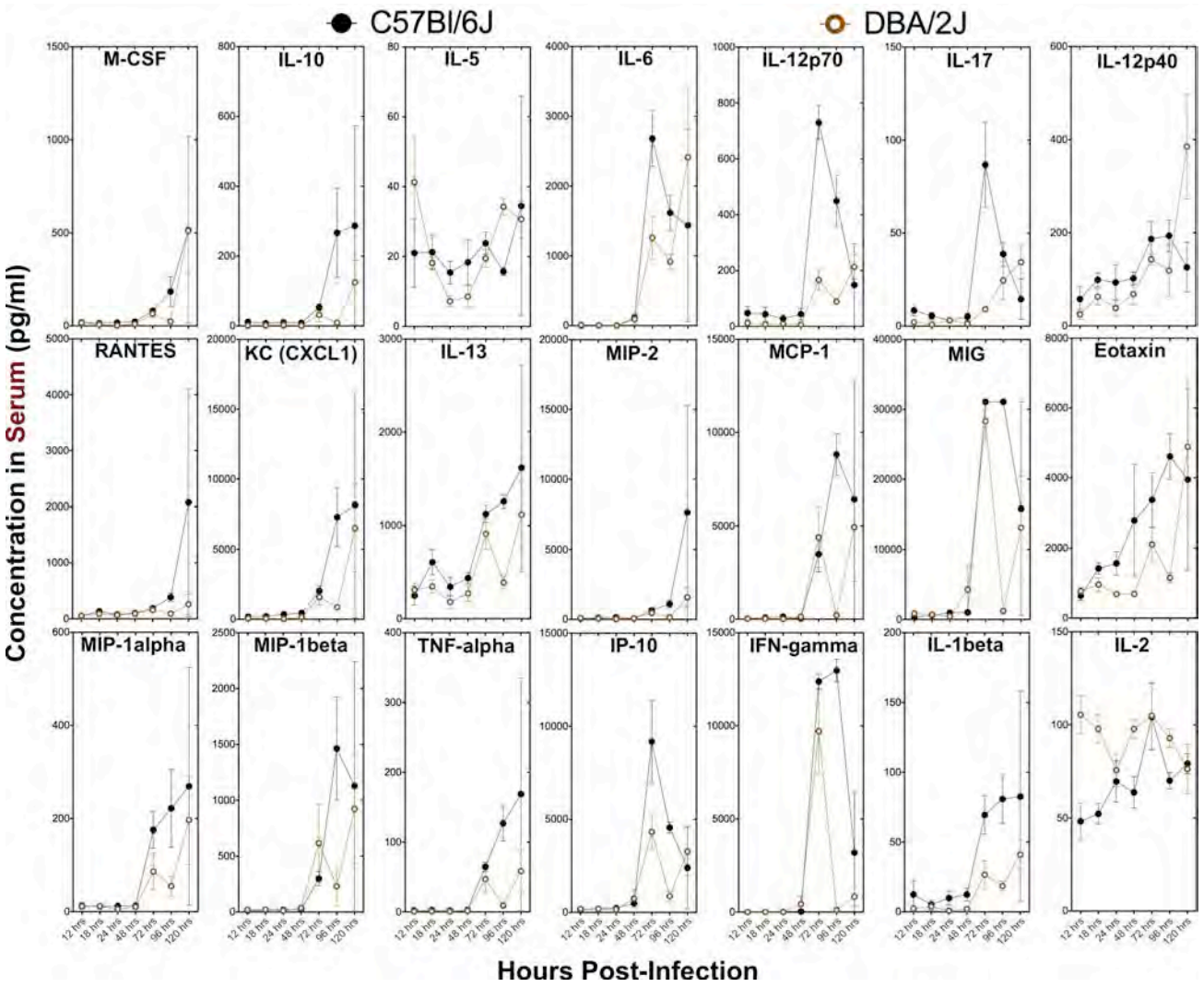

Figure 4. Kinetic monitoring of cytokine/chemokine levels in the peripheral circulation of B6 and D2 mice following pneumonic challenge with *Francisella tularensis* Schu S4. B6 and D2 mice (35/group) were challenged via intranasal instillation with 250 CFU FT Schu S4. At the indicated time points (12, 18, 24, 48, 72, 96, and 120 hrs post-infection), blood samples were collected via submandibular puncture. Quantitation of cytokine/chemokine levels in the serum samples was performed via Luminex-based multiplex analysis (32-plex Millipore kit).

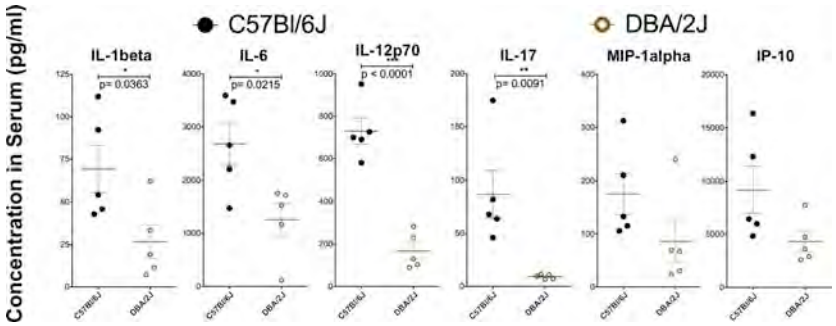

Figure 5. Differential expression of cytokines/chemokines by B6 vs. D2 mice 72-hours post-infection with *Francisella tularensis* Schu S4. B6 and D2 mice (5/group were challenged with 250 CFU FT Schu S4. Blood serum was collected via submandibular puncture 72-hours later. Cytokine/chemokine quantitations were performed via Luminex-based multiplex analysis (32-plex Millipore kit). Statistical analyses were performed using a student-t test and p values are indicated.

Key Research Accomplishments

- We have identified 16 distinct phenotypes of differential responsiveness of B6 vs. D2 mice to pneumonic FT infection (BAL cell numbers, 9 analytes in BALF, and 6 analytes in serum) on day 3 post-infection.
- We have identified 25 distinct phenotypes of differential responsiveness of B6 vs. D2 mice to pneumonic FT infection (6 analytes in BALF, and 19 analytes in serum) on day 4 post-infection.
- We have identified 11 distinct phenotypes of differential responsiveness of B6 vs. D2 mice to pneumonic FT infection (10 analytes in BALF, and 1 analytes in serum) on day 5 post-infection.

Reportable outcomes

Presentations

1. **Poster Presentation** at the International Toll 2012 Meeting: Decoding Innate Immunity. Riva del Garda, Italy, May 4-7, 2011. Ceballos-Olveda I, Sahoo M, **Bina JE**, **Miller MA**, **Re F**. "Role of inflammasome-dependent cytokines IL-1β and IL-18 during mouse ling infection with virulent *Francisella tularensis* SchuS4"
2. **Poster Presentation** at UTHSC A.A-St Jude Research Lectureship and Medical Student Poster Session. Wodowski A, Jayakar H, Parvathareddy J, Bina XR, **Bina JE**, **Miller MA**. 2011. "Visualization of Intranasal Dosing Efficiency Using Luminescent *Francisella tularensis*".
3. **Poster Presentation** at Regional Centers for Excellence Meeting. Llewellen AC, Zhao J, Song F, Flynn K, Xu Q, Napier BA, **Bina JE**, Cotter PA, Swanson MS, **Miller MA**, Raetz CRH, Weiss DS. 2012. "A novel conserved deacytylase required for lipid A modification and *Francisella* virulence".

Abstracts

1. Ceballos-Olveda I, Sahoo M, **Bina JE**, **Miller MA**, **Re F**. Role of inflammasome-dependent cytokines IL-1β and IL-18 during mouse ling infection with virulent *Francisella tularensis* SchuS4. In: Proceedings of the International Toll 2012 Meeting, Decoding Innate Immunity, Riva del Garda, Italy, May 4-7, 2011.
2. Wodowski A, Jayakar H, Parvathareddy J, Bina XR, **Bina JE**, **Miller MA**. 2011. Visualization of Intranasal Dosing Efficiency Using Luminescent *Francisella tularensis*. In: Proceedings of UTHSC A.A-St Jude Research Lectureship and Medical Student Poster Session, 2011.
3. Llewellen AC, Zhao J, Song F, Flynn K, Xu Q, Napier BA, **Bina JE**, Cotter PA, Swanson MS, **Miller MA**, Raetz CRH, Weiss DS. 2012. A novel conserved deacytylase required for lipid A modification and *Francisella* virulence. In: Proceedings of the Regional Centers for Excellence Meeting, 2012.S. Weiss. **201**2. In *Proceedings of the Regional Centers for Excellence Meeting, 201*2.

Publications

1. Clinton SR, **Bina JE**, Hatch TP, Whitt MA, **Miller MA**. 2010. Binding and activation of host plasminogen on the surfact of *Francisella tularensis*. BMC Microbiol. 10:76
2. Bina XR, **Miller MA**, **Bina JE**. 2011. Construction of a bioluminescence reporter plasmid for *Francisella tularensis*. Plasmid 64:156-161.

3. Jayakar HR, Parvathareddy J, Fitzpatrick EA, Bina XR, **Bina JE**, Re F, Emery FD, **Miller MA**. 2011. A galU Mutant of *Francisella tularensis* is Attenuated for Virulence in a Murine Pulmonary Model of Tularemia. BMC Microbio. 11:179. PMID:21819572 PMCID: PMC3173336.
4. **Miller MA**, Stabenow JM, Parvathareddy J, Wodowski AJ, Fabrizio TP, Bina XR, Zalduondo L, **Bina JE**. 2012. Visualization of intranasal dosing efficiency using luminescent *Francisella tularensis*.: effect of instillation volume and form of anesthesia. PLoS ONE; 7(2):e31359. PMID:22384012 PMCID: PMC3286442.
5. Napier BA, Meyer L, **Bina JE**, **Miller MA**, Sjostedt A, Weiss DS. 2012. Link between intraphogosomal biotin and rapid phagosomal escape in *Francisella*. Proc Natl Acad Sci USA 109(44):18084-9. PMID: 23071317 PMCID:PMC3497780.
6. Llewellyn AC, Zhao J, Song F, Parvathareddy J, Xu Q, Napier BA, Laroui H, Merlin D, **Bina JE**, Cotter PA, **Miller MA**, Raetz CRH, Weiss DS. NaxD is a deacetylase required for lipid A modification and *Francisella* pathogenesis. Molecular Microbiology 86(3):611-627.

Conclusions

We have laid the groundwork for QTL analyses that could identify host genetic loci that correlate with differential innate immune responses to pneumonic FT infection. These differences in innate immunity result (at least in part) in a 5-10 fold difference in bacterial burdens between B6 and D2 mice. Our results have also shown quite nicely that the innate response to FT challenge is significantly delayed compared to most infection models. Most of the cytokine levels in both B6 and D2 mice remained relatively flat until day three post-infection. This is unusual and in stark contract to the other two bacterial pathogens we have discussed in this progress report (*Acinetobacter baumannii* and *Burkholderia pseudomallei*).

Acinetobacter baumannii project

In the progress report from September 2010, we reported that we were having difficulty establishing pulmonary infection with *Acinetobacter baumannii* (Ab) that resulted in disease symptoms in either of the parental mouse strains. We performed a series of experiments using cyclophosphamide treatment in an effort to reduce the innate response to Ab in hopes of establishing a disease state in one or both of the parental strains. We were unable to establish symptomatic infections using this approach.

In an effort to identify a differential phenotype in the parental strains following pulmonary infection with Ab, we initiated studies to evaluate a series of immune parameters within the lung following intranasal infection with Ab. We performed time-course studies in which mice were infected with 1 x 10^6 CFU of Ab, and then a subset of the mice were sacrificed every 24 hours, bronchiolar lavage (BAL) was performed, and flow cytometric analyses was performed to determine the frequency of neutrophils within the BAL cell population.

The results of these studies have revealed that there is a significant difference in the recruitment of immune cells to the peritoneal cavity of B6 vs. D2 mice 24 hours after intranasal challenge (**Figure 1**). No differences were observed in mice sacrificed at later timepoints (data not shown). Flow cytometric analysis revealed that the bulk of the cells recruited to the lungs of D2 mice were neutrophils (data not shown).

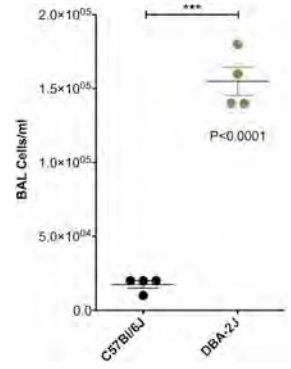

Figure 1. Differential recruitment of immune cells into the lungs following pulmonary infection with *Acinetobacter baumannii*. Mice (4/group) were challenged with either 1 x 10^6 CFU Ab via the intranasal route. The mice were sacrificed 24 hr later and bronchiolar lavage (BAL) was performed. BAL cells were counted using a hemocytometer. Statistical analysis was performed using an unpaired t-test.

We have initiated a series of studies using several lung parameters as phenotypic readouts for BXD analyses. Based on the data shown in **Figure 1**, recruitment of cell to the lungs is the one of the phenotypes of interest and is the one that we have concentrated most of our efforts on to this point. We have performed screening with 25 BXD strains (all between 10-12 weeks old) and have found that several of the BXD strains are phenotypically similar to D2 mice, some are phenotypically similar to B6 mice, and several strains display intermediate phenotypes (**Figure 2**). Some of the group sizes are too small to yield statistically relevant findings, and additional studies will be performed with these strains as mice of the appropriate age become available. Interval mapping (using GeneNetwork.org) using this cohort of animals reveals a suggestive QTL on chromosome 10 (**Figure 3**). We have established breeding cages for additional strains that will be used to continue

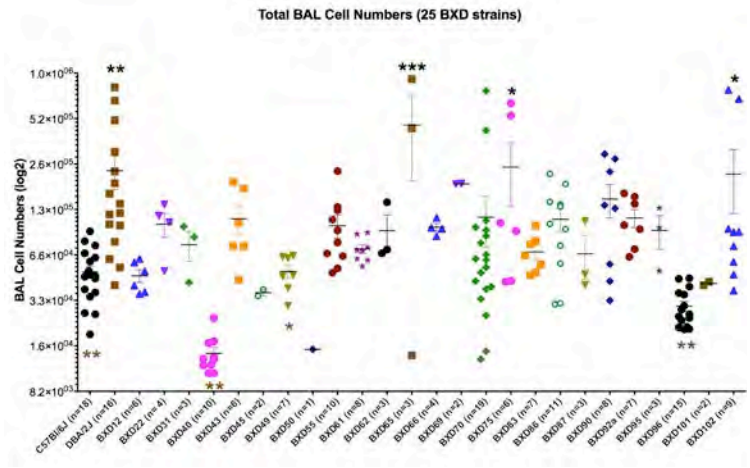

Figure 2. Differential recruitment of immune cells into the lungs of BXD strains following pulmonary infection with *Acinetobacter baumannii*. BXD mice were challenged with 1 x 10^7 CFU Ab via the intranasal route. The mice were sacrificed 24 hr later and bronchiolar lavage (BAL) was performed. BAL cells were counted using a Scepter cell counter. Statistical analysis was performed using one-way ANOVA using Dunnett post tests to compare each of the BXD strains with the C57Bl/6 (statistical significance is indicated in black) and with the DBA/2J mice (statistical significance indicated in brown). Statistica significance is as follows: p<0.05 *, p<0.01 **, and p<0.001 ***.

this line of investigation and to confirm/narrow the interval on chromosome 10 that appears to correlate with the differential innate immune responses of B6 and D2 mice following *Acinetobacter* infection.

We have also been collecting bronchiolar lavage fluids (BALF) and serum samples upon sacrifice of each of the mice shown in **Figure 2**. Each of the samples will be subjected to multiplex cytokine quantitative analyses using a Luminex 32-plex cytokine/chemokine kit.

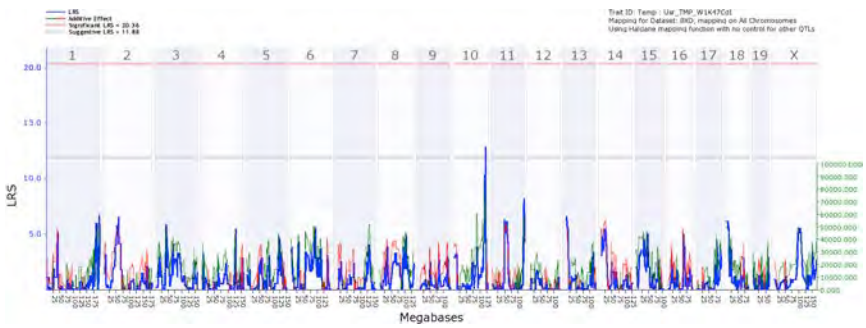

Figure 3. Interval map using recruitment of cells to the lungs of Acinetobacter-infected mice as the query phenotype. A cohort of mice which includes 25 BXD strain were infected intranasally with 1 x 10^7 CFU of Acinetobacter baumannii. Twenty-four hous later, the maice were sacrificed and bronchiolar lavage was performed on each mouse. The number of cells collected from the lungs of each mouse was determined and used as a phenotypic readout for differential innate responsiveness to *Acinetobacter*. Interval mapping was performed using the in silico resources within GeneNetwork.org. to identify genetic loci that correlate with differential recruitment of immune cells to the lungs of infected mice.

Approximately half of the BALF samples have already been analyzed and it is apparent that there are significant differences in the production of a number of the analytes by the parental and BXD strains following Ab infection. In BALF samples, we have observed differences in production of 24 of the 32 analytes tested (IFN-g, IL-1a, IL-1b, IL-2, IL-4, IL-3, IL-6, G-CSF, IL-9, IL-10, IL-12p40, IL-12p70, LIF, IL-13, LIX, IL-15, IL-17, IP-10, KC, M-CSF, MIP-2, MIG, VEGF, TNF-a). Interval mapping of these differential cytokine/chemokine phenotypes have identified several QTL that correlate with differential expression of many of these cytokines. The most commonly observed QTLs are on chromosomes 5 (centered at approximately 100Mb) and 6 (centered at approximately 26Mb). As shown in **figure 4**, either significant or suggestive QTLs were observed for each of the cytokines at a similar region of chromosome 5, and suggestive QTLs were observed at a similar region of chromosome 6 for four of the six cytokines shown.

We surveyed the genes that are within the suggested interval of chromosome 5 in an effort to identify genes that have obvious roles in the production of immune responses (**Figure 5**). Many of the prospective genes that were identified are likely to play a role in innate resistance to bacterial pathogens. For example, Cmklr1, a genetic locus on chromosome 5, encodes chemokine-like receptor-1. This receptor is expressed on a number of immune cells including plasmacytoid dendritic cells, myeloid dendritic cells, macrophages, and NK cells [1]. After activation of this receptor, these

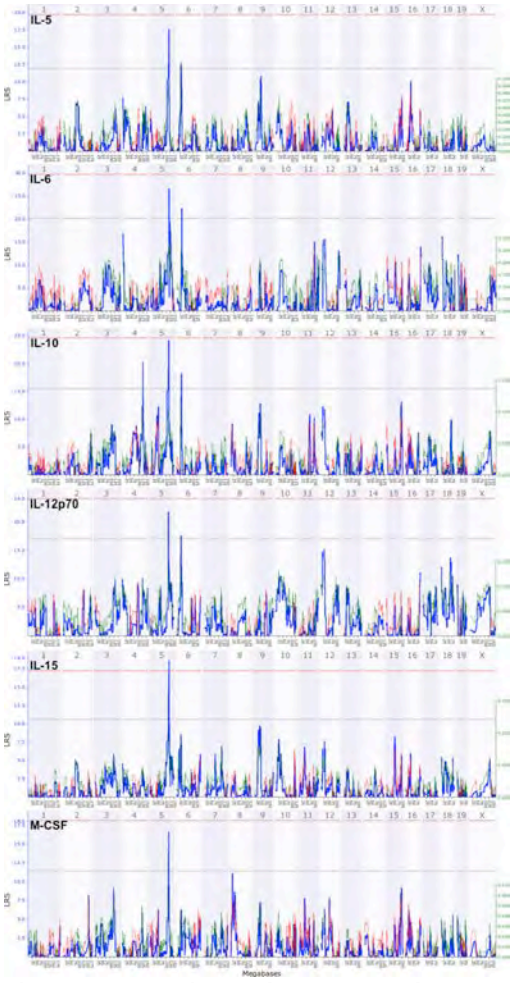

Figure 4. Interval mapping of a panel of differentially expressed cytokines/ chemokines. Interval mapping was performed using the in silico resources within GeneNetwork.org to identify genetic loci that correlate with differential disease-state expression of IL-5, IL-6, IL-10, IL-12p70, IL-15, and M-CSF in the lungs of *Acinetobacter*-infected mice.

cells synthesize and secrete a number of proinflammatory cytokines, including IL-6 and TNFα [2]. Activation of this receptor causes initiation of signaling cascades such as ERK1 and NF-kB [3].

Gpr81, which encodes G-protein coupled receptor (GPCRs) 81, was also found within the loci of the suggestive QTL on chromosome 5. GPCRs are expressed on inflammatory cells such as polymorphonuclear leukocytes, monocytes and macrophages for classic chemoattractants and chemokines. These receptors also play a crucial role in the migration of phagocytes to sites of inflammation [4].
Other genes of interest that lie within this locus encode the IL-31 receptor and neutrophil cytostolic factor (IL-31r and NCF1respectively). The IL-31 receptor is expressed on a number of cell types including monocytes, epithelial cells and T cells and has role in limiting type 2 inflammation in the lung [5, 6]. NCF1 encodes neutrophil cytostolic factor (p47hox). This protein has been implicated as a regulator for IL-4 signaling pathways that are important for macrophage cell fate choice. Furthermore, this protein is a subunit of the NADPH oxidase enzyme complex, which plays an essential role in the function of phagocytes [7].

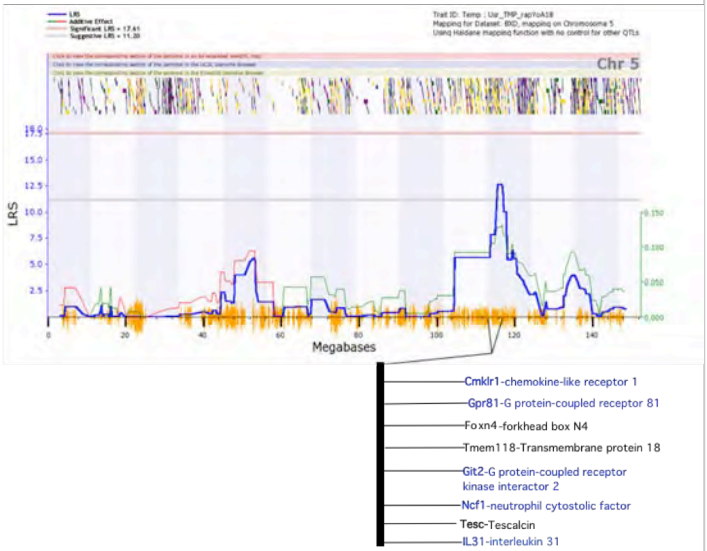

Figure 5. Identity of host genes encoded within the suggestive QTL on chromosome 5 that may be potentially involved in immune processes. Genes that are potentially involved in immune processes are listed in blue.

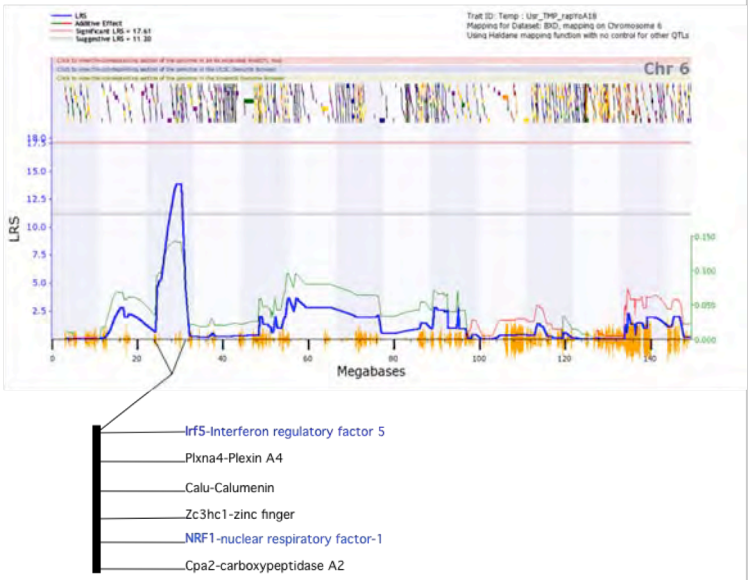

Figure 6. Identity of host genes encoded within the suggestive QTL on chromosome 6 that are potentially involved in immune processes. Genes that are potentially involved in immune processes are listed in blue.

Genes of interest within the interval identified on chromosome 6 (**Figure 6**) include Irf5, which encodes the protein interferon regulatory factor 5. This protein binds to specific regions of DNA that regulate the activity of genes that produce interferons and other cytokines. Irf5 has also been shown to stimulate the activity of natural killer cells [8]. Another gene of interest within this QTL is NRF1 (Nuclear respiratory factor-1) gene that is an early phase component of the host antibacterial defenses [9].

Linkage analysis of several other cytokine phenotypes identified suggesting QTLs on chromosome 12 (**Figure 7**), significant and suggestive QTLs of chromosome 15 (**Figure 8**), and a significant QTL on chromosome 19 (**Figure 9**). Genes within the identified interval on chromosome 19 (**Figure 10**) that are of immediate interest include secretoglobin, and T-cell immune regulator (Tcirg1). Secretoglobins modulate inflammatory and immunologic responses to the environment at mucosal surfaces and inside the body and are associated with increased bronchial inflammation [10]. This multi-functional protein with anti-inflammatory/immunomodulatory properties has been implicated to have a homeostatic role against oxidative damage, inflammation, autoimmunity and cancer [10, 11]. Tcirg1 is a membrane protein that is induced after immune activation on the surface of certain peripheral human T and B cells as well as monocytes and IL-10 expressing T-cells. This gene has implicated in inhibiting T-cell proliferation by modulation of CTLA-4 expression [12]; of course, this function is unlikely to have any role in the innate response to *Acinetobacter*. Loci included the significant QTL region on chromosome 19 also encode several G-protein coupled receptors that as previously stated, are important for the migration of phagocytes.

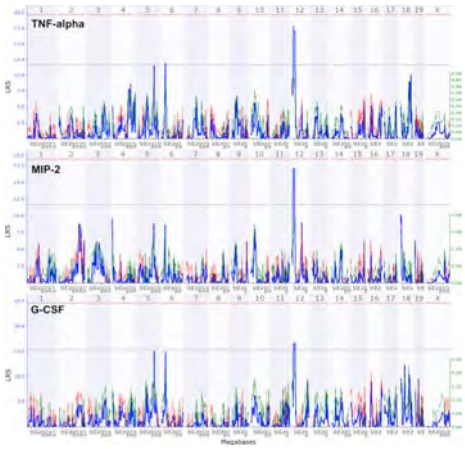

Figure 7. Interval mapping of a differentially expressed cytokines/ chemokines. Interval mapping was performed using the in silico resources within GeneNetwork.org to identify genetic loci that correlate with differential disease-state expression of TNF-alpha, MIP-2, and G-CSF in the lungs of *Acinetobacter*-infected mice.

Dr. Cui has performed a preliminary analysis of these data (only 17 BXD strains) and has identified a significant correlation between the levels of a number of these cytokines (**Figure 11**) and has identified three genetic genomic locations [Chr 6 near 65 Mb (mCV22576656), Chr 14 near 43 Mb (rs13482156), and Chr 19 near 51 Mb (rs3716572)] that each impact the level of several cytokines. We performed principal components analysis of the cytokines with an absolute correlation greater than 0.7 for the three loci and mapped the first principal component of each of the groups of cytokines (**Figure 12**). The first principal component of each of the sets of cytokines has a significant or highly suggestive QTL at the marker location. Several genes at these three loci, including a cluster of immunoglobulin kappa (IGK) genes on Chr 6, *Mbl1* and *Bmp4* on Chr 14, and *Nfkb2* on Chr 19, have been previously associated with immune responses. These locations are promising starting points for developing network models that explain variation in response to infection with *Acinetobacter*. We have also begun to analyze serum samples collected from this cohort of mice (13 strains) and have observed differences in the levels of 14 of the analytes tested (eotaxin, G-CSF, IFN-g, IL-1a, M-CSF, IL-6, IL-13, KC, LIX, MIP-1a, MIP-1b, RANTES, and TNFa). Preliminary analyses of these data

Figure 8. Interval mapping of phenotypic data from differentially-expressed cytokines/ chemokines. Interval mapping was performed using the in silico resources within GeneNetwork.org to identify genetic loci that correlate with differential disease-state expression of IL-1beta and IL-17 in the lungs of *Acinetobacter*-infected mice.

suggest that the loci on Chr 6 (mCV22576656) and Chr 14 (rs13482156) that were shown to influence the levels of cytokines in the BALF are also correlated with cytokine levels in the serum (**data not shown**).

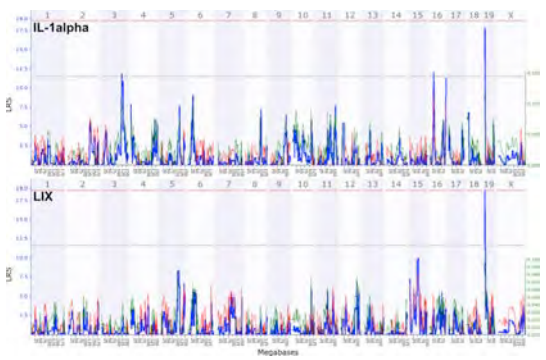

Figure 9. Interval mapping of phenotypic data from differentially-expressed cytokines/ chemokines. Interval mapping was performed using the in silico resources within GeneNetwork.org to identify genetic loci that correlate with differential disease-state expression of IL-1alpha and LIX in the lungs of *Acinetobacter*-infected mice.

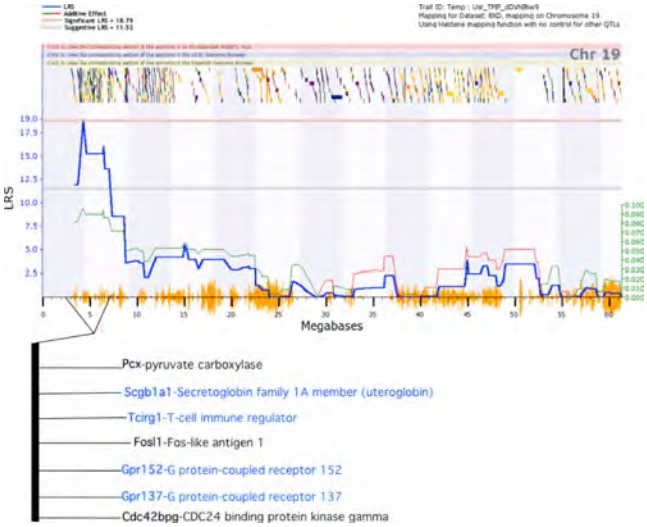

Figure 10. Identity of host genes encoded within the suggestive QTL on chromosome 19 are potentially involved in immune processes. Genes that are potentially involved in immune processes are listed in blue.

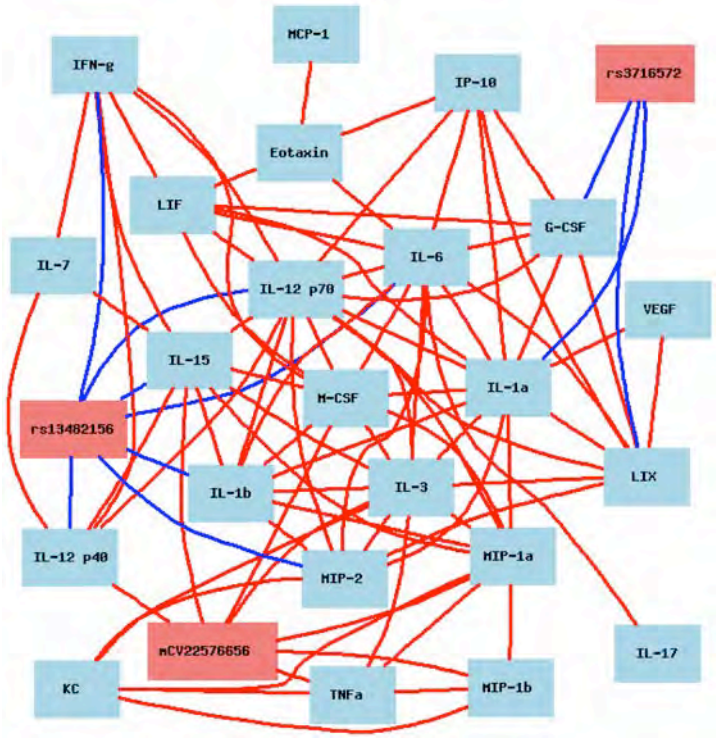

Figure 11. Correlation network for cytokine levels in the BALF of BXD strains infected with *Acinetobacter baumannii*. Three genotype markers (red boxes) on chromosomes 6, 14, and 19 are highly correlated with several cytokines. Pearson's correlation coefficient greater than 0.7 (solid lines) are shown.

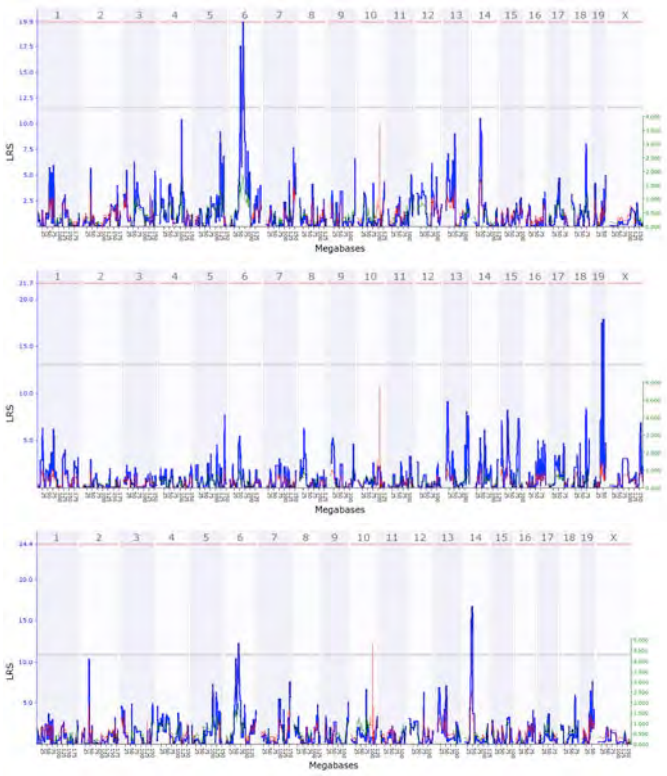

Figure 12. QTL mapping of first principal component for cytokines correlated (Pearson correlation coefficient > 0.7) with mCV22576656 (top), rs13482156 (middle), and rs3716572 (bottom).

We have also begun to analyze serum samples collected from this cohort of mice and have observed differences in the levels of 14 analytes of the analytes tested (eotaxin, G-CSF, IFN-g, IL-1a, M-CSF, IL-6, IL-13, KC, LIX, MIP-1a, MIP-1b, RANTES, and TNFa; **data not shown**). In summary, we have identified 38 phenotypes that may be useful in our search for host genetic elements that lead to differential innate immune responsiveness of B6 vs. D2 mice following infection with *Acinetobacter baumannii*.

Key Research Accomplishments:

- We have confirmed that B6 and D2 mice produce differential innate immune responses to pneumonic Ab infection

- We have identified a suggestive QTL on chromosome 10 that appears to correlate with the differential recruitment of immune cells to the lungs in response to pneumonic *Acinetobacter* infection.

- We have identified putative QTL's (chromosomes 5, 6, and 19) that correlate with a disease-state expression of a series of cytokines/chemokines in the lung compartment of *Acinetobacter*-infected.

- We have identified 39 total phenotypes that include cell recruitment to the lungs, differential expression of 24 cytokines/chemokines in the lung compartment, and 14 cytokine/chemokines that are differentially expressed in the circulation (serum) of acutely infected mice.

Reportable outcomes

Presentation

1. **Poster Presentation** at UTHSC A.A-St Jude Research Lectureship and Medical Student Poster Session, 2012. "Host Genetic Loci Correlating with Differential Innate Immune Responsiveness to *Acinetobacter baumannii* infection".

Abstract

1. Sneed A, Parvathareddy J, Emery FD, Cui Y, Williams R, Miller MA. Host Genetic Loci Correlating with Differential Innate Immune Responsiveness to *Acinetobacter baumannii* infection. In: Proceedings of UTHSC A.A-St Jude Research Lectureship and Medical Student Poster Session, 2012.

Publication

1. Emery F, Parvathareddy J, Van Hoang K, **Cui Y**, **Williams RW**, **Miller MA**. Quantitative trait loci that correlate with differential innate immune responses produced by mice suffering from acute pulmonary *Acinetobacter baumannii* infection. PLoS One (manuscript in preparation).

Conclusions:

We have identified a large number of clear phenotypic differences between the innate responsiveness of B6 and D2 mice to pulmonary infection with *Acinetobacter baumannii*. We have initiated studies in a cohort of BXD strains and hope to identify host genes that correlate with the differential responsiveness of the parental strains to *Acinetobacter*. Although we have

only completed analyses of relatively few BXD strains, we have already identified a significant correlation between several cytokines produced in the lungs and the differential responsiveness of B6 vs. D2 mice to *Acinetobacter* infection. Moreover, we have preliminarily identified a genetic locus on chromosome 10 that correlates with differential recruitment of immune cells to the lungs and four loci (on chromosomes 5, 6, 12, and 19) that appear to correlate with differential production of a number of cytokines/chemokines following pneumonic infection. Identification of this large panel of queriable phenotypes will allow for very interesting network modeling that has potential to identify gene networks that are involved in a variety of innate immune responses to *Acinetobacter* infection.

References:

1. Zabel, B.A., A.M. Silverio, and E.C. Butcher, *Chemokine-like receptor 1 expression and chemerin-directed chemotaxis distinguish plasmacytoid from myeloid dendritic cells in human blood.* Journal of immunology, 2005. **174**(1): p. 244-51.
2. Zabel, B.A., et al., *Chemokine-like receptor 1 expression by macrophages in vivo: regulation by TGF-beta and TLR ligands.* Experimental hematology, 2006. **34**(8): p. 1106-14.
3. Bondue, B., et al., *ChemR23 dampens lung inflammation and enhances anti-viral immunity in a mouse model of acute viral pneumonia.* PLoS pathogens, 2011. **7**(11): p. e1002358.
4. Sun, L. and R.D. Ye, *Role of G protein-coupled receptors in inflammation.* Acta Pharmacol Sin. **33**(3): p. 342-50.
5. Perrigoue, J.G., et al., *IL-31-IL-31R interactions negatively regulate type 2 inflammation in the lung.* The Journal of experimental medicine, 2007. **204**(3): p. 481-7.
6. Perrigoue, J.G., et al., *IL-31-IL-31R interactions limit the magnitude of Th2 cytokine-dependent immunity and inflammation following intestinal helminth infection.* Journal of immunology, 2009. **182**(10): p. 6088-94.
7. Yi, L., et al., *p47(phox) directs murine macrophage cell fate decisions.* The American journal of pathology, 2012. **180**(3): p. 1049-58.
8. Paun, A., et al., *Functional characterization of murine interferon regulatory factor 5 (IRF-5) and its role in the innate antiviral response.* The Journal of biological chemistry, 2008. **283**(21): p. 14295-308.
9. Suliman, H.B., et al., *Co-regulation of nuclear respiratory factor-1 by NFkappaB and CREB links LPS-induced inflammation to mitochondrial biogenesis.* Journal of cell science, 2010. **123**(Pt 15): p. 2565-75.
10. Heinzmann, A., *Association of uteroglobulin-related protein 1 with bronchial asthma.* Int. Arch. Allergy Immunology, 2003. **131**(4): p. 291-295.
11. Chiba, Y., T. Kusakabe, and S. Kimura, *Decreased expression of uteroglobin-related protein 1 in inflamed mouse airways is mediated by IL-9.* American journal of physiology. Lung cellular and molecular physiology, 2004. **287**(6): p. L1193-8.
12. Bulwin, G.C., et al., *TIRC7 inhibits T cell proliferation by modulation of CTLA-4 expression.* Journal of immunology, 2006. **177**(10): p. 6833-41.

Burkholderia pseudomallei project

Our initial studies with a pneumonic challenge model (intranasal instillation) confirmed the previously published observation that B6 mice are more resistant than D2 mice to Bp infection. We found that following intranasal instillation of 50 CFU of Bp strain 1026b, D2 mice typically succumbed to infection by day 4 post-infection while B6 mice survived the infection. Subsequent studies showed that the same results were obtained with challenge doses of up to 200 CFU/mouse.

Based on these findings, we initiated forward genetics studies with a cohort of BXD strains in an effort to identify host genetic loci that co-vary with the differential susceptibility observed in the parental strains. We screened a cohort of 35 BXD strains for susceptibility to pneumonic Bp infection. Groups of male mice were challenged with 50-100 CFU of Bp (from a diluted frozen stock) via intranasal instillation and then monitored for weight retention and survival. B6 and D2 mice were included in each of the 19 experiments that have been performed, and the D2 mice were always the last group to be challenged to ensure the "potency" of the challenge stock throughout the instillation process. We found that several of the BXD strains were highly susceptible to Bp (similar to D2 mice), others were relatively resistant to Bp (similar to B6 mice), and several strains displayed intermediate phenotypes (**Figure 1A**). Interval mapping (see Modeling Core description) using this cohort of animals revealed a significant QTL on chromosome 5 and suggestive QTLs on chromosomes 7 and 14 (**Figure 1B**) that co-vary with differential susceptibility / resistance to Bp. These findings indicated that susceptibility / resistance to Bp infection is a complex trait. Using a combination of genetic analyses (QTL mapping) and normative genomic/gene expression data from various tissues, we have identified several potential candidate genes within the interval on chromosomes 5, 7, and 14 that appear to be covariant with differential susceptibility to Bp infection (**Figure 2**). There are several genes within the QTL interval on chromosome 5 that appear to be strong candidate genes that are known to have roles in immunological processes. For instance, the *cox18* gene encodes a mitochondrial inner membrane protein that is involved with cytochrome C assembly. It is known that mutation of *Cox18* results in deficient cytochrome C oxidase activity that, in turn, eliminated activation of cell surface receptors involved in apoptosis (Souza et al, 2000) a process that is essential for limiting replication of some intracellular bacterial pathogens (Ceballos-Olvera et al, 2007; Ying et al, 2008). Another candidate gene in the interval, *G3bp2*, encodes GTPase activating protein-binding protein 2. This protein is known to interact with IκBα and has been implicated in the regulation of NF-κB (Prigent et al, 2000). The NF-κB family of transcription factors is a group of evolutionarily conserved proteins involved in lymphoid organogenesis, development of immune cells (Wong and Tergaonkar, 2009) and the coordination of many aspects of innate and adaptive immunity to infection. The *Cxcl11* gene encodes the chemokine C-X-C motif ligand 11. Expression of CXCL11 protein is high in peripheral blood leukocytes, liver and pancreas, with

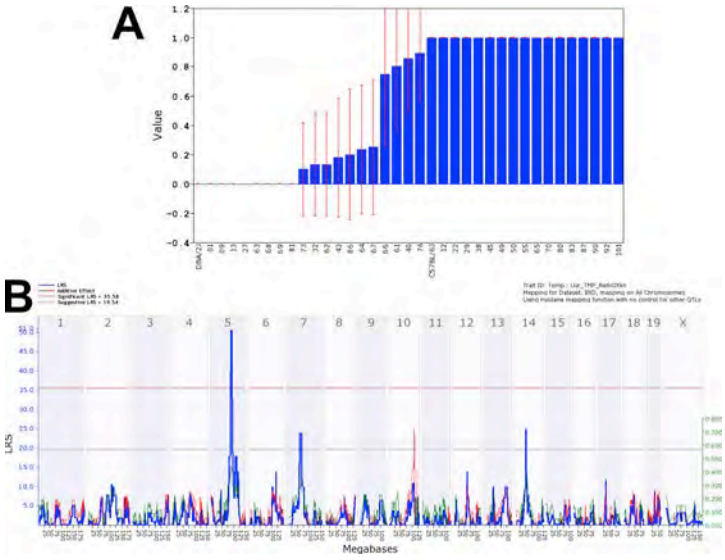

Figure 1. Interval map using survival of pneumonic challenge with *Burkholderia pseudomallei* as the query phenotype. A cohort of male mice which included 35 BXD strains, was infected intranasally with 50-100 CFU o *Burkholderia pseudomallei*. Infected mice were monitored for survival for up to 11 days post-infection and those that survived infection were given a value of "1" while those that succumbed to infection received a value of "0" (**Panel A**). Interva mapping was performed using the *in silico* resources within GeneNetwork.org to identify genetic loci that correlated with survival (**Panel B**).

modest levels in thymus, spleen and lung (Cole et al, 1998). CXCL11 expression is strongly increased in response to IFN-α or IFN-γ, and is involved in the recruitment of Th1 lymphocytes to sites of inflammation (Antonellia et al, 2013). This gene may be of importance because the attraction of leukocytes to tissues is essential for inflammation and the host response to infection (Luster 1998). Finally, *Bmp2k* (the gene that encodes BMP-2-inducible kinase) is also found within this QTL. Bone morphogenic proteins (BMPs) have no known role in immune responses, but they are known to play a key role in skeletal development and patterning (Hoffmann and Gross, 2001) and have been implicated in lung development, and adult lung homeostasis (Sountoulidis et al, 2012). None of the candidate genes with the highest correlation indices within the QTL on chromosome 7 (*Tubgcp5*, *Nipa1*, and *Snurp*) have any obvious role in host immune responses. *Tubgcp5* encodes a protein (gamma complex-associated protein 5) that has essential roles in mitotic spindle formation (Oakley et al, 1990; Xiong and Oakley, 2009) and microtubule nucleation and organization (Murphy et al, 2001; Xiong and Oakley, 2009). *Nipa1* encodes a protein (Prader Willi/Angelman syndrome 1 homolog) that plays a role in nervous system development and maintenance (Entrez Gene), and may function as a receptor or magnesium transporter (Goytain et al, 2007). *Snurp* encodes a protein (small nuclear ribonucleoprotein N) that is involved in transcriptional modification of RNA (Valadkhan, 2005). None of the candidate genes within the chromosome 14 interval appear to have roles in immune responses either, and they all have similar correlation indices; additional BXDs with break points within this interval will need to be added to the analysis to identify the most likely candidates.

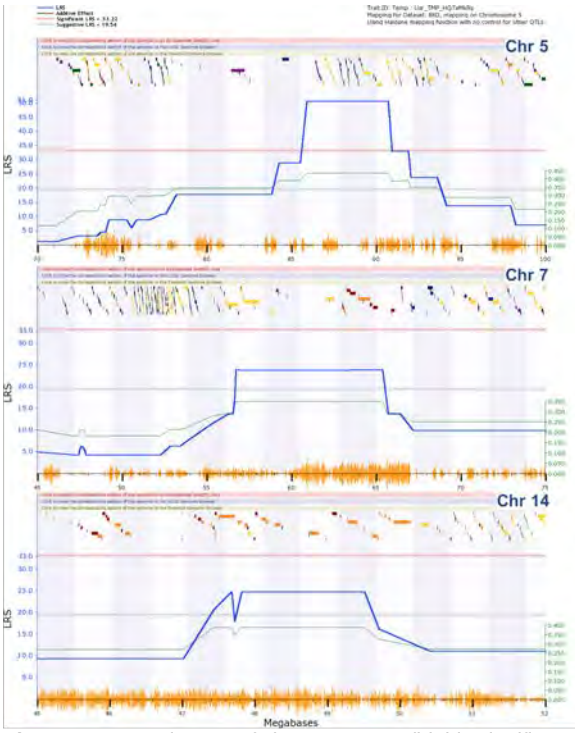

		Lung		Spleen	
Gene	Mb	LRS	Exp	LRS	Exp
Cox18	90.644	82.2	9.517	64.1	10.02
Afm	90.979	18.8	6.459	60.8	9.782
Thap6	92.392	23.2	6.951	71.7	8.546
G3bp2	92.483	26	10.44	188.1	6.731
Bpm2K	92.507	37.1	8.693	-	-
Cxcl11	92.789	-	-	77.3	6.962

		Lung		Spleen	
Gene	Mb	LRS	Exp	LRS	Exp
Tubgcp5	63.085	26.9	9.447	30.1	9.151
Nipa1	62.234	51.7	9.961	-	-
Apt10a	66.084	18.5	8.374	-	-
Snurp	67.120	48.0	5.945	-	-
Klf13	71.03	15.1	10.04	-	-

		Lung		Spleen	
Gene	Mb	LRS	Exp	LRS	Exp
Cgrrf1	47.474	20.3	10.04	-	-
Samd4	47.722	39.1	9.797	35.2	8.067
Miss	47.942	38	10.28	-	-
Peli2	x48.876x	35.8	8.511	-	-
Rnase4	51.725	34.1	12.84	-	-
Mett11d1	52.510	33.0	10.15	-	-

Figure 2. Interval maps of chromosome 5 (highly significant QTL), chromosome 7 (suggestive QTL and chromosome 14 (suggestive QTL). Candidate genes within each interval are indicated in the table to the right along with their LRS score and their relative expression levels in normative tissues

Interestingly, females from several of the BXD strains as well as female D2s were significantly more resistant to pneumonic Bp infection than their male counterparts. We are hopeful that identification of additional strains with this differential sex-related phenotype will lead to identification of correlating host genetic factor(s). We have also initiated studies to identify additional Bp disease-state phenotypic differences between the parental strains. Parental mice were challenged with 100 CFU via intranasal instillation and then sacrificed 24 hours later for collection of blood serum and bronchoalveolar lavage. BAL cells and BAL fluids/serum were collected from each mouse and subjected to flow cytometric analysis and multiplex cytokine/chemokine analysis (32-plex), respectively. Neutrophil recruitment was significantly higher (p=0.03) in D2 (compared to B6; data not shown). Multiplex cytokine analysis identified six analytes from the BALF and five analytes from the serum whose Bp disease-state levels were significantly different between the two parental mouse strains (**Figure 3**). Similar preliminary studies with a cohort of BXD strains suggested that we will be able to exploit these additional phenotypes as well as some additional lung cell phenotypes and cytokine/chemokine phenotypes (data not shown) for forward genetic analyses.

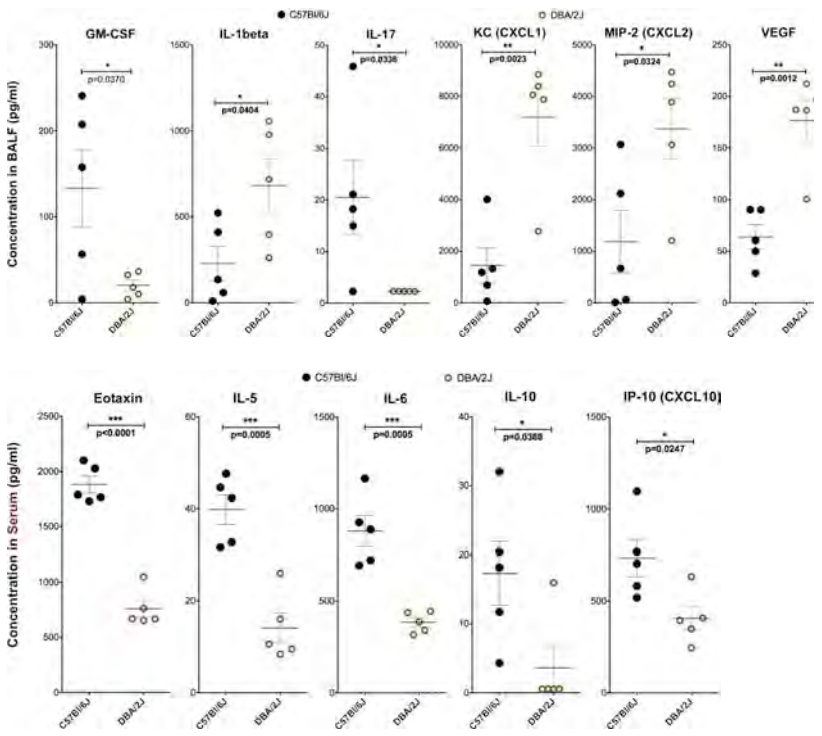

Figure 3. Differential disease-state cytokine expression in the lung compartment and in the peripheral circulation during acute *Burkholderia* infection of BXD parental mouse strains. BXD mice were challenged with 100 CFU Bp strain 1026b via the intranasal route, sacrificed 24 hr later, and bronchoalveolar lavage (BAL) and serum collection was performed. Multiplex cytokine/chemokine analysis (32-plex) was performed on BAL fluids (**Top Panel**) and serum samples (**Bottom Panel**). Statistical analysis was performed using unpaired student-t tests. Statistical significance is as follows: p<0.05 *, p<0.01 **, and p<0.001 ***

Reportable outcomes

Presentations

1. **Poster Presentation** at the International Toll 2012 Meeting: Decoding Innate Immunity. Riva del Garda, Italy, May 4-7, 2011. Sahoo M, Ceballos-Olveda I, Bina JE, Miller MA, Re F. "Critical role of the NLRC4 inflammasome and IL-18 during mouse lung infection with virulent *Burkholderia pseudomallei*".

Abstracts

1. Sahoo M, Ceballos-Olveda I, **Bina JE**, **Miller MA**, **Re F**. Critical role of the NLRC4 inflammasome and IL-18 during mouse lung infection with virulent *Burkholderia pseudomallei*. In: Proceedings of the International Toll 2012 Meeting, Decoding Innate Immunity, Riva del Garda, Italy, May 4-7, 2011.

Publications

1. Ceballos-Olvera I, Sahoo M, **Miller MA**, del Barrio L, **Re F**. 2011. Inflammasome-dependent Pyroptosis and IL-18 Protect against *Burkholderia pseudomallei* Lung Infection while IL-1β Is Deleterious. PLoS Pathog 7(12): e1002452.

2. Emery F, Parvathereddy J, **Williams, RW**, **Miller, MA**. Identification of Quantitative Trait Loci Correlating With Differential Susceptibility of Mice to Pneumonic *Burkholderia pseudomallei* Infection. PLoS One. (manuscript in preparation).

Conclusions

We have identified a significant QTL on chromosome 5 and two suggestive QTL on chromosomes 7 and 14 that are linked with differential susceptibility to pneumonic Bp infection. We have also identified 12 additional Bp disease-state phenotypic differences between the parental strains that should be useful in our search for host genetic elements that lead to differential innate immune responsiveness to infection with Bp.

References

1. Alessandro Antonellia, S. M. F., Caterina Mancusia, Valeria Mazzia, Cinzia Pupillib, Marco Centannic, Clodoveo Ferrid, Ele Ferranninia, and P. Fallahia. 2013. Interferon-α, -β and -γ induce CXCL11 secretion in human thyrocytes: Modulation by peroxisome proliferator-activated receptor γ agonists. Immunobiology 18(5):690-5.
2. Berl R. Oakley, C.Elizabeth Oakley, Yisang Yoon, and M. K. Jung. 1990. γ-tubulin is a component of the spindle pole body that is essential for microtubule function in Aspergillus nidulans. Cell 61:1289-1301.
3. Ceballos-Olvera, I., M. Sahoo, M. A. Miller, L. Del Barrio, and F. Re. 2011. Inflammasome-dependent pyroptosis and IL-18 protect against Burkholderia pseudomallei lung infection while IL-1beta is deleterious. PLoS Pathog 7:e1002452.
4. Cole, K. E., C. A. Strick, T. J. Paradis, K. T. Ogborne, M. Loetscher, R. P. Gladue, W. Lin, J. G. Boyd, B. Moser, D. E. Wood, B. G. Sahagan, and K. Neote. 1998. Interferon-inducible T cell alpha chemoattractant (I-TAC): a novel non-ELR CXC chemokine with potent activity on activated T cells through selective high affinity binding to CXCR3. J Exp Med 187:2009-2021.
5. Entrez Gene: NIPA1 non imprinted in Prader-Willi/Angelman syndrome 1.
6. Goytain, A., R. M. Hines, A. El-Husseini, and G. A. Quamme. 2007. NIPA1(SPG6), the basis for autosomal dominant form of hereditary spastic paraplegia, encodes a functional Mg2+ transporter. J Biol Chem 282:8060-8068.
7. Hoffmann, A., and G. Gross. 2001. BMP signaling pathways in cartilage and bone formation. Crit Rev Eukaryot Gene Expr 11:23-45.
8. Luster, A. D. 1998. Chemokines--chemotactic cytokines that mediate inflammation. N Engl J Med 338:436-445.
9. Murphy, S. M., A. M. Preble, U. K. Patel, K. L. O'Connell, D. P. Dias, M. Moritz, D. Agard, J. T. Stults, and T. Stearns. 2001. GCP5 and GCP6: two new members of the human gamma-tubulin complex. Mol Biol Cell 12:3340-3352.
10. Prigent, M., I. Barlat, H. Langen, and C. Dargemont. 2000. IkappaBalpha and IkappaBalpha /NF-kappa B complexes are retained in the cytoplasm through interaction with a novel partner, RasGAP SH3-binding protein 2. The Journal of biological chemistry 275:36441-36449.
11. Sountoulidis, A., A. Stavropoulos, S. Giaglis, E. Apostolou, R. Monteiro, S. M. Chuva de Sousa Lopes, H. Chen, B. R. Stripp, C. Mummery, E. Andreakos, and P. Sideras. 2012. Activation of the Canonical Bone Morphogenetic Protein (BMP) Pathway during Lung Morphogenesis and Adult Lung Tissue Repair. PLoS One 7:e41460

12. Souza, R. L., N. S. Green-Willms, T. D. Fox, A. Tzagoloff, and F. G. Nobrega. 2000. Cloning and characterization of COX18, a Saccharomyces cerevisiae PET gene required for the assembly of cytochrome oxidase. J Biol Chem 275:14898-14902.
13. Valadkhan, S. 2005. snRNAs as the catalysts of pre-mRNA splicing. Curr Opin Chem Biol 9:603-608.
14. Xiong, Y., and B. R. Oakley. 2009. In vivo analysis of the functions of gamma-tubulin-complex proteins. J Cell Sci 122:4218-4227.
15. Ying, S., M. Pettengill, E. R. Latham, A. Walch, D. M. Ojcius, and G. Hacker. 2008. Premature apoptosis of Chlamydia-infected cells disrupts chlamydial development. J Infect Dis 198:1536-1544

Studies with *SARS-CoV*

Investigation of SARS-Coronavirusis important since SARS-like pandemics remain a significant global health threat and information concerning the genetics of host disease susceptibility will inform us of methods that will be critical in managing large affected groups of people should a SARS-like pandemic arise. SARS-CoV is classified as an NIAID category C priority pathogen and due to its high pathogenicity, it was added to the list of HHS Select Agents in December 2012. Following the Guidance on the Inventory Requirements for Select Agents and Toxins, we have established a detailed inventory of our SARS-CoV (both Urbani and MA15) stocks and SARS-CoV-infected samples.

Our studies were focused on dissecting the host genetic basis and key virus-host interactions that determine disease severity of SARS using the ARI BXD strain set. Details of work accomplished from our studies during the period supported by the grant are provided below.

In the first year, we completed the Material Transfer Agreements with CDC and NIH for transferring the wild-type (Urbani strain) and mouse adapted (MA-15) SARS coronaviruses to UTHSC and obtained both viruses. The personnel engaged in the SARS project obtained DOJ clearance and were approved for access to select agents and/or toxins. They were enrolled in the UTHSC Animal Care and Use Occupational Health & Safety Program and fit-tested. Personnel received initial and annual refresher BSL-3 and select agent training. Personnel were SRA-approved, listed on the registration with DSAT, and received didactic and hand-on training by the Regional Biosafety Laboratory (RBL) biosafety officer and designated experienced users.

In a related project, we characterized the interferon (IFN) antagonism mediated by the papain-like proteases (PLPs) of two important human coronaviruses, SARS-CoV and NL63, in collaboration with S. Baker at Loyola University - Chicago. The results showed that the PLP2 of NL63, like what we have previously demonstrated for the PLP of SARS-CoV, blocks IFN induction by inhibiting the activation of IFN regulatory factor-3 (IRF3), a latent transcription factor pivotal for type I IFN synthesis. Furthermore, the PLP IFN antagonism is enhanced by, but is not strictly dependent on, the catalytic activity of the PLP enzyme. Results from these studies were published in J. Virology 2010.

In year 2, we grew the wild-type SARS-CoV (Urbani strain) stocks and determined their infectious titers. However, we encountered some difficulty in obtaining high-titer stocks for the mouse-adapted MA-15 virus – in the first couple of attempts the MA-15 virus only grew to titers in the 10^5 $TCID_{50}$/ml range in Vero-E6 cells. We thus spent some time optimizing the conditions for propagating the MA-15 virus. We finally worked out the conditions for generating MA-15 virus$\geq$ 2 X 10^6 $TCID_{50}$/ml and scaled up the culture to produce large quantity of virus stocks for the animal experiments.

In a related project, we continued the collaborative studies with S. Baker and Z. Chen (Beijing Institute of Radiation Medicine) on the mechanisms by which coronavirus PLPs inhibit IRF3-dependent innate immune responses. It was found that PLPs of SARS-CoV and NL63 associate with stimulator of interferon genes (STING), an adaptor protein in the IRF3 activation pathway, and that this interaction disrupts the assembly of signaling complexes involving MAVS, STING and IKKε and ubiquitination of these signaling molecules, both of which are required for viral activation of IRF3. These results were described in a paper published in PLoS One 2012.

In year 3, we performed animal studies to determine the differential susceptibility/resistance of mouse genotypes to SARS-CoV infection. To determine whether the BXD strain set is suitable

as a model system to dissect factors modulating SARS pathogenesis and disease severity, we investigated whether the parental strains, B6 and D2, differ in their susceptibilities to SARS-CoV infection. First, we examined our existing transcriptome data on the B6 and D2 strains and found that angiotensin converting enzyme 2 (ACE2), which is the entry receptor for SARS-CoV (Li et al, 2003), is expressed at comparable levels between these two parental strains (data not shown), excluding the possibility of ACE2 expression level as a confounding factor. We then challenged groups of 10-week old B6 and D2 strains via the intranasal route with 10^5 $TCID_{50}$ of the mouse-adapted MA15 virus (diluted in 50-µl PBS), and monitored mice for weight change and viral replication in the lungs for 9 days. As controls, we also inoculated 4 mice each strain with culture supernatants of Vero-E6 cells (the cell host for propagating the MA15 virus inocula) diluted in PBS. As shown in **Fig. 1**, neither B6 nor D2 strain receiving control inocula (i.e., mock infection) lost weight during the 9-day observation period, indicating that the light anesthesia and intranasal challenge procedures do not produce appreciable adverse effects on these mice, nor do the constituents in culture medium of Vero-E6 cells. In contrast, there was significant weight loss in both strains infected with the MA15 virus. B6 strain lost a little over 10% of their initial weight at 2-3 days post infection (d.p.i), followed by a relatively fast recovery starting on day 4. On 8-9 d.p.i., the B6 strain had regained weight to nearly pre-infection levels. This was similar to what was reported by Sheahan et al. In contrast, D2 strain had substantially more weight loss at 3-5 d.p.i. than B6 strain, and these mice did not start to recover until after 6 d.p.i. In addition, a total of two D2 mice died on 3 and 5 d.p.i., after losing 18% and 25% weight, respectively. Analyses of infectious viral titers in lung homogenates from a subset of infected mice revealed high levels of pulmonary viral replication in both strains for the first 4 d.p.i. (**Fig. 2**), with D2 strain harboring consistently 2-3 fold higher levels of viral replication. Strikingly, while lung viral titers had dropped to the 10^3 $TCID_{50}$/g tissue range in B6 strain at 5 d.p.i., viral replication remained high (at >10^5 $TCID_{50}$/g levels) in D2 strain. The 62-fold higher level of viral replication in D2 strain compared with B6 strain at this time point was consistent with the sustained weight loss seen in D2 strain at 5 d.p.i. (**Fig. 1**). Of note, when sacrificing mice for tissue collection, we consistently observed higher frequency of lung lobe consolidation in infected D2 mice than in infected B6 mice (data not shown).

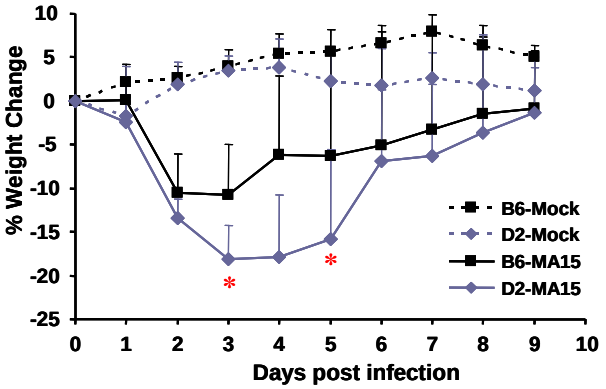

Fig. 1. Weight change of C57BL/6J and DBA/2J mice following challenge with mouse-adapted SARS-CoV, MA15. C57BL/6J (n=26) and DBA/2J (n=28) mice were inoculated with 10^5 $TCID_{50}$ of MA15 virus in PBS via the intranasal route. Control mice (Mock, 4/group) received Vero-E6 culture supernatant diluted in PBS. Mice were monitored daily for weight change and a subset of infected mice (3-5/group) were sacrificed on 1, 2, 3, 4, 5, and 9 days post infection for evaluation of viral replication in the lungs (see Fig. 2). Asterisk denotes 1 mouse (DBA/2J) death observed on 3 and 5 days post infection, respectively.

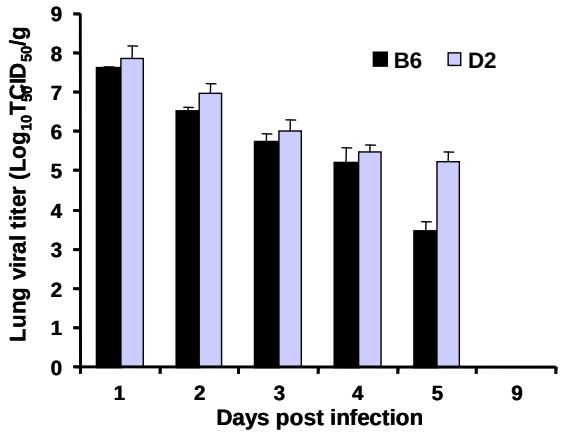

Fig. 2. Viral replication in the lungs of C57BL/6J and DBA/2J mice intranasally challenged with 10^5 $TCID_{50}$ of MA15 virus. Data shown are infectious viral titers in lung tissues from 3-5 mice/strain at each time point.

When the infection dose was increased to 5X10^5 $TCID_{50}$, there was no significant increase in the frequency of lethal infection in D2 strain, although weight loss was substantially prolonged (**Fig. 3**). In contrast, the weight loss kinetics in the vast majority of infected B6 strain followed a trend similar to that seen in low dose challenge (10^5 $TCID_{50}$, see **Fig. 1**), although we began to see a small number of deaths in the B6 group (two mice in total) at this high infection dose. Collectively, data from these experiments suggest that 1) D2 strain is substantially more susceptible to MA15 virus infection than B6 mice, as evidenced by developing a more severe disease (more substantial weight loss) and supporting higher and prolonged viral replication in the lung; 2) death/survival cannot be used as a phenotypic readout to differentiate between the two strains following infection by MA15 virus, which causes typically non-lethal disease in both strains (although more casualty was observed in MA15-infected D2 strain); and 3) Pathogen load (i.e., viral replication in the lung) around 5 d.p.i and weight loss around 3-5 d.p.i are good candidate infection markers that distinguish between B6 and D2 strains, although the challenge dose of MA15 virus and the time points that maximize the differences between the two parental strains for these phenotypes may need to be optimized. Taken together, the substantial difference in susceptibility to MA15 virus infection between the parental B6 and D2 strains support the feasibility of using the ARI BXD genotype set to identify host genes/pathways and molecular nodes/links that regulate the pathogenesis of and differential host responses to SARS-CoV infection.

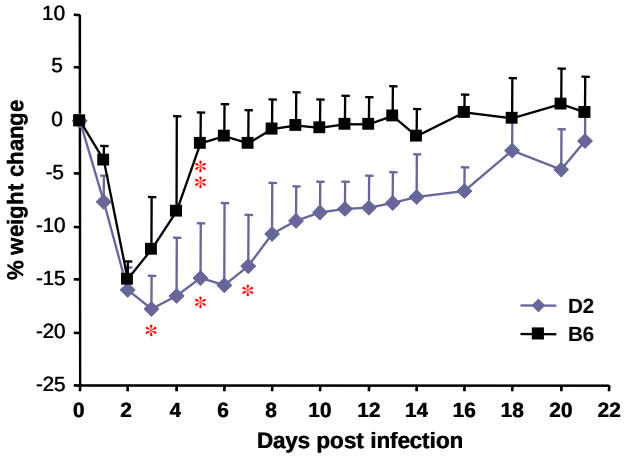

Fig. 3. Weight change of C57BL/6J (n=11) and DBA/2J (n=10) mice following intranasal challenge with high-dose (5X10^5 $TCID_{50}$) of MA15 virus. Asterisk denotes 1 mouse death. Note that of the two B6 mice scored as dead on day 5, 1 was euthanized due to weight loss > 25%. None of the mice on day 21 had detectable infectious virus in lung.

Reportable outcomes

Publications

1. Clementz MA, Chen Z, Banach BS, Wang Y, Sun L, Ratia K, Baez-Santos YM, Wang J, Takayama J, Ghosh AK, **Li K**, Mesecar AD, Baker SC. Deubiquitinating and interferon antagonism activities of coronavirus papain-like proteases. *Journal of Virology* 2010; 84: 4619-4629.
2. Sun L, Xing Y, Chen X, Zheng Y, Yang Y, Nichols DB, Clementz MA, Banach BS, **Li K**, Baker SC, and Chen Z. Coronavirus papain-like proteases negatively regulate antiviral innate immune response through disruption of STING-mediated signaling. PLoS ONE 2012; 7: e30802.

References

1. Li, W., M. J. Moore, N. Vasilieva, J. Sui, S. K. Wong, M. A. Berne, M. Somasundaran, J. L. Sullivan, K. Luzuriaga, T. C. Greenough, H. Choe, and M. Farzan. 2003. Angiotensin-converting enzyme 2 is a functional receptor for the SARS coronavirus. Nature 426:450-4.
2. Sheahan, T., T. E. Morrison, W. Funkhouser, S. Uematsu, S. Akira, R. S. Baric, and M. T. Heise. 2008. MyD88 is required for protection from lethal infection with a mouse-adapted SARS-CoV. PLoSPathog 4:e1000240.

Highly Pathogenic Influenza A virus (H5N1) project

Dr Boon transferred to Washington University at St Louis during the second year of the project. Below is a summary of the work accomplished during the period he was supported by the grant. During the second year of the proposal we continued to assess the susceptibility of several congenic mouse lines and initiated a second phenotypic screen for highly pathogenic H5N1 virus in the BXD mice. This work was done at St Jude Children's Research Hospital in the laboratory of Dr. Richard Webby.

Congenic mouse lines

The B6.D2.11D mouse line was obtained from Drs Davis and Lusis at UCLA and transferred to the animal facility at St Jude Children's Research Hospital. In year 1 we had assessed the susceptibility of this strain to a mouse adapted H1N1 virus (A/PR/8/34) and were preparing to do similar studies using the highly pathogenic H5N1 virus A/Hong Kong/213/03 virus (HK213). B6.D2.11D mice were experimentally inoculated with 10^4 EID_{50} of HK213 virus and morbidity and mortality were monitored (**Table 1**). Compared to the female C57BL/6 control mice, the B6.D2.11D mice lost more bodyweight at the later stages of the infection (day 13), however the difference was not statistically significant. Also, one of the 11D mice succumbed to infection, whereas none of the control mice did. A similar pattern of disease was observed in male mice; the B6.D2.11D male mice lost significantly more weight on day 10 compared to the male C57BL/6 control mice. Also on day 13, the bodyweight of the male B6.D2.11D mice was lower compared to the controls. Although the differences are small and the experiment requires validation, the data are promising and suggest the presence of a gene polymorphism in this locus exacerbating disease severity after H5N1 infection.

Table 1: Weight loss and Mortality in B6.D2.11D mice after inoculation with A/Hong Kong/213/03 virus

		Mortality	Morbidity (% weight loss after infection ± SEM)			
			Day 4	Day 7	Day 10	Day 13
Female	**C57BL/6**	0	94.7 ± 0.6	80.6 ± 0.7	80.1 ± 2.0	94.2 ± 2.8
	B6.D2.11D	25	94.7 ± 1.8	82.0 ± 1.2	79.7 ± 3.8	86.0 ± 4.4
Male	**C57BL/6**	0	94.7 ± 0.7	82.1 ± 1.0	89.4 ± 2.0	98.3 ± 1.4
	B6.D2.11D	0	92.3 ± 1.1	81.3 ± 0.9	80.1 ± 3.9	88.5 ± 4.3

Besides B6.D2.11D, we also obtained two other congenic mouse lines containing *Qivr*'s or QTL for influenza virus resistance on a pure C57BL/6 genetic background; B6.D2.17D and B6.D2.7C containing *Qivr17* and *Qivr7* respectively.

A breeding colony for B6.D2.17D has been established and several groups of mice have been infected with 10^4 or 10^5 EID_{50} of HK213 virus (**Table 2**). Morbidity and mortality after inoculation were monitored. Unfortunately no significant difference in mortality or morbidity was observed in the B6.D2.17D mice compared to C57BL/6 controls.

The B6.D2.7C congenic mice were difficult to generate. First the genotyping experiments discovered a change in the genotype and instead of an entire chromosome 7 of DBA/2J genetic origin we obtained mice containing only two-thirds of chromosome 7 of DBA/2J. Fortunately the B6.D2.7D mice, as they are referred to now, do contain the genetic locus (*Qivr7*) that we had previously identified. Next we produced several homozygous mice B6.D2.7D mice and established a colony. Finally, we have infected a large number of female and male B6.D2.7D

mice with 10^4 EID_{50} of HK213 virus. The morbidity and mortality of the B6.D2.7D mice was not significantly different from the wild type control animals (**Table 3**).

Table 2: Weight loss and Mortality in B6.D2.17D mice after inoculation with A/Hong Kong/213/03 virus

		Dose (EID_{50})	Mortality	Morbidity (% weight loss after infection)		
				Day 4	Day 7	Day 10
Female	**C57BL/6**	10^4	8	96	82	83
	B6.D2.17D	10^4	0	99	84	92
Male	**C57BL/6**	10^5	16	90	78	75
	B6.D2.17D	10^5	50	92	74	71

Table 3: Weight loss and Mortality in B6.D2.7D mice after inoculation with A/Hong Kong/213/03 virus

		Dose (EID_{50})	Mortality	Morbidity (% weight loss after infection)		
				Day 4	Day 8	Day 10
Female	**C57BL/6**	10^4	27	96	76	77
	B6.D2.7D	10^4	18	94	79	84

Novel H5N1 phenotype

While we have worked hard to identify the genes and their polymorphisms in previously identified influenza loci (*Qivr*) associated with death after HK213 virus infection, we have also started testing BXD strains for a second H5N1 phenotype. As reported in the Journal of Virology paper in 2009 from our group (Boon *et al*), DBA/2J and C57BL/6J mice differ considerably in their response to influenza virus infection with very low LD_{50} values, high influenza titers and excessive production of pro-inflammatory mediators in the DBA/2J mice. High viral titers and production of pro-inflammatory cytokines are hallmarks of H5N1 infection in humans. Therefore we aimed to identify the genetic locus associated with increased production of pro-inflammatory mediators TNFα, CCL2 and IFNα 48 hours after inoculation with H5N1. A total of 43 BXD strains were analyzed for the production of pro-inflammatory mediators and compared to the parental DBA/2 and C57BL/6 mice (**Figure 1**).

Preliminary QTL analysis using the free online QTL analysis tool at www.genenetwork.org, has indicated that a locus on Chromosome 6 is responsible for a significant portion of the observed phenotype for all three inflammatory mediators tested. Two other QTL's, one on chromosome 1 and another on chromosome 12, are considered suggestive. Interestingly, the locus on chromosome 12 contains the *Ahr* gene which is known to differ between C57BL/6 and DBA/2J mice.

Future work will concentrate on identifying the gene on chromosome 6 responsible for the excessive production of pro-inflammatory mediators. Based on additional work in the laboratory, we hypothesize that it is the higher viral load in DBA/2J mice that is initiating this difference in cytokine production and therefore the gene under investigation is likely to influence the replication dynamics of the virus. To validate the result, we have initiated the production of a congenic mouse line containing chromosome 6 of C57BL/6 mice on a DBA/2 background. Compared to the parental DBA/2J mice, the congenic strain will likely produce lower amounts of TNFα, CCL2 and IFNα.

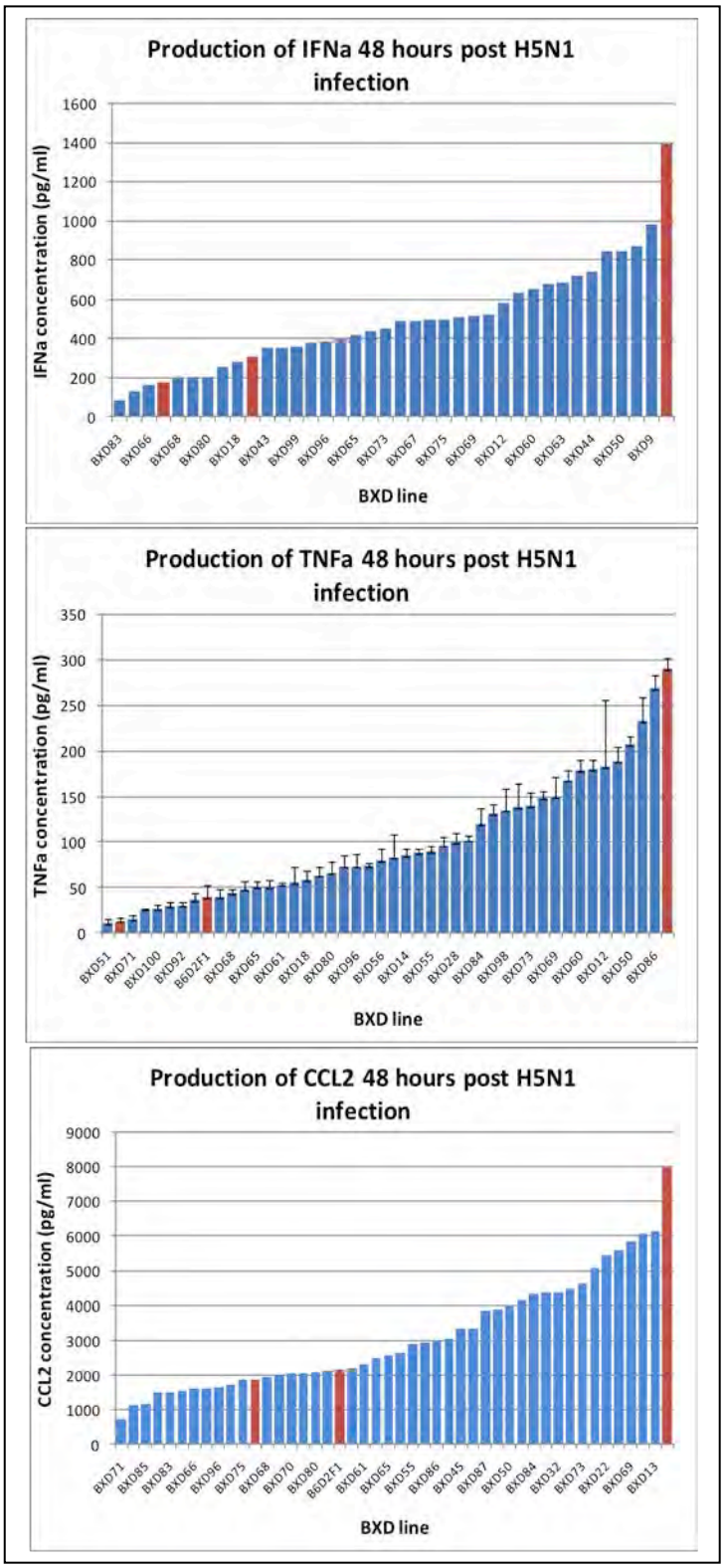

Figure 1: Production of pro-inflammatory cytokines 48 hours post inoculation with Highly pathogenic H5N1 influenza A virus. The production of IFNα[1] (top), TNFα (middle) and CCL2 (bottom) in 43 different BXD lines and the parental DBA/2, C57BL/6 plus the F1 strain. The red bars indicate (from left to right) C57BL/6, B6D2F1 and DBA/2J. Fewer strains were tested for the production of IFNα.

Reportable outcomes

Presentations

1. **Seminar** at University of Maryland, College Park, MD, March-2010, “H5N1 pathogenesis and the role of host genetic diversity”
2. **Oral presentation** at the BXD world meeting in Braunschweig, Germany, 2009, “H5N1 pathogenesis and the role of host genetic diversity”.
3. **Seminar** at Washington University School of Medicine, St Louis, MO, Feb-2010, “H5N1 pathogenesis and the role of host genetic diversity”.
4. **Seminar** at St Louis University, Infectious Disease Research Conference, St Louis, MO, April 2011, “H5N1 pathogenesis and the role of host genetic diversity”.
5. **Seminar** at Emory University, Microbiology and Molecular Genetics Seminar, Atlanta, GA, October 2011, “H5N1 pathogenesis and the role of host genetic diversity”.
6. **Seminar** at Washington University School of Medicine, Department of Medicine, Division of Pulmonary Medicine, Lung Biology and Genetics conference, St Louis, GA, April 2011, “H5N1 pathogenesis and the role of host genetic diversity”.

Abstracts

1. Abstract at the BXD World meeting in Braunschweig, Germany, 2009, “H5N1 pathogenesis and the role of host genetic diversity”.
2. Abstract for the Options for the Control of Influenza VII, Hong Kong, 2010, “Systems Biology Approach to H5N1 Influenza A virus Pathogenesis”.

Publication

1. **Boon ACM**, DeBeauchamp J, Krauss S, Rubrum A, Webb AD, Webster RG, McElhaney J, Webby RJ. 2010. Cross-reactive neutralizing antibodies directed against pandemic H1N1 2009 virus are protective in a highly sensitive DBA/2 influenza mouse model. J. Virol. 84:7662-7667.
2. **Boon ACM**, Finkelstein D, Zheng M, Liao G, Allard J, Klumpp K, Webster R, Peltz G, Webby RJ. 2011. H5N1 influenza virus pathogenesis in genetically diverse mice is mediated at the level of viral load. MBio. 2011 Sep 6;2(5).

Conclusions

- B6.D2.11D mice are possibly more susceptible to H5N1 influenza A virus with an increase in weight loss during the resolution phase of the infection.
- B6.D2.17D mice display no obvious phenotype upon inoculation with H5N1 virus.
- B6.D2.7D mice display no obvious phenotype upon inoculation with H5N1 virus.
- DBA/2 produce significantly higher amounts of pro-inflammatory cytokines TNFa, CCL2 and IFNa compared to C57BL/6 mice.
- Fourty-three BXD strains have been tested for the production of pro-inflammatory cytokines 48 hours post inoculation with HK213 H5N1 virus.
- A significant QTL associated with the early production of pro-inflammatory cytokines has been identified on chromosome 6.

Leishmania major project

We have successfully used the BXD resource to study the host response to *Leishmania major* (*Lm*), a protozoal parasite that causes an inflammatory disease in mice similar to cutaneous leishmaniasis in humans. We determined the optimal parasite dose ($1x10^6$), host gender (female), age (7-9 weeks) and optimal time (3 weeks post-infection) for reproducible and robust analysis of pathology and immune response. Using these parameters, we measured a minimal informative set of phenotypes as shown in **Table 1**.

Table 1

Phenotypes measured	**Frequency**	**Time**
clinical score (footpad swelling)	*weekly*	*over 8 weeks*
pathogen score (parasite burden in feet)	*once*	*3 weeks*
ex vivo cyto/chemokine expression (popliteal LN)	once	3 weeks
ex vivo cyto/chemokine expression (cardiac blood)	once	3 weeks
myelo/lymphoid immunophenotype (popliteal LN)	once	3 weeks
gene expression profile (popliteal LN)	once	3 weeks

The clinical course we observed was consistent with published reports [1, 2], with DBA/2 being more clinically resistant than C57BL/6. In contrast to the differential clinical course, parasite burdens were similar between the BXD parental strains, highlighting distinct underlying mechanisms, and suggesting that differences in the inflammatory response to *Lm* might be responsible for the contrasting clinical outcomes. In support of this interpretation, draining popliteal lymph node cellularity was significantly higher in C57BL/6 versus DBA/2.
To investigate the nature of the differential cellularity exhibited by DBA/2 and C57BL/6 in response to *Lm* infection, we performed FACS analysis of draining popliteal lymph node cells.

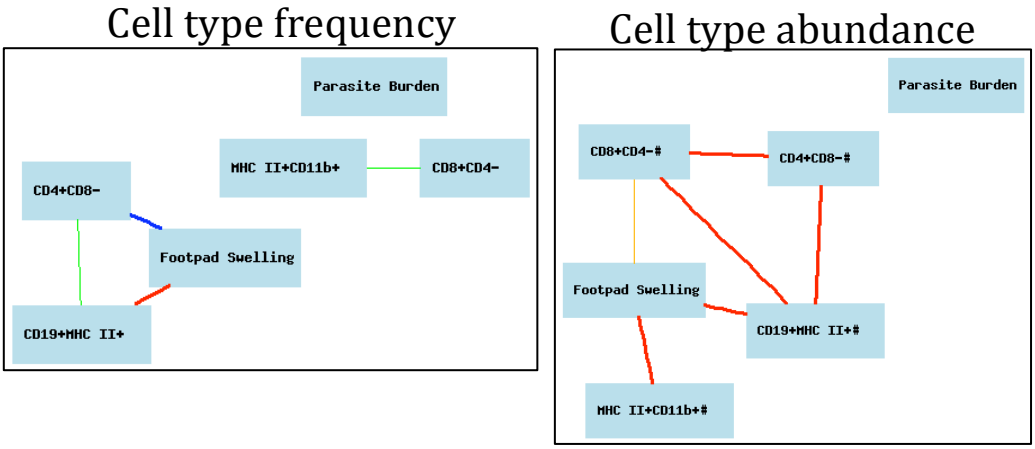

Figure 1. Correlation between CD19+MHC-II+ B-cells and clinical score (footpad swelling) depicted as the frequency and absolute number of indicated cell types in the popliteal lymph node.

We found that the number of MHC class II+, CD19+ B cells was significantly elevated in C57BL/6 versus DBA/2, accounting for the majority of the cellularity difference (**Figure 1**). The correlation between draining popliteal lymph node B cell abundance and clinical score has been noted previously and is thought to relate to the antigen presentation function of B cells [3, 4]. Thus, the hypothesis neutral BXD approach we have employed has succeeded in uncovering a key biological process validated by independent experimental evidence. We are now attempting to genetically dissect the molecular role of B cells in determining clinical outcome to *Lm*.

Although, parasite burden did not differ significantly between the parental strains, variation did exist among the BXD strains. Thus, we sought to determine whether popliteal lymph node cells exhibit additional differences that could potentially explain the differential parasite burdens exhibited by infected BXD mice. To accomplish this we used a Milliplex bead assay to measure cytokine and chemokine content in supernatants of 48-hour popliteal lymph node cultures. Indeed, GCSF level was found to be strongly correlated with parasite burden (**Figure 2**).

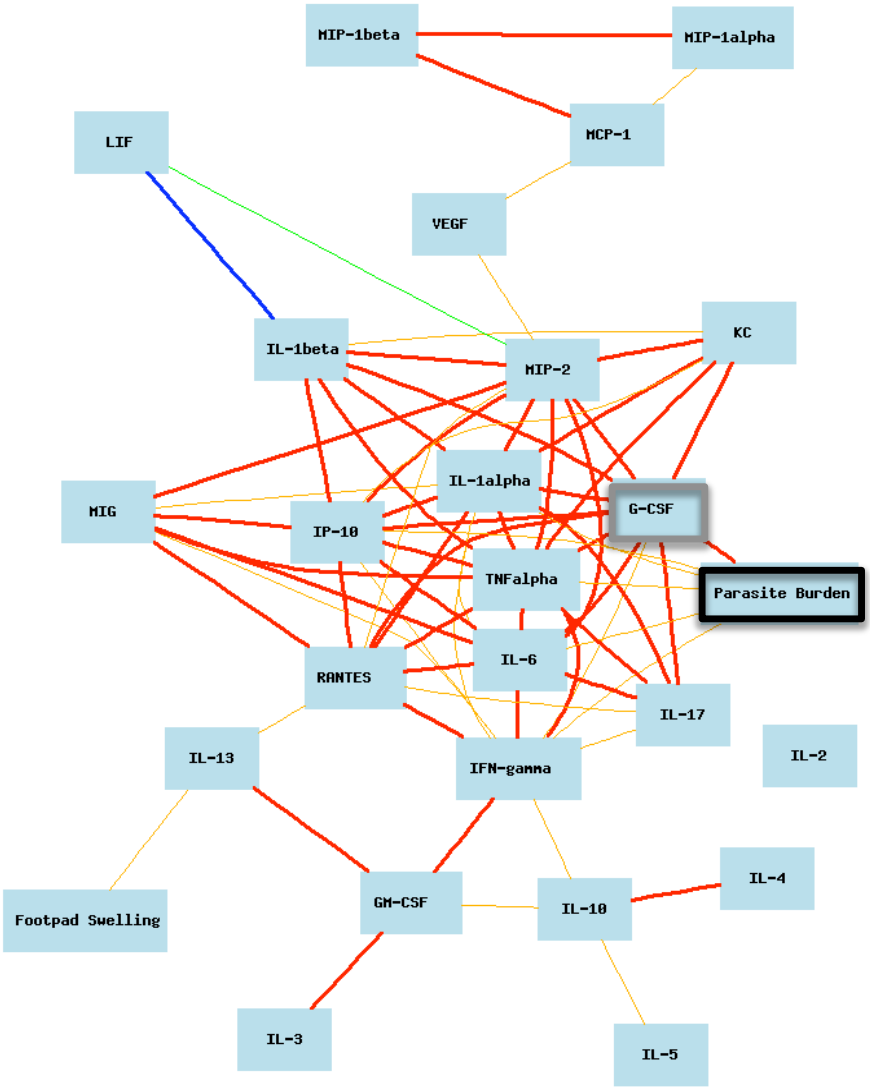

Figure 2. Correlation between GCSF level and parasite burden.

As was the case with clinical score and B cell abundance, the correlation between GCSF level and parasite burden had also been noted previously [5, 6]. In this case, the evidence suggested that neutrophils mobilized to the site of infection by GCSF ingest parasites and transmit them intact to macrophages wherein they replicate and from which they eventually spread.
Thus, the hypothesis neutral BXD approach has succeeded again in uncovering another key biological process that has been validated by independent experimental evidence.

Furthermore, analysis of the data in Gene Network reveals 2 suggestive loci regulating parasite burden (**Figure 3**). Although neither QTL interval contains the gene for GCSF, we hypothesize that the activities that map to each QTL will act in the GCSF/neutrophil/macrophage axis.

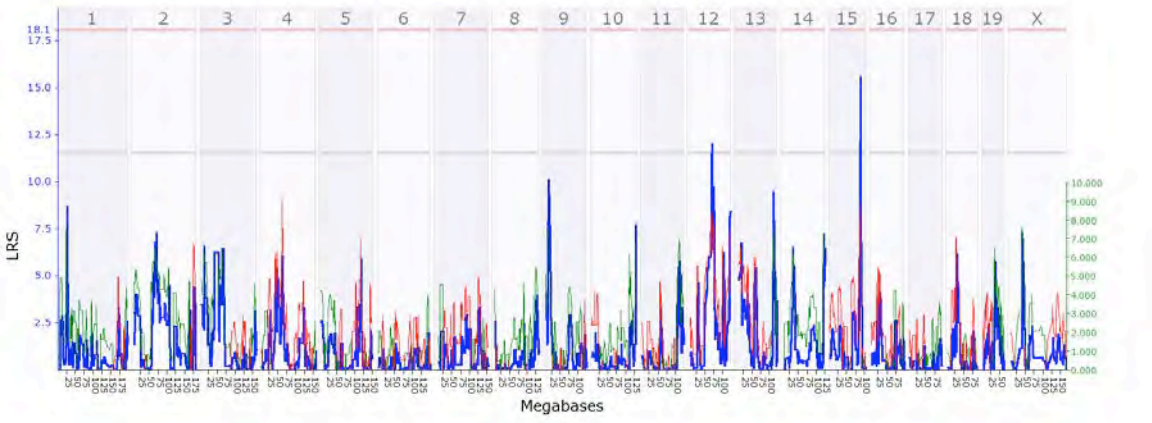

Figure 3. QTLs regulating parasite burden. Note suggestive QTLs on chromosomes 12 and 15.

Key Research Accomplishments

- Identified 2 suggestive loci regulating parasite burden.
- Identified one strong statistical correlation between ex vivo popliteal lymph node GCSF expression level and parasite burden.
- Identified one strong statistical correlation between popliteal lymph node B cell abundance and footpad swelling.
- Based on (2) and (3) above, we have determined that assessment of key phenotypes on as few as 30 BXD mice is sufficient to rapidly triangulate essential host immune features underlying clinical presentation and pathogen score (draining lymph node B cell abundance and GCSF level, respectively). The causal connections underlying statistical correlations unearthed in our analysis have been elucidated experimentally in multiple independent scientific reports [1-6]. Thus, our study serves as a proof of principle demonstration of the power and utility of the BXD resource (combined with appropriate phenotypic measures) to rapidly identify key features of the host response to a given infectious pathogen. An added benefit is the concomitant identification of genetic loci that regulate the uncovered features.

Reportable Outcomes

None

Conclusions

Though currently based on the analysis of up to 30 BXD strains (1-5 mice/strain), our analysis has sufficed to reveal two key correlations that previous more conventional studies have shown to be causal [1-6]. Our data indicate that clinical score (footpad swelling) is strongly correlated with B cell abundance in the draining popliteal lymph nodes. Further, they show that parasite burden is strongly correlated with popliteal lymph node GCSF level. Thus, our data reveal the power of the BXD approach to rapidly focus attention on key immunological parameters controlling the host response to a given infectious pathogen.

References

1. Reiner, S.L. and R.M. Locksley, *The regulation of immunity to Leishmania major.* Annu Rev Immunol, 1995. **13**: p. 151-77.
2. Baldwin, T.M., et al., *The site of Leishmania major infection determines disease severity and immune responses.* Infect Immun, 2003. **71**(12): p. 6830-4.
3. Smelt, S.C., et al., *B cell-deficient mice are highly resistant to Leishmania donovani infection, but develop neutrophil-mediated tissue pathology.* J Immunol, 2000. **164**(7): p. 3681-8.
4. Ronet, C., et al., *Leishmania major-specific B cells are necessary for Th2 cell development and susceptibility to L. major LV39 in BALB/c mice.* J Immunol, 2008. **180**(7): p. 4825-35.
5. Tacchini-Cottier, F., et al., *An immunomodulatory function for neutrophils during the induction of a CD4+ Th2 response in BALB/c mice infected with Leishmania major.* J Immunol, 2000. **165**(5): p. 2628-36.
6. Kohler, A., et al., *G-CSF-mediated thrombopoietin release triggers neutrophil motility and mobilization from bone marrow via induction of Cxcr2 ligands.* Blood, 2011. **117**(16): p. 4349-57.

Mouse Genomics Core

BXD strains colony for the DoD select agents

We maintained more than 500 cages for the DoD including most of the JAX BXD strains and all of the UTHSC strains. We are developing another 80 new BXD strains. Of these new strains, ~46 new strains have passed the 10th generation of inbreeding, and two strains (BXD113 and BXD125) have been inbred. We have genotyped all of the 80 new BXD strains with 50 UTHSC BXD strains together using GeneSeek SNP array at about 8000 SNPs density. Many alleles have showed homozygosis for most of the strains and therefore could be used to validate genetic modulators for some selected phenotype or gene expression.

Pathogen profiling

We have sequenced the genomes of 16 different strains of *Burkholderia*. DNA isolated from these samples was used to prepare barcoded fragment libraries for the Ion Torrent PGM. After preparation, the libraries were quantified by pooling and running a PGM 314 chip (~500,000 reads). The barcode quantification from this chip was then used to pool the libraries equally for a run on a PGM 318 chip (3.63M reads). The PGM platform is especially suited for this work due to speed of sequencing, low cost, and ease of use. Libraries can also be saved and re-sequenced on a relatively short time frame if the coverage is insufficient after the first run. Data collected here will be further analyzed.

Infectious disease gene expression profiling and genetic mapping

Over the last few years we have also generated and distributed a large number of immune related gene expression data sets that include spleens (109 strains), lung (57 strains), and T cells (33 strains). This data can be used to address central questions on the genetics of infection response, and to identify the candidate genes that confer susceptibility or resistance to infectious diseases. One example of candidate gene selection comes from spleen transcriptome-mapping data after oviduct infection with *Chlamydia*. The first step is to narrow down the list of candidate causal genes within a Quantitative Trait Locus (QTL)—a chromosomal region containing sequence variants strongly associated with phenotypic variation. For the oviduct infection study, a significant QTL has been mapped to distal chromosome 3 (**Figure 1**). There are more than 100 genes in this QTL region. We performed correlation analysis, expression QTL (eQTL) analysis, and co-localization analysis using spleen gene expression data above, and finally narrowed down candidate genes from 126 to 5. The expression of those 5 genes is significantly correlated with oviduct infection phenotype (P< 0.05), and the expression of each is cis-regulated (a gene variant located within or near the gene controls gene expression) with Likelihood ratio statistic (LRS) 17 and above (P< 0.05) (**Table 1**).

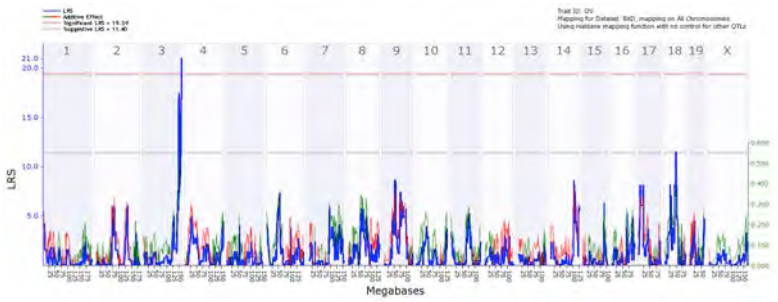

Fig 1. Interval mapping of oviduct gross pathology across the BXD strains reveals a QTL on distal Chr 3. The LRS values are plotted in blue across the genome and measure the strength of the association between chromosome and Mb position (top and bottom X-axis, respectively) and phenotype expression. Allele contribution is shown by the red (C57BL/6J) and green (DBA/2J) lines. Red and grey horizontal lines indicate genome-wide significance and suggestive thresholds, respectively.

Table 1. Candidate genes for a QTL of oviduct infection

Symbol	Gene (Chr: Mb)	Expression	Max LRS	eQTL (Chr: Mb)	r	p value
Lphn2	Chr3: 148.478819	8.55	55.4	Chr3: 148.26	-0.50	0.002
Syde2	Chr3: 145.651617	7.58	26.4	Chr3: 145.09	-0.59	0.000
Mcoln2	Chr3: 145.812797	9.78	25.6	Chr3: 144.42	0.35	0.037
Ttll7	Chr3: 146.606970	7.80	25.3	Chr3: 148.26	-0.43	0.008
Ankrd13c	Chr3: 157.610215	10.36	17.4	Chr3: 157.87	0.35	0.041

Subsequent gene function and gene network analysis suggest that *Syde2* is the strongest candidate gene. It may work with several other genes together to affect severity of oviduct infection.

In-house genomic sequencing of inbred mouse strains

We have recently completed the genomic sequencing of the DBA/2J strain at 100x coverage using both SOLiD and Illumina systems. We have generated ~150 Gb of well-aligned sequences (110 Gb using SOLiD and 40 Gb using Illumina GA2). All of the sequence data have been deposited in the NCBI Sequence Read Archive (SRA009489). We have combined these short sequences with the original Celera DBA/2J sequence (~1.3 x shotgun) (Mural et al, 2002) to produce a high quality consensus genome on a C57BL/6J reference genome framework (Church et al, 2009). Because both parental strains of the BXDs have now been well sequenced, we are able to generate a nearly comprehensive list of sequence variants that are segregating in the BXDs as common alleles. For example, we now have a list of approximately 5 million high quality SNPs, including 63 nonsense and ~11,000 missense mutations, 568K indels (2–10 nucleotides), 16K copy number variants (CNVs), and 600 inversions. The number of new SNPs that we have discovered roughly doubled the original set generated using Celera sequence. The DBA/2J genome has also recently been sequenced at 23x coverage by the Wellcome Trust as part of an effort to sequence 17 strains of commonly used inbred mice (Keane et al, 2011). Our higher coverage sequencing of the DBA/2J genome enabled us to call 0.6 million more SNPs compared to the Welcome Trust. For the first time, a nearly complete compendium of sequence variants is available for a large mouse cross—the BXD family of strains. This well-characterized genetic population provides a unique resource to study a wide variety of disease processes, including infectious-related diseases and phenotypes. We are currently sequencing 8 mate pair libraries, 2 of which have different insert sizes (1-2 KB), from select BXD strains. As a part of the "library complexity check" procedure, we sequenced a small portion of the library for BXD29 and BXD2 mice and found that greater than 95% of the reads have unique start positions when aligned against the reference genome.

Validation of sequence polymorphism between B6 and D2 mice.

To assess the validity of the coding SNPs, we performed conventional Sanger sequencing on all 63 nonsense mutations and 76 random selected missense mutations. This validation is designed to prioritize variants used for the reverse complex trait analysis below. For nonsense mutations, we obtained reliable Sanger results on 49 PCR products and confirmed that 42 are authentic with false positive rate of 14% (7/49). For non-synonymous mutations, we obtained 67 reliable PCR products and confirmed 63 with false positive rate of 6% (4/67).

Small indels in coding sequence can be highly disruptive, especially when they introduce frameshift mutations or extend the length of polyglutamine tracts in the protein product. Most small indels (98.74%) were in introns or intergenic regions, but 542 small deletions

and 641 small insertions were in coding exons. The small coding indels are enriched of trinucleotides, which account for 32% of small coding deletions and 38% of small coding insertions. Of these small indels, a subset of 50 (28 deletions and 22 insertions) is predicted to result in frame shift mutations in roughly half of the BXD lines (**Table 2**). We randomly selected 40 frame shift mutations for conventional Sanger validation. Thirty-three primer pairs produced reliable PCR products, 27 out of which were validated, indicating that the false positive rate is about 18% (6/33).

Table 2. Validated frame shift mutations between the B6 and D2 genomes

Chr	Start Position (bp)	Sequence	Indel type	Gene Symbol	Entrez GeneID	Exon #
		GAGAGAGAGAGAG		*C230029F*		
1	49,310,932	A	INS	*24Rik*	442837	2
1	171,252,513	TT	INS	*Adamts4*	24,913	1
2	35,043,207	TA	DEL	*Hc*	15139	6
2	87,949,277	A	INS	*Olfr1156*	258814	1
2	126,737,553	TGTATGTA	INS	*Usp8*	8492	9
3	41,742,027	T	DEL	*Sclt1*	67161	1
3	133,002,550	TGCCGTGTTTGAGA	INS	*Gstcd*	67553	9
4	117,070,923	T	DEL	*Eif2b3*	1867	1
5	38,300,289	G	DEL	*Otop1*	2196	6
5	96,828,404	GTAG	DEL	*Anxa3*	11745	7
5	131,476,702	G	INS	*Auts2*	319,974	7
6	5,272,293	A	INS	*Pon2*	3,326	6
6	131,221,840	AGAAATCCAC	INS	*Klra2*	16,633	7
		TGGCTTTGGTAAGA		*8430419L*		
6	135,225,279	AGCAGGGC	INS	*09Rik*	74525	5
		CAGCAGCACTGGGA				
		AAGGGGAAAGAGA				
7	16,336,830	GATTAGAGAGA	INS	*Sae1*	56,459	7
7	33,737,360	T	DEL	*Abpz*	2339	3
7	107,590,404	T	DEL	*Olfml1*	244198	3
8	4,275,857	T	DEL	*Pdgfrl*	68,797	6
8	41,309,537	C	DEL	*Pcm1*	18,536	25
8	114,133,648	G	DEL	*Nudt7*	67528	1
9	32,728,881	A	DEL	*Ets1*	23871	4
9	65,280,130	G	DEL	*Cilp*	214425	1
13	21,484,709	A	INS	*Zkscan4*	544922	3
14	51,039,518	T	INS	*Rnase9*	32841	2
		GGGCTTGGTGAAGG				
15	83,158,786	CTCAGGGCTGA	INS	*Cyb5r3*	19754	8
16	64,926,926	T	DEL	*Htr1f*	15,557	3
17	47,391,015	GG	INS	*Guca1b*	17477	3

Reverse complex trait analysis of immune system function

Genetic mapping usually proceeds through a forward genetics approach, starting with a complex phenotype that varies across a population followed by identification of the genes and variants that caused the phenotypic variation. Reverse complex trait analysis (RCTA) is a novel reverse genetics method that starts with identification of the nascent sequence variants rather than with engineered alleles or mutagenized stock. After we generated ~100x whole-genome shotgun coverage of DBA/2J (D2) combined with publicly available sequence from the C57BL/6J (B6) strain, we were able to generate a nearly comprehensive list of sequence variants, and identify the downstream effects of those sequence variants using BXD strains. In the past few years, we have identified 5 M SNPs, 568K insertions and deletions (Indels), and thousands of inversions and copy number variants (CNVs) segregating among the 80 BXD strains. Recently we explored possible functional consequences of sequence and structural variants using a large data set of expression profiles from the BXD family, and tested the method of RCTA in immune system function. For example, there is a single non-synonymous SNP in *Wdr26*, a gene with an important role in innate immune responses through suppression of the MAPK signaling pathway. Expression mapping showed that *Wdr26* is associated with a strong cis eQTL with an LRS of 40 in lung (**Figure 2**).

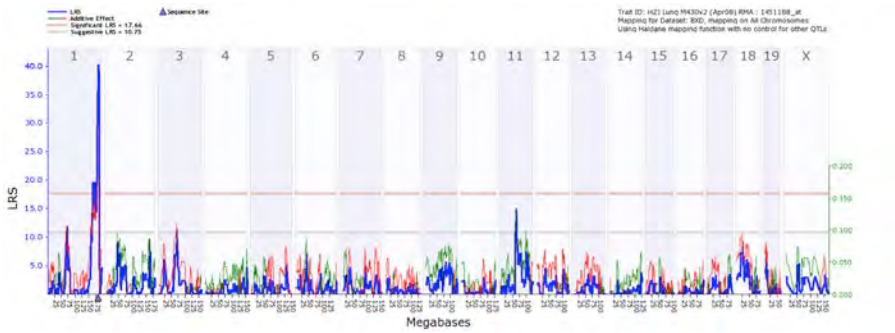

Fig 2. Interval mapping of Wdr26 expression showed it is cis-regulated.

Expression levels of *Wdr26* co-vary well (r = –0.7167, p = 0.0012) with T cell proliferation in the immune system (GN Trait ID 10237, **Figure 3**), a trait that maps very closely to *Wdr26* with an LRS > 49. The human ortholog, WDR26, directly binds free Gβγ and forms a complex with endogenous Gβγ in T cells, attenuating chemotaxis in the T cells, which corroborates the function of *Wdr26* in mouse. This example illustrates that the functional consequence of the single non-synonymous SNP in *Wdr26* can be readily determined by RCTA.

The identification of sequence variants that modulate phenotypes is fundamental to our understanding of the genetic basis of both Mendelian traits and quantitative complex traits. RCTA could efficiently link sequence variants to novel phenotypes. Through RCTA we can efficiently discover

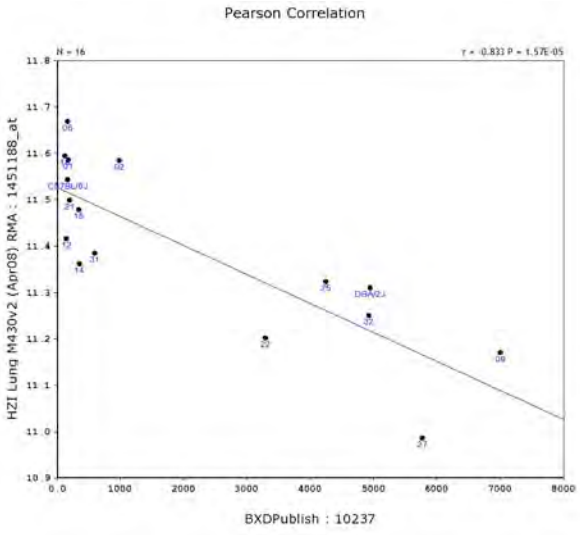

Fig 3. The expression of Wdr26 correlated with T cell proliferation very well (r = -8.330.0001).

, p <

the downstream consequences of DNA polymorphisms on RNA expression and infectious related phenotypes in specific BXD strains using the high coverage genomic sequence data.

Reportable outcomes

Presentation

1. **Oral presentation** at the UT-ORNL-KBRIN Bioinformatics Summit, Cadiz, KY, USA, 2010. "High-throughput sequencing of the DBA/2J mouse genome"

Abstract

1. **Miyairi I**, **Lu L**, **Williams RW**, **Byrne GI**. Genetic susceptibility to acute and chronic Chlamydia infection. The BXD World International Meeting on BXD Phenotyping, Braunschweig, Germany, Nov 30 – Dec 1, 2009.
2. Wang X, Mulligan MK, Mozhui K, **Lu L**, Chen Z, Nelson SF, Taylor WL, and **Williams RW**: Comparison of variant detections using whole genome sequencing of the DBA/2J mouse strain. The 10th Annual Complex Trait Consortium (CTC) Meeting, Washington DC, USA, June 22~25, 2011.

Publications

1. Wang X, Agarwala R, Capra JA, Chen Z, Church DM, Ciobanu DC, Li Z, **Lu L**, Mozhui K, Megan K Mulligan MK, Nelson SF, Pollard KS, Taylor WL, Thomason DB, **Williams RW**: High-throughput sequencing of the DBA/2J mouse genome. BMC Bioinformatics 2010, 11(Suppl 4):O7
2. Alberts R, **Lu L**, **Williams RW**, Schughart K. 2011. Genome-wide analysis of the mouse lung transcriptome reveals novel molecular gene interaction networks and cell-specific expression signatures. Respiratory Research 12:61
3. **Miyairi I**, Ziebarth J, Laxton JD, Wang X, van Rooijen N, **Williams RW**, **Lu L**, **Byrne GI**, **Cui Y**. 2012. Host genetics and Chlamydia disease: prediction and validation of disease severity mechanisms. PLoS ONE 7:e33781.PMCID: PMC3306297
4. Nedelko T, Kollmus H, Klawonn F, Spijker S, **Lu L**, Heszmann M, Alberts R, **Williams RW**, Schughart K. 2012. Distinct gene loci control the host response to influenza H1N1 virus infection in a time-dependent manner. BMC Genomics 13:411, PMID: 22905720 PMCID: PMC3479429
5. Wang X, Mulligan MK, Pandey A, **Lu L**, Biobanu DC, Nelson SF, Pollard KS, Taylor WL, Thomason DB, **Williams RW**: Sequencing the DBA/2J Mouse Genome: Reverse Genetics Using Test Cross Progeny. PLoS Biology, manuscript in preparation.

References

1. Mural R, Adams M, Myers E, Smith H, Miklos G, Wides R. A (2002) Comparison of Whole-Genome Shotgun-Derived Mouse Chromosome 16 and the Human Genome. Science. 296:1661-71
2. Church DM, Goodstadt L, Hillier LW, Zody MC, Goldstein S, She X, et al. (2009) Lineage-Specific Biology Revealed by a Finished Genome Assembly of the Mouse. PLoS Biology. 7:e1000112.
3. Keane TM, Goodstadt L, Danecek P, White MA, Wong K, et al. (2011) Mouse genomic variation and its effect on phenotypes and gene regulation. Nature 477: 289-294.

Modeling core – Construction of gene network models

Introduction

The primary objectives of the modeling group were (1) to develop tools for systems genetics analysis of infectious disease and (2) to use these tools to create network models that enhance understanding of responses to specific diseases or gene regulatory networks. Our work to meet the first objective culminated in the creation of the Bayesian Network Webserver (*BNW*, http://compbio.uthsc.edu/BNW), while we have utilized BNW and related methods to investigate variation in responses to infection to *Chlamydia psittaci* and in expression of immune-related genes within the BXD panel of recombinant inbred mice.

Body

A. The Bayesian Network Webserver

We developed the *Bayesian Network Webserver* (*BNW*, http://compbio.uthsc.edu/BNW), a comprehensive web-based tool for network modeling of systems genetics data. In addition to allowing our group to quickly generate network models linking genotype with gene expression traits and phenotypes after pathogen infection, *BNW* will be a valuable and accessible tool for network modeling by the larger research community. While Bayesian networks have been applied to many biological data sets, their widespread use has been limited by a lack of easy-to-use and comprehensive resources for creating and analyzing models. Successful Bayesian network modeling requires the integration of several distinct steps, ranging from structure learning to using models to create testable hypotheses. *BNW* integrates software we developed and used for network modeling datasets related to this grant, but is designed to be automated enough for use by researchers new to network modeling and flexible enough to be applied to a wide variety of data sets.

Steps in Bayesian network modeling:

Structure learning. The first step in Bayesian network modeling of a dataset is structure learning, or identifying which directed edges between variables (nodes) should be included in the network to represent the conditional dependencies observed in the data. As performing exhaustive searches during structure learning is an NP-hard problem, structure learning is often the most computationally intensive part of Bayesian network modeling. To reduce the speed of structure learning, BNW integrates several recent improvements in structure learning algorithms, allowing for an exhaustive search for hybrid networks containing as many as 19 variables within 2 minutes. Structure learning in BNW can be broken down into three main steps: calculating local network scores, determining the highest scoring global network structures, and, depending on user settings, performing model averaging over high scoring structures. The score of a local structure in a Bayesian network considers how well a node is explained by its immediate parents. To begin structure learning in BNW, we calculate all possible local scores by performing an exhaustive search of local structures given the structural constraints specified by the user. BNW uses a scoring metric that allows for the use of hybrid datasets through the use of conditional Gaussian distributions (1). After calculating local scores, BNW performs a search for the *k*-best global optimal structures, using a user-specified value of *k* (9, 10).

Model averaging. The Bayesian score metric inherently handles the problem of overfitting data to complex models (8). However, selecting a single best network model and ignoring all other models may still lead to over-fitting the data. Model averaging can be used to reduce this risk (2). An indicator function f is defined as: if a network G has the feature (here a feature is a directed edge representing a regulatory relationship), $f(G) = 1$, otherwise, $f(G) = 0$. The

posterior probability of a feature is $P(f(G) \mid D) = \sum_G f(G)P(G \mid D)$. This probability reflects our confidence in the feature f. The posterior probability of a feature can be estimated by averaging over the high scoring models visited during the search. We currently use model averaging when performing structure learning of small networks after exhaustive searches in *BNW*.

Parameter learning. We will use maximum likelihood to estimate the parameters of the conditional probability distributions (CPDs) by computing statistics from the data samples. The local conditional probabilities can be parameterized using finite mixture models, which are flexible methods for modeling complex probability distribution functions, and the EM algorithm to find the maximum likelihood estimates of the parameters of the CPDs. *BNW* currently uses the BayesNet Toolbox (6) to automatically perform parameter learning after structure learning and displays each discrete node as a bar chart and each continuous node as a line chart using Google Charts APIs.

Prediction after observed evidence and external intervention. To predict the effects of genetic and transcriptional variations/interventions with network models, we compute the probability distribution of the molecular traits, conditional on known evidence (e.g. the QTL genotype and/or gene expression level). The joint probability represented by a Bayesian network is given by the chain rule. Bayesian network models can be used to for predictions in two ways. First, networks can predict how *observing evidence* of some variables in the network impacts other network variables. For example, if a network model connecting genotype and gene expression was learned using a set of mouse strains, it could be used to predict gene expression for a new set of strains. The genotype for each of the new set of strains could be used as observed evidence when testing the predictions of other variables by the network. Bayesian networks can also be used to predict the effects of external interventions, which change not only the predicted values of nodes in the networks but also the network structure by removing the dependence of the intervened node on its parents.

Use of the Bayesian Network Webserver

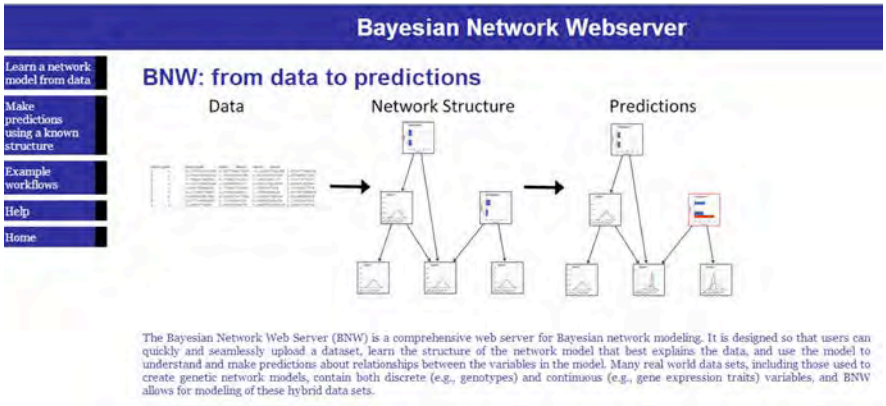

Figure 1 Screenshot of the *Bayesian Network Webserver* homepage

From the *BNW* homepage (**Figure 1**), users can select one of two options for network modeling of their data sets. First, they can select "Learn a network model from data", allowing them to upload a file containing a dataset, learn the structure and parameters of the network from the data, and investigate predictions of the network. Alternatively, they can select "Make predictions using a known structure", allowing them to upload a file containing the network structure and a separate file containing the data, learn the network parameters from the data, and then examine network predictions. A file containing the network structure can be downloaded from *BNW* after structure learning, allowing users to skip the structure learning step if they wish to investigate the same network during a return visit to the site.

After clicking “Learn a network model from data” on the *BNW* homepage, users upload a file containing their data. They then select whether they want to add any constraints when performing structure learning. The addition of constraints reduces the computational complexity of structure learning, aiding users in identifying biologically meaningful networks and allowing structure learning to be performed more quickly. Users who want to add structural constraints are presented with a structural constraint graphical interface built using HTML5 (**Figure 2**). The structural constraint interface is separated into three sections: a section for grouping nodes into different tiers, a section for specifying the interactions that are allowed within and between tiers, and a section for creating lists of specific required or banned directed edges. For genetic networks, the genetic causality identified by QTL mapping can be used as constraints in network modeling. For a set of genes regulated by a set of common QTLs, variables can be separated into a tier of genotype, a tier of cis-regulated genes, and a tier of trans-regulated genes using the *BNW* structure learning constraint interface. Then, restrictions can be added to ensure that: 1) QTL genotypes have no parents; and 2) *trans*-regulated gene expression traits cannot be the parents of *cis*-regulated genes. For nodes connecting QTL genotypes, gene expression traits, and phenotypes, we can add restraints that prevent phenotype nodes from being the parents of gene expression traits, as shown in **Figure 2**. Specific banned or required edges can be added to the network to include knowledge gained from previous experiments.

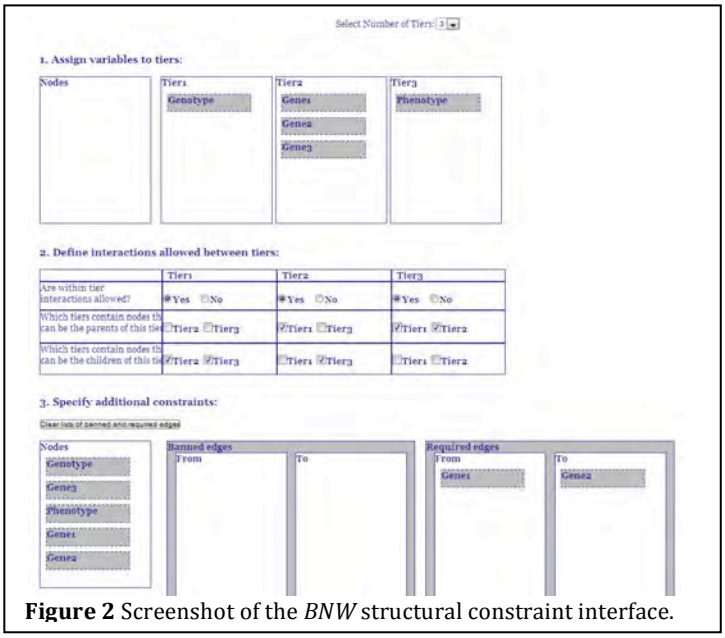

Figure 2 Screenshot of the *BNW* structural constraint interface.

After structure learning or entering a structure file, *BNW* automatically performs parameter learning and displays the network with discrete variables presented as bar charts and continuous variables as line charts (**Figure 3A**). BNW provides two modes for making predictions with the networks, an Evidence mode and an Intervention mode, that can be selected using a button at the top of webpage. User interaction with *BNW* for each mode is the same: the user simple clicks on one of the charts in the network and a pop-up window prompts users to enter a value for the variable. BNW then automatically calculates how the entered value impacts the network and displays the new predicted values for each variable. For both modes, the variable

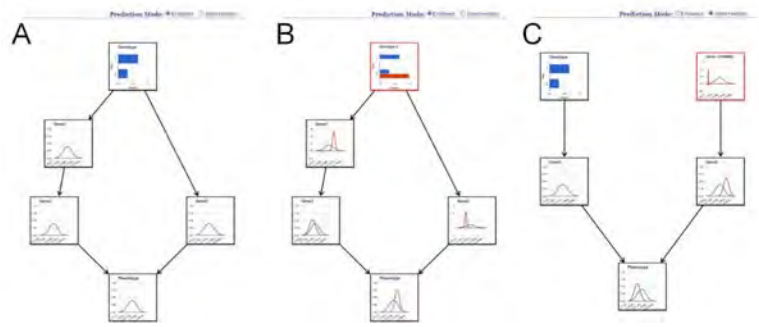

Figure 3 (A) Example of a network containing one discrete and four continuous variables after structure and parameter learning. (B) Use of the Evidence mode to predict the values of gene expression traits and phenotypes for samples with Genotype in state 2. (C) Use of the Intervention mode to predict how experimental intervention that removes Gene1 from a system impacts other variables in the network.

with the entered value is outlined in red and the new distributions are shown in red. As external intervention removes the dependence of a variable on its parents, the network structure may change when in the Intervention mode and only those variables downstream of the intervened variable will be impacted by the intervention. **Figures 3B** and **3C** show screenshots of *BNW* after entering data in Evidence and Intervention modes, respectively. For both cases, the entered value has a large impact on the predictions of the network.

We have included several features to help make *BNW* easy to use. First, the Help page provides detailed descriptions of the features of BNW, such as the structure learning constraint interface, and simple guidelines for formatting input data files. To aid users in selecting a structure learning method, the Help page also provides descriptions of the different methods as well as the network sizes that are appropriate for each method. Second, we include example workflows that take users through a step-by-step tour of features of *BNW*. Finally, each of the structure learning methods includes a sample dataset, allowing users to play with the interactive features of *BNW*.

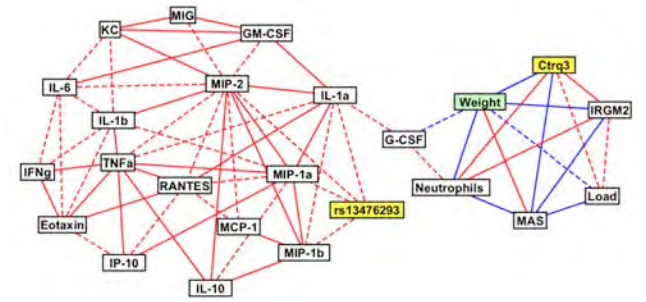

Figure 4 The correlation network of immune parameters during Chlamydia infection in BXD mice. Correlation network linking BXD genotypes (*Ctrq3* and rs13476293), *C. psittaci* load, inflammatory responses, cytokine profiles, IRGM2 protein expression pattern, and weight change after *C. psittaci* infection in BXD strains. Positive (red) and negative (blue) correlations between variables with magnitudes of Pearson's correlation coefficient greater than 0.6 (dashed lines) and 0.7 (solid lines) are shown.

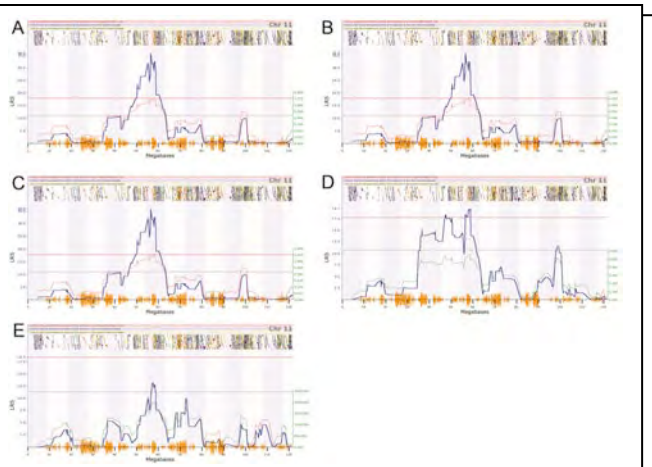

Figure 5 QTL mapping results for (A) day 6 weight, (B) neutrophils, (C) macrophage activation status, (D) *C. psittaci* load, and (E) G-CSF on chromosome 11. Significant QTLs ($p < 0.05$) are indicated by the solid red line.

Network modeling of *Chlamydia psittaci* infection

The C57BL/6J (B6) and DBA/2J (D2) strains of mice have a differential susceptibility (difference in 100% lethal dose > 1000,000 fold) to infection with *Chlamydia psittaci*; however, the specific molecular mechanism through which the genotype impacts disease status is unknown (5). To elucidate the pathways that connect *Ctrq3* genotype with disease outcome, we created a Bayesian network model including three levels of systems genetics data: (1) *Ctrq3* genotype, (2) intermediate immune-related phenotypes, including quantitative variables associated with cytokines, macrophages, neutrophils, and pathogen load, and (3) disease status as quantified by the ratio of weight 6 days after infection to weight at the time of infection.

The first step in our analysis was to determine which intermediate phenotypes to include in the model. Data for 32 cytokines, pathogen load, levels of macrophages and neutrophils, and macrophage activation status (MAS) were collected for 40 BXD strains infected with *Chlamydia psittaci*. We used two tools, correlation network analysis and QTL mapping, in the GeneNetwork web server (www.genenetwork.org) to determine which of these variables were associated with disease status. We found that many cytokines were highly correlated with each other, but had little association with diseases status (**Figure 4**). Disease status (weight) was

associated the level of the G-CSF cytokine, the level of neutrophils, pathogen load, and MAS. As expected, disease status was controlled by a QTL at *Ctrq3*. Neutrophils, load, and MAS also had significant QTLs at this location, but G-CSF did not (**Figure 5**). To further investigate the influence of the genetic polymorphisms at *Ctrq3*, we analyzed the expression pattern of the IRGM2 protein, an innate immune gene in the family of immunity-related GTPases located at *Ctrq3*, and found that it had two distinct isoforms that were highly correlated with *Ctrq3* genotype. We also investigated the protein expression level of IRGB10, but found that it did not correlate with weight. Of the 40 BXD strains studied, there was no discrepancy between the *Ctrq3* genotype and IRGM2 expression pattern. We, therefore, selected 5 variables to include in the Bayesian network model: genotype at *Ctrq3*/IRGM2 protein expression pattern, neutrophil level, pathogen load, MAS, and weight ratio.

Bayesian network modeling was performed using the methods outlined in the previous discussion of *BNW*. The network (**Figure 6A**) was constructed from data for C57BL/6J and 40 BXD strains using one discrete node, representing the *Ctrq3* genotype and IRGM2 protein expression pattern, and four continuous nodes (neutrophils, *C. psittaci* load, macrophage activation status, and the ratio of the weight of the mice 6 days after infection to the weight before infection), which were modeled with conditional Gaussian distributions. Leave-one-out cross validation was also used to test the performance of the hybrid Bayesian network. For each test strain, parameter learning of the remaining 40 strains and inference was performed with the Bayes Net Toolbox with a maximum likelihood approach. To evaluate the quality of the continuous predictions, we used the Q^2 parameter (3), which is given by:

$$Q^2 = 1 - \frac{\sum (y_i - \hat{y}_i)^2}{\sum (y_i - \bar{y})^2}$$

where y_i is the value of the ith sample, $\hat{y}_i$ is the predicted value of the ith sample, and $\bar{y}$ is the

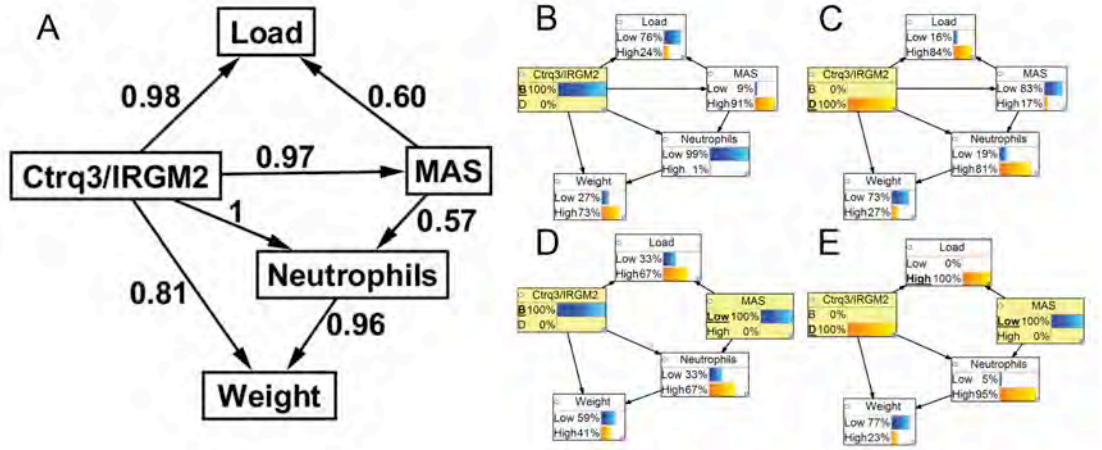

Figure 6 Bayesian network (BN) modeling of *C. psittaci* infection. (A) Structure of the BN. The number next to each directed arc of the BN indicates the confidence in the arc after model averaging, with higher numbers indicating higher confidence. (B and C) Predictions of the BN as a function of genotype at *Ctrq3*. BXD strains with the susceptible (D) genotype at the IRG locus tend to have lower MAS and weights and higher levels of neutrophils and pathogen load. (D and E) Predicted effect of interventional depletion of macrophages on the predictions of the BN. External depletion of macrophages is predicted to cause a decrease in weight and increases in neutrophils and pathogen load. For panels B to E, a threshold was determined by averaging the mean value of strains with a B genotype and the mean value of strains with a D genotype for the original data sample. Then, the probability that the predicted value for each variable was greater than (High) or less than (Low) this threshold was calculated from the conditional Gaussian distributions learned from the BN for the original data and after macrophage depletion. Nodes with a yellow background have been assigned the value to represent data for only a given genotype and intervention on the MAS.

sample mean. The values of Q^2 for MAS, neutrophil level, pathogen load, and weight were 0.51, 0.59, 0.45, and 0.68, respectively. Additionally, we discretized the original data and the predictions from the leave-one-out-cross validation for each strain and used this discretized data to test the accuracy of the predictions. A threshold for each of the continuous variables was determined by averaging the mean value of the original data for all strains with the B genotype and the mean value for all strains with the D genotype. Then, the continuous variables for the original data and the predictions were classified as being either High or Low through comparison with these threshold values for each strain. The accuracy was then determined by dividing the number of predictions that matched the original data by the total number of strains. For MAS, neutrophil level, pathogen load, and weight, the accuracy was accuracy 85%, 93%, 80%, and 88%, respectively.

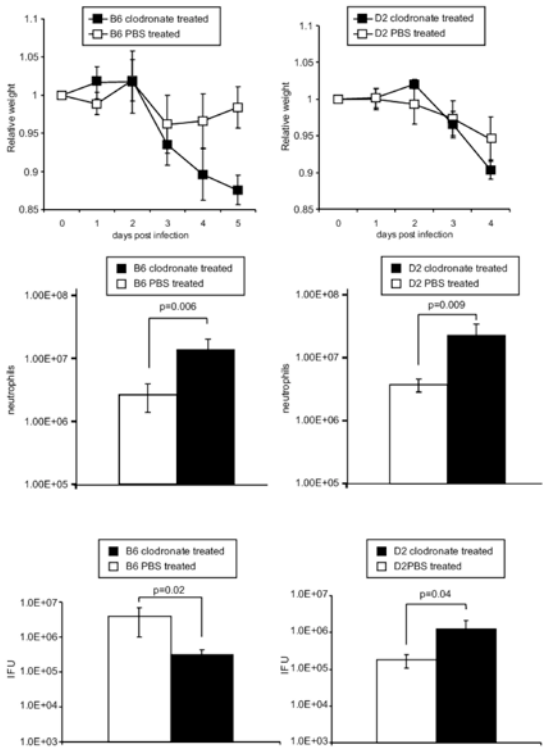

Figure 7 Impact of macrophage depletion on course of *C. psittaci* infection in B6 and D2 strains. B6 and D2 mice received either liposome clodronate or liposome PBS iv (day –1 post infection) and i.p. (day –1, 1, and 3 post infection) and infected with *C. psittaci* 10^4 IFU intraperitoneally (N=5/group). Mice were monitored daily for weight (Top) and appearance. Clodronate treated D2 strain became moribund on day 4 and B6 on day 5 post infection and were euthanized. (Middle) The number of neutrophils in the peritoneal lavage increased in both B6 and D2 strains treated with clodronate. (Bottom) Pathogen load in the peritoneal cavity was quantified. There was a statistically significant difference in final weight, number of neutrophils, and *C. psittaci* load for both B6 and D2 strains. Data is representative of two experiments.

The structure of the Bayesian network model is presented in **Figure 6A**. We further investigated two of the relationships implied by the network. First, MAS is central to the model, implying that MAS directly influences neutrophils and pathogen load, and also indirectly impacts disease status. We can use the model to predict the effects of external interventions, such as depleting the level of macrophages and MAS. The intervention sets of the value of the MAS node and relieves it from the influence of its parent node. Therefore, we predict the effects of macrophage depletion by removing the link *Ctrq3*/IRGM2 → MAS and setting MAS to the minimum value observed in the data used for parameter learning [action do (MAS = MIN), where MIN is the minimum observed MAS value]. The probabilistic inference of the effects of this influence was executed using the Bayes Net Toolbox. The model predicts that depletion of macrophages increases the levels of neutrophils and pathogen load and decreases weight (**Figure 6 panels B-E**). The magnitude of these changes is expected to be more significant in BXD strains with the resistant (D) genotype. We tested these predictions by performing chemical depletion of macrophages with clodronate before infecting B6 and D2 strains with *C. psittaci*. The results validated many of the model's predictions (**Figure 7**). In the D2 strain, depletion of macrophages increased neutrophil influx; and *C. psittaci* load and also induced a more rapid decline in weight. As predicted, in the resistant B6 strain, depletion of macrophages increased neutrophils and exacerbated the weight loss. These mice were moribund 5 days post-infection. In contrast to prediction, the B6 strain had decreased pathogen load after depleting macrophages. Pathogen load in the liver was

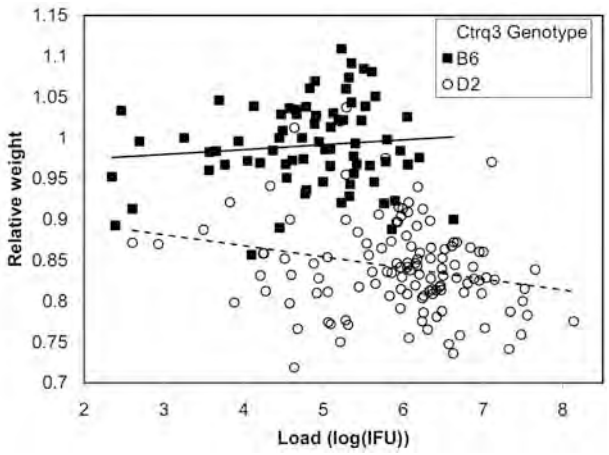

Figure 8 Genetic resistance and tolerance to Chlamydia infection in mice. Plot of weight change as a function of IFU for 197 BXD mice infected with *C. psittaci*. Mice with the susceptible D genotype at the *Ctrq3* (open symbols) lose weight as pathogen load increases, while mice with the resistant B genotype at the *Ctrq3* marker (filled circles) do not. The slopes of the linear regression lines for the B (solid line) and D (dashed line) data are significantly different (p = 0.02)

similar in B6 irrespective of whether macrophages were depleted or not (PBS control: 4.26 x 10^6 IFU/gram, Clodronate treated; 3.81 x 10^6 IFU/gram, p=0.06). Several reports have documented that IRGs reduce pathogen burden in vitro and in vivo, which is expected to influence disease severity (4, 5, 7). To investigate the possibility that the status of the *Irgm2* genotype switches disease modality, we performed the Bayesian analysis for strains with the B genotype at the *Ctrq3* locus separately from strains with the D genotype. As each data set only contained data from strains with one genotype, the genotype node was removed from the network, and the structure of the network, using model averaging of an exhaustive search of possible structures with deal, was learned for both the B and D data. For strains with the D genotype, a directed edge from pathogen load to weight ratio had a posterior probability of 0.64, while the same edge for strains with the B genotype had a posterior probability of only 0.16, indicating that weight change was dependent on *C. psittaci* load only for strains with the susceptible D genotype.The influence of load on disease outcome was much stronger for strains with the susceptible D genotype than strains with the resistant B genotype. Because of the genotype-specific switching between pathogen load and disease in the model, we expanded this analysis to 197 BXD mice and correlated the disease severity (weight) with pathogen load in individual mice according to the genotype at the IRG locus (**Figure 8**). Overall, mice with the B genotype had lower pathogen load compared to mice with a D genotype, although a considerable overlap existed. However, the mice with the B genotype were tolerant of increases in pathogen burden whereas mice with D genotype lost more weight with increases in pathogen burden as demonstrated by the differences in the slope of the load to weight linear regression lines (p = 0.02).

Network modeling of immune genes in the spleen of BXD mice

Gene expression in the spleen of young adult mice was profiled using the Affymetrix GeneChip Mouse Gene 1.0 ST array in a total of 108 strains, including 81 BXD strains. The data is freely available in the GeneNetwork website (www.genenetwork.org) and further details of the sample collection and processing are available at genenetwork.org/dbdoc/UTHSC_SPL_RMA_1210.html. To examine the expression of immune related gene in the spleen, we selected all 1249 genes with a 'immune system process' Gene Ontology annotation (GO:0002376). We then identified all probesets in the spleen gene expression dataset that target these genes. A total of 1421 probesets target these immune related genes, and this collection of probesets was used in all of the following analysis.

We performed gene expression quantitative trait locus (eQTL) mapping of the immune related genes using QTLReaper (www.genenetwork.org/qtlreaper.html) for the BXD strains. 414 of the probesets were associated with eQTLs with an LRS ≥ 15. We categorized these eQTLs into two groups: *cis*-eQTLs, in which the gene and associated marker were within 5 Mb, and *trans*-eQTLs, in which the gene and associated marker were separated by more than 5 Mb. We identified 140 *cis*-eQTLs and 274 *trans*-eQTLs. In general, the genetic variation that underlies a

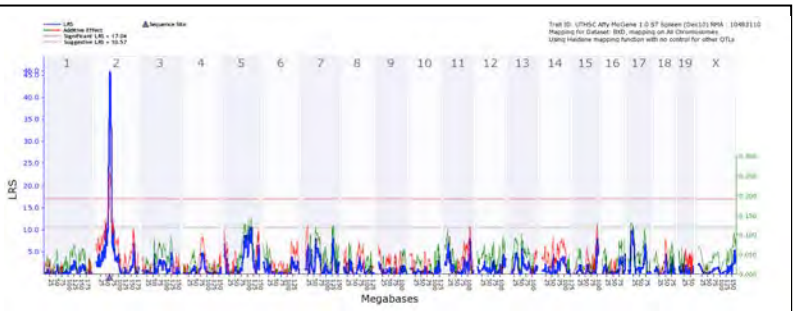

Figure 9 QTL mapping results for *Ifih1*. Significant QTLs ($p < 0.05$) are indicated by the peak solid red line, while suggestive QTLs ($p < 0.63$) are indicated with the solid grey line. The location of the gene is indicated by the purple triangle.

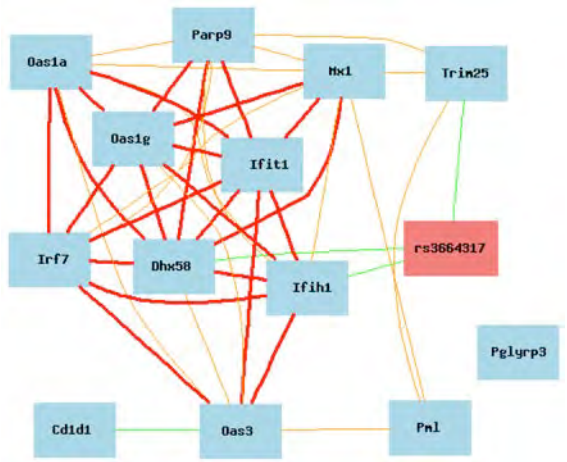

Figure 10 Correlation network of associations between a BXD genotype at 63.9 Mb on Chr 2 (rs3664317) and genes with eQTLs mapping near this locus. Correlations with Pearson's correlation > 0.7 (red), > 0.5 (orange), and < -0.5 (green) are shown.

cis-eQTL is believed to be found within the gene itself or to otherwise directly impact the expression of the gene. *Trans*-eQTLs, in contrast, are thought to result from an indirect mechanism. For example, a genetic variant located within the promoter region of gene A (*i.e.*, a *cis*-eQTL) may directly impact expression of gene A. If the expression of gene A, then, affects the expression of genes B and C, the genetic variant would also be in indirect factor (i.e., a *trans*-eQTL) that explains the variation in expression of genes B and C. As we investigated the eQTL mapping results, we found that *trans*-eQTLs were not evenly distributed across the genome. While the density of *trans*-eQTLs across the majority of the genome was low, there were several loci that contained several *trans*-eQTLs. For example, only 2 genes had a *trans*-eQTL that mapped to Chr 1 from 0-138 Mb, while 9 genes had a *trans*-eQTL that mapped to Chr 1 from 138-161 Mb. We identified a total of 9 genomic locations containing at least one *cis*-eQTL and at least three *trans*-eQTLs for the selected immune related genes. These 9 locations are promising starting points for modeling of immune gene networks in the spleen. Here, we will focus our discussion on creating models for two locations: Chr 2 near 65 Mb and Chr 17 near 35 Mb.

Modeling of impact of genetic variation on Chr 2 near 65 Mb:
Our first gene network model will investigate the impact of genetic variations at Chr 2 near 65 Mb on gene expression of immune related genes. One gene, *Ifih1*, located at 62.4 Mb on Chr 2 was regulated by a *cis*-eQTL at this location (**Figure 9**), and 12 genes had a *trans*-eQTL with LRS >= 15 at Chr 2 between 62 and 68 Mb. The genes with *trans*-eQTLs were highly correlated with one another and with *Ifih1* (**Figure 10**). The first step in creating a Bayesian network model is selecting the variables to include in the model. We selected the BXD genotype at rs3664317 (63.9 Mb on Chr 2) and *Ifih1* expression as two variables to include in the network. We removed genes that had low LRS values, low expression, low variance across strains, or a small difference in expression between the parental strains of the BXD mice. Of the genes with *trans*-eQTLs, we selected *Ifit1*, *Oas1a*, and *Oas1g*.
We then used our Bayesian network modeling pipeline to learn the structure of the gene network model. We have described our structure learning method previously. Briefly, we perform model averaging of the posterior probability of possible features (*i.e.*, directed edges) in the model over all possible models and include features with a posterior probability greater than 0.5 to include in the network. Our structure learning procedure allows for prior knowledge to be

included in the network by requiring that specific features are either included or excluded from the network structure. For example, if a regulatory relationship among genes is known, only network structures that include this relationship will be included in the network. Here, we prevented *Ifih1*, the *cis*-regulated gene, from being the child of any of the *trans*-regulated genes. **Figure 11** shows the structure of the gene network model of the Chr 2 eQTL. Some interesting relationships can be observed in the structure of the network. First, the genotype at rs3664317 influences the expression of *Ifih1* in all high scoring networks, as expected, but the genotype only influences the expression of the *trans*-regulated genes indirectly (i.e., *Ifih1* masks the influence of the genotype on the *trans*-regulated genes). Additionally, the network shows that there is a strong influence of the expression of *Ifih1* on *Ifit1* and *Oas1g* on *Oas1a*. We performed parameter learning as described previously and assessed the model using leave-one-out cross validation. The values of Q^2 for predictions of the expression of *Ifih1*, *Ifit1*, *Oas1g*, and *Oas1a* using leave-one-out cross validation were 0.43, 0.66, 0.70, and 0.76, respectively.

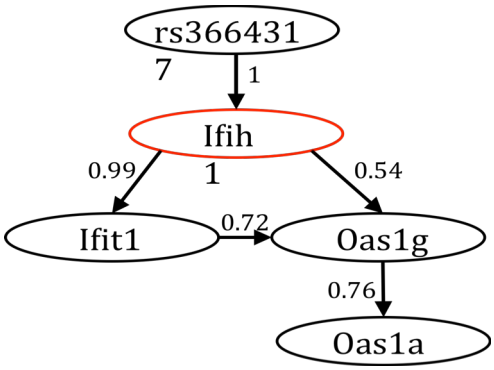

Figure 11 Structure of the Bayesian network model of influence of genetic variation at Chr 2 near 65 Mb on the expression of immune related genes. The number next to each directed edge of the BN indicates the confidence in the edge after model averaging as described in the text. *Cis*-regulated genes are shown in red.

Modeling of impact of genetic variation on Chr 17 near 35 Mb:
In contrast to the Chr 2 locus which contained only a single gene with a strong *cis*-eQTL, a locus on Chr 17 near 35 Mb contained several eQTLs for both *cis*- and *trans*-regulated immune related genes. Specifically, 17 and 15 probesets were regulated by *cis*- and *trans*-eQTL, respectively, located between 33 and 38 Mb on Chr 17 with an LRS > 15. The majority of the *cis*-regulated genes were related to the histocompatibility complex, including, for example, *H2-K1*, *H2-Oa*, and *H2-Q6*. Except for *H2-Ea-ps*, all of the *cis*-regulated genes were highly correlated with each other; *H2-Ea-ps* had higher expression in strains with the D allele at this locus, while the other H2 genes had higher expression in strains with the B allele. To reduce the amount of data needed to examine the *cis*-regulated genes and, potentially, reduce the noise in the data obtained from single probesets, we used principal component analysis tools that are available in the GeneNetwork to select the first principal component (PC1) of the H2 genes with *cis*-eQTLs at this locus, excluding *H2-Ea-ps*. PC1 had a highly significant eQTL at Chr 17 near 35 Mb, and we, therefore, used PC1 in our network modeling. While investigating the *trans*-regulated genes to select genes for use in building gene network models, we observed that 3 chemokine receptor genes (*Cxcr3*, *Ccl19*, *Cx3cr1*) had *trans*-eQTLs at Chr 17 near 35 Mb and included these genes in the model. Finally, we included rs13482958, which is located at 34.5 Mb on Chr 17, as the genotype node in the network. We used no restrictions when performing network structure learning.

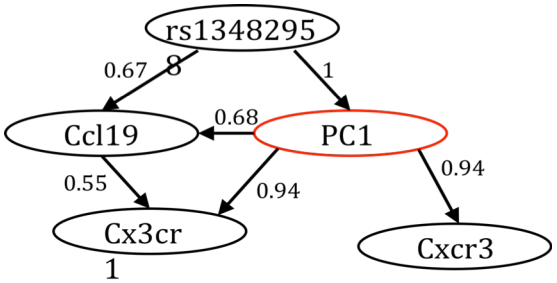

Figure 12 Structure of the Bayesian network model of influence of genetic variation at Chr 17 near 35 Mb on the expression of immune related genes. The number next to each directed edge of the BN indicates the confidence in the edge after model averaging as described in the text. PC1 is the first principal component of a cluster of histocompatibility complex genes that are located near rs13482958 and regulated by a *cis*-eQTL

Figure 12 shows the structure of the gene network model for genes regulated by the Chr 17 locus. In contrast to the behavior found for the for the Chr 2 locus (**Figure 11**), the effect of the genotype at the locus on all

of the *trans*-regulated genes is not masked by the expression of the *cis*-regulated genes, as *Ccl19* is the direct child of the genotype node. This result may be due to *Ccl19* being influenced by a specific *cis*-regulated gene whose expression was not sufficiently captured by PC1. We performed leave-one-out cross validation to evaluate the network. The values of Q^2 for predictions of PC1, *Ccl19*, *Cxcr1*, and *Cxcr3* were 0.69, 0.51, 0.46, and 0.38, respectively.

Key Research Accomplishments

Developed integrated method for Bayesian network structure learning, parameter learning, cross-validation, and prediction of effects of external interventions.
Implemented this method in the Bayesian Network Webserver, an easy-to-use tool for network modeling of systems genetics data
Created Bayesian network model connecting *Ctrq3* genotype with disease status in BXD mice after infection with *Chlamydia psittaci*
Used the model to predict the effects of an external intervention, specifically macrophage depletion, and experimentally verified many of these predictions
Found that genetic influence on of *Chlamydia* disease in strains with the resistant D genotype was a function of both increased resistance to and tolerance of high pathogen loads
Created gene network models of immune-related genes in the spleens of BXD mice

Reportable outcomes

Presentations

1. **Poster presentation** at the UT-ORNL-KBRIN Bioinformatics Summit, Cadiz, KY, USA, 2010. Linking genotype to phenotype with Bayesian network modeling of *Chlamydia infection*.
2. **Oral Presentation** at the 10th Annual UT-ORNL-KBRIN Bioinformatics Summit, Memphis, TN, USA, 2011. Ziebarth JD, Cui Y, Miyairi I. Using hybrid Bayesian network models to link genotype with phenotype in infectious diseases.

Publications

1. Ziebarth JD, Li B, **Miyairi I, Cui Y**. 2010. Linking genotype to phenotype with Bayesian network modeling of *Chlamydia infection*. BMC Bioinformatics 11(Suppl 4):P19
2. **Miyairi I**, Laxton J, Ziebarth J, **Williams R**, **Lu L**, **Byrne G**, **Cui Y**. Systems Genetics Analysis of *Chlamydia psittaci* infection. 2010. Proc. 12th Int. Symposium on Human Chlamydial infections, Schachter et al eds, pp 197-200, June 20-25, Hof bei Salzburg, Austria.
3. Bao L, Xia X, **Cui Y**. 2010. Expression QTL Modules as Functional Components Underlying Higher-Order Phenotypes. PLoS ONE 5(12): e14313.
4. **Miyairi I**, Ziebarth J, Laxton JD, Wang X, van Rooijen N, **Williams RW**, **Lu L**, **Byrne GI**, **Cui Y**. 2012. Host genetics and Chlamydia disease: prediction and validation of disease severity mechanisms. PLoS ONE 7(3): e33781.
5. Ziebarth J, Bhattacharya, A, **Cui, Y**. Bayesian Network Webserver: a comprehensive tool for biological network modeling. Submitted to Bioinformatics

Website

Bayesian Network Webserver (BNW http//compbio.uthsc.edu/BNW)

Conclusions

We have developed a comprehensive workflow for Bayesian network modeling of system genetics data and implemented this workflow in the *Bayesian Network Webserver*, to enabling network modeling for future investigation of responses to infectious diseases and other biological problems by our group, as well as the larger research community. We successfully employed the methods used in *BNW* to investigate differential susceptibility to infection with *Chlamydia psittaci* and differences in immune gene expression in BXD mice. We experimentally validated several of the predictions made by the *Chlamydia* model and, also, found that the resistant genotype was associated with both increased resistance to and tolerance of high pathogen loads after infection.

References

1. Boettcher, S. G., and C. Dethlefsen. 2003. deal: a package for learning Bayesian networks. J Stat Soft **8**:1-40.
2. Hartemink, A. J., D. K. Gifford, T. S. Jaakola, and R. A. Young. 2001. Using graphical models and genomic expression data to statistically validate models of genetic regulatory networks. Pac Symp Biocomput.
3. Hawkins, D. M., S. C. Basak, and D. Mills. 2003. Assessing model fit by cross-validation. J Chem Inf Comput Sci **43**:579-86.
4. MacMicking, J. D., G. A. Taylor, and J. D. McKinney. 2003. Immune control of tuberculosis by IFN-gamma-inducible LRG-47. Science **302**:654-59.
5. Miyairi, I., V. R. Tatireddiagar, O.S. Mahdi, L. A. Rose, R. J. Belland, L. Lu, R. W. Williams, and G. I. Byrne. 2007. The p47 GTPases Iigp2 and Irgb10 regulate innate immunity and inflammation to murine Chlamydia psittaci infection. J Immunol **179**:1814-24.
6. Murphy, K. 2001. The Bayes Net Toolbox for Matlab. Comp Sci Stat
7. Nelson, D. E., D. P. Virok, H. Wood, C. Roshick, R. M. Johnson, W. M. Whitmire, D. D. Crane, O. Steele-Mortimer, L. Kari, G. McClarty, and H. D. Caldwell. 2005. Chlamydial IFN-gamma immune evasion is linked to host infection tropism. Proc Natl Acad Sci U S A **102**:10658-63.
8. Pe'er, D. 2005. Bayesian network analysis of signaling networks: a primer. Sci STKE **2005**:pl4.
9. Silander, T., and P. Myllymaki. 2006. A simple approach for finding the globally optimal Bayesian network structure. Proceedings of the Converence in Artificial Intelligence (UAI2006), **2006**:445-52.
10. Tian, J., R. He, and L. Ram. 2010. Bayesian model averaging using the k-best Bayesian network structures. Proceedings of the Conference on Uncertainty in Artificial Intelligence (UAI2010) **2010**:589-97.

List of Personnel supported by the Grant between 06/1/2009 and 06/30/2013

Personnel	**Role**
Gerald I. Byrne	Principal Investigator
Mark A. Miller	Co-Investigator
Robert W. Williams	Co-Investigator
Lu Lu	Co-Investigator
Yan Cui	Co-Investigator
Kui Li	Co-Investigator
James E. Bina	Co-Investigator
Fabio Re	Co-Investigator
Isao Miyairi	Co-Investigator
Tony A. Marion	Co-Investigator
Mark Bix	Co-Investigator (St Jude)
Jacco Boon	Co-Investigator (St Jude/Washington University, St Louis)
Olaimatu S Mahdi	Project Manager
Xiaowen Renee Bina	Research Faculty
Jennifer M. Stabenow	RBL Facility Manager
Baoming Lin	Post-doctoral fellow
Jesse Dylan Ziebarth	Post-doctoral fellow
Himangi R. Jayakar	Post-doctoral fellow
Lishi Wang	Post-doctoral fellow
Li Lui	Post-doctoral fellow
Yang Shen	Post-doctoral fellow
Ky Van Hoang	Post-doctoral fellow
Laura Barrio Diaz	Post-doctoral fellow
Hossam Aly Abdelsamed	Post-doctoral fellow
Dahai Wei	Post-doctoral fellow
Jonathan Laxton	Research Assistant
Sarah Hasty	Research Assistant
Jyothi Parvathareddy	Research Assistant
Sandra N. Lester	Graduate student
Daniel R. Wells	Summer student

Personnel in bold were supported for the entire duration of the grant

List of presentations

1. **Oral presentation** at the BXD world meeting in Braunschweig, Germany, 2009, “H5N1 pathogenesis and the role of host genetic diversity” (**Boon**).
2. **Seminar** at Washington University School of Medicine, St Louis, MO, Feb-2010, “H5N1 pathogenesis and the role of host genetic diversity” (**Boon**).
3. **Seminar** at University of Maryland, College Park, MD, March-2010, “H5N1 pathogenesis and the role of host genetic diversity” (**Boon**).
4. **Poster presentation** at the UT-ORNL-KBRIN Bioinformatics Summit, Cadiz, KY, USA, March 19-21, 2010. Ziebarth JD, Li B, **Miyairi I**, **Cui I**. “Linking genotype to phenotype with Bayesian network modeling of *Chlamydia infection*”.
5. **Oral Presentation** at the UT-ORNL-KBRIN Bioinformatics Summit, Cadiz, KY, USA, 2010. Wang X, Agarwala R, Capra JA, Chen Z, Church DM, Cioanu DC, Li Z, **Lu L**, Mazhui K, Mulligan MK, Nelson SF, Pollard KS, Taylor WL, Thomason DB, **Williams RW**. “High-throughput sequencing of the DBA/2J mouse genome”.
6. **Seminar** at St Louis University, Infectious Disease Research Conference, St Louis, MO, April 2011, “H5N1 pathogenesis and the role of host genetic diversity” (**Boon**)
7. **Seminar** at Emory University, Microbiology and Molecular Genetics Seminar, Atlanta, GA, October 2011. “H5N1 pathogenesis and the role of host genetic diversity” (**Boon**).
8. **Seminar** at Washington University School of Medicine, Department of Medicine, Division of Pulmonary Medicine, Lung Biology and Genetics conference, St Louis, GA, April 2011. “H5N1 pathogenesis and the role of host genetic diversity” (**Boon**).
9. **Oral Presentation** at the 10th Annual UT-ORNL-KBRIN Bioinformatics Summit, Memphis, TN, USA, 2011. Ziebarth JD, **Cui Y**, **Miyairi I**. “Using hybrid Bayesian network models to link genotype with phenotype in infectious diseases”.
10. **Poster Presentation** at UTHSC A.A-St Jude Research Lectureship and Medical Student Poster Session, 2011. Wodowski A, Jayakar H, Parvathareddy J, Bina XR, **Bina JE**, **Miller MA**. 2011. “Visualization of Intranasal Dosing Efficiency Using Luminescent *Francisella tularensis*”.
11. **Poster Presentation** at the International Toll 2012 Meeting: Decoding Innate Immunity. Riva del Garda, Italy, May 4-7, 2011. Ceballos-Olveda I, Sahoo M, **Bina JE**, **Miller MA**, **Re F**. “Role of inflammasome-dependent cytokines IL-1β and IL-18 during mouse ling infection with virulent *Francisella tularensis* SchuS4”
12. **Poster Presentation** at the International Toll 2012 Meeting: Decoding Innate Immunity. Riva del Garda, Italy, May 4-7, 2011. Sahoo M, Ceballos-Olveda I, **Bina JE**, Miller MA, Re F. “Critical role of the NLRC4 inflammasome and IL-18 during mouse lung infection with virulent *Burkholderia pseudomallei*”.
13. **Poster Presentation** at Regional Centers for Excellence Meeting. Llewellen AC, Zhao J, Song F, Flynn K, Xu Q, Napier BA, **Bina JE**, Cotter PA, Swanson MS, **Miller MA**, Raetz CRH, Weiss DS. 2012. “A novel conserved deacytylase required for lipid A modification and *Francisella* virulence”.
14. **Poster Presentation** at UTHSC A.A-St Jude Research Lectureship and Medical Student Poster Session, 2012. “Host Genetic Loci Correlating with Differential Innate Immune Responsiveness to *Acinetobacter baumannii* infection”.

List of Abstracts/Conference Proceedings resulting from DoD grant support (2009 – present)

1. **Boon J**, **Lu L**, **Williams R**, Webby R. H5N1 pathogenesis and the role of host genetic diversity. The BXD World International Meeting on BXD Phenotyping, Braunschweig, Germany, Nov 30 – Dec 1, 2009.
2. **Miyairi I**, **Lu L**, **Williams RW**, **Byrne GI**. Genetic susceptibility to acute and chronic Chlamydia infection. The BXD World International Meeting on BXD Phenotyping, Braunschweig, Germany, Nov 30 – Dec 1, 2009.
3. **Boon A**, Debeauchamp J, Webby R. Systems Biology Approach to H5N1 Influenza A virus Pathogenesis. Options for the Control of Influenza VII, Hong Kong SAR, China, Sep 3-7, 2010.
4. Ceballos-Olveda I, Sahoo M, **Bina JE**, **Miller MA**, **Re F**. Role of inflammasome-dependent cytokines IL-1β and IL-18 during mouse ling infection with virulent *Francisella tularensis* SchuS4. In: Proceedings of the International Toll 2012 Meeting, Decoding Innate Immunity, Riva del Garda, Italy, May 4-7, 2011.
5. Sahoo M, Ceballos-Olveda I, **Bina JE**, **Miller MA**, **Re F**. Critical role of the NLRC4 inflammasome and IL-18 during mouse lung infection with virulent *Burkholderia pseudomallei*. In: Proceedings of the International Toll 2012 Meeting, Decoding Innate Immunity, Riva del Garda, Italy, May 4-7, 2011.
6. Wang X, Mulligan MK, Mozhui K, **Lu L**, Chen Z, Nelson SF, Taylor WL, and **Williams RW**. Comparison of variant detections using whole genome sequencing of the DBA/2J mouse strain. The 10th Annual Complex Trait Consortium (CTC) Meeting, Washington DC, USA, June 22-25, 2011.
7. Wodowski A, Jayakar H, Parvathareddy J, Bina XR, **Bina JE**, **Miller MA**. 2011. Visualization of Intranasal Dosing Efficiency Using Luminescent *Francisella tularensis*. In: Proceedings of UTHSC A.A-St Jude Research Lectureship and Medical Student Poster Session, 2011.
8. Llewellen AC, Zhao J, Song F, Flynn K, Xu Q, Napier BA, **Bina JE**, Cotter PA, Swanson MS, **Miller MA**, Raetz CRH, Weiss DS. 2012. A novel conserved deacytylase required for lipid A modification and *Francisella* virulence. In: Proceedings of the Regional Centers for Excellence Meeting, 2012.
9. Sneed A, Parvathareddy J, Emery FD, **Cui Y**, **Williams R**, **Miller MA**. Host Genetic Loci Correlating with Differential Innate Immune Responsiveness to *Acinetobacter baumannii* infection. In: Proceedings of UTHSC A.A-St Jude Research Lectureship and Medical Student Poster Session, 2012.

Abstract Form

The BXD World
International Meeting on BXD Phenotyping

November 30 – December 1, 2009

Title H5N1 pathogenesis and the role of host genetic diversity

---

Authors Jacco Boon, Lu Lu, Robert Williams, Richard Webby

Text (max. 250 words)

Despite the prevalence of H5N1 influenza viruses in global avian populations, the number of human cases is comparatively few. Although viral factors almost certainly play a role in limiting human infection and disease, it is likely that host genetics contribute substantially. Indeed, a better understanding of the role of host factors in the infectious process is an important goal for controlling and treating infectious agents of all types. To investigate host factors in the context of influenza infection we determined the 50% mouse lethal dose (MLD50) of the H5N1 virus (A/Hong Kong/213/03 (HK213)) in sixteen inbred mouse strains. The maximum MLD50 differences between the strains were 5-logs for HK213. Disease severity following HK213 infection was associated with differences in replication kinetics and a higher production of pro-inflammatory cytokines. Recombinant inbred BXD strains, derived from DBA/2J (susceptible to infection) and C57BL/6 (resistant to infection) mice were utilized to map survival to 3 quantitative trait loci. Analysis of gene expression of lung tissue from infected and uninfected resistant and susceptible mouse strains identified several candidate genes as host components modulating the infectious process.

Please fill out the form, save the document on your computer and send as e-mail attachment or Fax to:

Mrs. Sylvana Foth
Dept. of Experimental Mouse Genetics,
Helmholtz Centre for Infection Research,

Fax ++49-531-6181-1199
E mail: BXD@helmholtz-hzi.de

Abstract

The BXD World
International Meeting on BXD Phenotyping

November 30 – December 1, 2009

Title : Genetic susceptibilty to acute and chronic Chlamydia infection.

Authors Isao Miyairi, Lu Lu, Robert W. Williams, and Gerald I. Byrne.

Text (max. 250 words)

Reports suggest susceptibility to Chlamydia in animal models is dependant on the model being studied. We previously showed that two p47GTPases; Irgb10 and Irgm2 encoded on Chr11 (ctrq3) confer a 10000 fold difference in susceptibility to C57BL6J and DBA2J in an acute systemic (i.p.) Chlamydia psittaci infection model. Subsequent analysis of peak pathogen load and weight in BXD strains also reveal the ctrq3 locus in defining susceptitibility. Twenty BXD strains that survive beyond the first week of infection were followed until 30 days post infection and their spleen weight and Chlamydia load was measured by quantitative PCR. Results reveal a 2.5 log fold variation in Chlamydia load. QTL analysis of Chlamydia load reveals a significant LRS of 33.57 at Chr17 corresponding to the MHC class II locus and suggestive LRS of 16.53 at both Chr9 and Chr11 (not ctrq3). Trait correlations of the load and spleen weight was significant at r=0.855 (p=8.21E-17). Results demonstrate the important factor of timing in defining susceptibility factors to the dynamic process of infectious diseases

Systems Biology Approach to H5N1 Influenza A virus Pathogenesis

Adrianus Boon[1], Jennifer Debeauchamp[1], Richard Webby[1]
[1] St Jude Children's Research Hospital, Memphis, TN, USA

The genotype of the host has been implicated in the severity of and susceptibility to influenza A virus infections. The exact mechanism and genetic polymorphisms responsible are currently unknown and require a systems biology approach to uncover. Earlier work on recombinant inbred BXD mice, derived from resistant C57BL/6 and susceptible DBA/2 mouse strains, identified three genomic loci, known as *Qivr* (QTL for influenza virus resistance), that were associated with resistance to severe highly pathogenic H5N1 disease and mortality. In a second genetic screen we used chromosomal substitution strains (CSS) derived from C57BL/6 and another susceptible mouse strain, A/J, in which a single chromosome of C57BL/6J is substituted with the homologous chromosome of A/J. Of the nineteen CSS strains tested, C57BL/6J-Chr. 4 A/J and C57BL/6J-Chr. 17 A/J were significantly more susceptible to highly pathogenic H5N1 influenza A virus than the parental C57BL/6J, indicating that genetic polymorphisms on these chromosomes are responsible for the increased susceptibility of A/J mice. The increased susceptibility of C57BL/6-Chr. 4 A/J mice was associated with higher virus titers at days 2, 7 and 9 post infection and increased expression of IFN-b1 and type I interferon induced proteins like Ptx3. To help identify the genetic polymorphism within the newly identified *Qivr* on Chr. 4, we have produced a series of congenic mouse strains containing C57BL/6 x A/J chimeras of chromosome 4. Preliminary analysis suggests that the polymorphism is located between 39 and 135Mb on chromosome 4. In conclusion, the application of systems biology to H5N1 pathogenesis has yielded significant results that will allow us to identify essential host proteins involved in resistance to severe influenza disease.

Role of inflammasome-dependent cytokines IL-1b and IL-18 during mouse lung infection with virulent *Francisella tularensis* SchuS4

Ivonne Ceballos-Olvera, Manoranjan Sahoo, James E. Bina, Mark A. Miller, and Fabio Re

Department of Microbiology, Immunology, and Biochemistry, The University of Tennessee Health Science Center, Memphis, TN 38163

Francisella tularensis (Ft), a gram-negative facultative intracellular bacterium, is the etiologic agent of tularemia and a category A bioterrorism agent. Several studies have shown that the innate immune response to Ft infection is primarily mediated by activation of TLR2, by bacterial lipoproteins, and of caspase-1, through the AIM2 inflammasome, leading to secretion of bioactive IL-1b and IL-18. However, most of these studies were conducted using attenuated *Francisella* strains while relatively few studies have examined the innate immune response to the virulent SchuS4 Ft strain. We have examined the role of the inflammasome and characterized the functions of the proinflammatory cytokines IL-1b and IL-18 in mice that were infected intranasally with either the attenuated LVS or the virulent SchuS4 strains of Ft. Our results show that IL-1RI-, IL-18-, and IL-1RI/IL-18-deficient mice are more susceptible to Ft infection than the inflammasome-deficient mice. This was likely due to infammasome-independent generation of IL-1b and IL-18 in the lungs of infected mice. We also demonstrate that IL-18 plays a role in the very early phase of the infection through its induction of IFNg. The function of IL-1 appears to be required at later time points and is essential for development of a protective adaptive response mediated by Th17 cells.

Critical role of the NLRC4 inflammasome and IL-18 during mouse lung infection with virulent *Burkholderia pseudomallei*

Manoranjan Sahoo, Ivonne Ceballos-Olvera, James E. Bina, Mark A. Miller, and Fabio Re

Department of Microbiology, Immunology, and Biochemistry, The University of Tennessee Health Science Center, Memphis, TN 38163

Burkholderia pseudomallei (Bp), a Gram-negative flagellated bacterium that is capable of replicating in macrophages, is the etiologic agent of the disease melioidosis and a category A bioterrorism agent. Little is known about the interaction of Bp with the host innate immune system. It has been shown that TLR4 and TLR5 are activated during infection with Bp and that the type III secretion apparatus of Bp activates the NLRC4 inflammasome in vitro. However, the role of the inflammasome and of the proinflammatory cytokines IL-1b and IL-18 during melioidosis in mice has not yet been investigated. Here we showed that Bp infection of the lung leads to NLRC4-dependent production of IL-1b and IL-18. Mice deficient in the inflammasome components ASC, caspase-1, and NLRC4, but not NLRP3, were dramatically more susceptible to lung infection with Bp. Analysis of IL-1RI- and IL-18-deficient mice infected with Bp revealed that IL-18 is essential for survival. The primary role of IL-18 during melioidosis appears to be the induction of IFNg production. In contrast, the survival of infected IL-1RI-deficient mice was undistinguishable from that of wild type mice indicating that IL-1 does not play a prominent role in the pathogenesis of melioidosis.

Comparison of variant detection using whole genome sequencing of the DBA/2J mouse strain

Xusheng Wang[1], Megan K. Mulligan[1], Khyobeni Mozhui[1], Lu Lu[1], Zugen Chen[2], Stanley F. Nelson[2], William L. Taylor[1], Robert W. Williams[1]

1. University of Tennessee Health Science Center, Memphis TN 38163
2. University of California, Los Angeles CA 90095

Introduction

Next Generation Sequencing (NGS) technology is now widely used to detect sequence and structural variants. Here we ask how coverage depth and platform affect the rate of detection of major classes of variants.

Results

We generated ~58X coverage for the DBA/2J genome using Illumina GAII and HiSeq2000 systems and ~42X using ABI SOLiD. We used six paired end libraries with insert lengths from 200 to 4,000 bp, and aligned against the C57BL/6J genome. We detected 4.16 million SNPs using Illumina and 4.09 M using SOLiD, of which 3.38 M SNPs were common. Unshared SNPs were validated 93% of the time by resequencing with a total yield (~99.7% true) of 4.87 M between strains. Each platform detects an large cohort of unique SNPs (15% per platform). We detected 0.56 M and 0.22 M indels using Illumina and SOLiD, respectively. Only 0.11 M were common. Finally, we identified 5,600 and 8,800 structural deletions using Illumina and SOLiD or which only 1,223 were common. An analysis of Illumina subsamples at 10, 20, 30, 40, and 55X demonstrates that platforms can rapidly reach a premature SNP detection asymptote that cannot be overcome simply by higher coverage. Indel and CNV detection is more challenging and even at 100–120X we appear to be far from a ~~"full~~ disclosure" on sequence variants even in these two strains. As is true for SNPs, each platform detects unique and genuine subsets of indels and CNVs. This incompleteness problem is compounded by the fact that assembly is biased by using a C57BL/6J scaffold and limitations of approaches used to detect variants.

Conclusion

Sequencing data from multiple platforms with high coverage will be necessary for the next few years to extract the majority of variants, particularly large structural variants.

Methods

Genomic DNA was isolated from liver of two DBA/2J females. We sequenced DNA using ABI SOLiD and Illumina GA2/Hiseq2000 platforms. GA2/Hiseq2000 reads were paired-end 100 bp-long whereas SOLiD reads were mate-paired and 25 and 50 bp-long. We also generated an amplification-free Illumina sequencing-library, which enables us much improve de novo assembly of GC-biased regions and thereby detect more variants.

●***Mapping and alignment***
Reads were mapped to the C57BL/6J reference mouse genome (mm9) using MAQ and the SOLiD Corona Lite Pipeline for GA2 and SOLiD reads, respectively.

●***Single nucleotide polymorphisms (SNPs) calling***
SNPs from GA2/Hiseq2000 data sets were identified by MAQ SNP calling with a minimal read depth of 3 and a minimum consensus quality scores of 30 (P < 10E-3). SNPs from SOLiD data sets were also detected with a minimal read depth of 3 and a stringent confidence value of 0.5.

●***Insertions and deletions***
Indels were detected by MAQs and ABI Corona pipeline for GA2/ Hiseq2000 and SOLiD data sets, respectively. Large deletions (1 bp – 10 kb) and medium-sized insertions (1 – 86 bp) were detected using GA2/HiSeq2000 reads. Smaller insertions (1 – 11 bp) and deletions (1 - 36 bp) were detected using 50 bp SOLiD reads .

●***Copy number variants (CNVs)***
Copy number variants were analyzed using an event-wise testing (EWT) method that is based on read depth and significance testing A common method was used for both platforms.

●***Variants detection at different levels of coverage***
We generated 55X coverage using Illumina. We divided data into 10, 20, 30, 40 and 55X coverage—lane by lane—to detect SNPs, indels, and CNVs as described above. The sum of all variants detected using the combined 100X coverage was used as a reference against which subsamples were evaluated.

Summary of sequencing data for the DBA/2J genome

Summary of sequencing data

Platform	ABI SOLiD	Illumina GA2
Run number	15	3
Read Length	25 bp / 50 bp	100 bp
Clone insert size	1k to 4k	200 bp
Mapped reads	3.06 billion	1.43 billion
Mapped nucleotides	108 billion	153 billion
Coverage	~ 42X	~58X

Assumed C57BL/6J reference genome size is 2.6 Gb. Read depth was determined by calculating all mapped nucleotides divided by the size of mouse genome.

Distribution of coverage

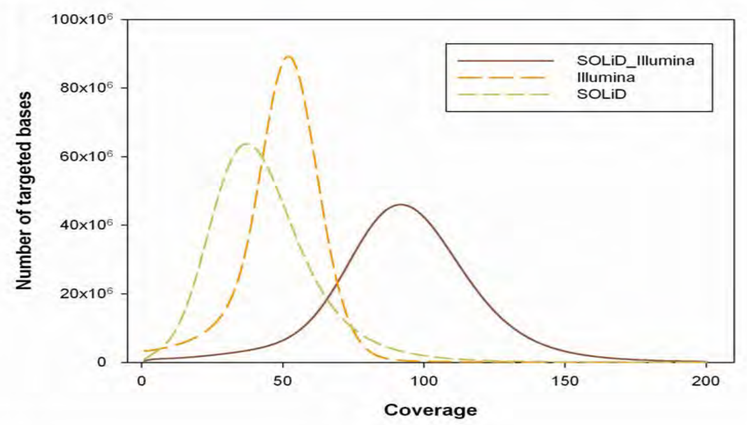

Variants comparison between SOLiD and Illumina

SNPs

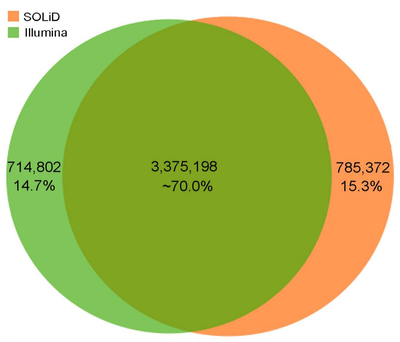

Genomes of DBA/2J and C57BL/6J differ from each other at 4.875 million SNPs

Platform	N SNPs	False Positive
SOLiD	4,160,570	0.44%
Illumina	4,090,000	0.65%

Insertions

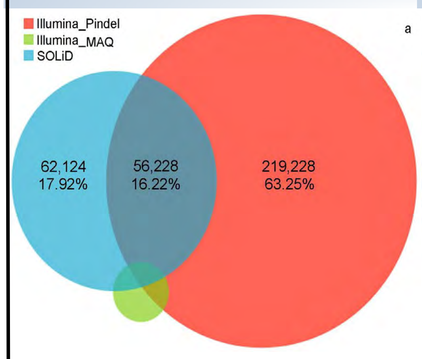

Deletions

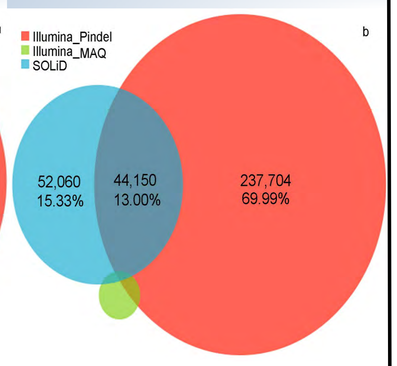

More than half of indels were detected exclusively by Illumina , whereas ~15% were detected exclusively by SOLiD.

Variants detection at different levels of coverage

SNPs

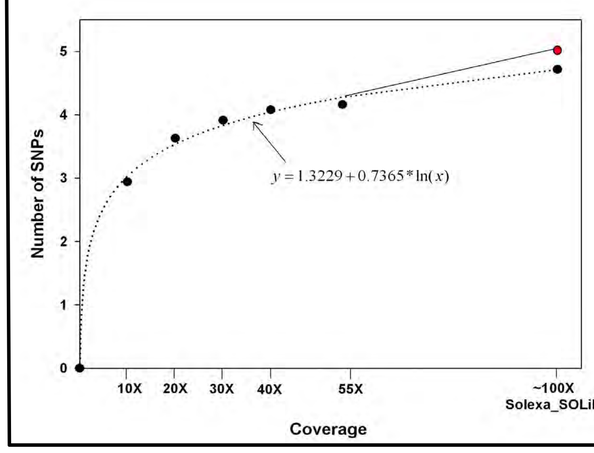

SNP summary:
1. A total number of 4.875 million SNPs were detected by combining Illumina and SOLiD data (red dot).
2. We estimate that 100X Illumina data would detect 4.71 million SNPs (black dot).
3. 98% at SNPs are detected at 40X.

Insertions

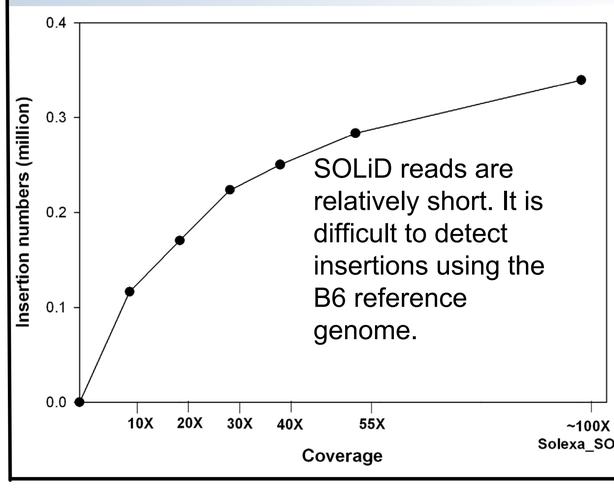

SOLiD reads are relatively short. It is difficult to detect insertions using the B6 reference genome.

CNVs

Loss

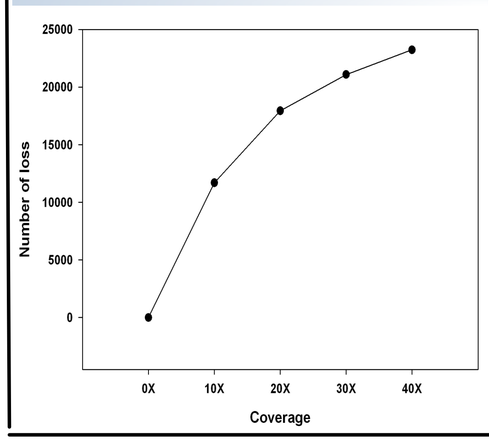

Gain

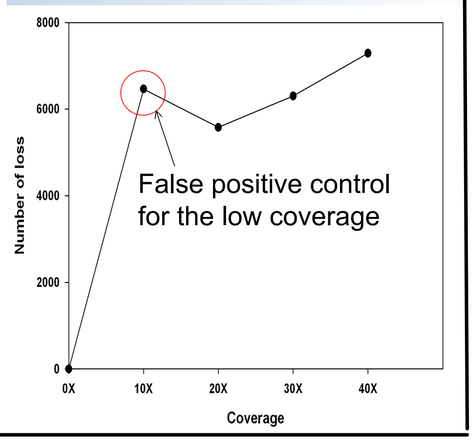

Deletions

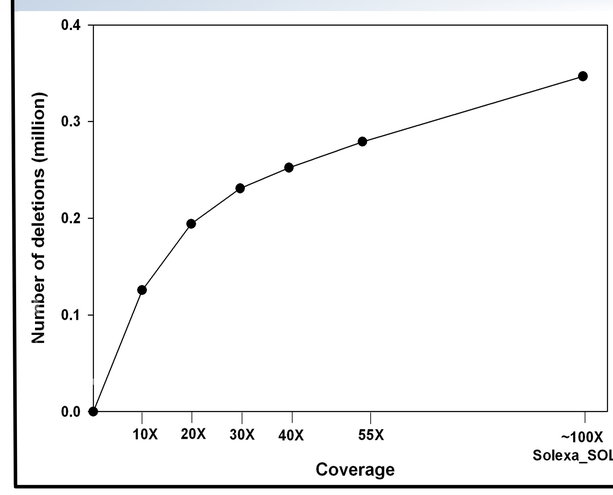

Acknowledgments

This work supported by the UT Center for Integrative and Translational Genomics and grants from NIAAA Integrative Neuroscience Initiative on Alcoholism (U01AA13499, U24AA13513 and U01AA014425).

Visualization of Intranasal Dosing Efficiency Using Luminescent *Francisella tularensis*

Mark A. Miller *PhD, Himangi Jayakar PhD, Jyothi Parvathareddy, Xiaowen R. Bina PhD,* ***James E. Bina*** *PhD, University of Tennessee Health Science Center, Memphis, TN*

OBJECTIVE: Administration of drugs, vaccine candidate, and/or pathogenic challenges to mice via the intranasal route is a widely used experimental procedure. However, there is a paucity of published literature describing the efficiency of intranasal dosing. We have hypothesized that a luminescent murine model of *Francisella tularensis* live vaccine strain (FTLVS) infection would allow visualization and evaluation of the efficiency of intranasal dosing.

STUDY DESIGN: FTLVS was transformed with a novel reporter plasmid (pXB173-lux) that constitutively expresses the *Photorhabdus luminescens lux* operon from a *Francisella* promoter. We evaluated the ability of FTLVS to retain the reporter plasmid when grown in the absence of antibiotic selection *in vitro* and *in vivo*. Individual bacterial colonies plated from either serially passaged broth cultures or the spleens of infected mice (over a five-day period), were scored for light production. We then used FTLVS bearing the luminescent reporter plasmid to determine the ideal bolus volume for intransal delivery of liquid suspensions into the lungs. Mice were challenged with FTLVS-pXB173-lux (1×10^6 CFU) in a total volume of 5µl, 10µl, 25µl, or 50µl of vehicle per nare. Whole-animal live IVIS imaging was then performed to visualize dissemination of luminescent bacteria in real-time.

RESULTS: Transformation of FTLVS with the pXB173-lux vector rendered FTLVS luminescent, and the vector was retained at a relatively high rate by the bacteria during both *in vitro* and *in vivo* growth. Dosing experiments using luminescent bacteria and IVIS whole-animal imaging yielded convincing visual evidence that intranasal administration of bacteria in volumes of 5-10 µl/nare initiated an upper airway infection but failed to efficiently deliver bacteria into the lungs. However, dosing in a volume of 25-50 µl/nare results in pulmonary delivery of the bacteria. These images also revealed that an upper airway infection with FTLVS failed to disseminate to the lungs.

CONCLUSION: Intranasal administration of mice with an FTLVS suspension in a dose volume of 5 µl/nare typically resulted in infection of the upper airways but very inefficient delivery into the pulmonary compartment. Efficient delivery of an FTLVS suspension into the lungs via the intranasal route requires a dose volume of approximately 25 µl/nare.

EMAIL CONTACT: awodowsk@uthsc.edu

This project was made possible by NIH grant #U54 AI057157 from the Southeastern Regional Center of Excellence for Emerging Infections and Biodefense, by NIH grants AI074582, AI079482, and AI061260, and by Department of Defense Army grant W81XHW-05-1-0227

Host Genetic Loci Correlating with Differential Innate Immune Responsiveness to *Acinetobacter baumannii* infection

Andrew Sneed, Jyothi Parvathareddy, Felicia D. Emery, Yan Cui PhD, Robert A. Williams PhD, and Mark A. Miller PhD, University of Tennessee HSC (Department of Microbiology, Immunology & Biochemistry)

Abstract

Acinetobacter baumannii has become one of the most important causes of nosocomial infections, and as such, this bacterial pathogen is of serious public health concern. Infections with this opportunistic organism are difficult to treat because *Acinetobacter* encodes a wide array of antibiotic resistance genes. Although *Acinetobacter* causes some maladies that are rather benign, it can also cause high morbidity/mortality illnesses that include pneumonias, wound infections, and bacteremic disease.

Our goal is to use a murine model of *Acinetobacter* infection to gain a better understanding of the interactions between this bacterium and its hosts. Preliminary studies revealed that *Acinetobacter* infection elicits phenotypically distinct innate immune responses in C57BL/6J and DBA/2J mice. Therefore, we decided to utilize a powerful mouse genetics resource (that was developed by Dr. Robert Williams and colleagues here at the UTHSC) to elucidate the host gene network that controls innate immune responses to *Acinetobacter*. This genetics resource consists of a panel of fully genotyped recombinant inbred mice that were derived from the C57BL/6J and DBA/2J parental inbred strains (commonly referred to as BXD mice) and a powerful array of complementary computer-based modeling approaches collectively known as the GeneNetwork. Using these resources, we have performed preliminary interval mapping that has identified a locus on chromosome 10 that appears to correlate with the differential recruitment of immune cells to the lungs following pneumonic infection with *Acinetobacter*. We have also identified a number of additional phenotypic differences in the innate immune responses produced by the parental mouse strains that can be used as readouts for interval mapping studies in BXD mice. These readouts include several cytokines that are differentially expressed in the lung compartment following infection. Preliminary studies using these readouts have identified genetic loci on chromosomes 6, 14, and 19 that correlate well with the production of several cytokines during the innate immune response to *Acinetobacter* infection.

These results form the foundation for work that will significantly increase our understanding of the interactions between *Acinetobacter* and its hosts. Moreover, these studies could facilitate a much better global understanding of the multifactorial events that result in innate immune cell recruitment to the lungs following pneumonic bacterial infection.

Contact
asneed1103@gmail.com

This project was made possible by DoD/US Army Grant W81XHW-05-1-0227.

List of Publications resulting from DoD grant support (2009 – 2013)

1. Clinton SR, Bina JE, Hatch TP, Whitt MA, **Miller MA.** 2010. Binding and activation of host plasminogen on the surface of *Francisella tularensis*. BMC Microbiol10:76.
2. Bina XR, **Miller MA**, **Bina JE**. 2010. Construction of a bioluminescence reporter plasmid for *Francisella tularensis***.** Plasmid 64(3):156-61., PMID: 20620161, PMCID: PMC2943566
3. **Boon AC**, Debeauchamp J, Krauss S, Rubrum A, Webb AD, Webster RG, McElhaney J, Webby RJ. 2010. Cross-reactive neutralizing antibodies directed against pandemic H1N1 2009 virus are protective in a highly sensitive DBA/2 influenza mouse model. J. Virol. 84:7662-7.
4. Clementz MA, Chen Z, Banach BS, Wang Y, Sun L, Ratia K, Baez-Santos YM, Wang J, Takayama J, Ghosh AK, **Li K**, Mesecar AD, Baker SC. 2010. Deubiquitinating and interferon antagonism activities of coronavirus papain-like proteases. J. Virol. 84:4619-4629.
5. **Miyairi I**, Laxton J, Ziebarth J, **Williams R**, **Lu L**, **Byrne G**, **Cui Y**. 2010. Systems Genetics Analysis of *Chlamydia psittaci* Infection. Proc. 12th Int. Symposium on Human Chlamydial Infections, Schachter et al eds, pp 197-200, June 20-25, Hof bei Salzburg, Austria.
6. Ziebarth JD, Li B, **Miyairi I, Cui I**. 2010. Linking genotype to phenotype with Bayesian network modeling of *Chlamydia infection*. BMC Bioinformatics 11(Suppl 4):P19.
7. Wang X, Agarwala R, Capra JA, Chen Z, Church DM, Ciobanu DC, Li Z, **Lu L,** Mozhui K, Mulligan MK, Nelson SF, Pollard KS, Taylor WL, Thomason DB, **Williams RW**. 2010. High-throughput sequencing of the DBA/2J mouse genome. BMC Bioinformatics 11(Suppl 4):O7
8. Bao L, Xia X and **Cui Y**. 2010. Expression QTL modules as functional components underlying higher-order phenotypes. PLoS ONE. 5(12): e14313
9. Jayakar HR, Parvathareddy J, Fitzpatrick EA, Bina XR, **Bina JE**, Re F, Emery FD, **Miller MA**. 2011. A *galU* Mutant of *Francisella tularensis* is Attenuated for Virulence in a Murine Pulmonary Model of Tularemia. BMC Microbio. 11:179. PMID:21819572 PMCID: PMC3173336.
10. **Boon ACM**, Finkelstein D, Sheng M, Liao G, Allard J, Klumpp K, Webster R, Peltz G, Webby RJ. 2011. H5N1 Influenza Virus Pathogenesis in Genetically Diverse Mice Is Mediated at the Level of Viral Load. mBio 2(5):e00171-11.
11. Alberts R, **Lu L**, **Williams RW**, Schughart K. 2011. Genome-wide analysis of the mouse lung transcriptome reveals novel molecular gene interaction networks and cell-specific expression signatures. Respiratory Research 12:61
12. Ceballos-Olvera I, Sahoo M., **Miller MA**, del Barrio L, **Re F**. 2011. Inflammasome-dependent pyroptosis and IL-18 protect against *Burkholderia pseudomallei* lung infection while IL-1b is deleterious detrimental. PLoS Path. 7(12): e1002452. *PMID- 22241982*
13. Sun L, Xing Y, Chen X, Zheng Y, Yang Y, Nichols DB, Clementz MA, Banach BS, **Li K**, Baker SC, and Chen Z. 2012. Coronavirus papain-like proteases negatively regulate antiviral innate immune response through disruption of STING-mediated signaling. PLoS ONE 7:e30802.
14. **Miyairi I**, Ziebarth J, Laxton JD, Wang X, van Rooijen N, **Williams RW**, **Lu L**, **Byrne GI**, **Cui Y**. 2012. Host genetics and Chlamydia disease: prediction and validation of disease severity mechanisms. PLoS ONE 7:e33781.
15. **Miller MA**, Stabenow JM, Parvathareddy J, Wodowski AJ, Fabrizio TP, Bina XR, Zalduondo L, **Bina JE**. 2012. Visualization of intranasal dosing efficiency using luminescent *Francisella tularensis*.: effect of instillation volume and form of anesthesia. PLoS ONE; 7(2):e31359. PMID:22384012.

16. **Byrne GI,** Beatty WL. 2012. Chlamydial Persistence Redux. In: M. Tang, P.M. Bavoil (ed). Intracellular Pathogens I *Chlamydiales*. ASM Press, Washington DC, pp 265-284.
17. Napier BA, Meyer L, **Bina JE**, **Miller MA**, Sjostedt A, Weiss DS. 2012. Link between intraphogosomal biotin and rapid phagosomal escape in Francisella. Proc Natl Acad Sci USA 109(44):18084-9. PMID: 23071317 PMCID:PMC3497780.
18. Llewellyn AC, Zhao J, Song F, Parvathareddy J, Xu Q, Napier BA, Laroui H, Merlin D, **Bina JE**, Cotter PA, **Miller MA**, Raetz CRH, Weiss DS. 2012. NaxD is a deacetylase required for lipid A modification and *Francisella* pathogenesis. Molecular Microbiology 86(3):611-627.
19. Nedelko T, Kollmus H, Klawonn F, Spijker S, **Lu L**, Heszmann M, Alberts R, **Williams RW**, Schughart K. 2012. Distinct gene loci control the host response to influenza H1N1 virus infection in a time-dependent manner. BMC Genomics 13:411, PMID: 22905720 PMCID: PMC3479429
20. Abdelsamed H, Peters J, **Byrne GI**. 2013. Genetic Variation in *Chlamydia trachomatis* and their Hosts: Impact on Disease Severity and Tissue Tropism. Future Microbiology. In press.

Clinton et al. BMC Microbiology 2010, 10:76
http://www.biomedcentral.com/1471-2180/10/76

BMC Microbiology

RESEARCH ARTICLE Open Access

Binding and activation of host plasminogen on the surface of *Francisella tularensis*

Shawn R Clinton, James E Bina, Thomas P Hatch, Michael A Whitt, Mark A Miller*

Abstract

Background: *Francisella tularensis* (FT) is a gram-negative facultative intracellular coccobacillus and is the causal agent of a life-threatening zoonotic disease known as tularemia. Although FT preferentially infects phagocytic cells of the host, recent evidence suggests that a significant number of bacteria can be found extracellularly in the plasma fraction of the blood during active infection. This observation suggests that the interaction between FT and host plasma components may play an important role in survival and dissemination of the bacterium during the course of infection. Plasminogen (PLG) is a protein zymogen that is found in abundance in the blood of mammalian hosts. A number of both gram-positive and gram-negative bacterial pathogens have the ability to bind to PLG, giving them a survival advantage by increasing their ability to penetrate extracellular matrices and cross tissue barriers.

Results: We show that PLG binds to the surface of FT and that surface-bound PLG can be activated to plasmin in the presence of tissue PLG activator *in vitro*. In addition, using Far-Western blotting assays coupled with proteomic analyses of FT outer membrane preparations, we have identified several putative PLG-binding proteins of FT.

Conclusions: The ability of FT to acquire surface bound PLG that can be activated on its surface may be an important virulence mechanism that results in an increase in initial infectivity, survival, and/or dissemination of this bacterium *in vivo*.

Background

Francisella tularensis (FT) is a Gram-negative intracellular pathogen that is the etiological agent of a multi-syndromic disease with a high morbidity/mortality that is referred to as tularemia. The pneumonic form of tularemia is of particular concern because of the high mortality rate (up to 60%) following inhalation of as few as ten organisms [1-4]. *Francisella* species are found throughout the Northern Hemisphere and infect a variety of vertebrate and invertebrate hosts [5,6]. Infections with FT can be contracted from blood sucking insects, such as the deer fly [5,7], mosquitoes [8,9], and ticks [5,7,10], and by open-wound contact with infected animal tissue [5,11,12].

Upon entry into a susceptible vertebrate host, FT is readily phagocytized by resident macrophages and dendritic cells and quickly escapes into the cytoplasm [13,14] where it multiplies. Late in its replicative cycle, FT induces apoptotic death of the host phagocyte, resulting in release of progeny bacteria that can infect new host cells. Recent studies have shown that significant numbers of FT are found in the acellular plasma fraction of mice infected intradermally or intranasally with either FT Live Vaccine Strain (LVS) (Type B) or FT Schu S4 (Type A) [15], and intranasally with FT *novicida* [16]. These findings suggest that, in addition to utilizing the intracellular cytoplasmic niche for replication and protection from humoral immunity, FT may also have a significant extracellular phase. Several studies have shown that deposition of host complement component C3 on the surface of FT is required for opsonophagocytosis by activating CR3 and CR4-mediated phagocytosis by macrophages and dendritic cells [14,17,18]. It is also known that FT is relatively resistant to complement-mediated lysis [19]. A recent report suggested that resistance of FT to membrane attack complex-mediated lysis may be due (at least in part) to its ability to bind to factor H from host plasma [20]. It is possible that the ability of FT to bind to factor

* Correspondence: mamiller@uthsc.edu
Department of Molecular Sciences, The University of Tennessee Health Science Center, 858 Madison Avenue, Memphis, Tennessee 38163, USA

H and potentially to other host plasma components plays a significant role in its pathogenesis.

It has been long established that a broad spectrum of both gram-positive and gram-negative bacterial pathogens gain a survival advantage by interacting with components of the host coagulation/fibrinolytic system in humans [21-24]. For instance, the ability to acquire surface-associated plasmin has been documented as an important virulence mechanism in Group A streptococci [25], *Borrelia burgdorferi* [26], and *Yersinia pestis* [27] by aiding in the organism's ability to penetrate the extracellular matrix and to disseminate to distal sites in the host. Plasminogen (PLG) is a 92-kDa glycoprotein zymogen that is involved in fibrinolysis. This precursor protein is converted to an active serine protease (plasmin) by cleavage of the peptide bond between residues $R^{560}$and V^{561} *in vivo* via urokinase-type (uPA) and/or tissue-type (tPA) PLG activators. Plasmin has an important role in blood clot resolution because of its role in the degradation of fibrin polymers. Because plasmin has other substrates that include pro-collagenases, pro-metalloproteinases, and extracellular matrix proteins, such as fibronectin, laminin, and vitronectin, the ability of a bacterium to acquire surface-associated plasmin can result in an enhanced ability of the pathogen to penetrate the extracellular matrix and to disseminate to distal sites in the host [21,23,25]. In this report we show that PLG binds to the surface of FT *in vitro* and that surface-bound PLG can be converted to the active plasmin form. In addition, using a combination of Far-Western blotting analyses coupled with proteomic methodologies, we have identified several FT proteins that can bind to human PLG *in vitro*.

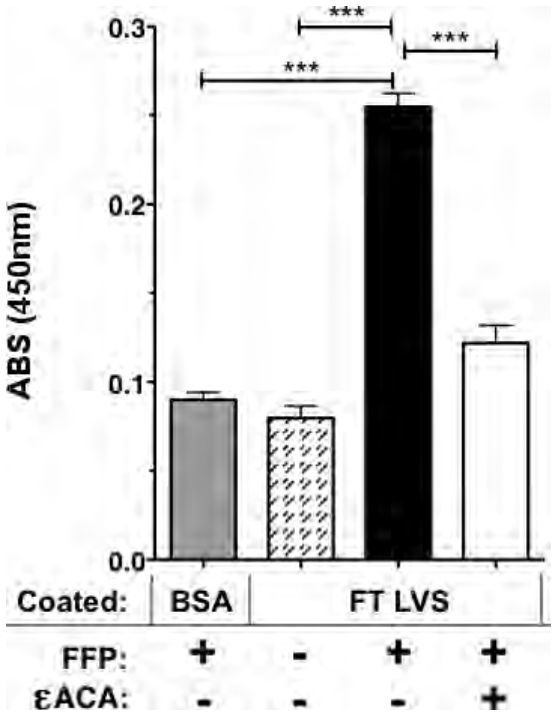

Figure 1 FT binds to PLG from human plasma. FTLVS cultured to mid-log phase in BHI broth were bound to wells of microtiter plates and then incubated for 1 hour with fresh frozen human plasma (FFP) in the presence or absence of 100 mM ε-amino caproic acid (εACA), a PLG-binding inhibitor. A modified ELISA was performed to measure FTLVS-bound PLG. The results shown are representative of 3 experiments of similar design. Bars indicate +/- SEM in triplicate. Statistical analysis was performed via one-way ANOVA using a Dunnett's Multiple Comparison post-test (*** P < .001).

Results

Binding of PLG from fresh human plasma to the surface of FTLVS

We used an ELISA assay to determine that PLG in fresh frozen plasma (FFP) binds to FTLVS grown to mid-log phase in BHI (Figure 1). Binding was inhibited when ε-aminocaproic acid (εACA), known to inhibit binding of PLG to lysine groups in proteins, was included in the incubation mixture. To help eliminate the possibility of non-specific binding of PLG due to its high concentrations in human plasma and also to rule out the contributions of other plasma proteins, we used purified human Glu-PLG (huPLG) and noted similar results to those observed when FFP was used (Figure 2A). We also found that huPLG binds to the highly virulent Schu S4 strain of FT at moderately higher levels than observed with FTLVS (Figure 2B). We confirmed that binding of huPLG to FT is a lysine-dependent interaction by showing that increasing concentrations of εACA can inhibit binding of huPLG to FTLVS in a dose-dependent fashion (Figure 3). When similar concentrations of glycine were used as an inhibitor control, no inhibition of huPLG binding was observed (data not shown). Confocal microscopic analyses suggested that huPLG binds to the surface of FT (Figure 4); however, it is possible that some of the staining observed was the result of huPLG penetration into the outer envelope of FT. Although is has been reported that culture media composition can have a significant impact of the surface properties and virulence characteristics of FTLVS [28], we observed no differences in the ability of PLG to bind to the surface of FTLVS grown in modified Mueller-Hinton medium vs. brain-heart infusion broth (data not shown).

Plasmin activation on the surface of FT LVS *in vitro* by a PLG activator

In other bacterial systems, surface-bound PLG can be converted to its proteolytically active plasmin form that contributes to the organism's virulence [21-24]. To test whether huPLG bound to FTLVS can be converted to plasmin, we used a chromogenic plasmin substrate

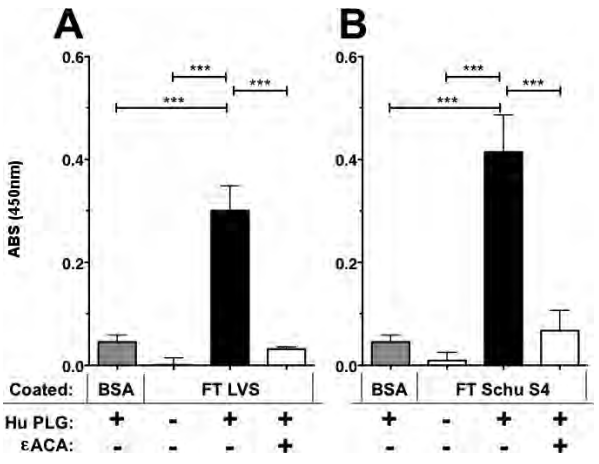

Figure 2 Purified huPLG binds to FTLVS and FTSchuS4. FTLVS (**Panel A**) and FTSchuS4 (**Panel B**) were bound to microtiter wells and incubated for 2 hours with purified huPLG (3 μg/ml) in the presence or absence of 10 mM εACA). A modified ELISA was performed to measure FTLVS-bound huPLG. The results shown are representative of four (**Panel A**) and one (**Panel B**) experiments, respectively, of similar design. Bars indicate +/- SEM in triplicate. Statistical analysis was performed via one-way ANOVA using a Dunnett's Multiple Comparison post-test (*** $P < .001$).

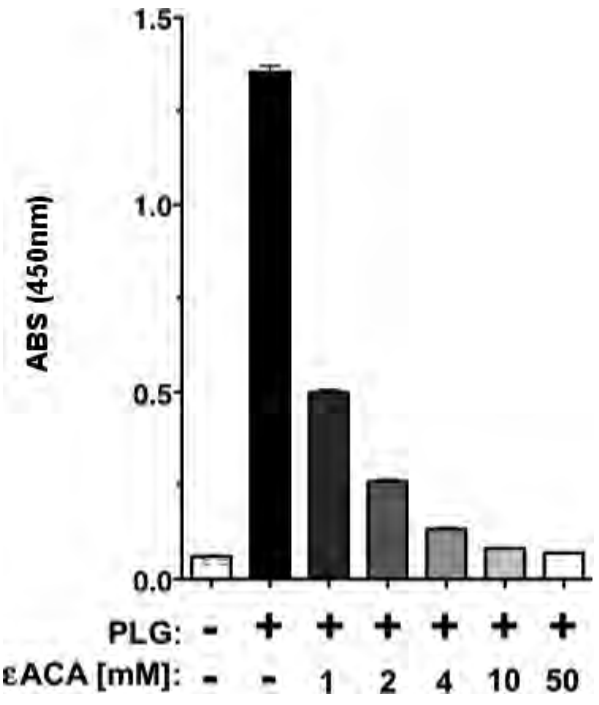

Figure 3 εACA inhibits huPLG binding to FT in a dose-dependent fashion. FTLVS was coated onto microtiter plate wells and incubated for 2 hours with purified huPLG (3 μg/mL) in the presence or absence of titrated concentrations of εACA. The results shown are representative of 3 experiments of similar design. Bars indicate +/- SEM in triplicate. Statistical analysis performed via one-way ANOVA using a Kruskal-Wallis test determined a p-value of < 0.0001.

(H-D-Val-Leu-Lys-pNA) to detect proteolytic activity following the addition of tissue PLG activator (tPA) (Figure 5). We also found that plasmin on the surface of FT can break down fibronectin (Figure 6), suggesting that FT-bound plasmin can potentially participate in the degradation of extracellular matrices.

Identification of putative *Francisella* PLG-binding membrane proteins

We used Far-Western Blot methodology and mass spectrometry to identify potential PLG receptors in the Sarkosyl soluble and insoluble FTLVS membrane fractions (Figure 7). Sarkosyl is a weak anionic detergent in which many outer membrane proteins of Gram-negative bacteria are insoluble [29]. We transferred the Sarkosyl-treated proteins to a PVDF membrane and incubated the membrane with PLG and identified bound PLG by reaction with anti-PLG mAbs (Figure 7a). We used the relative migration rates of the reactive bands to identify the reactive proteins on a duplicate Coomassie-stained polyacrylamide gel (Figure 7b), which were then excised for proteomic analysis by mass spectrometry. Several prominent PLG-binding proteins were noted in the total membrane fraction of FTLVS, all but one of which was found in the Sarkosyl insoluble fraction (Figure 7b). The identity of the prominent proteins from this assay (Figure 7c) are the products of the following genes: FTL_1328 (outer membrane associated protein, fopA1), FTL_1042 (FKBP-type peptidyl-prolyl cis-trans isomerase family protein), FTL_0336 (peptidoglycan-associated lipoprotein), FTL_0421 (hypothetical lipoprotein, lpn-A), and FTL_0645 (hypothetical lipoprotein).

Discussion

Until recently FT has been considered an intracellular pathogen whose dissemination to tissues distal to the site of initial infection was highly dependent on its ability survive within host macrophages. The observation that FT can be found in relatively high numbers in the acellular plasma fraction of its mammalian host [15,16] suggested that FT may have a significant extracellular component to its life cycle and that interactions between FT and one or more plasma proteins could contribute to its ability to disseminate within the host. There are a number of examples of bacterial pathogens that utilize interactions with host plasma components to enhance their ability to colonize and to penetrate the extracellular matrices of host cells/tissues. A wide range of bacterial pathogens (including *Francisella*) subvert the destructive mechanisms of the complement cascade by acquiring surface-bound complement control proteins [20,30-34]. Moreover, a number of Gram-positive bacterial pathogens including *streptococcal* spp. [35,36], *staphylococcal* spp. [37-40], and *Bacillus anthracis* [41,42],

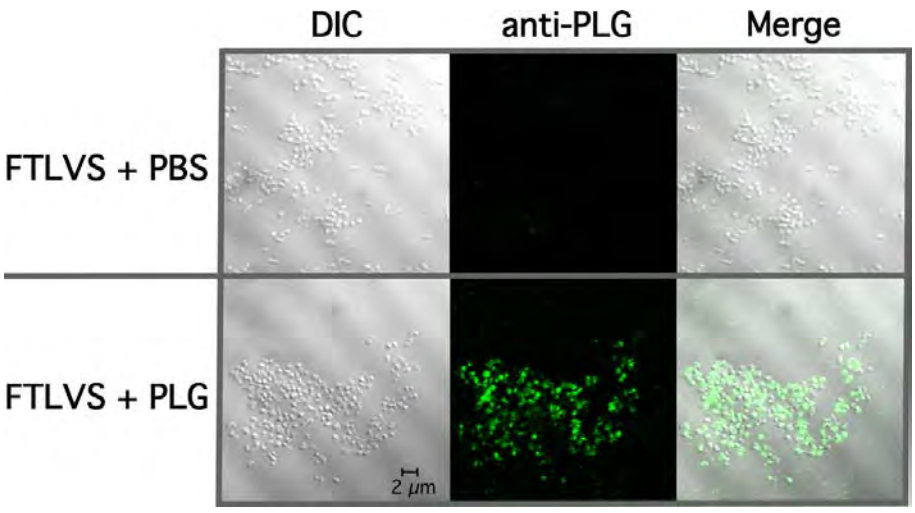

Figure 4 PLG binds to the outer envelope of FT. Laser scanning confocal microscopy of PLG-associated FTLVS was performed as described in "Materials and Methods". Bound huPLG ligand was detected using sheep anti-human PLG antibody followed by incubation with Dylight-488 conjugated donkey, anti-sheep/goat IgG secondary antibody. Samples were visualized using a Zeiss LSM 510 confocal microscope.

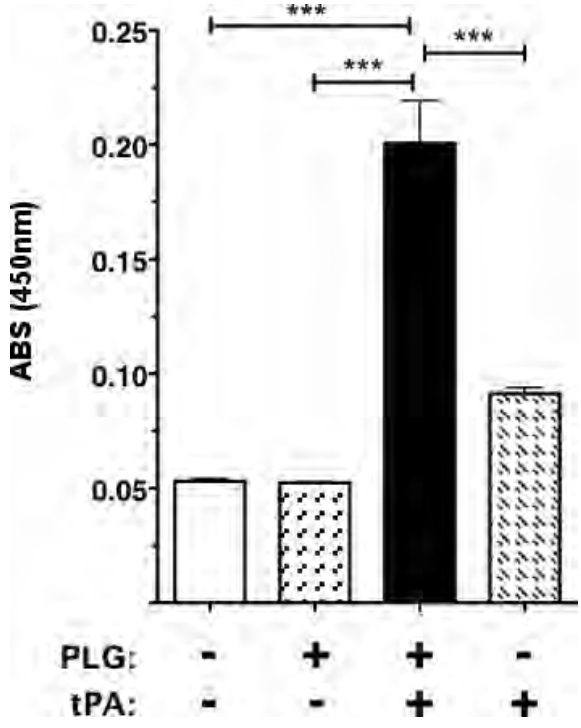

Figure 5 FT surface-bound huPLG can be converted to plasmin. FTLVS was incubated with huPLG at a concentration of 96 μg/mL. After removal of unbound huPLG, a chromogenic plasmin substrate (D-VLK-pNA), tissue PLG activator (tPA), or both were then added to test the proteolytic ability of each sample preparation. Conversion of the chromogenic substrate was measured by comparison of Δ405 nm. The results shown are representative of 3 experiments of similar design. Bars indicate +/- SEM in triplicate. Statistical analysis was performed via one-way ANOVA using a Dunnett's Multiple Comparison post-test (*** $P < .001$).

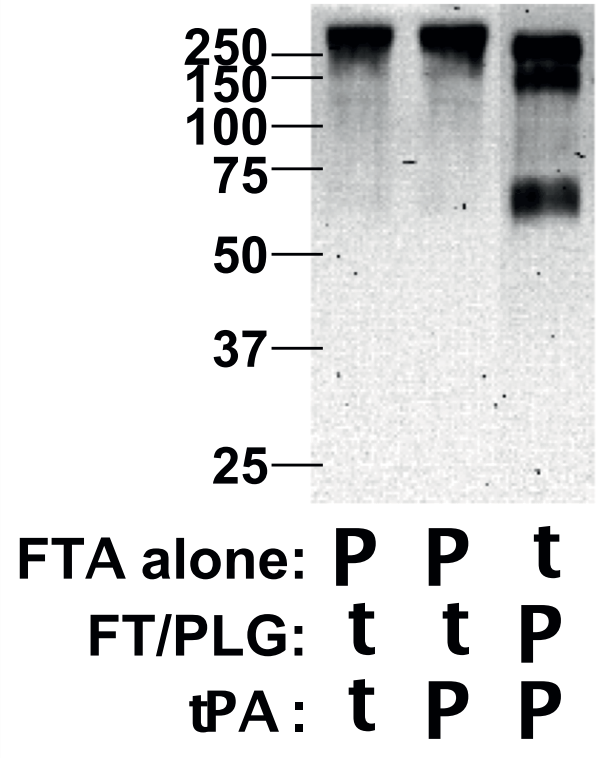

Figure 6 Fibronectin is a substrate for plasmin bound to FT. FTLVS (10^9 CFU) were incubated with 100 μg of huPLG and 0.5 μg tissue tPA for 1 hour at 37°C. After removal of unbound huPLG and tPA, 3 μg fibronectin was added and allowed to incubate for 24 hours at 37°C. Supernatant from each preparation were separated by SDS-PAGE and transferred to PVDF membrane. Degradation of fibronectin was detected by Western blot analysis as described in "Materials and Methods".

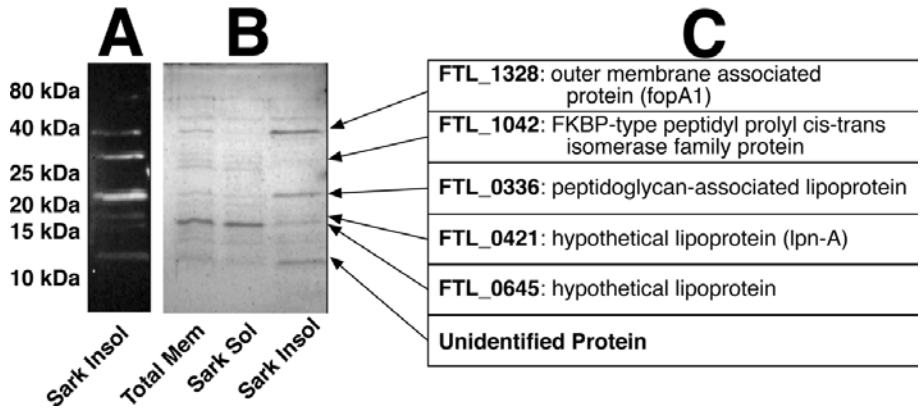

Figure 7 Identification of putative PLG-binding proteins of FT. Sarkosyl-soluble and insoluble protein fractions of FTLVS were separated by SDS-PAGE and transferred to PVDF membrane. Membranes were then blotted with huPLG (3 ug/mL) followed by anti-PLG antibody and HRP-conjugated secondary antibody to detect PLG-binding proteins (**Panel A**). Protein bands on an identical Coomassie Blue-stained SDS-PAGE gel corresponding to those identified via blotting (**Panel B**) were excised and identified using proteomic methodologies (**Panel C**).

as well as Gram-negative bacteria such as *Pseudomonas aeruginosa* [43] have been shown to augment their invasive capacity by interacting with fibrinogen, fibronectin, and/or PLG. *Yersinia pestis* is probably the best-characterized example of a pathogen that exploits the host fibrinolytic system to penetrate host tissues. *Yersinia* expresses a surface serine protease (designated Pla) whose substrates include several complement components, PLG, and alpha2-antiplasmin (the primary circulating inhibitor of plasmin). Pla also has adhesin activity and binds to laminin (a glycoprotein of mammalian basement membranes). Because Pla upregulates plasmin activity, and because laminin is a substrate of plasmin, *Yersinia* can very efficiently penetrate basement membranes of host tissues [for review, see Suomalainen et. al. [44]]. Clearly, interaction with plasma components is a strategy that is used by many bacterial pathogens to gain a survival advantage within their hosts.

The goal of the studies described here was to determine whether FT has the potential to use the host fibrinolytic system (specifically PLG) to enhance its ability to penetrate/disseminate following infection of a mammalian host. Our results indicate that both FTLVS and FTSchuS4 are able to acquire surface bound PLG *in vitro* and that this zymogen can be converted by a host-derived PLG activator into its active serine protease form (plasmin) while bound to FTLVS. The ability of PLG to bind its ligands typically involves its lysine-binding kringle domains. This specific interaction between PLG and exposed lysine residues can be inhibited with the lysine-analogue εACA and, to a lesser extent, with free lysine. Our findings revealed that binding of PLG to the surface of FTLVS could be inhibited by εACA in a dose-dependent fashion. Moreover, we showed that plasmin bound to the surface of FT could degrade fibronectin. This finding supports our hypothesis that the ability of FT to bind to serum plasmin may enhance its ability to penetrate extracellular matrices, enhancing its ability to disseminate *in vivo*.

Using a ligand-blotting technique coupled with proteomic methodologies we identified five FTLVS proteins that were able to bind to PLG, each of which are highly conserved among the various FT type A and B strains. Three of these proteins are lipoproteins (gene products of FTL_0336, FTL_0421, and FTL_0645). Two of the lipoproteins are unique to FT, while the third, peptidoglycan-associated lipoprotein (PAL), is highly conserved among gram-negative bacteria. The specific use of surface-exposed lipoproteins as receptors for host PLG is not unusual and has been well documented in other human bacterial pathogens, such as some members of the genus *Borrelia* and *Treponema*. Several members of the genus *Borrelia* use complement regulator-acquiring surface proteins (CRASP) to bind both PLG and complement factor H to aid in the ability of the organism to both disseminate and to resist innate immunity [45-50]. An additional example of a PLG-binding lipoprotein is OppA of *Treponema denticola*, which has been suggested to play a role in periodontal disease in humans [51]. With this in mind, there lies the possibility that lipoproteins of *Francisella* species may have the capacity to bind multiple host-derived proteins in addition to PLG.

Here we have shown that FT can bind to PLG and that surface-bound PLG can be activated by tPA to its proteolytic form (plasmin). The binding of PLG on the surface of FT could play a role in several phases of tularemia, including the initial entry into the host through insect bites and/or broken skin where active fibrinolytic processes would provide an early

opportunity for FT to acquire proteolytic activity that might augment the establishment or dissemination of infection. During later phases of tularemia the acquisition of plasmin on the cell surface may contribute to its pathogenicity by degrading host innate effector molecules and extracellular matrix components. Based on the new report that FT-bound plasmin can degrade immunoglobulins [52], as well as the established ability of FT to acquire surface-bound factor H [20], it also appears likely that FT uses plasma components to interfere with host humoral immune mechanisms throughout the course of FT infection. Future studies to identify additional plasma components that can be surface acquired by FT may uncover additional virulence mechanisms used by this pathogen during its extracellular life cycle.

Conclusions

FT interacts with at least two serum components (plasmin, and complement factor H), and it seems likely that FT also uses interactions with additional host serum components to gain a survival advantage. Our lab is examining FT interactions with additional targets, including fibrinogen and fibronectin, both of which are substrates for plasmin and are host components that are known to be exploited by numerous pathogens for adhesion to and penetration of extracellular matrix layers. The interaction of FT with host serum components may play a significant role in the survival and dissemination of this highly pathogenic bacterium. Gaining a better understanding of these interactions could be a critical step in the development of therapeutic and prophylactic interventions for tularemic disease.

Methods

Bacterial strains and culture

F. tularensis Live Vaccine Strain (FTLVS) was a kind gift of Dr. Karen Elkins (FDA, Bethesda, MD). FT Schu S4 was obtained from the CDC. All bacterial cultures were grown overnight in Brain-Heart Infusion broth (37 g/L, pH 6.8) from frozen stocks at 37°C with shaking to mid-log phase (OD_{600} = ~0.7) before use.

Reagents

Human fresh frozen plasma (FFP) was purchased from Lifeblood Mid-South Regional Blood Center (Memphis, TN). Purified human Glu-PLG (huPLG), human single-chain tissue PLG activator (tPA), and the plasmin colorimetric substrate (H-D-Val-Leu-Lys-pNA) were purchased from Molecular Innovations (Novi, MI). Bovine serum albumin (fraction V) was purchased from Thermo-Fisher Scientific (Pittsburgh, PA). Polyclonal sheep anti-human PLG, anti-human fibronectin, and donkey anti-sheep/goat IgG:Dylight-488 antibody preparations purchased from AbD Serotec (Raleigh, NC). Monoclonal anti-goat/sheep IgG-horseradish peroxidase conjugated secondary antibody (clone GT-34) and ε-aminocaproic acid (A7824) were purchased from Sigma-Aldrich (St. Louis, MO). Ninety-six well MAXISORP ELISA plates were purchased from Nunc (Rochester, NY).

PLG binding ELISA assays

FTLVS was cultured overnight to mid-log phase, pelleted at 6,400 × g for 30 minutes, washed twice with phosphate-buffered saline (PBS), and resuspended in PBS with 0.1% Na azide to an OD_{600} = 0.1. The resulting bacterial suspension was added to microtiter plates (100 μL/well; approximately 2.5×10^8 bacterial cells) before being incubated overnight at 4°C to facilitate binding. The wells were then washed twice with 200 μL of Tris-buffered saline (TBS) pH 7.45 containing 0.05% Tween-20 (TBST) to remove unbound bacteria and then pre-blocked with 200 μL of TBST containing 1% bovine serum albumin (1% BSA-TBST) for 1 hour at RT° to prevent non-specific protein binding. After removal of the blocking solution, 90% citrated human plasma or 3 μg/mL huPLG in 1% BSA-TBST was added to each well (100 μL), with or without the indicated concentrations of ε-amino caproic acid (εACA), and incubated for 1-2 hours at 37°C with gentle rocking. Wells were washed three times with TBST and then sheep anti-human PLG-specific antibody (1:2,000 dilution in 1% BSA-TBST) was added (100 μL/well) and allowed to incubate for 1 hour at 37°C. Unbound primary antibodies were removed by washing three times with TBST, followed by the addition of HRP-conjugated anti-sheep/goat IgG mAb (GT-34, 1:5,000 dilution in 1% BSA-TBST; 100 μL/well) and incubation for 1 hour at 37°C. Unbound secondary antibodies were removed by washing four times with TBST, and OptEIA TMB colorimetric substrate solution (Becton-Dickenson, Franklin Lakes, NJ) was added to each well (100 μL/well) and incubated at 37°C for 20 min. to allow color development. Absorbance at 450 nm was determined using a SpectraMAX 340 plate reader (Molecular Devices, Sunnyvale, CA).

Indirect immunofluorescence assays

FTLVS was cultured and washed as described above. After diluting the washed bacteria to OD_{600} = 0.1, 1 mL aliquots were incubated with a total of 40 μgs of PLG or PBS (negative control) for 30 minutes at 37°C with gentle rotation. Bacteria were then washed three times with PBS by centrifugation, resuspended in 100 μL of PBS, followed by spotting 20 μL of each sample onto glass coverslips. The samples were then air-dried overnight at 37°C. After methanol fixation, the coverslips were blocked with 1% BSA-PBS at room temperature before adding sheep anti-human PLG (1:100 diluted in 1%

BSA-PBS) for 30 minutes at room temperature. The coverslips were gently washed with PBS before adding donkey anti-sheep/goat IgG:Dylight-488 (1:100 diluted in 1% BSA-PBS), followed by incubation for 30 minutes at room temperature. After washing again with PBS, coverslips were mounted onto glass slides using 100% glycerol containing 0.1 M n-propyl gallate and images were collected on a Zeiss LSM 510 confocal microscope with an Axiovert 100 M base with a 100× Plan Apochromat 1.4 NA oil DIC objective using the argon laser for 488 nm excitation and 505-530 nm bandpass emission filter for imaging Dylight488 fluorescence and the HeNe1 543 nm laser for illumination of the DIC images. Both images were collected using identical detector gain and amplifier offset settings, and the images shown are 1.0 μm optical slices. Digital images were visualized using Zeiss AxioVision LE software.

Chromogenic plasmin activation assay

FTLVS was cultured overnight to mid-log phase, washed twice with TBS and then resuspended in TBS to an OD_{600} of 0.7. Aliquots of the bacterial suspension (50 μL) was added to 50 μL of TBS alone or TBS containing huPLG (192 μg/mL) and incubated for 1 hour at 37°C. The cells were washed 3× with TBST containing 0.1% BSA, and pellets were resuspended in 200 μL of TBS and then split into two 100 μL aliquots. 50 μL of 50 mM Tris-HCl (pH 7.45) with or without 333 μM of the chromogenic plasmin substrate (H-D-Val-Leu-Lys-pNA) and 50 μL 1.2 μg of tPA or TBS alone was added to each sample and incubated at 37°C for 3 h. Bacteria were pelleted via centrifugation and 150 μL of each supernatant was pipetted into a 96-well plate and absorbance at 405 nm was determined as a measure of plasmin activity.

Membrane protein fractionation

Outer membrane enriched fractions were isolated by a procedure adapted from de Bruin, et al [53]. FTLVS were grown in BHI broth (500 ml) to mid-log phase and then were pelleted via centrifugation at 6,400 × g for 30 minutes. Cells were resuspended in cold PBS and then lysed by sonication. Unlysed bacterial cells were separated from the whole-cell lysate by centrifugation at 10,000 × g for 20 minutes at 4°C. The insoluble membrane fraction was then isolated by ultracentrifugation for 1 hour at 100,000 × g at 4°C. After removal of the soluble protein fraction, the pelleted total membrane fraction was resuspended in 1% sarkosyl with vortexing and subjected to a second round of ultracentrifugation for 1 hour at 100,000 × g at 4°C. The Sarkosyl-insoluble pellet was resuspended in 50 mM Tris pH 8. The protein concentration of both the Sarkosyl-soluble and Sarkosyl-insoluble fractions was determined using the DC protein assay (Bio-Rad, Hercules, CA) according to manufacturer directions. Samples were stored at -20°C until use.

Fibronectin degradation assay

Overnight cultures of FTLVS were washed three times with PBS, 10^9 CFU were pipetted into 1.5 mL tubes, and bacteria were pelleted via centrifugation at 18,900 × g for 10 minutes. Bacterial pellets were then resuspended in 50 μl of PBS with or without PLG (2 mg/ml), followed by the addition of 50 μl of tPA (10 μg/mL) and incubation at 37°C with gentle shaking for 1 hour. The bacterial suspensions were pelleted via centrifugation at 18,900 × g, washed 3× with PBS and resuspended with 100 μl of 50 mM Tris, 100 mM NaCl, 5 mM $CaCl_2$) with 3 μg fibronectin (BD Biosciences) and incubation at 37°C with gentle shaking for 24 hours. After the incubation was complete, bacteria were pelleted via centrifugation at 18,900 × g and the supernatants were solublized by boiling in 2× SDS-PAGE sample buffer containing 2-mercaptoethanol. Samples were subjected to 10% SDS-PAGE and then electrophoretically transferred to a PVDF membrane (Immobilon-P, Millipore). The PVDF membrane was pre-blocked with 1% BSA-TBST for 1 hour at RT to minimize non-specific protein binding, and was then incubated with sheep anti-human fibronectin-specific antibody (diluted 1:2000 in 1% BSA-TBST) for 1 hour at RT with gentle rocking. The PVDF membrane was washed three times with TBST to remove unbound primary antibody. The membrane was then incubated in a solution of anti-sheep/goat IgG monoclonal antibody (GT-34, diluted 1:5000 in 1%BSA-TBST) with rocking for 1 hr at RT. The PVDF membranes were washed 3 times with TBST to remove unbound secondary antibody. The blot was developed using Pierce PicoWest chemiluminescence reagents and images were captured using a Bio-Rad ChemiDoc XRS system.

Far-Western blotting analysis

Approximately 100 μg of each protein fraction was precipitated using ice-cold acetone, pelleted via centrifugation at 18,900 × g for 15 minutes, and air-dried at room temperature. The samples were then solublized by boiling in 1× SDS-PAGE sample buffer containing 2-mercaptoethanol. Duplicate 20 μL aliquots of each sample were subjected to 15% SDS-PAGE to separate the proteins based on their size. One set of the samples was then electrophoretically transferred to a PVDF membrane (Immobilon-Psq, Millipore). The PVDF membrane was pre-blocked with 1% BSA-TBST for 1 hour at room temperature to minimize non-specific protein binding and was then incubated in a solution of huPLG (3 ug/mL in 1% BSA-TBST) for one hour with rocking

at 37°C. Unbound PLG was removed by washing three times with TBST. Sheep anti-human PLG-specific antibody (diluted 1:2,000 in 1% BSA-TBST) was added (100 μL/well) and allowed to incubate for 1 hour at RT° with rocking. The PVDF membrane was washed three times with TBST to remove unbound primary antibody. The membrane was then incubated in a solution of anti-sheep/goat IgG monoclonal antibody (GT-34, diluted 1:5,000 in 1%BSA-TBST) with rocking for 1 hr at room temperature. The PVDF membranes were washed three times with TBST to remove unbound secondary antibody. The blot was developed using Pierce PicoWest chemiluminescence reagents and imaged using a Bio-Rad ChemiDoc XRS system.

Proteomic identification of PLG-binding FT proteins

Protein bands were excised from Coomassie-stained SDS-PAGE gels, cut into small pieces, incubated in 50% acetonitrile/100 mM ammonium bicarbonate until colorless, and dried via vacuum centrifugation. The protein was digested by adding 20 μl of a 20 ng/μl trypsin solution and incubating overnight at 37°C. Peptides were extracted from the gel slices via sonication in 50 μl 60% acetonitrile/5%TFA, dried via vacuum centrifugation, and reconstituted in 15 μl 0.1% TFA. Tryptic peptides were desalted/enriched using a C18 ZipTip column (Millipore, Billerica, MA) according to manufacturer's instructions and the eluant was spotted on a MALDI plate and dried. Samples were analyzed using a MALDI-LTQ mass spectrometer (ThermoFinnigan, San Jose, CA). A full MS scan in high-mass range (m/z 600-4000, 5 microscans) was performed. The 50 most intense peaks in the full MS spectrum were selected, and MSMS scans were performed for those ions in high-mass range (m/z 50-4000, 5 microscans), the normalized collision energy for MSMS was 35. Xcalibur software was used to process the mass spectrometric data, and the NCBInr database and the Bioworks 3.2 search engine software were used for database searching.

Acknowledgements

The project described was supported by NIH grant #U54 AI057157 from Southeastern Regional Center of Excellence for Emerging Infections and Biodefense, by NIH grants AI074582 and AI079482 (to JEB) and AI061260 (to MAM), and by Department of Defense Army grant W81XHW-05-1-0227. The authors also thank Cory Blackwell and Himangi Jayakar for helpful discussions. We also thank Jyothi Parvathareddy, and Janice Collum for their technical assistance.

Authors' contributions

SRC conceived and performed all of the experimental work for the study and drafted the manuscript. JEB, TPH, and MAW both participated in the design of the study and played an important role in drafting the manuscript. MAM participated in the design and coordination of all studies, performed the statistical analyses, and helped to draft the manuscript. All authors read and approved the final manuscript.

Received: 10 August 2009 Accepted: 12 March 2010
Published: 12 March 2010

References

1. Hoel T, Scheel O, Nordahl SH, Sandvik T: **Water- and airborne Francisella tularensis biovar palaearctica isolated from human blood.** *Infection* 1991, **19(5)**:348-350.
2. Siret V, Barataud D, Prat M, Vaillant V, Ansart S, Le Coustumier A, Vaissaire J, Raffi F, Garre M, Capek I: **An outbreak of airborne tularaemia in France, August 2004.** *Euro Surveill* 2006, **11(2)**:58-60.
3. Feldman KA, Enscore RE, Lathrop SL, Matyas BT, McGuill M, Schriefer ME, Stiles-Enos D, Dennis DT, Petersen LR, Hayes EB: **An outbreak of primary pneumonic tularemia on Martha's Vineyard.** *N Engl J Med* 2001, **345(22)**:1601-1606.
4. Syrjala H, Kujala P, Myllyla V, Salminen A: **Airborne transmission of tularemia in farmers.** *Scand J Infect Dis* 1985, **17(4)**:371-375.
5. Francis E: **Landmark article April 25, 1925: Tularemia. By Edward Francis.** *JAMA* 1983, **250(23)**:3216-3224.
6. Hopla CE: **The ecology of tularemia.** *Adv Vet Sci Comp Med* 1974, **18(0)**:25-53.
7. **Tularemia transmitted by insect bites–Wyoming, 2001-2003.** *MMWR Morb Mortal Wkly Rep* , 2005/02/25 2005, **54**:170-173.
8. Eliasson H, Lindback J, Nuorti JP, Arneborn M, Giesecke J, Tegnell A: **The 2000 tularemia outbreak: a case-control study of risk factors in disease-endemic and emergent areas, Sweden.** *Emerg Infect Dis* 2002, **8(9)**:956-960.
9. Skierska B: **[Mosquitoes in the northern part of Szczecin region and their role in epidemiology of tularemia.].** *Biul Panstw Inst Med Morsk Trop J W Gdansku* 1955, **6**:267-275.
10. Hubalek Z, Treml F, Halouzka J, Juricova Z, Hunady M, Janik V: **Frequent isolation of Francisella tularensis from Dermacentor reticulatus ticks in an enzootic focus of tularaemia.** *Med Vet Entomol* 1996, **10(3)**:241-246.
11. Emmons RW, Ruskin J, Bissett ML, Uyeda DA, Wood RM, Lear CL: **Tularemia in a mule deer.** *J Wildl Dis* 1976, **12(3)**:459-463.
12. Greco D, Ninu E: **A family outbreak of tularemia.** *Eur J Epidemiol* 1985, **1(3)**:232-233.
13. Golovliov I, Baranov V, Krocova Z, Kovarova H, Sjostedt A: **An attenuated strain of the facultative intracellular bacterium Francisella tularensis can escape the phagosome of monocytic cells.** *Infect Immun* 2003, **71(10)**:5940-5950.
14. Clemens DL, Lee BY, Horwitz MA: **Francisella tularensis enters macrophages via a novel process involving pseudopod loops.** *Infect Immun* 2005, **73(9)**:5892-5902.
15. Forestal CA, Malik M, Catlett SV, Savitt AG, Benach JL, Sellati TJ, Furie MB: **Francisella tularensis has a significant extracellular phase in infected mice.** *J Infect Dis* 2007, **196(1)**:134-137.
16. Yu JJ, Raulie EK, Murthy AK, Guentzel MN, Klose KE, Arulanandam BP: **The presence of infectious extracellular Francisella tularensis subsp. novicida in murine plasma after pulmonary challenge.** *Eur J Clin Microbiol Infect Dis* 2008, **27(4)**:323-325.
17. Ben Nasr A, Haithcoat J, Masterson JE, Gunn JS, Eaves-Pyles T, Klimpel GR: **Critical role for serum opsonins and complement receptors CR3 (CD11b/CD18) and CR4 (CD11c/CD18) in phagocytosis of Francisella tularensis by human dendritic cells (DC): uptake of Francisella leads to activation of immature DC and intracellular survival of the bacteria.** *J Leukoc Biol* 2006, **80(4)**:774-786.
18. Barker JH, McCaffrey RL, Baman NK, Allen LA, Weiss JP, Nauseef WM: **The role of complement opsonization in interactions between F. tularensis subsp. novicida and human neutrophils.** *Microbes Infect* 2009, **11(8-9)**:762-9.
19. Sandstrom G, Lofgren S, Tarnvik A: **A capsule-deficient mutant of Francisella tularensis LVS exhibits enhanced sensitivity to killing by serum but diminished sensitivity to killing by polymorphonuclear leukocytes.** *Infect Immun* 1988, **56(5)**:1194-1202.
20. Ben Nasr A, Klimpel GR: **Subversion of complement activation at the bacterial surface promotes serum resistance and opsonophagocytosis of Francisella tularensis.** *J Leukoc Biol* 2008, **84(1)**:77-85.
21. Lahteenmaki K, Kuusela P, Korhonen TK: **Bacterial plasminogen activators and receptors.** *FEMS Microbiol Rev* 2001, **25(5)**:531-552.
22. Sun H: **The interaction between pathogens and the host coagulation system.** *Physiology (Bethesda)* 2006, **21**:281-288.

23. Lahteenmaki K, Edelman S, Korhonen TK: **Bacterial metastasis: the host plasminogen system in bacterial invasion.** *Trends Microbiol* 2005, **13(2)**:79-85.
24. Degen JL, Bugge TH, Goguen JD: **Fibrin and fibrinolysis in infection and host defense.** *J Thromb Haemost* 2007, **5(Suppl 1)**:24-31.
25. Li Z, Ploplis VA, French EL, Boyle MD: **Interaction between group A streptococci and the plasmin(ogen) system promotes virulence in a mouse skin infection model.** *J Infect Dis* 1999, **179(4)**:907-914.
26. Coleman JL, Gebbia JA, Piesman J, Degen JL, Bugge TH, Benach JL: **Plasminogen is required for efficient dissemination of B. burgdorferi in ticks and for enhancement of spirochetemia in mice.** *Cell* 1997, **89(7)**:1111-1119.
27. Sodeinde OA, Subrahmanyam YV, Stark K, Quan T, Bao Y, Goguen JD: **A surface protease and the invasive character of plague.** *Science* 1992, **258(5084)**:1004-1007.
28. Hazlett KR, Caldon SD, McArthur DG, Cirillo KA, Kirimanjeswara GS, Magguilli ML, Malik M, Shah A, Broderick S, Golovliov I, *et al*: **Adaptation of Francisella tularensis to the mammalian environment is governed by cues which can be mimicked in vitro.** *Infect Immun* 2008, **76(10)**:4479-4488.
29. Filip C, Fletcher G, Wulff JL, Earhart CF: **Solubilization of the cytoplasmic membrane of Escherichia coli by the ionic detergent sodium-lauryl sarcosinate.** *J Bacteriol* 1973, **115(3)**:717-722.
30. Friberg N, Carlson P, Kentala E, Mattila PS, Kuusela P, Meri S, Jarva H: **Factor H binding as a complement evasion mechanism for an anaerobic pathogen, Fusobacterium necrophorum.** *J Immunol* 2008, **181(12)**:8624-8632.
31. Verma A, Hellwage J, Artiushin S, Zipfel PF, Kraiczy P, Timoney JF, Stevenson B: **LfhA, a novel factor H-binding protein of Leptospira interrogans.** *Infect Immun* 2006, **74(5)**:2659-2666.
32. Hellwage J, Meri T, Heikkila T, Alitalo A, Panelius J, Lahdenne P, Seppala IJ, Meri S: **The complement regulator factor H binds to the surface protein OspE of Borrelia burgdorferi.** *J Biol Chem* 2001, **276(11)**:8427-8435.
33. Horstmann RD, Sievertsen HJ, Knobloch J, Fischetti VA: **Antiphagocytic activity of streptococcal M protein: selective binding of complement control protein factor H.** *Proc Natl Acad Sci USA* 1988, **85(5)**:1657-1661.
34. Ram S, Sharma AK, Simpson SD, Gulati S, McQuillen DP, Pangburn MK, Rice PA: **A novel sialic acid binding site on factor H mediates serum resistance of sialylated Neisseria gonorrhoeae.** *J Exp Med* 1998, **187(5)**:743-752.
35. Bergmann S, Rohde M, Chhatwal GS, Hammerschmidt S: **Characterization of plasmin(ogen) binding to Streptococcus pneumoniae.** *Indian J Med Res* 2004, **119(Suppl)**:29-32.
36. Sun H, Ringdahl U, Homeister JW, Fay WP, Engleberg NC, Yang AY, Rozek LS, Wang X, Sjobring U, Ginsburg D: **Plasminogen is a critical host pathogenicity factor for group A streptococcal infection.** *Science* 2004, **305(5688)**:1283-1286.
37. Espersen F: **Interactions between human plasma proteins and cell wall components of Staphylococcus aureus.** *Dan Med Bull* 1987, **34(2)**:59-69.
38. Hauck CR, Ohlsen K: **Sticky connections: extracellular matrix protein recognition and integrin-mediated cellular invasion by Staphylococcus aureus.** *Curr Opin Microbiol* 2006, **9(1)**:5-11.
39. Josefsson E, Higgins J, Foster TJ, Tarkowski A: **Fibrinogen binding sites P336 and Y338 of clumping factor A are crucial for Staphylococcus aureus virulence.** *PLoS ONE* 2008, **3(5)**:e2206.
40. Menzies BE: **The role of fibronectin binding proteins in the pathogenesis of Staphylococcus aureus infections.** *Curr Opin Infect Dis* 2003, **16(3)**:225-229.
41. Agarwal S, Kulshreshtha P, Bambah Mukku D, Bhatnagar R: **alpha-Enolase binds to human plasminogen on the surface of Bacillus anthracis.** *Biochim Biophys Acta* 2008, **1784(7-8)**:986-994.
42. Fricke B, Drossler K, Willhardt I, Schierhorn A, Menge S, Rucknagel P: **The cell envelope-bound metalloprotease (camelysin) from Bacillus cereus is a possible pathogenic factor.** *Biochim Biophys Acta* 2001, **1537(2)**:132-146.
43. Kunert A, Losse J, Gruszin C, Huhn M, Kaendler K, Mikkat S, Volke D, Hoffmann R, Jokiranta TS, Seeberger H, *et al*: **Immune evasion of the human pathogen Pseudomonas aeruginosa: elongation factor Tuf is a factor H and plasminogen binding protein.** *J Immunol* 2007, **179(5)**:2979-2988.
44. Suomalainen M, Haiko J, Ramu P, Lobo L, Kukkonen M, Westerlund-Wikstrom B, Virkola R, Lahteenmaki K, Korhonen TK: **Using every trick in the book: the Pla surface protease of Yersinia pestis.** *Adv Exp Med Biol* 2007, **603**:268-278.
45. Kraiczy P, Hartmann K, Hellwage J, Skerka C, Kirschfink M, Brade V, Zipfel PF, Wallich R, Stevenson B: **Immunological characterization of the complement regulator factor H-binding CRASP and Erp proteins of Borrelia burgdorferi.** *Int J Med Microbiol* 2004, **293(Suppl 37)**:152-157.
46. Kraiczy P, Hellwage J, Skerka C, Becker H, Kirschfink M, Simon MM, Brade V, Zipfel PF, Wallich R: **Complement resistance of Borrelia burgdorferi correlates with the expression of BbCRASP-1, a novel linear plasmid-encoded surface protein that interacts with human factor H and FHL-1 and is unrelated to Erp proteins.** *J Biol Chem* 2004, **279(4)**:2421-2429.
47. Kraiczy P, Hellwage J, Skerka C, Kirschfink M, Brade V, Zipfel PF, Wallich R: **Immune evasion of Borrelia burgdorferi: mapping of a complement-inhibitor factor H-binding site of BbCRASP-3, a novel member of the Erp protein family.** *Eur J Immunol* 2003, **33(3)**:697-707.
48. Kraiczy P, Skerka C, Brade V, Zipfel PF: **Further characterization of complement regulator-acquiring surface proteins of Borrelia burgdorferi.** *Infect Immun* 2001, **69(12)**:7800-7809.
49. Kraiczy P, Skerka C, Zipfel PF, Brade V: **Complement regulator-acquiring surface proteins of Borrelia burgdorferi: a new protein family involved in complement resistance.** *Wien Klin Wochenschr* 2002, **114(13-14)**:568-573.
50. Wallich R, Pattathu J, Kitiratschky V, Brenner C, Zipfel PF, Brade V, Simon MM, Kraiczy P: **Identification and functional characterization of complement regulator-acquiring surface protein 1 of the Lyme disease spirochetes Borrelia afzelii and Borrelia garinii.** *Infect Immun* 2005, **73(4)**:2351-2359.
51. Fenno JC, Tamura M, Hannam PM, Wong GW, Chan RA, McBride BC: **Identification of a Treponema denticola OppA homologue that binds host proteins present in the subgingival environment.** *Infect Immun* 2000, **68(4)**:1884-1892.
52. Crane DD, Warner SL, Bosio CM: **A novel role for plasmin-mediated degradation of opsonizing antibody in the evasion of host immunity by virulent, but not attenuated, Francisella tularensis.** *J Immunol* 2009, **183(7)**:4593-4600.
53. de Bruin OM, Ludu JS, Nano FE: **The Francisella pathogenicity island protein IglA localizes to the bacterial cytoplasm and is needed for intracellular growth.** *BMC Microbiol* 2007, **7**:1.

doi:10.1186/1471-2180-10-76
Cite this article as: Clinton *et al.*: Binding and activation of host plasminogen on the surface of *Francisella tularensis*. *BMC Microbiology* 2010 **10**:76.

Plasmid 64 (2010) 156–161

Contents lists available at ScienceDirect

Plasmid

journal homepage: www.elsevier.com/locate/yplas

Construction of a bioluminescence reporter plasmid for *Francisella tularensis*

Xiaowen R. Bina, Mark A. Miller, James E. Bina *

The University of Tennessee Health Science Center, Department of Molecular Sciences, 858 Madison Avenue, Memphis, TN 38163, USA

ARTICLE INFO

Article history:
Received 21 March 2010
Accepted 4 July 2010
Available online 8 July 2010

Communicated by J. Casadesus

Keywords:
Francisella tularensis
Plasmid
Luminescence

ABSTRACT

A *Francisella tularensis* shuttle vector that constitutively expresses the *Photorhabdus luminescens* lux operon in type A and type B strains of *F. tularensis* was constructed. The bioluminescence reporter plasmid was introduced into the live vaccine strain of *F. tularensis* and used to follow *F. tularensis* growth in a murine intranasal challenge model in real-time by bioluminescence imaging. The results show that the new bioluminescence reporter plasmid represents a useful tool for tularemia research that is suitable for following *F. tularensis* growth in both in vitro and in vivo model systems.

1. Introduction

Francisella tularensis is a gram negative facultative intracellular bacterium that causes the zoonotic disease tularemia. *F. tularensis* infection of humans can occur by a number of routes, including the handling of infected animals, arthropod bites (Evans, 1985; Francis, 1937; Tarnvik, 1989), ingestion (Anda et al., 2001; Greco et al., 1987; Karpoff and Antononoff, 1936), and by inhalation (Syrjala et al., 1985; Teutsch et al., 1979). *F. tularensis* is highly infectious and as few as 10 bacteria can cause disease (Cross, 2000). The high infectivity and ease of dissemination of *F. tularensis* by aerosols has raised concerns about the potential use of *F. tularensis* as a biological weapon (Sjostedt, 2007) and provided the rationale for the development of new tularemia therapeutics.

A major focus of *F. tularensis* research is to decipher the molecular mechanisms that contribute to *F. tularensis* pathogenesis. The strategy for identification of virulence associated genes has largely focused on generating mutations in putative virulence genes and assessing the resultant strains for growth attenuation in a murine tularemia model. The traditional method for assessing *F. tularensis* growth and dissemination in vivo requires challenging large numbers of animals with the test and control *F. tularensis* strains. Thereafter, several animals are sacrificed from each group and dissected at each time point over a time course. *F. tularensis* titers are then determined in each mouse by plating serial dilutions of organ homogenates onto agar plates. This method requires large numbers of experimental animals and is laborious. In addition, the requirement for repeated animal sacrifice, dissection and tissue handling increases the potential for occupational exposure of researchers to *F. tularensis*, a category A select agent.

Technological advances in small animal imaging have made it possible to monitor in real-time the growth and dissemination of fluorescent or bioluminescent-labeled bacteria in individual animals over the entire course of infection, offering a powerful alternative to traditional methodologies. Bioluminescence has proven to be particularly useful for this application. Bioluminescence reporters have several advantages over fluorescence reporters for in vivo imaging studies. Luminescence reporters are more sensitive and have lower background levels, and they do not share the auto-fluorescence or signal quenching issues that limit the utility of fluorescent reporters for in vitro

* Corresponding author. Fax: +1 901 448 7360.
E-mail address: JBina@uthsc.edu (J.E. Bina).

0147-619X/$ - see front matter © 2010 Elsevier Inc. All rights reserved.
doi:10.1016/j.plasmid.2010.07.001

and in vivo imaging applications. In addition, there are numerous methods available for the detection of bioluminescence (e.g. CCD camera, plate reader, film exposure, scintillation counter). Bioluminescence reporters have a number of applications in bacterial pathogenesis including the quantification of gene expression, virulence analysis, and the evaluation of therapeutic agents. Bioluminescence tagging vectors that express the *Photorhabdus luminescens* lux operon have been used to follow in real-time the growth and dissemination of a number of pathogens in animal models. However, to date bioluminescence reporters have not yet been published for use in *F. tularensis*.

In this work we describe the construction of a new *F. tularensis* reporter plasmid that constitutively expresses the *P. luminescens* lux operon. We show that the presence of this plasmid in type A and type B *F. tularensis* results in bioluminescence production which could be used to follow *F. tularensis* growth and dissemination in vitro and in vivo.

2. Materials and methods

2.1. Bacterial strains and growth conditions

F. tularensis strains LVS (live vaccine strain) and Schu S4 were obtained from the Centers for Disease Control and Prevention (CDC, Atlanta, GA). All work involving Schu S4 was performed in a CDC-approved BSL3 facility at The University of Tennessee Health Sciences Center in accordance with approved BSL3 protocols. *F. tularensis* strains were cultured in modified Mueller Hinton broth (MH broth supplemented with 10 g/L tryptone, 0.1% glucose, 0.025% ferrous pyrophosphate, 0.1% L-cysteine, and 2.5% calf serum) or on BHI-chocolate agar (BHI agar supplemented with 1% hemoglobin and 1% IsoVitalex). *Eschericia coli* strain EC100λpir (Epicentre, Madison, WI) was used as a host for the cloning experiments and was grown in Luria–Bertani (LB) broth or on LB agar at 37 °C. Antibiotics were used at the following concentrations when necessary: kanamycin (km) at 50 μg/mL for *E. coli* and 10 μg/mL for *F. tularensis*; cefprozil was used at 300 μg/mL for *F. tularensis*; carbenicillin was used at 100 μg/mL for *E. coli*.

2.2. Recombinant DNA methods

Recombinant DNA methods were performed according to standard protocols. Restriction enzymes were purchased from New England Biolabs (Beverly, MA). PCR amplification was performed using Biolase DNA polymerase (Bioline, Taunton, MA) or Pfu DNA polymerase (Stratagene, Cedar Creek, TX). *F. tularensis* was transformed by electroporation as previously described (Bina et al., 2006) except that outgrowth following electroporation was limited to one hour (for Schu S4) or two hours (for LVS) before plating onto selective media.

2.3. Construction of pXB173-lux

The *Francisella–E. coli* shuttle vector pXB167 (Bina et al., 2006) was used as a starting template for construction of pXB173-lux. The initial step in construction was to replace the ColE1 origin of replication with a cassette encoding the R6K origin of replication and the conjugal origin (*oriT*) from pBSL238 (Alexeyev and Shokolenko, 1995). This was accomplished by digestion of pXB167 with AclI and PacI restriction endonucleases to remove the ColE1 origin of replication. The resulting 4090 bp fragment was made blunt-ended by treatment with the Klenow fragment of DNA polymerase before being ligated to the 784 bp *ori*R6 k and *oriT* PCR amplicon that was obtained from pBSL238 by PCR using the *oriF* (5′-CGATCTACTATGCCATGTCAGCCGTTAAGTGTTCC-3′) and *oriR* (5′-GGGATATCGGGGATCAATTCCGTGATAGGTGG-3′) primers to produce pXB168 (Fig. 1).

We then replaced the *gfp* gene in pXB168 with the *aph*3′ gene that encoded kanamycin resistance. This was accomplished by digestion of pXB168 with BamHI and ClaI restriction enzymes to remove the *gfp* allele. The resulting 4119 bp fragment was rendered blunt-ended by treatment with Klenow fragment before being ligated to the 901 bp kanamycin resistance gene (*aph*3′) which was obtained from TN:EZ by PCR using the (Epicentre, Madison, WI) using the KanF (5′-AAGGCGCGCCACGCGTAGGAGTTTGT TATGAGCCATATTCAACGGGAA-3′) and KanR (5'-GCACGCG TCAAGTCAGCGTAATGCTCTGCCAG-3') primers to generate pXB169. pXB173-lux was then generated by digestion of

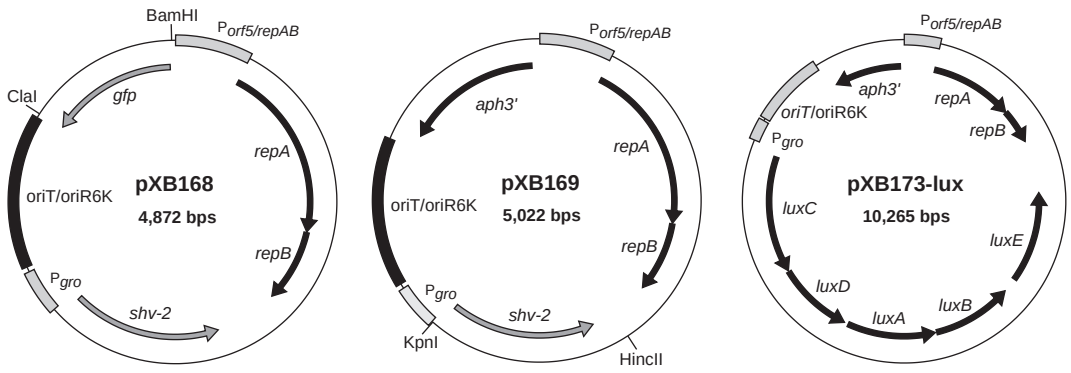

Fig. 1. Construction of pXB173-lux. Plasmid pXB168 is derived from pXB167 (Bina et al., 2006). Only relevant restriction sites are shown. The details for construction are given in Section 2.3.

pXB169 with KpnI and HinCII restriction enzymes to remove the *shv-2* allele. The resulting 3987 bp fragment was then ligated with the 5.9 kb lux operon that was derived from digestion of pXB128-lux (Bina laboratory collection) with KpnI and XmaI restriction enzymes. The results of this ligation placed the lux operon downstream and in the same orientation as the constitutively expressed Francisella *gro* promoter (indicated as P_{gro} in Fig. 1). The DNA sequence of pXB173-lux was confirmed by DNA sequencing at the Molecular Resource Center of The University of Tennessee Health Science Center (Memphis, TN). The DNA sequence of pXB173-lux has been deposited in Genbank with the accession number HM017829.

2.4. Bioluminescence detection and animal challenge studies

The limit of bioluminescence detection of LVS-pXB173-lux was determined by making serial LVS-pXB173 culture dilutions in white 96-well microtiter plates. Bioluminescence production was then quantified by use of an IVIS Spectrum imaging system (Caliper Life Sciences, Hopkinton, MA) according to the manufacturer's directions.

The utility of pXB173-lux in *F. tularensis* was assessed in a murine intranasal challenge model as previously described (Lavine et al., 2007). Briefly, 12 week-old female BALB/c mice were challenged intranasally with $\sim 5 \times 10^5$ CFU of *F. tularensis* LVS-pXB173-lux in a total volume of 50 μl that was administered as 25 μl per naris. Bioluminescence was then used as a reporter to following bacterial dissemination starting at 3 h post-challenge and then at 24-h intervals until the conclusion of the experiment. Bioluminescence production in the mice was quantified by use of the IVIS Spectrum imaging system according to the manufacturer's directions.

Bioluminescence production in Type A *F. tularensis* strain Schu S4 was assessed by use of the IVIS Spectrum to image an agar plate that had been inoculated with both the LVS and Schu S4 strains of *F. tularensis* bearing the pXB173-lux vector. Due to BSL3 restrictions we are currently unable to image mice infected with *F. tularensis* Schu S4 on the IVIS imaging system.

2.5. Plasmid stability determination

The stability of pXB173-lux in *F. tularensis* Schu S4 was assessed in vitro as follows. A fresh overnight culture of *F. tularensis* Schu S4-pXB173 was successively cultured in MH broth without km for four days. The presence of the plasmid was then determined by plating serial dilutions of the culture on days 1 and 4 onto BHI-chocolate agar plates with and without km. The ratio of km-resistant to km-sensitive bacteria was then calculated to determine pXB173-lux stability in the absence of antibiotic selection. In vivo stability of pXB173-lux was determined by intranasal infection of mice with $\sim 10^3$ cfu of *F. tularensis* Schu S4-pXB173. The spleen was then collected from one mouse on days 1, 5 and 6 and homogenized in 1 ml of PBS before 0.25 ml of 5× disruption buffer (2.5% saponin, 15% BSA, in PBS) was added with light vortexing. Serial dilutions of the spleen homogenates were then plated onto BHI-chocolate agar plates with and without km. The ratio of km-resistant to km-sensitive bacteria was then calculated as an indicator of in vivo plasmid stability.

3. Results and discussion

3.1. Construction of pXB169

We previously described the construction of three shuttle vectors (pXB136, pXB160 and pXB167) (Bina et al., 2006) that were derived from pFNLTP6::gfp (Maier et al., 2004). In electroporation experiments we observed that pXB136 could be efficiently transformed into Schu S4 with selection for cefprozil resistance, however, we were not able to recover Schu S4 transformants when selecting for kanamycin resistance (data not shown). Since the kanamycin resistance locus in pXB136 is derived from the pFNLTP shuttle vectors, this observation is consistent with previous findings that pFNLTP-based vectors transformed poorly into Schu S4 (LoVullo et al., 2006) and suggested that the poor transformation and plasmid instability observed in pXB136 was likely due to inefficient expression of the kanamycin resistance allele in type A *F. tularensis* strains. In silico analysis of pXB136 suggested that the *repAB* locus in pXB136 (and in the pFNLTP vectors) contained a divergently transcribed promoter, denoted as P_{orf5} in Fig. 1, located 808 bp upstream of the kanamycin resistance gene (i.e. *aph*3′). Downstream of the P_{orf5} is *orf*5′ which encodes a truncated gene that was hypothesized to form part of a two component toxin–antitoxin system that was present in the parent plasmid pFNL10 (Pavlov et al., 1996). Downstream of *orf5*′ was the f1 origin of replication and the *aph*3′ gene which originated from pCR2.1-TOPO (Maier et al., 2004). As P_{orf5} was derived from pFNL10, we hypothesized that it likely encoded an active *F. tularensis* promoter and contributed to *aph*3′ expression in pXB136 and that the intervening 808 bp sequence inhibited *aph*3′ expression in Schu S4. To test this hypothesis we deleted the 808 bp intervening region. The resulting plasmid retained kanamycin resistance in *E. coli* and LVS and gained the ability to be retained by Schu S4. The resulting plasmid transformed into Schu S4 at an efficiency that was equivalent to what was observed with LVS ($\sim 10^5$ cfu/μg DNA). Collectively these results suggested that the *repAB* promoter region contained a divergently transcribed promoter that was constitutively expressed in both *E. coli* and *F. tularensis*. It is unclear why pXB136 and the pFNLTP plasmids display different stabilities in LVS and Schu S4 with selection for kanamycin resistance.

3.2. Construction of pXB173-lux

Having established that the Schu S4 stability problems associated with our previous vectors was likely due to expression of the kanamycin resistance allele and not some inherent problem with the plasmid construct, we set out to design a new shuttle vector that could be used as a bioluminescence reporter in *F. tularensis*. To construct the bioluminescence reporter plasmid we first replaced the high copy number origin of replication that was present in pXB167 with a low copy number origin of replication and a conjugal origin of transfer. This was accomplished by

replacement of the pXB167 ColE1 origin of replication with a cassette that encoded the R6K origin of replication and the RP4 origin of transfer to generate pXB168. This effectively reduced the plasmid copy number in *E. coli* and introduced an origin of transfer to facilitate conjugal transfer of the plasmid into *F. tularensis*. Conjugation represents a very efficient and easy method for introduction of plasmids into *F. tularensis*. The *shv*-2 marker was then replaced with the *aph*3′ allele as kanamycin resistance is the most reliable and widespread genetic marker used in type A *F. tularensis* strains (e.g. Schu S4). We used the *orf5* promoter to drive expression of *aph*3′ so that we could use the P_{gro} promoter to drive expression of the lux reporter construct (see below). The resulting plasmid, pXB169, was transformed into Schu S4 with high efficiency ($\sim 10^5$ transformants per μg/DNA).

The bioluminescence reporter plasmid pXB173-lux (Fig. 1) was then generated from pXB169 by cloning the *P. luminescens* lux operon downstream of the *F. tularensis gro* promoter. The *P. luminescens* lux operon contains the genes that are required for production of both luciferase (*luxAB*) and luciferin (*luxCDE*) and expression of the lux operon results in concomitant light production. Since the *F. tularensis gro* promoter is constitutively expressed in *E. coli* and *F. tularensis*, the presence of pXB173-lux in *E. coli*, LVS and Schu S4 results in constitutive bioluminescence production as observed in Fig. 2. The in vitro detection limit for LVS-pXB173-lux in white 96-well microtiter plates was ~2000 cfu per well which suggests that pXB173-lux likely can be used to follow *F. tularensis* growth in cell culture studies.

3.3. Use of pXB173-lux to follow F. tularensis dissemination in mice

We documented the utility of pXB173-lux by testing whether it could be used as a reporter to follow *F. tulanensis* growth in a murine model of tularemia in real-time. We therefore challenged two BALB/c mice with $\sim 10^5$ cfu of LVS-pXB173-lux by the intranasal route (Fig. 3). In the first mouse, the majority of the LVS inoculum was detected in the stomach at 3 h post-challenge, suggesting that at least a portion of the intranasal challenge dose failed to reach the lungs and was swallowed. Twenty-four-hours later, the bioluminescence production in the stomach of mouse one had resolved and LVS was clearly visualized in the lungs of both animals and in the upper respiratory tract of mouse two. The upper airway infection intensified over the six day course of the experiment in mouse two. It is unclear whether this upper respiratory tract infection occurs in natural inhalation infections or is an artifact of the intranasal inoculation method that is widely used by the tularemia research community. The images also showed that LVS disseminated to the cervical lymph nodes of mouse one (day 3) and mouse two (day 2) and that colonization of the lymph nodes intensified throughout the study period. Beginning on day 3 post-challenge LVS was observed in the liver of both mice, and by day 4 post-challenge, the

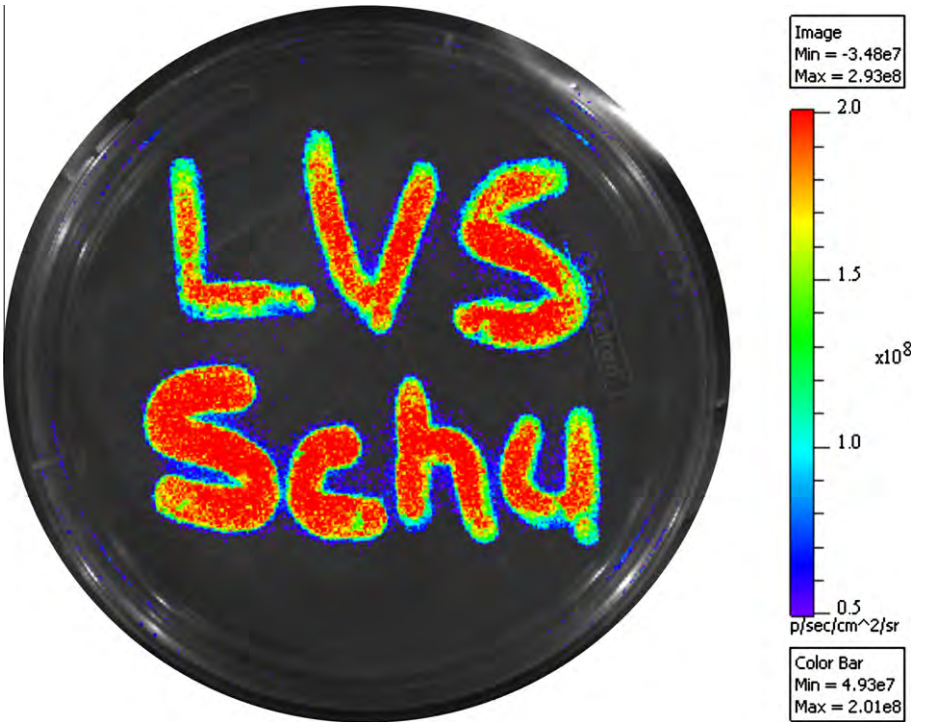

Fig. 2. Bioluminescence production by *F. tularensis*. Overnight cultures of *F. tularensis* containing pXB173-lux (LVS on the upper half of plate; Schu S4 on the lower half of plate) were inoculated onto the surface of a modified Mueller–Hinton agar plate using a Dacron-tipped swab and incubated at 37 °C for 18 h when the plate was imaged for bioluminescence production using an IVIS spectrum imaging system. Photon emission intensity is represented as a pseudocolor image that is superimposed onto the surface of the inoculated agar plate. (For interpretation of the references to colour in this figure legend, the reader is referred to the web version of this article.)

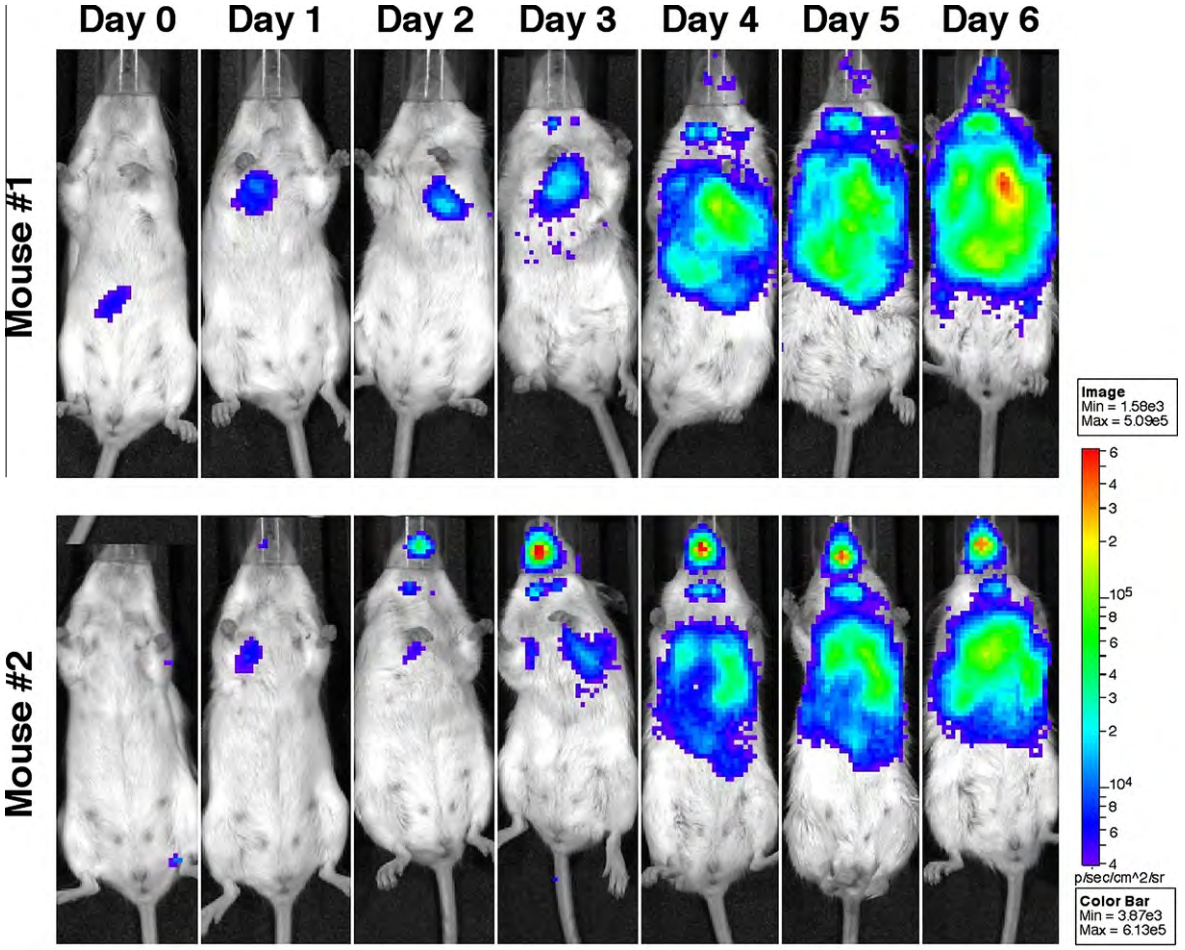

Fig. 3. Visualization of *F. tularensis* LVS-pXB173-lux in mice by bioluminescence imaging. Two twelve week-old BALB/c mice were challenged with 5×10^5 CFU *F. tularensis* LVS-pXB173-lux in a total volume of 50 μl of PBS via the intranasal route. Bioluminescence production in the mice was then visualized using an IVIS Spectrum Imaging system at 24-h intervals beginning 3 h after administration of the challenge dose. Exposure times varied based on bioluminescent signal intensities in an effort to collect between 600 and 60,000 counts, and image scaling was normalized by converting total counts to photons/s. Results shown here are representative of several experiments of similar design. (For interpretation of the references to colour in this figure legend, the reader is referred to the web version of this article.)

livers of both mice were heavily colonized. On day 6, both mice exhibited extensive bacterial dissemination which correlated with other signs of severe tularemic disease (i.e. significant weight loss, ruffled fur and reduced physical activity) and the experiment was terminated. These results validate that pXB173-lux can be used as a reporter to follow *F. tularensis* dissemination in mice.

The stability of pXB173-lux in *F. tularensis* Schu S4 was assessed to validate the use of this plasmid in a Type A strain background. The plasmid was well maintained in vitro with 85% of the bacteria retaining the plasmid following growth for four successive subcultures in the absence of antibiotic selection. In vivo stability was similar to the in vitro results with 82% and 75% and of the bacteria retaining the plasmid on days 5 and 6 post-challenge, respectively. This demonstrates that pXB173-lux is stable in *F. tularensis* Schu S4, while the data presented in Fig. 2 demonstrate that the lux reporter works in *F. tularensis* Schu S4. Collectively these results strongly suggest that pXB173-lux will be useful for in vivo studies with Type A *F. tularensis* strains as we have documented with *F. tularensis* LVS.

The results presented above show that bioluminescence is a highly sensitive reporter that can be used to follow *F. tularensis* growth in mice in real-time. Bioluminescence represents a new tool for the tularemia research community that has not been previously available. In particular, the use of pXB173-lux can greatly facilitate animal and cell culture studies with virulent type A *F. tularensis* strains. As most analyses previously depended on terminal end point assays, the use of bioluminescence should greatly reduce both the labor cost and number of animals that are required for these assays while limiting the potential for occupational exposure of researchers to a potentially fatal pathogen.

Acknowledgments

This work was supported by NIH grant #U54 AI057157 from Southeastern Regional Center of Excellence for

Emerging Infections and Biodefense, by NIH grants AI074582 and AI079482 (to JEB), AI061260 (to MAM), and by DOD grant W81XHW-05-1-0227. Its contents are solely the responsibility of the authors and do not necessarily represent the official views of the NIH.

References

Alexeyev, M.F., Shokolenko, I.N., 1995. RP4 oriT and RP4 oriT-R6K oriV DNA cassettes for construction of specialized vectors. Biotechniques 19, 22–24, 26.

Anda, P. et al., 2001. Waterborne outbreak of tularemia associated with crayfish fishing. Emerging Infectious Diseases 7, 575–582.

Bina, X.R. et al., 2006. The Bla2 beta-lactamase from the live-vaccine strain of *Francisella tularensis* encodes a functional protein that is only active against penicillin-class beta-lactam antibiotics. Archives of Microbiology 186, 219–228.

Cross, T.J.A.R.L.P., 2000. *Francisella tularensis* (tularemia). In: Mandell, G.L., Bennett, J.E., Dolin, R. (Eds.), Principles and Practice of Infectious Diseases. Churchill Livingston, Philadelphia.

Evans, M.E., 1985. *Francisella tularensis*. Infection Control 6, 381–383.

Francis, E., 1937. Sources of infection and seasonal incidence of tularemia in man. Public Health Reports 52, 103.

Greco, D. et al., 1987. A waterborne tularemia outbreak. European Journal of Epidemiology 3, 35–38.

Karpoff, S.P., Antononoff, N.I., 1936. The spread of tularemia through water as a new factor in its epidemiology. Journal of Bacteriology 32, 243.

Lavine, C.L. et al., 2007. Immunization with heat-killed *Francisella tularensis* LVS elicits protective antibody-mediated immunity. European Journal of Immunology 37, 3007–3020.

LoVullo, E.D. et al., 2006. Genetic tools for highly pathogenic *Francisella tularensis* subsp. *tularensis*. Microbiology 152, 3425–3435.

Maier, T.M. et al., 2004. Construction and characterization of a highly efficient *Francisella* shuttle plasmid. Applied Environmental Microbiology 70, 7511–7519.

Pavlov, V.M. et al., 1996. Cryptic plasmid pFNL10 from *Francisella novicida*-like F6168: the base of plasmid vectors for *Francisella tularensis*. FEMS Immunology and Medical Microbiology 13, 253–256.

Sjostedt, A., 2007. Tularemia: history, epidemiology, pathogen physiology, and clinical manifestations. Annals of the New York Academy of Sciences 1105, 1–29.

Syrjala, H. et al., 1985. Airborne transmission of tularemia in farmers. Scandinavian Journal of Infectious Diseases 17, 371–375.

Tarnvik, A., 1989. Nature of protective immunity to *Francisella tularensis*. Reviews of Infectious Diseases 11, 440–451.

Teutsch, S.M. et al., 1979. Pneumonic tularemia on Martha's Vineyard. New England Journal of Medicine 301, 826–828.

JOURNAL OF VIROLOGY, Aug. 2010, p. 7662–7667 Vol. 84, No. 15
0022-538X/10/$12.00 doi:10.1128/JVI.02444-09

Cross-Reactive Neutralizing Antibodies Directed against Pandemic H1N1 2009 Virus Are Protective in a Highly Sensitive DBA/2 Mouse Influenza Model[▽]

Adrianus C. M. Boon,[1] Jennifer deBeauchamp,[1] Scott Krauss,[1] Adam Rubrum,[1] Ashley D. Webb,[1] Robert G. Webster,[1] Janet McElhaney,[2] and Richard J. Webby[1]*

Department of Infectious Diseases, St. Jude Children's Research Hospital, Memphis, Tennessee 38105[1], and Department of Medicine, University of British Columbia, Vancouver, British Columbia, Canada[2]

Received 19 November 2009/Accepted 11 May 2010

Our ability to rapidly respond to an emerging influenza pandemic is hampered somewhat by the lack of a susceptible small-animal model. To develop a more sensitive model, we pathotyped 18 low-pathogenic non-mouse-adapted influenza A viruses of human and avian origin in DBA/2 and C57BL/6 mice. The majority of the isolates (13/18) induced severe morbidity and mortality in DBA/2 mice upon intranasal challenge with 1 million infectious doses. Also, at a 100-fold-lower dose, more than 50% of the viruses induced severe weight loss, and mice succumbed to the infection. In contrast, only two virus strains were pathogenic for C57BL/6 mice upon high-dose inoculation. Therefore, DBA/2 mice are a suitable model to validate influenza A virus vaccines and antiviral therapies without the need for extensive viral adaptation. Correspondingly, we used the DBA/2 model to assess the level of protection afforded by preexisting pandemic H1N1 2009 virus (H1N1pdm) cross-reactive human antibodies detected by a hemagglutination inhibition assay. Passive transfer of these antibodies prior to infection protected mice from H1N1pdm-induced pathogenicity, demonstrating the effectiveness of these cross-reactive neutralizing antibodies *in vivo*.

Respiratory tract infections are the third leading cause of mortality in the world (27). Influenza, a disease of the airways caused by influenza viruses, is responsible for approximately half a million deaths and 3 to 5 million hospitalizations per year (28). In addition to the annual disease burden, influenza A virus is more notoriously known for its ability to cause pandemics. Three pandemics have been reported in the twentieth century: the first that occurred in 1918 (Spanish influenza) killed 20 to 50 million individuals (15); the other two in 1957 and 1968, although less lethal, killed millions due to the lack of preexisting immunity. In April 2009, two cases of febrile illness were confirmed to be caused by swine-origin influenza A virus (H1N1) (4, 8). Continuous spread within North America and other parts of the world has signaled the first influenza pandemic of this century.

To study the pathogenicity of influenza A viruses, including the current pandemic A (H1N1) 2009 virus (H1N1pdm), in mammalian hosts and to determine the effectiveness of pharmaceutical interventions, it is essential to have a sensitive animal model. Although influenza has some important differences in mice and humans, a murine model is the only animal model thus far described that allows for relatively high group numbers and any relatively high throughput. Unfortunately, only a few strains of influenza A virus—almost exclusively belonging to the highly pathogenic avian influenza virus isolates of the H5 and H7 subtypes—are pathogenic in most commonly used mouse strains without adaptation through serial passaging. The hemagglutinin (HA) proteins of these H5 and H7 viruses contain a basic amino acid cleavage site, allowing them to spread systemically (12, 19, 26). Most other subtypes of influenza virus, including H1N1 and H3N2, either do not infect or cause very mild disease in mice. The requirement for adaptation of a pandemic virus to commonly used mouse strains can lead to a delay in the gathering of important data to help guide public health control strategies. As such, the lack of a sensitive small-animal model to study the infection dynamics of various subtypes of avian influenza viruses severely hampers the rapid and effective response required during a pandemic or prepandemic situation.

This study was designed to demonstrate the utility of DBA/2 mice, previously reported to be susceptible to highly pathogenic influenza viruses (1), to study infections caused by several influenza A virus subtypes isolated from birds or humans without the need for prior adaptation. To assess the utility of the model to respond to emerging strains, we used DBA/2 mice to examine the functional activity of sera from individuals previously shown to have preexisting cross-reactive H1N1pdm antibodies. It is hypothesized that these individuals may be partially protected from infection because of the presence of cross-reactive neutralizing antibodies produced after infection with a different but related H1N1 virus. This hypothesis is supported by *in vitro* microneutralization and hemagglutination inhibition (HI) assays (2, 10); however, it is not yet known whether these antibodies are also functional *in vivo*.

MATERIALS AND METHODS

Mice and viruses. Six- to 10-week-old female C57BL/6 and DBA/2 mice were purchased from Jackson Laboratories (Bar Harbor, ME) and housed in the Animal Resource Center at St. Jude Children's Research Hospital (St. Jude). The mice received food and water *ad libitum*, and all experiments were con-

* Corresponding author. Mailing address: St. Jude Children's Research Hospital, Department of Infectious Diseases, Mailstop 330, 262 Danny Thomas Place, Memphis, TN 38105. Phone: (901) 595 3014. Fax: (901) 595 8559. E-mail: Richard.Webby@stjude.org.

▽ Published ahead of print on 19 May 2010.

TABLE 1. Percent mortality in DBA/2 and C57BL/6 mice inoculated with various isolates of influenza A virus

Influenza A virus isolate	Subtype	% Mortality by mouse strain and dose		
		DBA/2 mice		C57BL/6 mice at 10^6 EID_{50}
		10^6 EID_{50}	10^4 EID_{50}	
A/Puerto Rico/8/1934	H1N1	100	100	100
A/Memphis/3/2008[a]	H1N1	100	88	0
A/California/4/2009[b]	H1N1	100	100	60
A/mallard/Alberta/79/2003	H2N3	33	0	ND[d]
A/mallard/Alberta/33/2004	H2N4	0	0	0
X31 (A/Hong Kong/1/1968)[c]	H3N2	100	100	0
A/pintail duck/Alberta/66/2005	H4N1	20	0	0
A/mallard/Alberta/147/2007	H4N6	0	ND	ND
A/Hong Kong/213/2003[a]	H5N1	100	100	76
A/Vietnam/1203/2004[a]	H5N1	100	100	100
A/shorebird/Delaware/101/2004	H5N7	20	0	0
A/ruddy turnstone/Delaware/103/2007	H5N9	100	25	ND
A/teal/Hong Kong/W312/1997	H6N1	100	100	40
A/mallard/Alberta/154/2003	H6N5	100	40	0
A/shorebird/Delaware/22/2006	H7N3	100	100	0
A/Netherlands/33/2003[a]	H7N7	100	100	100
A/mallard/Alberta/177/2004	H7N9	0	0	0
A/quail/Hong Kong/G1/1997	H9N2	100	0	0
A/duck/Hong Kong/Y280/1997	H9N2	100	20	0
A/mallard/Alberta/162/2007	H9N5	0	0	ND
A/mallard/Alberta/221/2006	H9N6	0	0	ND
A/blue-winged teal/Alberta/271/2007	H10N5	100	75	0
A/mallard/Alberta/56/2004	H10N7	100	75	0

[a] Human influenza A virus isolate.
[b] Human 2009 pandemic H1N1 virus isolate.
[c] X31 is a 6:2 reassortant virus containing six gene segments from A/Puerto Rico/8/1934 virus and the HA and NA gene segments from A/Hong Kong/1/68/.
[d] ND, not done.

ducted in accordance with rules of the Institutional Animal Control and Use Committee of St. Jude.

Twenty-three influenza A viruses (Table 1) from nine different hemagglutinin subtypes (H1 to H7, H9, and H10) were propagated in the chorioallantoic cavity of 10-day-old embryonated chicken eggs. The allantoic fluid containing infectious particles was harvested 48 h after inoculation, and the infectious titers (50% egg infectious doses [EID_{50}]) of the viruses were determined. All virus stocks had minimum titers of $10^{8.5}$ EID_{50}/ml.

Inoculation of mice with influenza A virus. C57BL/6 and DBA/2 mice were inoculated with influenza A viruses intranasally in 30 μl of sterile phosphate-buffered saline (PBS) after sedation with avertin (2,2,2-tribromoethanol; Sigma-Aldrich, MO). The 50% mouse lethal dose (MLD_{50}) was determined after mice were infected with 10-fold serial dilutions of the viruses from 10^6 EID_{50} to 10^1 EID_{50}. Morbidity and mortality were monitored for 21 days, and the MLD_{50} values were calculated by the Reed-Munch method (20). Groups of five mice per inoculum size per isolate were tested with the exception of seasonal H1N1 (at 10^6 EID_{50}, $n = 6$; at 10^4 EID_{50}, $n = 8$), H1N1pdm (10^4 EID_{50}, $n = 9$), H2N3 (10^6 EID_{50}, $n = 3$; 10^4 EID_{50}, $n = 4$), H2N4 (10^4 EID_{50}, $n = 4$), H4N6 (10^6 EID_{50}, $n = 3$), H5N9 (10^6 EID_{50}, $n = 6$; 10^4 EID_{50}, $n = 4$), H5N7 (10^6 EID_{50}, $n = 10$), H7N3 (10^6 EID_{50}, $n = 9$; 10^4 EID_{50}, $n = 4$), H7N9 (10^4 EID_{50}, $n = 4$), H9N2/Y280 (10^6 EID_{50}, $n = 10$), H9N5 (10^6 and 10^4 EID_{50}, $n = 4$), H10N5 (10^6 EID_{50}, $n = 6$; 10^4 EID_{50}, $n = 8$), and H10N7 (10^4 EID_{50}, $n = 4$) for DBA/2 mice and H5N7 (10^6 EID_{50}, $n = 8$), H6N5 (10^6 EID_{50}, $n = 6$), H7N3 (10^6 EID_{50}, $n = 10$), H7N9 (10^6 EID_{50}, $n = 4$), and H9N2 (10^6 EID_{50}, $n = 4$) for C57BL/6.

Lung viral titers. Lungs were collected on days 2 and 7 postinoculation with 10^4 EID_{50} of influenza A virus and stored at −80°C. They were homogenized in 1.0 ml of minimal essential medium, and homogenates were spun for 5 min at 1,000 × *g* to remove cellular debris. The supernatant was used to quantify the amount of infectious virus present in the lungs. Depending on the virus isolate, virus titers were determined in eggs or Madin-Darby canine kidney (MDCK) cells as described previously (1).

Hemagglutination inhibition and virus neutralization assays. Influenza A virus-neutralizing activity in serum was quantified by hemagglutination inhibition and virus microneutralization (VN) assay. Sera were first treated with receptor-destroying enzyme (RDE) (RDE II Seiken; Denka Seiken UK Ltd., United Kingdom) for 18 h at 37°C, followed by a 30-min inactivation at 56°C. HI assays were done with 4 hemagglutination units of the virus and 0.5% turkey red blood cells (H1N1pdm) or 0.5% chicken red blood cells (avian virus isolates), as described previously (10). For a VN assay the serum was diluted 2-fold starting at a 1:10 dilution in PBS and incubated for 1 h at 37°C with 100 50% tissue culture infective doses ($TCID_{50}$) of A/California/4/09 virus. Next, 100 μl of the mixture of virus and serum was added to MDCK cells for 1 h at 37°C. Following the aspiration of the supernatant, cells were washed with PBS, and 200 μl of fresh minimal essential medium supplemented with 0.1% bovine serum albumin (A8412; Sigma-Aldrich), antibiotics (Invitrogen, NY), vitamins (Invitrogen), and 1 μg/ml tosylsulfonyl phenylalanyl chloromethyl ketone (TPCK)-trypsin (Worthington, NJ) was added. After 3 to 4 days at 37°C, the assay was developed by HA assay using turkey red blood cells. The average HI and VN titers were calculated following $\log_2$ transformation of the highest serum dilution able to inhibit hemagglutination or virus replication, respectively.

Passive antibody transfer. Human sera were collected as part of a clinical trial conducted during the influenza seasons of 2007 to 2008 and 2008 to 2009 in the Greater Vancouver Area of British Columbia, Canada, or in the vicinity of the Greater Hartford Area of Connecticut. All participants received the standard dose of the licensed trivalent split-virus influenza vaccine containing A/Solomon Islands/3/2006-like (H1N1), A/Wisconsin/67/2005-like (H3N2), and B/Malaysia/2506/2004-like viruses in 2007 to 2008 or A/Brisbane/59/2007 (H1N1)-like, A/Brisbane/10/2007 (H3N2)-like, and B/Florida/4/2006-like viruses in 2008 to 2009. Sera were collected before vaccination and 4 weeks after vaccination. Postvaccination sera from individuals aged 65 years and older with detectable HI and VN titers toward H1N1pdm (A/California/4/2009) were pooled and heat inactivated for 30 min at 56°C. To study the effect of neutralizing antibodies, we used age-matched pooled human sera without detectable HI and VN titers to H1N1pdm (A/California/4/2009), seasonal H1N1 (A/Brisbane/59/2007), and H7N3 (A/shorebird/Delaware/22/2006) viruses. Ferret polyclonal sera obtained from ferrets 14 days after inoculation with the H1N1pdm virus (HI titer of 2,560; VN titer of 320) or PBS was used as a positive or negative control, respectively. A total of 400 μl of pooled human sera, diluted 1:1 in PBS, was injected intraperitoneally into 10 mice 24 h prior to inoculation with a lethal dose of virus. The positive and negative controls were also injected into 10 mice each for the H1N1pdm experiment, while five PBS control mice were included in the H7N3 and seasonal H1N1 follow-up experiment.

Cytokine analysis. Lungs were collected on days 2 and 7 postinoculation with 10^4 EID_{50} of influenza A virus, and concentrations of CCL2, CCL5, interleukin-6 (IL-6), tumor necrosis factor-alpha (TNF-α), and interferon-gamma (IFN-γ) were determined as described previously (1). Enzyme-linked immunosorbent assays (ELISAs) were performed according to the manufacturer's instructions (Quantikine kits; R&D Systems, Minneapolis, MN). At least four animals infected with a particular strain of influenza A virus were tested for one cytokine at a given time point.

Statistical analysis. Statistical analyses of differences in mortality were determined by using the log rank test. The Student's *t* test was used to analyze differences in lung virus titers between the different strains of mice following ln transformation of the data as well as to determine statistical significance in cytokine and chemokine production and weight loss after influenza A virus infection.

RESULTS

Increased susceptibility of DBA/2 mice to influenza A virus isolates. To assess the utility of DBA/2 mice as a more universal small-animal model for influenza, we tested a range of different viral subtypes for their ability to induce morbidity and mortality in this host. A set of 23 viruses belonging to nine different hemagglutinin subtypes was selected and used to inoculate DBA/2 mice. At a dose of 10^6 EID_{50}, 18 (78%) of the viruses were pathogenic, and mice succumbed to infection at 5 to 12 days postinoculation, depending on the virus isolate (Table 1). Inoculation with a lower dose of virus (10^4 EID_{50}) caused severe weight loss and death of DBA/2 mice in 14 of 22 (64%) virus isolates tested (Table 1). These isolates included a seasonal human H1N1 virus from 2008 and both H10 viruses. The ability to induce severe disease, as measured by weight loss and mortality, in DBA/2 mice was not limited to certain subtypes of influenza virus; however, virus isolates of the H2 and

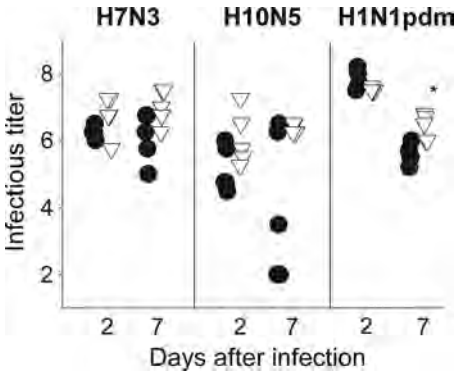

FIG. 1. Virus titer in lungs of C57BL/6 (●) and DBA/2 (▽) mice at 2 and 7 days postinoculation with 10^4 EID_{50} of A/shorebird/Delaware/22/2006 (H7N3), A/blue winged-teal/Alberta/271/2007 (H10N5), and A/California/4/2009 (H1N1pdm). *, $P < 0.01$. Infectious titer values on the *y* axis represent EID_{50}/ml for H7N3 and H10N5 viruses and $TCID_{50}$/ml for H1N1pdm.

H4 subtypes were only mildly pathogenic. Few isolates were pathogenic at 10^2 EID_{50}, and these included the two mouse-adapted influenza A viruses (A/Puerto Rico/8/1934, 100% mortality; X31, 60% mortality), two highly pathogenic H5N1 influenza A viruses (A/Hong Kong/213/2003, 84% mortality; A/Vietnam/1203/2004, 100% mortality), a low-pathogenic H7N3 (A/shorebird/Delaware/22/2006, 45% mortality) virus, and the H1N1pdm (100% mortality). Eighteen isolates were also tested in C57BL/6 mice at a dose of 10^6 EID_{50}. Only the mouse-adapted virus A/Puerto Rico/8/1934 virus, three highly pathogenic viruses, an H6N1 virus (A/teal/Hong Kong/W312/1997), and the H1N1pdm virus caused severe disease and mortality (Table 1).

Nonadapted avian influenza A viruses can replicate to high titers in C57BL/6 and DBA/2 mice. We hypothesize that the large difference in the degrees of pathogenicity of avian influenza A viruses between DBA/2 and C57BL/6 mice may be due to increased replication efficiency. To test this, we measured day 2 and day 7 postinoculation pulmonary viral loads in mice infected with 10^4 EID_{50} of H7N3 or H10N5 virus (Fig. 1). These avian virus isolates were selected for their exceptionally large difference in pathology scores between DBA/2 and C57BL/6 mice. High-dose inoculation (10^6 EID_{50}) with H7N3 or H10N5 virus induced 7% and 4% maximum weight loss in C57BL/6 mice, while DBA/2 mice succumbed to infection with 10^2 or 10^4 EID_{50}, respectively. On day 2 postinoculation, lung viral titers of DBA/2 and C57BL/6 mice were similar for both H7N3 ($10^{6.25}$ versus $10^{6.75}$ EID_{50}/ml, respectively) and H10N5 virus ($10^{5.3}$ versus $10^{6.0}$ EID_{50}/ml, respectively) (Fig. 1). Interestingly, titers in H7N3-infected lungs were approximately 1 $\log_{10}$ higher than those in H10N5-infected lungs. At day 7 postinoculation, H7N3-infected lungs of DBA/2 mice had higher virus loads than those of C57BL/6 mice ($P < 0.05$) (Fig. 1). Lungs of H10N5-infected DBA/2 mice also contained more virus than those of C57BL/6 mice; however, this difference was not significant ($P = 0.07$).

To assess the ability of other non- or low-pathogenic avian influenza A virus isolates to infect mice, we measured the serological response against the challenge virus in convalescent-phase serum as a surrogate marker for viral replication. In C57BL/6 mice, an HI titer was detected postinoculation with five of the eight virus isolates studied, suggesting that the majority of the isolates replicate in the respiratory tract of mice (Table 2). Inoculation of three viruses, an H4N1, H6N5, and an H5N7 virus, did not cause seroconversion in C57BL/6 mice. Because DBA/2 mice are generally more susceptible to influenza virus infection and because fewer isolates were non- or low-pathogenic isolates, we tested convalescent-phase serum following inoculation with only five virus isolates. Of the five convalescent-phase sera tested, three contained a detectable HI titer whereas two (an H4N6 and an H9N6 virus) did not (Table 2). These data suggest that most influenza virus isolates are capable of replicating in the respiratory tract of mice, but the outcome after infection depends entirely on the mouse strain, virus strain, or a combination of both.

Pandemic H1N1 2009 virus A/California/4/2009 is highly pathogenic in DBA/2 mice. Based on the results presented above, we next looked at the replication of the H1N1pdm viruses in DBA/2 and C57BL/6 mice. Inoculation of mice with 10^6 to 10^2 EID_{50} of A/California/4/09, a representative H1N1pdm virus, resulted in 100% mortality after 8 to 12 days, and inoculation with 10^1 EID_{50} caused significant weight loss in 100% and mortality in 50% of DBA/2 mice (Table 1). In contrast, C57BL/6 mice lost a significant amount of weight (14%; $P < 0.05$) by day 7 when inoculated with 10^6 EID_{50}, and 60% of the mice died. Inoculation with 10^5 to 10^4 EID_{50} did not cause death of C57BL/6 mice. Therefore, the MLD_{50} for A/California/4/2009 was 10^5-fold lower in DBA/2 than in C57BL/6 mice, a finding consistent with results with other virus strains.

Increased pathogenicity is often associated with higher viral loads and increased levels of proinflammatory cytokines such as CCL2, IL-6, and TNF-α. At day 2 postinoculation with 10^4 EID_{50} of H1N1pdm, lung viral titers of DBA/2 mice and C57BL/6 mice were similar (Fig. 1). There were also no significant differences in the levels of CCL2, CCL5, and IL-6 between the strains (Table 3), but levels of TNF-α were significantly higher in DBA/2 than C57BL/6 mice ($P < 0.01$). At day 7 postinfection, lung homogenates of DBA/2 mice had higher viral loads than C57BL/6 mice ($P < 0.01$) (Fig. 1) as well as significantly higher concentrations of CCL2 and IL-6 ($P < 0.01$) (Table 3).

TABLE 2. Serum antibody responses in mice infected with 10^6 EID_{50} of non- or low-pathogenic influenza A viruses

Influenza A virus isolate	Subtype	HI titer[a]	
		DBA/2 mice	C57BL/6 mice
A/Memphis/3/2008	H1N1	ND[2]	40
A/mallard/Alberta/33/2004	H2N4	40	20
A/pintail duck/Alberta/66/2005	H4N1	ND	<10
A/mallard/Alberta/147/2007	H4N6	<10	ND
A/shorebird/Delaware/101/2004	H5N7	40	<10
A/mallard/Alberta/154/2003	H6N5	ND	<10
A/mallard/Alberta/177/2004	H7N9	40	80
A/mallard/Alberta/221/2006	H9N6	<10	ND
A/blue-winged teal/Alberta/271/2007	H10N5	ND	160
A/mallard/Alberta/56/2004	H10N7	ND	40

[a] Average geometric mean titer as measured by the HI assay. An HI titer of <10 is undetectable. ND, not done.

TABLE 3. Concentrations of proinflammatory cytokines in lungs of C57BL/6 and DBA/2 mice infected with 10^4 EID_{50} of pandemic H1N1 2009 virus

Cytokine	Cytokine concn (pg/ml) by mouse strain at:[a]			
	Day 2		Day 7	
	DBA/2	C57BL/6	DBA/2	C57BL/6
CCL2	4,013	3,387	10,145*	4,520
CCL5	4,212	2,924	5,703	7,060
IL-6	710	950	1,057*	735
TNF-α	236*	102	96	109
IFN-γ	46	42	1,097	900

[a] The asterisk indicates a significant difference ($P < 0.05$) in cytokine concentrations between C57BL/6 and DBA/2 mice on day 2 or 7 after infection.

Passive transfer of cross-reactive human neutralizing antibodies protects against H1N1pdm-induced pathogenicity. To assess the functionality of human cross-reactive polyclonal antibodies, passive antibody transfer experiments were performed using the highly susceptible DBA/2 mice. Human sera were obtained from individuals not previously exposed to the H1N1pdm virus but who had cross-reactive neutralizing antibodies to it, with an HI titer of 160 and VN titer of 95. Twenty-four hours after passive transfer, mice were inoculated with 10^2 EID_{50} (3 to 5 50% lethal doses [LD_{50}]) of A/California/4/2009 virus, and morbidity and mortality were assessed. As expected, all control mice treated with PBS died within 10 days of inoculation (Fig. 2a). Mice treated with ferret serum containing high levels of H1N1pdm-specific neutralizing antibodies did not succumb to infection ($P < 0.001$) and lost significantly less weight on days 7, 10, 13, and 15 than mice in all other groups ($P < 0.01$) (Fig. 2b). DBA/2 mice injected with pooled human serum containing cross-reactive antibodies had a higher survival rate (75%) than mice in the PBS control group (0%; $P < 0.01$) and mice receiving human serum without detectable cross-neutralizing antibodies (15%; $P < 0.05$). Increased survival of the mice injected with cross-neutralizing antibodies was accompanied by a decrease in percent weight loss on days 10 (11%) and 13 (20%) postinfection ($P < 0.01$) (Fig. 2b). These data indicate that H1N1pdm-specific neutralizing antibodies induced after infection with a related H1N1 virus can protect DBA/2 mice from a lethal challenge and are likely responsible for the age-related attack rates seen in humans. The protective effect of human serum without any neutralizing antibodies was validated using two additional challenge models, a seasonal H1N1 (A/Memphis/33/2008) and an avian H7N3 (A/shorebird/Delaware/22/2006) virus isolate. The survival rates increased significantly for the seasonal H1N1 virus (90%; $P < 0.01$) but not for H7N3 (17%; $P > 0.05$), suggesting that *in vitro* HI or VN assays underestimate the levels of preexisting neutralizing immunity to influenza A virus strain in humans.

DISCUSSION

The present study establishes that DBA/2 mice are very susceptible to most influenza A virus isolates and that infection often results in debilitating pneumonia and subsequent death. This sensitivity of DBA/2 mice was used to demonstrate that H1N1pdm is more pathogenic than the circulating seasonal H1N1 viruses and that preexisting human cross-reactive neutralizing antibodies can prevent H1N1pdm-induced mortality and morbidity.

Small-animal models, like mouse models, have frequently been used for influenza virus research, including areas such as pathogenesis, vaccine efficacy, and antiviral therapies. The preferred strains, C57BL/6 and BALB/c, display few clinical symptoms upon high-dose inoculation with most influenza A virus isolates, and only highly pathogenic or mouse-adapted viruses cause severe morbidity and mortality at low doses. As such, it was generally believed that mice are resistant to most human and avian influenza A viruses. The current study, as well as a recent report by Driskell et al (6), provides substantial evidence to suggest that BALB/c and C57BL/6 mice are susceptible to infection with many different influenza A virus isolates (H1 to H7 and H9 to H11) even if the infection does not cause significant disease. In contrast, DBA/2 mice become sick and often succumb to infection with the majority of the tested isolates. This enhanced susceptibility of DBA/2 mice was previously reported for highly pathogenic and mouse-adapted influenza viruses (1, 23) and now includes many nonadapted avian influenza isolates.

The mechanism for the difference in susceptibilities between

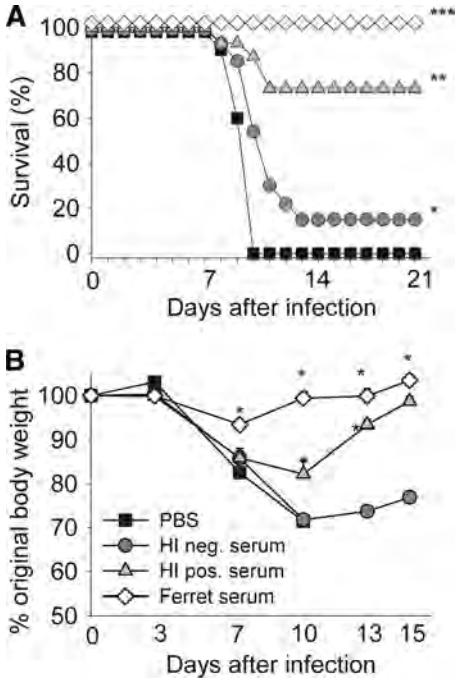

FIG. 2. Human cross-reactive 2009 pandemic H1N1-neutralizing antibodies are functional *in vivo*. Human serum pools with (H1 pos) or without (H1 neg) a detectable cross-reactive 2009 pandemic H1N1 (A/California/4/2009)-neutralizing antibody titer were injected intraperitoneally 24 h prior to intranasal lethal challenge. Control mice were injected with PBS or convalescent-phase serum obtained from 2009 pandemic H1N1 virus-infected ferrets. Survival was monitored for 21 days, and weight loss was monitored for 16 days. Data shown in panel A are the cumulative results of two experiments, and those in panel B represent the average weight loss of one indicative experiment. (A) ***, $P < 0.001$ compared to results for other groups; **, $P < 0.01$ compared to results for PBS control group and $P < 0.05$ compared to results for H1-negative group; *, $P < 0.01$ compared to results for PBS control group. (B) *, $P < 0.01$ compared to results for other groups..

C57BL/6 and DBA/2 mice is not yet fully understood but involves multiple genetic differences between the two mouse lineages, affecting several pathways and processes (1). Certain influenza viruses grow to higher titers in DBA/2 mice (A/Hong Kong/213/2003 [H5N1] or A/Memphis/33/2008 [H1N1]) (data not shown) while others do not (H7N3 and H10N5) (this study). Irrespective of the difference in viral loads, DBA/2 mice respond more vigorously, producing larger quantities of certain proinflammatory molecules like TNF-α, which was shown to correlate with increased morbidity and mortality in humans (5). Previous work has shown that the lack of a functional hemolytic complement (Hc) in DBA/2 mice may result in a less effective adaptive immune response, increasing the viral load during later stages of the infection (1, 11). In the same study, histopathologic evaluation of DBA/2 and C57BL/6 mice after H5N1 virus infection was able to clearly show more extensive involvement of the entire lung as well as necrotic epithelium on day 4 in the DBA/2 mice. At day 7 there was a dramatic difference in the numbers of cells that stained positive for influenza virus between the two strains. In the C57BL/6 mice, an inflammatory response was observed in the parenchyma, with multifocal macrophages within the infiltrate that stained positive for influenza virus. In contrast, the DBA/2 mice maintained widespread intensely positive staining of the airway epithelium, alveolar macrophages, and type I and type II cells in the alveolar wall. Overall, the combined effect of poor clearance, excessive inflammation, and elevated virus titers likely creates a highly pathogenic environment in DBA/2 mice.

The exceptional susceptibility of DBA/2 mice for influenza virus infections was used to demonstrate the effectiveness of H1N1pdm cross-neutralizing human antibodies in reducing H1N1pdm-driven mortality. Approximately 50% of the U.S. population over 75 years of age has low levels of preexposure cross-reactive antibodies to H1N1pdm (13). The age of these individuals suggests that these antibodies were generated between 1918 and 1930 when an antigenically similar H1N1 virus was possibly circulating among humans. We show in this study that these cross-reactive antibodies are also fully functional *in vivo* and may offer some degree of protection to an otherwise at-risk elderly population against the current H1N1pdm. The identity of the neutralizing epitopes has yet to be identified but could be located within the antigenic site Sa (29). Interestingly, there was a small but significant level of protection when mice were injected with human serum without detectable levels of virus-neutralizing antibodies. The protection was specific for H1N1 viruses since the transfer of HI negative serum did not affect the survival after challenge with an H7N3 virus. The protection is possibly mediated by antibodies specific for the M2 protein (18, 24, 25) or to nonneutralizing epitopes on the HA or neuraminidase (NA) (3, 14, 16, 21, 22). These data also suggest that the current *in vitro* assays (HI and VN) are underestimating the level of preexisting protective immunity in the human population. Addition of serum factors, like C1q, has been shown to increase the sensitivity of these assays (7, 17). The limited capacity of HI or VN assays to detect neutralizing antibodies was previously noted in preclinical H5N1 ferret vaccine studies. A single dose of inactivated H5N1 vaccine did not induce a detectable HI or VN titer; however, the animals were protected from a lethal challenge with highly pathogenic H5N1 virus (9).

Although the DBA/2 mouse model will provide a useful analytical tool to study viruses and antiviral therapies, the model may not necessarily reflect the natural response to influenza viruses in humans. With the exception of highly pathogenic H5N1 viruses, one should be careful in interpreting pathogenesis data upon infection with these avian isolates as described in the current study.

To summarize, we have confirmed that the DBA/2 mouse model is a suitable and highly susceptible animal model to study infection of influenza A viruses of various subtypes, including those previously known to infect humans. Also, this model will allow us to define the requirements of viruses of avian origin to infect mammalian hosts and rapidly evaluate vaccines or antiviral therapies in the event of a pandemic emergency.

ACKNOWLEDGMENTS

We thank David Walker for isolating and propagating influenza A virus isolates. We also acknowledge Nancy Cox, Sasha Klimov, and Ruben Donis of the Centers of Disease Control, Ron Fouchier of Erasmus Medical Center, Malik Peiris and Guan Yi of the University of Hong Kong, and the World Health Organization Global Influenza Surveillance Network as a source of influenza A viruses. Finally, we thank M. Ducatez and S. Schultz-Cherry for critically reviewing the paper.

This project was funded in part by grants from the National Institute of Allergy and Infectious Diseases, National Institutes of Health, Department of Health and Human Services, under contract HHSN266200700005C, by Department of Defense award W81XWH-09-1-0391, by the Centers of Infectious Diseases Control at St. Jude Children's Research Hospital, and by the American Lebanese Syrian Associated Charities.

REFERENCES

1. **Boon, A. C., J. Debeauchamp, A. Hollmann, J. Luke, M. Kotb, S. Rowe, D. Finkelstein, G. Neale, L. Lu, R. W. Williams, and R. J. Webby.** 2009. Host genetic variation affects resistance to infection with a highly pathogenic H5N1 influenza A virus in mice. J. Virol. **83:**10417–10426.
2. **Centers for Disease Control and Prevention.** 2009. Serum cross-reactive antibody response to a novel influenza A (H1N1) virus after vaccination with seasonal influenza vaccine. MMWR Morb. Mortal. Wkly. Rep. **58:**521–524.
3. **Chen, Z., S. Kadowaki, Y. Hagiwara, T. Yoshikawa, K. Matsuo, T. Kurata, and S. Tamura.** 2000. Cross-protection against a lethal influenza virus infection by DNA vaccine to neuraminidase. Vaccine **18:**3214–3222.
4. **Dawood, F. S., S. Jain, L. Finelli, M. W. Shaw, S. Lindstrom, R. J. Garten, L. V. Gubareva, X. Xu, C. B. Bridges, and T. M. Uyeki.** 2009. Emergence of a novel swine-origin influenza A (H1N1) virus in humans. N. Engl. J. Med. **360:**2605–2615.
5. **de Jong, M. D., C. P. Simmons, T. T. Thanh, V. M. Hien, G. J. Smith, T. N. Chau, D. M. Hoang, N. V. Chau, T. H. Khanh, V. C. Dong, P. T. Qui, B. V. Cam, d. Q. Ha, Y. Guan, J. S. Peiris, N. T. Chinh, T. T. Hien, and J. Farrar.** 2006. Fatal outcome of human influenza A (H5N1) is associated with high viral load and hypercytokinemia. Nat. Med. **12:**1203–1207.
6. **Driskell, E. A., C. A. Jones, D. E. Stallknecht, E. W. Howerth, and S. M. Tompkins.** 2010. Avian influenza virus isolates from wild birds replicate and cause disease in a mouse model of infection. Virology **399:**280–289.
7. **Feng, J. Q., K. Mozdzanowska, and W. Gerhard.** 2002. Complement component C1q enhances the biological activity of influenza virus hemagglutinin-specific antibodies depending on their fine antigen specificity and heavy-chain isotype. J. Virol. **76:**1369–1378.
8. **Garten, R. J., C. T. Davis, C. A. Russell, B. Shu, S. Lindstrom, A. Balish, W. M. Sessions, X. Xu, E. Skepner, V. Deyde, M. Okomo-Adhiambo, L. Gubareva, J. Barnes, C. B. Smith, S. L. Emery, M. J. Hillman, P. Rivailler, J. Smagala, M. de Graaf, D. F. Burke, R. A. Fouchier, C. Pappas, C. M. Alpuche-Aranda, H. Lopez-Gatell, H. Olivera, I. Lopez, C. A. Myers, D. Faix, P. J. Blair, C. Yu, K. M. Keene, P. D. Dotson, Jr., D. Boxrud, A. R. Sambol, S. H. Abid, K. St. George, T. Bannerman, A. L. Moore, D. J. Stringer, P. Blevins, G. J. Demmler-Harrison, M. Ginsberg, P. Kriner, S. Waterman, S. Smole, H. F. Guevara, E. A. Belongia, P. A. Clark, S. T. Beatrice, R. Donis, J. Katz, L. Finelli, C. B. Bridges, M. Shaw, D. B. Jernigan, T. M. Uyeki, D. J. Smith, A. I. Klimov, and N. J. Cox.** 2009. Antigenic and genetic characteristics of swine-origin 2009 A(H1N1) influenza viruses circulating in humans. Science **325:**197–201.

9. **Govorkova, E. A., R. J. Webby, J. Humberd, J. P. Seiler, and R. G. Webster.** 2006. Immunization with reverse-genetics-produced H5N1 influenza vaccine protects ferrets against homologous and heterologous challenge. J. Infect. Dis. **194:**159–167.
10. **Hancock, K., V. Veguilla, X. Lu, W. Zhong, E. N. Butler, H. Sun, F. Liu, L. Dong, J. R. Devos, P. M. Gargiullo, T. L. Brammer, N. J. Cox, T. M. Tumpey, and J. M. Katz.** 2009. Cross-reactive antibody responses to the 2009 pandemic H1N1 influenza virus. N. Engl. J. Med. **361:**1945–1952.
11. **Hicks, J. T., F. A. Ennis, E. Kim, and M. Verbonitz.** 1978. The importance of an intact complement pathway in recovery from a primary viral infection: influenza in decomplemented and in C5-deficient mice. J. Immunol. **121:** 1437–1445.
12. **Horimoto, T., and Y. Kawaoka.** 1994. Reverse genetics provides direct evidence for a correlation of hemagglutinin cleavability and virulence of an avian influenza A virus. J. Virol. **68:**3120–3128.
13. **Itoh, Y., K. Shinya, M. Kiso, T. Watanabe, Y. Sakoda, M. Hatta, Y. Muramoto, D. Tamura, Y. Sakai-Tagawa, T. Noda, S. Sakabe, M. Imai, Y. Hatta, S. Watanabe, C. Li, S. Yamada, K. Fujii, S. Murakami, H. Imai, S. Kakugawa, M. Ito, R. Takano, K. Iwatsuki-Horimoto, M. Shimojima, T. Horimoto, H. Goto, K. Takahashi, A. Makino, H. Ishigaki, M. Nakayama, M. Okamatsu, K. Takahashi, D. Warshauer, P. A. Shult, R. Saito, H. Suzuki, Y. Furuta, M. Yamashita, K. Mitamura, K. Nakano, M. Nakamura, R. Brockman-Schneider, H. Mitamura, M. Yamazaki, N. Sugaya, M. Suresh, M. Ozawa, G. Neumann, J. Gern, H. Kida, K. Ogasawara, and Y. Kawaoka.** 2009. In vitro and in vivo characterization of new swine-origin H1N1 influenza viruses. Nature **460:**1021–1025.
14. **Johansson, B. E., D. J. Bucher, and E. D. Kilbourne.** 1989. Purified influenza virus hemagglutinin and neuraminidase are equivalent in stimulation of antibody response but induce contrasting types of immunity to infection. J. Virol. **63:**1239–1246.
15. **Johnson, N. P., and J. Mueller.** 2002. Updating the accounts: global mortality of the 1918–1920 "Spanish" influenza pandemic. Bull. Hist Med. **76:** 105–115.
16. **McLain, L., and N. J. Dimmock.** 1989. Protection of mice from lethal influenza by adoptive transfer of non-neutralizing haemagglutination-inhibiting IgG obtained from the lungs of infected animals treated with defective interfering virus. J. Gen. Virol. **70:**2615–2624.
17. **Mehlhop, E., S. Nelson, C. A. Jost, S. Gorlatov, S. Johnson, D. H. Fremont, M. S. Diamond, and T. C. Pierson.** 2009. Complement protein C1q reduces the stoichiometric threshold for antibody-mediated neutralization of West Nile virus. Cell Host Microbe **6:**381–391.
18. **Mozdzanowska, K., K. Maiese, M. Furchner, and W. Gerhard.** 1999. Treatment of influenza virus-infected SCID mice with nonneutralizing antibodies specific for the transmembrane proteins matrix 2 and neuraminidase reduces the pulmonary virus titer but fails to clear the infection. Virology **254:**138–146.
19. **Ohuchi, M., M. Orlich, R. Ohuchi, B. E. Simpson, W. Garten, H. D. Klenk, and R. Rott.** 1989. Mutations at the cleavage site of the hemagglutinin after the pathogenicity of influenza virus A/chick/Penn/83 (H5N2). Virology **168:** 274–280.
20. **Reed, L. J., and H. Muench.** 1938. A simple method for estimating fifty percent endpoints. Am. J. Hyg. **27:**493–497.
21. **Sambhara, S., A. Kurichh, R. Miranda, T. Tumpey, T. Rowe, M. Renshaw, R. Arpino, A. Tamane, A. Kandil, O. James, B. Underdown, M. Klein, J. Katz, and D. Burt.** 2001. Heterosubtypic immunity against human influenza A viruses, including recently emerged avian H5 and H9 viruses, induced by FLU-ISCOM vaccine in mice requires both cytotoxic T-lymphocyte and macrophage function. Cell Immunol. **211:**143–153.
22. **Sandbulte, M. R., G. S. Jimenez, A. C. Boon, L. R. Smith, J. J. Treanor, and R. J. Webby.** 2007. Cross-reactive neuraminidase antibodies afford partial protection against H5N1 in mice and are present in unexposed humans. PLoS Med. **4:**e59.
23. **Srivastava, B., P. Blazejewska, M. Hessmann, D. Bruder, R. Geffers, S. Mauel, A. D. Gruber, and K. Schughart.** 2009. Host genetic background strongly influences the response to influenza a virus infections. PLoS One **4:**e4857.
24. **Tompkins, S. M., Z. S. Zhao, C. Y. Lo, J. A. Misplon, T. Liu, Z. Ye, R. J. Hogan, Z. Wu, K. A. Benton, T. M. Tumpey, and S. L. Epstein.** 2007. Matrix protein 2 vaccination and protection against influenza viruses, including subtype H5N1. Emerg. Infect. Dis. **13:**426–435.
25. **Treanor, J. J., E. L. Tierney, S. L. Zebedee, R. A. Lamb, and B. R. Murphy.** 1990. Passively transferred monoclonal antibody to the M2 protein inhibits influenza A virus replication in mice. J. Virol. **64:**1375–1377.
26. **Vey, M., M. Orlich, S. Adler, H. D. Klenk, R. Rott, and W. Garten.** 1992. Hemagglutinin activation of pathogenic avian influenza viruses of serotype H7 requires the protease recognition motif R-X-K/R-R. Virology **188:**408–413.
27. **World Health Organization.** 2008. The global burden of disease: 2004 update. World Health Organization, Geneva, Switzerland.
28. **World Health Organization.** 2009. Fact sheet number 211: influenza (seasonal). World Health Organization, Geneva, Switzerland. http://www.who.int/mediacentre/factisheets/fs211/en/.
29. **Xu, R., D. C. Ekiert, J. C. Krause, R. Hai, J. E. Crowe, Jr., and I. A. Wilson.** 2010. Structural basis of preexisting immunity to the 2009 H1N1 pandemic influenza virus. Science **328:**357–360.

JOURNAL OF VIROLOGY, May 2010, p. 4619–4629 Vol. 84, No. 9
0022-538X/10/$12.00 doi:10.1128/JVI.02406-09

Deubiquitinating and Interferon Antagonism Activities of Coronavirus Papain-Like Proteases▽

Mark A. Clementz,[1]† Zhongbin Chen,[2]† Bridget S. Banach,[1] Yanhua Wang,[2] Li Sun,[2] Kiira Ratia,[3] Yahira M. Baez-Santos,[3] Jie Wang,[4] Jun Takayama,[5] Arun K. Ghosh,[5] Kui Li,[4] Andrew D. Mesecar,[3] and Susan C. Baker[1]*

Department of Microbiology and Immunology, Loyola University Chicago Stritch School of Medicine, Maywood, Illinois 60153[1]; Division of Infection and Immunity, Department of Electromagnetic and Laser Biology, Beijing Institute of Radiation Medicine, Beijing 100850, China[2]; Department of Medicinal Chemistry and Pharmacognosy, University of Illinois, Chicago, Illinois 60607[3]; Department of Molecular Sciences, University of Tennessee Health Science Center, Memphis, Tennessee 38163[4]; and Department of Chemistry, Purdue University, West Lafayette, Indiana 47907[5]

Received 13 November 2009/Accepted 15 February 2010

Coronaviruses encode multifunctional proteins that are critical for viral replication and for blocking the innate immune response to viral infection. One such multifunctional domain is the coronavirus papain-like protease (PLP), which processes the viral replicase polyprotein, has deubiquitinating (DUB) activity, and antagonizes the induction of type I interferon (IFN). Here we characterized the DUB and IFN antagonism activities of the PLP domains of human coronavirus NL63 and severe acute respiratory syndrome (SARS) coronavirus to determine if DUB activity mediates interferon antagonism. We found that NL63 PLP2 deconjugated ubiquitin (Ub) and the Ub-line molecule ISG15 from cellular substrates and processed both lysine-48- and lysine-63- linked polyubiquitin chains. This PLP2 DUB activity was dependent on an intact catalytic cysteine residue. We demonstrated that in contrast to PLP2 DUB activity, PLP2-mediated interferon antagonism did not require enzymatic activity. Furthermore, addition of an inhibitor that blocks coronavirus protease/DUB activity did not abrogate interferon antagonism. These results indicated that a component of coronavirus PLP-mediated interferon antagonism was independent of protease and DUB activity. Overall, these results demonstrate the multifunctional nature of the coronavirus PLP domain as a viral protease, DUB, and IFN antagonist and suggest that these independent activities may provide multiple targets for antiviral therapies.

The front-line defense of a host cell against virus infection is the innate immune system, which utilizes multiple membrane and cytoplasmic sensors, such as toll-like receptors (TLRs) and RNA helicases, to detect pathogen-associated molecular patterns like viral RNA (3, 9, 31, 47, 54). Activation of these sensors by viral RNA intermediates sets off a cascade of signaling events that ultimately turn on transcription factors, such as NF-κB, ATF2/c-Jun, IRF-7, and IRF-3. These activated transcription factors translocate to the nucleus and upregulate transcription of interferon (IFN) mRNAs. The translation and subsequent secretion of IFNs activates cells to upregulate interferon-stimulated genes (ISGs) to establish an antiviral state hostile to viral replication. Of importance for this study, many of the signaling events that link the sensors to the transcription factors are mediated by the activities of kinases and ubiquitinating enzymes that modify and activate critical intermediates in the cascade (7, 8, 20, 25). For example, signaling from RIG-I can proceed through MAVS/TRAF3/TANK to TBKI and inducible IκB kinase (IKKi), which ultimately phosphorylate IRF-3. Recent studies indicate that both TRAF3 and TANK are modified by lysine-63-linked polyubiquitination and can be inactivated by DUBA, a cellular deubiquitinating (DUB) enzyme (28). Thus, ubiquitinating enzymes and DUBs are critical players in modulating the innate immune response.

For positive-strand RNA viruses that replicate in the cytoplasm of the cell using double-stranded RNA intermediates, the cytoplasmic innate immune sensors and subsequent signaling cascades represent a minefield that must be either neutralized, navigated by stealth, or both. Recent studies have revealed that viral proteases can act as "multitaskers" during viral replication by not only processing viral polyproteins but also cleaving/inactivating key players in the innate immune response. For example, the hepatitis C virus NS3-4A protease cleaves the viral replicase polyprotein and inactivates the key signaling proteins TRIF and MAVS (36, 38, 42, 46). Picornavirus 3C protease is essential for processing the replicase polyprotein and inactivating NF-κB and RIG-I (2, 49). In these studies, the catalytic function of the viral proteases was essential for the inactivation of host factors involved in signaling the innate immune response. Recently the coronavirus papain-like protease domains have also been identified as modulators of the innate immune response; however, the mechanisms of inhibition are not entirely clear (13, 16, 70).

Coronaviruses are enveloped viruses with large RNA genomes (28 to 32 kb) that cause disease in humans ranging from common colds (human coronavirus [CoV] 229E [HCoV-229E] and OC43) to croup and pneumonia, seen mostly in very young and old populations (HCoV-NL63 and -HKU1), to severe acute respiratory syndrome (SARS) coronavirus (SARS-CoV) with 10% mortality (53). Upon entry, coronavirus genomic

* Corresponding author. Mailing address: Department of Microbiology and Immunology, Loyola University Medical Center, Bldg. 105, Rm. 3929, 2160 South First Avenue, Maywood, IL 60153. Phone: (708) 216-6910. Fax: (708) 216-9574. E-mail: sbaker1@lumc.edu.
† These authors contributed equally to this work.
▽ Published ahead of print on 24 February 2010.

RNA is translated to produce two large polyproteins, pp1a and pp1ab. These polyproteins are processed by viral cysteine proteases, papain-like (PLPs/PLpro) and picornavirus 3C-like (3CLpro), to generate mature nonstructural proteins (nsp's) that assemble with host cell membranes to form double membrane vesicles (DMVs) (18, 19, 61). These DMVs are the site of viral RNA synthesis producing double-stranded intermediates and genomic/subgenomic mRNAs. Interestingly, robust replication of SARS-CoV was shown to trigger low but detectable levels of beta interferon (IFN-β) (13, 62, 63). The low-level IFN response to a vigorously replicating RNA virus suggests that SARS-CoV either evades or inactivates the innate immune response. Indeed, recent studies indicate that SARS-CoV encodes multiple proteins, such as nsp1, protein 3b, protein 6, and the nucleocapsid protein that modulate multiple pathways of the innate immune response (17, 27, 30, 48, 68). In addition, we showed that the SARS-CoV papain-like protease (PLpro) domain acts as an interferon antagonist that blocks the phosphorylation and subsequent nuclear translocation of IRF-3 (13). We also showed via X-ray structural studies that the SARS-CoV PLpro domain is similar to cellular deubiquitinating enzymes (57), and we and others demonstrated that PLpro is both a protease and a DUB (4, 39, 40). Initially, we hypothesized that either the protease or DUB activity would be required for modulating the innate immune response, but we found that inactivation of the catalytic cysteine residue of PLpro, which ablates both proteolysis and deubiquitinating activity, decreased but did not abrogate PLpro's ability to block activation of interferon (13). These results are consistent with a protease/DUB-independent mechanism that contributes to interferon antagonism. Frieman and coworkers also showed that catalytic mutants of PLpro retained interferon antagonism, and they reported that deletion of the PLP ubiquitin-like (Ubl) domain upstream of the catalytic site resulted in a loss of antagonism (16). Studies by Zheng et al. of the PLP domain of murine hepatitis virus (MHV) suggested that viral DUB activity may be required for interferon antagonism, although they reported that MHV PLP2 catalytic cysteine mutants became less efficient at, but did not eliminate, blockade of the interferon response (70). Therefore, further studies are required to clarify the role of coronavirus protease/DUB activity in PLP-mediated interferon antagonism.

In this study, we analyzed the DUB and IFN antagonism profiles of the papain-like proteases of human coronavirus NL63 and SARS-CoV (group 1 and group 2 coronaviruses, respectively). We show that HCoV-NL63 PLP2 is a deubiquitinating and deISGylating (ISG15-removing) enzyme. HCoV-NL63 infection, like that of SARS-CoV, triggers a weak type I IFN response in human airway epithelial cell cultures. We also evaluated the role of PLP2 and PLpro enzymatic activity in interferon antagonism. By generating dose-response profiles of IFN antagonism, we found that the papain-like proteases do not require enzymatic activity to inhibit type I IFN induction. Using a pharmacological approach, we found that the inhibition of PLpro did not alter the antagonism of IRF-3-dependent reporters but did affect an NF-κB- dependent reporter. Overall, we show that multifunctional coronavirus PLPs target the activities of key transcription factors involved in the induction of type I interferons and thereby hinder the activation of the innate immune system.

MATERIALS AND METHODS

Cells and HCoV-NL63. HeLa cells, HEK293 cells, and HEK293-TLR3 (stable expression of human TLR3 receptor) cells were cultured using Dulbecco's modified Eagle's medium containing 10% (vol/vol) fetal calf serum, supplemented with penicillin (100 U/ml) and streptomycin (100 μg/ml). The HCoV-NL63 (P8) virus and LLC-MK2 cells were kindly provided by Lia van der Hoek (University of Amsterdam, Amsterdam, Netherlands) and propagated as described previously (12). A plaque-purified isolate of HCoV-NL63 was kindly provided by Christian Drosten and propagated in CaCo2-TC7 cells (21). This virus stock was used to infect human airway epithelial cells as described previously (1).

Plasmid DNA. pcDNA3.1-Flag-Ub was kindly provided by Adriano Marchese (Loyola University Medical Center). IFN-β-Luc was kindly provided by John Hiscott (Jewish General Hospital, Montreal, Canada). pISRE-Luc has been previously described (35). pRL-TK *Renilla* luciferase reporter was purchased from Promega. N-RIG-Flag, NF-κB-Luc, and nsp2/3-GFP were kindly provided by Ralph Baric (University of North Carolina). pcDNA3-myc6-mISG15 was kindly provided by Min-Jung Kim (Pohang University of Science and Technology, Pohang, Republic of Korea). pcDNA3-Ube1L and pcDNA3-UbcH8 were kind gifts from Robert M. Krug (University of Texas).

PLP1 and PLP2 core domain synthesis, cloning, and site-directed mutagenesis. To obtain high expression in eukaryote cells, the codon usage of the HCoV-NL63 PLP1 core domain (amino acids 1018 to 1277 of HCoV-NL63) and PLP2 core domain (amino acids 1570 to 1884) were optimized based on human codon usage frequency, and the potential splicing sites and poly(A) signal sequences were removed and cloned into pcDNA3.1-V5/HisB at the BamHI and EcoRI sites as an in-frame fusion with the V5 peptide. The native viral sequence for the remainder of nsp3 (including the transmembrane domain downstream of PLP2) was cloned into pcDNA3.1-PLP2(N) using the existing EcoRI site and XhoI to generate transmembrane (TM)-containing PLP2 (PLP2-TM) in frame with the V5 peptide. To generate specific mutations in the catalytic residues (C1062 and H1212 in PLP1 and C1678 and H1836 in PLP2), mutagenic primers were incorporated into newly synthesized DNA using the QuikChange II XL site-directed mutagenesis protocol (Stratagene, La Jolla, CA) according to the manufacturer's instruction. Mutated nucleotides are indicated in bold. PLP1 C1062A was amplified using the forward primer 5′ AAC AAC GCC TGG ATC AGC ACC ACC CTG GTG CAA CTG 3′ and reverse primer 5′ GAT CCA GGC GTT GTT GTC GCT CTG GTC CAG CAC CCG 3′. PLP1 H1212A was amplified using the forward primer 5′ AGC GGC GCC TAC CAG ACC AAC CTG TAC AGC TTC AAC 3′ and reverse primer 5′ CTG GTA GGC GCC GCT GCC CTT CAC GCC CAG GTA CAC 3′. PLP2 C1678A was amplified using the forward primer 5′ AAC AAC GCC TGG GTG AAC GCC ACC TGC ATC ATC CTG 3′ and reverse primer 5′ CAC CCA GGC GTT GTT GTC GGT GGT GCC CAG CAC CCG 3′. PLP2 H1836A was amplified using the forward primer 5′ AAC GGC GCC TAC GTG GTG TAC GAC GCC GCC AAC AAC 3′ and reverse primer 5′ CAC GTA GGC GCC GTT GTC GAA GCT GCC GCT GAA GG 3′. The primers used for mutagenesis were designed according to the modified methods of Zheng et al. (71). All introduced mutations were confirmed by DNA sequencing.

Assay of deubiquitinating activity in cultured cells. The effect of HCoV-NL63 PLP1 and PLP2 on ubiquitinated proteins in cultured cells was assessed as described previously (14). Briefly, HeLa cells cultured in 60-mm dishes were cotransfected with 0.4 μg of pcDNA3.1-Flag-Ub plus appropriate amounts of constructs containing PLP1, PLP2, or the corresponding catalytic mutants. Transfection was performed with Lipofectamine 2000 per the manufacturer's instructions. The empty vector pcDNA3.1/V5-HisB was used to standardize the total amount of DNA used for transfection. After 48 h, cells were harvested by adding 250 μl 2× LBA, containing 20 mM *N*-ethylmaleimide (NEM) (Calbiochem) and 20 mM iodoacetamine (Sigma). Cell lysates were then analyzed for ubiquitin (Ub)-conjugated proteins by Western blotting with anti-Flag M2 antibody (1:10,000) (Sigma). Proteins were separated via SDS-PAGE, followed by transfer to a polyvinylidene difluoride (PVDF) membrane in transfer buffer (0.025 M Tris, 0.192 M glycine, and 20% methanol) for 2 h at 4°C. The membrane was blocked using 5% dried skim milk in Tris-buffered saline (TBS) (0.9% NaCl, 10 mM Tris-HCl, pH 7.5) plus 0.1% Tween 20 (TBST) for 2 h at room temperature. The blot was probed with the indicated antibody overnight at 4°C. The membrane was washed in TBST three times for 20 min (each). Following the washes, the membrane was incubated with peroxidase-conjugated secondary antibody (donkey anti-rabbit or goat anti-mouse IgG horseradish peroxidase [HRP]) (Amersham) at a dilution of 1:10,000 for 2 h at room temperature. The membrane was then washed three times with TBST and detected with Western Lightning Chemoluminescence Reagent Plus (PerkinElmer LAS Inc.). To confirm the expression levels of PLP1, PLP2, and the mutants, anti-V5 antibody

(Invitrogen) was used to detect the V5-tagged proteins. Calnexin was detected with anti-calnexin monoclonal antibody (MAb) (BD Transduction Lab) as a protein loading control.

NL63 PLP2 cleavage of K48- and K63-linked ubiquitin chains. The NL63 PLP2 wild-type protein was purified as previously described (4, 12), and ubiquitin chains were purchased from Boston Biochem (K48-Ub_6 [catalog no. UC-217] and K63-Ub_6 [catalog no. UC-317]). Proteolytic cleavage of K48-linked or K63-linked ubiquitin chains was carried out under the following conditions: 0.01 μg of purified PLP2 was incubated with 2.5 to 5 μg of K48-Ub_6 or K63-Ub_6 at 25°C in a 10- to 20-μl volume containing 50 mM HEPES, pH 7.5, 0.1 mg/ml bovine serum albumin (BSA), 100 mM NaCl, and 2 mM dithiothreitol (DTT). A control reaction was incubated under identical conditions with the exclusion of enzyme. At specified time points, the reactions were quenched with the addition of SDS-PAGE sample loading dye to a 1× concentration (25 mM Tris, pH 6.8, 280 mM β-mercaptoethanol, 4% glycerol, 0.8% SDS, 0.02% bromophenol blue) and heat treated at 95°C for 5 min. The samples were analyzed by electrophoresis on a 15% SDS-PAGE gel and stained with Coomassie dye.

Assay of deISGylating activity in cultured cells. The effect of HCoV-NL63 PLP2 on ISGylated proteins in cultured cells was assessed as described previously (69). Briefly, HEK293 cells cultured in 60-mm dishes were cotransfected with 0.5 μg of pcDNA3-myc6-mISG15, 0.25 μg of pcDNA3-Ube1L, and 0.25 μg of pcDNA3-UbcH8 plus appropriate amounts of constructs containing PLP2 or the corresponding catalytic mutant with a total of 2 μg of plasmid DNA for each transfection. The empty vector pcDNA3.1/V5-HisB was used to standardize the total amount of DNA used for transfection. Transfection was performed with Lipofectamine 2000 per the manufacturer's instructions. After 30 h, cells were harvested by adding 250 μl 2× LBA containing 20 mM *N*-ethylmaleimide (Calbiochem) and 20 mM iodoacetamine (Sigma). Cell lysates were then analyzed for ISG-conjugated proteins by Western blotting with monoclonal anti-myc antibody (1:2,000; MBL Companies, Japan) as described above. To confirm the expression levels of PLP2 and the mutants, anti-V5 antibody (1:5,000; Invitrogen) was used to detect the V5-tagged proteins. Actin was detected with antiactin MAb (Beyotime Institute of Biotechnology, China) as a protein loading control.

Enzyme-linked immunosorbent assay for IFN-β secretion in HAE culture supernatants. Human airway epithelial (HAE) cultures were generated as previously described (1). Cultures were inoculated with 100 μl of 10^5 PFU/ml HCoV-NL63, 2,000 hemagglutinating units (HAU)/ml Sendai virus (SeV), or medium for 1 h at 37°C, after which the inoculum was removed and apical washes with 200 μl of F12 medium (Gibco) were performed at indicated times. The IFN-β concentration was determined by a commercial enzyme-linked immunosorbent assay (ELISA) (PBL Biomedical Laboratories) according to the manufacturer's instructions. Data were analyzed and plotted using the GraphPad Prism 5.0 software program.

Luciferase reporter gene assay. To determine if PLpro and/or PLP2 modulates IFN expression in host cells, the IFN-β-Luc reporter, consisting of the IFN-β promoter upstream of firefly luciferase, was transfected into HEK293 cells along with PLpro, ΔUbl-PLpro-Sol, ΔUbl-PLpro-TM, PLP2, PLP2-TM, or the C1678A and H1836A PLP2 catalytic mutants in the soluble or transmembrane versions. pRL-TK, encoding *Renilla* luciferase under the control of the herpes simplex thymidine kinase promoter (low to moderate *Renilla* expression), was used for normalization of transfection efficiency. HEK293 cells were transfected by Lipofectamine 2000 or LT1 transfection reagent (MirusBio) according to the manufacturer's instructions and incubated for 24 h. Cells were then mock infected or infected with Sendai virus (Cantell strain; Charles River Laboratories) at the dose of 100 HAU/ml for 16 h or transfected with N-RIG-Flag for 24 h to activate the RIG-I-dependent IFN pathway. To detect TLR3-dependent IFN expression, HEK293-TLR3 cells were transfected with IFN-β-Luc and PLP2 for 24 h. Cells were then treated with poly(IC) for 6 h as described previously (13). Firefly luciferase and *Renilla* luciferase activities were assayed using the Dual-Luciferase reporter assay kit (Promega) and a luminometer.

Drug inhibition of SARS-CoV PLpro. HEK293 cells were transfected with plasmids encoding PLpro-TM (13), IFN-β-Luc, ISRE-Luc, NF-κB-Luc, pRL-TK, nsp2/3-GFP substrate, and/or N-RIG-Flag. The pcDNA3.1/V5-HisB vector was used to standardize the DNA concentration for transfection. Dimethyl sulfoxide (DMSO) vehicle control or 100 μM GRL-0617S (56) was added at the time of transfection. Tumor necrosis factor alpha (TNF-α) (10 ng/ml) from Roche was used to stimulate the NF-κB-Luc reporter (6 h of stimulation). Cell lysates were prepared per the manufacturer's instruction using 1× passive lysis buffer (Promega), and luciferase activity was measured using the Dual-Luciferase reporter assay kit (Promega) and a luminometer. Cell lysates were also mixed 1:1 with 2× sample buffer and subjected to Western blotting as described above. PLpro-TM was detected with anti-V5 (Invitrogen), and nsp2/3-GFP and nsp3-GFP were detected with rabbit anti-green fluorescent protein (anti-GFP) (Invitrogen).

RESULTS

NL63 PLP2 but not PLP1 has deubiquitinating activity. Previously we showed that HCoV-NL63 replicase nonstructural protein 3 (nsp3) encodes two papain-like proteases, PLP1 and PLP2, that process the amino-terminal end of the replicase polyprotein (Fig. 1A). In addition, we have shown that PLP2 can process K48-linked polyubiquitin chains, suggesting that this protease has deubiquitinating activity (12). Both the polyprotein cleavage and K48-linked polyubiquitin chain processing are dependent on a cysteine residue in the catalytic triad of this cysteine protease (12). To determine if one or both of these NL63 PLPs can remove ubiquitin conjugated to cellular proteins, HeLa cells were transfected with plasmid DNA encoding PLP1 or PLP2 along with pcDNA3.1-3×Flag-Ub, and the effect of expression of PLP1 and PLP2 on the extent of ubiquitinated cellular proteins was assessed via Western blotting with anti-Flag antibodies. We found that increasing expression of PLP2 resulted in a dramatic reduction in the level of Ub-conjugated proteins (Fig. 1B). We noted that PLP2 appears to have global DUB activity, since no particular cellular substrates were spared. As expected, this PLP2 DUB activity is dependent on an intact catalytic cysteine residue 1678, and mutation of this residue to alanine resulted in the loss of DUB activity (Fig. 1C). In contrast, PLP1 did not show any significant reduction of Flag-Ub conjugates at the concentrations tested (Fig. 1D). These results indicate that NL63 PLP2, like SARS-CoV PLpro, has potent DUB activity that can remove ubiquitin conjugates from many cellular substrates.

NL63 PLP2 processes lysine-63-linked in addition to lysine-48-linked polyubiquitin. Cellular proteins can be covalently modified with ubiquitin at one or multiple lysines through an isopeptide bond that links the carboxy terminus of ubiquitin to a lysine on the target protein. Ubiquitin itself contains seven lysines that can be further conjugated to the C terminus of another ubiquitin molecule, forming different types of polyubiquitin-linked chains on the targeted protein. The two most common types of polyubiquitin chains are linked through ubiquitin lysine 48 (K48) and lysine 63 (K63). These modifications play key regulatory roles in protein degradation and pathway signaling and have been associated with controlling several pathways of innate and adaptive immunity (7). Previous studies indicated that SARS-CoV PLpro processes both K48- and K63-linked ubiquitin (39, 40). To assess if HCoV-NL63 PLP2 has isopeptidase activity that will deconjugate K63-linked ubiquitin in addition to K48-linked isopeptidase activity, purified PLP2 enzyme was incubated with hexameric K48-linked and K63-linked polyubiquitin chains. SDS-PAGE analysis of the cleavage products shows that PLP2 can cleave the substrates *in vitro* (Fig. 2), and with prolonged incubation times, both chains can be reduced to monoubiquitin (data not shown). These data show that both major forms of polyubiquitin can be recognized and degraded by HCoV-NL63 PLP2.

PLP2 possesses deISGylating activity. Several viral DUBs, including SARS-CoV PLpro, can also deconjugate Ub-like moieties such as ISG15 (39, 40). Conjugation of ISG15 has been shown to be important for protection against viral infection

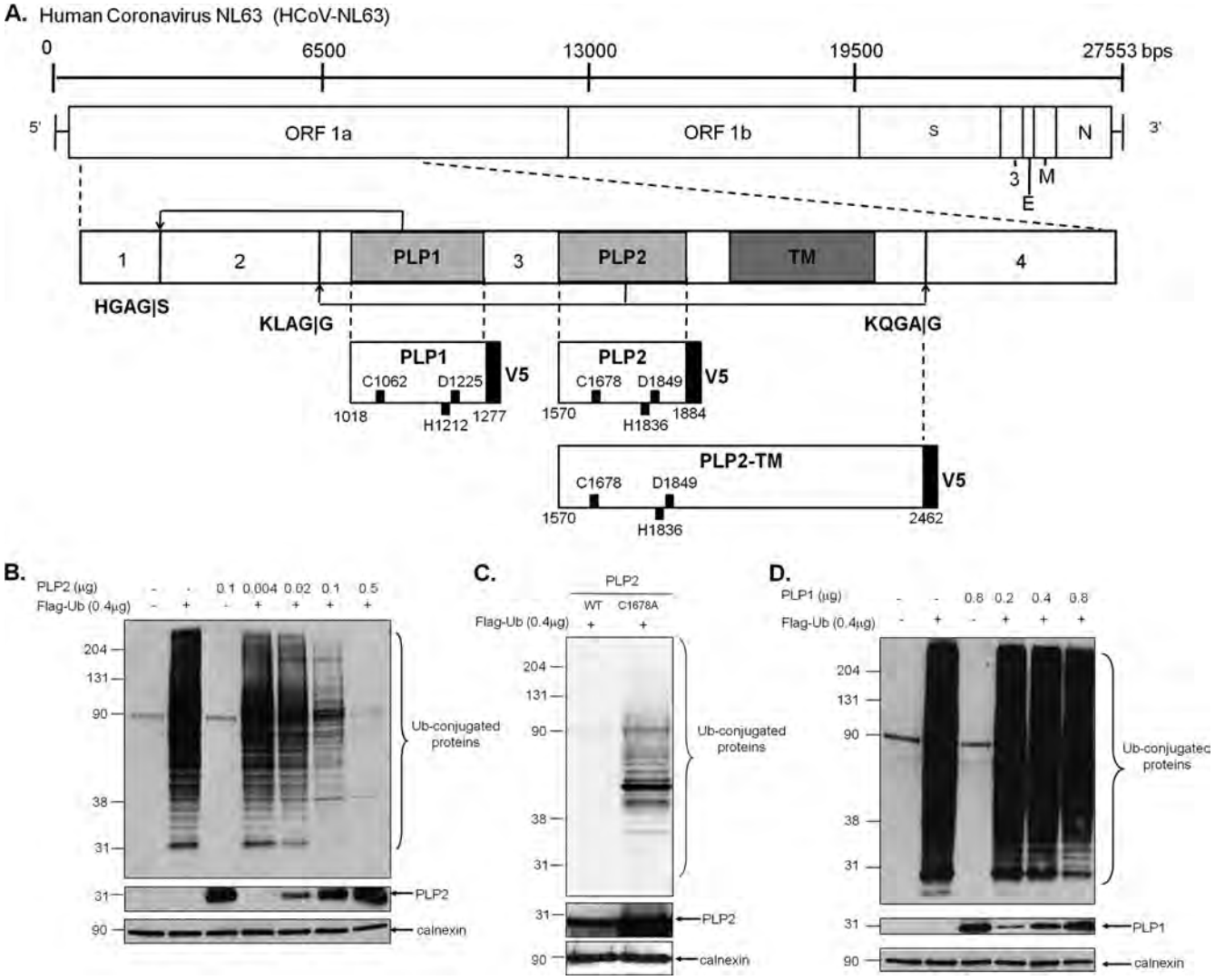

FIG. 1. HCoV-NL63 PLP2, but not PLP1, has a dose-dependent global deubiquitinating activity in cultured cells. (A) Schematic diagram of the NL63 genomic RNA and the resulting polyprotein 1ab, which contains three viral proteases. PLP1 and PLP2 cleavage sites are indicated, as are the resulting nonstructural proteins. The V5-tagged constructs of PLP2 used in this study are listed, and the catalytic residues numbering from ORF 1a are shown. DNA encoding HCoV-NL63 PLP2 (B), PLP2 C1678A (C), or PLP1 (D) was transfected into HeLa cells along with pcDNA3.1-3×Flag-Ub. Cell lysates were prepared at 24 h posttransfection and analyzed for Flag-Ub-conjugated proteins by Western blotting with an anti-Flag antibody. Mouse anti-V5 was used to confirm the expression of PLP1 and PLP2, and anticalnexin antibody was used to detect calnexin, which serves as a protein loading control. Molecular weight markers shown on the left of each gel are in thousands.

(15, 33, 34). We assessed whether HCoV-NL63 PLP2 can deISGylate cellular c-myc-tagged ISG15 (c-myc-ISG15) conjugates. HeLa cells were transfected with increasing amounts of plasmid DNA encoding PLP2 along with c-myc-ISG15 and the ISG15 conjugation machinery Ube1L and UbcH8 to enhance ISGylation of host cell proteins. The ability of PLP2 to deISGylate cellular proteins was then assayed via Western blotting with anti-myc antibody. We found that expression of increasing amounts of PLP2 was associated with a dramatic reduction in the levels of ISGylated cellular proteins (Fig. 3A), in agreement with a previous report (50). The deISGylating activity was dependent on intact catalytic residues C1678 and H1836, since mutation of these residues to alanine resulted in the loss of deISGylating activity (Fig. 3B). Thus, HCoV-NL63 PLP2 is a potent DUB/deISGylating enzyme that acts on many modified cellular substrates.

IFN-β release from human airway epithelial (HAE) cell cultures. HAE cultures are a useful model system for studying human respiratory viruses, including HCoV-NL63, since they mimic human bronchial epithelium, which is the primary site of infection (1, 60). HAE cell cultures were infected with HCoV-NL63 or Sendai virus, and apical wash samples were collected at 24, 48, 72, 96, and 144 h postinfection. The presence of secreted IFN-β in the apical wash was measured by ELISA. Mock-infected cultures released no detectable IFN-β, whereas cultures inoculated with a potent IFN inducer, Sendai virus, released more than 400 pg/ml of IFN-β. In contrast, inoculation of HAE cultures with HCoV-NL63 stimulated low but

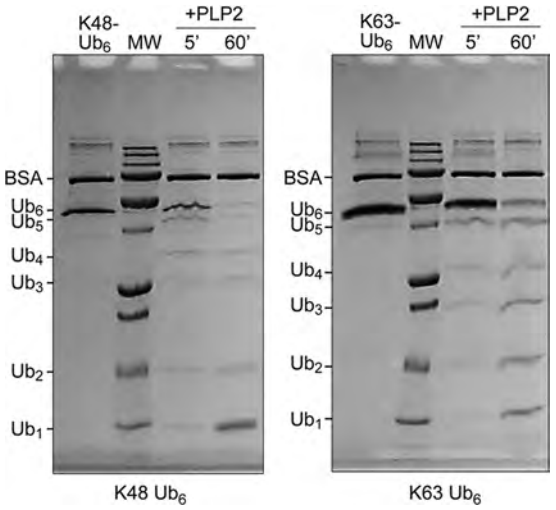

FIG. 2. Processing of K48- and K63-linked ubiquitin chains by PLP2. NL63 PLP2 was incubated with K48-linked (left) or K63-linked (right) Ub_6 chains for the indicated time points before being analyzed by SDS-PAGE. Uncleaved Ub_6 is run in the first lane of each gel. The expected sizes of the Ub species are indicated to the left of all gels. Molecular weight (MW) markers include 250,000-, 100,000-, 75,000-, 50,000-, 37,000-, 25,000-, 20,000-, 15,000-, and 10,000-molecular-weight bands.

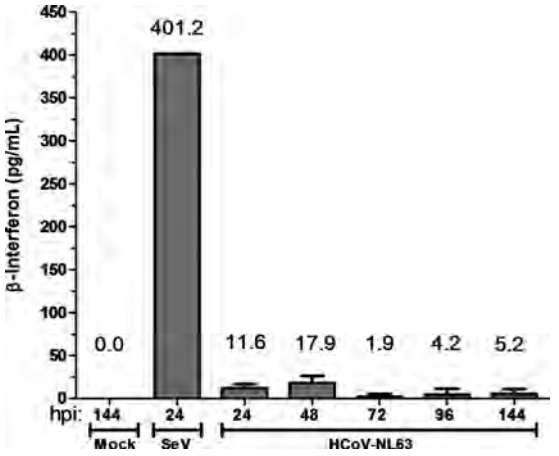

FIG. 4. Evaluating interferon-β secretion from human airway epithelial (HAE) cell cultures following HCoV-NL63 infection. Apical washes were collected from HAE cultures at 24, 48, 72, 96, and 120 h postinfection, and secreted IFN-β was measured by ELISA. Supernatant from HAE cells infected with Sendai virus (SeV) for 24 h was used as a positive control.

detectable levels of IFN-β from 24 to 144 h postinfection (Fig. 4). These results are reminiscent of the reports of low but detectable levels of IFN-β produced from SARS-CoV-infected cells (13, 63) and indicate that either HCoV-NL63 is a weak inducer of the IFN-β response or, like SARS-CoV, HCoV-NL63 encodes potent IFN antagonists.

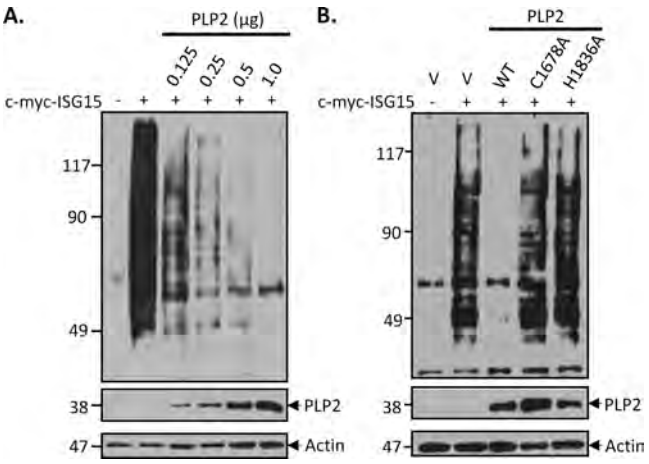

FIG. 3. NL63 PLP2 has global deISGylating activity in cultured cells. HEK293 cells were transfected with pcDNA3-myc6-mISG15, pcDNA3-Ube1L, and pcDNA3-UbcH8 plus indicated amounts of the PLP2 expression construct (A) or PLP2 expression construct and the corresponding catalytic mutants (B). To ensure that the total amount (2 μg/transfection) of plasmids for transfection was equal under every condition, empty vector pcDNA3.1/V5-HisB (v) was used to standardize the total amount of DNA. After 30 h, cells were harvested, and cell lysates were analyzed for ISG-conjugated proteins by Western blotting with monoclonal anti-myc antibody. Expression levels of V5-tagged PLP2 and mutant enzymes were detected with anti-V5 antibody. Actin was detected with antiactin MAb antibody as a protein loading control.

PLP2 inhibits both RIG-I- and TLR3-dependent IFN-β expression. To determine if PLP2 is an IFN antagonist, we transfected HEK293 cells with plasmids encoding HCoV-NL63 PLP2 or SARS-CoV PLpro along with IFN-β–luciferase and *Renilla* luciferase reporters for 24 h. Then, the RIG-I-dependent pathway leading to IFN-β expression was activated by Sendai virus infection for 16 h or by a dominant active N-terminal portion of RIG-I (N-RIG). We found that activation of the IFN-β promoter by Sendai virus (Fig. 5A) or N-RIG (Fig. 5B) was inhibited in the presence of either NL63 PLP2 or SARS-CoV PLpro. To determine if HCoV-NL63 PLP2 inhibits its TLR3-mediated activation of IFN-β production, PLP2 and the reporters were transfected into HEK293-TLR3 cells, and then the TLR3-mediated pathway was activated by addition of poly(IC) to the cell culture medium. We found that activation of the IFN-β promoter by the TLR3-mediated pathway was significantly inhibited by HCoV-NL63 PLP2 and SARS-CoV PLpro (Fig. 5C). These results demonstrate that the IFN antagonism mediated by coronavirus PLPs is conserved in two distinct viruses, although there is only 19% amino acid identity between the catalytic domains of HCoV-NL63 PLP2 and SARS-CoV PLpro in this region of nsp3 (4).

Mutation of the catalytic residues does not abolish HCoV-NL63 PLP2 IFN antagonism. To further elucidate the interferon antagonism profile of PLP2, a dose-dependent IFN antagonism profile was generated. Concurrently, to determine if IFN antagonism is dependent on catalytic activity, plasmid DNAs encoding PLP2 or the C1678A (devoid of enzymatic activity) and H1836A (severely reduced) catalytic mutants were transfected with the IFN-β and pRL-TK reporters into HEK293 cells, and IFN-β reporter activity was assessed. N-RIG was used to stimulate IFN-β induction. We found that, like the PLP2 wild type, both PLP2 C1678A and PLP2 H1836A exhibit dose-dependent inhibition of IFN-β promoter activity; however, the catalytic mutants were less efficient than wild-type PLP2 (Fig. 6A). Expression of the proteases was verified

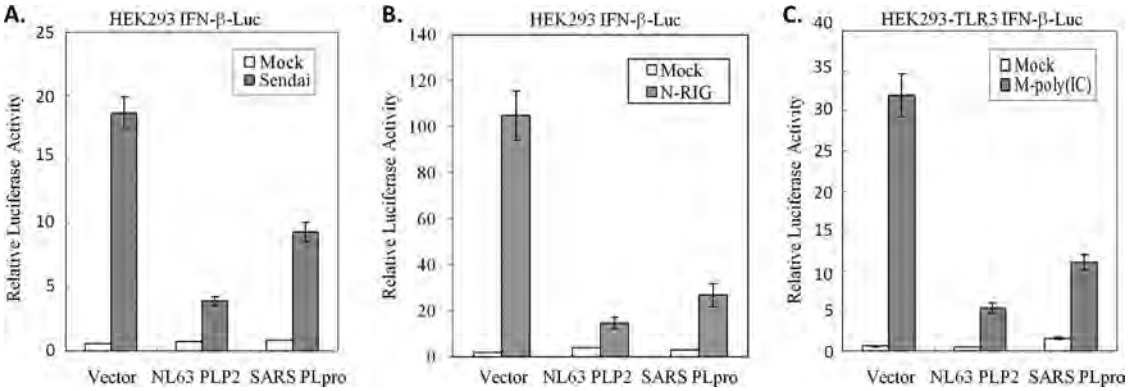

FIG. 5. PLP2 inhibits both RIG-I- and TLR3-dependent IFN-β induction. (A) HEK293 cells were transfected with IFN-β-Luc, pRL-TK, and either 300 ng of HCoV-NL63 PLP2 or 300 ng of SARS-CoV PLpro. At 24 h posttransfection, cells were either mock infected or infected with Sendai virus for 16 h. Following infection, cell lysates were prepared and assayed using the Dual-Luciferase reporter assay. (B) HEK293 cells were transfected with IFN-β-Luc, pRL-TK, 200 ng N-RIG, and either 300 ng of HCoV-NL63 PLP2 or 300 ng of SARS-CoV PLpro. At 24 h posttransfection, cell lysates were prepared and assayed using the Dual-Luciferase reporter assay. (C) HEK293-TLR3 cells were transfected with IFN-β-Luc, pRL-TK, and either 300 ng of HCoV-NL63 PLP2 or 300 ng of SARS-CoV PLpro. At 24 h posttransfection, cells were either mock treated or treated with poly(IC) for 6 h. Following poly(IC) treatment, cell lysates were prepared and assayed using the Dual-Luciferase reporter assay. Error bars indicate standard deviations from the means for triplicates.

by Western blotting (Fig. 6B). These results indicate that enzymatic activity of PLP2 is not strictly required for inhibition of antiviral IFN expression.

The transmembrane (TM) form of PLP2 is also an IFN antagonist. The PLP domains are part of a larger nsp3 protein in SARS-CoV and HCoV-NL63 that is membrane bound. Previously we showed that the biologically relevant transmembrane-containing form of SARS-CoV PLpro, termed PLpro-TM, is a potent IFN antagonist (13). To determine if the membrane-tethered version of HCoV-NL63 PLP2 can function as an interferon antagonist, the NL63 TM sequence was cloned into the PLP2 construct in frame with the V5 epitope tag, and the resulting construct was designated PLP2-TM. HEK293 cells were transfected with PLP2-TM or the catalytic mutant PLP2-TM C1678A or PLP2-TM H1836A, along with the IFN-β and pRL-TK reporters. N-RIG was used to stimulate IFN-β induction. We found that PLP2-TM and the catalytic mutants were able to inhibit N-RIG-induced IFN-β reporter activity in a dose-dependent manner, although like the soluble version of PLP2, the catalytic mutants were less efficient than the wild type (Fig. 7A). Expression of the proteases was verified by Western blotting (Fig. 7B). These data corroborate our previous results indicating that the catalytic site is not essential for IFN-β antagonism by HCoV-NL63 PLP2.

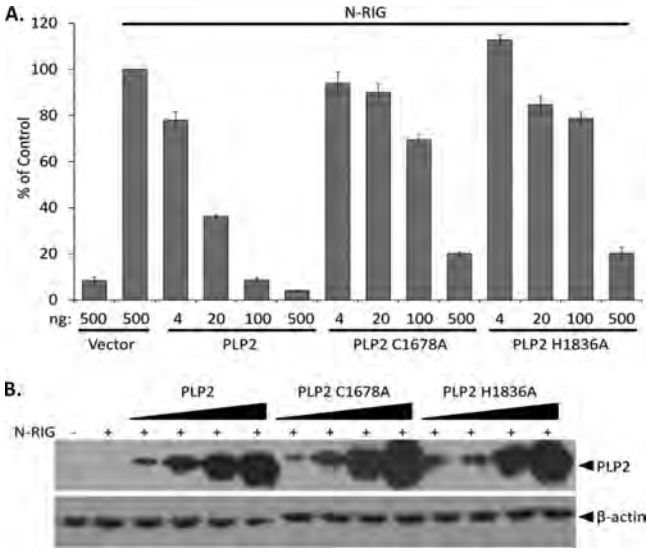

FIG. 6. HCoV-NL63 PLP2 and the catalytic mutants inhibit RIG-I-mediated IFN induction in a dose-dependent manner. PLP2 and the C1678A and H1836A catalytic mutants were cotransfected with IFN-β-Luc and pRL-TK reporters into HEK293 cells. A dominant active N-terminal portion of RIG-I was used to stimulate IFN-β induction. At 24 h posttransfection, cell lysates were harvested and assayed for luciferase activity via the Dual-Luciferase reporter assay. Values are expressed as percentages of N-RIG-stimulated luciferase controls set to 100. Error bars indicate standard deviations from the means for triplicates. (B) The cell lysates described above were mixed with 2× sample buffer and subjected to 12.5% SDS-PAGE. Following transfer to nitrocellulose, the membrane was blotted with mouse anti-V5 to detect the proteases and antiactin as a loading control.

PLpro IFN antagonism is not dependent on the ubiquitin-like domain. In addition to the downstream TM domain, a previous study suggested that the upstream ubiquitin-like domain (Ubl) plays a role in the IFN antagonism of SARS-CoV PLpro, since deletion of this domain in the soluble version of PLpro results in a loss of IFN antagonism (16). Currently, no analogous domain has been identified in HCoV-NL63 PLP2. To determine the role of the Ubl domain in the more biologically relevant transmembrane form of PLpro, we generated identical Ubl deletions (ΔUbl) of PLpro in both the soluble and transmembrane forms and performed a dose-response profile of IFN antagonism. In contrast to results of the study by Frieman and coworkers, we found that ΔUbl-PLpro-Sol was as potent as wild-type PLpro in inhibiting N-RIG-induced IFN-β reporter activity, as was ΔUbl-PLpro-TM (Fig. 8B). Expression of the proteases was verified by Western blotting (Fig. 8C). These results indicate that the Ubl domain of PLpro has no effect on antagonism of type I IFN induction.

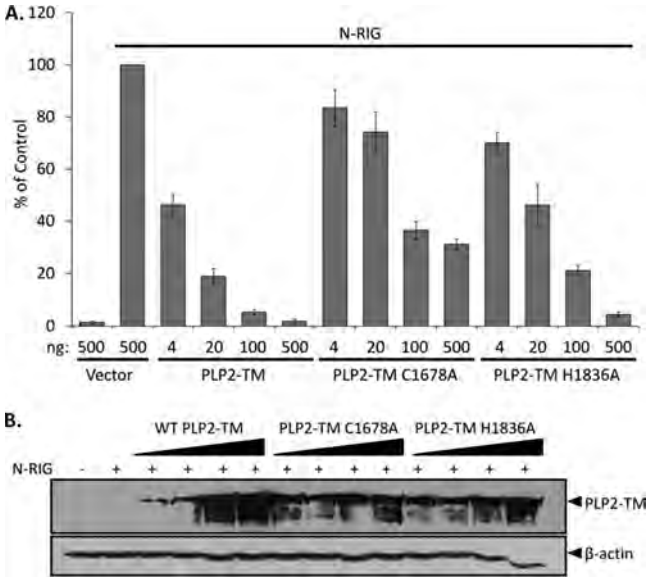

FIG. 7. The transmembrane form of HCoV-NL63 PLP2 and catalytic mutants inhibit RIG-I-mediated IFN-β induction in a dose-dependent manner. The native downstream hydrophobic domain was cloned into the PLP2 plasmid, and the catalytic cysteine or histidine residue was mutated to alanine. (A) HEK293 cells were transfected with the indicated amounts of PLP2-TM, PLP2-TM C1678A, or PLP2-TM H1836A along with the IFN-β-Luc and pRL-TK reporters. N-RIG was used to stimulate IFN-β induction. At 24 h posttransfection, cell lysates were harvested and assayed for luciferase activity via the Dual-Luciferase reporter assay. Values are expressed as percentages of N-RIG-stimulated luciferase controls set to 100. Error bars indicate standard deviations from the means for triplicates. (B) The cell lysates described above were mixed with 2× sample buffer and subjected to 12.5% SDS-PAGE. Following transfer to nitrocellulose, the membrane was blotted with mouse anti-V5 to detect the proteases and antiactin as a loading control.

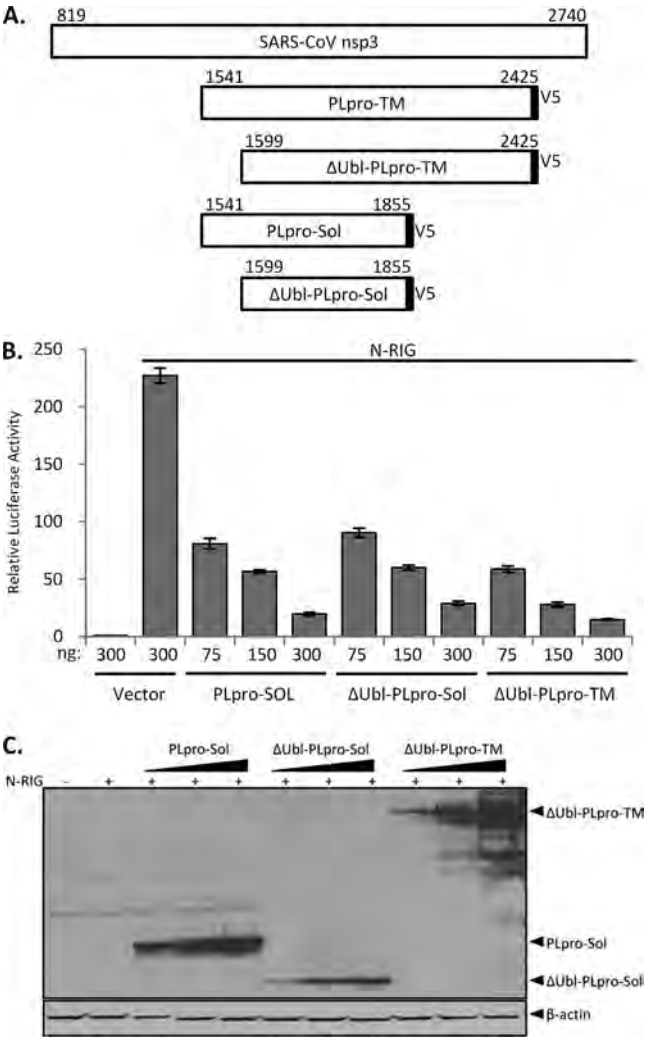

FIG. 8. The ubiquitin-like domain of SARS-CoV PLpro is not required for IFN antagonism. (A) Schematic diagram of nsp3 and the various V5-tagged deletion constructs. Numbers above the constructs indicate the amino acid numbers counting from ORF 1a. (B) HEK293 cells were transfected with the indicated amounts PLpro-Sol, ΔUbl-PLpro-Sol, or ΔUbl-PLpro-TM along with the IFN-β-Luc and pRL-TK reporters. A dominant active N-terminal portion of RIG-I was used to stimulate IFN-β induction. At 24 h posttransfection, cell lysates were harvested and assayed for luciferase activity via the Dual-Luciferase reporter assay. Values expressed are relative to results for cells transfected with the reporters alone. Error bars indicate standard deviations from the means for triplicates. (C) The cell lysates described above were mixed with 2× sample buffer and subjected to 12.5% SDS-PAGE. Following transfer to nitrocellulose, the membrane was blotted with mouse anti-V5 to detect the proteases and antiactin as a loading control.

Inhibition of SARS-CoV PLpro by protease inhibitor GRL-0617S has no effect on IFN-β or IFN-stimulated response element (ISRE) reporter activity but abrogates inhibition of NF-κB reporter activity. The mutagenesis data for PLP2 suggest that the catalytic residues (and thus catalytic activity) are not required for interferon antagonism, and Devaraj et al. reached a similar conclusion for SARS-CoV PLpro (13). To further evaluate the role of protease/DUB activity in interferon antagonism of wild-type PLpro, we added a protease inhibitor (GRL-0617S) that has been developed and shown to specifically and selectively block protease and DUB activity of SARS-CoV PLpro (56) and assessed the ability of PLpro to inhibit activation of IFN-β-Luc, ISRE-Luc, or NF-κB-Luc reporter activity. HEK293 cells were transfected with plasmid DNA encoding the transmembrane form of PLpro-TM (amino acids 1541 to 2425 of SARS-CoV ORF 1a), previously shown to be a potent IFN antagonist (13), and pRL-TK along with the IFN-β, ISRE, or NF-κB reporter, and an nsp2/3-GFP substrate. At the time of transfection, the cells were treated with 100 μM GRL-0617S (10 times the 50% effective concentration [EC_{50}]) or DMSO (vehicle control). At 24 h after transfection, cell lysates were generated and evaluated for induction of the reporters and proteolytic processing of the nsp2/3 substrate. We found that inhibition of protease activity by GRL-0617S had no effect on the IFN-β reporter (Fig. 9A) and little to no effect on the ISRE reporter, which is dependent on IRF-3 (Fig. 9B). We did detect an alleviation of PLpro-mediated inhibition of the NF-κB reporter by GRL-0617S (compare Fig. 9A and 9B with 9C). These results indicate that protease/DUB activity may be important for PLpro-mediated inhibition of NF-κB activity but not essential for inhibition of IRF-3 activity. To demonstrate efficacy of the protease inhibitor, cell lysates used in the reporter assay were assessed for nsp2/3-GFP substrate

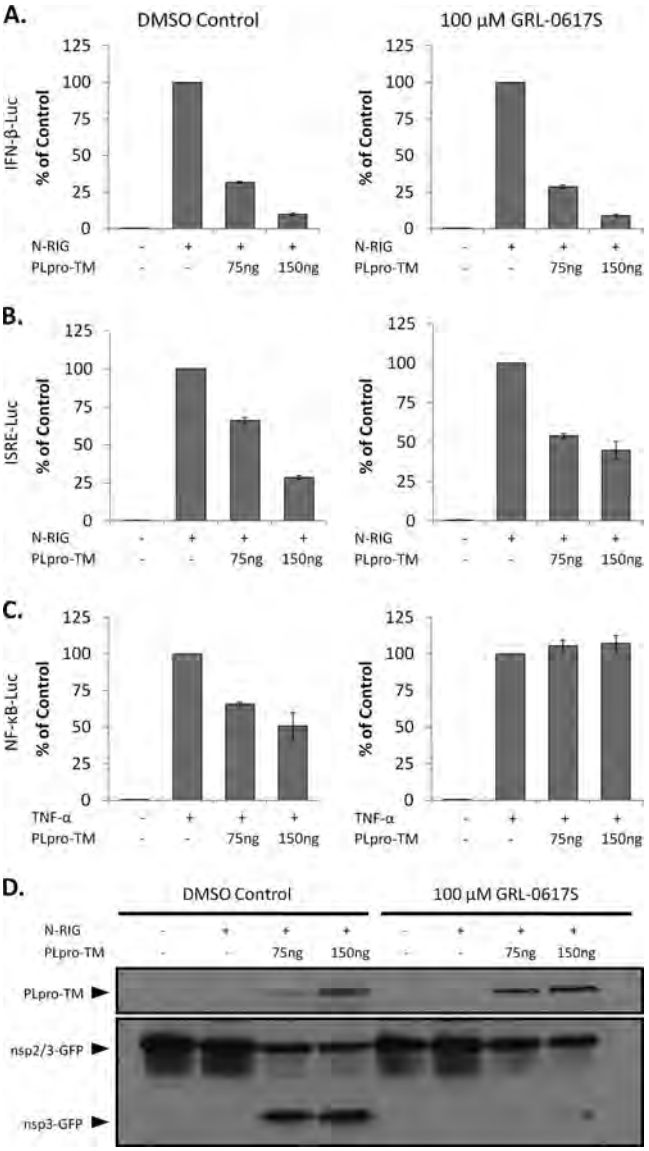

FIG. 9. SARS-CoV PLpro inhibits IFN-β and ISRE but not NF-κB reporter activity in a dose-dependent manner in the presence or absence of a protease inhibitor. HEK293 cells were transfected with the indicated amounts of PLpro-TM, pRL-TK, nsp2/3-GFP, and either IFN-β-Luc (A), ISRE-Luc (B), or NF-κB-Luc (C). N-RIG was used to stimulate IFN-β and ISRE. TNF-α (10 ng/ml) was used to stimulate the NF-κB-Luc reporter. DMSO vehicle control or 100 μM GRL-0617S was added at the time of transfection. At 24 h posttransfection, cell lysates were harvested and assayed for luciferase activity via the Dual-Luciferase reporter assay. Values are expressed as percentages of N-RIG- or TNF-α-stimulated luciferase controls, set to 100. Error bars indicate standard deviations from the means from triplicates. (D) The cell lysates described above were mixed with 2× sample buffer and subjected to 12.5% SDS-PAGE. Following transfer to nitrocellulose, the membrane was blotted with mouse anti-V5 to detect PLpro-TM and rabbit anti-GFP to detect the nsp2/3-GFP substrate and the nsp3-GFP cleavage product.

cleavage. The nsp2/3-GFP substrate contains a region of nsp2/nsp3 (including the cleavage site) fused in-frame with GFP and was previously shown to be a substrate for PLpro (16). As shown in Fig. 9D, the nsp3-GFP cleavage product was readily detected in cell lysates that contain PLpro in the absence of GRL-0617S. In contrast, the processing of nsp2/3-GFP and liberation of nsp3-GFP was almost completely abrogated in the presence of the drug. Overall, these data provide further support that there is a catalysis-independent component to type I IFN antagonism by the papain-like proteases of human coronaviruses.

DISCUSSION

In this study, we describe the multifunctional nature of the papain-like protease domains of NL63 and SARS coronaviruses. These coronavirus PLP domains act as viral proteases, deubiquitinating/deISGylating enzymes, and are able to antagonize innate immune induction of type I interferon. We found that PLP interferon antagonism is enhanced by, but is not strictly dependent on, the catalytic activity of the enzyme. Inhibition of coronavirus protease and DUB activity by mutagenesis or pharmacological means did not abrogate interferon antagonism. Therefore, these distinct PLP activities provide multiple targets for antiviral therapies.

The recognition of the DUB/deISGylating activity of SARS-CoV PLpro and HCoV-NL63 PLP2 provides new opportunities to investigate how the virus is modifying the host cell environment. Posttranslational modification of proteins by ubiquitin and ubiquitin-like (Ubl) molecules, such as SUMO, ISG15, and Nedd8, plays a critical role in the regulatory processes of virtually all aspects of cell biology (14, 15, 20, 22, 25, 29, 34, 41, 55). These modifications, though covalent, are highly reversible. Deubiquitinating enzymes can deconjugate Ub and Ub-like moieties and thus modulate the activities of ubiquitinated proteins. There are about 100 DUBs encoded in the human genome, and most of the known DUBs are cysteine proteases, characterized by a Cys-His-Asp catalytic triad (51). Several RNA viruses encode cysteine proteases to generate mature viral proteins necessary for replication, and many have been found to be multifunctional proteins. Like SARS-CoV PLpro and HCoV-NL63 PLP2, the protease of a nairovirus, Crimean Congo hemorrhagic fever virus (CCHFV), and the proteases of arteriviruses, including equine arteritis virus (EAV) and porcine respiratory and reproductive syndrome virus (PRRSV), have DUB and deISGylase activity (4, 15, 39). The contribution of these enzymatic activities to inhibition of type I IFN induction is currently poorly understood. A vast array of proteins involved in the type I IFN signaling cascade are activated by ubiquitination. Induction of IFN-β, for example, requires the activation of IRF-3 and NF-κB (45, 55). Ubiquitination is known to be intimately involved in the activation of NF-κB. Polyubiquitination of receptor-interacting protein (RIP), TNF receptor-associated factor 6 (TRAF6), and TNF receptor-associated factor 2 (TRAF2) activates these signaling intermediates, which leads to the polyubiquitination of IκB. IκB, which binds to and holds NF-κB inactive in the cytoplasm, is degraded via the proteasome, thereby freeing NF-κB to translocate to the nucleus and induce IFN-β transcription (20). Here we have shown that HCoV-NL63 PLP2 has a profound and global deconjugation effect on ubiquitinated cellular conjugates, suggesting that the DUB activity of PLP2 may modulate NF-κB activation. In addition, we demonstrate that protease inhibitors, which block coronavirus

DUB activity, abrogate the moderate inhibition of NF-κB reporter activity imposed by transient, ectopic expression of PLpro. These results support a role for coronavirus DUBs in modulating the NF-κB response during coronavirus replication. However, further investigation is needed to delineate the physiological effect of coronavirus PLPs on NF-κB signaling, since SARS-CoV PLpro did not inhibit virus- or double-stranded RNA (dsRNA)-induced activation of two well-characterized NF-κB-dependent genes, encoding interleukin 6 (IL-6) and A20, when it was stably expressed in HeLa cells in a tetracycline-regulated fashion (13).

The effect of ISGylation of cellular proteins on the antiviral response is far less understood. It is known that ISG15 conjugation is required for protection against lethal Sindbis virus infection of IFN-α/β receptor knockout mice (15). Also, ISGylation has been shown to influence the activation of the JAK/STAT pathway, involved in type I IFN signaling (44). Intriguingly, IRF-3 also undergoes ISGylation during viral infections, which was found to enhance innate antiviral responses by inhibiting virus-induced IRF-3 degradation (43). We found that HCoV-NL63 PLP2 globally deconjugates ISG15 similarly to its deconjugation of Ub, and this activity depends on the catalytic sites of PLP2. Although the contribution of the deISGylation activity of PLP2 to IFN antagonism remains to be further investigated, deISGylation of IRF-3 is unlikely to be a significant contributing factor, since the PLP catalytic mutants devoid of deISGylation activity still effectively inhibited IFN induction.

Using human airway epithelial cells, which represent a cell culture model for respiratory infection, we found that IFN-β release induced by HCoV-NL63 was weak but measurable. This finding is similar to weak IFN induction by the far more pathogenic human coronavirus SARS-CoV, suggesting that antagonism of type I IFN is a common trait of coronavirus infection (13, 58, 63). In addition to PLpro, SARS-CoV encodes several other IFN antagonists. ORF 3b, ORF 6, and nucleocapsid inhibit type I IFN induction via inhibition of IRF-3 phosphorylation and its subsequent nuclear translocation (30). ORF 6 and nsp1 have been shown to inhibit IFN signaling by interfering with the activity of STAT1 (17, 27, 48). Mouse hepatitis virus also encodes several IFN antagonists, including nsp1, nucleocapsid, and PLP2 (58, 68, 70). Thus, there is clear evolutionary pressure to encode and maintain multiple IFN antagonists. It has yet to be determined if nsp1 and nucleocapsid from HCoV-NL63 are IFN antagonists as well.

Using reporter assays, we found that HCoV-NL63 PLP2 can antagonize type I IFN induction independently of catalytic activity. Catalytic mutants of PLP2 can dose-dependently inhibit IFN-β induction; however, this inhibition is reduced compared to equivalent amounts of wild-type PLP2. In addition, we note that the presence of the transmembrane domain confers enhanced IFN antagonism, particularly in the catalytic mutants. We speculate that the TM domain may facilitate either protein folding or interaction with cellular protein partners. Overall, the antagonism profile of HCoV-NL63 PLP2 is remarkably similar to that of PLpro of SARS-CoV. In fact, using a known specific inhibitor of SARS-CoV PLpro (GRL-0617S), we found that PLpro can effectively inhibit type I IFN induction despite a profound reduction in proteolysis, which corroborates the notion of a catalysis-independent mechanism for type I IFN antagonism. Previously we showed that SARS-CoV PLpro is able to inhibit the phosphorylation and nuclear accumulation of IRF-3 following Sendai virus infection (13). We found that HCoV-NL63 PLP2 was also able to inhibit the translocation of IRF-3 to the nucleus (data not shown); however, the mechanism of this inhibition is not yet clear. We are actively searching for cellular factors that associate with HCoV-NL63 PLP2 as well as SARS-CoV PLpro.

The crystal structure of SARS-CoV PLpro has identified a unique domain that has remarkable similarity to ubiquitin (57). Frieman and coworkers reported that removal of the Ubl domain in the soluble version of PLpro resulted in a loss of IFN antagonism (16). However, we note that the authors of that study assessed IFN antagonism using one concentration of PLpro. In this study, by performing a dose-response profile of IFN antagonism, we found that deletion of the Ubl domain from both the soluble and the transmembrane version of PLpro had no effect on IFN antagonism. Thus, it is critical to assess the effect of IFN antagonism across a range of protein concentrations to fully evaluate the activity of these proteases.

Many viruses have been shown to inhibit the transcriptional activity of IRF-3 in a wide variety of ways (9, 24, 52). Some viruses inhibit IRF-3 phosphorylation, dimerization, and/or translocation to the nucleus. Others can induce IRF-3 degradation or sequester the transcription factor (11, 23). The mechanism of inhibition that can lead to these phenotypes can occur directly on IRF-3 or may affect any of the vast array of proteins upstream of IRF-3 in the type I IFN induction cascade. For example, the VP35 protein of Ebola Zaire virus (EBOV) has been shown to impact IRF-3 activity by binding dsRNA, thus preventing detection by RIG-I (5, 6). In addition, VP35 was shown to interact with Ubc9 (SUMO E2 enzyme), PIAS1 (SUMO E3 ligase), and IRF-7, leading to SUMOylation of IRF-7 and transcriptional repression of the IFN-β promoter (10). Respiratory syncytial virus (RSV) encodes two proteins, NS1 and NS2, that act individually or cooperatively to inhibit the activity of IRF-3. It was reported that these proteins reduce the expression of key kinases involved in IRF-3 phosphorylation (TRAF3 and IκB kinase epsilon [IKKε]), but how NS1 and NS2 induce TRAF3 and IKKε degradation is still unclear (64). Coronavirus PLPs could be acting on an as yet unidentified cellular factor involved in the IFN induction cascade. For example, in a recent study by Schröder et al., a new protein, DEAD box protein 3 (DDX3), was found to be involved in the type I IFN cascade. DDX3 was identified by coimmunoprecipitation with an IFN antagonist from vaccinia virus (VACV) protein K7 (59). Alternatively, it is intriguing to speculate that coronavirus PLPs may function by sequestering polyubiquitin complexes or membrane-associated factors, such as STING/MITA (26, 67, 72). Previously we showed that the block must be downstream of TBK1 but at or upstream of IRF-3 since a constitutively active form of IRF-3 is not blocked by PLpro (13). Further studies are needed to elucidate the mechanism by which coronavirus PLPs modulate IRF-3 activity.

The multiple enzymatic activities of SARS-CoV PLpro and HCoV-NL63 PLP2 may all influence the host cell type I IFN response. The DUB activity of these proteins could modulate the activity of key players in the signaling cascade that are known to be activated by lysine-48- or lysine-63-linked poly-

ubiquitination. Our data suggest that catalytic activity may contribute to IFN antagonism but ablation of proteolysis does not abrogate IFN antagonism. Thus, coronavirus PLPs also possess a catalytic activity-independent mechanism that acts to inhibit IFN induction. We are currently working to delineate both the DUB and catalytic activity-independent mechanism by which coronavirus PLPs inhibit type I IFN induction.

The data presented in this study draw significant parallels between the single papain-like protease of SARS-CoV PLpro and the second papain-like protease of HCoV-NL63 PLP2. Despite modest sequence identity (~19%), these two proteases have similar enzymatic activities and can inhibit type I IFN induction independently of catalytic activity. Since coronavirus PLpro/PLP2 domains are required for viral replication, they are attractive targets for antiviral therapeutics. Indeed, inhibitors of SARS-CoV PLpro have been shown to block virus replication (56). Though less pathogenic than SARS-CoV, HCoV-NL63 causes significant morbidity in children, the elderly, and immune-compromised individuals and has been shown to be an etiological agent causing croup (65, 66). In addition, we now recognize that bats and other mammals can serve as reservoirs for potentially emerging pandemic coronaviruses (32, 37). Thus, further studies of these multifunctional coronavirus PLPs are needed to determine if both protease inhibitors and blockers of interferon antagonism can be developed to reduce replication and pathogenesis of human and zoonotic coronaviruses.

ACKNOWLEDGMENTS

We thank members of the Baker lab for helpful discussions.

The work was supported by NIH grant P01AI060915 (to S.C.B., A.K.G., and A.D.M.), DoD grant W81XWH-09-01-0391 (to Gerald Byrne), and grants from the National Natural Science Foundation of China (30870536 and 30972761 to Z.C.) and Beijing Municipal Natural Science Foundation (7092075 to Z.C.). M.A.C. and B.S.B. were supported by NIH training grant T32AI007508.

REFERENCES

1. **Banach, B., J. M. Orenstein, L. M. Fox, S. H. Randell, A. H. Rowley, and S. C. Baker.** 2009. Human airway epithelial cell culture to identify new respiratory viruses: coronavirus NL63 as a model. J. Virol. Methods **156:**19–26.
2. **Barral, P. M., D. Sarkar, P. B. Fisher, and V. R. Racaniello.** 2009. RIG-I is cleaved during picornavirus infection. Virology **391:**171–176.
3. **Barral, P. M., D. Sarkar, Z. Z. Su, G. N. Barber, R. DeSalle, V. R. Racaniello, and P. B. Fisher.** 2009. Functions of the cytoplasmic RNA sensors RIG-I and MDA-5: key regulators of innate immunity. Pharmacol. Ther. **124:**219–234.
4. **Barretto, N., D. Jukneliene, K. Ratia, Z. Chen, A. D. Mesecar, and S. C. Baker.** 2005. The papain-like protease of severe acute respiratory syndrome coronavirus has deubiquitinating activity. J. Virol. **79:**15189–15198.
5. **Basler, C. F., A. Mikulasova, L. Martinez-Sobrido, J. Paragas, E. Muhlberger, M. Bray, H. D. Klenk, P. Palese, and A. Garcia-Sastre.** 2003. The Ebola virus VP35 protein inhibits activation of interferon regulatory factor 3. J. Virol. **77:**7945–7956.
6. **Basler, C. F., X. Wang, E. Muhlberger, V. Volchkov, J. Paragas, H. D. Klenk, A. Garcia-Sastre, and P. Palese.** 2000. The Ebola virus VP35 protein functions as a type I IFN antagonist. Proc. Natl. Acad. Sci. U. S. A. **97:**12289–12294.
7. **Bhoj, V. G., and Z. J. Chen.** 2009. Ubiquitylation in innate and adaptive immunity. Nature **458:**430–437.
8. **Bibeau-Poirier, A., and M. J. Servant.** 2008. Roles of ubiquitination in pattern-recognition receptors and type I interferon receptor signaling. Cytokine **43:**359–367.
9. **Bowie, A. G., and L. Unterholzner.** 2008. Viral evasion and subversion of pattern-recognition receptor signalling. Nat. Rev. Immunol. **8:**911–922.
10. **Chang, T. H., T. Kubota, M. Matsuoka, S. Jones, S. B. Bradfute, M. Bray, and K. Ozato.** 2009. Ebola Zaire virus blocks type I interferon production by exploiting the host SUMO modification machinery. PLoS Pathog. **5:**e1000493.
11. **Chen, Z., R. Rijnbrand, R. K. Jangra, S. G. Devaraj, L. Qu, Y. Ma, S. M. Lemon, and K. Li.** 2007. Ubiquitination and proteasomal degradation of interferon regulatory factor-3 induced by Npro from a cytopathic bovine viral diarrhea virus. Virology **366:**277–292.
12. **Chen, Z., Y. Wang, K. Ratia, A. D. Mesecar, K. D. Wilkinson, and S. C. Baker.** 2007. Proteolytic processing and deubiquitinating activity of papain-like proteases of human coronavirus NL63. J. Virol. **81:**6007–6018.
13. **Devaraj, S. G., N. Wang, Z. Chen, Z. Chen, M. Tseng, N. Barretto, R. Lin, C. J. Peters, C. T. Tseng, S. C. Baker, and K. Li.** 2007. Regulation of IRF-3-dependent innate immunity by the papain-like protease domain of the severe acute respiratory syndrome coronavirus. J. Biol. Chem. **282:**32208–32221.
14. **Evans, P. C., H. Ovaa, M. Hamon, P. J. Kilshaw, S. Hamm, S. Bauer, H. L. Ploegh, and T. S. Smith.** 2004. Zinc-finger protein A20, a regulator of inflammation and cell survival, has de-ubiquitinating activity. Biochem. J. **378:**727–734.
15. **Frias-Staheli, N., N. V. Giannakopoulos, M. Kikkert, S. L. Taylor, A. Bridgen, J. Paragas, J. A. Richt, R. R. Rowland, C. S. Schmaljohn, D. J. Lenschow, E. J. Snijder, A. Garcia-Sastre, and H. W. Virgin IV.** 2007. Ovarian tumor domain-containing viral proteases evade ubiquitin- and ISG15-dependent innate immune responses. Cell Host Microbe **2:**404–416.
16. **Frieman, M., K. Ratia, R. E. Johnston, A. D. Mesecar, and R. S. Baric.** 2009. Severe acute respiratory syndrome coronavirus papain-like protease ubiquitin-like domain and catalytic domain regulate antagonism of IRF3 and NF-kappaB signaling. J. Virol. **83:**6689–6705.
17. **Frieman, M., B. Yount, M. Heise, S. A. Kopecky-Bromberg, P. Palese, and R. S. Baric.** 2007. Severe acute respiratory syndrome coronavirus ORF6 antagonizes STAT1 function by sequestering nuclear import factors on the rough endoplasmic reticulum/Golgi membrane. J. Virol. **81:**9812–9824.
18. **Goldsmith, C. S., K. M. Tatti, T. G. Ksiazek, P. E. Rollin, J. A. Comer, W. W. Lee, P. A. Rota, B. Bankamp, W. J. Bellini, and S. R. Zaki.** 2004. Ultrastructural characterization of SARS coronavirus. Emerg. Infect. Dis. **10:**320–326.
19. **Gosert, R., A. Kanjanahaluethai, D. Egger, K. Bienz, and S. C. Baker.** 2002. RNA replication of mouse hepatitis virus takes place at double-membrane vesicles. J. Virol. **76:**3697–3708.
20. **Haglund, K., and I. Dikic.** 2005. Ubiquitylation and cell signaling. EMBO J. **24:**3353–3359.
21. **Herzog, P., C. Drosten, and M. A. Muller.** 2008. Plaque assay for human coronavirus NL63 using human colon carcinoma cells. Virol. J. **5:**138.
22. **Hicke, L., and R. Dunn.** 2003. Regulation of membrane protein transport by ubiquitin and ubiquitin-binding proteins. Annu. Rev. Cell Dev. Biol. **19:**141–172.
23. **Higgs, R., J. Ni Gabhann, N. Ben Larbi, E. P. Breen, K. A. Fitzgerald, and C. A. Jefferies.** 2008. The E3 ubiquitin ligase Ro52 negatively regulates IFN-beta production post-pathogen recognition by polyubiquitin-mediated degradation of IRF3. J. Immunol. **181:**1780–1786.
24. **Honda, K., and T. Taniguchi.** 2006. IRFs: master regulators of signalling by Toll-like receptors and cytosolic pattern-recognition receptors. Nat. Rev. Immunol. **6:**644–658.
25. **Isaacson, M. K., and H. L. Ploegh.** 2009. Ubiquitination, ubiquitin-like modifiers, and deubiquitination in viral infection. Cell Host Microbe **5:**559–570.
26. **Ishikawa, H., and G. N. Barber.** 2008. STING is an endoplasmic reticulum adaptor that facilitates innate immune signalling. Nature **455:**674–678.
27. **Kamitani, W., K. Narayanan, C. Huang, K. Lokugamage, T. Ikegami, N. Ito, H. Kubo, and S. Makino.** 2006. Severe acute respiratory syndrome coronavirus nsp1 protein suppresses host gene expression by promoting host mRNA degradation. Proc. Natl. Acad. Sci. U. S. A. **103:**12885–12890.
28. **Kayagaki, N., Q. Phung, S. Chan, R. Chaudhari, C. Quan, K. M. O'Rourke, M. Eby, E. Pietras, G. Cheng, J. F. Bazan, Z. Zhang, D. Arnott, and V. M. Dixit.** 2007. DUBA: a deubiquitinase that regulates type I interferon production. Science **318:**1628–1632.
29. **Kirkin, V., and I. Dikic.** 2007. Role of ubiquitin- and Ubl-binding proteins in cell signaling. Curr. Opin. Cell Biol. **19:**199–205.
30. **Kopecky-Bromberg, S. A., L. Martinez-Sobrido, M. Frieman, R. A. Baric, and P. Palese.** 2007. Severe acute respiratory syndrome coronavirus open reading frame (ORF) 3b, ORF 6, and nucleocapsid proteins function as interferon antagonists. J. Virol. **81:**548–557.
31. **Koyama, S., K. J. Ishii, C. Coban, and S. Akira.** 2008. Innate immune response to viral infection. Cytokine **43:**336–341.
32. **Lau, S. K., P. C. Woo, K. S. Li, Y. Huang, H. W. Tsoi, B. H. Wong, S. S. Wong, S. Y. Leung, K. H. Chan, and K. Y. Yuen.** 2005. Severe acute respiratory syndrome coronavirus-like virus in Chinese horseshoe bats. Proc. Natl. Acad. Sci. U. S. A. **102:**14040–14045.
33. **Lenschow, D. J., N. V. Giannakopoulos, L. J. Gunn, C. Johnston, A. K. O'Guin, R. E. Schmidt, B. Levine, and H. W. Virgin IV.** 2005. Identification of interferon-stimulated gene 15 as an antiviral molecule during Sindbis virus infection in vivo. J. Virol. **79:**13974–13983.
34. **Lenschow, D. J., C. Lai, N. Frias-Staheli, N. V. Giannakopoulos, A. Lutz, T. Wolff, A. Osiak, B. Levine, R. E. Schmidt, A. Garcia-Sastre, D. A. Leib, A. Pekosz, K. P. Knobeloch, I. Horak, and H. W. Virgin IV.** 2007. IFN-stimu-

lated gene 15 functions as a critical antiviral molecule against influenza, herpes, and Sindbis viruses. Proc. Natl. Acad. Sci. U. S. A. **104:**1371–1376.
35. **Li, K., Z. Chen, N. Kato, M. Gale, Jr., and S. M. Lemon.** 2005. Distinct poly(I-C) and virus-activated signaling pathways leading to interferon-beta production in hepatocytes. J. Biol. Chem. **280:**16739–16747.
36. **Li, K., E. Foy, J. C. Ferreon, M. Nakamura, A. C. Ferreon, M. Ikeda, S. C. Ray, M. Gale, Jr., and S. M. Lemon.** 2005. Immune evasion by hepatitis C virus NS3/4A protease-mediated cleavage of the Toll-like receptor 3 adaptor protein TRIF. Proc. Natl. Acad. Sci. U. S. A. **102:**2992–2997.
37. **Li, W., Z. Shi, M. Yu, W. Ren, C. Smith, J. H. Epstein, H. Wang, G. Crameri, Z. Hu, H. Zhang, J. Zhang, J. McEachern, H. Field, P. Daszak, B. T. Eaton, S. Zhang, and L. F. Wang.** 2005. Bats are natural reservoirs of SARS-like coronaviruses. Science **310:**676–679.
38. **Li, X. D., L. Sun, R. B. Seth, G. Pineda, and Z. J. Chen.** 2005. Hepatitis C virus protease NS3/4A cleaves mitochondrial antiviral signaling protein off the mitochondria to evade innate immunity. Proc. Natl. Acad. Sci. U. S. A. **102:**17717–17722.
39. **Lindner, H. A., N. Fotouhi-Ardakani, V. Lytvyn, P. Lachance, T. Sulea, and R. Menard.** 2005. The papain-like protease from the severe acute respiratory syndrome coronavirus is a deubiquitinating enzyme. J. Virol. **79:**15199–15208.
40. **Lindner, H. A., V. Lytvyn, H. Qi, P. Lachance, E. Ziomek, and R. Menard.** 2007. Selectivity in ISG15 and ubiquitin recognition by the SARS coronavirus papain-like protease. Arch. Biochem. Biophys. **466:**8–14.
41. **Liu, Y. C., J. Penninger, and M. Karin.** 2005. Immunity by ubiquitylation: a reversible process of modification. Nat. Rev. Immunol. **5:**941–952.
42. **Loo, Y. M., D. M. Owen, K. Li, A. K. Erickson, C. L. Johnson, P. M. Fish, D. S. Carney, T. Wang, H. Ishida, M. Yoneyama, T. Fujita, T. Saito, W. M. Lee, C. H. Hagedorn, D. T. Lau, S. A. Weinman, S. M. Lemon, and M. Gale, Jr.** 2006. Viral and therapeutic control of IFN-beta promoter stimulator 1 during hepatitis C virus infection. Proc. Natl. Acad. Sci. U. S. A. **103:**6001–6006.
43. **Lu, G., J. T. Reinert, I. Pitha-Rowe, A. Okumura, M. Kellum, K. P. Knobeloch, B. Hassel, and P. M. Pitha.** 2006. ISG15 enhances the innate antiviral response by inhibition of IRF-3 degradation. Cell Mol. Biol. (Noisy-le-grand) **52:**29–41.
44. **Malakhova, O. A., and D. E. Zhang.** 2008. ISG15 inhibits Nedd4 ubiquitin E3 activity and enhances the innate antiviral response. J. Biol. Chem. **283:**8783–8787.
45. **Maniatis, T., J. V. Falvo, T. H. Kim, T. K. Kim, C. H. Lin, B. S. Parekh, and M. G. Wathelet.** 1998. Structure and function of the interferon-beta enhanceosome. Cold Spring Harb. Symp. Quant. Biol. **63:**609–620.
46. **Meylan, E., J. Curran, K. Hofmann, D. Moradpour, M. Binder, R. Bartenschlager, and J. Tschopp.** 2005. Cardif is an adaptor protein in the RIG-I antiviral pathway and is targeted by hepatitis C virus. Nature **437:**1167–1172.
47. **Meylan, E., and J. Tschopp.** 2006. Toll-like receptors and RNA helicases: two parallel ways to trigger antiviral responses. Mol. Cell **22:**561–569.
48. **Narayanan, K., C. Huang, K. Lokugamage, W. Kamitani, T. Ikegami, C. T. Tseng, and S. Makino.** 2008. Severe acute respiratory syndrome coronavirus nsp1 suppresses host gene expression, including that of type I interferon, in infected cells. J. Virol. **82:**4471–4479.
49. **Neznanov, N., K. M. Chumakov, L. Neznanova, A. Almasan, A. K. Banerjee, and A. V. Gudkov.** 2005. Proteolytic cleavage of the p65-RelA subunit of NF-kappaB during poliovirus infection. J. Biol. Chem. **280:**24153–24158.
50. **Nicholson, B., C. A. Leach, S. J. Goldenberg, D. M. Francis, M. P. Kodrasov, X. Tian, J. Shanks, D. E. Sterner, A. Bernal, M. R. Mattern, K. D. Wilkinson, and T. R. Butt.** 2008. Characterization of ubiquitin and ubiquitin-like-protein isopeptidase activities. Protein Sci. **17:**1035–1043.
51. **Nijman, S. M., M. P. Luna-Vargas, A. Velds, T. R. Brummelkamp, A. M. Dirac, T. K. Sixma, and R. Bernards.** 2005. A genomic and functional inventory of deubiquitinating enzymes. Cell **123:**773–786.
52. **Ozato, K., P. Tailor, and T. Kubota.** 2007. The interferon regulatory factor family in host defense: mechanism of action. J. Biol. Chem. **282:**20065–20069.
53. **Perlman, S., and J. Netland.** 2009. Coronaviruses post-SARS: update on replication and pathogenesis. Nat. Rev. Microbiol. **7:**439–450.
54. **Pichlmair, A., and C. Reis e Sousa.** 2007. Innate recognition of viruses. Immunity **27:**370–383.
55. **Platanias, L. C.** 2005. Mechanisms of type-I- and type-II-interferon-mediated signalling. Nat. Rev. Immunol. **5:**375–386.
56. **Ratia, K., S. Pegan, J. Takayama, K. Sleeman, M. Coughlin, S. Baliji, R. Chaudhuri, W. Fu, B. S. Prabhakar, M. E. Johnson, S. C. Baker, A. K. Ghosh, and A. D. Mesecar.** 2008. A noncovalent class of papain-like protease/deubiquitinase inhibitors blocks SARS virus replication. Proc. Natl. Acad. Sci. U. S. A. **105:**16119–16124.
57. **Ratia, K., K. S. Saikatendu, B. D. Santarsiero, N. Barretto, S. C. Baker, R. C. Stevens, and A. D. Mesecar.** 2006. Severe acute respiratory syndrome coronavirus papain-like protease: structure of a viral deubiquitinating enzyme. Proc. Natl. Acad. Sci. U. S. A. **103:**5717–5722.
58. **Roth-Cross, J. K., L. Martinez-Sobrido, E. P. Scott, A. Garcia-Sastre, and S. R. Weiss.** 2007. Inhibition of the alpha/beta interferon response by mouse hepatitis virus at multiple levels. J. Virol. **81:**7189–7199.
59. **Schroder, M., M. Baran, and A. G. Bowie.** 2008. Viral targeting of DEAD box protein 3 reveals its role in TBK1/IKKepsilon-mediated IRF activation. EMBO J. **27:**2147–2157.
60. **Sheahan, T., B. Rockx, E. Donaldson, A. Sims, R. Pickles, D. Corti, and R. Baric.** 2008. Mechanisms of zoonotic severe acute respiratory syndrome coronavirus host range expansion in human airway epithelium. J. Virol. **82:**2274–2285.
61. **Snijder, E. J., Y. van der Meer, J. Zevenhoven-Dobbe, J. J. Onderwater, J. van der Meulen, H. K. Koerten, and A. M. Mommaas.** 2006. Ultrastructure and origin of membrane vesicles associated with the severe acute respiratory syndrome coronavirus replication complex. J. Virol. **80:**5927–5940.
62. **Spiegel, M., A. Pichlmair, L. Martinez-Sobrido, J. Cros, A. Garcia-Sastre, O. Haller, and F. Weber.** 2005. Inhibition of Beta interferon induction by severe acute respiratory syndrome coronavirus suggests a two-step model for activation of interferon regulatory factor 3. J. Virol. **79:**2079–2086.
63. **Spiegel, M., K. Schneider, F. Weber, M. Weidmann, and F. T. Hufert.** 2006. Interaction of severe acute respiratory syndrome-associated coronavirus with dendritic cells. J. Gen. Virol. **87:**1953–1960.
64. **Swedan, S., A. Musiyenko, and S. Barik.** 2009. Respiratory syncytial virus nonstructural proteins decrease multiple members of the cellular interferon pathways. J. Virol. **83:**9682–9693.
65. **van der Hoek, L., K. Sure, G. Ihorst, A. Stang, K. Pyrc, M. F. Jebbink, G. Petersen, J. Forster, B. Berkhout, and K. Uberla.** 2005. Croup is associated with the novel coronavirus NL63. PLoS Med. **2:**e240.
66. **van der Hoek, L., K. Sure, G. Ihorst, A. Stang, K. Pyrc, M. F. Jebbink, G. Petersen, J. Forster, B. Berkhout, and K. Uberla.** 2006. Human coronavirus NL63 infection is associated with croup. Adv. Exp. Med. Biol. **581:**485–491.
67. **Xia, Z. P., L. Sun, X. Chen, G. Pineda, X. Jiang, A. Adhikari, W. Zeng, and Z. J. Chen.** 2009. Direct activation of protein kinases by unanchored polyubiquitin chains. Nature **461:**114–119.
68. **Ye, Y., K. Hauns, J. O. Langland, B. L. Jacobs, and B. G. Hogue.** 2007. Mouse hepatitis coronavirus A59 nucleocapsid protein is a type I interferon antagonist. J. Virol. **81:**2554–2563.
69. **Zhao, C., C. Denison, J. M. Huibregtse, S. Gygi, and R. M. Krug.** 2005. Human ISG15 conjugation targets both IFN-induced and constitutively expressed proteins functioning in diverse cellular pathways. Proc. Natl. Acad. Sci. U. S. A. **102:**10200–10205.
70. **Zheng, D., G. Chen, B. Guo, G. Cheng, and H. Tang.** 2008. PLP2, a potent deubiquitinase from murine hepatitis virus, strongly inhibits cellular type I interferon production. Cell Res. **18:**1105–1113.
71. **Zheng, L., U. Baumann, and J. L. Reymond.** 2004. An efficient one-step site-directed and site-saturation mutagenesis protocol. Nucleic Acids Res. **32:**e115.
72. **Zhong, B., Y. Yang, S. Li, Y. Y. Wang, Y. Li, F. Diao, C. Lei, X. He, L. Zhang, P. Tien, and H. B. Shu.** 2008. The adaptor protein MITA links virus-sensing receptors to IRF3 transcription factor activation. Immunity **29:**538–550.

SYSTEMS GENETICS ANALYSIS OF CHLAMYDIA PSITTACI INFECTION

I. Miyairi[1, 2], J. Laxton[1], J. Ziebarth[1], R. Williams[3], L. Lu[3], G. Byrne[1], Y. Cui[1].

Department of Molecular Sciences[1], Pediatrics[2], and Anatomy and Neurobiology[3], University of Tennessee Health Science Center, Memphis, TN, USA.

Introduction

Individual differences in susceptibility to infectious diseases have been mapped to numerous disease defining genetic polymorphisms or quantitative trait loci (QTL) by forward genetics (1-3). However, such genotype-phenotype associations do not provide information on the causal pathways of how disease occurs. Inbred mouse models have been widely utilized for identification of susceptibility genes and systems genetics. Recombinant inbred (RI) strains contain unique, approximately equal proportions of genetic contributions from two progenitor inbred strains. A panel of 78 established BXD RI strains derived from C57BL/6J (B6) and DBA/2J (D2) strains have been genotyped over 13,377 SNP markers and are available for repeated testing. Combined with a web-based analytical tool (GeneNetwork.org) this allows high precision Quantitative trait loci (QTL) mapping. In a previous analysis, we determined that a QTL on chromosome 11 containing two polymorphic innate immune genes (Irgm3 and Irgb10) in the family of immunity-related GTPases (IRG) were responsible for the innate difference in susceptibility to a systemic infection to *C.psittaci* between the B6 and D2 mice (3). Characterization of the immunological differences between the B6 and D2 mice revealed significant differences in *Chlamydia* load, inflammatory responses, and cytokine profiles. While the IRGs were shown to control *Chlamydia* load (2), alternative immunomodulatory functions of this gene have been implicated (4-5). In our model it is unclear whether the various immunological differences are a function of pathogen load, immunomodulatory functions or yet unrelated to the IRGs.

We hypothesized that a multiscale analysis of BXD genotype, pathogen load, and immune parameters can be combined to define causative immune pathways induced by *Chlamydia psittaci* infection.

Methods

1. Infection and sample collection.

Chlamydia infection: 8-10 week old male mice (C57BL/6J, DBA/2J, and 57 BXD strains) were infected in groups of 2-5/strain for a total of 372 mice. *C. psittaci* 6BC strains were propagated in L cells, titrated and stored at -80C°. Intraperitoneal infection with *C.psittaci* 6BC (10^4 IFU) was performed using the same stock source to minimize variations across experiments.

Monitoring and sample collection: Infected mice were monitored daily for weight changes. On day 6-post infection, mice were euthanized to obtain peritoneal lavage samples for pathogen load, flow cytometry, and cytokine analysis.

2. Assessment of immune phenotypes.

Chlamydia load: Titration was performed by a cell culture based IFU assay.

Flow cytometry: Standard methods were used. Briefly, murine peritoneal exudates were blocked with Fc block and incubated with fluorochrome-conjugated Abs. The following Abs was used: (Macrophage) F4/80-APC, (Neutrophil) Ly6G-PE, (Class II) IA/AE-Alexa488, (Myeloid) and CD11b-PE-Cy7. Data was expressed as percent of macrophages or neutrophils in the CD11b expressing myeloid cells. Class II expression was used as a marker for macrophage activation status and data was expressed as percent of F4/80 expression cells that also expressed class II.

Cytokine analysis: Peritoneal lavage supernatants were stored in -80°C till assessment. We used the Mouse 32-plex kit to analyze levels of 32 cytokines.

3. Data analysis.

QTL analysis: We used interval mapping method available on the GeneNetwork.org interface to identify genetic loci regulating infection/immune phenotypes. Interval Mapping is a statistical test of association between trait values and the genotypes of marker loci through the genome. A significant association is interpreted as indicating the presence of a QTL linked to the marker that shows the association.

Correlation analysis: The correlation analysis was performed using Pearson and Spearman correlations and a network graph was drawn using a built in function in the GeneNetwork. This function enables graphical association among large groups of phenotypes.

Results

1. Immune phenotype data

Mice exhibited a range of disease manifestation ranging from 30 % weight reduction to 10 % weight increase in 6 days. *Chlamydia* load ranged from 4 to 6.5 log IFU/mouse. Neutrophils ranged 2-40% of the myeloid population. Of the macrophage population 2-80% expressed Class II. A measurable difference was observed in at 22 of the 32 cytokines examined.

2. QTL analysis

The majority of the variability observed in weight change, macrophage activation status, *Chlamydia* load, and neutrophil recruitment was attributed to the previously reported chromosome 11 locus. While many other traits were influenced by the chromosome 11 locus, subset of chemokines were controlled by a combination of minor QTLs on chromosomes 4, 5, 9, and 16 whereas IFNγ, TNFα, IL10 levels were under the primary control of a QTL on chromosome 8 (Table).

3. Correlation analysis

The strongest positive correlation with the disease phenotype (weight) was found with macrophage activation status, rather than *Chlamydia* load (Table). The macrophage activation status itself had a strong negative correlation with *Chlamydia* load as well as percentage of neutrophils in the inflammatory cell population. The level of cytokines such as IFNγ and TNFα were not associated with the weight changes observed in this model.

In order to determine whether the phenotype was a direct consequence of the pathogen burden we examined the correlation of pathogen load with weights of individual mice according to the genotype at chromosome 11 encoding the IRGs. Results demonstrated that mice that have the B6 genotype at the locus are tolerant to increases in the pathogen load. Also, there was a significant overlap in the pathogen load between two genotypes. These findings suggest the IRGs encoded in chromosome 11 locus affect disease outcome by a mechanism of tolerance (ability to withstand increasing pathogen burden) rather than resistance (ability to restrict pathogen load).

Discussion

Results indicate the involvement of multiple QTL in determining the immune phenotypes associated with a systemic *Chlamydia psittaci* infection. A systems approach utilized in this study allows us to infer immune responses and its hierarchy that contribute to disease process. Specifically, the disease status controlled by the chromosome 11, which is most likely the IRGs,

appeared to be a function of the macrophage activation status rather than direct *Chlamydia* load. In this model the macrophage activation status influences *Chlamydia* load as well as the inflammatory cell population. While, this will require further validation, this likely represents the multiple functions of the IRG. Cytokine levels that intuitively would be associated with disease severity such as IFNγ and TNFα were found to fluctuate independent of disease status and were controlled by other genetic loci. Candidate genes on the chromosome 8 interval are currently under investigation.

Table: QTL mapping results and Pearson correlation coefficient.

Phenotype	QTL (Chromosome)	Macro	Neutro	Weight	Chlamydia	TNFa	Mip2	IFNg
Mac activation status	Chr11	1						
Neutrophils	Chr11	-0.726	1					
Weight	Chr11	0.738	-0.673	1				
Chlamydia load	Chr11, 5	-0.736	0.556	-0.69	1			
TNFa	Chr 8, 11	-0.307	0.404	-0.25	0.374	1		
Mip2	Chr 4, 5, 9, 11, 16	-0.531	0.282	-0.354	0.269	0.149	1	
IFNg	Chr 1, 8	-0.261	0.356	-0.246	0.242	0.712	0.106	1

High positive correlations 0.7 to 1, Moderate positive correlation 0.5 to 0.7, High negative correlation –0.7 to -1.0, Moderate negative correlation –0.5 to –0.7.

Acknowledgements: This work was funded by AI081050 (IM, YC), 09GBIA2050135 (IM), BAA08-1 (GIB, IM), AI19782 (GIB), AI30040 (GIB).

References

1. Bernstein-Hanley, I., Z. R. Balsara, W. Ulmer, J. Coers, M. N. Starnbach, and W. F. Dietrich. 2006. Genetic analysis of susceptibility to Chlamydia trachomatis in mouse. Genes Immun 7:122-9.

2. Bernstein-Hanley, I., J. Coers, Z. R. Balsara, G. A. Taylor, M. N. Starnbach, and W. F. Dietrich. 2006. The p47 GTPases Igtp and Irgb10 map to the Chlamydia trachomatis susceptibility locus Ctrq-3 and mediate cellular resistance in mice. Proc Natl Acad Sci U S A 103:14092-7.

3. Miyairi, I., V. R. Tatireddigari, O. S. Mahdi, L. A. Rose, R. J. Belland, L. Lu, R. W. Williams, and G. I. Byrne. 2007. The p47 GTPases Iigp2 and Irgb10 regulate innate immunity and inflammation to murine Chlamydia psittaci infection. J Immunol 179:1814-24.

4. Howard J. 2008. The IRG proteins: a function in search of a mechanism. Immunobiology;213(3-4):367-75.

5. Taylor GA, Feng CG, Sher A. 2007. Control of IFN-gamma-mediated host resistance to intracellular pathogens by immunity-related GTPases (p47 GTPases). Microbes Infect. 9:1644-51.

Ziebarth et al. BMC Bioinformatics 2010, 11(Suppl 4):P19
http://www.biomedcentral.com/1471-2105/11/S4/P19

BMC Bioinformatics

POSTER PRESENTATION Open Access

Linking genotype to phenotype with Bayesian network modeling of *Chlamydia* infection

Jesse D Ziebarth[1*], Bao Li[1], Isao Miyairi[1,2], Yan Cui[1,3]

From UT-ORNL-KBRIN Bioinformatics Summit 2010
Cadiz, KY, USA. 19-21 March 2010

Background

Understanding the causal pathways that link genotypes with gene expression and higher order phenotypes, such as disease susceptibility, has been a recent goal of systems genetic studies. Pairwise correlations can select genes and phenotypes that are associated with a common genetic locus; however, the directions of these links are more difficult to determine. We propose a method in which Bayesian networks are used to establish causal pathways from genotype to gene expression to phenotype and apply it to mice infected with *Chlamydia psittaci*.

Results

Recombinant inbred BXD mice strains have been previously used to study the genetic differences that cause a much greater resistance to *Chlamydia psittaci* infection in C57BL/6J mice compared with DBA/2J mice [1]. Gene expression levels and higher order phenotypes, such as pathogen load and survival, were collected for 44 BXD strains. Directed graphs linking SNPs [2] in the BXD genomes to this data were created with QTL mapping and the Bayesian network method. Figure 1 shows a selection of the resulting causal pathways; many of the genes in these pathways are known to be associated with immune response or GTPase activity, which has been linked to *Chlamydia psittaci* infection [1].

Acknowledgements
This work was support by NIH grant AI081050 and DOD grant W81XHW-05-01-0227.

Author details
[1]Department of Molecular Sciences, University of Tennessee Health Science Center, Memphis, TN 38163, USA. [2]Department of Pediatrics, University of Tennessee Health Science Center, Memphis, TN 38163, USA. [3]Center of Integrative and Translational Genomics, University of Tennessee Health Science Center, Memphis, TN 38163, USA.

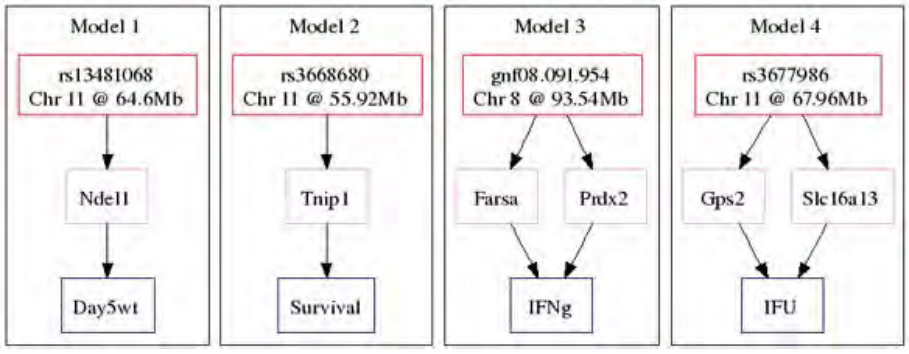

Figure 1 Causal pathways linking genotype SNPs to gene expression levels to phenotypes in BXD mice infected with *Chlamydia psittaci*

* Correspondence: jziebart@uthsc.edu
[1]Department of Molecular Sciences, University of Tennessee Health Science Center, Memphis, TN 38163, USA

Published: 23 July 2010

References

1. Miyairi I, Tatireddigari VRRA, Mahdi OS, Rose LA, Belland RJ, Lu L, Williams RW, Byrne GI: **The p47 GTPases *Iigp2 and Irgb10* regulate innate immunity and inflammation to murine *Chlamydia psittaci* infection.** *J Immunol* 2007, **179**:1814-1824.
2. **BXD Genotypes at the GeneNetwork.** [http://www.genenetwork.org/genotypes/BXD.geno].

doi:10.1186/1471-2105-11-S4-P19
Cite this article as: Ziebarth *et al.*: Linking genotype to phenotype with Bayesian network modeling of *Chlamydia* infection. *BMC Bioinformatics* 2010 **11**(Suppl 4):P19.

BMC Bioinformatics

ORAL PRESENTATION Open Access

High-throughput sequencing of the DBA/2J mouse genome

Xusheng Wang[1], Richa Agarwala[2], John A Capra[3], Zugen Chen[4], Deanna M Church[2], Daniel C Ciobanu[5], Zhengsheng Li[1], Lu Lu[1], Khyobeni Mozhui[1], Megan K Mulligan[1], Stanley F Nelson[4], Katherine S Pollard[3], Williams L Taylor[1], Donald B Thomason[1], Robert W Williams[1*]

From UT-ORNL-KBRIN Bioinformatics Summit 2010
Cadiz, KY, USA. 19-21 March 2010

Background

The DBA/2J mouse is not only the oldest inbred strain, but also one of the most widely used strains. DBA/2J exhibits many unique anatomical, physiological, and behavior traits. In addition, DBA/2J is one parent of the large BXD family of recombinant inbred strains [1]. The genome of the other parent of this BXD family—C57BL/6J—has been sequenced and serves as the mouse reference genome [2]. We sequenced the genome of DBA/2J using SOLiD and Illumina high throughput short read protocols to generate a comprehensive set of ~5 million sequence variants segregating in the BXD family that ultimately cause developmental, anatomical, functional and behavioral differences among these 80+ strains.

Results

We generated approximately 13.2 and 38.9× whole-genome short reads of DBA/2J females using Illumina GA2 and ABI SOLiD massively parallel DNA sequencing platforms. Comparing to the C57BL/6J reference genome sequence, we identified over 4.5 million single nucleotide polymorphisms (SNPs), including 84 nonsense and ~11,000 missense mutations, 78% of which are novel. We also detected ~568,000 insertions and deletions (indels) within single short reads and ~9,400 between mate-paired reads. Approximately 300 inversions were detected by SOLiD mate-pair reads, 46 of which span at least one exon. In addition, we identified ~22,000 copy number variants (CNVs) in the range of 1 Kb to 100 Kb (Figure 1).

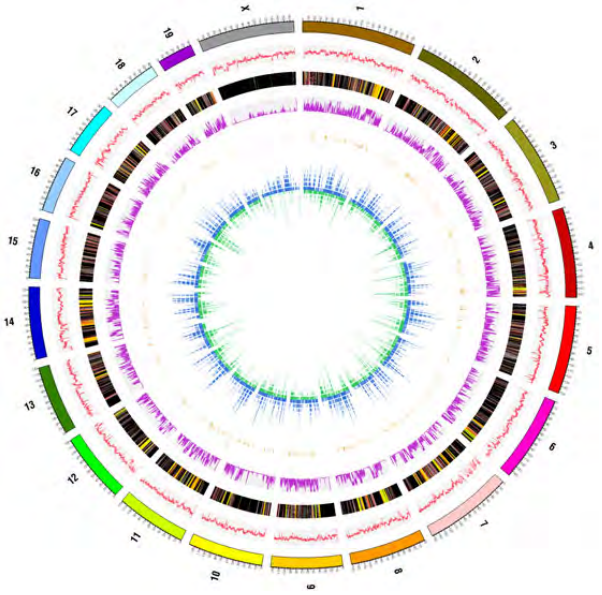

Figure 1 Concentric circles represent the sequence and structural variation across mouse chromosomes. Moving inward from the outer circle, circle 1 denotes each chromosome. Circle 2, read depth with 100kb window. Circle 3, SNP density with 100kb windows (black is lowest density and orange is highest density). Circle 4, Indels density with 100kb window. Circle 4, Inversion. Circle 5, CNVs, blue (outward) denotes loss of CNVs and green (inward) denotes gains of CNVs.

Conclusion

Our study generates the first consensus sequence for the DBA/2J and creates a compendium of sequence and structural variations that will be used by the community of researchers who study complex traits in mouse models. The sequence data provide a novel resource with which to initiate reverse genetic analysis of complex

* Correspondence: rwilliam@nb.uthsc.edu
[1]University of Tennessee Health Science Center, Memphis, TN 38163, USA

traits, particularly by exploiting strong alleles (premature stop codons, frame-shift mutations, and deletion) that differentially affect members of the BXD strain family. The DBA/2J genome is also an essential prerequisite to unbiased alignment of RNA-seq and ChIP-seq data generated using BXD strains and any other cross involving these two common parental strains.

Author details
[1]University of Tennessee Health Science Center, Memphis, TN 38163, USA. [2]National Center for Biotechnology Information, National Library of Medicine, National Institutes of Health, Bethesda, MD 20894, USA. [3]Gladstone Institutes, University of California, San Francisco, CA 94158, USA. [4]University of California, Los Angeles, CA 90095, USA. [5]University of Nebraska, Lincoln, NE 68588, USA.

Published: 23 July 2010

References

1. Peirce JL, Lu L, Gu J, Silver LM, Williams RW: **A new set of BXD recombinant inbred lines from advanced intercross populations in mice.** *BMC genetics* 2004, **5**:7.
2. Waterston RH, Lindblad-Toh K, Birney E, Rogers J, Abril JF, Agarwal P, Agarwala R, Ainscough R, Alexandersson M, An P: **Initial sequencing and comparative analysis of the mouse genome.** *Nature* 2002, **420(6915)**:520-562.

doi:10.1186/1471-2105-11-S4-O7
Cite this article as: Wang *et al.*: High-throughput sequencing of the DBA/2J mouse genome. *BMC Bioinformatics* 2010 **11**(Suppl 4):O7.

OPEN ACCESS Freely available online

PLoS one

Expression QTL Modules as Functional Components Underlying Higher-Order Phenotypes

Lei Bao[1]*¤, Xuefeng Xia[3], Yan Cui[1,2]*

1 Department of Molecular Sciences, University of Tennessee Health Science Center, Memphis, Tennessee, United States of America, **2** Center for Integrative and Translational Genomics, University of Tennessee Health Science Center, Memphis, Tennessee, United States of America, **3** Institute of Bioinformatics, Tsinghua University, Beijing, China

Abstract

Systems genetics studies often involve the mapping of numerous regulatory relations between genetic loci and expression traits. These regulatory relations form a bipartite network consisting of genetic loci and expression phenotypes. Modular network organizations may arise from the pleiotropic and polygenic regulation of gene expression. Here we analyzed the expression QTL (eQTL) networks derived from expression genetic data of yeast and mouse liver and found 65 and 98 modules respectively. Computer simulation result showed that such modules rarely occurred in randomized networks with the same number of nodes and edges and same degree distribution. We also found significant within-module functional coherence. The analysis of genetic overlaps and the evidences from biomedical literature have linked some eQTL modules to physiological phenotypes. Functional coherence within the eQTL modules and genetic overlaps between the modules and physiological phenotypes suggests that eQTL modules may act as functional units underlying the higher-order phenotypes.

Citation: Bao L, Xia X, Cui Y (2010) Expression QTL Modules as Functional Components Underlying Higher-Order Phenotypes. PLoS ONE 5(12): e14313. doi:10.1371/journal.pone.0014313

Editor: Cathal Seoighe, National University of Ireland Galway, Ireland

Received July 22, 2010; **Accepted** November 23, 2010; **Published** December 13, 2010

Funding: This work was supported in part by NIH grants NR009270, AI081050, a Department of Defense grant W81XHW-05-01-0227 and an American Heart Association grant 0830134N. The funders had no role in study design, data collection and analysis, decision to publish, or preparation of the manuscript.

Competing Interests: The authors have declared that no competing interests exist.

* E-mail: lebao@ucsd.edu (LB); ycui2@uthsc.edu (YC)

¤ Current address: Moores Cancer Center, University of California San Diego, San Diego, California, United States of America

Introduction

Recent advances in the integration of quantitative genetics and expression genomics have provided a global view of gene expression traits and their implications in high-order phenotype variations [1,2,3,4,5,6,7,8]. The Genetical Genomics [9] approach systematically associates gene expression traits with regulatory genomic regions called expression quantitative trait loci (eQTLs) [10]. Typically, this high-throughput approach identifies a large set of regulatory relations between genetic markers and expression traits, which compose bipartite networks that consist of two types of nodes, representing expression traits and eQTLs respectively.

A module is usually defined as a subset of components in a network that interact with each other and act in concert to regulate biological processes, while maintaining relative independence from other components in the network. Studies on the architecture of biological networks, including protein-protein interaction networks, metabolic networks, and transcriptional regulatory networks [11,12,13] have revealed that modularity is a common organizational principle of these networks. In a previous work we discovered transcription modules and their associations with higher-order phenotypes [14]. Recently a Bayesian method for eQTL network partition was developed by Zhang et al. [15]. The application of their method to a yeast eQTL network identified 20 modules with one eQTL and 9 modules with two eQTLs [15].

In this work we define eQTL module as a set of highly connected nodes with at least two eQTLs in different chromosomes. We analyzed the eQTL networks constructed from a yeast dataset and a mouse liver dataset and found 65 and 98 modules respectively. We also studied the associations between the eQTL modules and higher-order phenotypes. Genes in many eQTL modules showed significant functional coherence. Fifty yeast morphologic phenotypes were mapped to genetic loci that overlapped with the eQTLs in 19 modules. We identified an eQTL module sharing genetic components with a mouse obesity phenotype — the gonadal fat mass (GFM), and evidences from previous studies strongly support the functional relevance between the module genes and obesity. The analysis of eQTL modules may provide important insights into the functional components underlying complex phenotypes.

Results

Formulation of the Module Detection Problem and Simulation Results

We exploited a network approach to systematically analyze large numbers of modulatory relations between genetic loci and gene expression traits. A module in an eQTL network is defined as a set of highly connected nodes — eQTLs and genes whose expression levels are regulated by some or all of the eQTLs. Only eQTLs located on different chromosomes are allowed to be included in a module to avoid trivial results caused by the linkage

between markers. A conceptual representation of eQTL module is shown in Figure 1. Module detection in an eQTL network can be formulated as an optimization problem: searching for a set of $m+n$ nodes that maximizes the objective function $Q(m, n, k) = k/(m \times n)$, where m is the number of eQTLs, n is the number of target genes and k is the number of edges between them. In this bipartite network, genes can be connected to QTLs, but there is no edge between genes and between QTLs. The maximum number of edges between n genes and m QTLs is $m \times n$, therefore Q is a value between zero and one. The objective function $Q(m, n, k)$ is a measurement of the connection density of a module. For a set of completely connected nodes, $Q = 1$; for a set of unconnected nodes, $Q = 0$. In this work, a module must have a Q value of 0.66 or above. Intuitively, this density criterion requires that on average each gene node are connected to about 2/3 or more of the QTL nodes and *vice versa*. Besides this density criterion, a module must also be statistically significant, which means the module should be highly unlikely to arise by chance in a randomized network with the same numbers of nodes and edges and the same degree distribution. The details of the module detection method are described in Materials and Methods.

A simulation study was performed to assess the performance of the module detection method. We generated random bipartite networks with prescribed modules and used normalized mutual information (NMI) [16] to evaluate the consistency between the prescribed modules and the modules identified by the search method. NMI is a robust performance indictor based on the confusion matrix [16]. The rows of the confusion matrix correspond to the prescribed modules, and the columns correspond to the identified modules. The confusion matrix contains the number of overlapped nodes between the prescribed modules and the identified module. If the identified modules completely match the prescribed modules, NMI takes the maximum value of 1.0; if the identified modules are unrelated to the simulated module, NMI becomes 0. The simulated eQTL networks consisted of 1200–1500 nodes and 3000–3500 edges, and contained 10 modules with 2–3 eQTL nodes and 20–150 gene nodes (typical sizes of the modules found in this work). Five independent simulation runs were performed with each of the following module homogeneity values: 0.2, 0.3, 0.4, 0.5, 0.6, 0.7, 0.8 and 0.9 (Figure 2). We then used our module detection algorithm to identify modules in the simulated networks. The details of the simulation procedure are described in Materials and Methods. The module homogeneity (p) controls the formation of the modular structures of the simulated network. For $p = 1$, the simulated network has a clear-cut modular structure. For $p = 0$, the prescribed modules become random partitions of the simulated network and therefore the network has no modular structure at all. The module detection algorithm is expected to be able to identify the prescribed modules correctly when p is high, while no module can be identified by any algorithm when p is too low. Our module detection method performed reasonably well with a NMI value above 0.8 when the module homogeneity was higher than 0.6, and the NMI value was very close to its maximum value of 1.0 when the module homogeneity is higher than 0.9. The NMI dropped quickly when the module homogeneity was below 0.5. This is because the modular structure became much fuzzier with such low module homogeneity values. For example, at a module homogeneity value of 0.5, on average only half of the edges connected to the nodes of a module come from members of the same module and the other half of the connections are randomly connected to nodes outside the module.

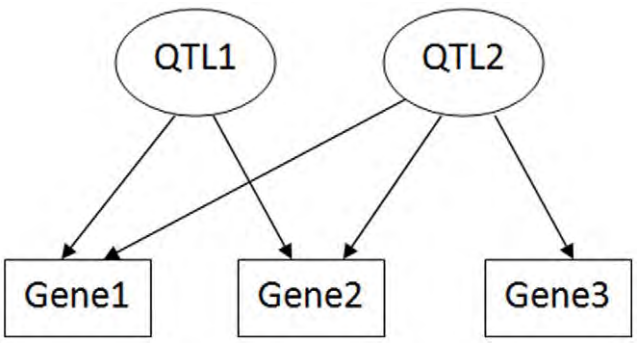

Figure 1. A conceptual representation of eQTL module. This module contains two eQTLs and three genes. The Q value of this module is 5/6.
doi:10.1371/journal.pone.0014313.g001

Expression QTL Network and Modules

The yeast eQTL network is a connected graph of 493 eQTL nodes, 4583 gene nodes, and 33,584 edges. The median degrees for the eQTL nodes and gene nodes are 25 and 7 respectively. In the yeast network, we identified 65 modules (Table S1). The number of eQTLs in each module ranges from 2 to 3, and the number of target genes ranges from 4 to 276. These modules contain 1756 unique genes, covering 38.3% of the genes in the yeast eQTL network. Three identified modules and their neighboring gene nodes in the yeast eQTL network are displayed in Figure 3. The mouse liver eQTL network is a connected graph of 408 eQTL nodes, 4086 gene nodes, and 11,458 edges. The median degrees for the eQTL nodes and gene nodes are 15 and 2 respectively. In the mouse liver network, we identified 98 modules (Table S2). The number of eQTLs in each module ranges from 2 to 4, and the number of target genes ranges from 4 to 84. These modules contain 989 unique genes, covering 24.2% of the genes in the mouse eQTL network. The size distributions of the yeast and mouse modules are shown in Figure 4. We found that these modules were highly unlikely to occur simply by chance in randomly rewired networks with the same number of nodes and edges and same degree distribution (P-value $<10^{-4}$). Therefore statistically significant modular structures exist in these eQTL networks. The modular structures of genotype-phenotype map has also been observed in some classical multiple-trait association studies [17,18].

Functional coherence of module genes

We used the Ontologizer software [19] to assess the enrichment of GO terms in each module. Ontologizer uses Parent-Child Analysis, which takes the structure of the GO hierarchy and parent-child relations into consideration when it performs the enrichment analysis. The Westfall-Young-Single-Step method [20] was used for multiple testing correction. A total of 42 yeast modules and 21 mouse modules were associated with at least one GO term at the significance level of $P<0.05$ (Tables S3 and S4).

Some modules were associated with common GO terms. For example, yeast module 63 and 64 were associated with 8 common GO terms (e.g. organelle lumen, ribosome biogenesis and assembly), and yeast module 45 and 61 were associated with 25 common GO terms (Table S3). They were identified as separate modules in the eQTL network, however there might be moderate but genuine links connecting them. These links are the weaker associations between gene expression traits of one module and eQTLs of another module, which did not pass the significance test used in eQTL mapping. We added the moderate links (with P-values <0.01 but ≥ 0.001) to the yeast eQTL

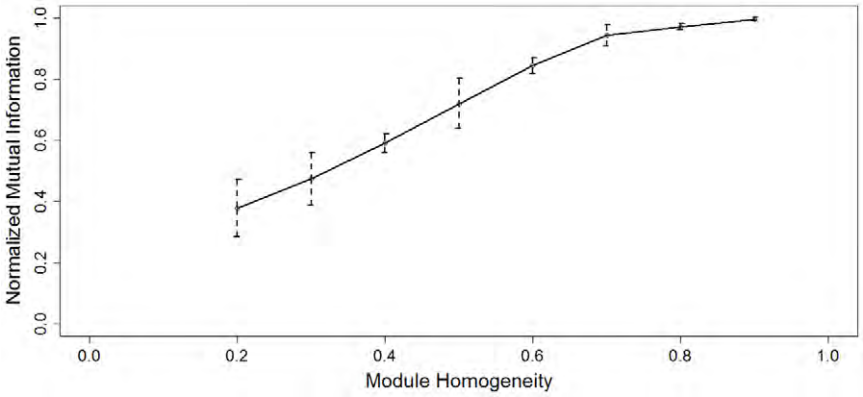

Figure 2. The performance of module detection algorithm as a function of module homogeneity. The error bars mark the interval of minus and plus one standard deviation.
doi:10.1371/journal.pone.0014313.g002

network to test if the distribution of the moderate links would suggest potential relations between the modules. We randomly rewired the moderate links in the eQTL network and counted the number of moderate links that connected each pair of modules. For each pair of modules, the maximum number of moderate links from 1000 such randomly rewired networks was compared to the number of moderate links bridging the two modules in the original network. We then sorted the module pairs by the ratio of these two numbers (original vs. rewired maximum) in a descending order. The top 20 (1%) yeast module pairs are listed in Table S5. Among the 2080 possible yeast module pairs, modules 45 and 61 ranked 18th with a ratio of 4.6, and modules 63 and 64 ranked 19th with a ratio of 4.5. There were many more (4.6 and 4.5 fold respectively) moderate links bridging these module pairs in the original eQTL network than that expected by chance in the randomly rewired networks. Other top ranked

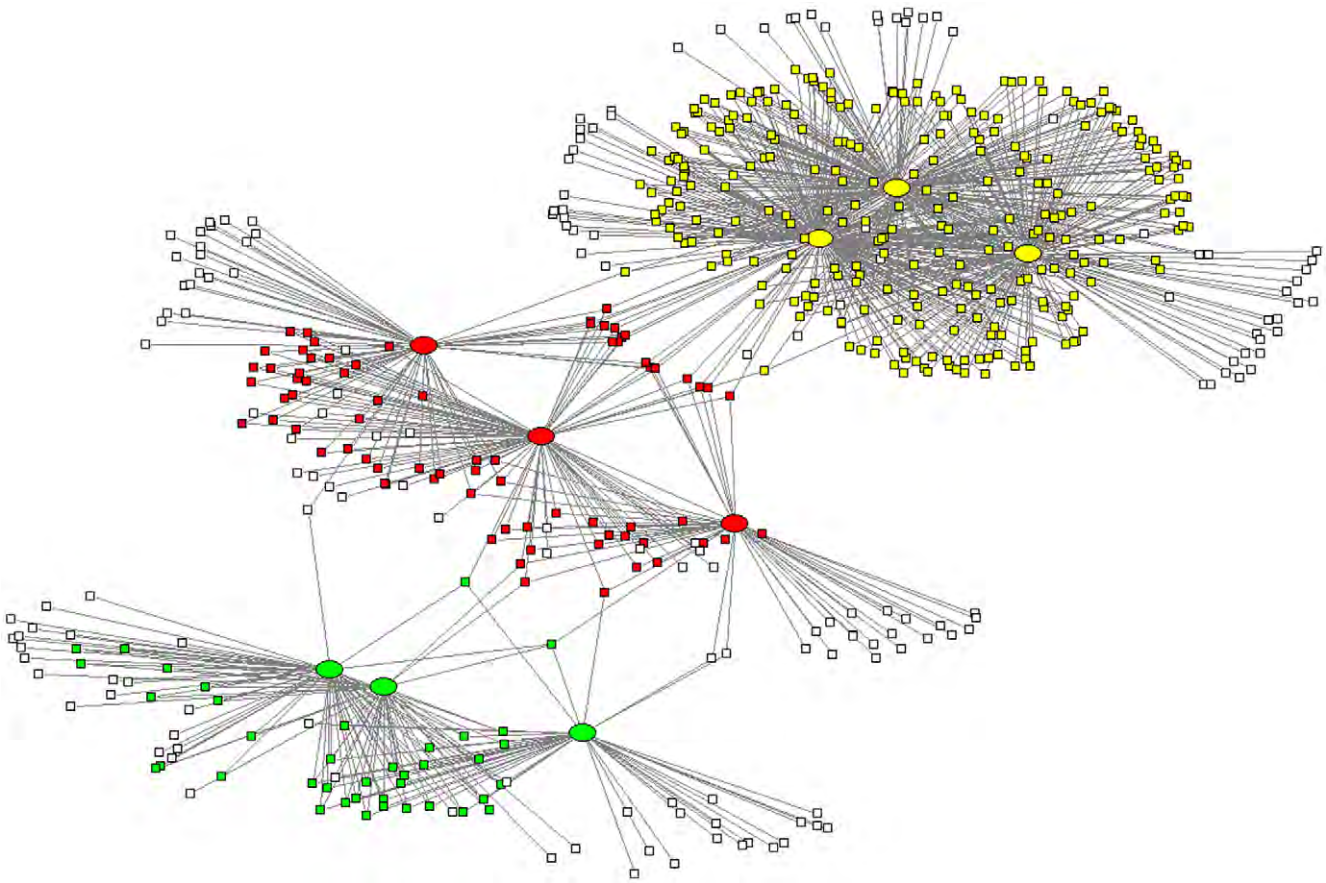

Figure 3. Three modules in the yeast eQTL network. The ellipses represents eQTLs, squares represent genes. White squares represent genes that do not belong to the three modules. Green: Module 48; Yellow: Module 64; Red: Module 55.
doi:10.1371/journal.pone.0014313.g003

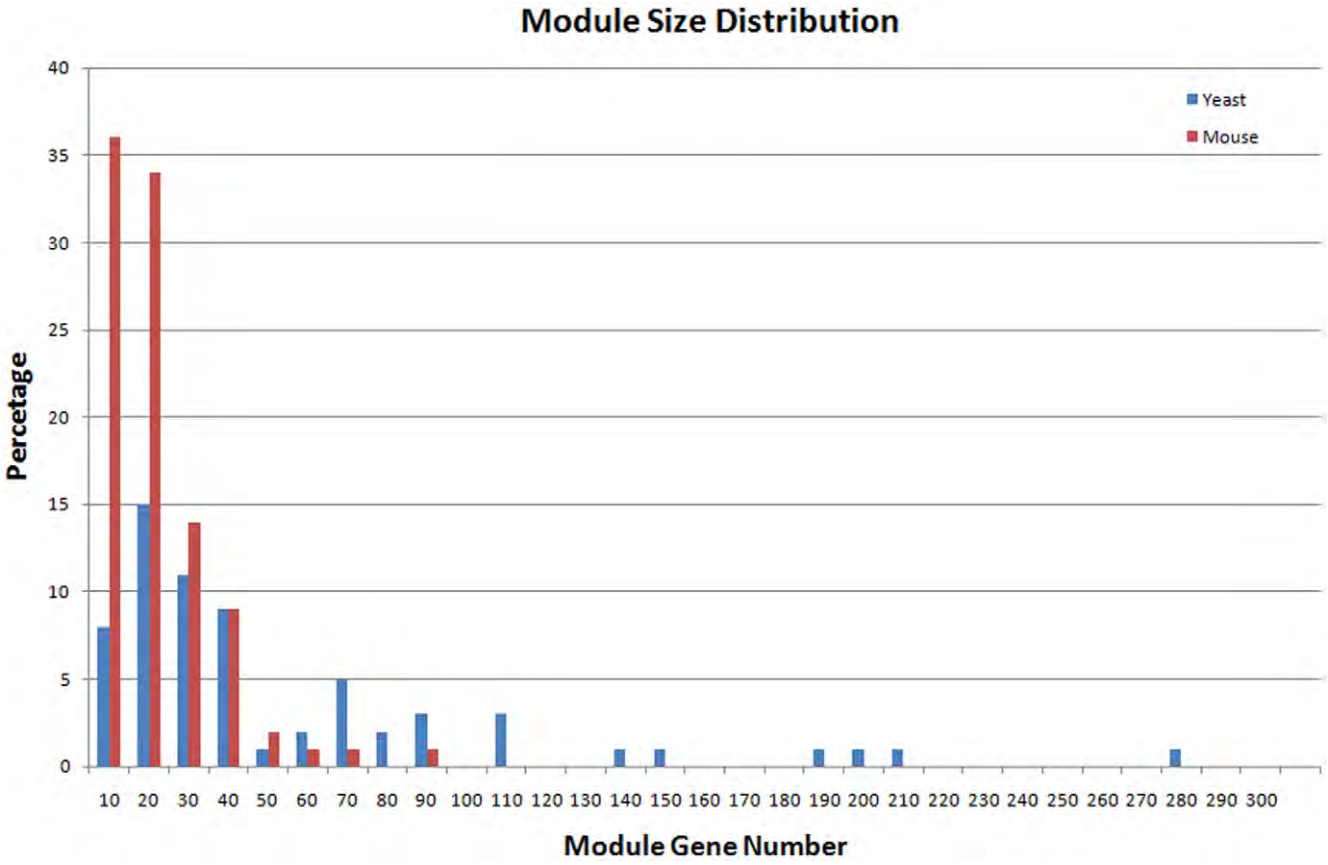

Figure 4. The size distributions of the yeast and mouse modules.
doi:10.1371/journal.pone.0014313.g004

module pairs that share common GO terms include: Module 46 and 64, Module 26 and 64, and Module 55 and 60. The non-random distribution of the moderate links may help us to identify modules that are more likely being functionally related.

Linking eQTL modules to physiological phenotypes

One major goal of systems genetics is to identify gene expression modules underlying higher-order phenotypes. Recently, Nogami et al. [21] measured more than 500 yeast morphologic phenotypes and mapped 7 significant QTLs (false discovery rate [FDR] = 0.05) (Table 2 and Table S4 of [21]). We assessed the genetic overlap between these 7 morphologic QTLs and the yeast eQTL modules we identified. We found that QTLs on three chromosomes were shared by morphologic phenotypes and the modules (Table 1). The morphologic phenotypes can be classified into six categories, each representing an aspect of cellular morphology (Table 2 of [21]). Phenotypes of same category were usually mapped to QTLs on same chromosome. But there was a surprising exception where the phenotypes concerning DNA region size, position, and shape were mapped to two unlinked loci on Chromosome 14 and 15, respectively [21]. The eQTL module analysis may provide a possible explanation to the exception. The modules with eQTLs on Chromosome 14 and 15 were associated with different GO terms. Three modules (28, 45, and 61) with eQTLs on Chromosome 14 were associated with protein metabolism while three modules (7, 9, and 51) with the QTLs on Chromosome 15 were associated with mitochondrial oxidative phosphorylation and energy generation. This indicates different molecular pathways may underlie the phenotypes mapped to chromosome 14 and those mapped to chromosome 15 though they all belong to same category.

We also analyzed the physiological relevance of the mouse liver eQTL modules. The obesity phenotype gonadal fat mass (GFM) was genetically dissected, and five "clinical" QTLs (cQTLs) regulating this phenotype were mapped in a previous study (Table 2 of [22]). We analyzed the overlaps between the module QTLs and these five cQTLs. Three modules (50, 74, and 84) had eQTLs that overlapped with a cQTL on chromosome 19. Module 74 was of particular interest because it had another eQTL located near a cQTL on chromosome 5. The distance between the two QTL markers is about 20 Mb. This module contains three eQTLs and 21 genes, seven of which were uncharacterized expressed sequence tags (ESTs) (Figure 5). There is literature evidence for seven of the module genes (i.e. 50% of the genes in this module with known functions) being related to obesity. *Lcat* (lecithin cholesterol acyltransferase) is involved in lipid metabolism which affects the GFM trait [23]. Other module genes related to lipid metabolism and obesity include *Anxa5* (annexin A5) [24], *Ccna2* (cyclin A2) [25], *Ces5* (carboxylesterase 5) [26], *Cyp2c38* (cytochrome P450, family 2, subfamily c, polypeptide 38) [27], *Setd8* (SET domain containing 8) [28], and *Slc16a11* (monocarboxylic acid transporters, member 11) [29]. Thus, literature evidence supports the association between GFM trait and the eQTL module.

Discussion

In this work we exploited a network approach to systematically analyze large numbers of modulatory relations between genetic

Table 1. Genetic overlap of yeast eQTL modules and morphologic phenotypes.

Phenotype category	QTL (bp)	Module ID
DNA region size, position and shape	chr14:440000-460000	21, 28, 50, 59, 61, 62, 63
	chr14: 480000-500000	24, 52, 58
	chr14: 500000-520000	13, 45
DNA region size, position and shape	chr15: 520000-540000	9
	chr15: 540000-560000	7, 21, 51
Mother cell size and shape	chr8: 60000-80000	56, 58
	chr8: 80000-100000	27, 37
	chr8: 100000-120000	43

doi:10.1371/journal.pone.0014313.t001

loci and gene expression traits. Like many other biological networks eQTL networks have evolved functional modules. Such modular structures may confer selective advantage by allowing the optimization of gene expression within each module and therefore minimizing the impact of genetic variants outside the module.

Recently Zhang et al. [15] used a Bayesian partition method to identify eQTL modules from the same yeast dataset used in this work. They identified 20 yeast modules with one eQTL and 9 modules with two eQTLs. In this work we are interested in detecting eQTL modules with complex genetic architectures. Therefore we focused on modules with at least two QTLs in different chromosomes, and identified 21 yeast modules with two eQTLs and 44 yeast modules with three eQTLs. The Bayesian partition method [15] essentially performs eQTL mapping and module identification simultaneously. Our module detection method takes the eQTL mapping results as the input and can be used with any eQTL mapping method; therefore it provides the flexibility to reanalyze the eQTL network when new algorithms for eQTL mapping become available.

Epistasis is a higher-order genetic interaction that go beyond the pair-wise regulatory relations between a QTL and a trait. To test the epistatic effects within the eQTL modules, we employed a regression based model selection approach to find the best eQTL model for each module gene. The expression values of each

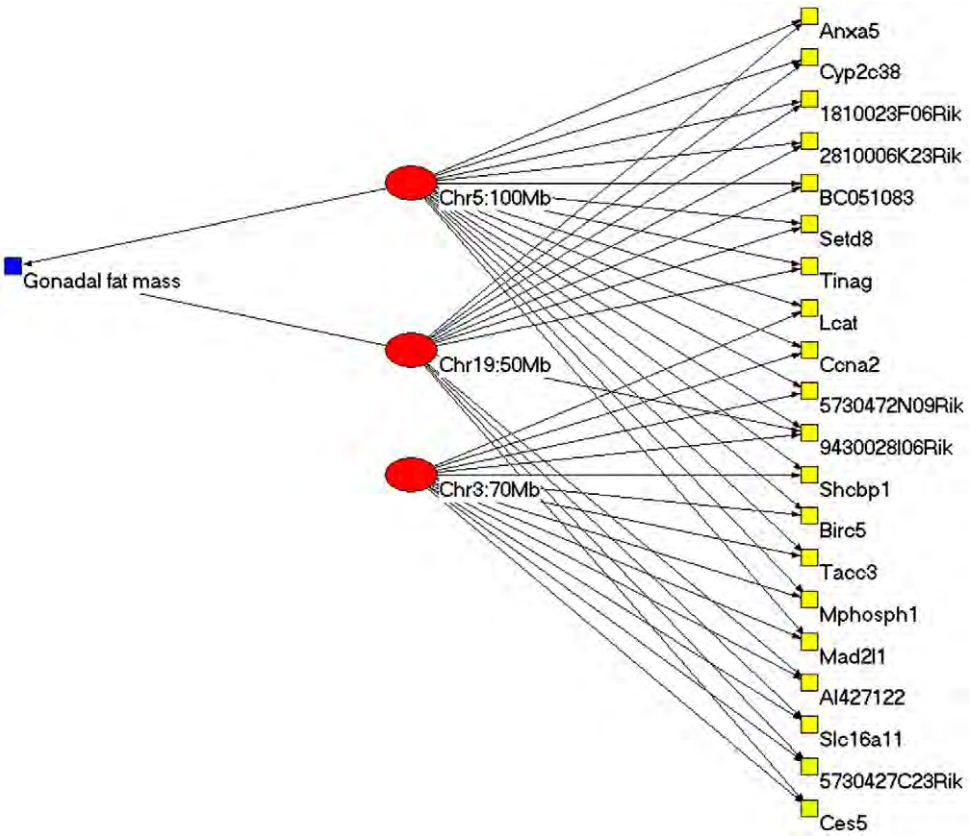

Figure 5. Genetic overlaps between Mouse gonadal fat mass (GFM) trait and module 74. Red ellipses represent QTLs, yellow squares represent genes and the blue square represents the GFM trait.
doi:10.1371/journal.pone.0014313.g005

module gene were regressed on the genotypes of the module eQTLs with or without interaction terms. Including interaction terms in an eQTL model may improve the model fit but also increases the model complexity. We used the standard Akaike Information Criterion to select the eQTL model with the best tradeoff between goodness-of-fit and model complexity [30]. Then for each module, we computed the proportion of module genes that could be best modeled by including the epistatic interactions. We found that this proportion ranged from 0% to 59% in the yeast modules with a median of 19%. Only four modules do not include epistatic QTLs. These results have revealed the genetic complexity of the eQTL modules.

We compared the eQTL modules of the two organisms and found that 21 (32.3%) and 44 (67.7%) yeast modules have two and three eQTLs respectively, while 12 (12.2%) and 85 (86.7%) mouse modules have two and three eQTLs respectively, and one mouse module has four eQTLs. The median module gene numbers for the yeast and the mouse modules are 27 and 14 respectively. The higher percentage of mouse modules with three eQTLs and the lower number of genes in mouse modules (Fig. 4) indicates that the regulation of gene expression in mouse is more genetically complex than that in yeast.

Materials and Methods

Construction of eQTL networks

We used two data sets, a yeast dataset [31,32] and a mouse liver dataset [22], to construct the eQTL networks. The yeast data set contained genotype data of 2957 markers and gene expression data of 6216 open reading frames in 112 F1 segregants that were generated by crossing the BY4716 strain with the RM11-1a strain. Linkage analysis was performed using the Wilcoxon test, and statistical significance was estimated by permutations [31]. Significant linkage results with P-values <0.001 were used to construct the eQTL network. We divided the yeast genome into bins of 20 Kb and mapped QTLs onto them. In an eQTL network, two types of nodes were used to represent eQTLs and gene expression traits respectively, and edges represent the modulatory relations between the QTLs and gene expression traits. Gene expression traits mapped to only one eQTL were not included in the network because such nodes would not belong to any module.

The mouse liver data set contained expression data of 23,574 mouse transcripts in the livers of 334 F2 mice generated by crossing the C57BL/6J ApoE$^{-/-}$ strain with the C3H/HeJ ApoE$^{-/-}$ strain [22]. Using this data set, Wang et al. [22] mapped suggestive and significant eQTLs (Table S1 of [22]). Again, we used $P<0.001$ as the cutoff value to construct the eQTL network. We divided the mouse genome into bins of 5 Mb and mapped QTLs onto them. The QTLs modulating the GFM trait of these mice were also mapped by Wang et al. (Table 2 of [22]).

Module detection

We employed a two-step search algorithm: in the first step we tried to find as many seed modules as possible and in the second step we merged overlapping seed modules. We searched for seed modules within a range of m (the number of eQTL nodes) from 2 to 6 and n (the number of gene nodes) from 4 to 14. For each combination of m and n, we started with a randomly picked, connected set of m eQTL nodes and n gene nodes. In each following step, one node in the current set was randomly selected and an attempt was made to replace it with a randomly picked node that does not belong to the current set but is connected to the current set by one or more edges. At the end of every 25 steps, one node in the current set was replaced with a node that had no connection to the current set to avoid getting stuck in local maxima. Changes were accepted or rejected according to the Metropolis criteria [33,34], i.e. a move was accepted with a probability of the smaller of 1.0 or $\exp[(Q_{new}-Q_{old})\times 10]$ where Q_{new} and Q_{old} were the new and old Q values. The optimization continued until $Q=1$ or 500 moves had been made. One thousand such searches with different random starts were performed and all identified seed modules (i.e., sets of connected node with a $Q \geq 0.66$ and a P-value $<10^{-4}$) were recorded. These seed modules were then merged iteratively. Each time two overlapping seed modules were merged if and only if the resulting module still had a $Q \geq 0.66$ and a P-value $<10^{-4}$. This process continued until no further merging was possible. The P-values for modules of different sizes (i.e. each combination of m and n) were estimated by random rewiring. One thousand networks were generated by randomly rewiring the edges of the original eQTL network, while keeping the edge degree of each node unchanged. The rewiring scheme is adopted from [35]. Two edges (A–B and C–D) are randomly selected and then rewired such that the new edges are A–D and B–C, provided neither of these new edges exists in the current network. This rewiring scheme is equivalent to randomly switching pairs of 0 and 1 in the rows of the adjacency matrix while keeping the raw and column margins unchanged. We then applied the module detection algorithm to these randomized networks to estimate the statistical significance of the Q value for each combination of m and n. One thousand independent searches with different random starts were performed for each randomized network.

Simulation

In order to access the performance of our model detection algorithm, we generated random networks with prescribed modular structure and then used our method to identify the predefined modules. We adopted the module simulation method for bipartite network as described in [36] with minor changes to accommodate the module density criterion (Q value) used in this work. We first predefined the module membership for all the eQTL and gene nodes being considered. We also predefined N_i, the number of gene nodes within the i-th module. For each eQTL node, we connected it to N_i gene nodes: with probability p, a gene node randomly selected from the same module was connected to the eQTL; otherwise a gene node randomly selected from the whole gene node set was connected to the eQTL. The parameter p controls the degree of homogeneity of a module and hence is called module homogeneity. If a module generated this way did not satisfy our module density criterion ($Q\geq 0.66$), we extracted a subset of nodes from the module that met this criterion as the final module. The normalized mutual information (NMI) was used to assess the performance of the search algorithm. Given a confusion matrix in which rows are prescribed modules and columns are detected modules, NMI is defined as

$$\frac{-2\sum_{M1}\sum_{M2} N_{ij}\times\log\left(\frac{N_{ij}\times N}{N_{i.}\times N_{.j}}\right)}{\sum_{M1} N_{i.}\times\log\left(\frac{N_{i.}}{N}\right)+\sum_{M2} N_{.j}\times\log\left(\frac{N_{.j}}{N}\right)},$$

where N_{ij} is an element of the confusion matrix specifying the number of overlapped nodes between the i-th prescribed module and the j-th detected module. $N_{i.}$ and $N_{.j}$ are the row means and column means respectively, and M_1 and M_2 are the number of prescribed and detected modules [16].

Supporting Information

Table S1 List of Yeast Modules
Found at: doi:10.1371/journal.pone.0014313.s001 (0.57 MB XLS)

Table S2 List of Mouse Liver Modules
Found at: doi:10.1371/journal.pone.0014313.s002 (0.19 MB XLS)

Table S3 Gene Ontology Analysis of Yeast Modules
Found at: doi:10.1371/journal.pone.0014313.s003 (0.06 MB XLS)

Table S4 Gene Ontology Analysis of Mouse Liver Modules
Found at: doi:10.1371/journal.pone.0014313.s004 (0.03 MB XLS)

Table S5 Yeast module pairs with significant numbers of moderate between-module links
Found at: doi:10.1371/journal.pone.0014313.s005 (0.02 MB XLS)

Acknowledgments

We thank Dr. Rachel Brem for providing the yeast genotype data and eQTL mapping results. We thank Dr. Gael Yvert for providing yeast morphological trait data.

Author Contributions

Conceived and designed the experiments: LB YC. Performed the experiments: LB. Analyzed the data: LB. Contributed reagents/materials/analysis tools: XX. Wrote the paper: LB YC.

References

1. Rockman MV, Kruglyak L (2006) Genetics of global gene expression. Nat Rev Genet 7: 862–872.
2. Quigley D, Balmain A (2009) Systems genetics analysis of cancer susceptibility: from mouse models to humans. Nat Rev Genet 10: 651–657.
3. Ayroles JF, Carbone MA, Stone EA, Jordan KW, Lyman RF, et al. (2009) Systems genetics of complex traits in Drosophila melanogaster. Nat Genet 41: 299–307.
4. Schadt EE (2009) Molecular networks as sensors and drivers of common human diseases. Nature 461: 218–223.
5. Rockman MV (2008) Reverse engineering the genotype-phenotype map with natural genetic variation. Nature 456: 738.
6. Emilsson V, Thorleifsson G, Zhang B, Leonardson AS, Zink F, et al. (2008) Genetics of gene expression and its effect on disease. Nature 452: 423–428.
7. Chen Y, Zhu J, Lum PY, Yang X, Pinto S, et al. (2008) Variations in DNA elucidate molecular networks that cause disease. Nature 452: 429–435.
8. Bao L, Peirce JL, Zhou M, Li H, Goldowitz D, et al. (2007) An integrative genomics strategy for systematic characterization of genetic loci modulating phenotypes. Hum Mol Genet 16: 1381–1390.
9. Jansen RC, Nap JP (2001) Genetical genomics: the added value from segregation. Trends Genet 17: 388–391.
10. Schadt EE, Monks SA, Drake TA, Lusis AJ, Che N, et al. (2003) Genetics of gene expression surveyed in maize, mouse and man. Nature 422: 297–302.
11. Barabasi A-L, Oltvai ZN (2004) Network biology: understanding the cell's functional organization. Nat Rev Genet 5: 101–113.
12. Rives AW, Galitski T (2003) Modular organization of cellular networks. Proceedings of the National Academy of Sciences of the United States of America 100: 1128–1133.
13. Segal E, Shapira M, Regev A, Pe'er D, Botstein D, et al. (2003) Module networks: identifying regulatory modules and their condition-specific regulators from gene expression data. Nat Genet 34: 166–176.
14. Li H, Chen H, Bao L, Manly KF, Chesler EJ, et al. (2006) Integrative Genetic Analysis of Transcription Modules: Towards Filling the Gap between Genetic Loci and Inherited Traits. Hum Mol Genet 15: 481–492.
15. Zhang W, Zhu J, Schadt EE, Liu JS (2010) A Bayesian Partition Method for Detecting Pleiotropic and Epistatic eQTL Modules. PLoS Comput Biol 6: e1000642.
16. Danon L, Diaz-Guilera A, Duch J, Arenas A (2005) Comparing community structure identification. Journal of Statistical Mechanics-Theory and Experiment. 10 p.
17. Klingenberg CP, Leamy LJ, Cheverud JM (2004) Integration and modularity of quantitative trait locus effects on geometric shape in the mouse mandible. Genetics 166: 1909–1921.
18. Mezey JG, Cheverud JM, Wagner GP (2000) Is the genotype-phenotype map modular? A statistical approach using mouse quantitative trait loci data. Genetics 156: 305–311.
19. Robinson PN, Wollstein A, Bohme U, Beattie B (2004) Ontologizing gene-expression microarray data: characterizing clusters with Gene Ontology. Bioinformatics 20: 979–981.
20. Westfall PH, Zaykin DV, Young SS (2002) Multiple tests for genetic effects in association studies. Methods Mol Biol 184: 143–168.
21. Nogami S, Ohya Y, Yvert G (2007) Genetic complexity and quantitative trait loci mapping of yeast morphological traits. PLoS Genet 3: e31.
22. Wang S, Yehya N, Schadt EE, Wang H, Drake TA, et al. (2006) Genetic and genomic analysis of a fat mass trait with complex inheritance reveals marked sex specificity. PLoS Genet 2: e15.
23. Greaves KA, Going SB, Fernandez ML, Milliken LA, Lohman TG, et al. (2003) Cholesteryl ester transfer protein and lecithin:cholesterol acyltransferase activities in hispanic and anglo postmenopausal women: associations with total and regional body fat. Metabolism 52: 282–289.
24. van Tits L, de Graaf J, Toenhake H, van Heerde W, Stalenhoef A (2005) C-Reactive Protein and Annexin A5 Bind to Distinct Sites of Negatively Charged Phospholipids Present in Oxidized Low-Density Lipoprotein. Arterioscler Thromb Vasc Biol 25: 717–722.
25. Laudes M, Bilkovski R, Oberhauser F, Droste A, Gomolka M, et al. (2008) Transcription factor FBI-1 acts as a dual regulator in adipogenesis by coordinated regulation of cyclin-A and E2F-4. Journal of Molecular Medicine 86: 597–608.
26. Soni KG, Lehner R, Metalnikov P, O'Donnell P, Semache M, et al. (2004) Carboxylesterase 3 (EC 3.1.1.1) is a major adipocyte lipase. J Biol Chem 279: 40683–40689.
27. Kudo T, Shimada T, Toda T, Igeta S, Suzuki W, et al. (2009) Altered expression of CYP in TSOD mice: a model of type 2 diabetes and obesity. Xenobiotica 39: 889–902.
28. Wakabayashi K-i, Okamura M, Tsutsumi S, Nishikawa NS, Tanaka T, et al. (2009) The Peroxisome Proliferator-Activated Receptor {gamma}/Retinoid X Receptor {alpha} Heterodimer Targets the Histone Modification Enzyme PR-Set7/Setd8 Gene and Regulates Adipogenesis through a Positive Feedback Loop. Mol Cell Biol 29: 3544–3555.
29. Merezhinskaya N, Fishbein WN (2009) Monocarboxylate transporters: past, present, and future. Histol Histopathol 24: 243–264.
30. Akaike H (1974) A New Look at the Statistical Model Identification. IEEE Trans Autom Control 19: 716–723.
31. Brem RB, Kruglyak L (2005) The landscape of genetic complexity across 5,700 gene expression traits in yeast. Proc Natl Acad Sci USA 102: 1572–1577.
32. Brem RB, Storey JD, Whittle J, Kruglyak L (2005) Genetic interactions between polymorphisms that affect gene expression in yeast. Nature 436: 701–703.
33. Metropolis N, Rosenbluth AW, Rosenbluth MN, Teller AH, Teller E (1953) Equation of state calculations by fast computing machines. The Journal of Chemical Physics 21: 1087–1092.
34. Spirin V, Mirny LA (2003) Protein complexes and functional modules in molecular networks. Proceedings of the National Academy of Sciences of the United States of America 100: 12123–12128.
35. Maslov S, Sneppen K (2002) Specificity and Stability in Topology of Protein Networks. Science 296: 910–913.
36. Guimera R, Sales-Pardo M, Amaral LAN (2007) Module identification in bipartite and directed networks. Physical Review E 76: 8.

BMC Microbiology

RESEARCH ARTICLE Open Access

A *galU* mutant of *francisella tularensis* is attenuated for virulence in a murine pulmonary model of tularemia

Himangi R Jayakar[1,2], Jyothi Parvathareddy[1], Elizabeth A Fitzpatrick[1], Xiaowen R Bina[1], James E Bina[1], Fabio Re[1], Felicia D Emery[1] and Mark A Miller[1*]

Abstract

Background: A number of studies have revealed that *Francisella tularensis* (FT) suppresses innate immune responses such as chemokine/cytokine production and neutrophil recruitment in the lungs following pulmonary infection via an unidentified mechanism. The ability of FT to evade early innate immune responses could be a very important virulence mechanism for this highly infectious bacterial pathogen.

Results: Here we describe the characterization of a *galU* mutant strain of FT live vaccine strain (LVS). We show that the *galU* mutant was highly attenuated in a murine model of tularemia and elicited more robust innate immune responses than the wild-type (WT) strain. These studies document that the kinetics of chemokine expression and neutrophil recruitment into the lungs of mice challenged with the *galU* mutant strain are significantly more rapid than observed with WT FT, despite the fact that there were no observed differences in TLR2 or TLR4 signaling or replication/dissemination kinetics during the early stages of infection. We also show that the *galU* mutant had a hypercytotoxic phenotype and more rapidly induced the production of IL-1β following infection either *in vitro* or *in vivo*, indicating that attenuation of the *galU* mutant strain may be due (in part) to more rapid activation of the inflammasome and/or earlier death of FT infected cells. Furthermore, we show that infection of mice with the *galU* mutant strain elicits protective immunity to subsequent challenge with WT FT.

Conclusions: Disruption of the *galU* gene of FTLVS has little (if any) effect on *in vivo* infectivity, replication, or dissemination characteristics, but is highly attenuating for virulence. The attenuated phenotype of this mutant strain of FT appears to be related to its increased ability to induce innate inflammatory responsiveness, resulting in more rapid recruitment of neutrophils to the lungs following pneumonic infection, and/or to its ability to kill infected cells in an accelerated fashion. These results have identified two potentially important virulence mechanisms used by FT. These findings could also have implications for design of a live attenuated vaccine strain of FT because sublethal infection of mice with the *galU* mutant strain of FTLVS promoted development of protective immunity to WT FTLVS.

Background

Francisella tularensis (FT) is a gram-negative intracellular bacterium that is the causal agent of tularemia. The *Francisellaceae* family of bacteria has a single genus, *Francisella*, which has been divided into two species: 1) *Francisella philomiragia* (a muskrat pathogen) and 2) *Francisella tularensis*. *Francisella tularensis* is further subdivided into four subspecies: *tularensis* (type A), *holarctica* (type B), *novicida*, and *mediasiatica* [1]. Of these, only subsp. *tularensis* and subsp. *holarctica* cause disease in humans [2]. FT *tularensis* is considered a prime candidate for use as a biological weapon because it is relatively easy to propagate and disseminate via aerosolization and because of the high morbidity and mortality associated with aerosol infection (LD_{50}<10 CFU) [3,4]. The live vaccine strain (FT LVS), which was derived from FT *holarctica*, is only moderately virulent in humans [5]

* Correspondence: mamiller@uthsc.edu
[1]Department of Microbiology, Immunology, and Biochemistry, The University of Tennessee Health Science Center, 858 Madison Avenue, Memphis, Tennessee 38163, USA
Full list of author information is available at the end of the article

and retains virulence in mice. Because LVS causes an infection in mice that is similar to the human form of disease, the murine FT LVS infection model serves as an appropriate animal model of human tularemic disease [6-8].

FT is well adapted for growth and survival within host macrophages, as evidenced by its ability to inhibit phagosome/lysosome fusion and the respiratory burst, and to escape from the phagosome and replicate within the macrophage cytoplasm [9-11]. Moreover, it has been reported that the virulence of FT depends on its ability to escape into the host cytoplasm [10,12,13]. However, like many other successful pathogens, the key to the pathogenesis of FT may be in its ability to overcome, evade, and/or suppress innate host immune responses. For instance, FT is known to be relatively resistant to cationic antimicrobial peptides (CAMPs), which may in part be responsible for its ability to overcome host innate immunity [14,15]. In fact, it has been shown that FT mutant strains that are CAMP-sensitive are attenuated for virulence in mice [16,17]. FT is also able to evade (in part) innate immune detection because its lipopolysaccharide (LPS) has unusual modifications that render it immunologically inert and unable to stimulate TLR4 [17-19]. Indeed, FT *novicida* mutants that lacked these modifications and produced TLR4-stimulating LPS were able to induce stronger proinflammatory cytokine production and host innate responses resulting in rapid clearance and an attenuated phenotype in mice [17,20]. FT also appears to actively suppress acute inflammatory responses at early times after infection in lungs by a mechanism that has not yet been defined [21]. Following pulmonary infection of mice with FT, there is an initial lag in recruitment of neutrophils as well as a minimal proinflammatory cytokine response in the first 24-48 hours following infection with FT [22,23]. This quiescent period is typically followed by a massive neutrophil influx and profound upregulation of cytokine production that appears to contribute to FT pathogenesis [15,24,25]. The ability of WT FT to delay recruitment of neutrophils appears to be a critical virulence mechanism because FT mutants that fail to delay influx of neutrophils are rapidly cleared from the host and are attenuated for virulence [17,20]. Additionally, pretreatment of mice with rIL-12 resulted in early neutrophil recruitment to lungs and rapid immune clearance following infection with WT FT [26]. These data suggest that the kinetics, rather than the magnitude, of neutrophil recruitment at the site of infection are important for resolution of FT infection.

The efficacy of innate immune responses is largely dependent on interactions between host pattern recognition receptors with cell envelope components of the invading pathogen. Because WT FT appears to utilize undefined mechanism(s) to modulate innate immune signaling events to gain a survival advantage in mammalian hosts, we postulated that mutations that altered the cell envelope structure of FT would attenuate the virulence of the bacterium. In this report we have tested the hypothesis that *galU* is required for FT pathogenesis. The *galU* gene (FTL_1357) encodes for the production of UTP-glucose-1-phosphate uridyl transferase (or alternatively UDP-glucose pyrophosphorylase), an enzyme that catalyzes the formation of UDP-glucose from glucose-1-phosphate and UTP and is known to have a key role in biosynthesis of cell-envelope-associated carbohydrates (e.g. LPS and capsule) in a variety of bacteria [27-32]. The findings reported here revealed that disruption of the FT *galU* gene was highly attenuating *in vivo*, and that the reduction in virulence correlated with changes in the kinetics of chemokine production and neutrophil recruitment into the lungs following pulmonary infection. The *galU* mutant strain induced more rapid production of IL-1β *in vivo* and *in vitro* and it displayed a hypercytotoxic phenotype. We also found that mice that survived infection with the FT *galU* mutant strain developed protective immunity to subsequent challenge with WT FT.

Results

Effect of *galU* mutation on growth and intracellular survival of FT *in vitro*

The *galU* gene is highly conserved among the three major subspecies of FT (100% identity between *galU* genes of SchuS4 and LVS, 98.5% identity shared between FT *novicida* and LVS). In gram-negative bacteria, *galU* is typically part of an operon that is involved in galactose utilization and in the production of various exopolysaccharides [27,30,31]. The *galU* mutant strain characterized here was isolated from a random transposon library of FT LVS and was isolated as a polymyxin B hypersensitive strain (Figure 1A). The increased sensitivity of this *galU* mutant strain to cationic antimicrobials does not appear to be due to generalized outer envelope disintegrity because the mutant bacterium does not exhibit hypersensitivity to deoxycholate (an anionic bile acid) (Figure 1A) or the antibiotics chloramphenicol or tetracycline (data not shown).

The galU gene product is also known to be involved (but not required) in the catabolism of glucose and is required for the catabolism of galactose in bacteria and yeast [31,33,34]. Therefore, we predicted that the *galU* mutant strain would display a mild growth defect in minimal medium containing glucose as a sole sugar source, and would have a more marked growth defect when cultured in medium containing galactose as a sole source of sugar. To determine whether the *galU* mutant had a galactose utilization phenotype, we characterized its growth in Mueller-Hinton broth (MHB) supplemented with either glucose or galactose as a sole sugar source (it is important to note

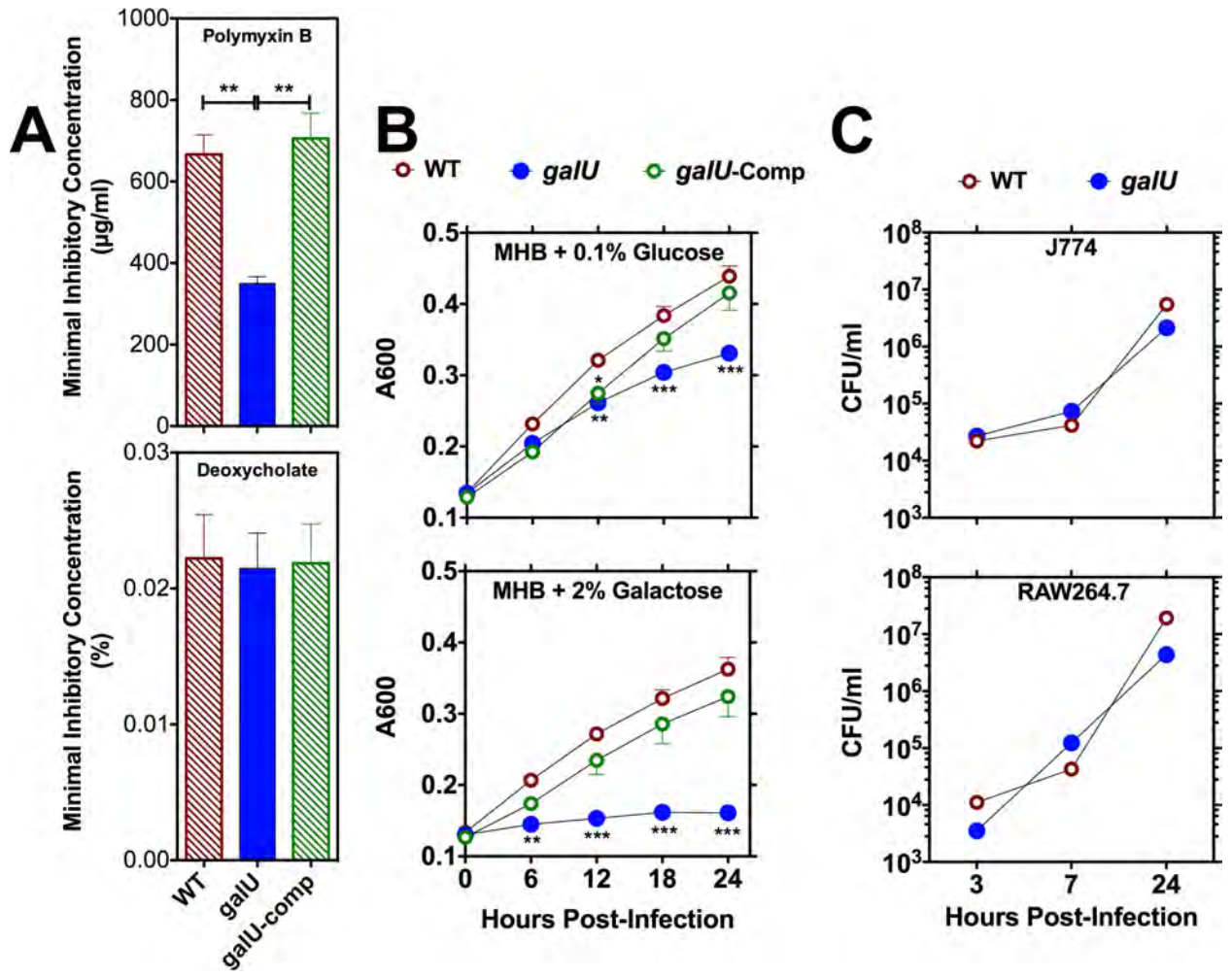

Figure 1 Growth kinetics of the *galU* mutant *in vitro*. Growth of wild-type, *galU* mutant, and *galU*-complemented strains of FT after 48 hrs of culture was measured by the gradient plating technique to determine their sensitivity to polymyxin-B and deoxycholate. All data points represent the mean (± SEM) of triplicate samples. Statistical analyses were performed via one-way ANOVA with Bonferroni post-tests. Statistically significant differences are indicated as follows: $P < 0.01$ (**) (**Panel A**). Growth of each strain cultured in MHB supplemented with either 0.1% glucose or 2% D-galactose (**Panel B**) or within macrophage-like murine cell lines (J774 or RAW264.7 at an MOI of 10, **Panel C**) was monitored over a 24 hour period. All data points represent the mean (± SEM) of triplicate samples. Each panel is representative of at least three experiments of similar design. Statistical analyses were performed via two-way ANOVA with Bonferroni post-tests. Statistically significant differences are indicated as follows: $P < 0.01$ (**) and $P < 0.001$ (***).

that our standard medium for culture of FT is MHB supplemented with 0.1% glucose as the sole source of sugar). As predicted, the *galU* mutant strain of FT displayed a mild growth defect in MHB supplemented with glucose and a severe growth defect in MHB supplemented with galactose. Complementation of the *galU* mutation restored WT growth kinetics in MHB supplemented with either glucose or galactose (Figure 1B).

To determine if mutation of the *galU* gene resulted in an intracellular growth defect, we evaluated the ability of the WT and *galU* mutant strains of FT to grow within murine macrophage-like cells *in vitro*. The replication kinetics of the *galU* mutant within J774 or RAW 264.7 cells were indistinguishable from those of the WT strain (Figure 1C), indicating that mutation of the *galU* gene had no effect on uptake or intracellular survival/replication of the bacterium.

Virulence of the *galU* mutant *in vivo*

To determine whether the *galU* gene is important for FT virulence, C57Bl/6J mice (5/group) were inoculated intranasally with 5×10^4 CFU ($50 \times LD_{50}$) of either the *galU* mutant or WT FT and then were monitored for 15 days. Each of the mice challenged with the *galU* mutant experienced transient weight loss but survived and completely cleared the infection, while all of the mice

challenged with WT FT lost weight continually until they succumbed to tularemia (Figure 2A and 2B). An additional challenge trial in which C57Bl/6 mice (4/group) were challenged with higher numbers of the *galU* mutant (up to 10^7 CFU) revealed that this mutant is highly attenuated, with an LD_{50} that is at least 5 logs higher than that of WT FT (Figure 2C). Moreover, trans-complementation of the *galU* mutation completely restored virulence of the mutant strain (Figure 2A). These findings indicated that FT virulence in mice is dependent on the expression of a functional *galU* gene product.

To determine whether the reduced virulence of the *galU* mutant was the result of defective replication and/or dissemination of the bacterium *in vivo*, we performed a kinetic analysis of bacterial burdens following infection. C57Bl/6J mice (16/group) were challenged with 5×10^4 CFU of either the *galU* mutant or WT FT and then four mice were sacrificed at each time point (24, 48, 72, and 96 h post-infection) for bacterial burden determinations from the lungs, livers, and spleens (Figure 3). The bacterial burdens observed in the *galU* mutant- and WT-infected mice were similar in each of the tissues for the first 48 h, indicating that mutation of *galU* did not confer any significant defects in replication or dissemination of FT *in vivo*. However, the burdens observed in the *galU* mutant-infected mice were significantly lower ($p < 0.01$) in the spleens and livers ($p < 0.001$) of infected mice at the 96 h time point. Collectively, these results reveal that despite its normal replication/dissemination phenotypes, the *galU* mutant is more readily cleared than WT FT.

Mutation of *galU* alters the kinetics of innate immune responses

To determine whether differences in innate immune recognition of infection might be responsible for the dramatic difference in the outcome of disease with the *galU* mutant vs. WT FT, we analyzed the kinetics of immune cell infiltration into the lungs following infection. BALF were collected from each mouse at the time of sacrifice and a series of flow cytometric analyses was performed. The numbers of macrophages, dendritic cells, and NK cells recruited into the lungs of mice infected with the *galU* mutant and WT FT were similar at each time point (data not shown). However, higher numbers of neutrophils were observed in the lungs of mice infected with the *galU* mutant at the 24- and 48-hour time points, with peak numbers of neutrophils measured at 48 hours post-infection (Figure 4A). In contrast, the kinetics of recruitment of neutrophils into the lungs of mice infected with WT FT was much slower (Figure 4A), peaking five days post-infection (data not shown).

Using a Luminex multiplex kit, we also measured the levels of a panel of cytokines/chemokines in the BALF collected from each mouse and found that the levels of

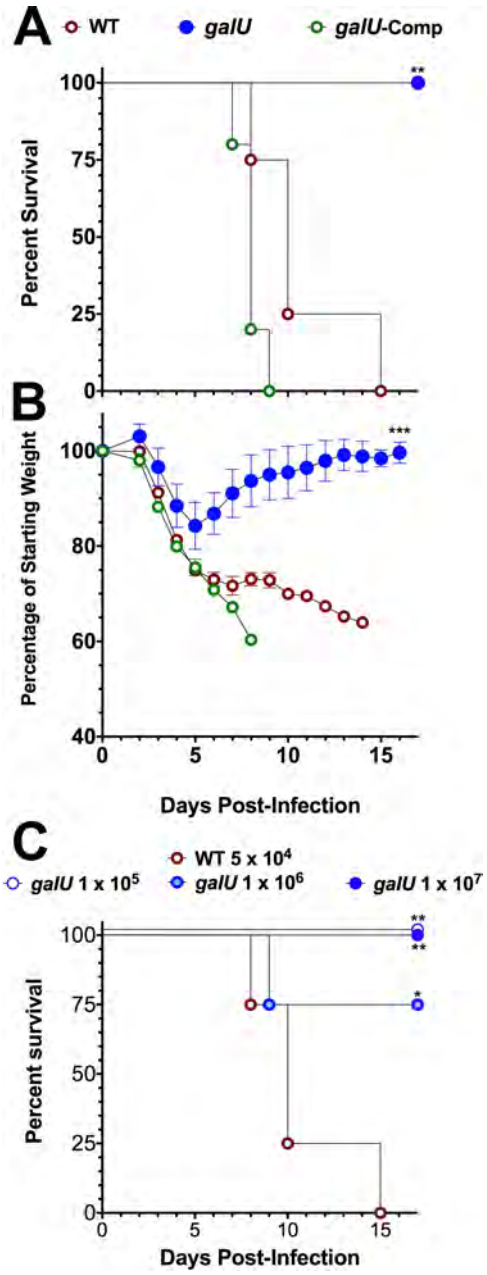

Figure 2 Mutation of the *galU* gene attenuates virulence of FT. C57BL/6 mice were infected intranasally with 5×10^4 CFU of WT (n = 9), the *galU* mutant (n = 10), or the *galU*-complemented strain (n = 5) strain of FTLVS, and their survival (**Panel A**) and weight (**Panel B**) were monitored. Statistical analyses of survival curves was performed using Gehan-Breslow-Wilcoxon tests and a p value of 0.005 is indicated (**). Statistical analysis of body weight retention was performed via one-way ANOVA with a Bonferroni multiple comparisons post-test and a p value of <0.0001 is indicated (***). **Panel C**: Survival was also monitored in C57Bl/6J mice challenged with a range of higher doses of the *galU* mutant (1×10^5-1×10^7 CFU; n = 4) or WT FT (5×10^4 CFU; n = 5). Statistical analysis of survival curves was performed using Gehan-Breslow-Wilcoxon tests and p values of 0.027 (*) and 0.009 (**) are indicated. Results shown are representative of two experiments of similar design.

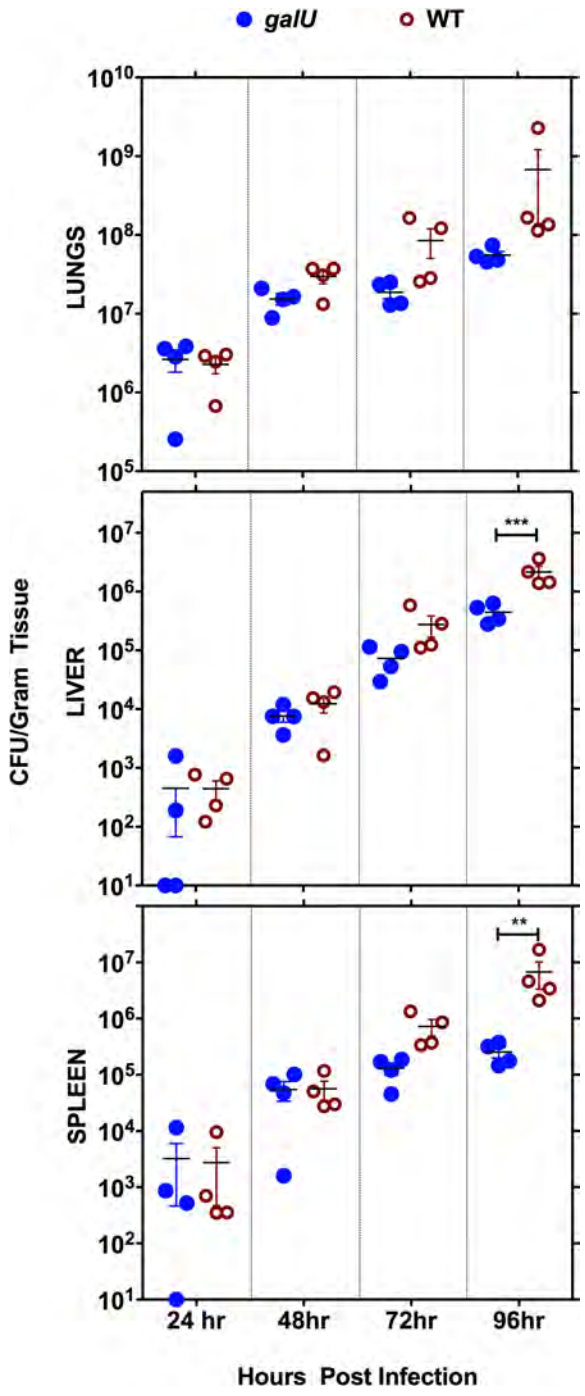

Figure 3 Mutation of the *galU* gene does not attenuate infectivity of FT *in vivo*. C57BL/6 mice (4/group) were infected intranasally with 5×10^4 CFU ($50 \times LD_{50}$ for FT LVS) of either the WT or *galU* mutant strain of FT LVS. Organs were harvested at 24, 48, 72 and 96 hours p.i. and CFU/g of organ was determined for lungs, liver, and spleen. The lower limit of detection was 20 CFU/g. Statistical analyses were performed via two-way ANOVA with a Bonferroni multiple comparisons post test and all significant differences are indicated as follows: ** $P < 0.01$ and *** $P < 0.0001$. The data shown is representative of two independent experiments of similar design.

several neutrophil chemoattractants CXCL1/KC [35], granulocyte colony stimulating factor or G-CSF [36], CXCL10/IP-10 [37], TNF-α [38], MIP-1α/CCL3 and MIP-1β/CCL4 [39], CXCL2/MIP-2 [40], and CCL2/MCP-1 [41] were all present at significantly higher levels in the lungs of *galU* mutant-infected mice ($p < 0.05$) at the 24 or 48 h time points (Figure 4B and 4C), correlating well with the peak of neutrophil recruitment at 48 h post-infection. The levels of these same chemokines/cytokines peaked in the lungs of WT FT-infected mice 72-96 hours post-infection (data not shown), corresponding well with the peak of neutrophil recruitment into the lungs on day five post-challenge.

It was recently reported that mutations that result in alterations in LPS structure, making the bacterium more likely to be recognized through TLR4 signaling, could result in robust chemokine expression and early neutrophil recruitment [17,20]. To determine if the altered kinetics of innate immune responses observed for the *galU* mutant strain resulted from gross alterations to its LPS structure, we extracted LPS from WT, *galU* mutant, and *wbtA* mutant (O-antigen deficient) strains of FT and performed Western blot analysis using a FT LPS-specific mAb. No obvious alteration in LPS laddering was observed, suggesting that mutation of *galU* did not result in gross changes in synthesis of the O-antigen component of LPS (Figure 5A). We also analyzed the ability of LPS derived from the *galU* mutant to initiate TLR4-mediated signaling. Using HeLa cells that stably express either TLR2 or TLR4/MD2 that had been transfected with a vector bearing a NFκB-responsive luciferase reporter construct, we determined that neither *galU* mutant or WT FT lysates were able to stimulate TLR4 while both stimulated TLR2 to the same extent (Figure 5B), suggesting that the lipid A portion of the mutant LPS was not altered.

To further investigate whether the *galU* gene resulted in gross change(s) to the outer envelope of FT, experiments were performed to measure the relative sensitivity of *galU* mutant and WT FT to serum components. The *galU* mutant, WT, and *galU*-complemented strains of FT all displayed a similar pattern of serum sensitivity. In contrast, an O-antigen-deficient (Δ*wbtA* mutant) strain of FT was highly sensitive to serum. Interestingly, the *galU*, WT, and *galU*-complemented strains were equally sensitive to heat-inactivated serum, while the *wbtA* mutant strain displayed no sensitivity to serum that had been heat inactivated (Figure 5C).

IL-1 expression/activation induced by the *galU* mutant vs. WT FT

Activation of the AIM2 inflammasome and production of IL-1β and IL-18 are known to be a critical component of the innate immune response to FT infection [42].

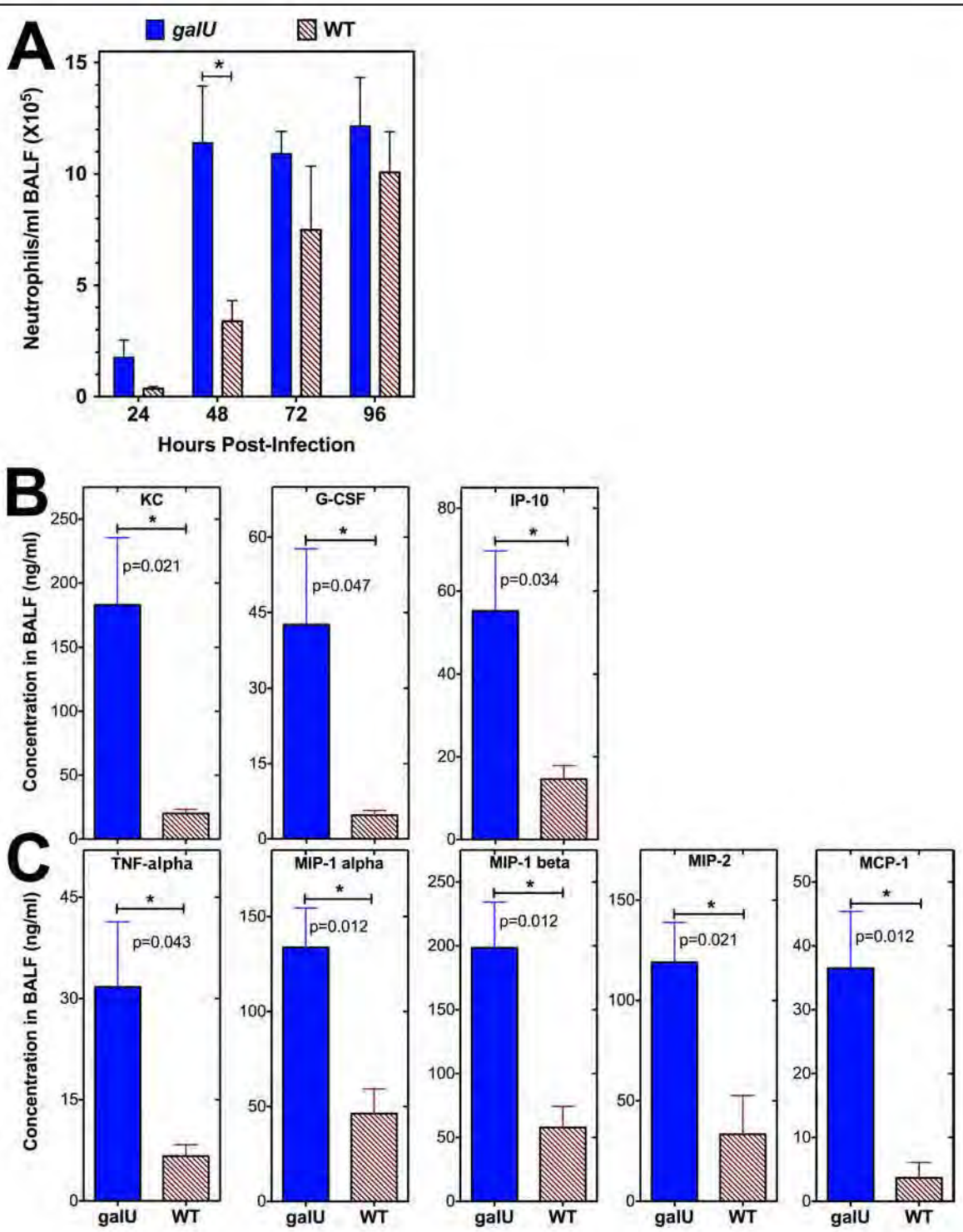

Figure 4 Neutrophil recruitment and chemokine expression in the lungs following infection with the *galU* mutant. C57Bl/6J mice (4/group) were infected intranasally with 5×10^4 CFU (or $50 \times LD_{50}$) of either the WT or *galU* mutant strain of FT and BALF was collected from individual mice at 24, 48, 72 and 96 hours post-infection. Flow cytometric analyses were performed on the cells recovered from BALF to determine the numbers of neutrophils at each timepoint. Statistical analyses were performed via two-way ANOVA with a Bonferroni multiple comparisons post-test and statistically significant differences ($P < 0.05$) are indicated (*) (**Panel A**). The concentrations of KC, G-CSF, MIG, and IL-10 (**Panel A**) and TNF-α, MIP-1α, MIP-1β, MIP-2, and MCP-1 (**Panel B**) in BALF at the 24 and 48 hour time points, respectively, were determined using a Luminex multiplex kit. Statistical analyses were performed using unpaired t tests. Statistically significant differences (*) and p values are indicated in each panel. The data shown is representative of three independent experiments of similar design.

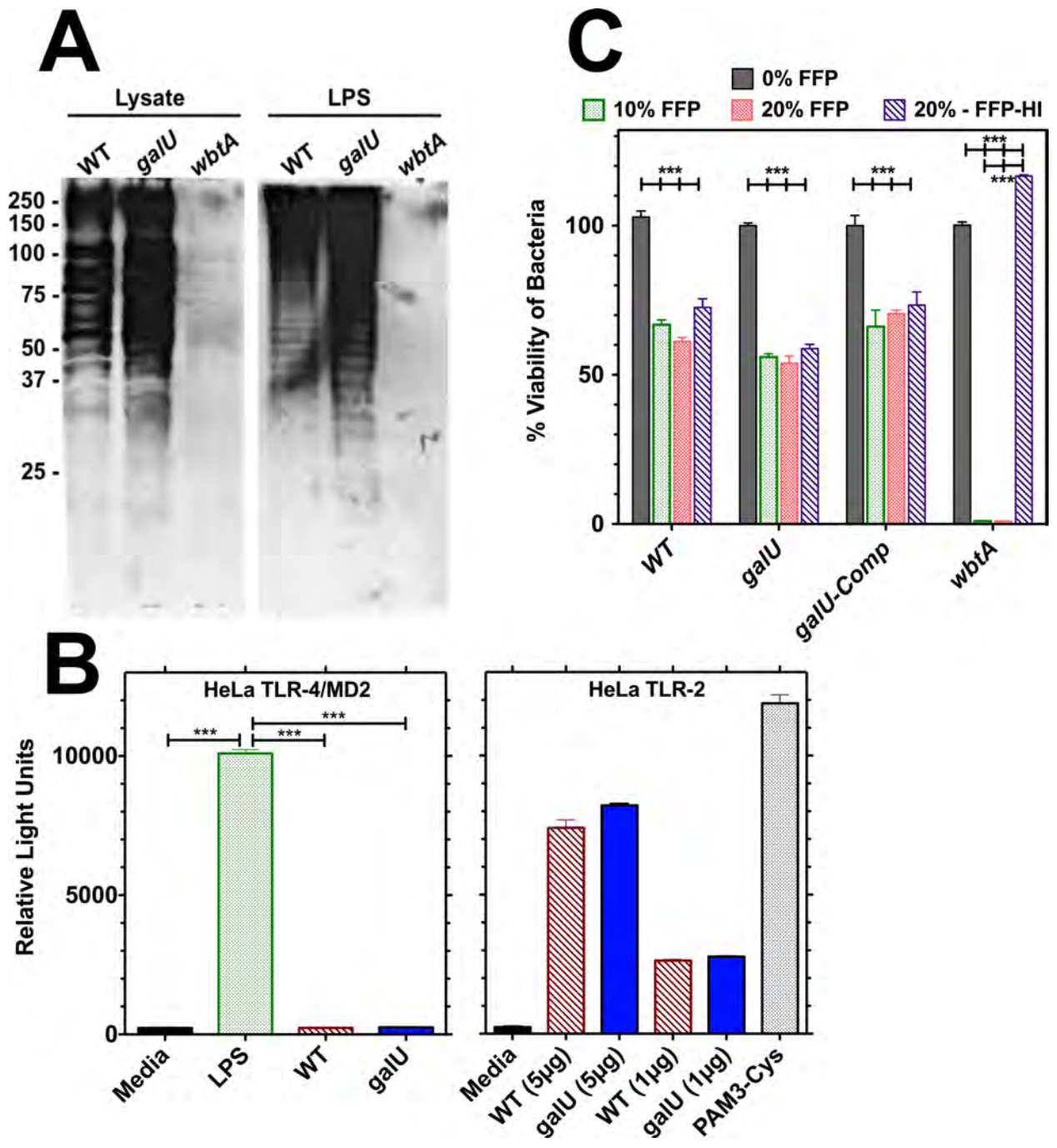

Figure 5 Mutation of *galU* does not cause gross changes in O-antigen synthesis, serum sensitivity, or TLR signaling. **Panel A:** Bacterial cell lysates (10 µg/lane) and LPS preparations of WT, *galU* mutant, and *wbtA*-mutant (O-antigen deficient) FT strains were subjected to SDS-PAGE and Western blotting using an FT LPS-specific monoclonal antibody preparation. **Panel B**: HeLa-TLR4/MD-2 or HeLa-TLR2 were transiently transfected with a ELAM-luciferase reporter construct, CMV-CD14 and CMV-β-Gal (for normalization) and stimulated for 6 hours with 2µg or 10µg of the indicated FT lysates. NF-κB activation was measured via a luciferase assay. Statistical analyses were performed via one-way ANOVA and significant differences ($P < 0.0001$) are indicated (***). **Panel C**: Bacteria were incubated for 2 h at 37°C in either PBS alone or PBS containing either 10% or 20% fresh frozen human plasma (FFP) or 20% heat-inactivated (HI-FFP). Viable bacteria were then enumerated by dilution plating. 100% viability was defined as the number of bacteria recovered from PBS containing no serum (0% FFP), and results were plotted as the mean (± SEM) of triplicate samples. Statistical analyses were performed via one-way ANOVA and statistically significant differences ($P < 0.0001$) are indicated (***).

We compared the kinetics of IL-1β production following infection (*in vitro* and *in vivo*) with either the *galU* mutant or WT strain of FT. RNase protection analysis revealed that IL-1β mRNA levels (as well as those of several other cytokines) were similar in bone marrow-derived dendritic cells (BMDC) that had been infected for 8 h with either the *galU* mutant, WT, or *galU*-complemented strains of FT (Figure 6A), confirming the comparable abilities of the *galU* mutant and WT strains to stimulate TLR-mediated events such as cytokine expression. However, 24 h after infection of a macrophage-like cell line (THP-1) or BMDCs with the *galU* mutant, the amount of IL-1β released into culture supernatants was significantly higher ($p < 0.0001$ and $p < 0.01$, respectively) than was observed following infection with WT FT (Figure 6B). The *galU* mutant also induced accelerated kinetics of IL-1β protein production *in vivo* (Figure 6C). Moreover, the kinetics of IL-1α protein production is more rapid following infection with the *galU* mutant strain of FT (Figure 6C).

Cytotoxicity of the *galU* mutant

In light of the findings that mutation of the *galU* gene resulted in altered kinetics of innate signaling and earlier production of IL-1β than was observed with WT FT, we speculated that the *galU* mutant might induce death of the host cell more rapidly than WT FT. To investigate this possibility, we evaluated the relative abilities of the

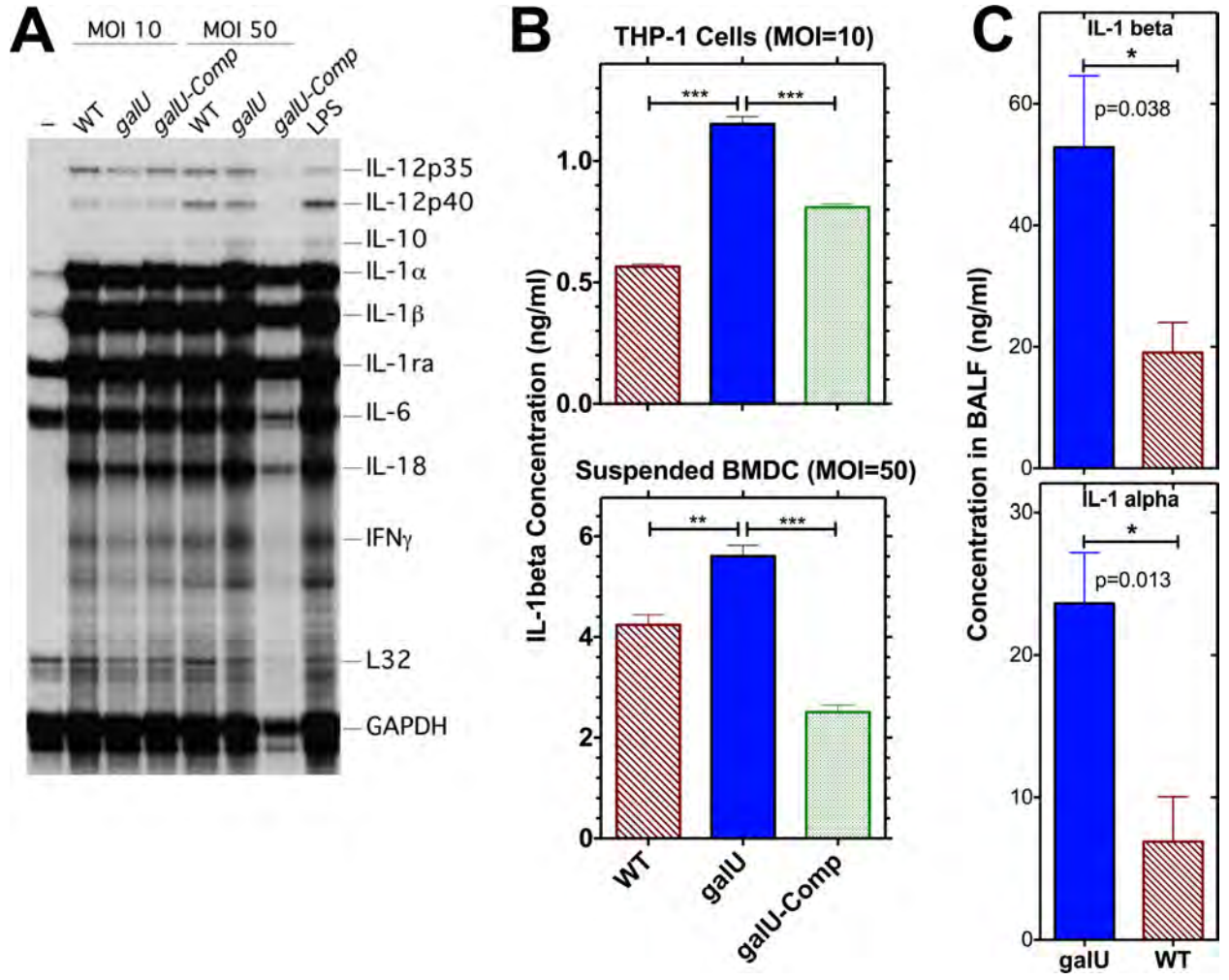

Figure 6 *galU* mutant and WT FT differentially induce cleavage of pro-IL-1β to the active IL-1β form. **Panel A**: BMDC were infected with WT, *galU* mutant, and *galU*-complemented strains of FT at the indicated MOI, and total RNA was extracted 8 h later and subjected to RNase protection analysis. **Panel B**: IL-1β concentrations in culture supernatants from THP-1 and BMDC following infection (24 h) *in vitro* with either WT, *galU* mutant, or *galU*-complemented strains of FT were determined via ELISA, and statistical analyses were performed via one-way ANOVA with a Bonferroni multiple comparisons post-test (p values are indicated as follows: ** $P < 0.01$, and *** $P < 0.0001$). **Panel C**: IL-1β and IL-1α concentrations in BALF collected from mice 48 hrs following intranasal infection with either WT or *galU* mutant strains of FT were determined via multiplex cytokine analysis. Statistical analyses were performed via unpaired t tests and two-tailed p values are indicated.

galU mutant and WT FT strains to kill their host cells *in vitro*. A macrophage-like cell line (J774) was infected with either the *galU* mutant or WT FT strains at an MOI of 100 and incubated for 24 hours. LDH activity in the culture medium was then determined as a measure of host cell death. A significantly higher amount of LDH activity was measured in the supernatants of J774 cells that had been infected with the *galU* mutant compared to those infected with WT FT ($p < 0.0001$), indicating that the *galU* mutant was hyper-cytotoxic. Complementation of the *galU* mutation *in trans* partially restored the cytotoxicity phenotype. For comparative purposes, a *wbtA* mutant strain of FT was also included and was shown to have cytotoxicity characteristics similar to those of WT FT (Figure 7).

Immunization with the *galU* mutant confers immunity to WT FT challenge

Because infection with the *galU* mutant elicited a robust innate immune response and infected mice were able to clear the infection, we assessed the efficacy of the *galU* mutant strain as a live attenuated vaccine strain. Two months following the initial inoculation, mice that survived infection with the *galU* mutant, as well as a naïve group of mice, were challenged with a large dose of WT ($50 \times LD_{50}$) via the intranasal route and were monitored for survival. The *galU* mutant-immunized mice experienced transient weight loss following challenge, but displayed no other visible symptoms of tularemic disease and survived the infection. In contrast, each of the naive mice displayed the typical visible signs of tularemia (lack of grooming, hunched posture, reduced motor activity, etc.) and succumbed to WT FT infection by day 8 post-challenge (Figure 8).

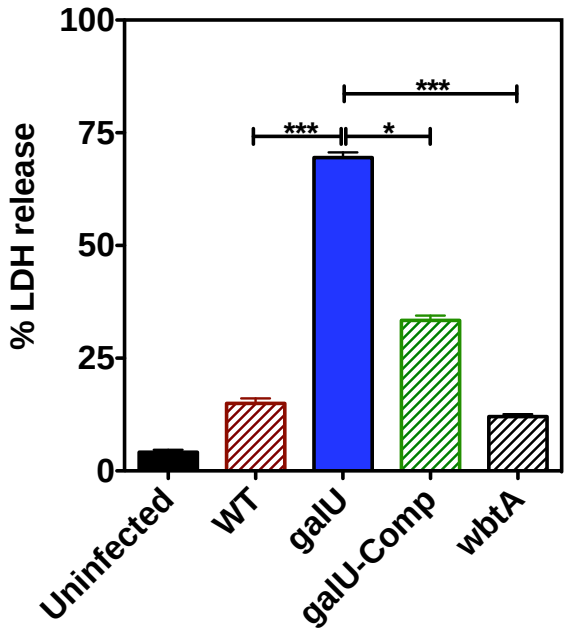

Figure 7 Mutation of the *galU* gene increases cytotoxicity of FT. Murine macrophage-like cells (J774) were infected with the WT, *galU* mutant, the *galU*-complemented, or *wbtA* mutant (O-antigen-deficient) FT LVS strains at an MOI of 100. Host cell death was determined by measuring LDH released from infected cells 24-hours post-infection. All data points represent the mean (± SEM) of triplicate samples and the data shown is representative of three experiments of similar design. Statistical analyses were performed via one-way ANOVA with a Bonferroni multiple comparisons post-test (*** indicates a p-value of <0.0001).

Discussion

A major focus of FT research continues to be the identification of virulence-mechanisms used by this extremely virulent pathogen. A number of virulence determinants have been identified, but there remains much to discover regarding the virulence mechanisms used by FT to survive and cause disease within its mammalian hosts. In this report we show that mutation of *galU* results in a dramatic attenuation of FTLVS virulence that appears to be unrelated to any *in vivo* infectivity or growth defects. Although it is known that mutation of the *galU* gene leaves some other bacterial pathogens attenuated for virulence [27,32,43,44], this is the first report examining the role of *galU* in the pathogenesis of FT.

Neutrophils are a critical component of the innate immune responses to bacterial infection, and the recruitment of these cells into the lungs following pneumonic infection typically peaks by 48-hours post-infection [45-47]. However, it has been reported elsewhere [22,25] and confirmed here that neutrophil recruitment following wild type FT infection in the lungs is not detected until approximately 72 h post-infection. Because it is known that neutrophils are required for control of FT infection [48], it is reasonable to speculate that the ability of FT to delay the kinetics of neutrophil recruitment into the lungs following pulmonary infection may be an important virulence determinant. Interestingly, a comparative analysis following pulmonary infection of mice with the *galU* mutant and WT strains of FT revealed that the kinetics of neutrophil recruitment (and production of chemokines/cytokines involved in neutrophil recruitment) occurs much more rapidly following infection with the *galU* mutant (peaks at 48 h post-infection). Kinetic analyses of bacterial burdens in the lungs, spleens, and livers of mice following infection with the *galU* mutant and WT strains of FT revealed that the two strains disseminated and replicated at comparable rates, but the bacterial burdens in *galU*-infected animals became significantly lower than in WT-infected animals by 72 h post-infection. The significant difference in bacterial

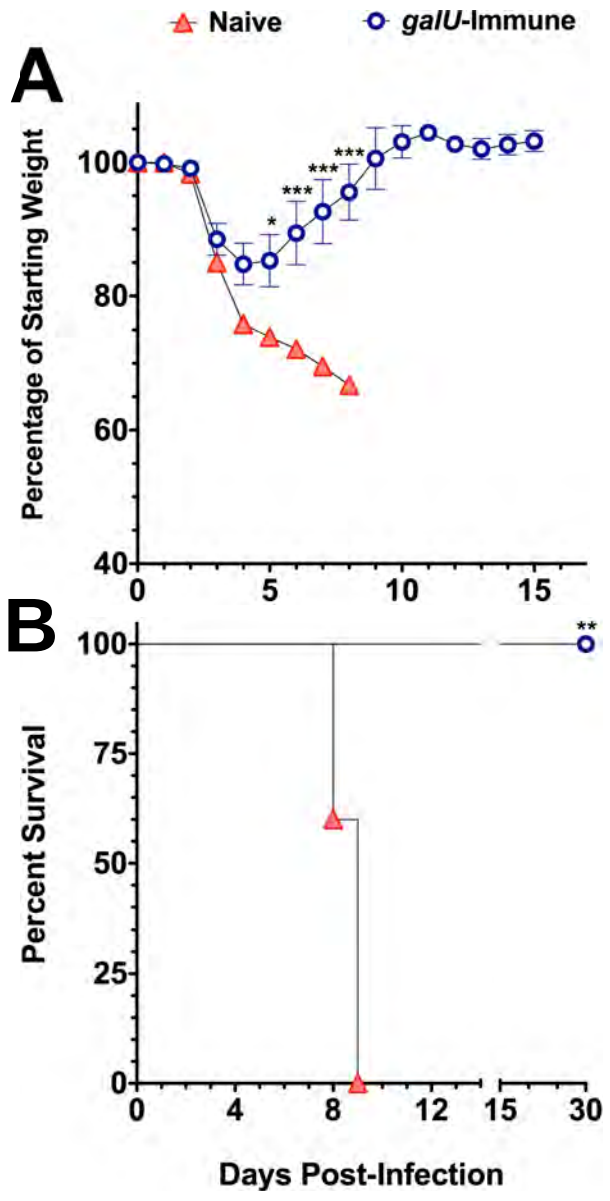

Figure 8 Infection with the *galU* mutant of FT LVS elicits protective immunity WT FT LVS. C57Bl/6J mice (n = 5) that had survived intranasal challenge with the *galU* mutant FT strain and naïve control mice (n = 5) were challenged intranasally with 5×10^4 CFU ($50 \times LD_{50}$) of WT FT LVS eight weeks following the initial infection. The body weight (**Panel A**) and survival (**Panel B**) of mice were monitored for survival for 30 days. Statistical analyses of changes in body weight were performed via two-way ANOVA using a Bonferroni multiple comparisons post-test and p-values are indicated as follows: * $P < 0.05$ and *** $P < 0.001$. Statistical analysis of the survival data was performed using a Gehan-Breslow-Wilcoxon test (** indicates a p-value of 0.0043).

burdens observed in *galU* mutant- vs. WT FT-infected mice 3-4 days post-infection may have been (at least in part) due to differences in the kinetics of neutrophil recruitment.

It remains unclear whether FT actively suppresses innate immune responses during the early stages of infection, or if the delayed response is due to poor recognition of FT through host pattern recognition receptors. It has been well documented that FT produces an atypical LPS that is not recognized via TLR4 [49-51] and that FT is recognized via the TLR2 signaling pathway [52-55]. Because the *galU* gene has been shown to be important for LPS production [27,31,32,43,56] in a number of other bacterial systems, we performed a series of studies to determine whether differences in the LPS expressed by the FT *galU* mutant might contribute to its reduced virulence. A western blot of both bacterial extracts and LPS preparations revealed no obvious differences in the O-antigen laddering between the *galU* mutant and WT strains of FT, suggesting that mutation of *galU* did not have any gross effects on O-antigen synthesis. Because it has been reported elsewhere [57] and confirmed here (*wbtA* mutant) that the absence of O-antigen is a major determinant of susceptibility to complement-mediated killing, our findings that the *galU* mutant displayed a WT serum sensitivity phenotype also suggested that O-antigen synthesis was not significantly altered by mutation of the *galU* gene. This finding contrasted with reports that *galU* mutant strains of *P. aeruginosa* and *V. cholerae* displayed increased serum sensitivity [31,44]. We also observed no differences between the *galU* mutant and WT strains of FT with respect to signaling via the TLR2 and TLR4 recognition pathways. It remains possible that mutation of *galU* results in minor O-antigen compositional changes, alterations in the core oligosaccharides, or differences in the carbohydrate modification of surface proteins of FT. Moreover, in light of the published finding that mutations causing alterations in the lipid A of FT *novicida* [17,20] are highly attenuating for virulence *in vivo* (possibly due to altered kinetics of cytokine/chemokine production and neutrophil mobilization), we posit that mutation of the *galU* gene may have an impact on the lipid A moieties of FT. A complete analysis of the carbohydrate components of the FT *galU* mutant is needed to identify such differences.

Recent studies have revealed that the innate immune response to FT infection is complex and involves multiple signaling pathways. Others and we have previously shown that FT elicits a powerful inflammatory response that is primarily mediated by TLR2 and caspase-1 activation [52-55]. More recently, it has been demonstrated that the AIM-2 inflammasome mediates caspase-1 activation and secretion of mature IL-1β and IL-18 during FT infection [42,58,59]. We predicted that the ability of the *galU* mutant strain of FT to accelerate the kinetics of inflammatory cytokine production/neutrophil mobilization *in vivo* might be due to more rapid activation of the inflammasome. To address this hypothesis, we measured

IL-1β protein production by either THP-1 cells or BMDCs infected for 24 h *in vitro* and found that the *galU* mutant induced higher concentrations of IL-1β than did WT FT. However, RNase protection assays revealed that the differences in IL-1β production by *galU* mutant- vs. WT FT-infected cells were not the result of differential transcription of the IL-1β gene and, therefore, were likely due to more robust activation of the inflammasome. Our findings that production of IL-1β (as well as IL-1α) was induced significantly earlier in the lungs of *galU* mutant vs. WT FT-infected mice were also consistent with the hypothesis. Moreover, we showed that macrophage-like J774 cells infected *in vitro* with the *galU* mutant are killed more rapidly than those infected with WT FT and that WT cytotoxicity could be partially restored by complementation *in trans* with the *galU* gene. These findings were consistent with the possibility that the *galU* mutant more rapidly activates the inflammasome that, in turn, initiates host cell death via pyroptosis and limits the ability of the bacteria to replicate [60]. Based on findings with other mutant strains that display a hypercytolytic phenotype [61,62], it could be speculated that such a change in the *in vivo* life cycle of FT could result in significant attenuation of virulence like that observed for the *galU* mutant. Overall, the findings shown here with FTLVSΔ*galU* are consistent with recently published studies showing that mutation of either *mviN* (FTL_1305 [63]) or *ripA* (FTL_1914 [64]) results in attenuated FT strains that activate the inflammasome more efficiently. Additional studies designed to delineate the signaling pathway(s) that enable early inflammasome activation by the *galU* mutant strain of FT are warranted.

Because the *galU* mutant was so severely attenuated for virulence, in spite of its normal ability to replicate and disseminate *in vivo*, and because there still is no well-defined and efficacious vaccine for FT, we performed a vaccine trial with the *galU* mutant strain. Mice that had been infected with the *galU* mutant and had survived the infection were challenged intranasally two months later with a large dose (50 × LD_{50}) of WT FT LVS and all were found to be immune to FT. These findings, coupled with the fact that the *galU* gene is 100% conserved between the LVS and Schu S4 strains, suggest that a *galU* mutant strain in the Schu S4 background could have strong prophylactic potential as a live attenuated vaccine strain. Studies to characterize *galU* in FT SchuS4 are currently underway in our laboratory.

Conclusions

Disruption of the *galU* gene of FTLVS has little if any effect on its infectivity, replication, or dissemination *in vitro*, but it resulted in highly significant virulence attenuation. The reduced virulence of the *galU* mutant appears to be related to its increased ability to induce innate immune responses following infection. Inflammatory responses and chemokine/cytokine production elicited by WT FT proceeds with much slower kinetics than typically observed for other bacterial pathogens. In contrast, the kinetics of chemokine/cytokine expression and neutrophil recruitment is more rapid following infection with the *galU* mutant strain, likely resulting in more rapid uptake and killing of bacteria by neutrophils. These studies also revealed that disruption of the *galU* gene results in a hypercytotoxic phenotype that could be due (at least in part) to activation of the AIM-2 inflammasome. The accelerated death of cells infected with the *galU* mutant strain presumably interferes with the normal replicative cycle of the bacterium, resulting in the significant difference in bacterial burdens in the liver and spleen of mice infected with the *galU* mutant vs. WT strains of FTLVS observed 4 days post-infection and contributing to the reduction in FTLVSΔ*galU* virulence. These findings underscore the need for studies designed to understand the mechanisms used by WT FT to alter the kinetics of innate immune responses following infection. A thorough comparative analysis of the outer envelope of the WT and *galU* mutant strains of FTLVS coupled with a more detailed analysis of the innate signaling that results following infection with these two strains of FT could lead to a better understanding of the ability of FT to avoid detection by the innate immune system during the early stages of infection. The findings presented here also suggest that a *galU* mutant strain of FT has high potential as a platform for development of a live attenuated tularemia vaccine strain.

Methods

Bacteria and Culture Conditions

FTLVS was a kind gift of Dr. Karen Elkins (FDA, Bethesda, MD). The FTLVS *galU* mutant strain was identified by screening a LVS transposon mutant library for mutants exhibiting elevated susceptibility to polymyxin B. Transposon insertion in to the *galU* gene was verified by DNA sequencing and the polymyxin B hypersensitive phenotype was verified by complementation. The results of this screen will be described in a future publication. FT strains were grown at 37°C in Mueller-Hinton (DIFCO/Becton Dickinson, Sparks, MD) broth modified with 2.5% ferric pyrophosphate, 0.1% glucose, and 10% cysteine (MMH). The *galU* mutant was grown under kanamycin selection (10 μg/mL). Complementation studies were performed as follows. The *galU* gene was amplified by PCR from the LVS genome using primers: forward primer: 5'-CTCGTGGATCCGCTAAAATGAAAATAAGAAAAGC-3' and reverse primer: 5'-ATCGCTAATCGATAAGCTATCTATTTTGAAGG-3'. The resulting amplicon was digested with BamHI and

ClaI restriction endonucleases before being ligated to similarly digested pXB167 [65], which placed the *galU* gene downstream and in the same orientation as the constitutively expressed *orf5* promoter. The resulting plasmid, pXB167-*galU*, was then introduced into the indicated strains by electroporation as previously described [15,65]. The *galU*-complemented strain was grown in presence of kanamycin (10 μg/mL) and carbenicillin (350 μg/mL). Bacterial stocks were made from overnight cultures of bacteria grown to OD_{600} of 0.7-0.9, and aliquots were frozen at -80°C.

Antimicrobial Susceptibility Determination

Antimicrobial susceptibility was determined by the gradient agar plate method [15,66]. The gradient agar plates were prepared in 90 mm × 90 mm Petri plates as follows. Thirty-five milliliters of BHI-chocolate agar (without the test compound) was poured into the square Petri dish and allowed to harden as a wedge by elevating one side of the plate. After the agar solidified, 35 mL of BHI-chocolate agar containing the test compound were added to the leveled plate and allowed to solidify. The antibiotic gradient plates were allowed to develop for 2 h and inoculated within 3 h after preparation. Growth was measured after two days of incubation at 37°C. All tests were performed in triplicate. Minimal inhibitory concentrations (MIC) were determined as follows: MIC = distance of growth (mm) × concentration of drug (ex. μm/mL)/90 (mm).

Mice

C57BL/6 mice were purchased from Charles River Laboratories. Mice were age-matched and used between 8 and 16 weeks of age. Mice were housed in microisolator cages with food and water available *ad libitum*. All experimental protocols were reviewed and approved by the University of Tennessee Health Science Center IACUC.

Intranasal Challenge of Mice with FT

Mice were lightly anesthetized using isoflurane administered with a Vapor Stick nebulizer. Frozen stocks of FT were thawed anew for each experiment, diluted in phosphate-buffered saline (PBS), and administered intranasally (20 μl/naris). The CFUs of FT in the inocula were verified by dilution plating. Following challenge, all mice were monitored daily for signs of illness (decreased mobility, ruffled fur, hunched gait) and weight loss. Upon sacrifice, bronchoalveolar lavage was performed and spleens, livers and lungs were collected for bacterial burden assessment.

Bacterial Burden Determination

Spleens, livers and lungs of challenged mice were removed aseptically and homogenized (using a tissue homogenizer) in one milliliter of sterile PBS. To disrupt cells (releasing FT), 0.25 mL disruption buffer (2.5% saponin, 15% BSA, in PBS) was added with light vortexing. Appropriate dilutions of each sample were then plated in duplicate using an Eddy Jet spiral plater (Neutec Group Inc., Farmingdale, NY) on MMH agar plates (supplemented with 5% calf serum) and incubated at 37°C for 48-72 hours. Colonies were counted using a Flash & Go automated colony counter (Neutec Group Inc.).

Cell Culture, Macrophage Infection, and Cytotoxicity Assays

J774 and RAW264.7 cells (ATCC) were propagated in Dulbecco's Modified Eagle's Medium (DMEM) containing 10% fetal bovine serum. For replication assays, cells were seeded in 24 well tissue culture plates at a density of 2×10^5 cells per well. Twenty-four-hours later, FT was added (MOI of 10) and incubated for 2 h. Gentamicin was then added (50μg/mL) and incubated for 1 hour to kill extracellular bacteria. Cells were then washed two times with DMEM and incubated in fresh culture medium at 37°C. At each experimental time point, cells were washed with PBS to remove any bacteria released during the incubation period, lysed in PBS containing 0.1% deoxycholate, and the number of viable bacteria released from the cells was determined via dilution plating.

For cytotoxicity (LDH) assays, J774 cells were seeded into a 96 well plates and allowed to adhere overnight. FT was added to wells (MOI of 100) and the plates were centrifuged (800 × g, 5 min) to facilitate contact between the cells and bacteria. After 2 hours of co-culture with bacteria, the culture supernatant was aspirated and replaced with fresh media containing gentamicin (50μg/mL) and the plates were incubated at 37°C, 5%CO_2 for 24 hrs. Culture supernatants were then analyzed for LDH release using the CytoTox Non-Radioactive Cytotoxicity Assay (Promega) according to the manufacturer's protocol. The total LDH release (100% LDH in cells) was determined by lysis of uninfected cells. The background LDH value was defined as the level of LDH in the supernatants collected from intact uninfected cells. The percentage of LDH release was calculated as follows: (Sample LDH value - background LDH value)/(Total LDH release value - Background LDH release value) × 100.

Mouse bone marrow-derived dendritic cells (BMDC) were generated by incubating bone marrow in RPMI 1640-10%FCS supplemented with rmGM-CSF (20 ng/mL) (R&D Systems, Minneapolis, MN) for 8 days. This procedure routinely results in 60-80% $CD11c^+$ cells.

Bronchoalveolar Lavage (BAL) and Flow Cytometric Analysis

BAL was performed as described previously [45]. Briefly, BAL was performed by intratracheal injection of 1 mL of PBS into the lungs with immediate vacuum aspiration.

The amount of fluid (BALF) recovered was routinely around 800 μl. Cells were recovered from BALF by centrifugation and their viability was determined by trypan blue exclusion. Protease inhibitor cocktail (Pierce, Rockford, IL) was added to the BALF immediately after recovery and the BALF was frozen at -80°C till further use.

Flow cytometry was performed on isolated BAL cells using fluorochrome conjugated antibodies specific for CD45, CD11b, F4/80, GR1, and NK1.1 (eBioscience CA, USA). A minimum of 50,000 events/sample was collected on a BD Biosciences LSRII cytometer (BD Biosciences, San Jose, CA). Expression of cell surface markers was analyzed using DIVA software. The percentage of neutrophils was determined using gates set on live cells and CD45 expression, and neutrophils were identified as $CD11b^{high}$ /$Gr1^{high}$. Dendritic cells and NK cells were identified as $CD11b^{high}$/$GR1^{lo}$/$F480^{lo}$ and $CD45^{high}$/$NK1.1^{high}$, respectively.

Chemokine/Cytokine Measurements from BALF

The concentrations of each of the chemokines/cytokines from BALF were determined via multiplex analysis using a Luminex Milliplex Analyzer (Millipore Corp., Billerica, MA). A 32-plex Milliplex Cytokine/Chemokine Immunoassay (Millipore) was used according to manufacturer's instructions to simultaneously measure the following: eotaxin, G-CSF, GM-CSF, IFN-γ, IL-1α, IL-1β, IL-2, IL-3, IL-4, IL-5, IL-6, IL-7, IL-9, IL-10, IL-12 (p40), IL-12 (p70), IL-13, IL-15, IL-17, IP-10, KC, LIF, LIX, MCP-1, M-CSF, MIG, MIP-1β, MIP-1α, MIP-2, RANTES, TNFα, and VEGF. All determinations were performed with duplicate samples, and data analysis was performed using Luminex xPonent and Milliplex Analyst software packages (Millipore).

Galactose Sensitivity

FT strains were grown overnight in MHB containing 0.1% glucose and then pelleted, washed and resuspended in PBS. Each strain was then diluted to 5×10^7 CFU/mL and inoculated in fresh MHB containing either 0.1% glucose or 2% D-galactose as the sole sugar source and incubated at 37°C for 24 hours. Optical density at 600 nm was monitored hourly as a measure of growth.

LPS Isolation

Bacterial cultures in mid-logarithmic growth phase were pelleted by centrifugation at 4000 rpm for 20 min and then resuspended in PBS. LPS was isolated from the bacteria using LPS extraction kit (Intron Biotechnologies, Boca Raton, FL) as per the manufacturer's directions.

SDS-PAGE and Western Blotting

Bacterial cell lysates (5 μg/lane) and LPS extracts were electrophoresed on 4-20% gradient polyacrylamide gel and transferred to nitrocellulose membrane. The membrane was then blocked with 5% BSA (in PBS+0.1% Tween-20) and probed with an FT LVS O-antigen-specific mAb (unpublished, see below). Bound antibodies were detected by probing with HRP-conjugated goat anti-mouse secondary antibody (Jackson Research Labs) and visualized by addition of Western Lightning Plus-ECL Enhanced Chemiluminescence substrate (Perkin Elmer, Shelton, CT).

The O-antigen-specific mAb used for the Western analysis was generated as follows: Six-week old female C57/BL6 mice were immunized (i.p.) three times at two-week intervals with 5×10^7 heat-killed FTLVS. Three weeks later each mouse was challenged/boosted via intraperitoneal inoculation with 10^6 live FTLVS. Six weeks later, the FT immune mice with high titer anti-FT IgG were boosted via intraperitoneal injection of 5×10^7 heat-killed FTLVS. Spleens were removed three days later, and splenocytes were fused with P3 × 63-Ag8.653 plasmacytoma cells as previously described [67]. Thirteen days after fusion, hybridoma cell supernatants were screened via direct ELISA for IgG reactive with sonicated FT-antigen and whole FT bacteria. The O-antigen-specific hybridoma was cloned via limiting dilution and mAbs were purified from culture supernatants via affinity chromatography using protein G-sepharose columns (Pierce/ThermoFisher Scientific, Rockford, IL).

Sensitivity to Human Serum

Overnight cultures of the indicated FT strains were pelleted via centrifugation at 4000 rpm for 20 min and washed once with PBS. The bacteria (1×10^7 CFU) were suspended in 100 μl PBS and incubated with an equal amount of human fresh frozen plasma (citrate was used as the anticoagulant) at varying concentrations for 2 h at 37°C. Surviving bacteria were enumerated by dilution plating on MMH plates.

TLR4/TLR2 Signaling Luciferase Assay

HeLa-TLR4/MD2 or HeLa-TLR2 [68] were transiently transfected in 24-well plates using Effectene reagent (Qiagen) with 0.4μg of ELAM-luciferase, 0.2μg of pcDNA-CD14 and 0.1μg of CMV-β-Gal expression plasmids (recipe for 24 wells). Forty-eight hours after transfection, the cells were stimulated for 6 hours with FT lysates. LPS (10 ng/mL) from ***E. coli*** strain LCD25 (List Biological, Campbell, CA) and PAM3-Cys (1μg/mL; Invivogen, San Diego, CA) were used as controls for TLR4 and TLR2 signaling, respectively. Luciferase assays were performed using Promega (Madison, WI) reagents according to the manufacturer recommendations. Efficiency of transfection was normalized by measuring β-Gal in cell lysates.

RNase Protection Assays

BMDC seeded into 24-well tissue culture plates (2×10^6/well) were infected with FT and then total RNA was isolated 8 hr later using TRizol reagent (Life Technologies, Grand Island, NY). RNase protection assays were performed with 4μg of total RNA using a BD-Pharmingen (San Diego, CA) Riboquant kit and the mCK-2 multi-probe template set.

Quantitation of IL-1β Production *In Vitro*

BMDC or THP-1 cells were seeded into 24-well tissue culture plates (2×10^6/well) and infected with FT. Gentamicin was added to the medium 3 hours later. IL-1β was measured in conditioned supernatants 24 hr post-infection using an ELISA kit (eBiosciences, San Diego, CA).

Statistical Methodology

Statistical analyses of each figure were performed using GraphPad Prism software (GraphPad Software, La Jolla, CA). The specific statistical method used for each dataset is described in the figure legends.

List of Abbreviations

FT: *Francisella tularensis*; LVS: live vaccine strain; FTLVS: *Francisella tularensis* live vaccine strain; LD_{50}: lethal dose 50; CAMPs: cationic antimicrobial peptides; LPS: lipopolysaccharide; WT: wild type; MHB: Muller-Hinton Broth; MMH: modified Mueller-Hinton Broth; PBS: phosphate-buffered saline (PBS),; BAL: Bronchoalveolar lavage; BALF: bronchiolar lavage fluid; BMDC: bone marrow-derived dendritic cells.

Acknowledgements and Funding

The project described was supported by NIH grant #U54 AI057157 from Southeastern Regional Center of Excellence for Emerging Infections and Biodefense, by NIH grants AI079482 (to JEB) and AI061260 (to MAM), and by Department of Defense Army grant W81XHW-05-1-0227. The authors also thank Janice Collum and Tim Higgins for their technical assistance.

Author details

[1]Department of Microbiology, Immunology, and Biochemistry, The University of Tennessee Health Science Center, 858 Madison Avenue, Memphis, Tennessee 38163, USA. [2]Department of Immunology and Microbial Sciences, The Scripps Research Institute, 10550 North Torrey Pines Road, La Jolla, CA 92037, USA.

Authors' contributions

HRJ conceived of and performed most of the experimental work for the study and drafted the manuscript. JP participated in the bulk of the experimental work. EAF participated in and assisted in design of the flow cytometric analyses. JEB and XRB created the transposon library and isolated the *galU* mutant strain of FTLVS. FR assisted in design of and performance of RNase protection and IL-1β measurements from infected cells in vitro. FDE performed the antimicrobial sensitivity assays. MAM oversaw the design and coordination of all studies, performed the statistical analyses, and helped to draft the manuscript. All authors have read and approved the final manuscript.

Competing interests

The authors declare that they have no competing interests.

Received: 6 April 2011 Accepted: 5 August 2011
Published: 5 August 2011

References

1. Dennis DT, Inglesby TV, Henderson DA, Bartlett JG, Ascher MS, Eitzen E, Fine AD, Friedlander AM, Hauer J, Layton M, *et al*: **Tularemia as a biological weapon: medical and public health management.** *JAMA* 2001, **285(21)**:2763-2773.
2. Twine S, Bystrom M, Chen W, Forsman M, Golovliov I, Johansson A, Kelly J, Lindgren H, Svensson K, Zingmark C, *et al*: **A mutant of *Francisella tularensis* strain SCHU S4 lacking the ability to express a 58-kilodalton protein is attenuated for virulence and is an effective live vaccine.** *Infect Immun* 2005, **73(12)**:8345-8352.
3. Saslaw S, Eigelsbach HT, Prior JA, Wilson HE, Carhart S: **Tularemia vaccine study. II. Respiratory challenge.** *Arch Intern Med* 1961, **107**:702-714.
4. Saslaw S, Eigelsbach HT, Wilson HE, Prior JA, Carhart S: **Tularemia vaccine study. I. Intracutaneous challenge.** *Arch Intern Med* 1961, **107**:689-701.
5. Eigelsbach HT, Downs CM: **Prophylactic effectiveness of live and killed tularemia vaccines. I. Production of vaccine and evaluation in the white mouse and guinea pig.** *J Immunol* 1961, **87**:415-425.
6. Larsson P, Oyston PC, Chain P, Chu MC, Duffield M, Fuxelius HH, Garcia E, Halltorp G, Johansson D, Isherwood KE, *et al*: **The complete genome sequence of *Francisella tularensis*, the causative agent of tularemia.** *Nat Genet* 2005, **37(2)**:153-159.
7. Gallagher LA, Ramage E, Jacobs MA, Kaul R, Brittnacher M, Manoil C: **A comprehensive transposon mutant library of *Francisella novicida*, a bioweapon surrogate.** *Proc Natl Acad Sci USA* 2007, **104(3)**:1009-1014.
8. Su J, Yang J, Zhao D, Kawula TH, Banas JA, Zhang JR: **Genome-wide identification of *Francisella tularensis* virulence determinants.** *Infect Immun* 2007, **75(6)**:3089-3101.
9. Anthony LD, Burke RD, Nano FE: **Growth of *Francisella* spp. in rodent macrophages.** *Infect Immun* 1991, **59(9)**:3291-3296.
10. Clemens DL, Lee BY, Horwitz MA: **Virulent and avirulent strains of *Francisella tularensis* prevent acidification and maturation of their phagosomes and escape into the cytoplasm in human macrophages.** *Infect Immun* 2004, **72(6)**:3204-3217.
11. Golovliov I, Baranov V, Krocova Z, Kovarova H, Sjostedt A: **An attenuated strain of the facultative intracellular bacterium *Francisella tularensis* can escape the phagosome of monocytic cells.** *Infect Immun* 2003, **71(10)**:5940-5950.
12. Santic M, Molmeret M, Klose KE, Jones S, Kwaik YA: **The *Francisella tularensis* pathogenicity island protein IglC and its regulator MglA are essential for modulating phagosome biogenesis and subsequent bacterial escape into the cytoplasm.** *Cell Microbiol* 2005, **7(7)**:969-979.
13. Qin A, Scott DW, Thompson JA, Mann BJ: **Identification of an essential *Francisella tularensis* subsp. tularensis virulence factor.** *Infect Immun* 2009, **77(1)**:152-161.
14. Gil H, Platz GJ, Forestal CA, Monfett M, Bakshi CS, Sellati TJ, Furie MB, Benach JL, Thanassi DG: **Deletion of TolC orthologs in *Francisella tularensis* identifies roles in multidrug resistance and virulence.** *Proc Natl Acad Sci USA* 2006, **103(34)**:12897-12902.
15. Bina XR, Lavine CL, Miller MA, Bina JE: **The AcrAB RND efflux system from the live vaccine strain of *Francisella tularensis* is a multiple drug efflux system that is required for virulence in mice.** *FEMS Microbiol Lett* 2008, **279(2)**:226-233.
16. Mohapatra NP, Soni S, Bell BL, Warren R, Ernst RK, Muszynski A, Carlson RW, Gunn JS: **Identification of an orphan response regulator required for the virulence of *Francisella* spp. and transcription of pathogenicity island genes.** *Infect Immun* 2007, **75(7)**:3305-3314.
17. Wang X, Ribeiro AA, Guan Z, Abraham SN, Raetz CR: **Attenuated virulence of a *Francisella* mutant lacking the lipid A 4'-phosphatase.** *Proc Natl Acad Sci USA* 2007, **104(10)**:4136-4141.
18. Vinogradov E, Perry MB, Conlan JW: **Structural analysis of *Francisella tularensis* lipopolysaccharide.** *Eur J Biochem* 2002, **269(24)**:6112-6118.
19. Phillips NJ, Schilling B, McLendon MK, Apicella MA, Gibson BW: **Novel modification of lipid A of *Francisella tularensis*.** *Infect Immun* 2004, **72(9)**:5340-5348.
20. Kanistanon D, Hajjar AM, Pelletier MR, Gallagher LA, Kalhorn T, Shaffer SA, Goodlett DR, Rohmer L, Brittnacher MJ, Skerrett SJ, *et al*: **A *Francisella* mutant in lipid A carbohydrate modification elicits protective immunity.** *PLoS Pathog* 2008, **4(2)**:e24.
21. Bosio CM, Bielefeldt-Ohmann H, Belisle JT: **Active suppression of the pulmonary immune response by *Francisella tularensis* Schu4.** *J Immunol* 2007, **178(7)**:4538-4547.

22. Hall JD, Woolard MD, Gunn BM, Craven RR, Taft-Benz S, Frelinger JA, Kawula TH: **Infected-host-cell repertoire and cellular response in the lung following inhalation of *Francisella tularensis* Schu S4, LVS, or U112.** *Infect Immun* 2008, **76(12)**:5843-5852.
23. Mares CA, Ojeda SS, Li Q, Morris EG, Coalson JJ, Teale JM: **Aged mice display an altered pulmonary host response to *Francisella tularensis* live vaccine strain (LVS) infections.** *Exp Gerontol* 2010, **45(2)**:91-96.
24. Malik M, Bakshi CS, McCabe K, Catlett SV, Shah A, Singh R, Jackson PL, Gaggar A, Metzger DW, Melendez JA, *et al*: **Matrix metalloproteinase 9 activity enhances host susceptibility to pulmonary infection with type A and B strains of *Francisella tularensis*.** *J Immunol* 2007, **178(2)**:1013-1020.
25. Mares CA, Ojeda SS, Morris EG, Li Q, Teale JM: **Initial delay in the immune response to *Francisella tularensis* is followed by hypercytokinemia characteristic of severe sepsis and correlating with upregulation and release of damage-associated molecular patterns.** *Infect Immun* 2008, **76(7)**:3001-3010.
26. Kirimanjeswara GS, Olmos S, Bakshi CS, Metzger DW: **Humoral and cell-mediated immunity to the intracellular pathogen *Francisella tularensis*.** *Immunol Rev* 2008, **225**:244-255.
27. Chang HY, Lee JH, Deng WL, Fu TF, Peng HL: **Virulence and outer membrane properties of a *galU* mutant of *Klebsiella pneumoniae* CG43.** *Microb Pathog* 1996, **20(5)**:255-261.
28. Choudhury B, Carlson RW, Goldberg JB: **The structure of the lipopolysaccharide from a *galU* mutant of *Pseudomonas aeruginosa* serogroup-O11.** *Carbohydr Res* 2005, **340(18)**:2761-2772.
29. Genevaux P, Bauda P, DuBow MS, Oudega B: **Identification of Tn10 insertions in the *rfaG, rfaP*, and *galU* genes involved in lipopolysaccharide core biosynthesis that affect *Escherichia coli* adhesion.** *Arch Microbiol* 1999, **172(1)**:1-8.
30. Mollerach M, Lopez R, Garcia E: **Characterization of the *galU* gene of *Streptococcus pneumoniae* encoding a uridine diphosphoglucose pyrophosphorylase: a gene essential for capsular polysaccharide biosynthesis.** *J Exp Med* 1998, **188(11)**:2047-2056.
31. Nesper J, Lauriano CM, Klose KE, Kapfhammer D, Kraiss A, Reidl J: **Characterization of *Vibrio cholerae* O1 El tor *galU* and *galE* mutants: influence on lipopolysaccharide structure, colonization, and biofilm formation.** *Infect Immun* 2001, **69(1)**:435-445.
32. Sandlin RC, Lampel KA, Keasler SP, Goldberg MB, Stolzer AL, Maurelli AT: **Avirulence of rough mutants of *Shigella flexneri*: requirement of O antigen for correct unipolar localization of IcsA in the bacterial outer membrane.** *Infect Immun* 1995, **63(1)**:229-237.
33. Boels IC, Ramos A, Kleerebezem M, de Vos WM: **Functional analysis of the Lactococcus lactis galU and galE genes and their impact on sugar nucleotide and exopolysaccharide biosynthesis.** *Appl Environ Microbiol* 2001, **67(7)**:3033-3040.
34. Daran JM, Dallies N, Thines-Sempoux D, Paquet V, Francois J: **Genetic and biochemical characterization of the UGP1 gene encoding the UDP-glucose pyrophosphorylase from Saccharomyces cerevisiae.** *European journal of biochemistry/FEBS* 1995, **233(2)**:520-530.
35. Moser B, Clark-Lewis I, Zwahlen R, Baggiolini M: **Neutrophil-activating properties of the melanoma growth-stimulatory activity.** *J Exp Med* 1990, **171(5)**:1797-1802.
36. Thomas J, Liu F, Link DC: **Mechanisms of mobilization of hematopoietic progenitors with granulocyte colony-stimulating factor.** *Curr Opin Hematol* 2002, **9(3)**:183-189.
37. Taub DD, Lloyd AR, Conlon K, Wang JM, Ortaldo JR, Harada A, Matsushima K, Kelvin DJ, Oppenheim JJ: **Recombinant human interferon-inducible protein 10 is a chemoattractant for human monocytes and T lymphocytes and promotes T cell adhesion to endothelial cells.** *J Exp Med* 1993, **177(6)**:1809-1814.
38. Lukacs NW, Strieter RM, Chensue SW, Widmer M, Kunkel SL: **TNF-alpha mediates recruitment of neutrophils and eosinophils during airway inflammation.** *J Immunol* 1995, **154(10)**:5411-5417.
39. Wolpe SD, Davatelis G, Sherry B, Beutler B, Hesse DG, Nguyen HT, Moldawer LL, Nathan CF, Lowry SF, Cerami A: **Macrophages secrete a novel heparin-binding protein with inflammatory and neutrophil chemokinetic properties.** *J Exp Med* 1988, **167(2)**:570-581.
40. Wolpe SD, Sherry B, Juers D, Davatelis G, Yurt RW, Cerami A: **Identification and characterization of macrophage inflammatory protein 2.** *Proc Natl Acad Sci USA* 1989, **86(2)**:612-616.
41. Xu LL, Warren MK, Rose WL, Gong W, Wang JM: **Human recombinant monocyte chemotactic protein and other C-C chemokines bind and induce directional migration of dendritic cells in vitro.** *J Leukoc Biol* 1996, **60(3)**:365-371.
42. Fernandes-Alnemri T, Yu JW, Juliana C, Solorzano L, Kang S, Wu J, Datta P, McCormick M, Huang L, McDermott E, *et al*: **The AIM2 inflamma some is critical for innate immunity to *Francisella tularensis*.** *Nat Immunol* 2010, **11(5)**:385-393.
43. Vilches S, Canals R, Wilhelms M, Salo MT, Knirel YA, Vinogradov E, Merino S, Tomas JM: **Mesophilic *Aeromonas* UDP-glucose pyrophosphorylase (GalU) mutants show two types of lipopolysaccharide structures and reduced virulence.** *Microbiology* 2007, **153(Pt 8)**:2393-2404.
44. Priebe GP, Dean CR, Zaidi T, Meluleni GJ, Coleman FT, Coutinho YS, Noto MJ, Urban TA, Pier GB, Goldberg JB: **The *galU* Gene of *Pseudomonas aeruginosa* is required for corneal infection and efficient systemic spread following pneumonia but not for infection confined to the lung.** *Infect Immun* 2004, **72(7)**:4224-4232.
45. Nance SC, Yi AK, Re FC, Fitzpatrick EA: **MyD88 is necessary for neutrophil recruitment in hypersensitivity pneumonitis.** *J Leukoc Biol* 2008, **83(5)**:1207-1217.
46. Tsai WC, Strieter RM, Mehrad B, Newstead MW, Zeng X, Standiford TJ: **CXC chemokine receptor CXCR2 is essential for protective innate host response in murine *Pseudomonas aeruginosa* pneumonia.** *Infect Immun* 2000, **68(7)**:4289-4296.
47. Greenberger MJ, Strieter RM, Kunkel SL, Danforth JM, Laichalk LL, McGillicuddy DC, Standiford TJ: **Neutralization of macrophage inflammatory protein-2 attenuates neutrophil recruitment and bacterial clearance in murine *Klebsiella pneumonia*.** *J Infect Dis* 1996, **173(1)**:159-165.
48. Sjostedt A, Conlan JW, North RJ: **Neutrophils are critical for host defense against primary infection with the facultative intracellular bacterium *Francisella tularensis* in mice and participate in defense against reinfection.** *Infect Immun* 1994, **62(7)**:2779-2783.
49. Duenas AI, Aceves M, Orduna A, Diaz R, Sanchez Crespo M, Garcia-Rodriguez C: ***Francisella tularensis* LPS induces the production of cytokines in human monocytes and signals via Toll-like receptor 4 with much lower potency than *E. coli* LPS.** *Int Immunol* 2006, **18(5)**:785-795.
50. Chen W, KuoLee R, Shen H, Busa M, Conlan JW: **Toll-like receptor 4 (TLR4) does not confer a resistance advantage on mice against low-dose aerosol infection with virulent type A *Francisella tularensis*.** *Microb Pathog* 2004, **37(4)**:185-191.
51. Ancuta P, Pedron T, Girard R, Sandstrom G, Chaby R: **Inability of the *Francisella tularensis* lipopolysaccharide to mimic or to antagonize the induction of cell activation by endotoxins.** *Infect Immun* 1996, **64(6)**:2041-2046.
52. Cole LE, Shirey KA, Barry E, Santiago A, Rallabhandi P, Elkins KL, Puche AC, Michalek SM, Vogel SN: **Toll-like receptor 2-mediated signaling requirements for *Francisella tularensis* live vaccine strain infection of murine macrophages.** *Infect Immun* 2007, **75(8)**:4127-4137.
53. Li H, Nookala S, Bina XR, Bina JE, Re F: **Innate immune response to *Francisella tularensis* is mediated by TLR2 and caspase-1 activation.** *J Leukoc Biol* 2006, **80(4)**:766-773.
54. Malik M, Bakshi CS, Sahay B, Shah A, Lotz SA, Sellati TJ: **Toll-like receptor 2 is required for control of pulmonary infection with *Francisella tularensis*.** *Infect Immun* 2006, **74(6)**:3657-3662.
55. Thakran S, Li H, Lavine CL, Miller MA, Bina JE, Bina XR, Re F: **Identification of *Francisella tularensis* lipoproteins that stimulate the toll-like receptor (TLR)2/TLR1 heterodimer.** *J Biol Chem* 2008, **283(7)**:3751-3760.
56. Dean CR, Goldberg JB: ***Pseudomonas aeruginosa galU* is required for a complete lipopolysaccharide core and repairs a secondary mutation in a PA103(serogroup O11) *wbpM* mutant.** *FEMS Microbiol Lett* 2002, **210(2)**:277-283.
57. Clay CD, Soni S, Gunn JS, Schlesinger LS: **Evasion of complement-mediated lysis and complement C3 deposition are regulated by *Francisella tularensis* lipopolysaccharide O antigen.** *J Immunol* 2008, **181(8)**:5568-5578.
58. Jones JW, Kayagaki N, Broz P, Henry T, Newton K, O'Rourke K, Chan S, Dong J, Qu Y, Roose-Girma M, *et al*: **Absent in melanoma 2 is required for innate immune recognition of *Francisella tularensis*.** *Proc Natl Acad Sci USA* 2010, **107(21)**:9771-9776.

59. Rathinam VA, Jiang Z, Waggoner SN, Sharma S, Cole LE, Waggoner L, Vanaja SK, Monks BG, Ganesan S, Latz E, *et al*: **The AIM2 inflammasome is essential for host defense against cytosolic bacteria and DNA viruses.** *Nat Immunol* 2010, **11(5)**:395-402.
60. Willingham SB, Bergstralh DT, O'Connor W, Morrison AC, Taxman DJ, Duncan JA, Barnoy S, Venkatesan MM, Flavell RA, Deshmukh M, *et al*: **Microbial pathogen-induced necrotic cell death mediated by the inflammasome components CIAS1/cryopyrin/NLRP3 and ASC.** *Cell Host Microbe* 2007, **2(3)**:147-159.
61. Platz GJ, Bublitz DC, Mena P, Benach JL, Furie MB, Thanassi DG: **A *tolC* mutant of *Francisella tularensis* is hypercytotoxic compared to the wild type and elicits increased proinflammatory responses from host cells.** *Infect Immun* 2010, **78(3)**:1022-1031.
62. Weiss DS, Henry T, Monack DM: ***Francisella tularensis*: activation of the inflamma some.** *Ann N Y Acad Sci* 2007, **1105**:219-237.
63. Ulland TK, Buchan BW, Ketterer MR, Fernandes-Alnemri T, Meyerholz DK, Apicella MA, Alnemri ES, Jones BD, Nauseef WM, Sutterwala FS: **Cutting edge: mutation of Francisella tularensis mviN leads to increased macrophage absent in melanoma 2 inflamma some activation and a loss of virulence.** *J Immunol* 2010, **185(5)**:2670-2674.
64. Huang MT, Mortensen BL, Taxman DJ, Craven RR, Taft-Benz S, Kijek TM, Fuller JR, Davis BK, Allen IC, Brickey WJ, *et al*: **Deletion of ripA alleviates suppression of the inflammasome and MAPK by Francisella tularensis.** *J Immunol* 2010, **185(9)**:5476-5485.
65. Bina XR, Wang C, Miller MA, Bina JE: **The Bla2 beta-lactamase from the live-vaccine strain of *Francisella tularensis* encodes a functional protein that is only active against penicillin-class beta-lactam antibiotics.** *Arch Microbiol* 2006, **186(3)**:219-228.
66. Curiale MS, Levy SB: **Two complementation groups mediate tetracycline resistance determined by Tn10.** *J Bacteriol* 1982, **151(1)**:209-215.
67. Marion TN, Lawton AR, Kearney JF, Briles DE: **Anti-DNA autoantibodies in (NZB × NZW)F1 mice are clonally heterogeneous, but the majority share a common idiotype.** *J Immunol* 1982, **128(2)**:668-674.
68. Re F, Strominger JL: **Toll-like receptor 2 (TLR2) and TLR4 differentially activate human dendritic cells.** *J Biol Chem* 2001, **276(40)**:37692-37699.

doi:10.1186/1471-2180-11-179
Cite this article as: Jayakar *et al.*: A *galU* mutant of *francisella tularensis* is attenuated for virulence in a murine pulmonary model of tularemia. *BMC Microbiology* 2011 **11**:179.

H5N1 Influenza Virus Pathogenesis in Genetically Diverse Mice Is Mediated at the Level of Viral Load

Adrianus C. M. Boon,[a] David Finkelstein,[b] Ming Zheng,[c] Guochun Liao,[c] John Allard,[c] Klaus Klumpp,[c] Robert Webster,[a] Gary Peltz,[c] and Richard J. Webby[a]

Department of Infectious Diseases[a] and Hartwell Center for Bioinformatics and Biotechnology,[b] St. Jude Children's Research Hospital, Memphis, Tennessee, USA, and Roche Pharmaceuticals, Palo Alto, California, USA[c]

ABSTRACT **The genotype of the host is one of several factors involved in the pathogenesis of an infectious disease and may be a key parameter in the epidemiology of highly pathogenic H5N1 influenza virus infection in humans. Gene polymorphisms may affect the viral replication rate or alter the host's immune response to the virus. In humans, it is unclear which aspect dictates the severity of H5N1 virus disease. To identify the mechanism underlying differential responses to H5N1 virus infection in a genetically diverse population, we assessed the host responses and lung viral loads in 21 inbred mouse strains upon intranasal inoculation with A/Hong Kong/213/03 (H5N1). Resistant mouse strains survived large inocula while susceptible strains succumbed to infection with 1,000- to 10,000-fold-lower doses. Quantitative analysis of the viral load after inoculation with an intermediate dose found significant associations with lethality as early as 2 days postinoculation, earlier than any other disease indicator. The increased viral titers in the highly susceptible strains mediated a hyperinflamed environment, indicated by the distinct expression profiles and increased production of inflammatory mediators on day 3. Supporting the hypothesis that viral load rather than an inappropriate response to the virus was the key severity-determining factor, we performed quantitative real-time PCR measuring the cytokine/viral RNA ratio. No significant differences between susceptible and resistant mouse strains were detected, confirming that it is the host genetic component controlling viral load, and therefore replication dynamics, that is primarily responsible for a host's susceptibility to a given H5N1 virus.**

IMPORTANCE **Highly pathogenic H5N1 influenza virus has circulated in Southeast Asia since 2003 but has been confirmed in relatively few individuals. It has been postulated that host genetic polymorphisms increase the susceptibility to infection and severe disease. The mechanisms and host proteins affected during severe disease are unknown. Inbred mouse strains vary considerably in their ability to resist H5N1 virus and were used to identify the primary mechanism determining disease severity. After inoculation with H5N1, resistant mouse strains had reduced amounts of virus in their lungs, which subsequently resulted in lower production of proinflammatory mediators and less pathology. We therefore conclude that the host genetic component controlling disease severity is primarily influencing viral replication. This is an important concept, as it emphasizes the need to limit virus replication through antiviral therapies and it shows that the hyperinflammatory environment is simply a reflection of more viral genetic material inducing a response.**

Received 25 July 2011 **Accepted** 16 August 2011 **Published** 6 September 2011

Citation Boon ACM, et al. 2011. H5N1 influenza virus pathogenesis in genetically diverse mice is mediated at the level of viral load. mBio 2(5):e00171-11. doi:10.1128/mBio.00171-11.

Editor Terence Dermody, Vanderbilt University Medical Center

Address correspondence to Adrianus C. M. Boon, jboon@dom.wustl.edu.

Genetic polymorphisms within the genome of the infected host play an important role in the response to and outcome of microbial infections. In humans, several polymorphisms that affect HIV, hepatitis C virus (HCV), and herpes simplex virus (HSV) pathogenesis (1–6) have been described. However, very few data are available on how host genetic differences influence the course of influenza A virus infection, and what is available is at best inconclusive. Studies on highly pathogenic H5N1 influenza virus in Asia support the notion of host genetic polymorphisms affecting susceptibility to H5N1 virus (7, 8), with a high proportion of infected contacts being genetically related to the index case within family clusters. Also, during the 2009 H1N1 virus pandemic, individuals of indigenous descent in the Americas, Australia, and the Pacific had higher hospitalization rates than did the overall population (9, 10). Although the increased incidence of risk factors such as diabetes and asthma may have contributed to this difference, gene polymorphisms likely played an important role in susceptibility to influenza virus.

Despite the evidence favoring a role for host genetic polymorphisms in susceptibility to influenza virus infection, no human polymorphisms have been discovered. More importantly, we have yet to understand the mechanistic basis for the difference in pathogenesis: does the genetic change in susceptible hosts allow for increased replication dynamics of the virus or an altered immune environment, or does it completely change the hosts' response to the pathogen independently of viral burden? Existing

literature reporting large differences in the host responses after infection with low- or highly pathogenic viruses (11–17) would suggest that individuals with severe disease have an aberrant immune response to the virus. Alternatively, the genetic differences between the hosts allow for an increased virus replication rate, resulting in the induction of a more vigorous immune response. In humans, H5N1 virus pathogenesis is characterized by high viral load and increased production of proinflammatory cytokines culminating in severe disease and often death (i.e., 60% mortality rate in humans) (12, 15). Due to the correlative nature of the 2 parameters, it is unclear how they are linked and how each affects survival after infection. The importance of replication dynamics was recently highlighted in a paper by Hatta et al. demonstrating that the more virulent H5N1 virus also had the highest replication rate of the viruses studied (18).

To increase our understanding of H5N1 virus pathogenesis and to study the effects of host genetic variation, we initiated a large systematic effort to define the underlying mechanism involved in susceptibility or resistance to influenza virus infection. This knowledge is crucial for the identification of genes or gene networks associated with differences in pathogenesis. In summary, H5N1 virus pathogenesis in genetically diverse hosts is largely determined by the host factors controlling viral load in the lungs. Increased viral loads initiate the production of excessive amounts of proinflammatory cytokines, causing tissue damage and ultimately mortality of the susceptible host.

RESULTS

H5N1 virus pathogenic phenotypes among inbred mouse strains. We experimentally inoculated 21 mouse strains with the highly pathogenic H5N1 influenza A virus A/Hong Kong/213/03 (HK213) and monitored the animals for 30 days thereafter for signs of morbidity and mortality. The 50% mouse lethal dose (MLD_{50}) values varied from 40 50% egg infective doses (EID_{50}) for the influenza virus-susceptible strain DBA/2_S (susceptibility indicated by "S") to more than 10^6 EID_{50} for the influenza virus-resistant strains BALB/c_R and BALB/cBy_R (resistance indicated by "R") (Fig. 1).

Several strains were resistant to the high-dose challenge and had MLD_{50} values between 10^5 and 10^6 EID_{50}. Others were considered either susceptible ($MLD_{50} < 10^4$ EID_{50}) or highly susceptible ($MLD_{50} < 10^3$ EID_{50}). The diversity in pathogenic potential of a single highly pathogenic H5N1 virus prompted us to define a dose of virus that was lethal to the susceptible mouse strains but induced only mild morbidity without mortality in the resistant strains. Thus, we set the dose of 10^4 EID_{50} as the cutoff for H5N1 virus resistance/susceptibility and subsequently used it in all host response experiments.

Transfer of hematopoietic cells from resistant strains does not rescue the pathogenic phenotype of susceptible strains. An appropriate immune response mediated by hematopoietic cells is essential for clearance of influenza viruses and subsequent survival of the infected host. To test whether susceptible mouse strains have an inferior immune response due to one or more genetic polymorphisms, we generated chimeric DBA/2_S mice whose bone marrow (BM) was replaced with that of C57BL/6_R (DBA/2_{C57}), BALB/c_R (DBA/2_{BALB}), or DBA/2_S (DBA/$2_{DBA/2}$) as a control. Twelve weeks post-BM transfer, successful engraftment was determined using strain-specific cell surface markers. The chimeric mice were subsequently infected with 1 of 2 doses of HK213 virus.

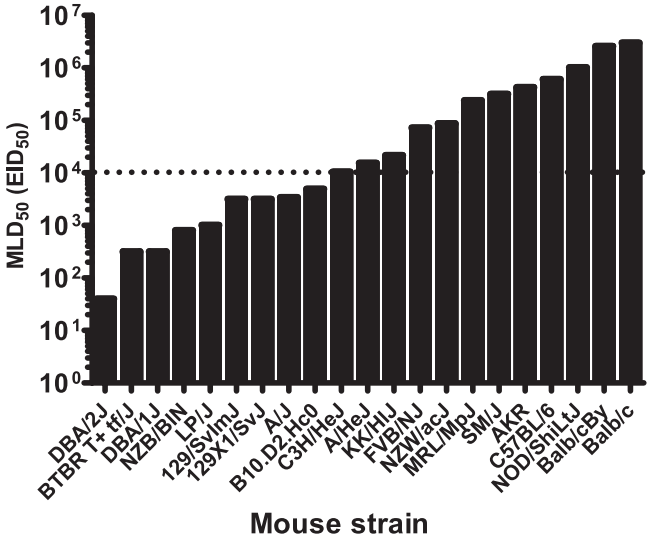

FIG 1 Pathogenic profile of 21 inbred mouse strains inoculated with highly pathogenic H5N1 influenza A virus. The 50% mouse lethal dose (MLD_{50}) of A/Hong Kong/213/03 virus is shown. A dose of 10^4 EID_{50} (dotted line) was set to distinguish influenza virus-resistant from influenza virus-susceptible mouse strains and used throughout the work to assess biological parameters associated with severity of disease and mortality.

At a dose of 10^4 EID_{50}, the DBA/2_{C57} and DBA/2_{BALB} mice succumbed to infection approximately 7 to 8 days postinoculation (dpi). This finding was similar to that seen in age-matched DBA/2 control mice and DBA/$2_{DBA/2}$ mice (Fig. 2A). Intranasal inoculation with a 10-fold-lower dose (10^3 EID_{50}) produced similar results: DBA/2_{BALB} mice died around the same time (postinoculation day 8) as did the DBA/$2_{DBA/2}$ control mice. DBA/2_{C57} mice survived a few days longer; however, all of the mice had died by day 12 postinoculation (Fig. 2B). Thus, the immune response of hematopoietic origin from resistant mouse strains was unable to rescue the phenotype of a susceptible strain, consistent with the hypothesis that the genetic polymorphism(s) affecting H5N1 virus pathogenesis in susceptible mouse strains promotes viral replication in the epithelial cells of the respiratory tract.

RNA expression profile early after H5N1 virus infection differentiates susceptible from resistant mouse strains. To identify differences in the molecular responses to HK213 virus infection in the susceptible and resistant mouse strains, we performed large-scale expression analysis of lung tissue before and at various time points after inoculation in 3 susceptible strains (DBA/2_S, 129/$SvIm_S$, and A/J_S) and 3 resistant strains (SM_R, C57BL/6_R, and BALB/c_R). Probes (26,000) that were detected in one or more strains at any time point after infection were included in subsequent analyses. Prior to detailed gene and pathway expression analysis, we performed an unsupervised principal component analysis (PCA) to identify similarities or differences in overall gene expression between strains of mice before inoculation and 1, 3 and 7 days postinoculation (dpi). If all biological replicates of a particular condition (mouse strain) form a cluster and are located elsewhere on the plot compared to the rest of the data, that particular mouse strain is considered to have a distinct expression profile. Our goal was to identify similarities and differences among the strains and correlate those with our disease phenotype. Prior to infection or shortly thereafter (day 1 postinfection), no

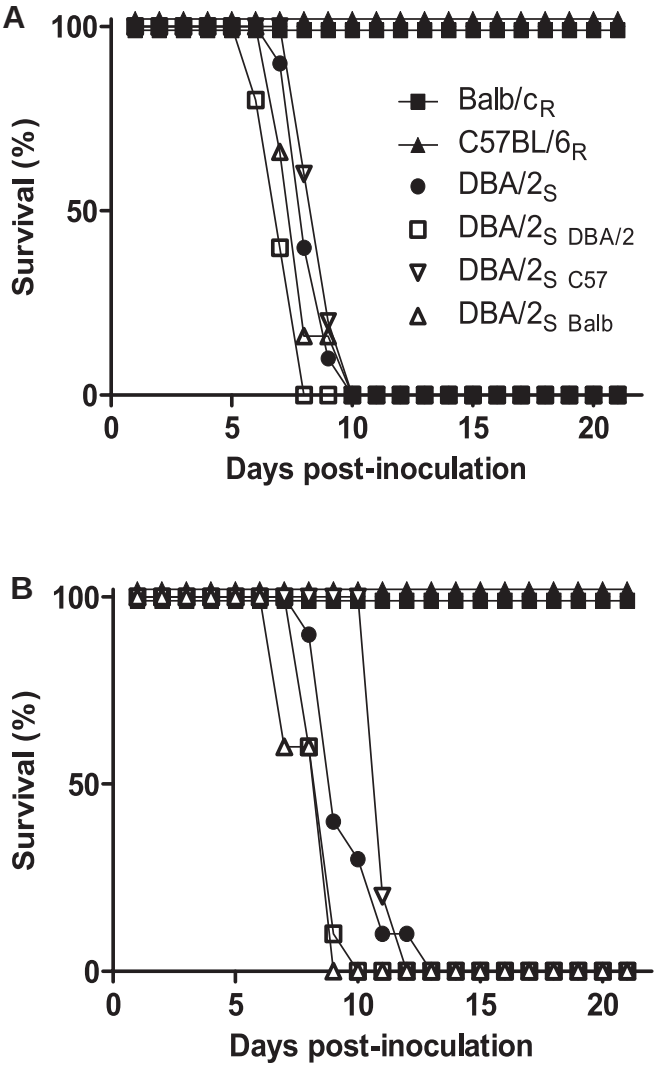

FIG 2 The hematopoietic component does not confer resistance in susceptible strains. Chimeric DBA/2$_S$ mice containing bone marrow from resistant (C57BL/6$_R$ or BALB/c$_R$) or susceptible (DBA/2$_S$) mice were inoculated with 10^4 EID$_{50}$ (A) or 10^3 EID$_{50}$ (B) of A/Hong Kong/213/03 virus and monitored for morbidity and mortality for 21 days.

clustering was observed, and individual data were scattered throughout the plot (Fig. 3). At day 3 postinfection, the expression profiles of the mice clustered into 3 groups. Group 1 (red circle) contained only highly susceptible strains (DBA/2$_S$ and 129/SvIm$_S$). Group 2 (green circle) was composed of resistant strains (C57BL/6$_R$ and BALB/c$_R$) only. Group 3 (blue circle) was composed of a susceptible strain and a resistant strain (A/J$_S$ and SM$_R$, respectively) and was situated between groups 1 and 2 on the second component. By day 7, the clustering of susceptible (group 1) and resistant (group 2) strains remained intact. More importantly, the susceptible strain in group 3, A/J$_S$, had joined group 1, and the resistant strain (SM$_R$) was found in close proximity to the other resistant strains of group 2. These plots clearly indicate that a gene expression signature is associated with death or survival in these mice but also that these signatures are not necessarily fixed until later in the infectious process.

Pathway analysis of the response to H5N1 virus infection in inbred mouse strains. To identify qualitative and quantitative differences in the host responses associated with survival, we probed the transcriptomes of susceptible and resistant mouse strains before and after inoculation with H5N1 virus. Because our phenotype occurred after H5N1 virus infection, we focused on genes whose expression increased or decreased ≥2-fold compared to that in uninfected controls in at least two of the three susceptible or resistant mouse strains; this approach yielded a comprehensive set of 2,038 genes.

At day 1 postinoculation, 76 genes were differentially expressed, of which the majority (64) were shared by the susceptible and resistant strains (see Fig. S1A in the supplemental material). By day 3, the number of differentially expressed genes increased dramatically to 829, and 569 (68.6%) of those were shared by the two groups. Surprisingly, only 28 (3.4%) genes were uniquely up- or downregulated in the resistant strains and 232 (70.5%) were found only in the susceptible strains. These included several genes that encode cytokines associated with increased inflammation, e.g., *Il28b*, *Ifna4*, *Ifna5*, and *Tnfrsf1b*. Similar results were found at day 7, with 582 of 1,084 (53.7%) genes differentially expressed in the susceptible strains only. Overall, these data suggest that the resistant mouse strains do not express a unique set of genes or a pathway(s) controlling replication or disease. Rather, the difference in expression profiles identified by PCA (Fig. 3) was caused by altered or increased gene expression in the susceptible mouse strains.

Next, we performed pathway analysis of the up- or downregulated genes within each mouse strain. At day 1 postinoculation, gene sets in 5 of 6 strains were enriched for the glutathione pathway (SM$_R$ was the exception). By day 3, the identified pathways were similar among all 6 strains (see Fig. S1B in the supplemental material), with significant *P* values for all the well-known pathways, including the cytokine-cytokine receptor interaction pathway, Toll-like receptor pathway, NOD-like receptor pathway, and chemokine signaling pathway. The increased expression of many of these pathway-associated genes in all strains suggested that the difference in resistance to H5N1 virus pathology is not due to a defect in innate or antiviral immune signaling in the susceptible strains. On the contrary, our analysis of the total number of genes identified within a particular pathway (Fig. S1C) showed many more upregulated genes in the DBA/2$_S$ and 129/SvIm$_S$ strains than in other strains. At day 7 postinfection, we found an enriched gene expression profile in the resistant mouse strains that is associated with systemic lupus erythematosus, cell adhesion molecules, the antigen processing and presentation pathway, and the graft-versus-host disease pathway. This profile is indicative of adequate virus-specific T- and B-cell responses in these mice. In contrast, the 3 susceptible strains continued to have many cytokine genes upregulated, as evidenced by the low *P* value for the cytokine-cytokine receptor interaction pathway (Fig. S1B and S1C; Table S1).

Finally, we performed statistical analysis on the array data to identify genes whose expression values correlated with the PCA clustering observed on days 3 and 7 postinoculation (see Table S2 in the supplemental material). The majority of the 85 identified genes belonged to proinflammatory pathways, including cytokine-cytokine receptor pathways, the Jak-Stat pathway, and innate sensing pathways like the Toll-like receptor pathway. To summarize, the difference between resistant and susceptible

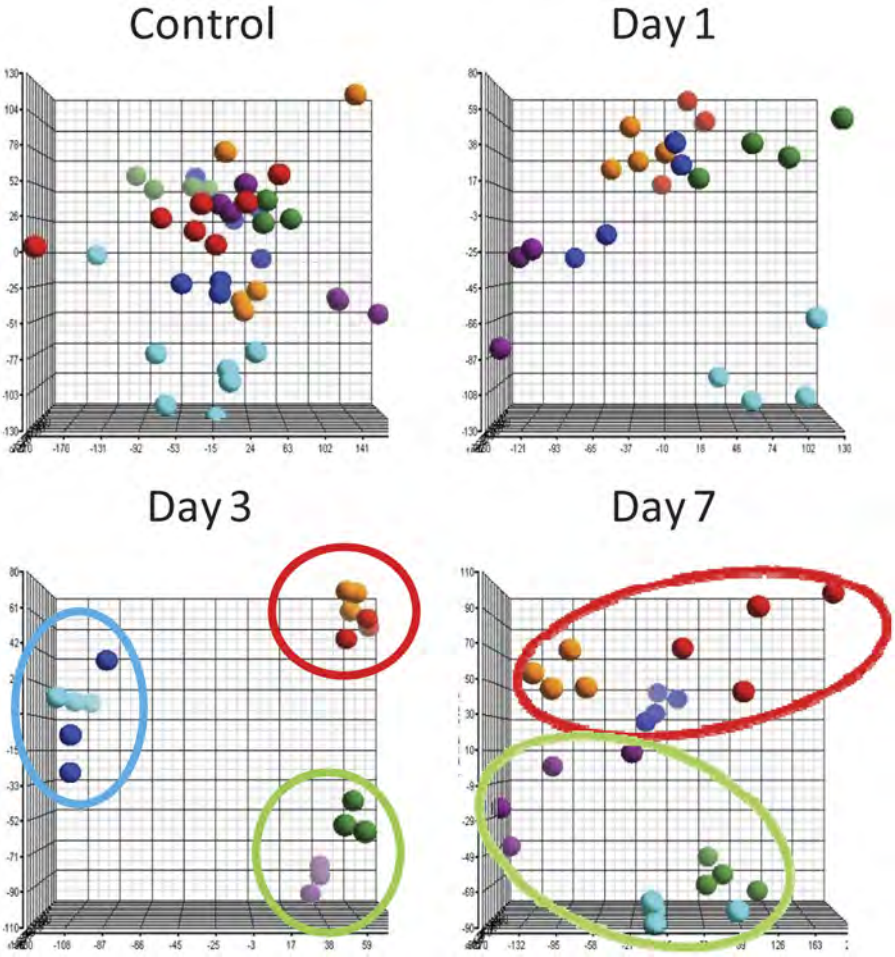

FIG 3 Principal component analysis identifies the gene expression profile associated with severity of H5N1 virus disease. Principal component analysis using ~26,000 probes in lung tissue RNA of DBA/2_S, 129/SvIm$_S$, A/J_S, SM$_R$, C57BL/6_R, and BALB/c_R mice prior to infection (control) and on days 1, 3, and 7 after inoculation with 10^4 EID$_{50}$ of A/Hong Kong/213/03. Each dot represents the RNA expression profile of a single mouse. Colored circles indicate the three clusters of highly susceptible (red), intermediate susceptible (blue), and resistant (green) mouse strains. The *x*, *y*, and *z* axes correspond to principal components 1, 2, and 3, respectively.

strains is predominantly quantitative, with the excessive production of proinflammatory cytokines in the susceptible strains most likely affecting downstream induction of robust adaptive immune responses. The overrepresentation of proinflammatory genes in the susceptible strains is indicative of ongoing viral replication and suggests higher replication rates and higher viral loads in these strains.

Increased production of inflammatory mediators in susceptible mouse strains. Many of the genes associated with severe disease that were identified by expression analysis are considered proinflammatory. Although inflammation is important for the induction of an innate and adaptive immune response, too much inflammation can be pathological and exacerbate disease. To validate the expression data and demonstrate increased production of proinflammatory mediators in the susceptible strains, we measured the production of CCL2, alpha interferon (IFN-α), IFN-β, tumor necrosis factor alpha (TNF-α), CXCL2, and CSF3 after inoculation with 10^4 EID$_{50}$ in 3 susceptible mouse strains (DBA/2_S, 129/SvIm$_S$, and A/J_S) and 3 resistant strains (SM$_R$, C57BL/6_R, and BALB/c_R). At day 3 postinfection, lung homogenates of susceptible strains contained significantly higher concentrations of proinflammatory cytokines than did those of most of the resistant strains (Fig. 4); however, intriguing patterns emerged. The concentration of CSF3 was significantly higher in all susceptible strains and in the SM$_R$ strain, which, based on expression analysis, clustered with the susceptible A/J_S strain. A similar pattern was found for IFN-α and IFN-β. In contrast, the production levels of CCL2 and CXCL2 were significantly higher in the DBA/2_S and 129/SvIm$_S$ strains than in the other 4 strains. Finally, we found significantly higher levels of TNF-α in the susceptible strains than in the resistant strains. The production of certain cytokines, i.e., CCL2, TNF-α, and CXCL2, was significantly correlated with the MLD$_{50}$ ($P < 0.01$; $R^2 = 0.77$, 0.96, and 0.72, respectively). These results were similar to those identified earlier by array analysis.

Viral load determines the outcome after infection with the HK213 virus. We hypothesized that increased pathogenicity coupled with enhanced inflammation in the susceptible strains may be the result of higher viral titers. To test this hypothesis, we quantified the amount of infectious virus at days 2, 4, and 7 postinoculation with 10^4 EID$_{50}$ of HK213 in the lungs of the 6 mouse

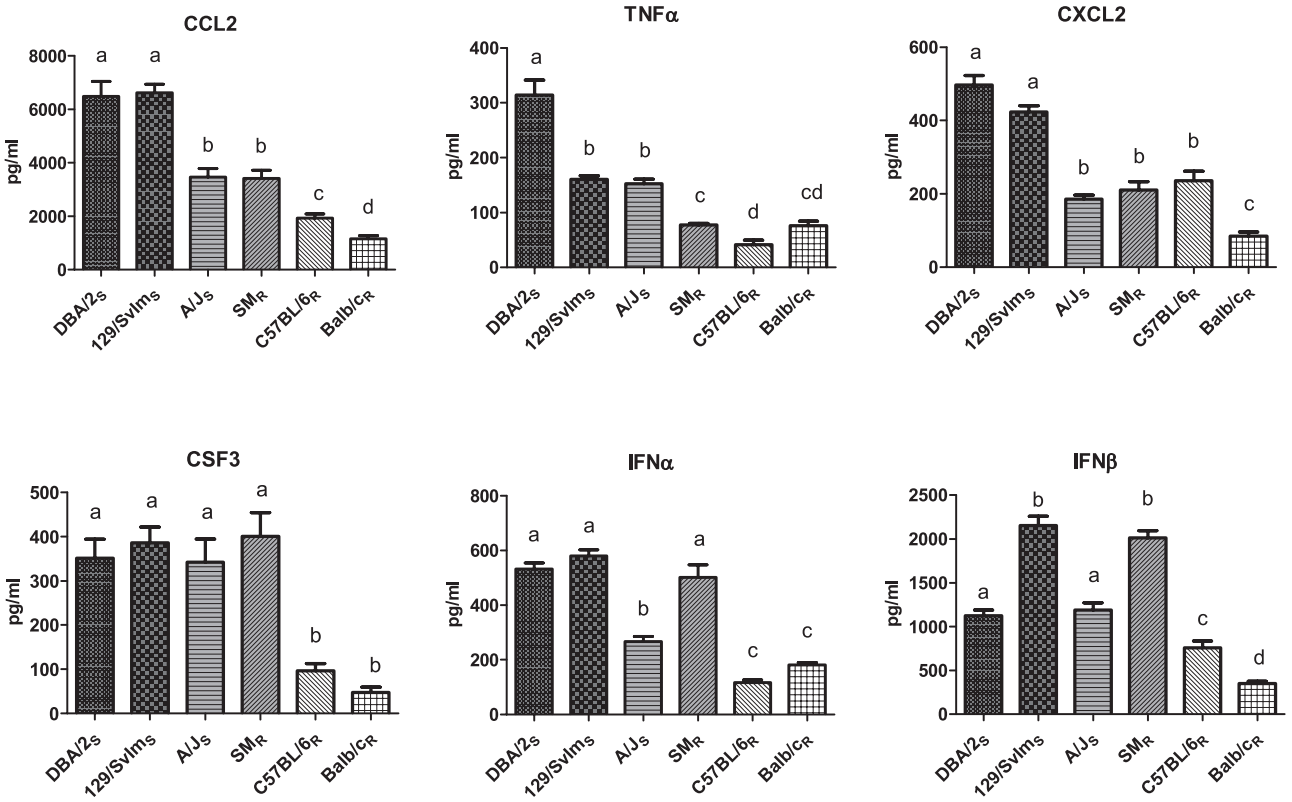

FIG 4 Elevated production of proinflammatory mediators in susceptible mouse strains after inoculation with H5N1 virus. Cytokine concentrations (pg/ml) were measured in homogenized lung tissues of DBA/2_S, 129/SvIm$_S$, A/J_S, SM_R, C57BL/6_R, and BALB/c_R mice 3 days after inoculation with highly pathogenic A/Hong Kong/213/03 H5N1 virus. Bars represent mean cytokine production levels + SEMs. Statistical significance ($P < 0.01$) between the six mouse strains is represented by letters above each column, with different letters signifying distinct statistical groups.

strains used for expression and cytokine analysis. At day 2, the virus titer ranged from $10^{4.9}$ 50% tissue culture infective doses ($TCID_{50}$)/ml in C57BL/6_R and SM_R strains to $10^{6.5}$ $TCID_{50}$/ml in the DBA/2_S strain (Table 1). The virus titer differed significantly between susceptible and resistant strains ($P < 0.05$), and it correlated well with the MLD_{50} ($R^2 = 0.70$, $P < 0.05$). In addition, we found significant associations between virus titer and MLD_{50} on day 4 ($R^2 = 0.82$, $P < 0.05$) and day 7 ($R^2 = 0.81$, $P < 0.05$). To estimate the viral burden over a period of 7 days, we calculated the area under the curve (AUC) for all 6 strains; again, we found a significant correlation with MLD_{50} ($R^2 = 0.87$, $P < 0.01$).

To confirm the association between high viral load and increased susceptibility, we applied computer-assisted immunohistochemical analysis of lung tissue from 3 susceptible strains (DBA/2_S, 129/SvIm$_S$, and A/J_S) and 2 resistant strains (C57BL/6_R and BALB/c_R) to detect the frequency of influenza A virus nucleoprotein-positive (NP^+) nuclei in cross sections of an entire formalin-fixed lung. Despite the small number of mice used in this experiment, it was clear that the susceptible strains had more NP^+ nuclei than did the resistant strains on days 2, 4, and 7 postinfection (see Table S3 in the supplemental material).

TABLE 1 Virus titers in the lungs of genetically diverse mouse strains inoculated with A/Hong Kong/213/03 H5N1 virus

Mouse strain	Virus titer[a] (log_{10} $TCID_{50}$/ml)			Viral burden[b] (AUC)
	Day 2	Day 4	Day 7	
DBA/2_S	6.5	5.7	4.8	34.6
129/SvIm$_S$	5.9	5.1	4.6	31.4
A/J_S	5.8	5.0	4.0	30.0
SM_R	4.9	4.6	3.2	26.1
C57BL/6_R	4.9	5.0	3.6	27.8
BALB/c_R	5.6	4.6	2.2	25.9

[a] Lung virus titers (50% tissue culture infectious doses [$TCID_{50}$s]) at days 2, 4, and 7 after inoculation with 10^4 EID_{50} of A/Hong Kong/213/03 influenza virus are shown.
[b] Area under the curve (AUC) for influenza virus titers between days 0 and 7 after inoculation with 10^4 EID_{50} of A/Hong Kong/213/03 influenza virus are shown.

To demonstrate the effect of increased viral load on proinflammatory cytokine production and survival, we inoculated DBA/2_S and C57BL/6_R mice with a 100-fold-higher dose (10^6 EID_{50}). As predicted, the production of CCL2 and TNF-α 3 dpi was significantly higher ($P < 0.01$) (see Fig. S4 in the supplemental material) in the mice inoculated with 10^6 EID_{50} than in the mice inoculated with 10^4 EID_{50}. More importantly, the amounts of CCL2 and TNF-α produced in the lethally infected C57BL/6_R mice were similar to those found in DBA/2_S mice infected with a much lower, but for this strain similarly lethal, dose of 10^4 EID_{50}.

Elevated production of proinflammatory mediators correlates with increased viral load in susceptible mouse strains. The newfound associations between viral loads, proinflammatory cytokine production, and outcome after infection were confirmed using quantitative real-time PCR on a select set of proinflammatory mediators in conjunction with influenza A virus matrix RNA species. Twenty-four hours postinoculation, the amount of influenza virus RNA was significantly higher (analysis of variance

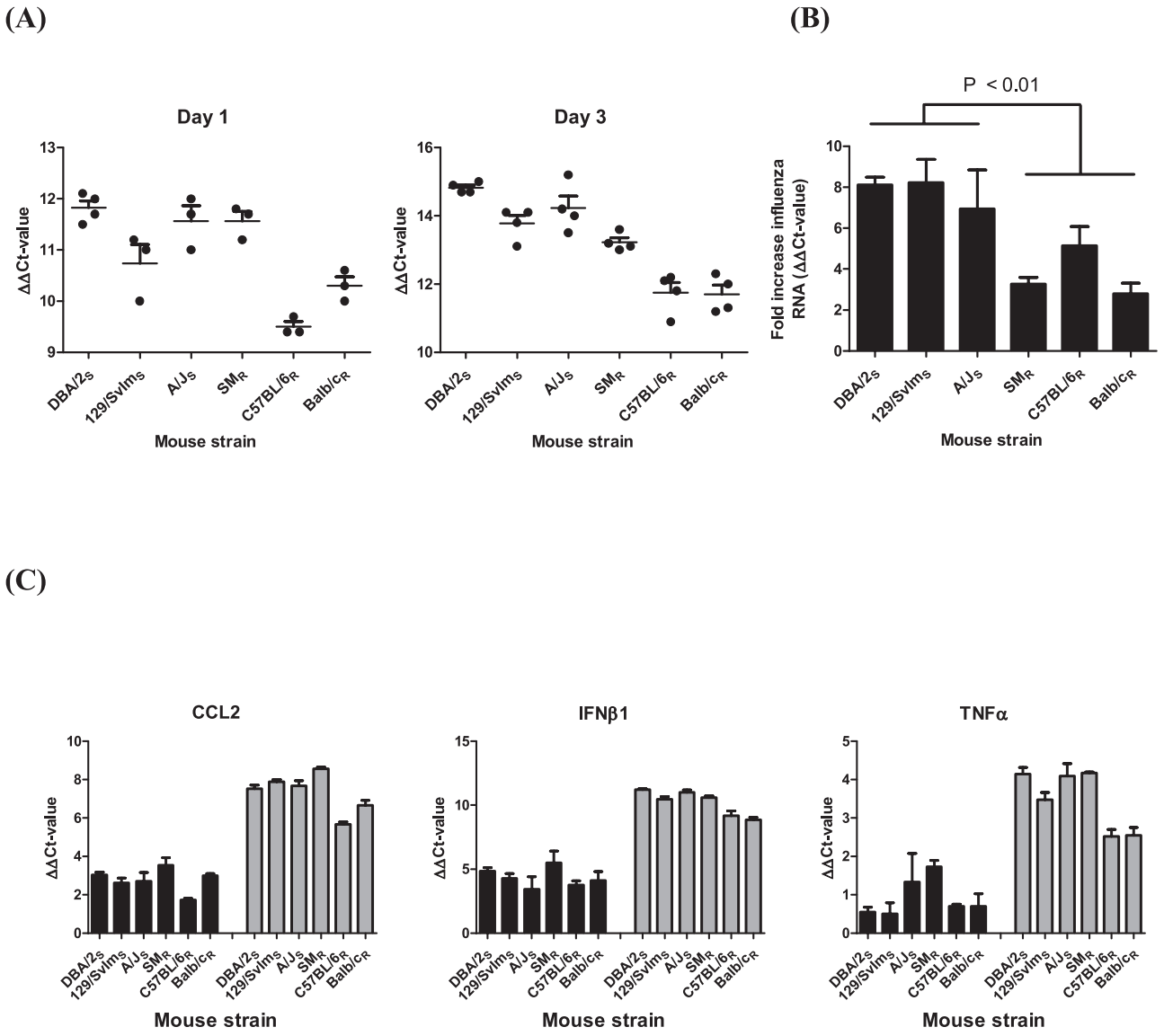

FIG 5 Viral load determines proinflammatory cytokine production in genetically diverse mice. (A) Higher viral load ($\Delta\Delta C_T$ value) in susceptible mouse strains ($DBA/2_S$, $129SvIm_S$, and A/J_S) than in the resistant strains $C57BL/6_R$ and $BALB/c_R$ 1 and 3 days postinoculation (dpi) with 10^4 EID_{50} of H5N1 virus. Dots indicate individual mice, and the average values + SEMs are indicated by the solid bars. (B) Resistant mouse strains (SM_R, $C57BL/6_R$, and $BALB/c_R$) more effectively limit virus replication between 1 and 3 dpi than do susceptible strains. Bars represent average fold increases in viral RNA + SEMs. (C) Higher viral load in susceptible mouse strains plus SM_R triggers an increase in production of proinflammatory mediators CCL2, IFN-β1, and TNF-α at 3 dpi (gray bars; $P < 0.01$) but not at 1 dpi (black bars; $P > 0.05$). Bars represent average $\Delta\Delta C_T$ values + SEMs.

[ANOVA], $P < 0.001$) in the three susceptible strains $DBA/2_S$, $129SvIm_S$, and A/J_S than in the two most resistant strains, $C57BL/6_R$ and $BALB/c_R$ (Fig. 5A). Not surprisingly the reduced viral load in the resistant strains minimized the production of proinflammatory cytokines on day 3 (Fig. 4) and allowed these two mouse strains to cluster at the transcriptional level (Fig. 3), displaying a "normal" inflammatory response to the invading pathogen. The third resistant strain, SM_R, had a high viral RNA load at 1 dpi similar to those of the susceptible strains and therefore clustered with a susceptible (A/J_S) strain at the transcriptional level and also produced more proinflammatory mediators. Three days postinoculation, the resistant $C57BL/6_R$ and $BALB/c_R$ strains continued to have smaller amounts of viral RNA (ANOVA, $P < 0.0001$) than did the susceptible strains. In addition, the viral load in the third resistant strain, SM_R, was lower than those in all three susceptible strains, providing further support for our hypothesis that viral load dictates the pathogenic response to infection in genetically diverse mice. Interestingly, the increase in amount of viral RNA between 1 and 3 dpi is significantly lower ($P < 0.01$) in the resistant strains than in the susceptible strains (Fig. 5B), confirming that lower viral load and early control of viral replication are key to minimizing disease and promoting survival.

To exclude the possibility that excessive production of cytokines promotes virus replication and therefore increases the viral load, we determined the mRNA levels of several proinflammatory

mediators after inoculation with H5N1 influenza A virus. On day 1 postinoculation, the increases in expression of *ccl2*, *ifnb1*, and *tnfa* (threshold cycle [$\Delta\Delta C_T$] value) were similar between all 6 mouse strains (Fig. 5C; see also Fig. S3 in the supplemental material), indicating that the production of proinflammatory cytokines is not responsible for the observed difference in viral RNA at 3 dpi. At 3 dpi, the fold increase in mRNA associated with *ccl2*, *ifnb1*, and *tnfa* was significantly lower ($P < 0.001$) in the resistant strains C57BL/6_R and BALB/c_R than in the three susceptible strains plus SM/J_R, providing further support that early viral load determines the inflammatory response and as such the outcome after infection.

To demonstrate that the genetic differences do not affect the production of proinflammatory cytokines per unit of viral RNA, we computed the ratio between cytokine RNA and viral RNA $\Delta\Delta C_T$ values (see Fig. S3 in the supplemental material). At 1 and 3 dpi, the ratios for IFN-β1 were similar across all strains tested. For the other cytokines, we observed significant differences in the expression ratios among the different mouse strains; however, limited evidence for an association of these differences with disease severity or susceptibility to H5N1 virus infection was found. Combined, these analyses suggest not that the increased susceptibility is caused by an intrinsic difference in the response to infection but rather that it is caused by a higher viral load inducing excessive production of proinflammatory cytokines and hence increased morbidity and mortality in the susceptible mouse strains.

DISCUSSION

Polymorphisms in the genome of the host play an important role in the severity of infection with a highly pathogenic H5N1 influenza A virus. The mechanism dictating the difference in H5N1 pathogenicities among genetically diverse hosts is, however, unknown. Detailed analysis of 6 H5N1 virus-infected inbred mouse strains demonstrated that the viral load is responsible for the heightened inflammation in susceptible hosts. This produces a pathogenic environment as early as 3 days postinoculation, ultimately causing the host to succumb.

Several studies have compared high- and low-pathogenic influenza A viruses in various host species and, without exception, identified a strong association between pathogenicity and excessive production of proinflammatory mediators (16, 18–25). Two possible mechanisms explain this difference: first, increased replication dynamics of the more pathogenic viruses may result in the infection of more epithelial cells and subsequent production of higher levels of cytokines. Second, altered intracellular signaling properties of viral proteins (e.g., PB1-F2, NS1, or hemagglutinin [HA]) of the pathogenic virus may trigger cells to produce more or different cytokines. Although both of these mechanisms are likely involved when comparing subtypes of influenza A viruses in a single homogenous host species, it is not well understood how a single highly pathogenic H5N1 virus produces such varied pathologies in genetically diverse hosts. Does the genetic change in susceptible hosts allow for increased replication dynamics or an altered immune environment, or does it completely change the hosts' response to the pathogen independently of viral burden?

Based on the data presented, we conclude that the susceptible host provides a milieu that allows for increased viral replication, which subsequently induces the production of more proinflammatory cytokines and tissue damage and ultimately results in the death of the animal. Although this study is the first of its kind, detailed analysis of H5N1 virus-infected humans in Vietnam also demonstrated a significant correlation between viral load, cytokine concentration, and severity of disease (12), thereby supporting the conclusion that differences in pathogenesis within a single host species are the result of variable replication dynamics.

The difference in viral load between susceptible and resistant strains was presented very early after inoculation (24 to 48 h), suggesting that the virus replication rate in the susceptible mouse strains is higher than that in the resistant strains. At this point, it is unclear whether this increase in replication rate is due to an inefficient antiviral mechanism or to an increase in cell metabolism and/or the availability of nutrients required for replication. The observation that the viral load increased nearly 8-fold in the susceptible strains between 1 and 3 dpi compared to <4-fold in the resistant strains suggests that the increased replication rate is caused by one or more defective antiviral effector molecules induced by the production of type I and II interferons shortly after infection. Alternatively, there could be a difference in infectious dose (50% infectious dose [ID_{50}]) between the resistant and susceptible mouse strains due to variations such as the sialic acid receptor content of the respiratory tract. Previously, we had shown a 100% infection rate in a resistant strain and a susceptible strain following inoculation with a very low dose of 100 EID_{50} of HK213, suggesting that the ID_{50}s are similar between resistant and susceptible mice and that this is unlikely the reason for the differences observed.

The importance of replication kinetics or polymerase activity in pathogenicity is well established (18, 26–30). The $PB2_{E627K}$ and $PB2_{D701N}$ mutations are associated with increased polymerase activity and faster replication; thus, viruses containing these mutations are often more pathogenic in mice (18, 27, 31). Molecular characterization of a variant PR8 virus adapted to induce severe disease in Mx1-positive mice found several mutations in the polymerase complex that allowed the virus to grow faster and therefore be more pathogenic than its wild-type counterpart (32). A recent comparison of A/Hong Kong/483/97 and A/Hong Kong/486/97 H5N1 viruses also surmised that replication rate regulates disease severity and the magnitude of the virus-specific $CD8^+$ T-cell response (18). After low-dose infection, the HK483 virus harboring a PB2 protein with a lysine residue at position 627 grew to significantly higher titers early during infection than did the variant containing a glutamic acid at this position. This difference in viral loads resulted in quantitative and qualitative differences in the cytotoxic T-cell responses that could be reversed upon administration of oseltamivir, a drug that limits viral replication. Combined, these studies suggest that the replication rate of the virus and hence viral load are responsible for the increase in inflammation and therefore pathogenesis of the virus. Reducing viral load or replication rate will most likely reduce morbidity and mortality upon infection.

As a result of the heightened viral load during the early stages of infection, the immune response in susceptible mice is excessive and can be detected within 3 days of infection. This relatively brief period of time has implications for potential intervention strategies for severe cases of influenza virus infection. It also explains the relatively short time period during which current commercially available antiviral therapy has proven effective. Similar observations have been made with monoclonal antibodies, whose treatment window is 3 to 4 days postinfection (33, 34). The opportunity to treat susceptible mice is much shorter (less than 1 day

postinfection) than that for resistant strains of mice (3 days postinfection [unpublished data]). In our study, one mouse strain that displayed an intermediate pathogenic profile (SM_R) recovered from the infection. This finding indicates that with the right treatment a pathogenic profile can be reversed and the animal can survive.

Clues about what biological trait is important for survival of influenza virus infection may be found in the A/J_S and SM_R strains. Although the strains had similar pathogenic expression profiles, the SM_R mice survived the infection while the A/J_S mice did not. The absence of glutathione metabolism pathway-associated gene expression in the SM_R mice may provide us with a mechanism for the difference in pathogenesis. Glutathione metabolism gene transcription is initiated early after infection to reduce harmful reactive oxygen species (ROS). Mice lacking a functional NADPH oxidase (Cybb-deficient mice) can no longer produce ROS, and intranasal infection with influenza virus was shown to increase the production of proinflammatory cytokines and promote cellular infiltration into the lungs (35, 36). Despite the increase in inflammation, Cybb-deficient mice had lower viral loads and improved resolution of the infection, similar to what we observed in SM_R mice. As such, further studies to determine the production of ROS and proinflammatory cytokines and to measure the induction of the glutathione metabolism response pathway in activated macrophages of SM_R and $C57BL/6_R$ mice would be of interest. A lack of ROS production, minimal expression of glutathione response genes, and reduced proinflammatory cytokine production in the SM mouse macrophages will form the basis for future studies into the role of ROS in influenza virus pathogenesis. An alternative explanation is the presence of one or more genetic changes affecting viral clearance. An example of this is the hemolytic complement (Hc) gene, which affects T-cell responses and therefore viral load at later time points during infection. The SM_R strain expresses a fully functional Hc gene; thus, viral load is reduced, inflammation is limited, and the animals are more likely to survive infection than are A/J_S mice, which do not express a fully functional Hc gene.

Although the susceptible strains and SM_R produced large amounts of proinflammatory cytokines (e.g., IFN-β and CSF3), certain cytokines were predominantly produced in the extremely susceptible strains such as $DBA/2_S$ and $129/SvIm_S$. The excessive production of certain proinflammatory mediators such as CSF3 and type I interferons may cause a mild, controllable form of inflammation, though the addition of a second signal such as CCL2 and/or TNF-α may create an uncontrollable cascade of events resulting in tissue damage and diminished adaptive immune responses in these mice. Results from *in vitro* experiments suggest that IFN-β and TNF-α act synergistically to induce a response quantitatively and qualitatively different from that of either cytokine alone (37, 38). Also, TNF-α affects morbidity after H5N1 virus infection (17, 39).

While the current study focused on identifying the mechanism of severe disease, e.g., virus replication, there is obvious merit in identifying the specific genetic polymorphisms responsible for this phenotype. The MLD_{50} curve for highly pathogenic H5N1 virus (Fig. 1) suggests that several genetic polymorphisms are involved. A similar complexity was previously identified with the recombinant inbred BXD strain family, in which 3 genetic loci contribute to the response to influenza virus infection (40). To identify the responsible polymorphisms, genetic tools like the BXD RI strains, consomic strain sets, or the Collaborative Cross will be extremely useful (41–44). Several of the candidate genes identified in our earlier BXD study were evaluated for their association with disease severity in our larger mouse panel using the available single nucleotide polymorphism (SNP) data. Hemolytic complement, on *Qivr2*, did not differentiate the resistant and susceptible mouse strains. *Qivr7* contains several potential antiviral genes (Trim genes); however, there are not enough public SNP data available to do the analysis. The candidate genes on *Qivr11* (*Grn*, *Ifi35*, and *Dhx58*) all associated significantly ($P < 0.01$) with disease severity and are currently under investigation for their role in influenza virus pathogenesis. Finally, none of the candidate genes on *Qivr17* (*Xdh*, *Eif2ak2*, *Emilin2*, and *Nlrc4*) separated with our phenotype.

In conclusion, gene polymorphisms in the genome of the infected host can have a profound impact on the course of an H5N1 influenza virus infection. Although featured as too much inflammation with excessive production of proinflammatory cytokines, the pathogenicity of influenza virus infection is rooted in increased virus titers in the lungs of the susceptible hosts.

MATERIALS AND METHODS

Inbred mouse strains and influenza A virus. Female mice (6 to 8 weeks old) from the following strains were purchased from Jackson Laboratories (Bar Harbor, ME) and housed in the Animal Resource Center at St. Jude Children's Research Hospital: C57BL/6J (stock no. 664), BALB/cJ (stock no. 651), SM/J (stock no. 687), DBA/2J (stock no. 671), FVB/NJ (stock no. 1800), LP/J (stock no. 676), NZB/BlnJ (stock no. 684), C3H/HeJ (stock no. 659), BALB/cByJ (stock no. 1026), AKR/J (stock no. 648), B10.D2-H2/oSnJ (stock no. 461), A/J (stock no. 646), A/HeJ (stock no. 645), 129/SvImJ (stock no. 2448), MRL/MpJ (stock no. 486), NZW/LacJ (stock no. 1058), BTBR T+ tf/J (stock no. 2282), KK/HlJ (stock no. 2106), 129X1/SvJ (stock no. 691), DBA/1J (stock no. 670), and NOD/ShiLtJ (stock no. 1976). Strain selection was based on representation in large mouse genetic databases like Haplotype Mapping by Roche Pharmaceuticals, Ancestry Mapping by Perlegen, and full-genome sequencing by the Sanger Institute (45–47). The mice received water and food *ad libitum*, and all experimental procedures were approved by the Animal Care and Use Committee of St. Jude Children's Research Hospital.

A reverse genetics variant of A/Hong Kong/213/03, a highly pathogenic H5N1 influenza A virus, was propagated in 10-day-old embryonated chicken eggs. The allantoic fluid containing the infectious virus was harvested, and the infectious virus titer was determined in eggs. The A/Hong Kong/213/03 virus (H5N1) variant contains 7 segments of A/Hong Kong/213/03 and 1 segment of A/Chicken/Hong Kong/52/03 H5N1 virus (40). This virus is referred to as HK213 throughout the paper.

Influenza A virus infection of mice. Experimental inoculation of mice with HK213 virus was done intranasally in 30 μl phosphate-buffered saline (PBS) as described previously (40, 48). MLD_{50} experiments were repeated, and the reported results were calculated from the cumulative results.

Generation of bone marrow chimera DBA/2 mice. $CD4^+$ and $CD8^+$ cells were depleted *in vivo* after intraperitoneal (i.p.) injection of $DBA/2_S$, $C57BL/6_R$, and $BALB/c_R$ donor mice with anti-CD4 and anti-CD8 antibodies. BM was then collected from the femurs of these mice, and approximately 6 million cells were injected intravenously into 9-Gy-irradiated $DBA/2_S$ mice. The mice were treated with Sulfatrim for 3.5 weeks to prevent any opportunistic infection.

At 12 weeks postengraftment, a small volume of peripheral blood was collected and subjected to flow cytometric analysis to test for the expression of cell surface markers of the respective donor mouse strains. In the $C57BL/6_R$ BM-recipient mice, we measured the percentage of $H\text{-}2^{b+}$ (C57BL/6) and $H\text{-}2^{k+}$ (DBA/2) cells within the $CD3^+$ T-cell population. In the $BALB/c_R$ BM-recipient mice, we measured the percentage of

CD22.1$^+$ (DBA/2) and CD22.2$^+$ (BALB/c) cells within the CD19$^+$ T-cell population. Animals in which more than 90% of the T or B cells were donor-derived cells were considered successful BM chimeras.

Lung viral titers and immunohistochemistry. Following intranasal inoculation with 10^4 EID_{50} of HK213 virus, lungs were harvested on days 2, 4, and 7 postinfection, and virus titers were determined on Madin-Darby canine kidney cells (40). At each time point, 4 to 6 animals from each mouse strain were used. The average virus titer was calculated, and the AUC was calculated between days 0 and 7 postinfection.

Immunohistochemical analysis was performed on formalin-fixed lung tissue harvested from HK213 virus-infected or uninfected $DBA/2_S$, $129/SvIm_S$, A/J_S, $C57BL/6_R$, and $BALB/c_R$ mice, as described previously (40). Digital images were obtained with a ScanScope (Aperio, Vista, CA), and the percentage of NP-positive nuclei was determined with ImageScope (Aperio, Vista, CA) using a nucleus-based algorithm.

Cytokine analysis. Lungs from 6 strains of mice inoculated with 10^4 EID_{50} of HK213 virus were harvested on day 3 postinfection and homogenized in 1.0 ml PBS for two 30-s intervals at 30 Hz (TissueLyser II; Qiagen, Valencia, CA). After centrifugation for 30 s at 16,000 × *g*, the supernatant was collected, divided into aliquots, and stored at −80°C. The homogenates were subsequently thawed to quantify the amounts of CCL2, TNF-α, CSF3, and CXCL2 in the lungs of infected animals by using Quantikine enzyme-linked immunosorbent assay (ELISA) kits (R&D Systems, Minneapolis, MN). The amounts of IFN-α and -β in the lung were determined with the respective ELISA kits (PBL Laboratories, Piscataway, NJ). For each cytokine at a given time point, 4 to 6 animals were tested, and the average concentration ± standard error of the mean (SEM) is reported.

RNA isolation and functional genomics. Six mouse strains, $DBA/2_S$, $129SvIm_S$, A/J_S, SM_R, $C57BL/6_R$, and $BALB/c_R$, were selected for an extensive RNA expression analysis before and after inoculation with 10^4 EID_{50} of HK213 virus. Lungs were isolated in 2 batches from uninfected mice and infected mice at days 1, 3, and 7 postinfection. RNA was extracted using TRIzol (Invitrogen, Carlsbad, CA), as previously reported (40) and submitted to a DNA cleanup protocol (Qiagen). Next, microarray analysis was done on RNA obtained from $DBA/2_S$, $129SvIm_S$, A/J_S, SM_R, $C57BL/6_R$, and $BALB/c_R$ mice, using Illumina MouseWG-6 v1.1 Expression BeadChips (Illumina, San Diego, CA). PCA analysis identified a large batch effect; however, both batches included uninfected samples, which allowed us to calculate fold differences in gene expression. Also, batches were done according to the day postinfection, and all 6 strains were assessed simultaneously for each day.

Before analysis, probes without a signal (i.e., detection *P* value of >0.05) in any of the 104 samples were removed from the data set. Signal values were ln-start transformed, ln(signal + 20), to stabilize variance across the range of intensities and approximate normalities in preparation for parametric tests. Using Partek Genomics Suite 6.3, we visualized the structure of the data via PCA. As a result of the complexity of the disease, we compared expression patterns of genes up- or downregulated in most of the susceptible or resistant strains. For a gene to qualify for an individual strain, we required a 2-fold increase or decrease in expression in the majority of the individual samples for that strain on that day. Once a gene qualified for a particular strain, we next assessed whether that gene was shared among the majority of the resistant or susceptible (2/3 or 3/4) mouse strains. Pathway analysis was performed using the online bioinformatics tool DAVID (49).

Quantitative real-time PCR. Samples of cDNA were prepared from lung tissue RNA (200 ng) by using Superscript III (Invitrogen) and random hexamers and used for quantitative real-time PCR. The C_T values for murine interleukin-6 (IL-6) (Mm00446190_m1), CCL2 (Mm00441242_m1), CCL4 (Mm00443111_m1), IFN-β1 (Mm00439552_s1), TNF-α (Mm99999068_m1), CSF3 (Mm00438334_m1), and β-actin were determined using commercially available primer-probe pairs from Applied Biosystems (Foster City, CA). To quantify the amount of virus in each RNA sample, we used the cDNA prepared with random hexamers in combination with a primer probe mix that was specific for the matrix gene (50). Baseline levels of each cytokine (ΔC_T value) were determined after normalization against β-actin, and the increase in expression ($\Delta\Delta C_T$ value) was calculated. No RNA species for IFN-β1, CSF3, or influenza virus matrix RNA were detected prior to infection. To calculate the increase, we used a C_T value of 40 for the uninfected samples. RNA samples ($n = 3$ to 4) were tested for each strain and time point prior to or after infection with HK213 virus.

Statistical analysis. Statistical analysis of differences in lung virus titers was determined by a Student *t* test following ln transformation of the data. Cytokine and chemokine production and quantitative PCR results were analyzed using a Student *t* test or ANOVA when comparing more than two groups. For Fig. 4, statistical significance between the six mouse strains is represented by letters above each column, with different letters signifying distinct statistical groups. Linear regression analyses were done to analyze the viral load ($\log_{10}$ $TCID_{50}$/ml and $\Delta\Delta C_T$ value) with MLD_{50} ($\log_{10}$ EID_{50}). *P* values less than 0.05 were considered significant.

ACKNOWLEDGMENTS

We thank Stacey Schultz-Cherry and Hui-Ling Yen for critically reviewing the manuscript and Paul Thomas for the anti-CD4 and -CD8 antibodies. We thank David Carey and Scott Krauss for their help in the ABSL3$^+$ facility.

This project was funded, in part, by grants from the National Institute of Allergy and Infectious Diseases, National Institutes of Health, Department of Health and Human Services, under contract no. HHSN266200700005C and by the American Lebanese Syrian Associated Charities (ALSAC).

SUPPLEMENTAL MATERIAL

Supplemental material for this article may be found at http://mbio.asm.org/lookup/suppl/doi:10.1128/mBio.00171-11/-/DCSupplemental.

Figure S1, PDF file, 0.1 MB.
Figure S2, PDF file, 0.1 MB.
Figure S3, PDF file, 0.1 MB.
Figure S4, PDF file, 0.1 MB.
Table S1, PDF file, 0.2 MB.
Table S2, PDF file, 0.1 MB.
Table S3, DOC file, 0.1 MB.

REFERENCES

1. **Casrouge A, et al.** 2006. Herpes simplex virus encephalitis in human UNC-93B deficiency. Science **314**:308–312.
2. **Pereyra F, et al.** 2010. The major genetic determinants of HIV-1 control affect HLA class I peptide presentation. Science **330**:1551–1557.
3. **Pérez de Diego R, et al.** 2010. Human TRAF3 adaptor molecule deficiency leads to impaired Toll-like receptor 3 response and susceptibility to herpes simplex encephalitis. Immunity **33**:400–411.
4. **Rauch A, et al.** 2010. Genetic variation in IL28B is associated with chronic hepatitis C and treatment failure: a genome-wide association study. Gastroenterology **138**:1338–1345.
5. **Thomas DL, et al.** 2009. Genetic variation in IL28B and spontaneous clearance of hepatitis C virus. Nature **461**:798–801.
6. **Zhang SY, et al.** 2007. TLR3 deficiency in patients with herpes simplex encephalitis. Science **317**:1522–1527.
7. **Horby P, et al.** 2010. What is the evidence of a role for host genetics in susceptibility to influenza A/H5N1? Epidemiol. Infect. **138**:1550–1558.
8. **Olsen SJ, et al.** 2005. Family clustering of avian influenza A (H5N1). Emerg. Infect. Dis. **11**:1799–1801.
9. **Flint SM, et al.** 2010. Disproportionate impact of pandemic (H1N1) 2009 influenza on indigenous people in the top end of Australia's northern territory. Med. J. Aust. **192**:617–622.
10. **La Ruche G, et al.** 2009. The 2009 pandemic H1N1 influenza and indigenous populations of the Americas and the Pacific. Euro Surveill. **14**: 19366.
11. **Chan RW, et al.** 2010. Influenza H5N1 and H1N1 virus replication and innate immune responses in bronchial epithelial cells are influenced by the state of differentiation. PLoS One **5**:e8713.
12. **de Jong MD, et al.** 2006. Fatal outcome of human influenza A (H5N1) is

associated with high viral load and hypercytokinemia. Nat. Med. **12**: 1203–1207.
13. **Hui KP, et al.** 2009. Induction of proinflammatory cytokines in primary human macrophages by influenza A virus (H5N1) is selectively regulated by IFN regulatory factor 3 and p38 MAPK. J. Immunol. **182**:1088–1098.
14. **Mok KP, et al.** 2009. Viral genetic determinants of H5N1 influenza viruses that contribute to cytokine dysregulation. J. Infect. Dis. **200**: 1104–1112.
15. **Peiris JS, et al.** 2004. Re-emergence of fatal human influenza A subtype H5N1 disease. Lancet **363**:617–619.
16. **Perrone LA, Plowden JK, Garcia-Sastre A, Katz JM, Tumpey TM.** 2008. H5N1 and 1918 pandemic influenza virus infection results in early and excessive infiltration of macrophages and neutrophils in the lungs of mice. PLoS Pathog. **4**:e1000115.
17. **Szretter KJ, et al.** 2007. Role of host cytokine responses in the pathogenesis of avian H5N1 influenza viruses in mice. J. Virol. **81**:2736–2744.
18. **Hatta Y, et al.** 2010. Viral replication rate regulates clinical outcome and CD8 T cell responses during highly pathogenic H5N1 influenza virus infection in mice. PLoS Pathog. **6**:e1001139.
19. **Baskin CR, et al.** 2009. Early and sustained innate immune response defines pathology and death in nonhuman primates infected by highly pathogenic influenza virus. Proc. Natl. Acad. Sci. U. S. A. **106**:3455–3460.
20. **Cilloniz C, et al.** 2010. Lethal dissemination of H5N1 influenza virus is associated with dysregulation of inflammation and lipoxin signaling in a mouse model of infection. J. Virol. **84**:7613–7624.
21. **Cilloniz C, et al.** 2009. Lethal influenza virus infection in macaques is associated with early dysregulation of inflammatory related genes. PLoS Pathog. **5**:e1000604.
22. **Fornek JL, et al.** 2009. A single-amino-acid substitution in a polymerase protein of an H5N1 influenza virus is associated with systemic infection and impaired T-cell activation in mice. J. Virol. **83**:11102–11115.
23. **Kobasa D, et al.** 2007. Aberrant innate immune response in lethal infection of macaques with the 1918 influenza virus. Nature **445**:319–323.
24. **Kobasa D, et al.** 2004. Enhanced virulence of influenza A viruses with the haemagglutinin of the 1918 pandemic virus. Nature **431**:703–707.
25. **Lee SM, et al.** 2008. Hyperinduction of cyclooxygenase-2-mediated proinflammatory cascade: a mechanism for the pathogenesis of avian influenza H5N1 infection. J. Infect. Dis. **198**:525–535.
26. **Chen LM, Davis CT, Zhou H, Cox NJ, Donis RO.** 2008. Genetic compatibility and virulence of reassortants derived from contemporary avian H5N1 and human H3N2 influenza A viruses. PLoS Pathog. **4**:e1000072.
27. **Hatta M, Gao P, Halfmann P, Kawaoka Y.** 2001. Molecular basis for high virulence of Hong Kong H5N1 influenza A viruses. Science **293**: 1840–1842.
28. **Hulse-Post DJ, et al.** 2007. Molecular changes in the polymerase genes (PA and PB1) associated with high pathogenicity of H5N1 influenza virus in mallard ducks. J. Virol. **81**:8515–8524.
29. **Leung BW, Chen H, Brownlee GG.** 2010. Correlation between polymerase activity and pathogenicity in two duck H5N1 influenza viruses suggests that the polymerase contributes to pathogenicity. Virology **401**: 96–106.
30. **Salomon R, et al.** 2006. The polymerase complex genes contribute to the high virulence of the human H5N1 influenza virus isolate A/Vietnam/1203/04. J. Exp. Med. **203**:689–697.
31. **Li Z, et al.** 2005. Molecular basis of replication of duck H5N1 influenza viruses in a mammalian mouse model. J. Virol. **79**:12058–12064.
32. **Grimm D, et al.** 2007. Replication fitness determines high virulence of influenza A virus in mice carrying functional Mx1 resistance gene. Proc. Natl. Acad. Sci. U. S. A. **104**:6806–6811.
33. **Hanson BJ, et al.** 2006. Passive immunoprophylaxis and therapy with humanized monoclonal antibody specific for influenza A H5 hemagglutinin in mice. Respir. Res. **7**:126.
34. **Simmons CP, et al.** 2007. Prophylactic and therapeutic efficacy of human monoclonal antibodies against H5N1 influenza. PLoS Med. **4**:e178.
35. **Snelgrove RJ, Edwards L, Rae AJ, Hussell T.** 2006. An absence of reactive oxygen species improves the resolution of lung influenza infection. Eur. J. Immunol. **36**:1364–1373.
36. **Vlahos R, et al.** 2011. Inhibition of Nox2 oxidase activity ameliorates influenza A virus-induced lung inflammation. PLoS Pathog. **7**:e1001271.
37. **Bartee E, McFadden G.** 2009. Human cancer cells have specifically lost the ability to induce the synergistic state caused by tumor necrosis factor plus interferon-beta. Cytokine **47**:199–205.
38. **Bartee E, Mohamed MR, Lopez MC, Baker HV, McFadden G.** 2009. The addition of tumor necrosis factor plus beta interferon induces a novel synergistic antiviral state against poxviruses in primary human fibroblasts. J. Virol. **83**:498–511.
39. **Belisle SE, et al.** 2010. Genomic profiling of tumor necrosis factor alpha (TNF-alpha) receptor and interleukin-1 receptor knockout mice reveals a link between TNF-alpha signaling and increased severity of 1918 pandemic influenza virus infection. J. Virol. **84**:12576–12588.
40. **Boon AC, et al.** 2009. Host genetic variation affects resistance to infection with a highly pathogenic H5N1 influenza A virus in mice. J. Virol. **83**: 10417–10426.
41. **Aylor DL, et al.** 2011. Genetic analysis of complex traits in the emerging Collaborative Cross. Genome Res. **21**:1213–1222.
42. **Chesler EJ, et al.** 2005. Complex trait analysis of gene expression uncovers polygenic and pleiotropic networks that modulate nervous system function. Nat. Genet. **37**:233–242.
43. **Iraqi FA, Churchill G, Mott R.** 2008. The Collaborative Cross, developing a resource for mammalian systems genetics: a status report of the Wellcome Trust cohort. Mamm. Genome **19**:379–381.
44. **Xiao J, et al.** 2010. A novel strategy for genetic dissection of complex traits: the population of specific chromosome substitution strains from laboratory and wild mice. Mamm. Genome **21**:370–376.
45. **Frazer KA, et al.** 2007. A sequence-based variation map of 8.27 million SNPs in inbred mouse strains. Nature **448**:1050–1053.
46. **Liao G, et al.** 2004. In silico genetics: identification of a functional element regulating H2-Ealpha gene expression. Science **306**:690–695.
47. **Zheng M, Shafer S, Liao G, Liu HH, Peltz G.** 2009. Computational genetic mapping in mice: the ship has sailed. Sci. Transl. Med. **1**:3ps4.
48. **Boon AC, et al.** 2010. Cross-reactive neutralizing antibodies directed against pandemic H1N1 2009 virus are protective in a highly sensitive DBA/2 mouse influenza model. J. Virol. **84**:7662–7667.
49. **Huang DW, Sherman BT, Lempicki RA.** 2009. Systematic and integrative analysis of large gene lists using DAVID bioinformatics resources. Nat. Protoc. **4**:44–57.
50. **Di Trani L, et al.** 2006. A sensitive one-step real-time PCR for detection of avian influenza viruses using a MGB probe and an internal positive control. BMC Infect. Dis. **6**:87.

RESPIRATORY RESEARCH

RESEARCH Open Access

Genome-wide analysis of the mouse lung transcriptome reveals novel molecular gene interaction networks and cell-specific expression signatures

Rudi Alberts[1], Lu Lu[2,3], Robert W Williams[2] and Klaus Schughart[1*]

Abstract

Background: The lung is critical in surveillance and initial defense against pathogens. In humans, as in mice, individual genetic differences strongly modulate pulmonary responses to infectious agents, severity of lung disease, and potential allergic reactions. In a first step towards understanding genetic predisposition and pulmonary molecular networks that underlie individual differences in disease vulnerability, we performed a global analysis of normative lung gene expression levels in inbred mouse strains and a large family of BXD strains that are widely used for systems genetics. Our goal is to provide a key community resource on the genetics of the normative lung transcriptome that can serve as a foundation for experimental analysis and allow predicting genetic predisposition and response to pathogens, allergens, and xenobiotics.

Methods: Steady-state polyA+ mRNA levels were assayed across a diverse and fully genotyped panel of 57 isogenic strains using the Affymetrix M430 2.0 array. Correlations of expression levels between genes were determined. Global expression QTL (eQTL) analysis and network covariance analysis was performed using tools and resources in GeneNetwork http://www.genenetwork.org.

Results: Expression values were highly variable across strains and in many cases exhibited a high heri-tability factor. Several genes which showed a restricted expression to lung tissue were identified. Using correlations between gene expression values across all strains, we defined and extended memberships of several important molecular networks in the lung. Furthermore, we were able to extract signatures of immune cell subpopulations and characterize co-variation and shared genetic modulation. Known QTL regions for respiratory infection susceptibility were investigated and several *cis*-eQTL genes were identified. Numerous *cis*- and *trans*-regulated *trans*cripts and chromosomal intervals with strong regulatory activity were mapped. The *Cyp1a1* P450 *trans*cript had a strong *trans*-acting eQTL (LOD 11.8) on Chr 12 at 36 ± 1 Mb. This interval contains the *trans*cription factor *Ahr* that has a critical mis-sense allele in the *DBA/2J* haplotype and evidently modulates transcriptional activation by AhR.

Conclusions: Large-scale gene expression analyses in genetic reference populations revealed lung-specific and immune-cell gene expression profiles and suggested specific gene regulatory interactions.

* Correspondence: klaus.schughart@helmholtz-hzi.de
[1]Department of Infection Genetics, Helmholtz Centre for Infection Research & University of Veterinary Medicine Hannover, Inhoffenstr. 7, D-38124 Braunschweig, Germany
Full list of author information is available at the end of the article

Background

The lung is the first line of defense against many pathogens and inhaled xenobiotics and is therefore a key part of the immune system. Host defense is strongly influenced by genetic differences and several studies have shown that the genetic background and sequence difference among humans and other host species modulate susceptibility and resistance to infectious diseases, allergens, and xenobiotics. Systems genetics is a modern extension of complex trait analysis that jointly analyzes and integrates large sets of genotypes and phenotypes to explain and predict variation in outcome measures and disease severity (for review see [1,2]). A typical systems genetics study relies on extensive single nucleotide polymorphism (SNP) data sets, matched data on RNA expression in key cells, tissues, or organs and a core set of key dependent measures such as disease susceptibility [3]. These data are collected across a panel or population of genetically diverse individuals or strains. This group of individuals represents a natural genetic perturbation, with well defined genotype and haplotype differences comprising the "treatment." The independent measurements in this case can consist either of the genotype or of crucial intervening variables such as the expression of genes and proteins.

In this study, we exploited a very well characterized panel of inbred strains of mice (a mouse genetic reference panel) that consists of two parts–a small set of standard inbred strains and a larger family of BXD type recombinant inbred strains. The genome of each BXD strain represents a mixture of the C57BL/6J and DBA/2J parental background and is homozygous at almost every genomic location. The genomic make-up of each BXD line has been determined by extensive mapping with molecular markers. After performing microarray expression analysis for each of the BXD mice, the expression level of each gene can be used as a quantitative trait (*e.g.* [4-6]). By comparing these expression values for all BXD mice with their molecular markers data along the genome, genomic expression quantitative trait loci (eQTL) can be identified that are likely to regulate the expression of one or several genes [2,5,7-12]. When an eQTL is located at the same genomic position as the gene itself (within a 10Mb interval of the gene) it is considered as a *cis*-eQTL. In this case, variations in the promoter sequence or in elements that determine the stability of the mRNA of the gene are the most likely causes for the observed differences in expression levels. If the eQTL is at a distant location from the regulated gene, the eQTL is referred to as a *trans*-eQTL.

Here, we performed a global gene expression analysis from the lungs of 47 BXD and eight widely used inbred strains. The aim of our study was to reveal genes and gene networks in mouse lung in steady state condition. We found that many genes had high variation in expression and that often this variation was highly heritable. This allowed us to identify many *cis*- and *trans*-eQTLs. In addition, we used the correlation structure in the data to obtain expression signatures for specific cell types within the lung.

Methods

Mouse strains and sample preparation

C57BL/6J, BALB/cByJ, FVB/NJ, and WSB/EiJ, as well as B6D2F1 and D2B6F1 lines were obtained from the University of Tennessee Health Science Center (UTHSC). DBA/2J, 129X1/SvJ, LP/J and SJL/J were obtained from The Jackson Laboratory. Mice from 38 BXD recombinant inbred strains were obtained from UTHSC and mice from nine BXD strains were obtained from The Jackson Laboratory. All animals were housed at UTHSC before sacrifice. Mice were killed by cervical dislocation and whole lungs including blood were removed and placed in RNAlater. Total RNA was extracted from the lungs using RNA STAT-60 (Tel-Test Inc.). RNA from two to five animals per strain were pooled and used for gene expression analysis. Animals used in this study were between 49 and 93 days of age. All inbred strains were profiled for both sexes, and for a given BXD strain either males or females were used. Mice were maintained under specific pathogen free conditions. All protocols involving mice were approved by the UTHSC Animal Care and Use Committee.

Microarray analysis

Gene expression profiling was performed using Affymetrix GeneChip Mouse Genome 430 2.0 Arrays at UTHSC. Samples were amplified according to the recommended protocols by the manufacturer (Affymetrix, Santa Clara, CA, USA). In all cases, 4-5 μg of each biotinylated cRNA preparation was fragmented and included in a hybridization cocktail containing four biotinylated hybridization controls (BioB, BioC, BioD, and Cre), as recommended by the manufacturer. Samples were hybridized for 16 hours. After hybridization, GeneChips were washed, stained with SAPE, and read using an Affymetrix GeneChip fluidic station and scanner.

Data preprocessing and analysis

Data analysis was performed using the GeneNetwork web service [13], a large resource with phenotypes and mRNA expression data for several genetic reference populations and multiple organisms. The expression data were preprocessed like all other datasets in GeneNetwork: adding an offset of 1 unit to each signal intensity value to ensure that the logarithm of all values were positive, computing the $\log_2$ value, performing a quantile normalization of the $\log_2$ values for the total set of

arrays using the same initial steps used by the RMA transform [14], computing the Z scores for each cell value, multiplying all Z scores by 2 and adding 8 to the value of all Z scores. The advantage of this variant of a Z transformation is that all values are positive and that 1 unit represents approximately a 2-fold difference in expression as determined using the spike-in control probe sets (see [8] for details). For correlation analyses we used Pearson's correlation unless otherwise stated. Heritability was determined using ANOVA with one factor mouse strain, and by dividing the mean between-mouse-strain variance by the sum of the mean between-mouse strain variance plus the mean within-strain variance.

QTL Mapping and expression analyses

All probe sets were mapped using standard interval mapping methods at 1 cM intervals (~2 Mb) along all autosomes and the X chromosome. This procedure generates estimates of linkage between variation in transcript expression levels and chromosomal location. The entire set of values can be used to construct a set of QTL maps for all chromosomes (except Chr Y and the mitochondrial genome) in which position is plotted on the x-axis and the strength of linkage–the likelihood ratio statistic (LRS) or log of the odds ratio (LOD)-is plotted on the y-axis. An LRS of 18 or higher is significant at a genome-wide p value of < 0.5. To compute LRS values we exploited the computationally efficient Haley-Knott regression equations [15] and a set of 3796 SNPs and microsatellite markers that we and others have genotyped over the past decade [16,17]. In order to rapidly map all 45,101 probe sets we used our customized QTL Reaper code http://qtlreaper.sourceforge.net/. QTL Reaper performs up to a million permutations of an expression trait to calculate the genome-wide empirical *p* value and the LRS scores associated with each interval or marker. The peak linkage value and position was databased in GeneNetwork and users can rapidly retrieve and view these mapping results for any probe set. Any of the QTL maps can also be rapidly regenerated using the same Haley-Knott methods, again using functions imbedded in GeneNetwork. GeneNetwork also enable a search for epistatic interactions (pair scanning function) and composite interval mapping with control for a single marker.

Data quality control

We used two simple but effective methods to confirm correct sample identification of all data entered into GeneNetwork. Expression of the *Xist* transcript (probe set 1427262_at) was used to validate the sex of the sample. *Xist* is involved in the inactivation of one X chromosome in females [18] and is only expressed at high levels in females. Other genes that show strong sex-specific expression are *Eif2s3y*, *Jarid1d* and *Ddx3y*. In addition, we investigated several genes that exhibit a strongly bimodal Mendelian expression pattern, meaning that one parental allele exhibits a high expression level whereas the other allele exhibits a low expression and only the F1 hybrids are intermediate. The expression level of such transcripts is directly correlated with the genotype at this locus and they can collectively be used to confirm sample genotype and hence strain. For example, expression of the *Rpgrip1* transcript (probe set 1421144_at) has a distinctly bimodal distribution, intermediate values for F1 animals, and is associated with a LOD score peak of 50 that corresponds precisely to the location of the cognate gene on Chr 14 at 52.5 Mb.

Results

Variation in gene expression

The Affymetrix M430 2.0 array that we used includes 45,101 probe sets and provides consensus estimates of expression for the vast majority of all protein coding genes. Table 1 gives an overview of the range of variation across strains in each of the probe sets used. Strikingly, more than 2,000 genes showed a range of expression that was larger than four-fold different between the strain with the lowest and the highest expression. Among the genes with the most extreme range in expression levels were *Krt4* (keratin 4), *Krt13* (keratin 13) and *Krtdap* (keratinocyte differentiation associated protein). Another gene with highly variable expression was *Cftr* (cystic fibrosis transmembrane conductance regulator homolog). This important lung disease-causing gene showed a four-fold variation in expression levels between strains. Several other genes with high variation were sex-specifically expressed genes, like *Xist* (inactive X specific transcripts), *Ddx3y* (DEAD (Asp-Glu-Ala-Asp) box polypeptide 3, Y-linked) and *Serpina1b* (serine (or cysteine) preptidase inhibitor, clade A, member 1B).

Table 1 Variation in gene expression for 45,101 probe sets.

Fold change range	Log_2 range	No. of genes
1-2	0-1	30,392
2-4	1-2	11,965
4-8	2-3	1,980
8-16	3-4	498
16-32	4-5	132
32-64	5-6	60
64-inf	6-inf	42

Fold changes between the lowest and highest expressed mouse stains per probe sets were cal-culated and divided in seven bins. The corresponding range on log_2 scale and the amount of genes in each range are given.

Heritability of variation in gene expression

To investigate to which extent the variation in expression was due to genetic effects, we calculated the heritability for each of the genes, which is the fraction of variation in expression caused by genetics. The heritability values ranged from as high as 0.96 (most of the variance was associated with between-strain differences) until as low as 0.01. Genes with the largest heritability were *Cdk17/Pctk2* (cyclin-dependent kinase 17, probe set 1446130_at), *Gm1337* (predicted gene 1337, 1443287_at) and *Pdxdc1/KIAA0251* (pyridoxal-dependent decarboxylase domain containing 1, 1452705_at), all having a value above 0.99. High heritability values indicate that it is likely to successfully map QTLs that influence gene expression values.

Lung-specific genes

The large dataset in GeneNetwork and its built-in features allowed us to compare the gene ex-pression patterns in the lung with data from 25 other tissues. First, we identified the most highly expressed genes in lung (Table 2 lists the 15 highest expression signals). Two of these genes were highly restricted to the lung and trachea: *Sftpc* (surfactant associated protein C) and *Ager* (advanced glycosylation end product-specific receptor) (Figure 1A, B) whereas *Scgb1a1* (secretoglobin, family 1A, member 1 (uteroglobin)) was highly expressed in lung but also showed expression in some other tissues (Figure 1C). On the other hand, *Hba-a1* (hemoglobin alpha, adult chain 1) was expressed at high levels in most tissues (Figure 1D). We then used *Stfpc* in a tissue

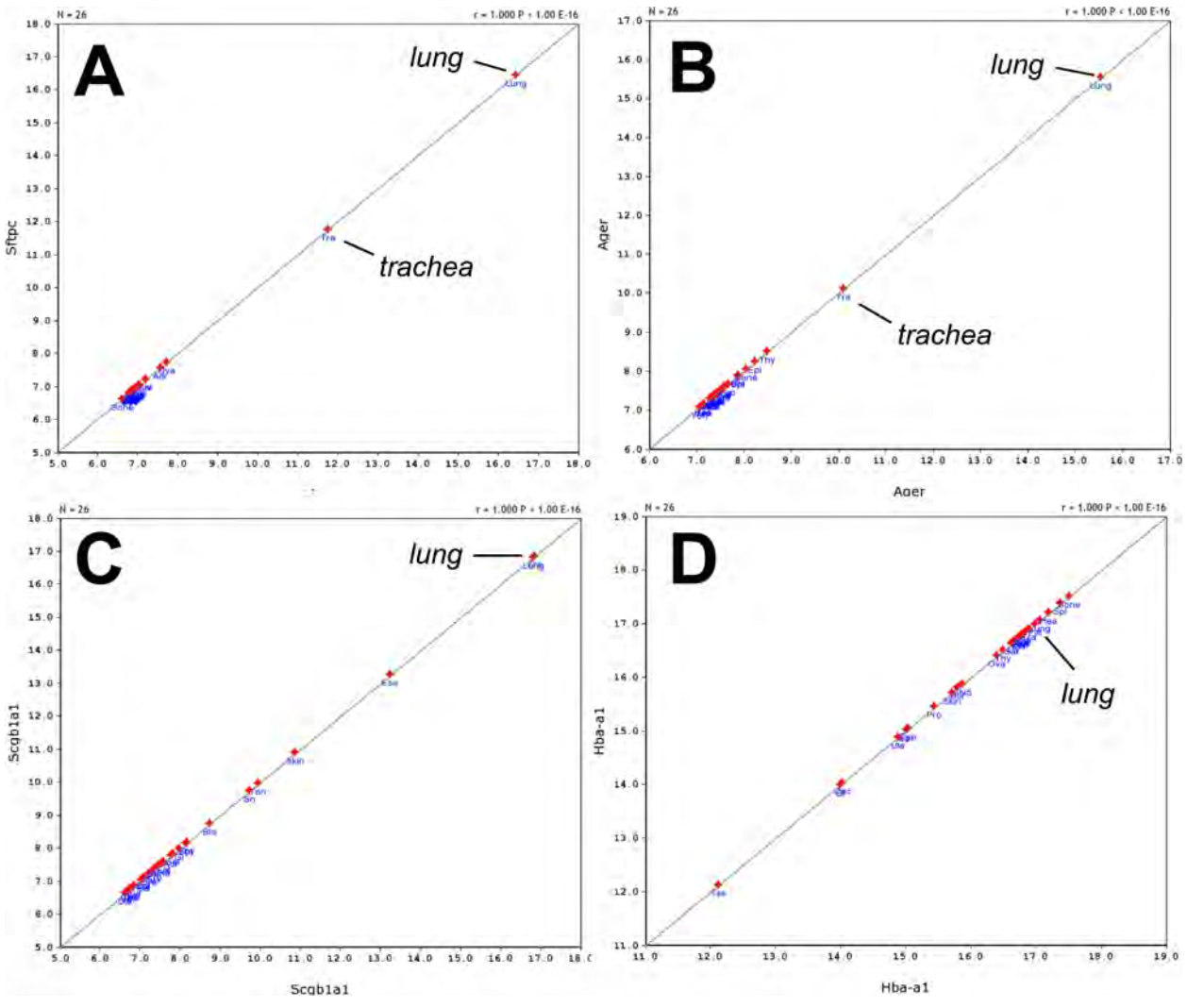

Figure 1 Tissue distribution in 25 other tissues of some of the most highly expressed genes in the lung. The expression levels for (A) *Stpc*, (B) *Ager*, (C) *Scgb1a1* and (D) *Hba-a1* in different tissues are shown. Please note that in this representation the gene is correlated with itself to illustrate only its issue distribution.

Table 2 List of 15 probe sets with highest expression signals in the lung

Probe set	Symbol	Description	Location (Chr, Mb)	Mean Expr	Tissue-specific expression
1428361_x_at	*Hba-a1*	hemoglobin alpha, adult chain 1	Chr11: 32.184441	15,10	MT
1418639_at	*Sftpc*	surfactant associated protein C	Chr14: 70.920826	14,92	LS
1452543_a_at	*Scgb1a1*	secretoglobin, family 1A, member 1 (uteroglobin)	Chr19: 9.158206	14,78	LHOT
1417184_s_at	*Hbb-b2*	hemoglobin, beta adult minor chain	Chr7: 110.976103	14,74	MT
1441958_s_at	*Ager*	advanced glycosylation end product-specific receptor	Chr17: 34.737745	14,69	LS
AFFX-b-ActinMur/M12481_3_at	*Actb*	actin beta, cytoplasmic	Chr5: 143.665528	14,67	MT
1452757_s_at	*Hba-a1*	hemoglobin alpha, adult chain 1	Chr11: 32.196742	14,66	MT
1416642_a_at	*Tpt1*	tumor protein, translationally-controlled 1	Chr14: 76.246098	14,62	MT
1418509_at	*Cbr2*	carbonyl reductase 2	Chr11: 120.628111	14,62	LHOT
1436996_x_at	*Lzp-s*	P lysozyme structural and lysozyme	Chr10: 116.724902	14,62	ND
1416624_a_at	*Uba52*	ubiquitin A-52 residue ribosomal protein fusion product 1	Chr8: 73.032191	14,58	MT
1427021_s_at	*Fth1*	ferritin heavy chain 1	Chr19: 10.057382	14,57	ND
AFFX-MURINE_B2_at	*B2*	AFFX-MURINE_B2_at short interspersed nuclear element (SINE) class of repeat (probes target Chr 1 and Chr 2 most heavily)	N/A	14,52	ND
1415906_at	*Tmsb4x*	thymosin, beta 4, X chromosome	ChrX: 163.645132	14,51	MT
1449436_s_at	*Ubb*	ubiquitin B	Chr11: 62.366564	14,50	MT

Mean Expr: mean expression in lung for BXD strains. LS: lung specific expression, LHOT: highly expressed in lung but also in other tissues, MT: expressed in many tissues or mainly in non-lung tissues, ND: no data for other tissues than lung available.

correlation analysis to identify other genes that may not be as highly expressed but still be restricted to lung tissue. The first 70 probe sets found were then analyzed as above for lung-specific expression, and 15 genes were identified (Table 3). A comparison to the expression patterns described in the BioGPS database [19] confirmed that the majority was only expressed in lung, most of them at high level. Two genes were not restricted to the lung according to BioGPS, and five genes were also found at lower levels in one other tissue (Table 3).

Identification of gene networks using correlations

The large data set for expression values for ~39,000 transcripts in 57 mouse strains allowed us to calculate correlations between any pair of genes. A Spearman rank correlation analysis identified 12,985 pairs of genes with a correlation value above 0.8, and 604 pairs showed a correlation value of 0.9 or higher. For example, the expression of *Klra3* (killer cell lectin-like receptor subfamilily A, member 3) was strongly correlated with the expression of *Gzma* (granzyme A) (Figure 2A). *Klra3* also appeared to be strongly correlated with *Il18rap* (interleukin 18 receptor accessory protein, Figure 2B). We then calculated the first principal component of the *Klra3*, *Gzma*, *Il18rap* and *Klrg1* (killer cell lectin-like receptor subfamily G, member 1) genes and used it to determine the correlations with all other genes in the lung data set. In this way, we could identify a network of nine genes exhibiting a correlation of >= 0.8 with this principal component (Figure 2C). One of the newly identified genes was *Prf1* (perforin 1) which was correlated with a p-value of $< 10^{-16}$ with the principal component (Figure 2D). If genes exhibit a strong correlation of their expression values, one may hypothesize that they are involved in the same biological process or pathway, or they may be expressed in the same cell type.

In a similar way, we identified another gene network of 20 genes that exhibited very high correlations of their

Table 3 List of genes with lung-restricted expression found by tissue correlation analysis with *Sftpc*

Probe set	Symbol	Description	Location (Chr, Mb)	Mean Expr	BioGPS expression
1418639_at	*Sftpc*	surfactant associated protein C	Chr14: 70.920826	14,92	high in lung, low in nucleus accumbens
1437028_at	*Sftpb*	surfactant associated protein B (nonciliated bronchiolar and alveolar type 2 cell signature)	Chr6: 72.260763	13,68	high in lung only
1422334_a_at	*Sftpa1*	surfactant associated protein A1	Chr14: 41.946994	14,24	high in lung only
1422346_at	*Nkx2-1 (Titf1)*	thyroid *trans*cription factor 1	Chr12: 57.634187	8,07	lung only
1417057_a_at	*Lamp3*	lysosomal-associated membrane protein 3	Chr16: 19.653875	12,09	high in lung, low in ES cells and some cell lines
1421404_at	*Cxcl15*	chemokine (C-X-C motif) ligand 15	Chr5: 91.230349	13,87	high in lung only
1441958_s_at	*Ager*	advanced glycosylation end product-specific receptor	Chr17: 34.737745	14,69	high in lung only
1436787_x_at	*Sec14l3*	SEC14-like protein 3	Chr11: 3.978573	13,21	only data for human available - not lung specific
1425218_a_at	*Scgb3a2*	secretoglobin, family 3A, member 2	Chr18: 43.924081	14,17	high in lung only
1449428_at	*Cldn18*	claudin 18	Chr9: 99.591247	12,70	highest in lung, lower in stomach
1449525_at	*Fmo3*	flavin containing monooxygenase 3	Chr1: 164.884088	10,90	high in lung, maybe weak in some other tissues
1425814_a_at	*Calcrl*	calcitonin receptor-like	Chr2: 84.170818	12,91	high in lung, weak in macrophages
1421373_at	*Cox4i2*	cytochrome c oxidase subunit IV isoform 2	Chr2: 152.582819	9,24	not specific for lung
1419699_at	*Scgb3a1*	secretoglobin, family 3A, member 1	Chr11: 49.477871	13,68	high in lung only
1451604_a_at	*Acvrl1*	activin A receptor, type II-like 1	Chr15: 100.968668	11,86	high in lung only
1420347_at	*Plunc*	palate, lung, and nasal epithelium carcinoma associated	Chr2: 153.973359	13,42	high in lung, low in heart

Mean Expr: mean expression in lung for BXD strains. BioGPS: evaluation of expression pattern as described in BioGPS.

expression levels across all mouse strains. All possible pairs of genes in this network showed a correlation above 0.95 (Figure 3). The network contained two keratin genes, *Krt4* (keratin 4) and *Krt13* (keratin 13) and genes involved in cytoskeleton functions, again pointing to a possible interaction of these genes in the same pathway or biological process. Further gene networks found by correlation studies were related to B and T cells (see below).

Correlation analysis identified gene expression signatures for T and B cells

The hemoglobin genes *Hba-a1* (hemoglobin alpha, adult chain 1) and *Hbb-b2* (hemoglobin beta, adult minor chain) were among the top 10 genes with highest expression values in our lung data set. The high levels of hemoglobin transcripts suggested that circulating blood cells, including immune cells, may also be analyzed in our data set. Therefore, we investigated the gene expression networks of known immune cell markers, *e.g. Cd3* genes as specific markers for T cells. We calculated the correlations of *Cd3d* (Cd3 antigen, delta polypeptide) expression levels over all BXD lines with all other genes. This analysis revealed 20 genes with a very highly correlated expression value (p-value below 10^{-14}, Figure 4). Most of these genes were known T cell markers or involved in T cell regulation. Eight out of the 12 genes with the strongest correlations were also exclusively expressed in T cells according to the BioGPS database (Wu et al., 2009): *Cd3d, Itk, Tcrb-13V Cd3e, Cd3g, Scap1, Cd6 and Cd5* (see Figure 4 for full gene names). Similarly, we searched for B cell-specific signatures starting with the B cell marker gene *Cd19* (CD19 antigen). The probe set "1450570_a_at" detected *Cd19* mRNA levels and showed a mean expression level of 9.3. We found 14 probe sets with a correlation above 0.80 (p-value < 10^{-14}, Figure 5). A comparison with the BioGPS database revealed that eight of them, *Cd19, Cd79b, Faim3, Cd79a, Blk, B3gnt5, Cd22 and Blr1 (*see Figure 5 for full gene names) were also exclusively

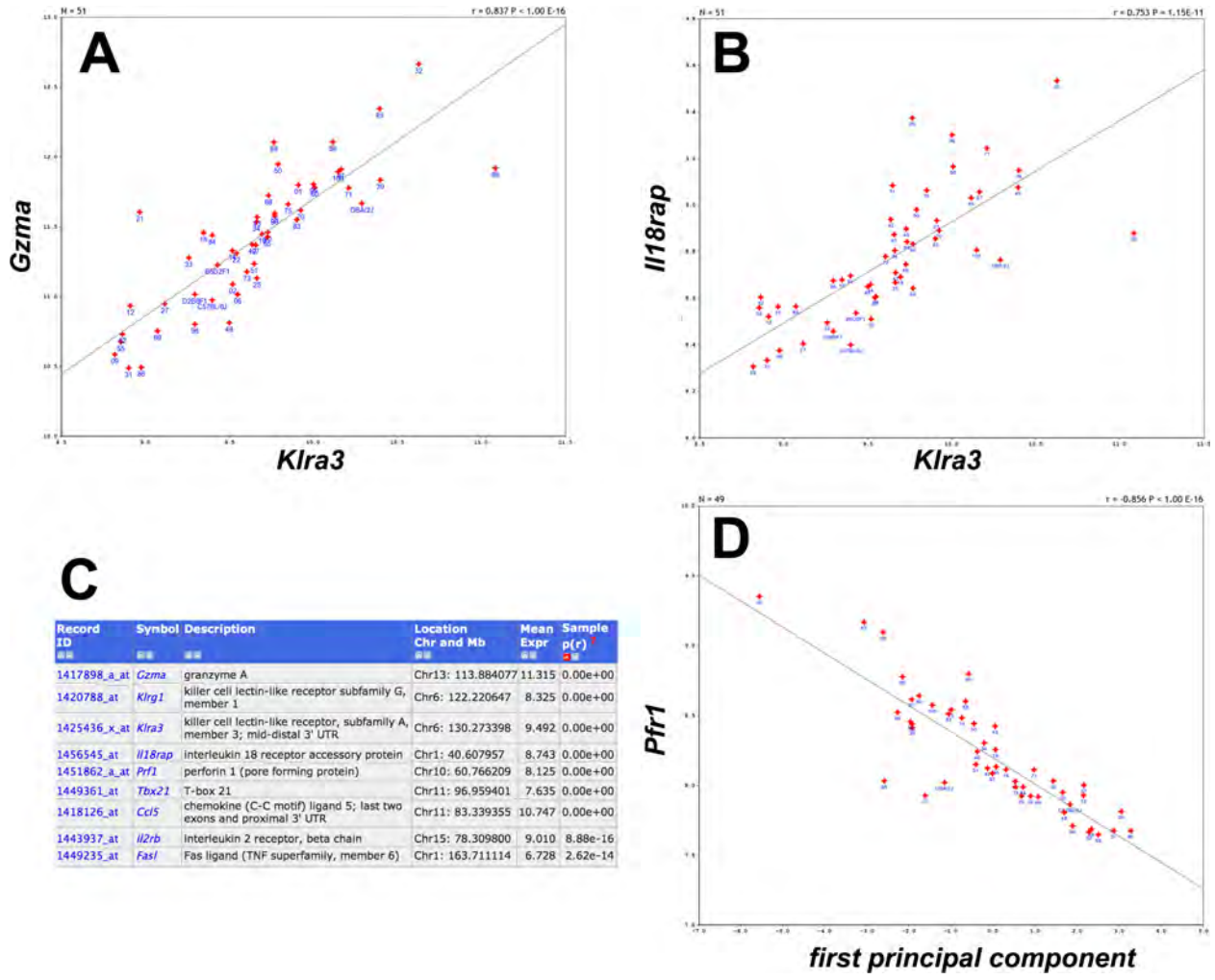

Record ID	Symbol	Description	Location Chr and Mb	Mean Expr	Sample p(r)
1417898_a_at	*Gzma*	granzyme A	Chr13: 113.884077	11.315	0.00e+00
1420788_at	*Klrg1*	killer cell lectin-like receptor subfamily G, member 1	Chr6: 122.220647	8.325	0.00e+00
1425436_x_at	*Klra3*	killer cell lectin-like receptor, subfamily A, member 3; mid-distal 3' UTR	Chr6: 130.273398	9.492	0.00e+00
1456545_at	*Il18rap*	interleukin 18 receptor accessory protein	Chr1: 40.607957	8.743	0.00e+00
1451862_a_at	*Prf1*	perforin 1 (pore forming protein)	Chr10: 60.766209	8.125	0.00e+00
1449361_at	*Tbx21*	T-box 21	Chr11: 96.959401	7.635	0.00e+00
1418126_at	*Ccl5*	chemokine (C-C motif) ligand 5; last two exons and proximal 3' UTR	Chr11: 83.339355	10.747	0.00e+00
1443937_at	*Il2rb*	interleukin 2 receptor, beta chain	Chr15: 78.309800	9.010	8.88e-16
1449235_at	*Fasl*	Fas ligand (TNF superfamily, member 6)	Chr1: 163.711114	6.728	2.62e-14

Figure 2 Expression signals for strongly correlated genes in the lung. Numbers indicate BXD strains, and the parental C57BL/6J and DBA/2J strains as well as F1 individuals are presented. Expression signals of (A) *Klra3* and *Gzma* ($p < 10^{-16}$) and (B) *Klra3* versus *Il18rap* ($p < 10^{-11}$) were strongly correlated. (C) List of nine genes highly correlated with the first principal component of the expression of *Gzma*, *Klrg1*, *Klra3* and *Il18rap*. (D) Strong correlation between the first principal component and *Prf1* ($p < 10^{-16}$). X- and Y-axis of the plots show the names of genes used for the analysis.

expressed in B cells. Therefore, these genes can be considered as T and B cell signature genes which may be used to follow the presence and infiltration of T and B cells in the lung under normal and pathological conditions.

Identification of candidate genes regulating phenotypic traits in the lung

Once a QTL for a phenotypic trait has been found, it will be important to identify the underlying quantitative gene (QTG) which is causing the variation. Searching *cis*-eQTLs in the QTL interval represents one suitable approach [8]. As a prototype for this approach in our lung data set, we examined two traits for which lung phenotypes were studied in the BXD population and which were available in GeneNetwork. Boon et al. [20] described several QTLs for the susceptibility of BXD mice to influenza A infections. We analyzed one significant QTL peak on chromosome 2 and two suggestive peaks on chromosomes 7 and 17. Seven *cis*-eQTL regulated genes were found in the chromosome 2 QTL interval (Table 4), including the *Hc* (hemolytic complement) gene which was shown to contribute to influenza susceptibility [20]. The analysis of the QTL region on chromosome 7 revealed 12 *cis*-regulated genes in the lung, including *Trim12* (tripartite motif protein 12) and *Trim34* (tripartite motif protein 34) which were also described as potential candidate QTGs by [20]. In the chromosome 17 QTL region, we found 17 *cis*-eQTL genes, of which *Prkcn* (protein kinase C, nu), *Qpct*

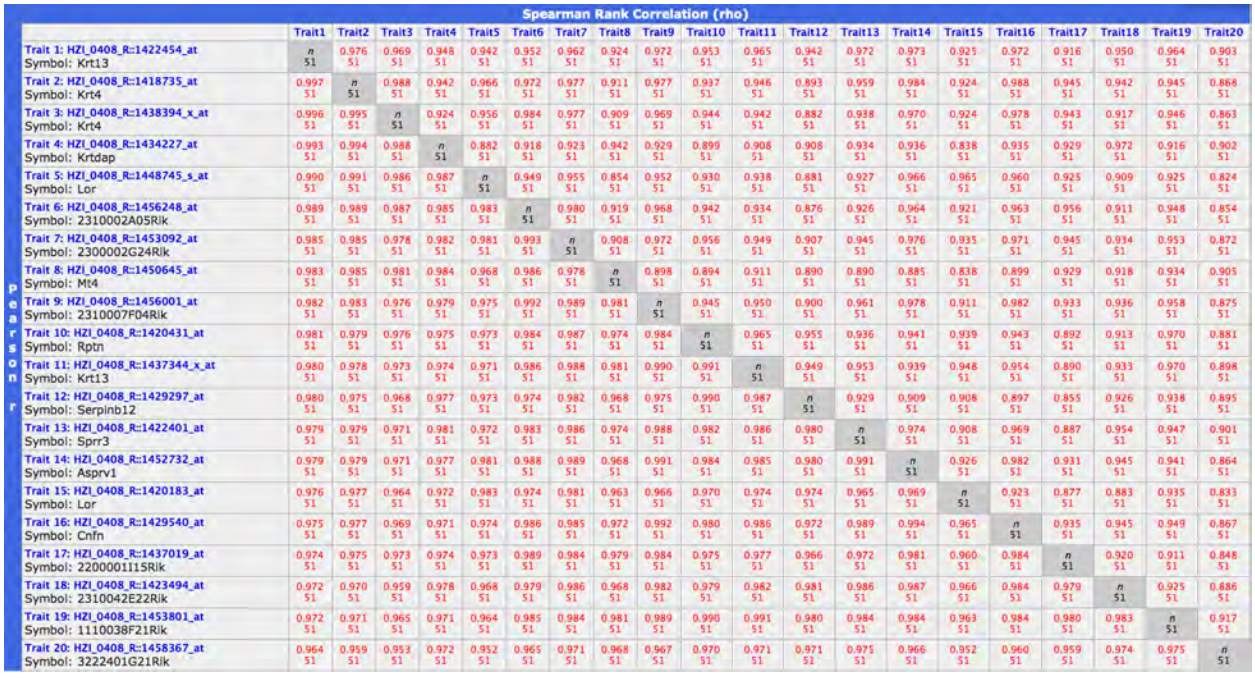

Spearman Rank Correlation (rho)

Pearson	Trait1	Trait2	Trait3	Trait4	Trait5	Trait6	Trait7	Trait8	Trait9	Trait10	Trait11	Trait12	Trait13	Trait14	Trait15	Trait16	Trait17	Trait18	Trait19	Trait20
Trait 1: HZI_0408_R::1422454_at Symbol: Krt13	n 51	0.976 51	0.969 51	0.948 51	0.942 51	0.952 51	0.962 51	0.924 51	0.972 51	0.953 51	0.965 51	0.942 51	0.972 51	0.973 51	0.925 51	0.972 51	0.918 51	0.950 51	0.964 51	0.903 51
Trait 2: HZI_0408_R::1418735_at Symbol: Krt4	0.997 51	n 51	0.988 51	0.942 51	0.966 51	0.972 51	0.977 51	0.911 51	0.977 51	0.937 51	0.946 51	0.893 51	0.959 51	0.984 51	0.924 51	0.988 51	0.945 51	0.942 51	0.945 51	0.868 51
Trait 3: HZI_0408_R::1438394_x_at Symbol: Krt4	0.996 51	0.995 51	n 51	0.924 51	0.956 51	0.984 51	0.977 51	0.909 51	0.969 51	0.944 51	0.942 51	0.882 51	0.938 51	0.970 51	0.924 51	0.978 51	0.943 51	0.917 51	0.946 51	0.863 51
Trait 4: HZI_0408_R::1434227_at Symbol: Krtdap	0.993 51	0.994 51	0.988 51	n 51	0.882 51	0.918 51	0.923 51	0.942 51	0.929 51	0.899 51	0.908 51	0.908 51	0.934 51	0.936 51	0.838 51	0.935 51	0.929 51	0.972 51	0.916 51	0.902 51
Trait 5: HZI_0408_R::1448745_s_at Symbol: Lor	0.990 51	0.991 51	0.986 51	0.987 51	n 51	0.949 51	0.955 51	0.854 51	0.952 51	0.930 51	0.938 51	0.881 51	0.927 51	0.966 51	0.965 51	0.960 51	0.925 51	0.909 51	0.925 51	0.824 51
Trait 6: HZI_0408_R::1456248_at Symbol: 2310002A05Rik	0.989 51	0.989 51	0.987 51	0.985 51	0.983 51	n 51	0.980 51	0.919 51	0.968 51	0.942 51	0.934 51	0.876 51	0.926 51	0.964 51	0.921 51	0.963 51	0.956 51	0.911 51	0.948 51	0.854 51
Trait 7: HZI_0408_R::1453092_at Symbol: 2300002G24Rik	0.985 51	0.985 51	0.978 51	0.982 51	0.981 51	0.993 51	n 51	0.908 51	0.972 51	0.956 51	0.949 51	0.907 51	0.945 51	0.976 51	0.935 51	0.971 51	0.945 51	0.934 51	0.953 51	0.872 51
Trait 8: HZI_0408_R::1450645_at Symbol: Mt4	0.983 51	0.985 51	0.981 51	0.984 51	0.968 51	0.986 51	0.978 51	n 51	0.898 51	0.894 51	0.911 51	0.890 51	0.890 51	0.885 51	0.838 51	0.899 51	0.929 51	0.918 51	0.934 51	0.905 51
Trait 9: HZI_0408_R::1456001_at Symbol: 2310007F04Rik	0.982 51	0.983 51	0.976 51	0.979 51	0.975 51	0.992 51	0.989 51	0.981 51	n 51	0.945 51	0.950 51	0.900 51	0.961 51	0.978 51	0.911 51	0.982 51	0.933 51	0.936 51	0.958 51	0.875 51
Trait 10: HZI_0408_R::1420431_at Symbol: Rptn	0.981 51	0.979 51	0.976 51	0.975 51	0.973 51	0.984 51	0.987 51	0.974 51	0.984 51	n 51	0.965 51	0.955 51	0.936 51	0.941 51	0.939 51	0.943 51	0.892 51	0.913 51	0.970 51	0.881 51
Trait 11: HZI_0408_R::1437344_x_at Symbol: Krt13	0.980 51	0.978 51	0.973 51	0.974 51	0.971 51	0.986 51	0.988 51	0.981 51	0.990 51	0.991 51	n 51	0.949 51	0.953 51	0.939 51	0.948 51	0.954 51	0.890 51	0.933 51	0.970 51	0.898 51
Trait 12: HZI_0408_R::1429297_at Symbol: Serpinb12	0.980 51	0.975 51	0.968 51	0.977 51	0.973 51	0.974 51	0.982 51	0.968 51	0.975 51	0.990 51	0.987 51	n 51	0.929 51	0.909 51	0.908 51	0.897 51	0.855 51	0.926 51	0.938 51	0.895 51
Trait 13: HZI_0408_R::1422401_at Symbol: Sprr3	0.979 51	0.979 51	0.971 51	0.981 51	0.972 51	0.983 51	0.986 51	0.974 51	0.988 51	0.982 51	0.986 51	0.980 51	n 51	0.974 51	0.908 51	0.969 51	0.887 51	0.954 51	0.947 51	0.901 51
Trait 14: HZI_0408_R::1452732_at Symbol: Asprv1	0.979 51	0.979 51	0.971 51	0.977 51	0.981 51	0.988 51	0.989 51	0.968 51	0.991 51	0.984 51	0.985 51	0.980 51	0.991 51	n 51	0.926 51	0.982 51	0.931 51	0.945 51	0.941 51	0.864 51
Trait 15: HZI_0408_R::1420183_at Symbol: Lor	0.976 51	0.977 51	0.964 51	0.972 51	0.983 51	0.974 51	0.981 51	0.963 51	0.966 51	0.970 51	0.974 51	0.974 51	0.965 51	0.969 51	n 51	0.923 51	0.877 51	0.883 51	0.935 51	0.833 51
Trait 16: HZI_0408_R::1429540_at Symbol: Cnfn	0.975 51	0.977 51	0.969 51	0.971 51	0.974 51	0.986 51	0.985 51	0.972 51	0.992 51	0.980 51	0.986 51	0.972 51	0.989 51	0.994 51	0.965 51	n 51	0.935 51	0.945 51	0.949 51	0.867 51
Trait 17: HZI_0408_R::1437019_at Symbol: 2200001I15Rik	0.974 51	0.975 51	0.973 51	0.974 51	0.973 51	0.989 51	0.984 51	0.979 51	0.984 51	0.975 51	0.977 51	0.966 51	0.972 51	0.981 51	0.960 51	0.984 51	n 51	0.920 51	0.911 51	0.848 51
Trait 18: HZI_0408_R::1423494_at Symbol: 2310042E22Rik	0.972 51	0.970 51	0.959 51	0.978 51	0.968 51	0.979 51	0.986 51	0.968 51	0.982 51	0.979 51	0.982 51	0.981 51	0.986 51	0.987 51	0.966 51	0.984 51	0.979 51	n 51	0.925 51	0.886 51
Trait 19: HZI_0408_R::1453801_at Symbol: 1110038F21Rik	0.972 51	0.971 51	0.965 51	0.971 51	0.964 51	0.985 51	0.984 51	0.981 51	0.989 51	0.990 51	0.991 51	0.980 51	0.984 51	0.984 51	0.963 51	0.984 51	0.980 51	0.983 51	n 51	0.917 51
Trait 20: HZI_0408_R::1458367_at Symbol: 3222401G21Rik	0.964 51	0.959 51	0.953 51	0.972 51	0.952 51	0.965 51	0.971 51	0.968 51	0.967 51	0.970 51	0.971 51	0.971 51	0.975 51	0.966 51	0.952 51	0.960 51	0.959 51	0.974 51	0.975 51	n 51

Figure 3 The cytokeratin network. Pearson correlations (listed below the diagonal) showed very high correlations between all pairs of the 20 selected genes. Spearman Rank correlations are shown above the diagonal.

(glutaminyl-peptide cyclo*trans*ferase (glutaminyl cyclase) and *Mta3* (metastasis associated 3) were suggested as potential QTGs by [20]. Another lung-specific phenotype in the GeneNetwork database is "Mycoplasmosis susceptibility, alveolar exudate" (GeneNetwork ID 10692, [21] and Cartner et al. unpublished). This trait showed a significant QTL on chromosome 10, between 105 and 130 Mb. The analysis of our lung expression data revealed 16 *cis*-eQTLs in the genomic interval (Table 5). Three of the *cis*-QTL genes have been

	Record ID	Symbol	Description	Location Chr and Mb	Mean Expr	Max LRS	Max LRS Location Chr and Mb	Sample r	N Cases	Sample p(r)	Lit Corr	Tissue r	Tissue p(r)
1	1422828_at	*Cd3d*	CD3 antigen, delta polypeptide	Chr9: 44.789979	9.770	13.2	Chr7: 81.491656	1.000	51	0.00e+00	1.000	1.000	N/A
2	1452405_x_at	*Tcra*	T-cell receptor alpha chain	Chr14: 54.842731	9.754	12.7	Chr11: 103.578807	0.917	51	0.00e+00	0.711	0.798	0.000
3	1425396_a_at	*Lck*	lymphocyte protein tyrosine kinase	Chr4: 129.225782	9.936	11.9	Chr7: 81.491656	0.907	51	0.00e+00	0.610	0.909	0.000
4	1417171_at	*Itk*	IL2-inducible T-cell kinase; mid distal 3' UTR	Chr11: 46.138692	8.208	11.3	Chr7: 81.491656	0.894	51	0.00e+00	0.619	0.883	0.000
5	1425854_x_at	*Tcrb-V13*	T-cell receptor beta, variable 13	Chr6: 41.496833	9.767	12.0	Chr7: 85.847907	0.879	51	0.00e+00	0.726	0.882	0.000
6	1422105_at	*Cd3e*	CD3 antigen, epsilon polypeptide; distal 3' UTR	Chr9: 44.806844	9.656	8.6	Chr7: 81.491656	0.872	51	0.00e+00	0.924	0.862	0.000
7	1426159_x_at	*Tcrb-V13*	T-cell receptor beta, variable 13	Chr6: 41.488285	10.520	10.8	Chr7: 85.847907	0.865	51	0.00e+00	0.726	0.882	0.000
8	1426113_x_at	*Tcra*	T-cell receptor alpha chain	Chr14: 54.843469	10.140	10.6	Chr11: 101.112194	0.864	51	0.00e+00	N/A	0.798	0.000
9	1419178_at	*Cd3g*	CD3 antigen, gamma polypeptide	Chr9: 44.777916	8.820	11.5	Chr9: 80.917762	0.863	51	0.00e+00	0.976	0.844	0.000
10	1452205_x_at	*Tcrb-V13*	T-cell receptor beta, variable 13	Chr6: 41.488510	9.520	12.5	Chr7: 85.847907	0.861	51	0.00e+00	0.726	0.882	0.000
11	1425226_x_at	*Tcrb-V13*	T-cell receptor beta, variable 13	Chr6: 41.488321	10.198	11.1	Chr7: 85.847907	0.860	51	0.00e+00	0.726	0.882	0.000
12	1416107_at	*Hmp19*	HMP19 protein, neuron specific gene family member 2 (hypothalamus golgi apparatus expressed 19 kDa protein, dopamine receptor binding); distal 3' UTR	Chr11: 31.958642	8.400	13.0	Chr7: 81.491656	0.850	51	0.00e+00	0.306	N/A	N/A
13	1460651_at	*Lat*	linker for activation of T cells	Chr7: 133.507917	9.211	14.0	Chr7: 90.186486	0.839	51	0.00e+00	0.667	0.878	0.000
14	1426772_x_at	*Tcrb-V13*	T-cell receptor beta, variable 13	Chr6: 41.496891	10.006	10.1	Chr7: 85.847907	0.837	51	0.00e+00	0.726	0.882	0.000
15	1434295_at	*Rasgrp1*	RAS guanyl releasing protein 1; distal 3' UTR	Chr2: 117.105846	8.530	11.5	Chr12: 101.866283	0.833	51	2.22e-16	0.609	0.452	0.020
16	1437249_at	*Scap1*	src family associated phosphoprotein 1; last three exons	Chr11: 96.592455	8.072	14.2	Chr7: 89.127385	0.822	51	6.66e-16	0.559	N/A	N/A
17	1435227_at	*Bcl11b*	B-cell leukemia/lymphoma 11B; distal 3' UTR	Chr12: 109.150912	8.565	10.1	Chr7: 81.491656	0.818	51	1.55e-15	0.580	0.413	0.036
18	1451910_a_at	*Cd6*	CD6 antigen	Chr19: 10.864137	7.856	9.3	Chr7: 125.263073	0.815	51	2.66e-15	0.733	0.864	0.000
19	1438392_at	*4833413G11Rik*	4833413G11Rik (Cd247 antigen-associated); 3' UTR (in Cd3z intron 1)	Chr1: 167.735938	7.114	10.5	Chr7: 81.491656	0.815	51	2.66e-15	N/A	N/A	N/A
20	1418353_at	*Cd5*	CD5 antigen	Chr19: 10.792689	7.984	11.3	Chr12: 118.628399	0.805	51	1.27e-14	0.789	0.708	0.000

Figure 4 Gene signatures for T-cells. List of the strongest correlates for *Cd3d* (probe set 1422828_at), all correlated at $p < 10^{-13}$.

	Record ID	Symbol	Description	Location Chr and Mb	Mean Expr	Max LRS	Max LRS Location Chr and Mb	Sample r	N Cases	Sample p(r)	Lit Corr	Tissue r	Tissue p(r)
1	1450570_a_at	*Cd19*	CD19 antigen	Chr7: 133.551983	9.343	10.1	Chr16: 73.748201	1.000	51	0.00e+00	1.000	1.000	N/A
2	1417640_at	*Cd79b*	CD79B antigen	Chr11: 106.172725	10.376	11.8	Chr5: 133.538653	0.917	51	0.00e+00	0.811	0.914	0.000
3	1429889_at	*Faim3*	Fas apoptotic inhibitory molecule 3	Chr1: 132.774829	9.773	12.6	Chr6: 88.537080	0.909	51	0.00e+00	0.462	0.887	0.000
4	1418830_at	*Cd79a*	CD79A antigen (immunoglobulin-associated alpha)	Chr12: 53.180027	9.950	15.4	Chr10: 13.407601	0.891	51	0.00e+00	0.858	0.961	0.000
5	1422775_at	*Blk*	B lymphoid kinase (oncogene); last exon and proximal half of 3' UTR	Chr14: 63.991841	8.724	13.1	Chr6: 88.537080	0.865	51	0.00e+00	0.713	0.928	0.000
6	1420994_at	*B3gnt5*	UDP-GlcNAc:betaGal beta-1,3-N-acetylglucosaminyltransferase 5; distal and far 3' UTR	Chr16: 19.771998	8.785	12.8	Chr10: 12.729006	0.847	51	0.00e+00	0.353	0.514	0.007
7	1419768_at	*Cd22*	CD22 antigen	Chr7: 31.650937	10.302	15.8	Chr7: 31.950330	0.846	51	0.00e+00	0.869	0.947	0.000
8	1419907_s_at	*Fcrla*	Fc receptor-like A;expressed sequence BB219290	Chr1: 172.847803	7.411	16.0	Chr15: 91.723348	0.837	51	0.00e+00	N/A	0.963	0.000
9	1422003_at	*Blr1*	Burkitt lymphoma receptor 1	Chr9: 44.320024	8.601	13.1	Chr6: 88.537080	0.834	51	0.00e+00	0.663	0.895	0.000
10	1419206_at	*Cd37*	CD37 antigen	Chr7: 52.489289	10.082	11.3	Chr10: 13.407601	0.829	51	2.22e-16	0.634	0.871	0.000
11	1460407_at	*Spib*	Spi-B transcription factor (Spi-1/PU.1 related)	Chr7: 51.781391	9.152	10.4	Chr1: 108.290874	0.829	51	2.22e-16	0.716	0.967	0.000
12	1423182_at	*Tnfrsf13b*	tumor necrosis factor receptor superfamily, member 13b	Chr11: 60.962284	9.318	20.4	Chr6: 88.537080	0.812	51	4.44e-15	0.747	0.792	0.000
13	1460419_a_at	*Prkcb*	protein kinase C, beta; distal 3' UTR	Chr7: 129.777363	9.675	13.2	Chr5: 147.658807	0.805	51	1.38e-14	0.432	N/A	N/A
14	1456632_at	*Bcl11a*	B-cell CLL/lymphoma 11A (zinc finger protein); distal 3' UTR or last intron	Chr11: 24.066781	7.033	12.3	Chr10: 12.729006	0.802	51	2.00e-14	0.563	0.648	0.000
15	1425736_at	*Cd37*	CD37 antigen	Chr7: 52.493149	9.102	15.2	Chr10: 12.729006	0.796	51	4.71e-14	0.634	0.871	0.000
16	1419307_at	*Tnfrsf13c*	tumor necrosis factor receptor superfamily, member 13c	Chr15: 82.052242	8.329	10.1	Chr8: 91.144186	0.796	51	5.20e-14	0.804	0.970	0.000
17	1456328_at	*A530094C12Rik*	RIKEN cDNA A530094C12 gene	Chr3: 135.716431	9.356	10.7	Chr15: 70.982535	0.789	51	1.27e-13	0.651	N/A	N/A
18	1419406_a_at	*Bcl11a*	B-cell CLL/lymphoma 11A (zinc finger protein)	Chr11: 24.072849	7.832	12.8	Chr15: 95.144975	0.788	51	1.56e-13	0.563	0.648	0.000
19	1438995_at	*Panx3*	pannexin 3	Chr13: 24.747062	8.779	10.2	Chr15: 95.144975	0.783	51	2.85e-13	0.222	0.056	0.786
20	1423478_at	*Prkcb1*	protein kinase C, beta 1; mid 3' UTR	Chr7: 129.771598	7.297	13.2	Chr5: 147.658807	0.781	51	3.74e-13	0.432	0.431	0.028

Figure 5 Gene signatures for B-cells. List of the strongest correlates for *Cd19* (probe set 1450570_at), all correlated at $p < 10^{-12}$.

associated previously with immune functions and thus represent suitable candidates to regulate this trait: *Chst* (carbohydrate (keratan sulfate Gal-6) sulfotransferase 1) was found to exhibit a critical role in lymphocyte trafficking during chronic inflammation [22]. The transcription factor *Maf* (avian musculoaponeurotic fibrosarcoma (v-maf) AS42 oncogene homolog) was shown to play a role in the transcriptional regulation of cytokine expression and immune cell markers, e.g. [23-29]. *Nrp1* (neuropilin 1) has been primarily described as neuronal receptor but appears also to play a role in the primary immune response and formation of the immunological synapse [30,31].

Cis- and trans-eQTLs

We then performed a search for eQTLs on a global level, for all probe sets. In this analysis 5,214 *cis*- and 15,485 *trans*-regulated genes were identified at an LRS threshold of 12 (Table 6 and Figure 6). When the LRS threshold was increased to 50, 1,332 *cis*-regulated genes were found, whereas the number of *trans*-regulated genes was reduced to 15. This observation indicates that many of the *trans*-eQTL showed a much lower significance value than the *cis*-eQTL. Next, we present examples for one *cis*- and one *trans*-eQTL. A strong eQTL was detected on chromosome 14, at 52 megabases (Mb; Figure 7B) regulating the expression levels of *Ang* (angiogenin, ribonuclease, RNase A family, 5) (Figure 7A). Since *Ang* is located at the same position as the eQTL (51.7 Mb on chromosome 14) it represents a *cis*-eQTL. Furthermore, a strong eQTL was found on chromosome 12 regulating the expression levels of the *Cyp1a1* gene (cytochrome P450, family 1, subfamily a, polypeptide 1) (Figure 7C,D). *Cyp1a1* is located on chromosome 9 and the corresponding eQTL was found on chromosome 12 (*trans*-eQTL). The eQTL significance interval contained nine genes, four of which were expressed in lung at a level above 10. *Ahr* (aryl-hydrocarbon receptor) was one of the four genes and was at the top of the QTL peak (Figure 8). It is the most likely candidate for *Cyp1a1* regulation. In conclusion, our data set contained a large number of genes whose expression levels are likely to be influenced by allelic variations in the genomes of C57BL/6J and DBA/2J. Therefore, the

Table 4 *Cis*-eQTLs identified in QTL inteval on chromosome 2 for influenza susceptibility

Probe set	Symbol	Description	Location (Chr, Mb)	Mean Expr	Max LRS
1423602_at	*Traf1*	Tnf receptor-associated factor 1	Chr2: 34.798805	9,28	21,1
1419407_at	*Hc*	hemolytic complement	Chr2: 34.838908	12,00	82,7
1441635_at	*Nr6a1*	nuclear receptor subfamily 6, group A, member 1	Chr2: 38.736451	7,51	20,2
1455743_at	*Olfml2a*	olfactomedin-like 2A	Chr2: 38.816929	8,28	63,2
1430379_at	*Zfhx1b*	zinc finger homeobox 1b	Chr2: 44.931019	9,08	82,4
1438516_at	*Rif1*	Rap1 interacting factor 1	Chr2: 51.975068	8,03	38,8
1444530_at	*Neb*	nebulin	Chr2: 51.991339	8,14	86,9

For each gene, only the highest LRS is shown. Mean Expr: mean expression in lung for BXD strains.

Table 5 *Cis*-eQTLs identified in QTL on chromosome 8 for Mycoplasmosis susceptibility trait

Probe set	Symbol	Description	Location (Chr, Mb)	Mean Expr	Max LRS
1435883_at	*AW413431*	expressed sequence AW413431	Chr8: 109.374192	8,27	37
1436986_at	*Sntb2*	syntrophin, basic 2	Chr8: 109.537595	6,94	23,6
1437003_at	*5730419l09Rik*	RIKEN cDNA 5730419l09 gene	Chr8: 109.543026	9,79	24,6
1451052_at	*Cog8*	component of oligomeric golgi complex 8	Chr8: 109.570082	10,35	23,7
1417766_at	*1810044O22Rik*	RIKEN cDNA 1810044O22 gene	Chr8: 109.710789	11,80	38
1429725_at	*Atbf1*	AT motif binding factor 1	Chr8: 111.481987	8,84	70,1
1453393_a_at	*Chst4*	carbohydrate (chondroitin 6/keratan) sulfo*trans*ferase 4	Chr8: 112.553165	7,33	71,9
1427513_at	*Nudt7*	nudix (nucleoside diphosphate linked moiety X)-type motif 7	Chr8: 116.678269	6,95	22,7
1446412_at	*Wwox*	WW domain-containing oxidoreductase	Chr8: 117.339587	7,46	94,7
1444073_at	*Maf*	avian musculoaponeurotic fibrosarcoma (v-maf) AS42 oncogene homolog	Chr8: 118.225461	7,93	121
1449964_a_at	*Mlycd*	malonyl-CoA decarboxylase (test Mendelian in BXDs with high DBA/2J allele)	Chr8: 121.934407	9,63	34,8
1418856_a_at	*Fanca*	Fanconi anemia, complementation group A	Chr8: 125.792224	7,98	78,5
1460109_at	*D8Ertd325e*	DNA segment, Chr 8, ERATO Doi 325, expressed	Chr8: 125.915951	7,60	89,8
1449307_at	*Dbndd1*	dysbindin (dystrobrevin binding protein 1)	Chr8: 126.029666	7,14	24,1
1446982_at	*Pard3*	par-3 (partitioning defective 3) homolog (C. elegans)	Chr8: 130.036847	8,02	87,9
1448944_at	*Nrp1*	neuropilin 1	Chr8: 131.027919	11,95	42,4

For each gene, only the highest LRS is shown. Mean Expr: mean expression in lung for BXD strains.

presence of pairs of regulated genes and their corresponding eQTLs predicts possible regulatory interactions and will allow searching for yet unknown regulatory networks.

Discussion

Here, we performed global gene expression profiling in eight inbred mouse strains and a cohort of BXD recombinant inbred strains from whole lung tissues. Our studies identified several lung-specific genes, large variations in gene expression levels, and a strong heritability in many gene expression traits. Correlation analysis of gene expression and genotypes identified potential gene interaction networks, pairs of *trans*- and *cis*-eQTLs, and genes with *cis*-eQTLs that may represent candidate genes involved in susceptibility to respiratory infections. In addition, one specific gene interaction pathway was identified in which *Ahr* regulates the *Cyp1a1* gene.

Using tissue correlations of gene expression patterns across the BXD strains, we identified 16 genes with a highly restricted expression in the lung of which 14 could be validated by comparison to the BioGPS database [19]. The second most strongly expressed gene in the lung tissues was *Sftpc* which has been shown to play a role in lung development and the prevention of pneumonitis and emphysema [32,33]. Also, *Sftpc* deficiency increases the severity of respiratory syncytial virus-induced pulmonary inflammation [34]. Furthermore, *Scgb1a1* and *Ager* were amongst the five most strongly expressed genes. *Scgb1a1* is expressed in lung clara cells and its deficiency results in enhanced susceptibility to environmental agents [35]. *Scgb3a1* (secretoglobin, family 3A, member 1) and *Scgb3a2* (secretoglobin, family 3A, member 2) were shown by others to be highly expressed in the lung and lower levels in other organs [36]. *Scgb3a2* is down-regulated in inflamed airways [37] and plays an important role in lung development [38]. *Sftpb* (surfactant associated protein B (non-ciliated bronchiolar and alveolar type 2 cell signature) is a hydrophobic peptide which enhances the surface properties of pulmonary surfactant and is expressed in non-ciliated bronchiolar and aleveolar type 2 cells [39]. Maintenance of *Sftpb* expression is critical for survival during acute lung injury [40] and reduction of alveolar expression causes surfactant dysfunction and respiratory failure [41]. *Plunc* (palate, lung, and nasal epithelium carcinoma associated) is expressed in the oral, lingual, pharyngeal and respiratory epithelia [42] and members of the *Plunc* gene family are thought to pay a role in the innate immune response [43]. The presence of Plunc protein in the lung decreases the levels of *Mycoplasma*

Table 6 Amount of *cis*- and *trans*-regulated *trans*cripts for different significance thresholds

Threshold (LRS)	No. of *cis* eQTLs	No. of *trans* eQTLs
12	5,214	15,485
16	4,391	3,149
20	3,666	536
30	2,500	48
50	1,332	15

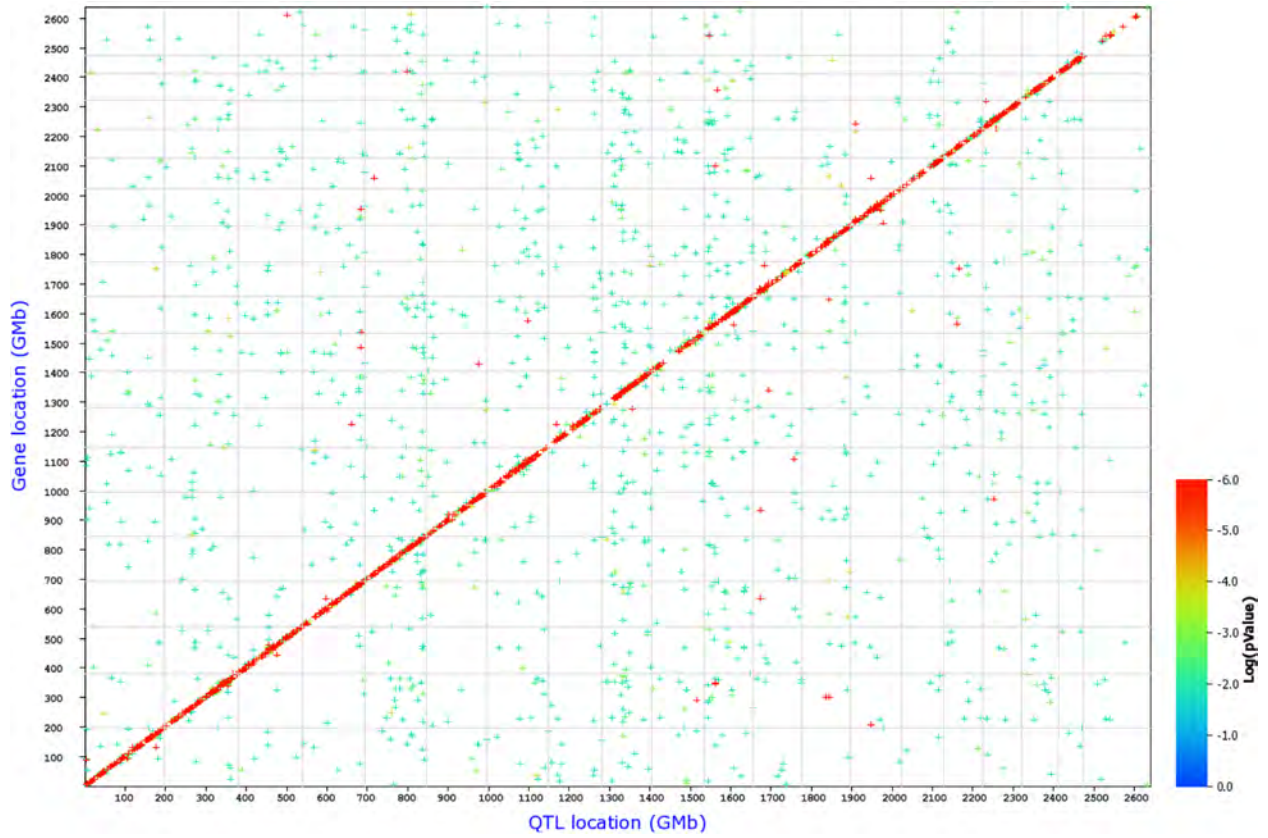

Figure 6 Genome-wide graph of *cis*- and *trans*-eQTLs. The positions of the eQTLs are plotted against the locations of the corresponding *trans*cript along the genome. *Cis*-regulated genes are located at the diagonal, all other dots represent *trans*-regulated genes. The significance level of each QTL is indicated by the color.

pneumoniae and its levels are reduced in allergic inflammatory conditions [44]. Thus, the lung data set allowed us to find important genes that are expressed primarily in the lung and are important for lung homeostasis and prevention of disease.

It should be noted that our analysis of genes with "restricted expression to the lung" is not ex-clusive; it only refers to the tissues that are represented in GeneNetwork and BioGPS. Also, the analysis performed here should not be considered to be comprehensive. More sophisticated approaches may be employed to identify additional genes which also fulfill the criterion of "lung-restricted" expression.

Furthermore, genes may not be apparent in the lung transcriptome because they are expressed only in a small fraction of cells within the lung. This issue of dilution of expression signals is an important one and we have studied it in several tissues with considerable care (eye, retina, and numerous brain regions) using the same genetic methods and the same array platform. We were consistently able to detect expression of genes that are only expressed in very small cell subpopulations (<0.1%) such as rare amacrine cell subclasses in the retina [8] or very rare oxytocin-expressing neurons (<2000) in whole brain samples. The reason for the increased sensitivity is that with such large sample sizes (~70 lung arrays) the signal-to-noise ratios are much better than standard studies using Affymetrix arrays. These stuides typically use far fewer arrays and do not use genetic methods to "validate" the source of signal.

The strong signal for hemoglobin and lymphocyte-specific genes clearly showed that gene ex-pression patterns of circulating blood cells are readily detectable in the lung transcriptome. This raises the question if an organ should be studied with or without containing blood. The correct answer to this question depends of course on the particular circumstances. However, we feel strongly that a global systems and genetic approach requires the analysis of the entire organ. The expression of genes is not cell-autonomous and depends on cellular micro envi-ronment, physical factors (gas pressure and gradients, etc), pathogen exposure, and many types of interactions. These factors also influence the expression of genes in blood cells. Therefore, we think that it is

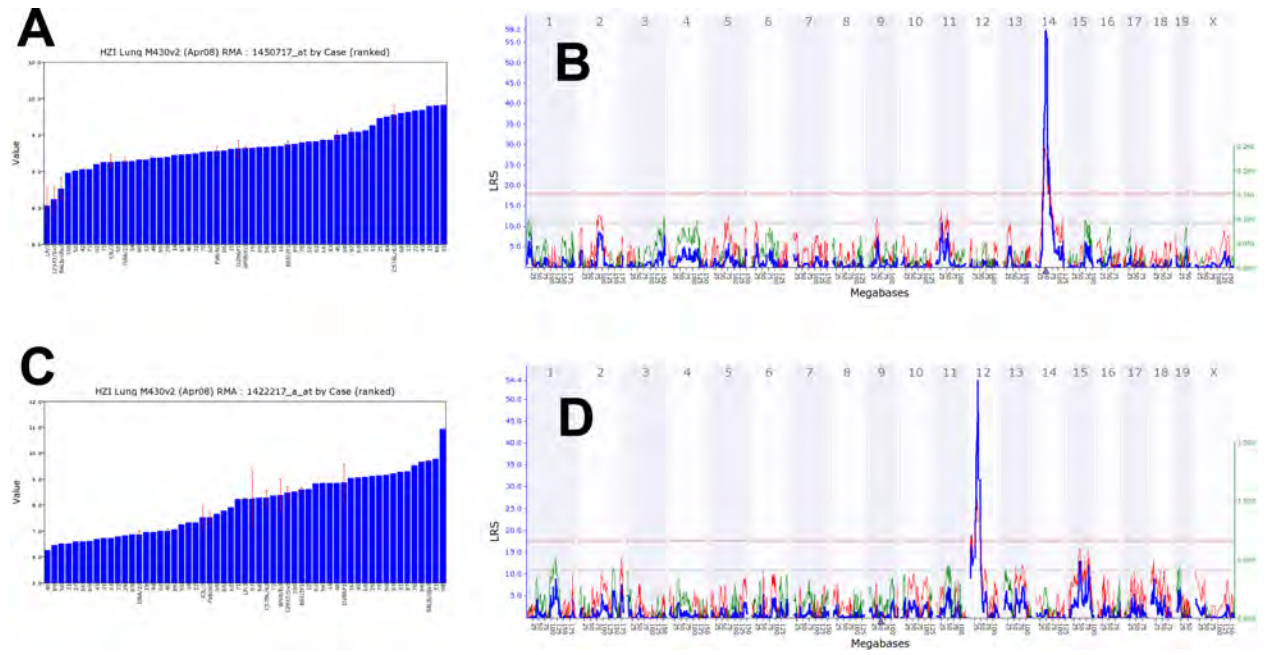

Figure 7 Examples for variations of expression levels in different BXD and inbred mouse strains and ge-nome-wide analysis of *cis*- and *trans*-eQTLs. (A) Log_2 expression levels for *Ang1* and (B) corresponding *cis*-eQTL signal. The numbers at the top are chromosomes. The blue line represents the significance level of the QTL expressed as LRS score (likelihood ratio statistic). A positive additive coefficient (green line) indicates that DBA/2J alleles increased trait values. A negative additive coefficient (red line) indicates that C57BL/6J alleles increased trait values. The two horizontal lines mark the genome-wide significance levels at $p < 0.05$ (red line) and $p < 0.63$ (gray line). *Ang1* is located on Chr 14 (triangle) and the QTL peak is at the same location as the gene. (C) Log_2 expression levels for *Cyp1a1* and (D) corresponding *trans* eQTL peak. *Cyp1a1* is on chromosome 9 (triangle) and the QTL was found on chromosome 12.

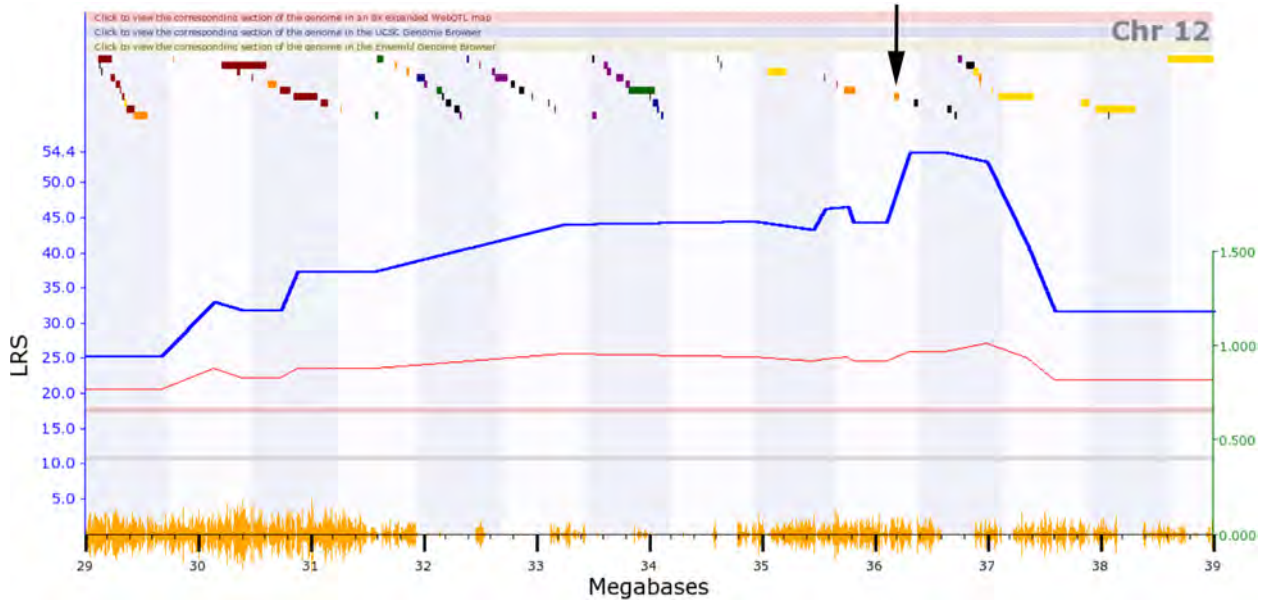

Figure 8 The *trans*cription factor *Ahr* is located within the *trans*-eQTL region for *Cyp1a1*. The strongest eQTL for *Cyp1a1* maps to Chromosome 12 and the QTL peaks between 36 and 37 megabases. The gene *Ahr*, indicated by an arrow, is located exactly at the top of the QTL peak.

imperative to look simultaneously at all cells in a function unit: in this case the whole lung plus its containing blood.

In conclusion, the combined analysis of expression levels and correlations in a variety of tissues tissue allowed us to determine genes with restricted or preferential expression in the lung. For several of these genes, an important function in the lung has been described and the same may be assumed for the others. This information will also contribute to a better understanding of the biological function of these genes.

Many phenotypic traits have been studied for the BXD mouse populations and several QTLs were identified which influence diseases or vulnerability in the lung. The detection of *cis* eQTLs in the very same tissue is one method to identify potential candidate genes under the QTL which may causally influence the trait. Here, we investigated two traits in more detail, susceptibility to influenza virus and susceptibility to mycoplasmosis. Several *cis*-eQTLs were found in the corresponding QTL regions and in each case, genes could be identified with a presumed role in the host immune defense (discussed already in the results section). Thus, the study of *cis*-eQTLs in our data set may provide valuable candidates for other quantitative trait genes that influence important lung phenotypes. Furthermore, we found 13 BXD lines with low expression signals for *Krt4*, *Krt13* and *Krtdap*. *Krt4* and *Krt13* have been shown to be responsible for White sponge nevus (WSN), also known as Cannon's disease, which is an autosomal dominant skin condition in humans [45-47]. We propose that the 13 mouse strains have genetic alterations which result in low transcript levels of these genes and they may represent a good model for Cannon's disease. It should be noted, however, that no *cis*-eQTLs found were found for any of the *Krt* genes.

We also identified a set of genes for which the expression levels correlated highly with members of the *Klr* gene family. *Klra3* and *Klrg1* are killer cell lectin-like receptors that are exclusively expressed on natural killer cells (NK cells). NK cells form a major component of the innate immune system and kill cells by releasing small cytoplasmic granules of proteins called perforins and granzymes [48]. Both *Gzma* and *Prf1* were in the gene network that we identified. In addition, correlations can also be used to expand already known gene networks in specific cell populations. When starting with the *Cd3* T cell marker and calculating correlations with all other transcripts measured, we identified a strongly correlated network of genes, in which most of the genes were known as T cell markers or to be involved in T cell activation or homeostasis. In a similar way, when starting with the *Cd19* B cell marker, we could identify a strongly correlated network of B cell signature genes. The analysis of these T cell and B cell expression signatures in the Bi-oGPS data base with expression profiles in mouse tissues revealed that indeed >90% of the T and B cell markers were specifically expressed in either T or B cells. Furthermore, most of the T and B cell signature genes represented genes with known function in B and T cell differentiation, activation and homeostasis. For example, the T cell signature included genes encoding subunits of the T cell receptor: *Cd3d* (CD3 antigen, delta po-lypeptide), *Cd3g* (CD3 antigen, gamma polypeptide), *Tcra* (T-cell receptor alpha chain) and *Tcrb-V13* (T-cell receptor beta, variable 13) and *Lat* (linker for activation of T cells) which are involved in T cell activation. The B cell signature contained components of the B cell antigen receptor complex, *Cd19* (CD19 antigen) and *Cd79a* (CD79A antigen (immunoglobulin-associated alpha)), as well as *Blk* (B lymphoid kinase) tyrosine kinase which is associated with the receptors. Also, the correlations for both signatures in the spleen expression data set in GeneNetwork could indeed confirm that the signatures were strongly correlated (data not shown). In summary, these studies demonstrate that correlation analyses are able to identify genes which very likely interact in a common network or biological process. The approach used here may thus have a great potential to identify new networks and biological processes in the lung. In addition, starting with a known bona-fide cell-specific gene and then analyzing gene expression values across strains, it is possible to identify a set of highly correlated genes. These gene sets genes can now be used as cell-specific signature genes in complex transcriptome studies, *e.g.* to detect infiltrating immune cells in the lungs after infection.

The genetic mapping of lung expression profiles revealed many *cis*- and *trans*-eQTLs, indicating that many gene expression patterns in lung have a strong genetic component. *Trans*-eQTLs allow the identification of gene-gene regulatory networks. As an example, we found that the transcription factor *Ahr* was present in a *trans*-eQTL region detected for the *Cyp1a1* gene. *Ahr* is a transcription factor known to induce *Cyp1a1* transcription levels after ligand binding [49-51]. Six binding sites for the Ahr receptor ligand have been revealed in the 700-basepair DNA domain upstream of *Cyp1a1* [52]. However, a critical leucine-to-proline substitution in *Ahr* results in a 15 to 20-fold reduction in the binding affinity of the proline variant found in DBA/2J compared to the leucine variant found in C57BL/6J [53]. Indeed, in our data set, expression values for *Cyp1a1*were low for BXD strains carrying the DBA/2J allele at the *Ahr* locus and high for the strains carrying the C57BL/6J allele. Since *Ahr* is not *cis*-regulated in lung, the downstream effects appear to be only caused by changes in Ahr protein binding affinity. Although the

interaction between *Cyp1a1* and *Ahr* as such is not a new finding, it is quite remarkable that the interaction becomes apparent in lungs which were not exposed to an inducing xenobiotic. Furthermore, we do not see this relationship in several other tissues, such as liver. Therefore, our observation suggests that in the lung, which is potentially exposed to many xenobiotics, the Ahr receptor may always be activated at a low level. Alternatively, *Ahr* expression may be stimulated by yet unknown ligands that are also present under normal environmental conditions.

Conclusions

Here, we showed that whole genome expression analysis of the lungs from a large set of strains of the BXD mouse population can be exploited to identify important gene regulatory networks. We found a large number of expression correlations and QTLs which can be further investigated to better understand molecular interaction networks in the lung. The search for *cis*-eQTLs in genomic intervals that were identified previously as QTLs for infectious diseases revealed several quantitative trait candidate genes. In addition, we demonstrated that the analysis of gene expression correlations, starting with a few cell-specific genes, could identify a larger set of genes which allows detecting the presence of B and T cells within the transcriptome of the whole lung. Such expression signatures will be very important to follow normal and abnormal host responses during infections and other diseases of the lung.

Acknowledgements

This work was supported by intra-mural grants from the Helmholtz-Association (Program "Infection and Immunity") and a research grant "FluResearchNet" (No. 01KI07137) from the German Ministry of Education and Research to KS. RWW acknowledges the support of the UTHSC Center for Integrative and Translational Genomics and NIH grant P20DA21131 and U01AA13499, and LL was supported by the NIH grant U01AA014425. We thank Dr. Yan Jiao and Weikuan Gu at UTHSC and the VA Medical Center, Memphis, for running the Affymetrix arrays in their core facility. We also thank the GeneNetwork development team, including Arthur Centeno, Xiaodong Zhou, Ning Liu, Zachary Sloan, and Lei Yan, for their help in integrating and error-checking the lung transcriptome data. We also thank Samuel C. Cartner for making the data on the Mycoplasmosis susceptibility phenotype available to us prior to publication.

Author details

[1]Department of Infection Genetics, Helmholtz Centre for Infection Research & University of Veterinary Medicine Hannover, Inhoffenstr. 7, D-38124 Braunschweig, Germany. [2]Department of Anatomy and Neurobiology, University of Tennessee Health Science Center, Memphis, Tennessee, USA. [3]Jiangsu Key Laboratory of Neuroregeneration, Nantong University, Nantong, China.

Authors' contributions

RA performed the bioinformatics analysis and wrote the manuscript. KS designed the experiments, performed the bioinformatics analysis and wrote the manuscript. LL and RWW prepared the study material and supervised the expression array studies. RW contributed to writing of the manuscript. All authors have read and approved the final manuscript.

Competing interests

The authors declare that they have no competing interests.

Received: 14 January 2011 Accepted: 2 May 2011 Published: 2 May 2011

References

1. Schughart K: **SYSGENET: a meeting report from a new European network for systems genetics.** *Mamm Genome* 2010, **21(7-8)**:331-336.
2. Morahan G, Peeva V, Mehta M, Williams R: **Systems genetics can provide new insights in to immune regulation and autoimmunity.** *J Autoimmun* 2008, **31(3)**:233-236.
3. Threadgill DW, Hunter KW, Williams RW: **Genetic dissection of complex and quantitative traits: from fantasy to reality via a community effort.** *Mamm Genome* 2002, **13(4)**:175-178.
4. Alberts R, Fu J, Swertz MA, Lubbers LA, Albers CJ, Jansen RC: **Combining microarrays and genetic analysis.** *Brief Bioinform* 2005, **6(2)**:135-145.
5. Chesler EJ, Lu L, Shou S, Qu Y, Gu J, Wang J, Hsu HC, Mountz JD, Baldwin NE, Langston MA, *et al*: **Complex trait analysis of gene expression uncovers polygenic and pleiotropic networks that modulate nervous system function.** *Nat Genet* 2005, **37(3)**:233-242.
6. Jansen RC, Nap JP: **Genetical genomics: the added value from segregation.** *Trends Genet* 2001, **17(7)**:388-391.
7. Rosen GD, Pung CJ, Owens CB, Caplow J, Kim H, Mozhui K, Lu L, Williams RW: **Genetic modulation of striatal volume by loci on Chrs 6 and 17 in BXD recombinant inbred mice.** *Genes Brain Behav* 2009, **8(3)**:296-308.
8. Geisert EE, Lu L, Freeman-Anderson NE, Templeton JP, Nassr M, Wang X, Gu W, Jiao Y, Williams RW: **Gene expression in the mouse eye: an online resource for genetics using 103 strains of mice.** *Mol Vis* 2009, **15**:1730-1763.
9. Gaglani SM, Lu L, Williams RW, Rosen GD: **The genetic control of neocortex volume and covariation with neocortical gene expression in mice.** *BMC Neurosci* 2009, **10**:44.
10. Gatti D, Maki A, Chesler EJ, Kirova R, Kosyk O, Lu L, Manly KF, Williams RW, Perkins A, Langston MA, *et al*: **Genome-level analysis of genetic regulation of liver gene expression networks.** *Hepatology* 2007, **46(2)**:548-557.
11. Bystrykh L, Weersing E, Dontje B, Sutton S, Pletcher MT, Wiltshire T, Su AI, Vellenga E, Wang J, Manly KF, *et al*: **Uncovering regulatory pathways that affect hematopoietic stem cell function using 'genetical genomics'.** *Nat Genet* 2005, **37(3)**:225-232.
12. Bao L, Wei L, Peirce JL, Homayouni R, Li H, Zhou M, Chen H, Lu L, Williams RW, Pfeffer LM, *et al*: **Combining gene expression QTL mapping and phenotypic spectrum analysis to uncover gene regulatory relationships.** *Mamm Genome* 2006, **17(6)**:575-583.
13. Chesler EJ, Lu L, Wang J, Williams RW, Manly KF: **WebQTL: rapid exploratory analysis of gene expression and genetic networks for brain and behavior.** *Nat Neurosci* 2004, **7(5)**:485-486.
14. Irizarry RA, Hobbs B, Collin F, Beazer-Barclay YD, Antonellis KJ, Scherf U, Speed TP: **Exploration, normalization, and summaries of high density oligonucleotide array probe level data.** *Biostatistics* 2003, **4(2)**:249-264.
15. Haley CS, Knott SA: **A simple regression method for mapping quantitative trait loci in line crosses using flanking markers.** *Heredity* 1992, **69(4)**:315-324.
16. Shifman S, Bell JT, Copley RR, Taylor MS, Williams RW, Mott R, Flint J: **A high-resolution single nucleotide polymorphism genetic map of the mouse genome.** *PLoS Biol* 2006, **4(12)**:e395.
17. Williams RW, Gu J, Qi S, Lu L: **The genetic structure of recombinant inbred mice: high-resolution consensus maps for complex trait analysis.** *Genome Biol* 2001, **2(11)**:RESEARCH0046.
18. Brockdorff N, Ashworth A, Kay GF, Cooper P, Smith S, McCabe VM, Norris DP, Penny GD, Patel D, Rastan S: **Conservation of position and exclusive expression of mouse Xist from the inactive X chromosome.** *Nature* 1991, **351(6324)**:329-331.
19. Wu C, Orozco C, Boyer J, Leglise M, Goodale J, Batalov S, Hodge CL, Haase J, Janes J, Huss JW, *et al*: **BioGPS: an extensible and customizable portal for querying and organizing gene annotation resources.** *Genome Biol* 2009, **10(11)**:R130.
20. Boon AC, deBeauchamp J, Hollmann A, Luke J, Kotb M, Rowe S, Finkelstein D, Neale G, Lu L, Williams RW, *et al*: **Host genetic variation affects resistance to infection with a highly pathogenic H5N1 influenza A virus in mice.** *J Virol* 2009, **83(20)**:10417-10426.

21. Cartner SC, Simecka JW, Briles DE, Cassell GH, Lindsey JR: **Resistance to mycoplasmal lung disease in mice is a complex genetic trait.** *Infect Immun* 1996, **64(12)**:5326-5331.
22. Hiraoka N, Kawashima H, Petryniak B, Nakayama J, Mitoma J, Marth JD, Lowe JB, Fukuda M: **Core 2 branching beta1,6-N-acetylglucosaminyltransferase and high endothelial venule-restricted sulfotransferase collaboratively control lymphocyte homing.** *J Biol Chem* 2004, **279(4)**:3058-3067.
23. Cao S, Liu J, Chesi M, Bergsagel PL, Ho IC, Donnelly RP, Ma X: **Differential regulation of IL-12 and IL-10 gene expression in macrophages by the basic leucine zipper transcription factor c-Maf fibrosarcoma.** *J Immunol* 2002, **169(10)**:5715-5725.
24. Cao S, Liu J, Song L, Ma X: **The protooncogene c-Maf is an essential transcription factor for IL-10 gene expression in macrophages.** *J Immunol* 2005, **174(6)**:3484-3492.
25. Hiramatsu Y, Suto A, Kashiwakuma D, Kanari H, Kagami S, Ikeda K, Hirose K, Watanabe N, Grusby MJ, Iwamoto I, *et al*: **c-Maf activates the promoter and enhancer of the IL-21 gene, and TGF-beta inhibits c-Maf-induced IL-21 production in CD4+ T cells.** *J Leukoc Biol* 2010, **87(4)**:703-712.
26. Nakamura M, Hamada M, Hasegawa K, Kusakabe M, Suzuki H, Greaves DR, Moriguchi T, Kudo T, Takahashi S: **c-Maf is essential for the F4/80 expression in macrophages in vivo.** *Gene* 2009, **445(1-2)**:66-72.
27. Pot C, Jin H, Awasthi A, Liu SM, Lai CY, Madan R, Sharpe AH, Karp CL, Miaw SC, Ho IC, *et al*: **Cutting edge: IL-27 induces the transcription factor c-Maf, cytokine IL-21, and the costimulatory recep-tor ICOS that coordinately act together to promote differentiation of IL-10-producing Tr1 cells.** *J Immunol* 2009, **183(2)**:797-801.
28. Voice J, Donnelly S, Dorsam G, Dolganov G, Paul S, Goetzl EJ: **c-Maf and JunB mediation of Th2 differentiation induced by the type 2 G protein-coupled receptor (VPAC2) for vasoactive intestinal peptide.** *J Immunol* 2004, **172(12)**:7289-7296.
29. Xu J, Yang Y, Qiu G, Lal G, Wu Z, Levy DE, Ochando JC, Bromberg JS, Ding Y: **c-Maf regulates IL-10 expression during Th17 polarization.** *J Immunol* 2009, **182(10)**:6226-6236.
30. Tordjman R, Lepelletier Y, Lemarchandel V, Cambot M, Gaulard P, Hermine O, Romeo PH: **A neuronal receptor, neuropilin-1, is essential for the initiation of the primary immune response.** *Nat Immunol* 2002, **3(5)**:477-482.
31. Wulfing C, Rupp F: **Neuropilin-1: another neuronal molecule in the "immunological synapse".** *Nat Immunol* 2002, **3(5)**:418-419.
32. Bridges JP, Wert SE, Nogee LM, Weaver TE: **Expression of a human surfactant protein C mutation associated with interstitial lung disease disrupts lung development in transgenic mice.** *J Biol Chem* 2003, **278(52)**:52739-52746.
33. Glasser SW, Detmer EA, Ikegami M, Na CL, Stahlman MT, Whitsett JA: **Pneumonitis and emphysema in sp-C gene targeted mice.** *J Biol Chem* 2003, **278(16)**:14291-14298.
34. Glasser SW, Witt TL, Senft AP, Baatz JE, Folger D, Maxfield MD, Akinbi HT, Newton DA, Prows DR, Korfhagen TR: **Surfactant protein C-deficient mice are susceptible to respiratory syncytial virus infection.** *Am J Physiol Lung Cell Mol Physiol* 2009, **297(1)**:L64-72.
35. Stripp BR, Reynolds SD, Boe IM, Lund J, Power JH, Coppens JT, Wong V, Reynolds PR, Plopper CG: **Clara cell secretory protein deficiency alters clara cell secretory apparatus and the protein composition of airway lining fluid.** *Am J Respir Cell Mol Biol* 2002, **27(2)**:170-178.
36. Porter D, Lahti-Domenici J, Torres-Arzayus M, Chin L, Polyak K: **Expression of high in normal-1 (HIN-1) and uteroglobin related protein-1 (UGRP-1) in adult and developing tissues.** *Mech Dev* 2002, **114(1-2)**:201-204.
37. Chiba Y, Kusakabe T, Kimura S: **Decreased expression of uteroglobin-related protein 1 in inflamed mouse airways is mediated by IL-9.** *Am J Physiol Lung Cell Mol Physiol* 2004, **287(6)**:L1193-1198.
38. Kurotani R, Tomita T, Yang Q, Carlson BA, Chen C, Kimura S: **Role of secretoglobin 3A2 in lung development.** *Am J Respir Crit Care Med* 2008, **178(4)**:389-398.
39. Bohinski RJ, Huffman JA, Whitsett JA, Lattier DL: **Cis-active elements controlling lung cell-specific expression of human pulmonary surfactant protein B gene.** *J Biol Chem* 1993, **268(15)**:11160-11166.
40. Bein K, Wesselkamper SC, Liu X, Dietsch M, Majumder N, Concel VJ, Medvedovic M, Sartor MA, Henning LN, Venditto C, *et al*: **Surfactant-associated protein B is critical to survival in nickel-induced injury in mice.** *Am J Respir Cell Mol Biol* 2009, **41(2)**:226-236.
41. Melton KR, Nesslein LL, Ikegami M, Tichelaar JW, Clark JC, Whitsett JA, Weaver TE: **SP-B deficiency causes respiratory failure in adult mice.** *Am J Physiol Lung Cell Mol Physiol* 2003, **285(3)**:L543-549.
42. LeClair EE, Nomellini V, Bahena M, Singleton V, Bingle L, Craven CJ, Bingle CD: **Cloning and expression of a mouse member of the PLUNC protein family exclusively expressed in tongue epithe-lium.** *Genomics* 2004, **83(4)**:658-666.
43. Bingle CD, Craven CJ: **PLUNC: a novel family of candidate host defence proteins expressed in the upper airways and nasopharynx.** *Hum Mol Genet* 2002, **11(8)**:937-943.
44. Chu HW, Thaikoottathil J, Rino JG, Zhang G, Wu Q, Moss T, Refaeli Y, Bowler R, Wenzel SE, Chen Z, *et al*: **Function and regulation of SPLUNC1 protein in Mycoplasma infection and allergic inflam-mation.** *J Immunol* 2007, **179(6)**:3995-4002.
45. Canon AB: **White sponge nevus of the mucosa (nevus spongiosus albus mucosa).** *Arch Dermatol Syphilol* 1935, **31**:365-370.
46. Terrinoni A, Rugg EL, Lane EB, Melino G, Felix DH, Munro CS, McLean WH: **A novel mutation in the keratin 13 gene causing oral white sponge nevus.** *J Dent Res* 2001, **80(3)**:919-923.
47. Rugg EL, McLean WH, Allison WE, Lunny DP, Macleod RI, Felix DH, Lane EB, Munro CS: **A mutation in the mucosal keratin K4 is associated with oral white sponge nevus.** *Nat Genet* 1995, **11(4)**:450-452.
48. Trapani JA, Smyth MJ: **Functional significance of the perforin/granzyme cell death pathway.** *Nat Rev Immunol* 2002, **2(10)**:735-747.
49. Nebert DW, Dalton TP, Okey AB, Gonzalez FJ: **Role of aryl hydrocarbon receptor-mediated induction of the CYP1 enzymes in environmental toxicity and cancer.** *J Biol Chem* 2004, **279(23)**:23847-23850.
50. Okey AB, Riddick DS, Harper PA: **The Ah receptor: mediator of the toxicity of 2,3,7,8-tetrachlorodibenzo-p-dioxin (TCDD) and related compounds.** *Toxicol Lett* 1994, **70(1)**:1-22.
51. Sutter CH, Yin H, Li Y, Mammen JS, Bodreddigari S, Stevens G, Cole JA, Sutter TR: **EGF receptor signaling blocks aryl hydrocarbon receptor-mediated transcription and cell differentiation in human epidermal keratinocytes.** *Proc Natl Acad Sci USA* 2009, **106(11)**:4266-4271.
52. Denison MS, Fisher JM, Whitlock JP Jr: **Protein-DNA interactions at recognition sites for the dioxin-Ah receptor complex.** *J Biol Chem* 1989, **264(28)**:16478-16482.
53. Chang C, Smith DR, Prasad VS, Sidman CL, Nebert DW, Puga A: **Ten nucleotide differences, five of which cause amino acid changes, are associated with the Ah receptor locus polymorphism of C57BL/6 and DBA/2 mice.** *Pharmacogenetics* 1993, **3(6)**:312-321.

doi:10.1186/1465-9921-12-61
Cite this article as: Alberts *et al.*: Genome-wide analysis of the mouse lung transcriptome reveals novel molecular gene interaction networks and cell-specific expression signatures. *Respiratory Research* 2011 **12**:61.

OPEN ACCESS Freely available online

PLoS PATHOGENS

Inflammasome-dependent Pyroptosis and IL-18 Protect against *Burkholderia pseudomallei* Lung Infection while IL-1β Is Deleterious

Ivonne Ceballos-Olvera, Manoranjan Sahoo, Mark A. Miller, Laura del Barrio, Fabio Re¤*

Department of Microbiology, Immunology, and Biochemistry, University of Tennessee Health Science Center, Memphis, Tennessee, United States of America

Abstract

Burkholderia pseudomallei is a Gram-negative bacterium that infects macrophages and other cell types and causes melioidosis. The interaction of *B. pseudomallei* with the inflammasome and the role of pyroptosis, IL-1β, and IL-18 during melioidosis have not been investigated in detail. Here we show that the Nod-like receptors (NLR) NLRP3 and NLRC4 differentially regulate pyroptosis and production of IL-1β and IL-18 and are critical for inflammasome-mediated resistance to melioidosis. *In vitro* production of IL-1β by macrophages or dendritic cells infected with *B. pseudomallei* was dependent on NLRC4 and NLRP3 while pyroptosis required only NLRC4. Mice deficient in the inflammasome components ASC, caspase-1, NLRC4, and NLRP3, were dramatically more susceptible to lung infection with *B. pseudomallei* than WT mice. The heightened susceptibility of *Nlrp3*$^{-/-}$ mice was due to decreased production of IL-18 and IL-1β. In contrast, *Nlrc4*$^{-/-}$ mice produced IL-1β and IL-18 in higher amount than WT mice and their high susceptibility was due to decreased pyroptosis and consequently higher bacterial burdens. Analyses of IL-18-deficient mice revealed that IL-18 is essential for survival primarily because of its ability to induce IFNγ production. In contrast, studies using IL-1RI-deficient mice or WT mice treated with either IL-1β or IL-1 receptor agonist revealed that IL-1β has deleterious effects during melioidosis. The detrimental role of IL-1β appeared to be due, in part, to excessive recruitment of neutrophils to the lung. Because neutrophils do not express NLRC4 and therefore fail to undergo pyroptosis, they may be permissive to *B. pseudomallei* intracellular growth. Administration of neutrophil-recruitment inhibitors IL-1ra or the CXCR2 neutrophil chemokine receptor antagonist antileukinate protected *Nlrc4*$^{-/-}$ mice from lethal doses of *B. pseudomallei* and decreased systemic dissemination of bacteria. Thus, the NLRP3 and NLRC4 inflammasomes have non-redundant protective roles in melioidosis: NLRC4 regulates pyroptosis while NLRP3 regulates production of protective IL-18 and deleterious IL-1β.

Citation: Ceballos-Olvera I, Sahoo M, Miller MA, del Barrio L, Re F (2011) Inflammasome-dependent Pyroptosis and IL-18 Protect against *Burkholderia pseudomallei* Lung Infection while IL-1β Is Deleterious. PLoS Pathog 7(12): e1002452. doi:10.1371/journal.ppat.1002452

Editor: Dana J. Philpott, University of Toronto, Canada

Received June 30, 2011; **Accepted** November 7, 2011; **Published** December 29, 2011

Funding: This work was supported by National Institutes of Health grants AI076835, AI081861 (F.R.) and Department of Defense Army grant W81XHW-05-1-0227. The funders had no role in study design, data collection and analysis, decision to publish, or preparation of the manuscript.

Competing Interests: The authors have declared that no competing interests exist.

* E-mail: fre@uthsc.edu; fabio.re@rosalindfranklin.edu

¤ Current address: Department of Microbiology and Immunology, Chicago Medical School, Rosalind Franklin University of Medicine and Science, North Chicago, Illinois, United States of America

Introduction

The ability to detect infection by pathogenic microbes and to restrict their growth are fundamental for the wellbeing of multicellular organisms. Pattern recognition receptors, including the Toll-like receptor (TLR) and the NLR, recognize microbial products and "danger signals" released by stressed cells and, in turn, activate signaling pathways that initiate the inflammatory response and regulate development of adaptive immunity. TLR are expressed on the cell surface or in endosomal compartments and their stimulation results in activation of the NF-κB, MAPK, and IRF signaling pathways culminating in transcriptional induction of a large number of genes. NLR, in contrast, are located in the cytoplasm, which they survey for evidence of danger or infection (reviewed in ref. [1]). Some NLR control activation of the inflammasome, a multiprotein complex that contains, in addition to a NLR, the adaptor molecule ASC and the protease caspase-1. Activation of caspase-1 in the context of the inflammasome is responsible for the proteolytic processing of the immature forms of IL-1β and IL-18, a modification required for the secretion and bio-activity of these proinflammatory cytokines. Activation of caspase-1 also triggers a form of cell death, known as pyroptosis, that effectively restricts intracellular bacterial growth [2,3]. Production of IL-1β and IL-18 and induction of pyroptosis have been shown to be protective effector mechanisms against many infectious agents. NLRP3 and NLRC4 are the best characterized NLR molecules. NLRP3 controls caspase-1 activation in response to "danger signals", several particles and crystals, and various bacteria, virus, and fungi. Although the logic that oversees the activation of the NLRP3 inflammasome is still elusive, it appears that disruption of cell membrane integrity may be a common event triggered by the NLRP3 activators. The NLRC4 inflammasome is responsive to a narrower spectrum of activators including cytoplasmically delivered bacterial flagellin and the basal rod constituent of various bacterial Type III secretion systems (T3SS). The T3SS apparatus is used by several bacteria, including *Salmonella*, *Yersinia*, *Pseudomonas*, *Shigella*, *Legionella*, *and Burkholderia* to inject virulence factors into the cytoplasm of target cells. Recent

Author Summary

The disease melioidosis is caused by the intracellular bacterium *Burkholderia pseudomallei*, a potential bioterrorism agent. Here we examined the interaction of *B. pseudomallei* with the inflammasome, an important innate immune pathway that regulates at least two host responses protective against infections: 1) secretion of the proinflammatory cytokines IL-1β and IL-18 and 2) induction of pyroptosis, a form of cell death that restricts intracellular bacteria growth. Using a mouse model of melioidosis we show that two distinct inflammasomes are activated by *B. pseudomallei* infection. One, containing the Nod-like receptor (NLR) NLRP3, mediates IL-1β and IL-18 induction. The other contains a different NLR called NLRC4 and mediates pyroptosis. Pyroptosis and IL-18 production were equally important for resistance to *B. pseudomallei*. Surprisingly, IL-1β was found to be deleterious in melioidosis. The detrimental role of IL-1β during melioidosis was due, in part, to excessive recruitment of neutrophils to the lung. We show that neutrophils do not express NLRC4, fail to undergo pyroptosis, and, therefore, may be permissive to *B. pseudomallei* intracellular replication leading to increased bacterial burden and morbidity/mortality. Thus, the NLRP3 and NLRC4 inflammasomes have non-redundant protective roles in melioidosis: NLRC4 regulates pyroptosis while NLRP3 regulates production of protective IL-18 and deleterious IL-1β.

works demonstrated that the specificity of the mouse NLRC4 for flagellin or rod proteins is determined by its interaction with the NLR molecules NAIP5 or NAIP2, respectively [4,5].

Burkholderia pseudomallei is a Gram-negative flagellate bacterium that causes melioidosis, a disease endemic to South-East Asia and other tropical regions [6,7] and the most common cause of pneumonia-derived sepsis in Thailand. Because melioidosis carries a high fatality rate, *B. pseudomallei* is classified as category B potential bioterrorism agent by the Center for Disease Control and NIAID. *B. pseudomallei* infection can be contracted through ingestion, inhalation, or subcutaneous inoculation and leads to broad-spectrum disease forms including pneumonia, septicemia, and organ abscesses. Following infection of macrophages and other non-phagocytic cell types, *B. pseudomallei* is able to escape the phagosome and invade and replicate in the host cell cytoplasm, directly spreading from cell to cell using actin-tail propulsion. Macrophages and IFNγ have been shown to play a critical role in protection from melioidosis [8–10] and several *B. pseudomallei* virulence factors have been identified including the bacterial capsule [11], the lipopolysaccharide [12], and one of the three T3SS possessed by *B. pseudomallei* [13]. Analysis of mouse strains with different susceptibility to *B. pseudomallei* infection indicates that the early phases of the infection are crucial for survival [14,15], emphasizing the necessity for better understanding of innate immune responses during melioidosis. With this goal in mind, using a murine model of melioidosis we have performed a detailed analysis of the role of the inflammasome components NLRP3, NLRC4, ASC, and caspase-1 and the effector mechanisms IL-1β, IL-18, and pyroptosis.

Results

NLRP3 and NLRC4 differentially regulate production of IL-1β and pyroptosis

To identify the pathway responsible for IL-1β and IL-18 secretion in response to infection with *B. pseudomallei*, bone marrow-derived macrophages (BMDM) or dendritic cells (BMDC) derived from WT mice or mice deficient in the inflammasome components ASC, NLRP3, NLRC4, or caspase-1 were infected *in vitro* with *B. pseudomallei* and secretion of IL-1β in culture supernatants was measured. As shown in figure 1A, secretion of IL-1β by *Asc*$^{-/-}$, *Nlrp3*$^{-/-}$, and *Casp1*$^{-/-}$ BMDM was markedly reduced compared to WT BMDM. Production of IL-1β during the first hours of the infection was also significantly reduced in *Nlrc4*$^{-/-}$ cells. However, later in the infection process (8 hours) *Nlrc4*$^{-/-}$ cells secreted IL-1β at levels considerably higher than WT cells. Secretion of IL-18 followed a similar pattern (data not shown). Immunoblotting of the supernatants confirmed processing of IL-1β and of caspase-1 to the mature 17 kDa and p20 forms, respectively (figure 1B). Interestingly, although caspase-1 was activated in *Asc*$^{-/-}$ cells, processing and secretion of IL-1β was not observed. NLRC4 possesses an amino-terminal CARD domain that can recruit and activate caspase-1 independently of ASC. It is unclear at present why activation of caspase-1 in *Asc*$^{-/-}$ cells is not sufficient to trigger secretion of mature IL-1β, a phenomenon previously reported by other groups [16]. The differences in IL-1β and IL-18 secretion were observed regardless of the number of bacteria used to infect cells (MOI 10, 50, or 100, data not shown) and were not due to differential induction of pro-IL-1β, which was present at comparable amounts in all the cell lysates. Thus, the NLRC4 and NLRP3 inflammasomes are both mediating release of IL-1β and IL-18 by myeloid cells infected with *B. pseudomallei*.

Inflammasome-mediated induction of pyroptosis has been demonstrated to be a mechanism that restricts growth of certain intracellular bacteria [2,3]. To measure induction of pyroptosis in cells infected with *B. pseudomallei* we used a kanamycin protection assay that allows only replication of intracellular bacteria whereas cells that undergo pyroptosis expose the bacteria to the microbicidal action of the antibiotic present in the medium. Induction of pyroptosis and intracellular bacterial replication were measured in WT or inflammasome-deficient BMDM infected with *B. pseudomallei*. As shown in figure 1C (upper graph), pyroptosis of infected cells (as measured by release of LDH in culture supernatants) was significantly reduced in *Casp1*$^{-/-}$ and *Nlrc4*$^{-/-}$ cells compared to WT and *Nlrp3*$^{-/-}$. Importantly, induction of pyroptosis was not lost in *Asc*$^{-/-}$ cells. NLRC4-mediated pyroptosis induced by other bacteria is also reported to be ASC-independent [16–19]. Consistent with the role of pyroptosis as a mechanism to restrict intracellular bacteria growth, considerably less intracellular bacteria were recovered from WT, *Nlrp3*$^{-/-}$, and *Asc*$^{-/-}$ cells than *Casp1*$^{-/-}$ or *Nlrc4*$^{-/-}$ cells at all time points (figure 1C, lower graph). Similar results regarding IL-1β processing and secretion and induction of pyroptosis were obtained using BMDC derived from the inflammasome–deficient mice (supplementary figure S1).

Taken together these results show that infection of macrophages and dendritic cells with *B. pseudomallei* leads to activation of the NLRC4 and NLRP3 inflammasomes. NLRC4 contributes to IL-1β during the early phase of the infection and induction of pyroptosis that restricts bacterial growth. NLRP3 does not control pyroptosis and primarily controls IL-1β secretion. It should be noted that the defective IL-1β production of *Nlrc4*$^{-/-}$ and *Nlrp3*$^{-/-}$ cells cannot be ascribed to the difference in induction of pyroptosis: thus *Nlrp3*$^{-/-}$ cells produce less cytokine than WT cells despite undergoing pyroptosis to the same extent as WT cells. Conversely, *Nlrc4*$^{-/-}$ cells, which are resistant to pyroptosis, still produce less cytokine than WT cells at the early time point. However, at later time points *Nlrc4*$^{-/-}$ cells produce considerably more IL-1β than WT cells. This is likely due to the fact that WT cells rapidly die after infection while *Nlrc4*$^{-/-}$ cells remain viable and continue to synthesize and secrete IL-1β.

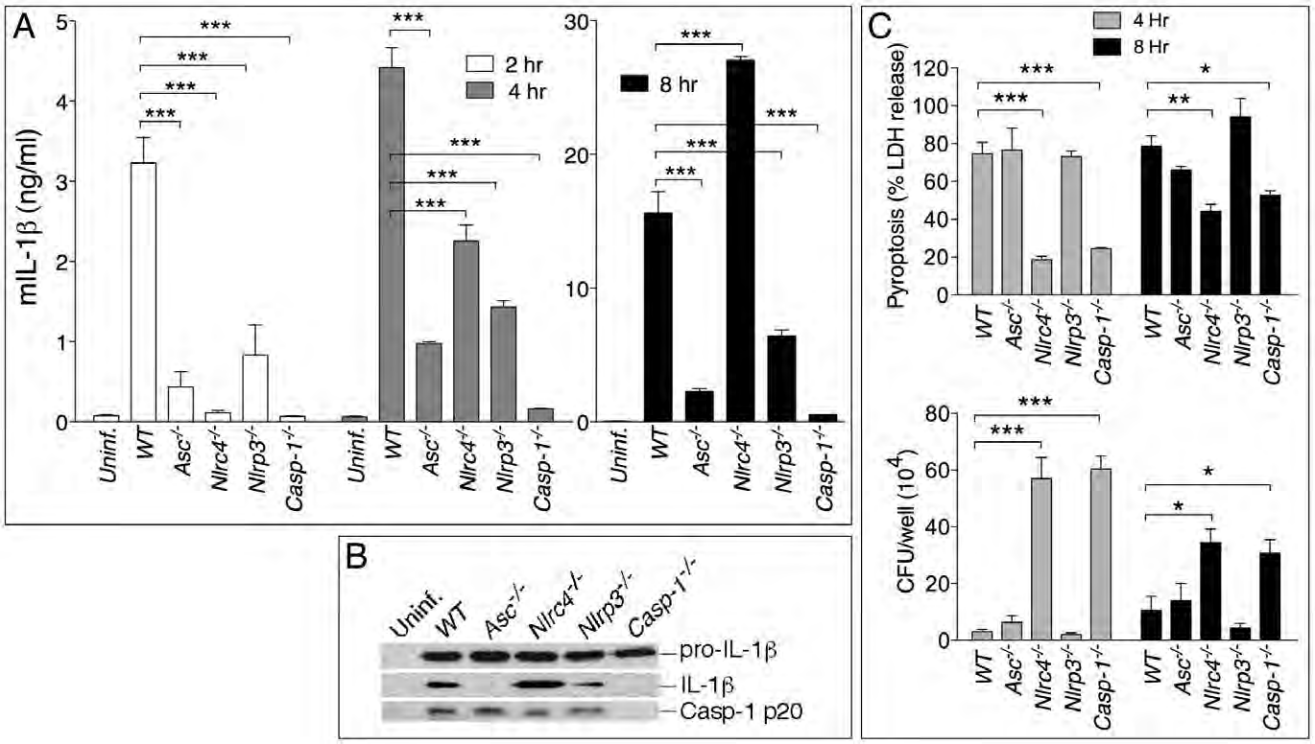

Figure 1. NLRP3 and NLRC4 differentially regulate production of IL-1β and pyroptosis. BMDM were infected with *B. pseudomallei* at MOI of 10. (A) Secretion of mature IL-1β was measured in conditioned supernatants of infected and uninfected cells at the indicated times. (B) Processing of IL-1β and caspase-1 was detected by immunoblot in 8 h conditioned supernatants from A. Pro-IL-1β was detected in cell lysate of the infected cells. (C) Induction of pyroptosis was measured as LDH release in conditioned supernatants of infected BMDM (MOI 10) (upper panel). Infected BMDM were lysed at the indicated time points after infection and intracellular bacteria growth was quantitated (lower panel). One experiment representative of three is shown. *$p<0.05$, **$p<0.01$, ***$p<0.001$ (1way ANOVA).
doi:10.1371/journal.ppat.1002452.g001

Role of inflammasomes in murine melioidosis

The role of the inflammasome during *in vivo B. pseudomallei* infection was next analyzed using a mouse model of melioidosis (figure 2). WT mice or inflammasome-deficient mice were infected intranasally with *B. pseudomallei* (100 CFU) and their weight (not shown) and survival were monitored (figure 2A). All mice started to lose weight 2 days post-infection. Generally, mice that survived the infection started to recover weight 7 days post-infection. *Casp1*$^{-/-}$, *Nlrc4*$^{-/-}$, and *Asc*$^{-/-}$ mice were extremely susceptible to melioidosis compared to WT mice. *Nlrp3*$^{-/-}$ mice were also considerably more susceptible than WT mice but slightly more resistant than the other inflammasome deficient mice. Measurement of the bacterial burdens in lungs, spleens, and livers of infected mice 24 hours (data not shown) and 48 hours post-infection revealed that *Nlrc4*$^{-/-}$ and *Casp1*$^{-/-}$ mice carried considerably higher burdens in all three organs than WT mice (figure 2B). Surprisingly, the bacterial burden of *Asc*$^{-/-}$ and *Nlrp3*$^{-/-}$ mice was not significantly different from that of WT mice at the tested time points despite their higher mortality.

Cytokine levels were measured in bronchio-alveolar lavage fluids (BALF) obtained from infected mice (figure 2C). Confirming the *in vitro* results, IL-1β and IL-18 levels were severely reduced in *Asc*$^{-/-}$, *Casp1*$^{-/-}$ and *Nlrp3*$^{-/-}$ mice. In contrast, IL-1β and IL-18 were present in the lungs of *Nlrc4*$^{-/-}$ mice in amounts considerably higher than WT mice. Immunoblotting experiments confirmed that the IL-1β measured by ELISA was in fact the p17 mature form of IL-1β (figure 2D). Thus, although the *in vitro* experiments demonstrated that both the NLRP3 and the NLRC4 inflammasome contribute to IL-1β and IL-18 production in response to *B. pseudomallei* infection, it is the NLRP3 inflammasome that primarily mediates production of these cytokines *in vivo*. The levels of several other proinflammatory cytokines, including IL-1α (figure S2), were significantly elevated in *Nlrc4*$^{-/-}$ BALF. It is interesting to note that the levels of IL-18 in BALF of *Asc*$^{-/-}$ and *Casp1*$^{-/-}$ mice, although very low, were higher than uninfected mice suggesting the existence of inflammasome-independent mechanisms to produce IL-1β and IL-18, as it has been previously shown in models of highly neutrophilic inflammation [20-23].

Histological analysis of the infected lungs revealed extensive inflammatory cell infiltration in the lung parenchyma (data not shown). The area of the inflammatory nodules, relative to the total area of the lung lobe, was calculated for each given section and found to be significantly greater in *Nlrc4*$^{-/-}$ mice compared to WT mice (figure 2E). This result was consistent with the elevated levels of inflammatory cytokines and chemokines produced by *Nlrc4*$^{-/-}$ mice. Taken together these results suggest a scenario where failure of *Nlrc4*$^{-/-}$ infected macrophages to undergo pyroptosis results in higher bacterial burden and continued production of IL-1β and other factors that attract more inflammatory cells, perpetuating lung inflammation and promoting bacteria dissemination.

Thus, our results identified two distinct infammasome-mediated mechanisms that efficiently restrict *B. pseudomallei* growth and pathogenesis: production of the cytokines IL-1β and IL-18 and induction of pyroptosis. The high susceptibility of *Nlrp3*$^{-/-}$ and *Asc*$^{-/-}$ mice to meliodiosis is due to defective cytokine production while that of the *Nlrc4*$^{-/-}$ mice likely results from defective pyroptosis. *Casp1*$^{-/-}$ mice are impaired in both inflammasome effector mechanisms and, therefore, we predicted that they would

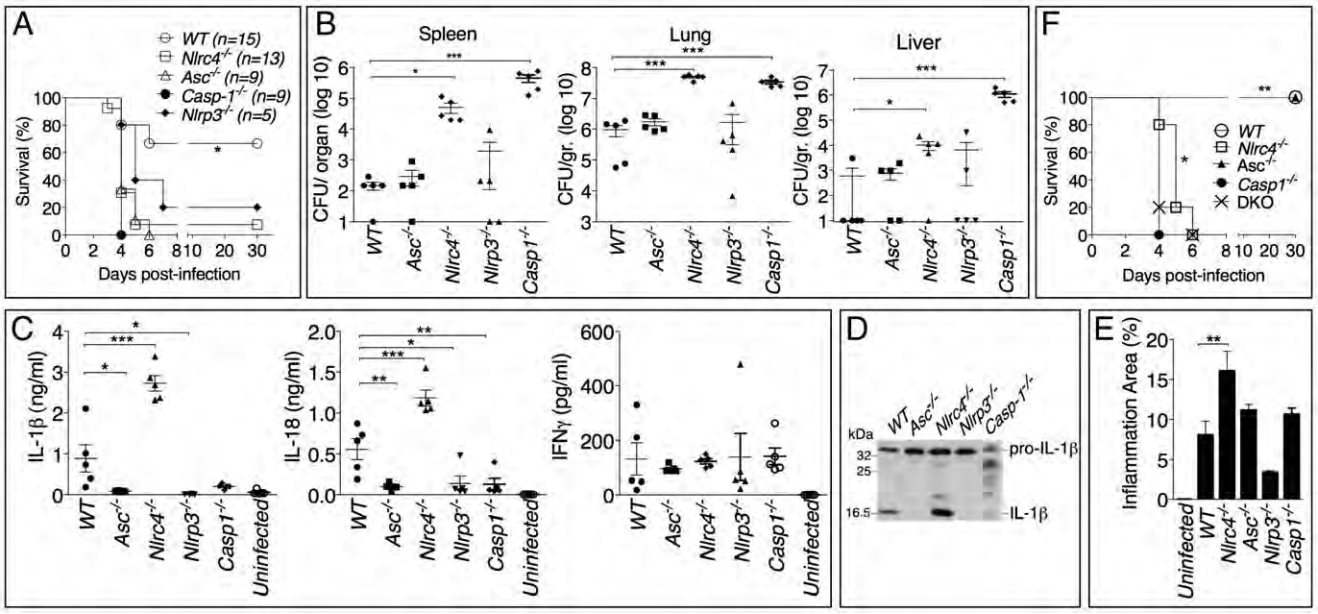

Figure 2. Differential contributions of NLRP3 and NLRC4 to melioidosis. (A) Mice were intranasally infected with *B. pseudomallei* (100 CFU) and their survival was monitored. *$p<0.05$ (Kaplan-Meier), WT compared to other genotypes (B) Mice were sacrificed 48 hours post-infection and the bacterial burdens were measured in organ homogenates. (C) Cytokines were measured in BALF obtained 48 hours post-infection. (D) Processing of IL-1β was detected by immunoblot in BALF from C. (E) Lung sections were stained with H&E and the total area of the inflammatory nodules was measured and expressed as percentage of the total lung lobe area. *$p<0.05$, **$p<0.01$, ***$p<0.001$ (1way ANOVA). (F) Mice were intranasaly infected with *B. pseudomallei* (25 CFU) and their survival was monitored. **$p<0.01$ WT compared to other genotypes and *p<0.05 *Casp-1*$^{-/-}$ compared to *Nlrc4*$^{-/-}$ (Kaplan-Meier).
doi:10.1371/journal.ppat.1002452.g002

be more vulnerable to *B. pseudomallei* than *Asc*$^{-/-}$ or *Il1-r1*$^{-/-}$*-Il-18*$^{-/-}$ double knock-out mice (DKO) (that are defective in cytokines but retain pyroptosis) or *Nlrc4*$^{-/-}$ mice (that retain IL-1β/IL-18 functionality but are deficient in pyroptosis). This prediction was found to be correct. As shown in figure 2F, when mice were infected with only 25 CFU (a non-lethal dose for WT mice) the mean time to death of *Nlrc4*$^{-/-}$ and *Il-1r1*$^{-/-}$*-Il-18*$^{-/-}$ DKO mice was slightly but significantly ($p<0.05$, Kaplan-Meier test) increased compared to *Casp1*$^{-/-}$ mice. Surprisingly, *Asc*$^{-/-}$ mice, which should be equivalent to DKO because of the absence of IL-1β or IL-18, survived the infection. This may be explained by the observation that IL-18, although drastically reduced, it is still detectable in *Asc*$^{-/-}$ mice at higher level than uninfected mice (figure 2C).

Role of IL-18 and IL-1β in murine melioidosis

We next analyzed the role of the inflammasome-dependent cytokines IL-1β and IL-18 during murine melioidosis. IL-18-deficient mice were extremely susceptible to *B. pseudomallei* infection even when infected with 25 CFU, a dose of bacteria that caused no mortality and only mild weight loss in WT mice (figure 3A). In contrast, *Il-1r1*$^{-/-}$ mice displayed increased resistance to *B. pseudomallei* infection compared to WT mice (figure 3A and see below). The survival of mice deficient in both IL-18 and IL-1RI (DKO) was indistinguishable from the *Il-18*$^{-/-}$ mice when the animals were infected with 100 CFU. However, in DKO mice infected with 25 CFU (figure 3A, right panel) the concomitant absence of IL-18 and IL-1RI provided a significant advantage over *Il-18*$^{-/-}$ mice ($p<0.05$) suggesting a detrimental role of IL-1RI-mediated signaling in melioidosis (see below).

Confirming the different susceptibilities of *Il-18*$^{-/-}$ and *Il-1r1*$^{-/-}$ mice to melioidosis, the bacterial burdens observed in the lungs, spleens, livers, and BALF of infected *Il-18*$^{-/-}$ mice were dramatically higher than that of WT mice even at early time points (24 hours post infection, figure 3B). In contrast, significantly lower amounts of bacteria were recovered 48 hours post infection from *Il-1r1*$^{-/-}$ mice compared to WT mice confirming their higher resistance.

Measurements of cytokines in the BALF obtained from mice at 24 and 48 hours post-infection (figure 3C) indicated that the levels of IFNγ were drastically reduced in *Il-18*$^{-/-}$ mice, a finding consistent with the established function of IL-18 as an IFNγ-inducing cytokine. Remarkably, IFNγ levels in *Il-1r1*$^{-/-}$ mice were greatly increased compared to WT mice. The levels of the neutrophil attractants Mip-2, KC, and IL-17 were also decreased in *Il-1r1*$^{-/-}$ mice and increased in *Il-18*$^{-/-}$ mice (figure S2). The number of inflammatory cells recovered from the BALF of infected *Il-1r1*$^{-/-}$ mice was significantly decreased compared to WT mice (see figure 4B, left panel). Histological analysis of the infected lungs revealed extensive inflammatory cell infiltration in the lung parenchyma of *Il-18*$^{-/-}$ mice (see figure 4C). The area of the inflammatory nodules, relative to the total area of the lung lobe, was calculated for each given section and found to be significantly greater in *Il-18*$^{-/-}$ mice compared to WT mice (figure 4D).

Considering that IFNγ is known to play a protective role during several bacterial infections, including *B. pseudomallei* [8–10], these results suggested that the reduced resistance of *Il-18*$^{-/-}$ mice to *B. pseudomallei* infection may be due to lack of IFNγ induction. To test this hypothesis, a group of *Il-18*$^{-/-}$ mice infected with *B. pseudomallei* were given daily intraperitoneal injections of either recombinant IFNγ or PBS. As shown in figure 3D, exogenous IFNγ completely protected the mice suggesting that IL-18 exerts its protective action primarily through induction of IFNγ.

Deleterious role of IL-1β in melioidosis

The results of figure 3 showed that *Il-1r1*$^{-/-}$ mice were more resistant to lung infection with *B. pseudomallei*. This appeared even

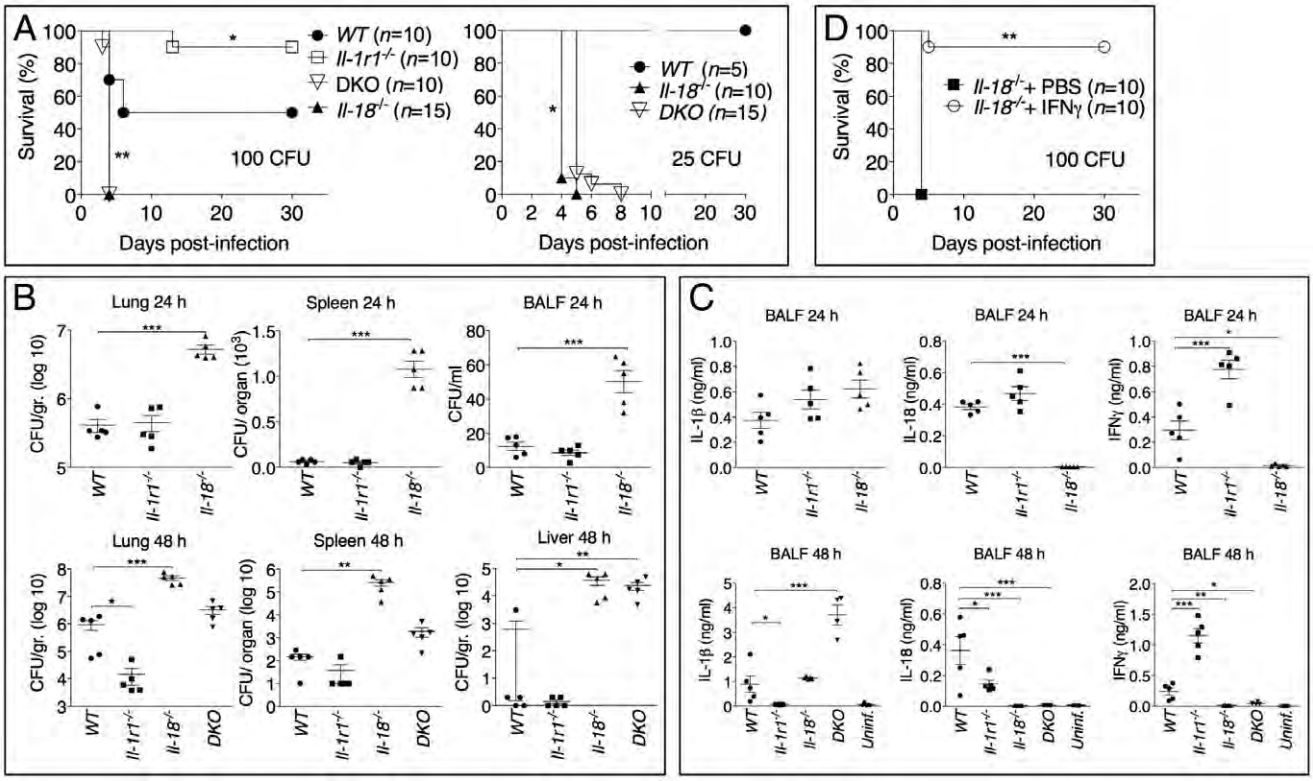

Figure 3. Differential contributions of IL-1 and IL-18 to melioidosis. (A) Mice were intranasaly infected with *B. pseudomallei* (100 CFU, left, or 25 CFU, right) and their survival was monitored. *$p<0.05$, **$p<0.01$ (Kaplan-Meier), WT compared to other genotypes (left), *Il-18*$^{-/-}$ compared to DKO (right). (B, C) Mice infected with *B. pseudomallei* (100 CFU) were sacrificed 24 hours or 48 hours postinfection and the bacterial burdens in organ homogenates and BALF (B) or cytokines levels in BALF (C) were measured. *$p<0.05$, **$p<0.01$, ***$p<0.001$ (1way ANOVA). (D) *Il-18*$^{-/-}$ mice were intranasally infected with *B. pseudomallei* (100 CFU) and their survival monitored. Mice were administered daily injections of PBS or IFNγ (1 μg) for the first 8 days. **$p<0.01$ (Kaplan-Meier).
doi:10.1371/journal.ppat.1002452.g003

more evident when mice were infected with higher doses of *B. pseudomallei* that killed all WT mice but only a fraction of the *Il-1r1*$^{-/-}$ mice (figure 4A). Recruitment of neutrophils, macrophages, and dendritic cells into alveolar spaces was decreased in *Il-1r1*$^{-/-}$ mice compared to WT mice (figure 4B, left graph). Lower levels of the neutrophil enzyme myeloperoxidase (MPO) were detected in the BALF of *Il-1r1*$^{-/-}$ mice compared to WT (figure S3). The extent of lung inflammation, as measured by the number and size of inflammatory nodules, was also significantly decreased in *Il-1r1*$^{-/-}$ mice (figure 4C, and 4D).

To further test the hypothesis that IL-1R-mediated signaling has a deleterious role in this model of melioidosis, WT mice were infected with 100 CFU *B. pseudomallei* and were given daily intraperitoneal injections of IL-1β or PBS (figure 4E). All mice that received the cytokine succumbed to the infection compared to significantly higher survival of the control group. Injection of IL-1β in non-infected mice had no deleterious effect aside from a transient, negligible weight loss (not shown). The bacteria burdens in organs of IL-1β-treated mice 72 hours post infection were dramatically higher than the control group and bacteremia was detected in IL-1β-treated mice but not control mice (figure 4F). Higher number of neutrophils, macrophages, and dendritic cells were found in the BALF of IL-1β-treated mice (figure 4B, center graph). This correlated with increased level of MPO in BALF (figure S3). The increased inflammatory cell recruitment to the lungs of IL-1β-treated mice was likely due to the induction, by IL-1β, of neutrophil chemoattractans KC (CXCL1) and MIP-2 (CXCL-2), which in fact were detected at very high levels in the BALF of IL-1β-treated mice (figure S2). Histological analysis of lung sections of mice treated with IL-1β showed a dramatic increase in the number and size of the foci of infiltrating inflammatory cells (figure 4C, lower left panels) and evidence of perivascular edema and airway obstruction (figure 4C, lower right panels).

If IL-1β in fact has a detrimental effect during melioidosis, inhibition of its activity should lower morbidity and mortality of mice infected with *B. pseudomallei*. As shown in figure 4G, administration of the IL-1 receptor antagonist IL-1ra protected mice from infection with lethal doses of *B. pseudomallei*. Mice treated with IL-1ra had decreased recruitment of inflammatory cells to the alveolar spaces (figure 4B, right graph) lower level of MPO in BALF (figure S3), and less severe lung pathology (data not shown).

Neutrophils fail to restrict *B. pseudomallei* intracellular growth and are resistant to pyroptosis

Surprisingly, in our experiments lower numbers of neutrophils in *Il-1r1*$^{-/-}$ mice correlated with lower bacterial burdens while IL-1β administration resulted in increased neutrophil recruitment *but also* increased bacterial burdens and systemic dissemination. These results would be consistent with the notion that neutrophils are not very effective at containing *B. pseudomallei* infection and, in fact, may foster its spread. In support of this idea, human neutrophils infected with *B. pseudomallei* underwent pyroptosis at a much slower rate than infected monocytes (figure 5A). Concomitantly, intra-

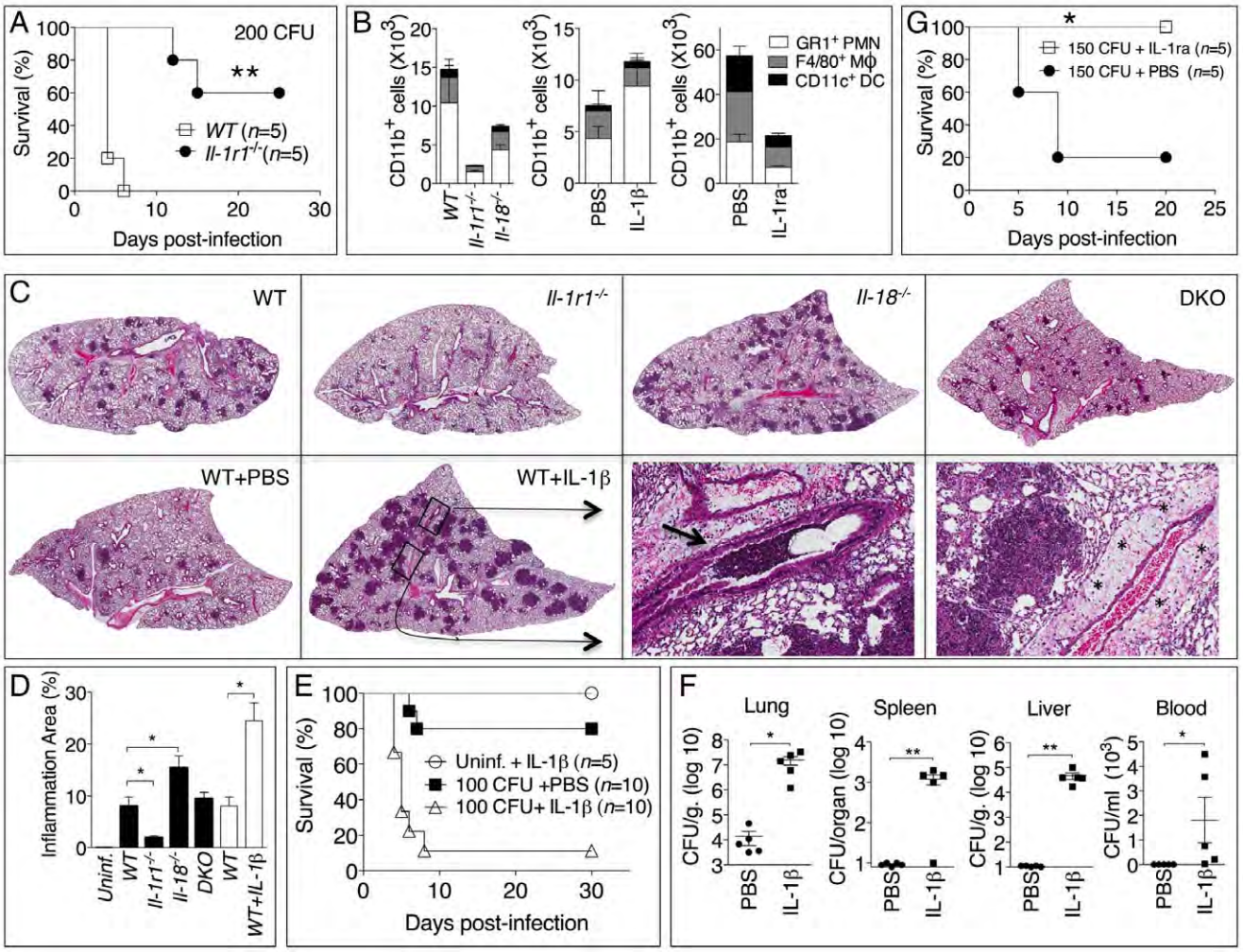

Figure 4. Deleterious role of IL-1β in melioidosis. (A) Mice were infected intranasally with *B. pseudomallei* (200 CFU) and their survival was monitored. (B) Flow cytometric analysis for myeloid cell composition of BALF obtained from the indicated infected mouse strains at 24 h (left); infected WT mice injected with IL-1β at 48 h (center graph); or infected WT mice injected with PBS or IL-1ra at 72 h. *$p<0.05$, ***$p<0.001$ (1way ANOVA). (C) Histopathology of lungs of infected mice of indicated genotype (0.8X magnification) at 48 h post-infection (upper row) or WT mice injected with PBS or IL-1β at 72 hrs post-infection (lower row). Bottom right panel shows 10X magnification of the indicated insets from WT+IL-1β showing airways obstruction (arrow head) and perivascular edema (asterisks). One image representative of five animals/experimental group. (D) The total area of the inflammatory nodules of lung sections of C was measured and expressed as percentage of the total lung lobe area. *$p<0.05$ (*t*-test). (E) WT mice were infected intranasally with *B. pseudomallei* (100 CFU) and received daily i.p. injections of PBS or IL-1β (1 μg). One group of mice were treated with IL-1β but not infected. **$p<0.01$, ***$p<0.001$ (Kaplan-Meyer). (F) Mice infected and IL-1β-injected as in E were sacrificed 72 h post-infection and the bacterial burden was measured in organs and blood. *$p<0.05$, **$p<0.01$ (1way ANOVA). (G) WT mice were infected intranasally with *B. pseudomallei* (150 CFU) and were administered daily injections of PBS or IL-1ra. *$p<0.05$ (Kaplan-Meyer).
doi:10.1371/journal.ppat.1002452.g004

cellular bacteria growth increased with time in infected neutrophils but decreased in monocytes. Consistent with previously published results [3], neutrophils did not express NLRC4 mRNA (figure 5B) suggesting they may be resistant to pyroptosis. Similar results were obtained using neutrophils and $CD11b^+$ monocytic cells isolated from mouse bone marrow (figure 5C). WT monocytes infected with *B. pseudomallei* underwent pyroptosis and failed to support bacteria replication whereas *Nlrc4*$^{-/-}$ cells were resistant to pyropotosis and supported *B. pseudomallei* intracellular replication. In contrast, both WT and *Nlrc4*$^{-/-}$ neutrophils did not undergo pyroptosis and supported *B. pseudomallei* intracellular replication to the same extent. These results suggest that the deleterious role of IL-1β during melioidosis may be due, in part, to excessive recruitment of neutrophils, a cell type that may be permissive for *B. pseudomallei* replication. We decided to test this hypothesis in *Nlrc4*$^{-/-}$ mice. As shown in figure 2E, infected *Nlrc4*$^{-/-}$ mice showed a significantly higher degree of lung inflammation. Consistent with higher neutrophil influx in the lung of *Nlrc4*$^{-/-}$ mice, the levels of the neutrophil enzyme MPO were significantly increased in their BALF compared to WT mice (figure 6A). To test the hypothesis that excessive neutrophil influx is deleterious during melioidosis, *Nlrc4*$^{-/-}$ mice were injected with IL-1ra or with antileukinate, a hexapeptide that acts as a CXCR2 neutrophil chemokine receptor antagonist. Both factors have been shown to inhibit neutrophil recruitment to inflammatory sites in different animal models including lung inflammation [24–26]. As shown in figure 6B, administration of IL-1ra or antileukinate protected *Nlrc4*$^{-/-}$ mice infected with low doses of *B. pseudomallei*. The number of inflammatory cells in the BALF of *Nlrc4*$^{-/-}$ mice treated with IL-1ra or antileukinate was reduced compared to mice who received

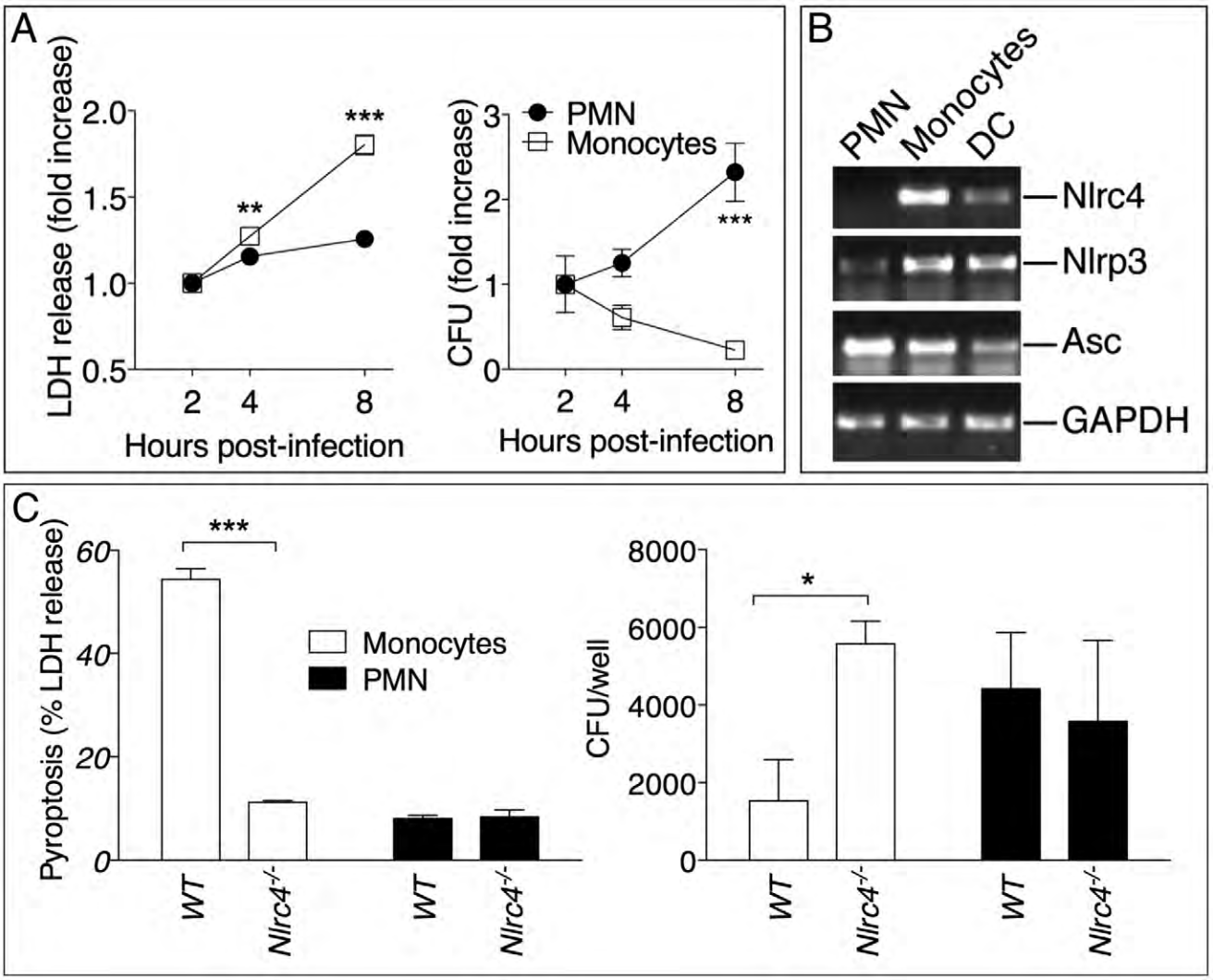

Figure 5. Neutrophils do not undergo pyroptosis and fail to restrict *B. pseudomallei* replication. (A) Human neutrophils or monocytes were infected with *B. pseudomallei* (MOI 50) and pyroptosis and intracellular bacterial growth were measured at the indicated time points. One experiment representative of two is shown. Data are shown as the fold increase normalized to the 2 h values. (B) RT-PCR analysis of total RNA from the indicated cell types. (C) WT or *Nlrc4*$^{-/-}$ mouse neutrophils and monocytic cells were infected with *B. pseudomallei* (MOI 50) and pyroptosis and intracellular bacterial growth were measured 8 hours post infection. * $p<0.05$, ** $p<0.01$, *** $p<0.001$ (2way ANOVA, post-test Bonferroni).
doi:10.1371/journal.ppat.1002452.g005

PBS injection (figure 6C) and lower levels of MPO were detected in the BALF of injected mice (figure S3). Moreover, systemic spread of bacteria to spleen or liver was reduced by administration of either drug (figure 6D).

Discussion

The inflammatory response to infection consists of several protective effector mechanisms that must be activated and orchestrated in order to maximize microbicidal functions and stimulation of adaptive immunity while, at the same time, minimize damage to the host tissues. Alteration in this balance may result in excessive and non-resolving inflammation that leads to severe morbidity and mortality [27]. It is becoming clear that to be effective but non-pathogenic the inflammatory response must be tailored to each specific pathogen. Here we have analyzed the role of a very important inflammatory pathway during infection with the lung pathogen *B. pseudomallei*. Using a murine model of melioidosis we have determined the role of various components of the inflammasome and the downstream effector mechanisms (production of IL-1β, IL-18, and pyroptosis) and we report several novel discoveries that greatly increase our understanding of the pathogenesis of melioidosis (see model in figure 7).

First, we found that both NLRC4 and NLRP3 play non-redundant roles during detection of *B. pseudomallei*. Analysis of *in vitro* infected macrophages or dendritic cells allowed us to estimate the relative contribution of NLRC4 and NLRP3 to IL-1β production. Our findings indicated that production of IL-1β is primarily dependent on the NLRP3 inflammasome. During the early phase of the infection the NLRC4 inflammasome also significantly contributes to IL-1β production. We posit that this pattern likely reflects the fact that the NLRC4 inflammasome responds to T3SS deployment, which occurs early in the infection cycle, while activation of NLRP3 may require escape from the phagosome, which is a relatively slower event [28]. *B. pseudomallei* , including the strain used in our study, possesses at least three T3SS

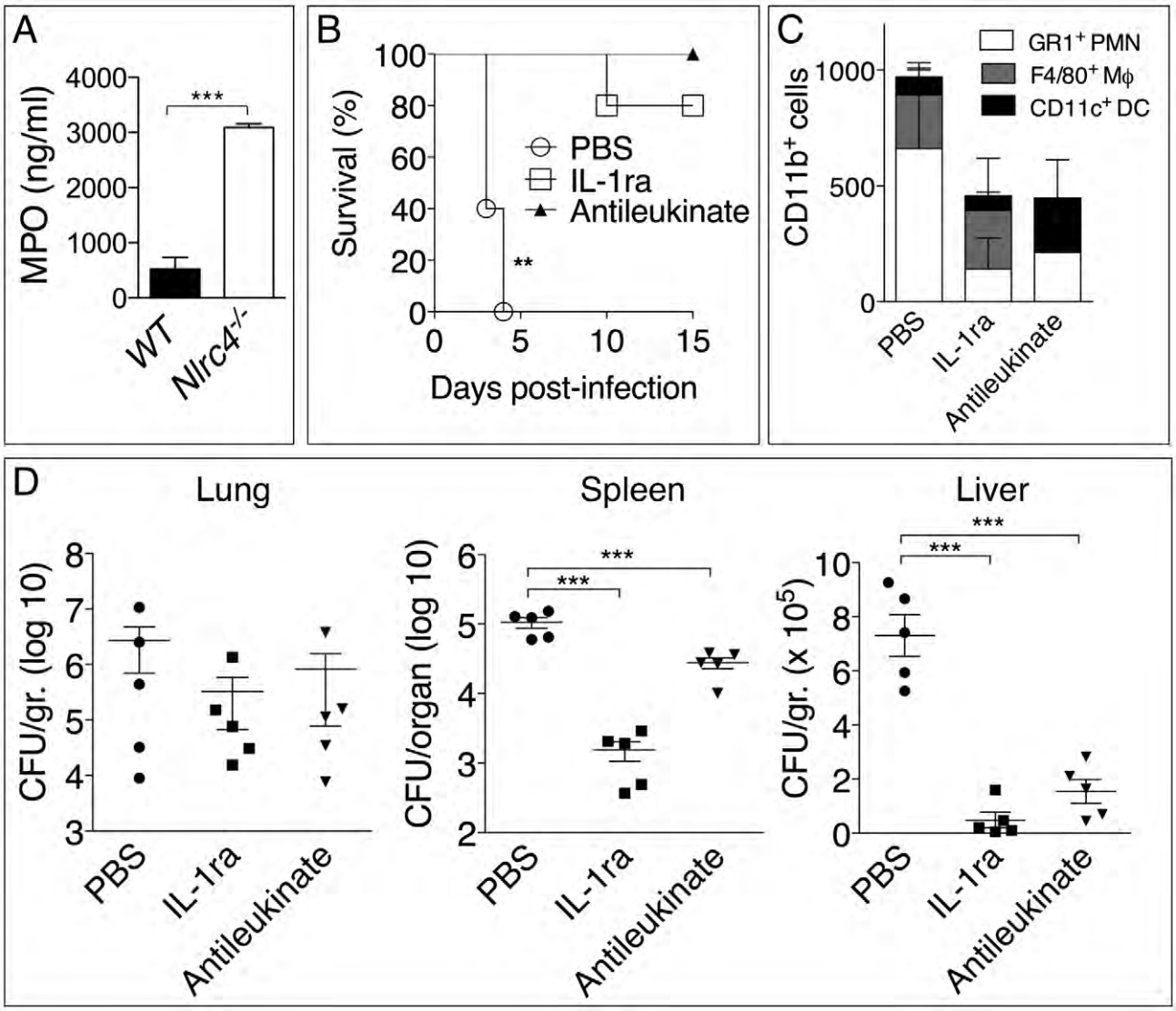

Figure 6. Inhibition of neutrophil recruitment to the lung protects *Nlrc4*$^{-/-}$ mice from melioidosis. (A) Myeloperoxidase was measured in BALF of WT and *Nlrc4*$^{-/-}$ mice. (B) *Nlrc4*$^{-/-}$ mice were infected intranasally with *B. pseudomallei* (25 CFU) and were administered daily injections of PBS or IL-1ra (i.p.) or antileukinate (s.c.). $^{**}p<0.01$, $^{***}p<0.001$ (Kaplan-Meyer). (C) Flow cytometric analysis for myeloid cell composition of BALF obtained from *Nlrc4*$^{-/-}$ mice infected and treated with IL-1ra or antileukinate. (D) *Nlrc4*$^{-/-}$ mice infected and treated with IL-1ra or antileukinate were sacrificed 48 h post-infection and the bacterial burden was measured in organs. $^{*}p<0.05$, $^{**}p<0.01$ (1way ANOVA).
doi:10.1371/journal.ppat.1002452.g006

gene clusters, one of which is similar to the *Salmonella* SP-1 pathogenicity island and has been shown to be an important virulence factor required for escape from the phagosome, induction of IL-1β production, and pathogenicity [13,28]. In addition to mediating host recognition of cytosol-delivered flagellin, NLRC4 also recognizes a structural motif found in the basal body rod components of the T3SS of various bacteria, including *B. pseudomallei* [29]. We have determined (data not shown) that transfection of *B. pseudomallei* flagellin protein into the cytoplasm of BMDC leads to NLRC4-dependent production of IL-1β. This result agrees with previously published evidence and indicates that *B. pseudomallei* (like some other bacteria) expresses multiple factors (e.g. flagellin, basal rods) that are recognized by the NLRC4 inflammasome. The mechanism responsible for NLRP3 activation by *B. pseudomallei* remains unclear.

In addition to controlling IL-1β and IL-18 production, NLRC4 also mediates pyroptosis, a form of cell death that is an effective mechanism to restrict growth and dissemination of intracellular bacteria [3]. Here we showed that *B. pseudomallei*-induced pyroptosis was caspase-1-dependent but ASC-independent, in agreement with works that showed ASC redundancy for pyroptosis induced by other bacteria [16–19]. However, the fact that production of IL-1β in response to *B. pseudomallei* infection is seriously compromised in *Asc*$^{-/-}$ cells indicates that this adaptor molecule plays a critical role in NLRC4-mediated cytokine production and suggests that NLRC4 can form two distinct inflammasomes: one that contains ASC and regulates IL-1β processing, and one devoid of ASC that activates caspase-1 and triggers pyroptosis, as recently proposed [30]. It has been recently shown [4,5] that NAIP molecules determine the specificity of NLRC4 for its activators and, we would further speculate, for its down-stream effector mechanisms. Whether NLRC4 relies on other molecules to recognize *B. pseudomallei* remains to be ascertained. We tested the susceptibility to *B. pseudomallei* of

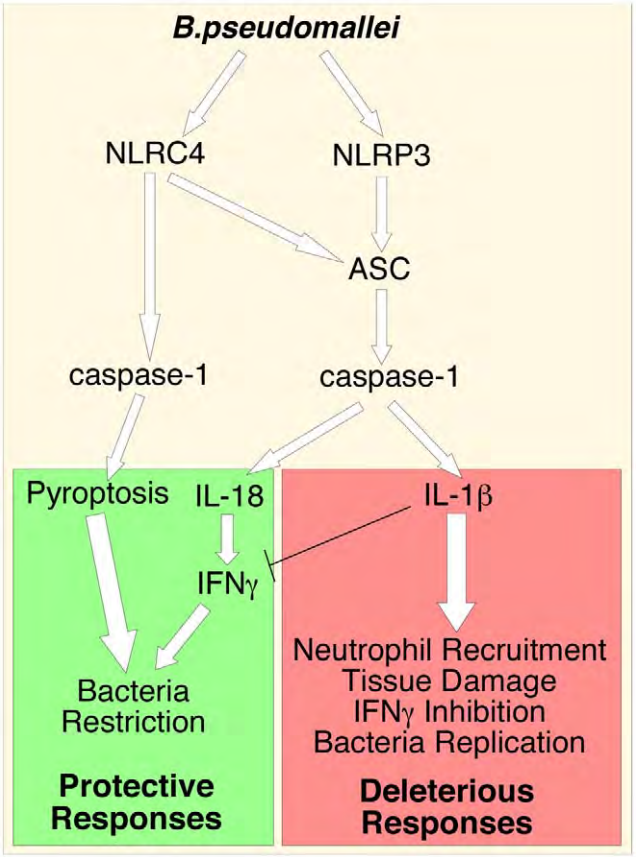

Figure 7. Inflammasomes-dependent protective and deleterious responses activated by *B. pseudomallei*. *B. pseudomallei* induces NLRC4-dependent pyroptosis that restricts intracellular bacterial growth. Activation of NLRP3-inflammasome leads to production of IL-18 and IL-1β. IL-18 is protective because of its induction of IFNγ. IL-1β deleterious role may be due to several reasons including excessive recruitment of neutrophils, which may support intracellular growth of *B. pseudomallei*, tissue damage, and inhibition of IFNγ production.
doi:10.1371/journal.ppat.1002452.g007

C57BL/6J-Chr13$^{A/J}$/NaJ mice, a consomic C57BL/6 strain that carries the A/J NAIP5 allele that renders them susceptible *to Legionella* infection [31-34], and found that they were indistinguishable from WT mice (data not shown).

Analysis of inflammasomes-deficient mice intranasaly infected with *B. pseudomallei* confirmed the importance of ASC, caspase-1, and both NLRP3 and NLRC4 inflammasomes for resistance to melioidosis. However, quite surprisingly, although production of IL-1β and IL-18 *in vitro* is mediated by both NLRP3 and NLRC4, *in vivo* it is exclusively dependent on the NLRP3-ASC-caspase-1 inflammasome (figure 2C). In contrast, *Nlrc4*$^{-/-}$ mice produce these cytokines in amounts that exceed even those detected in WT mice. Remarkably, despite the abundance of IL-1β and IL-18, *Nlrc4*$^{-/-}$ mice were dramatically more susceptible to melioidosis than WT mice, rapidly succumbed to the infection, and had very high organ's bacteria burden and worst neutrophilic lung inflammation. Thus, the critical role of NLRC4 during melioidosis is independent of IL-1β and IL-18 production. Rather, our results suggest that pyroptosis, which we show is defective in *Nlrc4*$^{-/-}$ cells, is a critical NLRC4 effector mechanism to fight *B. pseudomallei* and, in its absence, bacterial replication and IL-1β production proceeds unrestrained causing severe inflammation, morbidity and mortality. Moreover, our analysis indicates that pyroptosis and IL-18 are both required and contribute equally to resistance to melioidosis. Thus, deficiency of either is equally lethal while deficiency of both (*Casp1*$^{-/-}$ mice) further worsens the outcome. It is important to emphasize that our study is the first to demonstrate the importance of pyroptosis in the context of an infection with a clinically relevant human pathogen that has not been genetically manipulated, as opposed to the previous seminal work by Miao et al. [3] that elegantly employed genetically manipulated bacteria and mouse strains to identify pyroptosis as an effective innate immune defence mechanism against bacterial infections. Previous reports have demonstrated activation of both NLRP3 and NLRC4 inflammasomes in response to infection with *Legionella pneumophila* [16], *Listeria monocytogenes* [35], and *Salmonella typhimurium* [36]. However, in those infection models NLRP3 and NLRC4 appeared to play redundant roles while in our model we were able to assign distinct functions to each inflammasome.

A great number of publications have documented the role of IL-18 and IL-1β during infections with a variety of pathogens. Almost invariably, both cytokines were found to have a protective function. Remarkably, our results show that while *Il-18*$^{-/-}$ mice are profoundly vulnerable to melioidosis, as previously shown [37], *Il-1r1*$^{-/-}$ mice were unexpectedly more resistant than WT mice. The protective role of IL-18 during melioidosis appears to be related to its ability to induce IFNγ, as administration of exogenous IFNγ completely rescued the survival of *Il-18*$^{-/-}$ infected mice. IFNγ activates the microbicidal activity of macrophages and has been shown to be important for resistance against infection with many pathogens including *B. pseudomallei* [8–10]. It is interesting and surprising to see that *Asc*$^{-/-}$ and *Nlrp3*$^{-/-}$ mice, which are defective in IL-1β and IL-18 production, are more resistant to *B. pseudomallei* than mice lacking IL-18. It is worth noting that although IL-18 production is drastically reduced in *Asc*$^{-/-}$ and *Nlrp3*$^{-/-}$ mice, it is still detectable in these mice at higher level than uninfected mice. It is conceivable that this inflammasome-independent production of IL-18 may be sufficient to provide some level of protection to *Asc*$^{-/-}$ and *Nlrp3*$^{-/-}$ mice against infection with low *B. pseudomallei* CFU.

Our discovery that *Il-1r1*$^{-/-}$ mice were more resistant than WT to *B. pseudomallei* infection is quite surprising considering that this cytokine has been shown to be protective in several bacterial, viral, and fungal infection models [38]. Studies in humans have also shown that inhibition of the function of IL-1 using the IL-1R antagonist IL-1ra (Kineret) is associated with increased susceptibility to bacterial infection. Infected *Il-1r1*$^{-/-}$ mice had lower BALF levels of proinflammatory cytokines as well as a reduction of neutrophil influx into the lungs, bacterial burdens, and lung pathology. Consistent with a deleterious role of IL-1β in melioidosis, administration of recombinant IL-1β drastically increased mortality, inflammation, pathology, and bacteria burdens while administration of IL-1ra (Kineret) rescued the survival of WT mice infected with a lethal dose of *B. pseudomallei*.

The reason for the detrimental effect of IL-1β during melioidosis is unclear and it is likely that several factors determine this outcome. IL-1β is one of the most powerful proinflammatory cytokines, it affects virtually every organ, and several human pathologies are primarily driven by unrestrained IL-1β production. One possible mechanism to account for IL-1β's deleterious role in melioidosis may be related to its ability to inhibit IFNγ production through the induction of the cycloxigenase COX-2 and release of prostaglandin PGE_2 [39,40]. Our observation that the level of IFNγ, a protective factor against *B. pseudomallei*, was significantly higher in infected *Il-1r1*$^{-/-}$ than WT mice (figure 3C) supports this type of scenario in melioidosis. Interestingly IL-8, a potent neutrophil chemoattractant, was shown to enhance the

intracellular growth and survival of *B. cepacia* in bronchial epithelial cell lines [41]. Whether IL-1β promotes *B. pseudomallei* intracellular replication is not known but our preliminary results indicated that induction of pyroptosis by *B. pseudomallei* was not affected by IL-1β.

IL-1β regulates neutrophil recruitment to inflammatory sites through multiple mechanisms including induction of KC, MIP-2, and IL-17, inflammatory mediators whose expression in our experiments correlated with the presence/absence of IL-1RI-mediated signaling. Excessive PMN recruitment is known to cause tissue damage leading to functional impairment of multiple organs, including the lungs [42,43]. One of the most remarkable observations reported here is that the absence of IL-1 signaling was associated with reduced lung neutrophilic inflammation *but also* lower bacterial burdens in the lungs (figure 3B, 4B). Conversely, IL-1β administration resulted in increased neutrophil recruitment *but also* increased bacterial burdens and systemic dissemination. These results would be consistent with the idea that neutrophils are not very effective at containing *B. pseudomallei* infection and, in fact, may foster its spread despite their strong microbicidal activities. This notion is supported by our observation that human or mouse neutrophils infected with *B. pseudomallei* failed to undergo pyropotosis (figure 5), consistent with the finding that neutrophils do not express NLRC4 [3]. At the same time, intracellular *B. pseudomallei* replication proceeded unaffected in both WT and *Nlrc4*$^{-/-}$ neutrophils in agreement with a report that showed that *B. pseudomallei* is intrinsically resistant to killing by infected PMN [44]. In support for a deleterious role of neutrophils in melioidosis we found that inhibition of their recruitment by administration of IL-1ra or the CXCR2 neutrophil chemokine receptor antagonist antileukinate protected *Nlrc4*$^{-/-}$ mice from infection with low doses of *B. pseudomallei* and decreased systemic spread of bacteria (figure 6).

Taken together our results suggest the following scenario: failure of *Nlrc4*$^{-/-}$ infected macrophages to undergo pyroptosis results in higher bacteria burden and continued production of IL-1β and other factors that attract more inflammatory cells, including neutrophils, perpetuating excessive lung inflammation and promoting bacteria dissemination. It is tempting to speculate that IL-1β promotes *B. pseudomallei* growth possibly by increasing the local pool of infectable permissive cells, including PMN. Our conclusion that neutrophils are a permissive cell type for *B. pseudomallei* replication seems to contrast with a report [45] that indicated that depletion of neutrophils resulted in severe increase in mortality in a model of murine melioidosis. However, caution should be used in the interpretation of these types of experiments because systemic depletion of neutrophils devoids the host not only of their microbicidal function but also of the many immunomodulatory functions these cells exert [46]. Of note, mice deficient in osteopontin, a pleiotropic cytokine that is chemotactic for neutrophils, were shown to be more resistant to *B. pseudomallei* infection [47], supporting our conclusion that neutrophils have a detrimental role in melioidosis.

The notion that excessive inflammation may be detrimental in certain infection models is well accepted. For example, TLR-mediated signaling negatively affects the outcome of infections with West Nile Virus [48] or influenza virus [49]. The fact that IL-1β is deleterious in melioidosis but protective against other lung pathogens like *Klebsiella*, *Francisella*, *Mycobacterium*, Respiratory Syncytial Virus, and influenza virus likely reflects differences between the virulence strategy of *B. pseudomallei* and those other pathogens. The intensity, kinetics, and quality of the inflammatory response elicited by *B. pseudomallei* and its ability to suppress the induction of anti-inflammatory circuitries are phenomena that we are interested to investigate in detail. Despite an extensive literature search we could identify only a single report [26] where IL-1β was shown to be deleterious in bacterial infections. It was demonstrated that this cytokine had a negative effect on bacterial clearance in a model of pneumonia caused by *Pseudomonas aeruginosa*, an organism that shares features with *Burkholderia*, which was in fact previously classified in the *Pseudomonas* genus. Surprisingly, the same group also reported a deleterious role for IL-18 in this type of infection [50], a further indication that each pathogen displays unique virulence strategies. It has been shown that activation of the inflammasome exacerbates inflammation without restricting bacterial growth in a model of *Mycobacterial* infection [51]. That report did not examine the role of IL-1β but other work showed it is protective during tuberculosis [23].

This is the first report that has analyzed in detail the role of the inflammasome during melioidosis. Previous work has implicated caspase-1 [52] and IL-18 [37] in this infectious disease although the pathways that led to their activation were not investigated. Other species of *Burkholderia* have been used as model organisms to study aspects of inflammasome biology. Surprisingly, *B. thailandensis*, which is has been used as a model for melioidosis although it rarely causes disease in humans, was reported to cause similar disease in WT and IL-18- IL-1β-double deficient mice [3] suggesting that species of *Burkholderia* other than *B. pseudomallei* may not be reliable models for melioidosis.

In summary, our work shows that NLRP3 and NLRC4 play non-redundant roles during *B. pseudomallei* infection by differentially regulating pyroptosis and production of IL-1β and IL-18; it demonstrates that pyroptosis is an efficient effector mechanism to restrict *in vivo* bacterial growth and dissemination; it identifies a deleterious role of IL-1β in melioidosis possibly due to excessive recruitment of neutrophils, a cell type that may be permissive to replication of *B. pseudomallei*; and, finally, it indicates that inhibition of IL-1RI-mediated signaling may be a beneficial therapeutical approach for the treatment of melioidosis.

Materials and Methods

Ethics statement

All the animal experiments described in the present study were conducted in strict accordance with the recommendations in the *Guide for the Care and Use of Laboratory Animals* of the National Institutes of Health. All animal studies were conducted under a protocol approved by the University of Tennessee Health Science Center (UTHSC) Institutional Animal Care and Use Committee (IACUC, protocol #1854). All efforts were made to minimize suffering and ensure the highest ethical and humane standards. Research involving human blood is exempt from the human subjects regulations. Human neutrophils and monocytes were isolated from healthy donors Leukopacks obtained from Lifeblood Mid-South Regional Blood Center, Memphis TN. All leukopaks are obtained anonymously. The gender, race, and age of each donor are unknown to the investigators.

Mice

C57BL/6, *Il-1r1*$^{-/-}$, *Il-18*$^{-/-}$, C57BL/6J-Chr13$^{A/J}$/NaJ mice were purchased from Jackson lab. *Il-18*$^{-/-}$-*Il-1r1*$^{-/-}$ double deficient mice (DKO) were obtained by crossing the parental single knock-out mice. *Asc*$^{-/-}$, *Nlrp3*$^{-/-}$, *Nlrc4*$^{-/-}$ (from Vishva Dixit, Genentec) and *Casp1*$^{-/-}$ (from Fayyaz Sutterwala) were bred in our facility. All mouse strains were on C57BL/6 genetic background and were bred under specific pathogen-free conditions. Age-(8–12 weeks old) and sex-matched animals were used in all experiments. Generally, experimental groups were composed of at least 5 mice.

Animal and *in vitro* experiments involving *B. pseudomallei* were performed under biosafety level 3 conditions in accordance with standard operating procedures approved by the Regional Biocontainment Laboratory at UTHSC.

Bacteria, mice infection, and treatments

For all experiment the *B. pseudomallei* 1026b strain (a clinical virulent isolate) was used. Bacteria were grown in Luria broth (Difco) to mid-logarithmic phase, their titer was determined by plating serial dilutions on LB agar, and stocks were maintained frozen at −80°C in 20% glycerol. No loss in viability was observed over prolonged storage. For infections, frozen stocks were diluted in sterile PBS to the desired titer. Aliquots were plated on LB agar to confirm actual CFU. Mice were anesthetized with isoflurane using a Surgivet apparatus and 50 µl of bacteria suspension were applied to the nares. In some experiments, mice were injected i.p. daily with recombinant mouse IL-1β (1 µg) or IFNγ (1 µg). IL-1ra (Biovitrum) was administered by alternating s.c. and i.p. injections every 12 hours (60 mg/kg body weight). Antileukinate (American Peptide Company) was administered by s.c. injection (8 mg/kg body weight).

Generation of mouse BMDM and BMDC

Mouse macrophages or dendritic cells were generated by incubating bone marrow cells in RPMI 1640-10%FCS supplemented with either rmM-CSF or rmGM-CSF (20 ng/ml) for 8 days, respectively.

Isolation of mouse neutrophils

Neutrophils and monocytic cells were isolated from the bone marrow cells of WT or *Nlrc4*$^{-/-}$ mice using Miltenyi Ly6G microbeads. Flow-through cells, consisting mostly of monocytic cells, were further purified using Miltenyi CD11b microbeads.

Isolation of human neutrophils and monocytes

Human neutrophils and monocytes were isolated from healthy donors Leukopacks obtained from Lifeblood Mid-South Regional Blood Center, Memphis TN. Blood was mixed with Isolymph (CTL Scientific Supply Corp.) (5:1 ratio) and RBC were allowed to sediment for 60 min at RT. The leukocytes-enriched supernatant was washed, resuspended in PBS, and stratified over Isolymph cushion and centrifuged at 1,350 rpm for 40 min. The cell pellet containing RBC and neutrophils was treated with 0.2% NaCl for 30 seconds to lyse RBC and immediatedly treated with an equal volume of 1.6% NaCl. The PBMC containing ring from the Isolymph centrifugation step was collected, washed, and monocytes were purified using CD14 microbeads (Miltenyi). The procedure routinely yield populations of purity greater than 95%.

Pyroptosis and intracellular bacteria growth (kanamycin protection assay)

Release of LDH in tissue culture media, a reflection of pyroptosis, was measured using the Roche Cytotox detection kit. BMDM, PMN, or monocytes (5×10^5 cells) were plated in 24 well plates. Bacteria at different MOI were added to the cell culture and the plates were centrifuged at 1500 rpm for 10 minutes to maximize and synchronize infection and incubated for 30 minutes at 37°C. Cells were washed with PBS to remove extracellular bacteria and medium containing kanamycin (200 µg/ml) was added to inhibit extracellular bacteria growth. Media were collected at 1, 2, 4, 8, 12 hours post infection for LDH measurement. Cells were lysed in PBS-2% saponin-15% BSA and serial dilutions of the lysates were plated on LB agar plates containing streptomycin (100 µg/ml) using the Eddy Jet Spiral Plater (Neutec). Bacterial colonies were counted 48 hours later using the Flash & Grow Automated Bacterial Colony Counter (Neutec).

Determination of bacteria growth in tissue culture and organs

Organs aseptically collected were weighted and homogenized in 1 ml PBS using 1 mm zirconium beads and the Mini16 bead beater. Serial dilutions were plated as described above.

Western blot

Conditioned supernatants were separated by 12% PAGE electrophoresis, transferred to PVDF membranes, and probed with rabbit anti-caspase-1 (Upstate Biotechnologies) or goat anti-mIL-1β (R&D Systems).

BALF collection and cytokines measurements

BALF were collected from euthanized mice by intratracheal injection and aspiration of 1 ml PBS. Cytokines levels in tissue culture conditioned supernatants and BALF were measured using the Milliplex mouse cytokine/chemokine panel (Millipore) and confirmed by ELISA using the following paired antibodies kits: mIL-1β and mIFNγ (eBioscience), mIL-18 (MBL Nagoya, Japan). MPO level in BALF were measured using the HyCult Biotech ELISA kit.

Flow cytometry

Cells obtained from BALF were counted and stained with CD45, CD11b, CD11c, F4/80, GR1 (Ly6G), and analyzed with a LSRII BD flow cytometer.

Histology and measurement of area of inflammatory foci

Formalin-fixed paraffin-embedded lung sections were stained with H&E and scanned using the Aperio Scanscope XT. The Aperio ImageScope software was used to quantitate the area of the inflammatory foci compared to the total lung lobe area. Results from lungs from 5 animals per group were combined.

RT-PCR

Total RNA was extracted using Trizol (Invitrogen) and 100 ng were amplified (27 cycles) using Superscript III One-step RT-PCR (Invitrogen) and primers specific for human Nlrc4, Nlrp3, Asc, and GAPDH (primers' sequence available upon request).

Statistical analysis

All data were expressed as mean ± S.E.M. Survival curves were compared using the log rank Kaplan-Meier test. 1way ANOVA and Tukey Post-test was used for analysis of the rest of data unless specified in the figure legends. Significance was set at $p<0.05$. Statistical analyses were performed using the GraphPad Prism 5.0.

Accession numbers

UniProtKB/Swiss-Prot ID: IL-1β, P10749; IL-1R1, P13504; IL-18, P70380; NLRP3, Q8R4B8; NLRC4, Q3UP24; ASC, Q9EPB4; Casp-1, P29452; NAIP5, Q8CGT2.

Supporting Information

Figure S1 NLRP3 and NLRC4 differentially regulate production of IL-1β and IL-18 and pyroptosis. BMDC were infected with *B. pseudomallei* at MOI of 10. (A) Secretion of mature IL-1β was measured in conditioned supernatants at the

indicated times. (B) Processing of IL-1β and caspase-1 were detected by immunoblot in 8h conditioned supernatants from A. (C) BMDC infected with *B. pseudomallei* (MOI 10) were lysed at the indicated time points after infection and intracellular bacterial growth was quantitated (upper panel). Induction of pyroptosis was measured as LDH release in conditioned supernatants (lower panel). One experiment representative of four (A) or three (C) is shown. *$p<0.05$, **$p<0.01$, ***$p<0.001$ (1way ANOVA).
(TIF)

Figure S2 Cytokines and chemokines were measured in BALF obtained from the indicated mouse strains 48 hours or 72 hours post-infection, as shown. *$p<0.05$, **$p<0.01$, ***$p<0.001$ (1way ANOVA).
(TIF)

Figure S3 Myeloperoxidase (MPO) was measured in BALF of the indicated mouse strains corresponding to the experiments of figures 3B, 4F, and 6D. *p<0.05, **p<0.01, ***p<0.001 (1way ANOVA).
(TIF)

Acknowledgments

The authors wish to thank Jennifer Stabenow and Lilian Zalduondo at the UTHSC Regional Biocontainment Laboratory for help and training on biocontainment techniques and Hossam Abdelsamed for flow cytometry analysis.

Author Contributions

Conceived and designed the experiments: FR. Performed the experiments: ICO MS MAM LdB FR. Analyzed the data: ICO MS MAM LdB FR. Wrote the paper: FR.

References

1. Davis BK, Wen H, Ting JP (2011) The inflammasome NLRs in immunity, inflammation, and associated diseases. Annu Rev Immunol 29: 707–735.
2. Brodsky IE, Medzhitov R (2011) Pyroptosis: macrophage suicide exposes hidden invaders. Curr Biol 21: R72–75.
3. Miao EA, Leaf IA, Treuting PM, Mao DP, Dors M, et al. (2010) Caspase-1-induced pyroptosis is an innate immune effector mechanism against intracellular bacteria. Nat Immunol 11: 1136–1142.
4. Kofoed EM, Vance RE (2011) Innate immune recognition of bacterial ligands by NAIPs determines inflammasome specificity. Nature 477: 592–595.
5. Zhao Y, Yang J, Shi J, Gong YN, Lu Q, et al. (2011) The NLRC4 inflammasome receptors for bacterial flagellin and type III secretion apparatus. Nature 477: 596–600.
6. Cheng AC, Currie BJ (2005) Melioidosis: epidemiology, pathophysiology, and management. Clin Microbiol Rev 18: 383–416.
7. Wiersinga WJ, van der Poll T, White NJ, Day NP, Peacock SJ (2006) Melioidosis: insights into the pathogenicity of Burkholderia pseudomallei. Nat Rev Microbiol 4: 272–282.
8. Miyagi K, Kawakami K, Saito A (1997) Role of reactive nitrogen and oxygen intermediates in gamma interferon-stimulated murine macrophage bactericidal activity against Burkholderia pseudomallei. Infect Immun 65: 4108–4113.
9. Santanirand P, Harley VS, Dance DA, Raynes JG, Drasar BS, et al. (1997) Interferon-gamma mediates host resistance in a murine model of melioidosis. Biochem Soc Trans 25: 287S.
10. Jones AL, Beveridge TJ, Woods DE (1996) Intracellular survival of Burkholderia pseudomallei. Infect Immun 64: 782–790.
11. Reckseidler SL, DeShazer D, Sokol PA, Woods DE (2001) Detection of bacterial virulence genes by subtractive hybridization: identification of capsular polysaccharide of Burkholderia pseudomallei as a major virulence determinant. Infect Immun 69: 34–44.
12. DeShazer D, Brett PJ, Woods DE (1998) The type II O-antigenic polysaccharide moiety of Burkholderia pseudomallei lipopolysaccharide is required for serum resistance and virulence. Mol Microbiol 30: 1081–1100.
13. Warawa J, Woods DE (2005) Type III secretion system cluster 3 is required for maximal virulence of Burkholderia pseudomallei in a hamster infection model. FEMS Microbiol Lett 242: 101–108.
14. Liu B, Koo GC, Yap EH, Chua KL, Gan YH (2002) Model of differential susceptibility to mucosal Burkholderia pseudomallei infection. Infect Immun 70: 504–511.
15. Hoppe I, Brenneke B, Rohde M, Kreft A, Haussler S, et al. (1999) Characterization of a murine model of melioidosis: comparison of different strains of mice. Infect Immun 67: 2891–2900.
16. Case CL, Shin S, Roy CR (2009) Asc and Ipaf Inflammasomes direct distinct pathways for caspase-1 activation in response to Legionella pneumophila. Infect Immun 77: 1981–1991.
17. Mariathasan S, Newton K, Monack DM, Vucic D, French DM, et al. (2004) Differential activation of the inflammasome by caspase-1 adaptors ASC and Ipaf. Nature 430: 213–218.
18. Suzuki T, Franchi L, Toma C, Ashida H, Ogawa M, et al. (2007) Differential regulation of caspase-1 activation, pyroptosis, and autophagy via Ipaf and ASC in Shigella-infected macrophages. PLoS Pathog 3: e111.
19. Franchi L, Stoolman J, Kanneganti TD, Verma A, Ramphal R, et al. (2007) Critical role for Ipaf in Pseudomonas aeruginosa-induced caspase-1 activation. Eur J Immunol 37: 3030–3039.
20. Fantuzzi G, Ku G, Harding MW, Livingston DJ, Sipe JD, et al. (1997) Response to local inflammation of IL-1 beta-converting enzyme- deficient mice. J Immunol 158: 1818–1824.
21. Coeshott C, Ohnemus C, Pilyavskaya A, Ross S, Wieczorek M, et al. (1999) Converting enzyme-independent release of tumor necrosis factor alpha and IL-1beta from a stimulated human monocytic cell line in the presence of activated neutrophils or purified proteinase 3. Proc Natl Acad Sci U S A 96: 6261–6266.
22. Guma M, Ronacher L, Liu-Bryan R, Takai S, Karin M, et al. (2009) Caspase 1-independent activation of interleukin-1beta in neutrophil-predominant inflammation. Arthritis Rheum 60: 3642–3650.
23. Mayer-Barber KD, Barber DL, Shenderov K, White SD, Wilson MS, et al. (2010) Caspase-1 independent IL-1beta production is critical for host resistance to mycobacterium tuberculosis and does not require TLR signaling in vivo. J Immunol 184: 3326–3330.
24. Maus U, von Grote K, Kuziel WA, Mack M, Miller EJ, et al. (2002) The role of CC chemokine receptor 2 in alveolar monocyte and neutrophil immigration in intact mice. Am J Respir Crit Care Med 166: 268–273.
25. Hayashi S, Yatsunami J, Fukuno Y, Kawashima M, Miller EJ (2002) Antileukinate, a hexapeptide inhibitor of CXC-chemokine receptor, suppresses bleomycin-induced acute lung injury in mice. Lung 180: 339–348.
26. Schultz MJ, Rijneveld AW, Florquin S, Edwards CK, Dinarello CA, et al. (2002) Role of interleukin-1 in the pulmonary immune response during Pseudomonas aeruginosa pneumonia. Am J Physiol Lung Cell Mol Physiol 282: L285–290.
27. Nathan C, Ding A (2010) Nonresolving inflammation. Cell 140: 871–882.
28. Burtnick MN, Brett PJ, Nair V, Warawa JM, Woods DE, et al. (2008) Burkholderia pseudomallei type III secretion system mutants exhibit delayed vacuolar escape phenotypes in RAW 264.7 murine macrophages. Infect Immun 76: 2991–3000.
29. Miao EA, Mao DP, Yudkovsky N, Bonneau R, Lorang CG, et al. (2010) Innate immune detection of the type III secretion apparatus through the NLRC4 inflammasome. Proc Natl Acad Sci U S A 107: 3076–3080.
30. Broz P, von Moltke J, Jones JW, Vance RE, Monack DM (2010) Differential requirement for Caspase-1 autoproteolysis in pathogen-induced cell death and cytokine processing. Cell Host Microbe 8: 471–483.
31. Ren T, Zamboni DS, Roy CR, Dietrich WF, Vance RE (2006) Flagellin-deficient Legionella mutants evade caspase-1- and Naip5-mediated macrophage immunity. PLoS Pathog 2: e18.
32. Molofsky AB, Byrne BG, Whitfield NN, Madigan CA, Fuse ET, et al. (2006) Cytosolic recognition of flagellin by mouse macrophages restricts Legionella pneumophila infection. J Exp Med 203: 1093–1104.
33. Lightfield KL, Persson J, Trinidad NJ, Brubaker SW, Kofoed EM, et al. (2011) Differential requirements for NAIP5 in activation of the NLRC4 inflammasome. Infect Immun 79: 1606–1614.
34. Zamboni DS, Kobayashi KS, Kohlsdorf T, Ogura Y, Long EM, et al. (2006) The Birc1e cytosolic pattern-recognition receptor contributes to the detection and control of Legionella pneumophila infection. Nat Immunol 7: 318–325.
35. Warren SE, Mao DP, Rodriguez AE, Miao EA, Aderem A (2008) Multiple Nod-like receptors activate caspase 1 during Listeria monocytogenes infection. J Immunol 180: 7558–7564.
36. Broz P, Newton K, Lamkanfi M, Mariathasan S, Dixit VM, et al. (2010) Redundant roles for inflammasome receptors NLRP3 and NLRC4 in host defense against Salmonella. J Exp Med 207: 1745–1755.
37. Wiersinga WJ, Wieland CW, van der Windt GJ, de Boer A, Florquin S, et al. (2007) Endogenous interleukin-18 improves the early antimicrobial host response in severe melioidosis. Infect Immun 75: 3739–3746.
38. Dinarello CA (2009) Immunological and inflammatory functions of the interleukin-1 family. Annu Rev Immunol 27: 519–550.
39. Lemos HP, Grespan R, Vieira SM, Cunha TM, Verri WA, Jr., et al. (2009) Prostaglandin mediates IL-23/IL-17-induced neutrophil migration in inflammation by inhibiting IL-12 and IFNgamma production. Proc Natl Acad Sci U S A 106: 5954–5959.
40. Lee JK, Kim SH, Lewis EC, Azam T, Reznikov LL, et al. (2004) Differences in signaling pathways by IL-1beta and IL-18. Proc Natl Acad Sci U S A 101: 8815–8820.

41. Kaza SK, McClean S, Callaghan M (2008) IL-8 released from human lung epithelial cells induced by cystic fibrosis pathogens Burkholderia cepacia complex affects the growth and intracellular survival of bacteria. Int J Med Microbiol 301: 26–33.
42. Abraham E (2003) Neutrophils and acute lung injury. Crit Care Med 31: S195–199.
43. Zemans RL, Colgan SP, Downey GP (2009) Transepithelial migration of neutrophils: mechanisms and implications for acute lung injury. Am J Respir Cell Mol Biol 40: 519–535.
44. Chanchamroen S, Kewcharoenwong C, Susaengrat W, Ato M, Lertmemongkolchai G (2009) Human polymorphonuclear neutrophil responses to Burkholderia pseudomallei in healthy and diabetic subjects. Infect Immun 77: 456–463.
45. Easton A, Haque A, Chu K, Lukaszewski R, Bancroft GJ (2007) A critical role for neutrophils in resistance to experimental infection with Burkholderia pseudomallei. J Infect Dis 195: 99–107.
46. Cassatella MA, Locati M, Mantovani A (2009) Never underestimate the power of a neutrophil. Immunity 31: 698–700.
47. van der Windt GJ, Wiersinga WJ, Wieland CW, Tjia IC, Day NP, et al. (2010) Osteopontin impairs host defense during established gram-negative sepsis caused by Burkholderia pseudomallei (melioidosis). PLoS Negl Trop Dis: 4 pii. pp e806.
48. Wang T, Town T, Alexopoulou L, Anderson JF, Fikrig E, et al. (2004) Toll-like receptor 3 mediates West Nile virus entry into the brain causing lethal encephalitis. Nat Med 10: 1366–1373.
49. Le Goffic R, Balloy V, Lagranderie M, Alexopoulou L, Escriou N, et al. (2006) Detrimental contribution of the Toll-like receptor (TLR)3 to influenza A virus-induced acute pneumonia. PLoS Pathog 2: e53.
50. Schultz MJ, Knapp S, Florquin S, Pater J, Takeda K, et al. (2003) Interleukin-18 impairs the pulmonary host response to Pseudomonas aeruginosa. Infect Immun 71: 1630–1634.
51. Carlsson F, Kim J, Dumitru C, Barck KH, Carano RA, et al. (2010) Host-detrimental role of Esx-1-mediated inflammasome activation in mycobacterial infection. PLoS Pathog 6: e1000895.
52. Breitbach K, Sun GW, Kohler J, Eske K, Wongprompitak P, et al. (2009) Caspase-1 mediates resistance in murine melioidosis. Infect Immun 77: 1589–1595.

OPEN ACCESS Freely available online

PLoS one

Coronavirus Papain-like Proteases Negatively Regulate Antiviral Innate Immune Response through Disruption of STING-Mediated Signaling

Li Sun[1☯], Yaling Xing[1☯], Xiaojuan Chen[1], Yang Zheng[1], Yudong Yang[1], Daniel B. Nichols[2], Mark A. Clementz[2], Bridget S. Banach[2], Kui Li[3], Susan C. Baker[2]*, Zhongbin Chen[1]*

1 Division of Infection and Immunity, Department of Electromagnetic and Laser Biology, Beijing Institute of Radiation Medicine, Beijing, China, **2** Department of Microbiology and Immunology, Loyola University of Chicago Stritch School of Medicine, Maywood, Illinois, United States of America, **3** Department of Microbiology, Immunology and Biochemistry, University of Tennessee Health Science Center, Memphis, Tennessee, United States of America

Abstract

Viruses have evolved elaborate mechanisms to evade or inactivate the complex system of sensors and signaling molecules that make up the host innate immune response. Here we show that human coronavirus (HCoV) NL63 and severe acute respiratory syndrome (SARS) CoV papain-like proteases (PLP) antagonize innate immune signaling mediated by STING (stimulator of interferon genes, also known as MITA/ERIS/MYPS). STING resides in the endoplasmic reticulum and upon activation, forms dimers which assemble with MAVS, TBK-1 and IKKε, leading to IRF-3 activation and subsequent induction of interferon (IFN). We found that expression of the membrane anchored PLP domain from human HCoV-NL63 (PLP2-TM) or SARS-CoV (PLpro-TM) inhibits STING-mediated activation of IRF-3 nuclear translocation and induction of IRF-3 dependent promoters. Both catalytically active and inactive forms of CoV PLPs co-immunoprecipitated with STING, and viral replicase proteins co-localize with STING in HCoV-NL63-infected cells. Ectopic expression of catalytically active PLP2-TM blocks STING dimer formation and negatively regulates assembly of STING-MAVS-TBK1/IKKε complexes required for activation of IRF-3. STING dimerization was also substantially reduced in cells infected with SARS-CoV. Furthermore, the level of ubiquitinated forms of STING, RIG-I, TBK1 and IRF-3 are reduced in cells expressing wild type or catalytic mutants of PLP2-TM, likely contributing to disruption of signaling required for IFN induction. These results describe a new mechanism used by CoVs in which CoV PLPs negatively regulate antiviral defenses by disrupting the STING-mediated IFN induction.

Citation: Sun L, Xing Y, Chen X, Zheng Y, Yang Y, et al. (2012) Coronavirus Papain-like Proteases Negatively Regulate Antiviral Innate Immune Response through Disruption of STING-Mediated Signaling. PLoS ONE 7(2): e30802. doi:10.1371/journal.pone.0030802

Editor: Karen L. Mossman, McMaster University, Canada

Received November 11, 2011; **Accepted** December 21, 2011; **Published** February 1, 2012

Funding: National Natural Science Foundation of China (No. 30972761, No. 30870536, No. 81172799 to ZC), Beijing Natural Science Foundation (No. 7092075 to ZC) and National S&T Major Project (2008ZX10004-015 to ZC) and Chinese National High-Tech R&D Program ("863" Program) (2006AA02Z412 to ZC), and the National Institutes of Health, USA (AI060915 to SCB), and the U.S. Department of Defense (W81XWH-09-01-0391 to KL). The funders had no role in study design, data collection and analysis, decision to publish, or preparation of the manuscript.

Competing Interests: The authors have declared that no competing interests exist.

* E-mail: chenzb@bmi.ac.cn (ZC); sbaker1@lumc.edu (SCB)

☯ These authors contributed equally to this work.

Introduction

The innate immune system is the first line of defense that protects the host against viral infection. Viral infections are sensed by pattern-recognition receptors (PRRs) of the innate immune system that recognize pathogen-associated molecular patterns (PAMPs) and then trigger an antiviral response [1]. Viral nucleic acids, such as the viral genome or replicative intermediates produced during viral replication, can be recognized by toll-like receptors (TLR3/7/8/9) or the retinoid acid-inducible gene (RIG)-I-like helicase (RLH) family members RIG-I and melanoma differentiation-associated protein 5 (MDA-5) [2,3]. Viral double stranded RNA can be sensed by membrane bound TLRs or cytosolic sensors like MDA-5, whereas RIG-I detects intracellular viral RNAs bearing 5′-triphosphate ends with base-paired structures to activate antiviral signaling [4–7]. Upon engagement with viral RNA, these PRRs recruit different adaptor proteins (MAVS/IPS-1/VISA/Cardif for RIG-I, and TRIF for TLR3 and MyD88 for TLR7/8/9), and transduce signals to the downstream kinase complexes which activate IFN regulatory factor-3 (IRF-3), nuclear factor κB (NF-κB) and ATF-2/c-jun. These transcription factors coordinately regulate the expression of type I Interferons (IFN-β and -α). Type I IFNs induce the activation of STAT transcription factors that induce the expression of hundreds of IFN-stimulated genes (ISGs) which establish an antiviral state in surrounding cells, thereby limiting viral replication and spread.

Recent investigations into the induction of the type I IFN response identified a new player in the pathway, designated here as STING (stimulator of interferon genes; also called MITA, ERIS and MPYS) [8–11]. STING was identified by investigators screening cDNA libraries for genes that, when overexpressed, were sufficient to activate production of IFN. Further studies revealed that STING-knockout mice are susceptible to lethal infection with herpes simplex virus 1 and vesicular stomatitis virus, demonstrating the critical role of STING in facilitating immune

responses to viral pathogens [12]. STING, with four transmembrane domains in the N-terminal region, is detected in the endoplasmic reticulum (ER) and upon activation complexes with signaling components including TBK1, leading to phosphorylation of IRF-3 [8]. In addition, activation of STING induces its dimerization and ubiquitination, which are proposed to play important roles in the activation of IRF-3 signaling [9].

Coronaviruses (CoV) are positive strand RNA viruses that replicate in the cytoplasm of infected cells and produce a nested-set of double-stranded RNA intermediates during viral RNA synthesis [13]. Despite the generation of dsRNA intermediates, CoV infection generally does not induce high levels of IFN production [14–18]. The new-emerging and most pathogenic CoV, severe acute respiratory syndrome coronavirus (SARS-CoV) inhibits the induction of IFN-β through blocking translocation of the transcription factor interferon regulatory factor 3 (IRF-3) from the cytoplasm to the nucleus at a later time point in infection [15]. However, activation of innate immunity in specific cell types is likely essential for generating a protective immune response. Studies using knockout mice or siRNA treatment of cell lines indicate that PRR TLR-7 in plasmacytoid dendridric cells [19]; MDA5 in brain macrophages [20], MDA5 and RIG-I in oligodendrocytes [21], and the adapter protein MyD88 are critical for activation of the innate response and protection from lethal coronavirus infection [22]. These studies are consistent with the idea that coronavirus infection induces a type I interferon response in a subset of cells and that the ability to mount an effective innate immune response is essential for clearing the viral infection and generating protective immunity. Furthermore, recent studies indicate that the inefficient activation of the innate immune response may contribute to development of more severe disease [23], [24]. At least two mechanisms have been proposed to explain the low level of type I interferon response to coronavirus infection: the sequestering of viral RNA in double membrane vesicles [25], [26] which prevents or reduces recognition by PRRs; and/or the expression of viral proteins that antagonize the innate response (reviewed in [13]). The most pathogenic CoV, severe acute respiratory syndrome coronavirus (SARS-CoV), which resulted in a 10% mortality rate, encodes at least 6 innate immune antagonists, including nonstructural protein 1 (nsp1) [27], the papain-like protease domain in nsp3 [17], nucleocapsid protein [28,30], membrane protein [29] and the products of open reading frame 6 (ORF6) and ORF3b [30]. Another important human CoV is NL63, which causes croup in children and is associated with pneumonia in the elderly [31]. HCoV-NL63 also encodes a papain-like protease, termed PLP2, which antagonizes IFN induction [14]. These coronavirus papain-like protease domains (PLPs) are contained within the nonstructural protein 3 (nsp3), which is expressed as part of a replicase polyprotein. The PLPs along with a 3C-like protease (3CLpro) cleave the replicase polyprotein to generate nonstructural proteins (nsp's) that associate with ER membranes to generate convoluted membranes and double membrane vesicles (DMVs), which are the site of viral replication [25,26]. The CoV PLPs are tethered to the DMVs by a transmembrane domain (Figure 1A). Analysis of enzymatic activity and structural studies revealed that SARS-CoV PLpro and HCoV-NL63 PLP2 function as both proteases and deubiquitinating (DUB) enzymes [14,32–35]. Initially, we speculated that CoV PLPs may act as IFN antagonists via their protease or DUB activities, however we found that both catalytic dependent and catalytic independent mechanisms contribute to PLP-mediated IFN antagonism [14,17]. Our previous studies indicated that SARS-CoV PLpro inhibits host antiviral innate immune response by inhibiting phosphorylation, dimerization and nuclear translocation of IRF-3, likely by forming a complex with IRF-3 [17]. However, the precise mechanism by which CoV PLPs inhibit IRF-3 activation is still unclear. In this work, we demonstrate that CoV PLPs antagonize IRF-3 signaling by targeting the IRF-3 scaffolding protein STING for inhibition. We also characterize both catalytic-dependent and catalytic-independent roles for PLPs in blocking the activation of IFN response.

Results

CoV PLPs antagonize STING-mediated activation of IRF-3

To determine if CoV PLPs are capable of blocking STING-mediated activation of an IRF-3 dependent promoter [36,37], we assessed the level of IFN stimulated response element reporter (ISRE-Luc) activity in the presence of STING with increasing amounts of coronavirus PLPs. Stimulation of HEK-293T cells with STING alone resulted in greater than 20-fold increase in activity of the ISRE-dependent reporter. Co-expression of STING with wild-type PLP2-TM or PLpro-TM resulted in a dose dependent decrease in ISRE activity indicating that these PLPs can antagonize STING-mediated activation of an IRF-3 dependent promoter (Fig. 1 B and C and supporting information (SI) Fig. S1). To determine if this antagonism is dependent on PLP catalytic activity, cells were co-transfected with plasmid DNA expressing STING and catalytic cysteine mutants of either PLP2-TM or PLpro-TM. Consistent with previous studies, CoV PLP catalytic mutants also act as antagonists, although they are less effective than wild-type PLPs in antagonizing the IFN response [14,17]. The effect of PLP2-TM on STING-mediated activation was also visualized using confocal microscopy. HEK-293T cells were transfected with STING-HA in the absence or presence of PLP2-TM and the localization of IRF-3 was monitored by immunofluorescence assay. In cells expressing STING-HA, IRF-3 translocates to the nucleus. However, in cells co-expressing PLP2-TM, IRF-3 remains in the cytoplasm (Fig. 1D). In addition, STING-HA and PLP2-TM co-localize in the cytoplasm of transfected cells. These results indicate that CoV PLPs antagonize STING-mediated activation of IRF-3.

CoV PLPs associate with STING

One possible mechanism for HCoV PLPs antagonism of STING-mediated activation of IFN is to associate with STING, either directly or as part of a multi-protein complex. Co-immunoprecipitation experiments were performed to determine if CoV PLPs associate with STING. HEK-293T cells were co-transfected with plasmid DNA expressing an epitope tagged version of STING (STING-Flag) in the presence or absence of PLP2-TM and cell lysates were subjected to immunoprecipitation with anti-Flag antibody. The products of the immunoprecipitation were separated by SDS-PAGE and visualized by immunoblotting (Fig. 2A). The results show that both NL63 wild-type and catalytic mutant PLPs are detected in association with STING. Similar co-immunoprecipitation results were obtained using PLpro-TM (Fig. S2) Next, we wanted to determine if STING is sequestered in HCoV-NL63-infected cells. HEK293-ACE2 cells, which express angiotensin-converting enzyme 2 (ACE2), a key receptor for SARS and NL63 coronaviruses, were transfected with STING-V5, infected with HCoV-NL63 and analyzed by confocal microscopy at 24 hrs postinfection. HCoV-NL63 replicase protein nsp3 which contains the PLP2-TM region is detected as punctate, perinuclear staining in virus-infected cells [35,38]. Interestingly, we detected partial co-localization of STING and nsp3 in virus-infected cells suggesting that STING may be sequestered in the viral replication

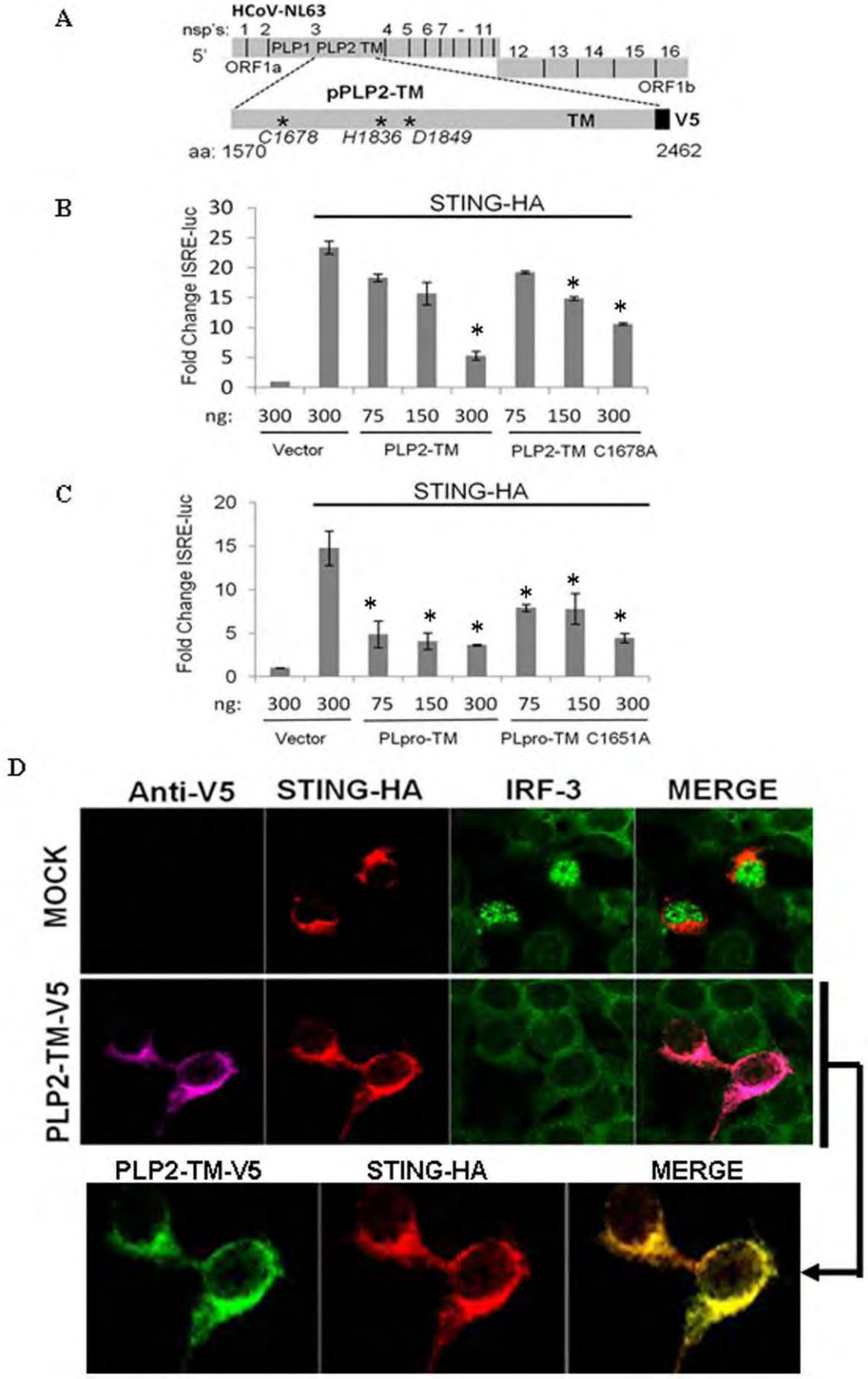
A
HCoV-NL63
nsp's: 1 2 3 4 5 6 7 - 11 12 13 14 15 16
5'
PLP1 PLP2 TM
ORF1a
ORF1b
pPLP2-TM
TM
V5
C1678 H1836 D1849
aa: 1570
2462
B
STING-HA
Fold Change ISRE-luc
30
25
20
15
10
5
0
ng: 300 300 75 150 300 75 150 300
Vector
PLP2-TM
PLP2-TM C1678A
C
STING-HA
Fold Change ISRE-luc
20
15
10
5
0
ng: 300 300 75 150 300 75 150 300
Vector
PLpro-TM
PLpro-TM C1651A
D
Anti-V5
STING-HA
IRF-3
MERGE
MOCK
PLP2-TM-V5
PLP2-TM-V5
STING-HA
MERGE

Figure 1. Expression of coronavirus PLPs blocks STING-mediated activation of the interferon stimulated response element (ISRE). (**A**) Schematic diagram of human coronaviruses (HCoV) NL63 illustrating the processing of replicase polyproteins to generate nonstructural proteins (nsp's). The papain-like protease domains, the catalytic residues that essential for protease catalytic activity [35], and the transmembrane (TM) domain within nsp3 are indicated. (**B** and **C**) HEK293T cells were transfected with the STING-HA, ISRE-luc reporter and either wild-type or catalytic mutants of HCoV-NL63 PLP2-TM or SARS-CoV PLpro-TM. Asterisks indicate statistical significance ($P<0.05$) in comparison with ISRE-reporter activity stimulated with STING. (**D**) Immunofluorescence microscopy of HEK-293T cells expressing STING-HA and PLP2-TM-V5. Cells were fixed at 24 hrs post-transfection and the localization of endogenous IRF-3 (anti-IRF-3, green) and the epitope-tagged products was visualized by confocal microscopy.
doi:10.1371/journal.pone.0030802.g001

complex and unable to mediate signaling (Fig. 2B). These results indicate that these CoV PLPs associate with STING either directly or as part of a multi-protein complex.

STING dimerization is reduced in the presence of CoV PLPs

Recent studies indicate that activation of the innate immune response signaling pathway induces dimerization and phosphorylation of STING, which are required for activation of the IFN response [9]. STING dimers can be visualized as a band at 80 kDa when resolved on SDS-PAGE [9]. We hypothesize that PLPs inhibit STING-mediated signaling through the disruption of assembly or stability of STING dimers. To test this hypothesis, cells were co-transfected with plasmid DNA expressing STING-Flag in the presence or absence of PLP2-TM and Sendai virus (SeV), and cell lysates were evaluated for STING dimers by immunoblotting with anti-Flag (Figure 3A). We detected STING dimers in STING-transfected and SeV-infected cells (Fig. 3A, lanes 2 and 4). In contrast, STING dimers were reduced in cells co-expressing PLP2-TM (Fig. 3A, lanes 3 and 5). Similar results were obtained when we evaluated PLpro-TM for disruption of STING dimers (Fig. S3), indicating that these CoV PLPs either prevent assembly or promote dissociation of STING dimers. A similar reduction in STING dimers was seen in cells transfected with STING-HA and infected with SARS-CoV (Fig. 3B, lane 2). In contract, STING dimers were not reduced when infected with SeV (Fig. 3B, lane 3). Collectively, these results indicate that STING dimerization was reduced in the presence of CoV PLPs, and was also substantially reduced in cells infected with SARS-CoV.

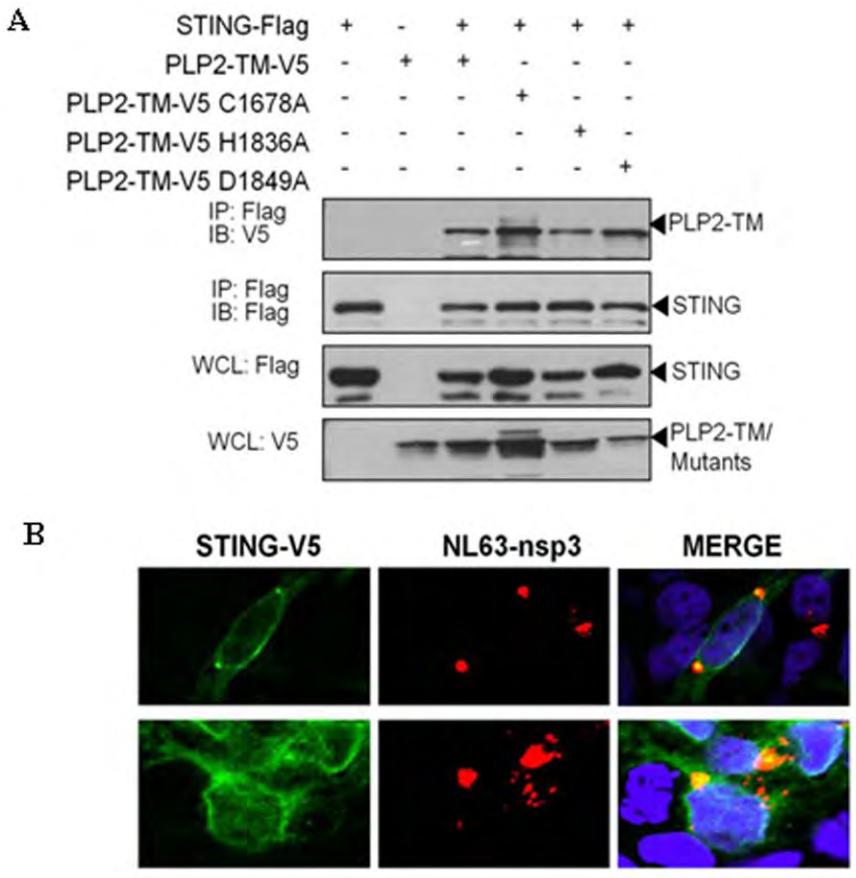

Figure 2. Coronavirus NL63 PLP2-TM associates with STING and nsp3 co-localizes with STING in virus-infected cells. (**A**) HEK293T cells were cotransfected with plasmid DNAs expressing STING-Flag and either wild type or catalytic mutants of NL63-PLP2-TM-V5. Cell lysates were prepared at 28 hrs post-transfection and subjected to immunoprecipitation (IP) with anti-Flag antibody. The products of the immunoprecipitation were separated by SDS-PAGE and subjected to immunoblotting (IB). STING-Flag, PLP2-TM-V5 and the catalytic mutant expression were selectively detected from whole cell lysates (WCL) using anti-Flag and anti-V5 antibodies. (**B**) HEK293-ACE2 cells were transfected with STING-V5 for 4 hours and then infected with HCoV-NL63 for 24 hrs and evaluated for expression of and localization of replicase product nsp3 (anti-nsp3, red) and STING-V5 (anti-V5, green).
doi:10.1371/journal.pone.0030802.g002

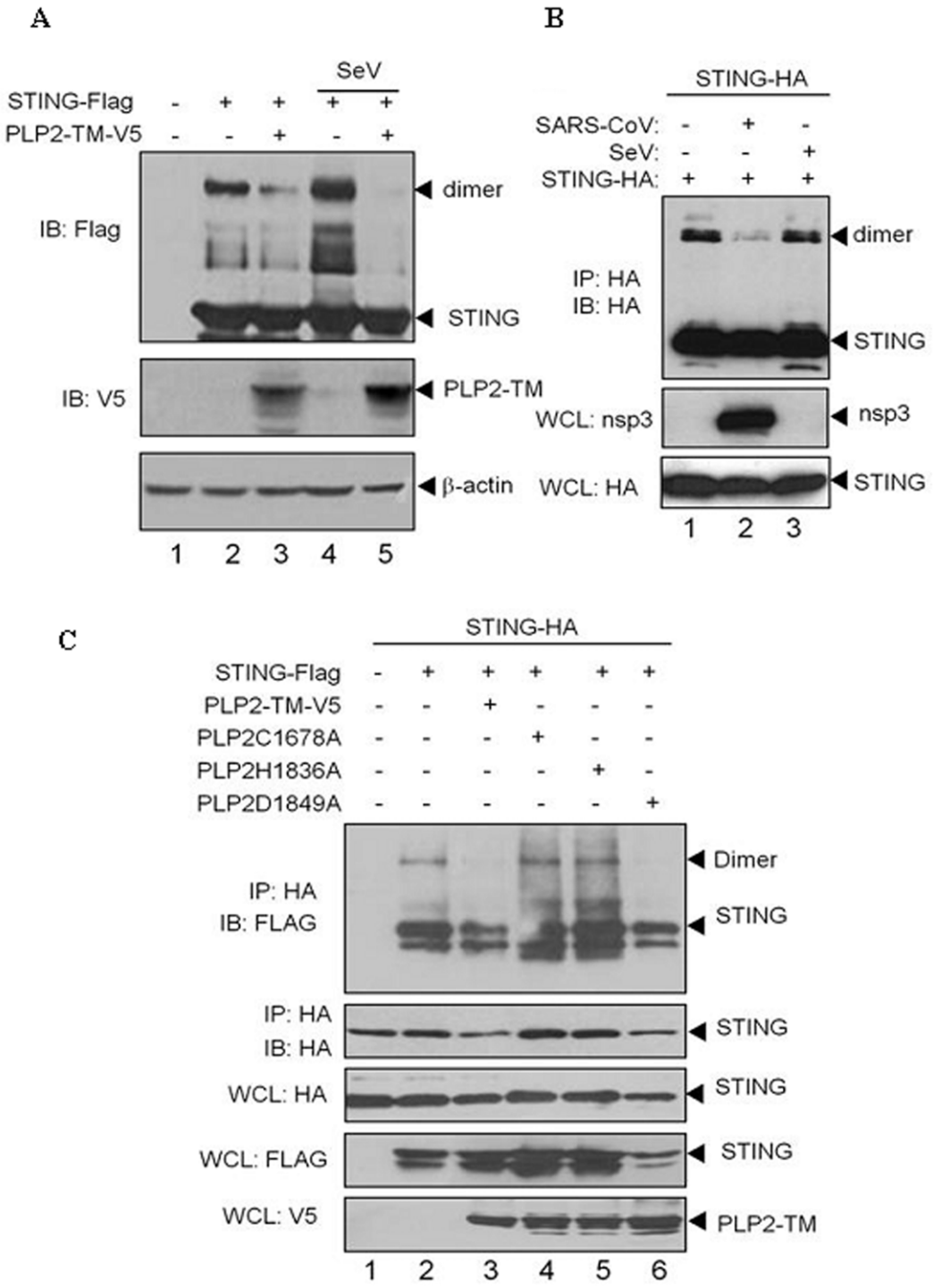

Figure 3. NL63 PLP2-TM interacts with STING and disrupts STING dimers. (**A**) HEK293T cells were co-transfected with plasmid DNA expressing STING-Flag, and/or PLP2-TM and/or infected with Sendai virus (SeV) as indicated above. The cell lysates were separated by SDS-PAGE and subjected to immunoblotting with antibodies as indicated on the left. (**B**) HEK293-ACE2 cells were transfected with plasmid DNA expressing STING-HA and infected with SARS-CoV as indicated and cell lysates were subjected to immunoprecipitation with anti-HA. The immunoprecipitated products were analyzed by SDS-PAGE and immunoblotted to access STING monomers and dimers. Whole cell lysates were immunoblotted to detected SARS-CoV replicase protein nsp3 and STING-HA. (**C**) Cells were co-transfected with STING-HA and STING-Flag with either wild-type or the indicated catalytic mutant of PLP2-TM and lysates were immunoprecipitated (IP) and immunoblotted (IB) to detect expression of each product.
doi:10.1371/journal.pone.0030802.g003

To determine if PLP catalytic activity is important for disruption of STING dimers, cells were co-transfected with plasmid DNA expressing STING-HA and STING-Flag and plasmid DNA expressing wt or catalytic mutants of PLP2-TM. Disruption of dimers was assessed by immunoprecipitation and immunoblotting (Fig. 3C). If STING-HA and STING-Flag form heterodimers,

then immunoprecipitation with anti-HA and immunoblotting with anti-Flag will allow detection of these heterodimers, as shown in Fig. 3C, lane 2. A reduction in STING dimers was detected in cells expressing wt PLP2-TM and the D1849A mutant which retains DUB activity (lanes 3 and 6), but not in cells expressing the C1678A or H1836A mutants which do not possess DUB activity [33]. These results indicate that PLP2 DUB activity is important for disruption of STING dimers. Similar results were obtained when we evaluated PLpro-TM for disruption of STING dimers (Fig. S3) A previous report indicates that only the dimer form of STING is ubiquitinated [9], which coupled with our observation that PLPs with DUB activity reduce the accumulation of STING dimers, supports a role for DUB activity in negatively regulating STING. Thus, these results are consistent with a role for viral DUB activity in antagonizing either the assembly or stability of STING dimers.

PLP2-TM disrupts MAVS-STING-IKKε interaction

Next, we wanted to determine if PLP2-TM altered the assembly of complexes required for activation of IRF-3 and the IFN response. MAVS, a mitochondrial-associated adaptor protein is a critical player in viral activation of the IFN response. Activation of MAVS mediates the assembly of a multi-protein complex that activates TBK-1/IKKε to phosphorylate IRF-3 [39]. Recent studies revealed that STING associates with MAVS to recruit TBK-1/IKKε and IRF-3 to a complex [8], and that activation of STING is critical for activation of IRF-3 [11,12]. Therefore, we investigated if PLP2-TM had any effect on assembly of these signaling complexes. HEK-293T cells were co-transfected with plasmid DNAs expressing STING-HA along with Flag-RIG-I, Flag-MAVS or Flag-IKKε in the presence or absence of PLP2-TM. Cell lysates were harvested and evaluated for co-immunoprecipitation of complexes by immunoblotting. We found that expression of PLP2-TM had no effect on co-immunoprecipitation of RIG-I with STING (Fig. 4A), but that co-immunoprecipitation of MAVS and IKKε was disrupted by expression of PLP2-TM (Fig. 4B, lane 4 and Fig. 4C, lane 4). Overall, these results are consistent with an important role for CoV PLPs in blocking activation of IFN by disrupting STING-mediated activation and complex formation.

PLP2-TM blocks ubiquitination of signaling molecules

Modification of signaling molecules by ubiquitination plays a critical role in activation of the IFN response [40–42]. Here, we asked if PLP2-TM can recognize and deubiquitinate key complexes in the IFN signaling pathway. HEK-293T cells were transfected with HA-Ub and epitope-tagged versions of either RIG-I, TBK-1, IRF-3 or STING and cell lysates were subjected to immunoprecipitation and immunoblotting to determine the ubiquitination status of the immunoprecipitated proteins (Fig. 5). We found that there was a dramatic reduction in the amount of ubiquitinated RIG-I (A), TBK-1 (B), IRF-3 (C) and STING (D) in cells expressing PLP2-TM. We also investigated the role of the PLP2-TM catalytic activity in mediating deubiquitination. Cells were transfected with HA-Ub and either wild-type or catalytic mutants of PLP2-TM and as expected, we detected a reduction in the level of ubiquitinated STING in the presence of wt and the D1849A mutant of PLP2-TM (Fig. 5D, lanes 4 and 7). Interestingly, expression of the PLP2-TM C1678A and H1836A mutants, which are catalytically inactive [35], still resulted in reduced levels of ubiquitined STING compared to the control (Fig. 5D, lanes 5 and 6). These results suggest that the catalytically inactive mutants of PLP2-TM may block access of STING to the ubiquitination machinery, thereby resulting in reduced levels of

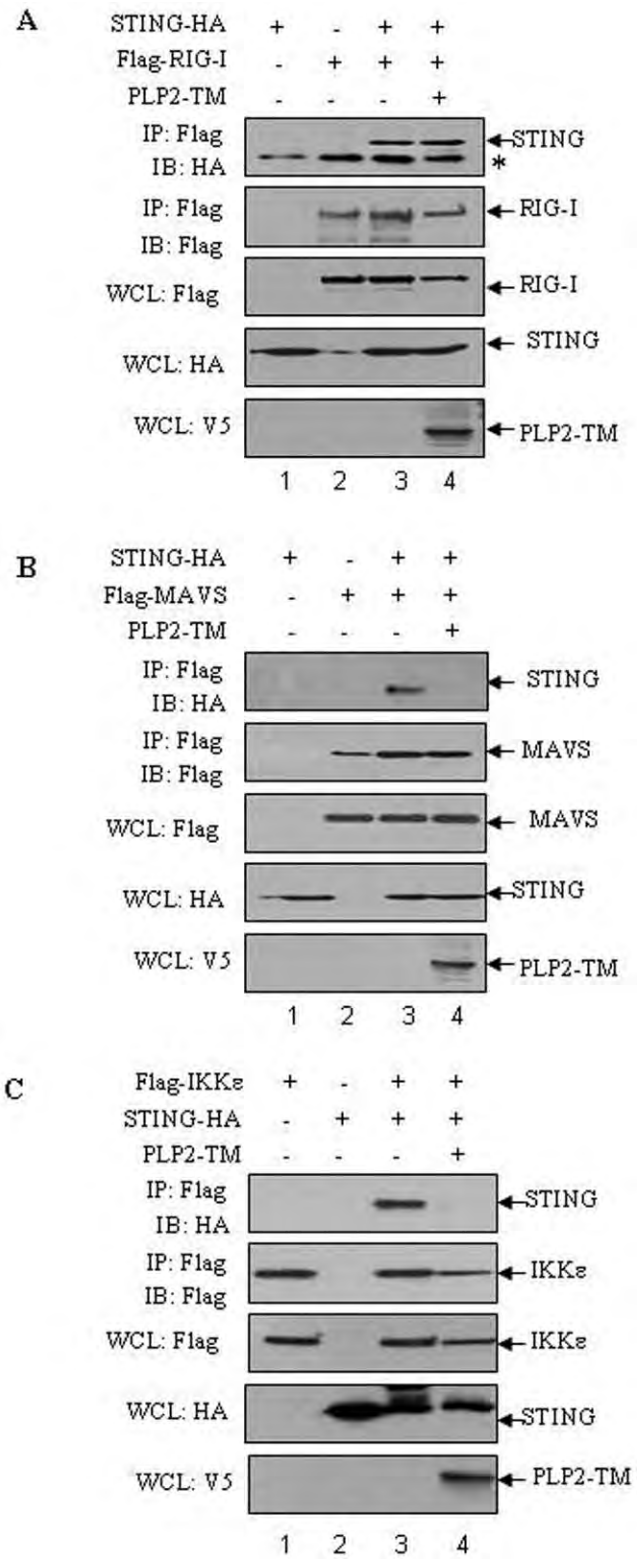

Figure 4. NL63 PLP2-TM disrupts signaling complex formation. HEK293T cells were co-transfected with STING-HA together with either Flag-tagged RIG-I (**A**), Flag-tagged MAVS (**B**) or Flag-tagged IKKε (**C**), and PLP2-TM-V5. At 28 h after transfection, cell lysates were prepared and subjected to immunoprecipitate (IP) and immunoblot (IB) with the indicated antibodies. The asterisk indicates the nonspecific band.
doi:10.1371/journal.pone.0030802.g004

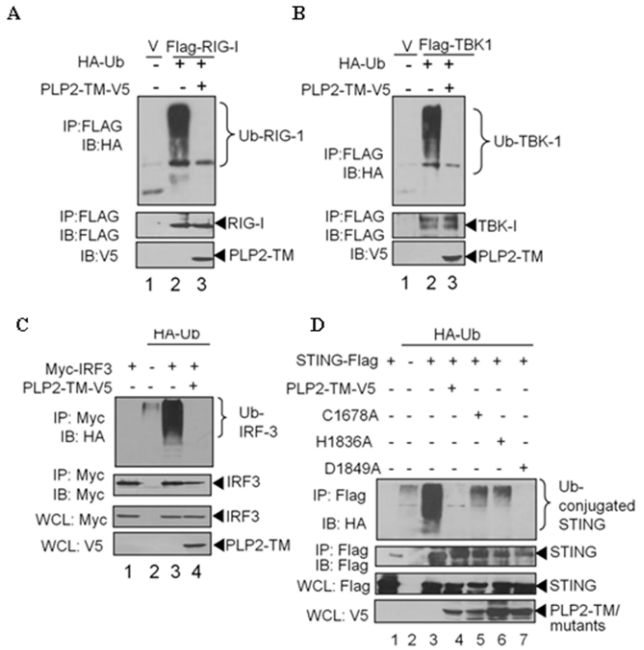

Figure 5. Reduction of ubiquitinated forms of RIG-I, STING, TBK1 and IRF-3 in the presence of NL63 PLP2-TM. HEK293 cells were transfected with Flag-tagged RIG-I(**A**), TBK1(**B**), myc-IRF-3(**C**), or STING-Flag (**D**) together with plasmid DNA expressing HA-tagged Ub in the presence or absence of V5-tagged PLP2-TM-V5. Cells were incubated for 24 hours after transfection and treated with 25 μM MG132 for 4 hours prior to harvesting lysates. Lysates were immunoprecipitated with the indicated antibody and the products were subjected to immunoblotting with anti-HA to evaluate ubiquitinated proteins (upper panels). The whole cell lysates (WCL) were blotted to evaluate expression of each epitope-tagged product (bottom panels).
doi:10.1371/journal.pone.0030802.g005

Ub-conjugated STING. Thus, the IFN antagonism of the catalytic mutants may be due to physical interaction with STING which blocks access of ubiquitin chains or Ub-ligases or other modifying enzymes that are required for efficient signaling [43,44]. A previous report indicates that only the dimer form of STING is ubiquitinated [9], which coupled with our observation that PLPs with DUB activity reduce the accumulation of STING dimers, supports a role for DUB activity in negatively regulating STING. Thus, these results are consistent with a role for viral DUB activity in antagonizing either the assembly or stability of STING dimers.

Discussion

In this study, we investigated the mechanisms of the IFN antagonism imposed by the coronavirus papain-like proteases (CoV PLPs). Previous studies suggested that CoV PLPs block IFN synthesis by inhibiting virus-activated IRF-3 phosphorylation and nuclear translocation, but the underlying mechanism was unclear [14,17,32]. Here we show that both SARS-CoV PLpro-TM and HCoV-NL63 PLP2-TM associate with an ER-associated protein, STING and block assembly or stability of STING dimers which are important for downstream signaling and induction of the IFN response. Importantly, we have demonstrated that STING colocalizes with nsp3 (which contains PLPs) in HCoV-NL63 infected cells, and that STING dimerization was substantially reduced in cells infected with SARS-CoV. In addition, we found that ubiquitination of signaling molecules is dramatically reduced in the presence of HCoV-NL63 PLP2-TM, which may contribute to destabilizing the signaling complex. Targeting of the signaling complex by blocking ubiquitination and disruption of STING dimers presents yet another mechanism used by coronaviruses to prevent activation of innate immunity and illustrates how coronavirus PLPs negatively regulate the IFN antiviral immune response in host cells.

Targeting the stimulator of IFN genes, STING

Recent studies have revealed the arsenal of proteins that viruses use to evade and subvert recognition by pattern-recognition receptors (PRRs) or activation of signaling molecules that are designed to respond to infectious agents [45]. STING is a key scaffolding protein that links the cytosolic viral RNA sensors RIG-I, rather than the MDA5, to the mitochondria protein MAVS [8,11]. These cytosolic sensors have been shown to be important for recognition of coronavirus RNA in oligodendrocytes [21] and brain macrophages/microglia [20]. Activation of STING, either by expression of N-RIG, the constitutive active caspase recruitment domain of RIG-I or ectopic expression of STING itself, induces the formation of STING dimers, which are modified by phosphorylation and ubiquitylation [9]. The activation of STING facilitates the recruitment of IRF-3 and TBK-1 into a complex where IRF-3 is phosphorylated. Phosphorylated IRF-3 forms dimers and is transported to the nucleus to activate transcription of type I IFN genes. CoV PLPs target STING and prevent this key scaffolding protein from activating IRF-3. Previously, we showed that PLpro blocks NF-κB-dependent promoter activity and that antagonism is abrogated using protease inhibitors [14]. Thus, CoV PLPs interact with key signaling molecules and exploit both catalytic dependent and catalytic-independent mechanisms to block the innate immune response. CoV-PLPs disrupt signal transduction to both IRF-3 and NF-κB, the key transcription factors required for activation of IFN-β (Fig. 6). Interestingly, CoV PLPs seem to exploit both catalytic dependent and independent mechanisms to block STING activity and a catalytic-dependent mechanism to disrupt NF-κB activity.

Previous studies have shown a role for viral proteases in cleavage of key IFN signaling molecules [45]. For example, the NS3/4A protease of hepatitis C virus and GB virus B and the 3ABC precursor of hepatitis A virus cleave MAVS/IPS-1, the mitochondria-associated signaling molecule, which blocks activation of IFN synthesis [46–51]. Therefore, it seemed reasonable to hypothesize that CoV PLPs exploited their protease or DUB activity to antagonize the innate immune response. However, we had previously shown that catalytically defective PLP mutants were still capable of inhibiting IRF-3 activation [17]. Furthermore, addition of a protease inhibitor that blocks both protease and DUB activity [52] failed to abrogate the PLP inhibition on activation of IRF-3 dependent promoters [14]. This led us to suspect that CoV PLPs were interacting with a component in the IFN signaling pathway. The fact that CoV PLPs are expressed as a polyprotein that localizes to the ER [25,26] led us to evaluate ER resident signaling molecules as targets of antagonism. The results presented in this study indicate that CoV PLPs are particularly potent antagonists because they can block: 1) STING dimerization; 2) the MAVS-STING-IKKε interaction required for signaling and 3) the ubiquitination of key signaling molecules such as RIG-I, STING, IRF-3 and TBK-1. Interestingly, catalytically inactive mutants of PLPs can interact, either directly or as part of a signaling complex, with STING and moderately inhibit IRF-3 activation for IFN induction, but wild type PLPs exhibit the most robust inhibition. We found that catalytic activity was important for blocking either the assembly or the stability of STING dimers. In addition, we found that PLP2-TM either

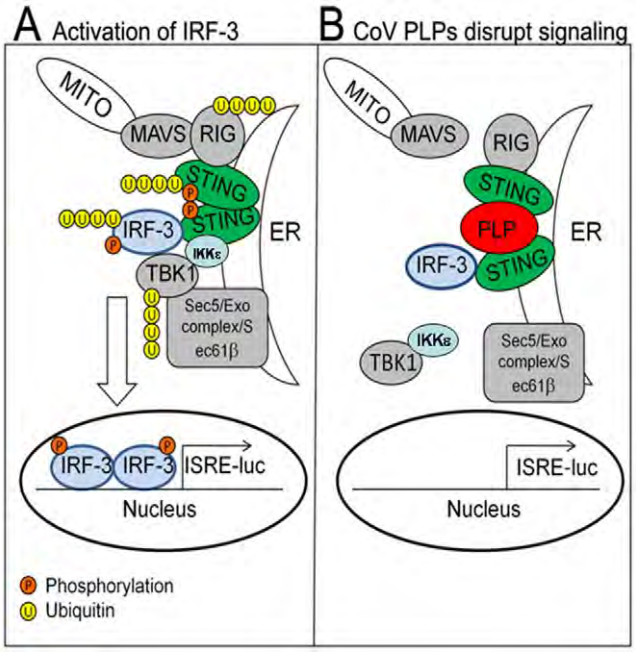

Figure 6. Model depicting the mechanisms used by CoV PLPs to block STING from signaling the activation of the IFN-β induction pathway. (**A**) Activation of sensors such as RIG-I induces interaction with the signaling complex including MAVS, STING, IRF-3 and TBK-1. Activated MAVS interacts with STING, which dimerizes, leading to the activation of IKK complex, TBK1 and IKKε [8]. The activation of this complex leads to the ubiquitination of RIG-I, STING, IRF-3 and TBK1 and the phosphorylatin of STING and IRF-3. Activated the transcription factor IRF-3 translocates to the nucleus inducing production of IFN. (**B**) Coronavirus papain-like protease domains (depicted here as PLP) interact with STING to block signaling by blocking assembly or stability of STING dimers and preventing the ubiquitination of signaling proteins, such as RIG-I, TBK1, and IRF-3.
doi:10.1371/journal.pone.0030802.g006

actively deubiquitinates or blocks the ubiquitination of the signaling molecules. This is consistent with these reported works that STING dimers were modified by ubiquitin [9]. By associating with STING, either directly or as part of a signaling complex, CoV PLPs can target and either block or deubiquitinate this important signaling molecule. Of course the question still remains if the PLP-STING interaction is direct or indirect, and what region(s) of the PLP are required for this potential interaction. These studies are currently ongoing. Understanding how to negatively regulate STING-mediated innate antiviral signaling by CoV PLPs may lead to the development of novel antiviral therapies and new insights for regulating the IFN response during acute and chronic infections.

DUBs as negative regulators of IFN activation

One of the striking findings in this report is the similarity in the function of CoV PLPs and cellular DUBs such as the NF-κB responsive gene A20, deubiquitinating enzyme A (DUBA), and the tumor suppressor protein associated with cylindromatosis (CYLD) [53–55]. Like CoV PLPs, cellular DUBs were identified as negative regulators of the innate immune response. A20 is considered a "central gatekeeper in inflammation and immunity" [56] because of its ability to interact with and mediate ubiquitin-editing on signaling molecules such as RIP1, TRAF6, RIP2 and NEMO. A20 DUB activity removes K-63 linked polyubiquitin chains from RIP1, TRAF6, RIP2 and NEMO which results in negative regulation of the innate immune response. In addition, A20 has been shown to act by antagonizing interactions between signaling molecules and ubiquitin conjugating enzymes [57]. Interestingly, both A20 and CoV PLPs can act on K-63 linked ubiquitin chains [14,58]. Further experiments are needed to determine if recognition, processing or sequestering of K-63 linked ubiquitin is important for CoV PLPs negative regulation of the IFN response. Cellular proteins DUBA and CYLD also negatively regulate the innate immune response. Kayagaki and co-workers found that DUBA targets and deubiquitinates TRAF3, a signaling molecule required for activation of IRF-3 [55]. They showed that reducing the expression of DUBA augments the IFN response to poly(I:C) whereas ectopic expression of DUBA blocks the IFN response. CYLD has been shown to deubiquitinate RIG-I to inhibit IFN production [53,54]. Ectopic expression of CYLD antagonizes the IFN response whereas siRNA-mediated knock-down of CYLD expression allows for a more robust IFN response. It seems that CoV PLPs are usurping the function of cellular DUBs by behaving as negative regulators of the innate immune response through targeting STING for both deubiquitination and dimer disruption.

Another possibility is that CoV PLPs function by sequestering STING as a mechanism of blocking activation of IFN. Both catalytically active and inactive CoV PLPs could interact and sequester STING and thereby prevent activation of IRF-3. Coronavirus PLPs are part of the viral replicase polyprotein that associates with ER membranes to form convoluted membranes and double membrane vesicles (DMVs) which are the sites of viral RNA synthesis [25,26,59]. Interestingly, STING also resides in the ER and upon activation assembles with Sec5 into exocyst vesicles [12]. The interaction of STING with PLP2-TM may block the signals required for STING to translocate to exocyst vesicles. Thus, further studies with CoV PLPs may reveal specific targets of STING that modulate this arm of the innate immune response.

In summary, the results of this study indicate that HCoV-NL63 and SARS-CoV PLPs inhibit host IFN-β production by targeting and nullifying STING. Blocking this key scaffolding protein prevents activation of IRF-3 and subsequent transcription of IFN-β. The antagonism functions of CoV PLPs are important negative regulators of the innate immune response and may be important in the virulence and pathogenesis of human coronavirus infection. Further characterization of the PLP-STING interaction may provide new targets for antiviral interventions.

Materials and Methods

Cells and virus

HEK293T cells [44] were cultured using Dulbecco's modified Eagle's medium containing 10% (v/v) fetal calf serum, supplemented with penicillin (100 U/ml) and streptomycin (100 μg/ml). HEK293-ACE2 cells, which express angiotensin-converting enzyme 2 (ACE2), a key receptor for SARS and NL63 coronaviruses, were kindly provided by Dr. Kui Li (University of Tennessee Health Science Center, Memphis, USA) and cultured as above with the addition of puromycin (10 μg/ml). HCoV-NL63 was propagated in LLC-MK2 cells [35] which were kindly provided by Lia van der Hoek (University of Amsterdam, The Netherlands) and as previously described [35]. SARS-CoV was propagated in VeroE6 cells as previously described [52]. All work with SARS-CoV was performed in a biosafety level 3 facility using approved protocols. Sendai virus was kindly provided to the Chen lab by Dr. Shaobo Xiao (Huazhong Agricultural University, Wuhan, China) or purchased from Charles River Laboratories.

Plasmid DNAs

DNA constructs containing wild type and catalytic mutants of NL63 PLP2-TM SARS-CoV PLpro-TM and plasmids of IFN-β-Luc, PRD(III-I)4-Luc, ISRE-Luc and HA-tagged Ub were previously described [14,17]. Flag-hIPS-1(MAVS), BOS-Myc-hIRF3, Flag-hTBK1, Flag-hRIG-I were kindly provided by Dr. Himanshu Kuma and Shizuo Akira (Immunology Frontier Research Center Osaka University, Osaka, Japan). pcDNA3.1-HA-ERIS (designated here as STING-HA) and pCMV14-Flag-ERIS (designated STING-Flag) were kindly provided by Dr. Zhengfan Jiang (School of Life Sciences, Peking University, Beijing, China).

Luciferase reporter gene assay

HEK293T cells were transfected with the indicated stimulator plasmid DNA (STING-HA), reporter plasmid DNA [pRL-TK, ISRE-Luc, IFN-β-Luc, or PRD(III-I)4-Luc] and either NL63 PLP2-TM or SARS-CoV PLpro-TM using either Lipofectamine 2000 or Mirus LT1 according to the manufacturer's protocol and incubated for 24 hours. Firefly luciferase and *Renilla* luciferase activities were assayed using the Dual Luciferase Reporter Assay Kit (Promega). Data were shown as mean relative luciferase (firefly luciferase activity divided by Renilla luciferase activity) with standard deviation from a representative experiment carried out in triplicate. For statistical analysis, the data between Vector (300 ng) and PLP (PLpro)-TM with various concentrations were subjected to unpaired, two-tailed Student's t test using the Microsoft SPSS 12.0 software, and P values of <0.05 were considered to indicate statistical significance.

Immunofluorescence assays

HEK293 or HEK293-ACE2 cells were plated on fibronectin treated glass coverslips in 12-well plates. To evaluate localization of STING and NL63 PLP2-TM, plasmid DNA expressing STING-HA (225 ng per well) was transfected in the presence or absence of 300 ng of PLP2-TM using Mirus LT1 according to the manufacturer's protocol. At 16 hours post transfection, cells were fixed with 3.7% formaldehyde for 10 min at room temperature. Cells were then incubated with 1:200 dilution of rabbit anti-IRF-3 (Active Motif), mouse anti-HA (Covance), and goat anti-V5 (Genscript) in ADPS (PBS+0.1% Triton-×100+5% fetal calf serum) for 1 hour at room temperature. Cells were washed three times with PBS and incubated with 1:200 dilution of chicken anti-rabbit Alexa Fluor (AF) 488, donkey anti-mouse AF568, and donkey anti-goat AF647 (Molecular Probes) in ADPS for 1 hour in the dark. Following the incubation, cells were washed three times with PBS, mounted, and imaged with the Zeiss LSM-510 confocal microscope.

To evaluate STING localization in NL63 infected cells, HEK293-ACE2 cells were transfected with 100 ng of a plasmid expressing human STING-V5 for 4 hours. Cells were subsequently infected with 200 µl of HCoV-NL63 (1×10^4 pfu/ml). At 24 hours post infection, cells were fixed with 3.7% formaldehyde for 10 minutes at room temperature. Cells were then diluted with a 1:1000 dilution of rabbit anti-nsp3 [35] and 1:1000 dilution of mouse anti-V5 for 1 hour at room temperature in ADPS. Cells were washed three times with PBS and incubated with a 1:200 dilution of goat anti-rabbit AF568 and chicken anti-mouse AF488, and 1:1000 dilution of DAPI for 30 minutes at room temperature in the dark. The cells were then washed three times with PBS, mounted, and imaged with the Zeiss LSM-510 confocal microscope.

Co-immunoprecipitation (Co-IP) analysis

HEK293T cells were seeded on 100-mm dishes at a density of 1×10^6 cells/dish. 12 hours later, cells were transiently transfected with a total of 10 µg of empty plasmid or indicated expression plasmids using Lipofectamine 2000 (Invitrogen). At 28 hours after transfection, cells were lysed in buffer containing 0.5% Triton-X-100, 150 mM NaCl, 12.5 mM β-glycerolphosphate, 1.5 mM MgCl2, 2 mM EGTA, 10 mM NaF, 1 mM Na_3VO_4, 2 mM DTT plus protease inhibitor cocktail (Sigma). The cell extracts were spun down at 5000× g for 10 minutes at 4°C. The protein concentration of each lysate was determined using the BCA Protein Assay (Bio-Rad) and the concentration was adjusted to 1 µg/µl, with 500 µl of lysate used for each IP. The lysates were precleared by adding 20 µl protein A+G Agarose (Beyotime Institute of Biotechnology, China) and 1 µg of normal IgG and incubating for 2 hours at 4°C, followed by spinning down the beads. The precleared supernatant was incubated with the designated antibody [Anti-Flag (Sigma) or anti-HA (MBL)/anti-Myc (MBL)] with rocking overnight at 4°C. The beads-antibody-antigen complex was spun down and washed 3 times with 1 ml of lysis buffer. The proteins were eluted from the beads in 30 µl of 2× SDS-PAGE sample buffer subjected to boiling for 10 min. The sample was separated by SDS-PAGE and transferred to PVDF membrane for western blotting.

Assessing ubiquitination of signaling molecules in cultured cells

The effect of HCoV-NL63 PLP2-TM on ubiquitinated proteins in cultured cells was assessed as described previously [53,55]. Briefly, Flag-tagged RIG-I, TBK1, STING, IRF-3 were co-transfected into HEK293T cells together with pcDNA3.1-HA-Ub, plus wild type or catalytic mutant PLP2-TM DNA using Lipofectamine 2000 according to the manufacturer's instructions. Empty vector pcDNA3.1/V5-HisB was used to standardize the total amount of DNA used for transfection. 24 post-transfection, cells were incubated with 25 µM MG132 for 4 hours, and then lysed in 300 µl of RIPA buffer (50 mM Tris-HCl pH 7.4, 150 mM NaCl, 2 mM EDTA, 1% NP-40, 0.1% SDS) containing protease inhibitor cocktail (1 mM, Roche) and 10 µM NEM, Non-covalently bound proteins were dissociated by boiling in 1% SDS, and samples diluted 1:10 in lysis buffer (50 mM Tris-HCl pH 7.4, 150 mM NaCl, 2 mM EDTA, 1% NP-40) containing protease inhibitor cocktail and 10 µM NEM. The soluble lysates were then immunoprecipitated with anti-Flag antibody followed by washing with RIPA buffer for three times. Flag-tagged proteins were resolved by SDS-PAGE and sequentially blotted with anti-HA and anti-Flag antibodies. 150 µl of lysate was used for each immunoprecipitation reaction. To confirm the PLP and the catalytic mutant expression level, western blotting with anti-V5 antibody (Invitrogen) was used to detect wild type and catalytic mutant PLP2-TM-V5 protein expression.

Detection of STING dimers

To assess STING dimers, HEK293T cells were transfected with STING-HA or STING-Flag (0.5 µg per 100 mm dish) and lysates subjected to immunoprecipitation and western blotting as described [9] with the indicated antibodies. To detect STING dimers induced by Sendai Virus (SeV) infection, HEK293T cells were transfected with STING-Flag and then infected with SeV (HAU = 100). 24 hours later, cells were lysed and immunoblotted with anti-Flag antibodies. To assess STING dimers in transfected and SARS-CoV- or Sendai Virus (SeV)- infected cells, HEK293-ACE2 cells were seeded at 10^5 cells/well in twelve well plates. 24 hours later, cells were transfected with either 0.5 µg of mSTING-HA expressing plasmid DNA or 0.5 µg pcDNA3.1V5-HisB vector DNA (Invitrogen). Following six hours of incubation, the cells were infected with either SARS-CoV Urbani (MOI = 0.1)

or SeV (HAU = 100). 24 hours later, the cells were lysed in 300 µl of lysis buffer containing 0.5% Triton-X-100, 150 mM NaCl, 12.5 mM β-glycerolphosphate, 1.5 mM MgCl2, 2 mM EGTA, 10 mM NaF, 1 mM Na_3VO_4, 2 mM DTT plus protease inhibitor cocktail (Sigma). 150 µl of lysate was used for each immunoprecipitation reaction. After preclearing the lysate with protein G magnetic beads (Millipore), 0.5 µg of rabbit anti-HA antibodies (Invitrogen) was incubated with the lysate overnight at 4°C. 25 µl protein G magnetic beads was added to the immunoprecipitation reactions and incubated for 2 hours at 4°C. Protein G magnetic beads were precipitated and washed 3 times with 1 ml lysis buffer. 80 µl of 2× sample buffer containing 10% glycerol, 5% -mercaptoethanol, 3% SDS, 12.5% upper buffer (0.5 M Trizma base and 0.4% SDS), and 0.01 mg bromophenol blue was added to the beads, and protein-antibody complexes were eluted by incubating at 37°C for 30 min. Samples were separated on SDS-PAGE gel and transferred to a PVDF membrane. Blots were incubated with mouse anti-HA antibody (Sigma) or anti-nsp3 antisera [17] at 0.5 µg/µl and 0.125 µg/µl concentrations, respectively. After washing three times in TBS-T buffer, blots were subsequently incubated with either goat-anti-mouse-HRP or donkey-anti-rabbit-HRP (Southern Biotech). Antibody-antigen reactions were detected using the Western Lighting Plus-ECL chemiluminescence reagents from Perkin Elmer.

Supporting Information

Figure S1 (**A**) Schematic diagram of SARS-CoV illustrating the processing of replicase polyproteins to generate nonstructural proteins (nsp's). The papain-like protease domains, the catalytic residues, and the transmembrane (TM) domain within nsp3 are indicated. (**B**) Western blot detection of STING-V5 and dose response of PLP2-TM-V5 and PLpro-TM-V5.
(TIF)

Figure S2 SARS-CoV PLpro-TM associates with STING. HEK293T cells were cotransfected with plasmid DNAs expressing STING-Flag and either wild type or catalytic mutants of PLpro-TM-V5. Cell lysates were prepared at 28 hrs post-transfection and subjected to immunoprecipitation (IP) with anti-Flag antibody. The products of the immunoprecipitation were separated by SDS-PAGE and subjected to immunoblotting (IB). STING-Flag, PLpro-TM-V5 and the catalytic mutant expression were selectively detected from whole cell lysates (WCL) using anti-Flag and anti-V5 antibodies.
(TIF)

Figure S3 SARS-CoV PLpro-TM interacts with STING and disrupts STING dimers. HEK293T cells were co-transfected with plasmid DNAs expressing STING-HA, and/or PLpro-TM and/or GFP-V5 as indicated above. At 24 hrs post-transfection, cell lysates were subjected to immunoprecipitation with the indicated antibody and the products were separated by SDS-PAGE and subjected to immunoblotting to detect STING monomer and dimer (upper panel). Whole cell lysates (WCL) were immunoblotted to detected expression of STING-HA, PLpro-TM-V5, and GFP-V5 (lower panel).
(TIF)

Acknowledgments

We would like to thank Dr. Himanshu Kuma, Dr. Shizuo Akira, Dr. Zhengfan Jiang, Dr. Min-Jung Kim, Dr. Robert M. Krug and Dr. Edward W. Harhaj for kindly providing the reporter plasmids and expression constructs. We also would like to thank Dr. Zhengfan Jiang for the helpful suggestion of STING dimer detection.

Author Contributions

Conceived and designed the experiments: ZC SCB KL. Performed the experiments: LS YX XC YZ YY DBN MAC BSB. Analyzed the data: LS YX ZC SCB. Wrote the paper: SCB ZC.

References

1. Kawai T, Akira S (2007) Antiviral signaling through pattern recognition receptors. J Biochem 141: 137–145.
2. Yoneyama M, Fujita T (2009) RNA recognition and signal transduction by RIG-I-like receptors. Immunol Rev 227: 54–65.
3. Barral PM, Sarkar D, Su ZZ, Barber GN, DeSalle R, et al. (2009) Functions of the cytoplasmic RNA sensors RIG-I and MDA-5: key regulators of innate immunity. Pharmacol Ther 124: 219–234.
4. Hornung V, Ellegast J, Kim S, Brzózka K, Jung A, et al. (2006) 5′-Triphosphate RNA is the ligand for RIG-I. Science 314: 994–997.
5. Pichlmair A, Schulz O, Tan CP, Näslund TI, Liljeström P, et al. (2006) RIG-I-mediated antiviral responses to single-stranded RNA bearing 5′-phosphates. Science 314: 997–1001.
6. Schmidt A, Schwerd T, Hamm W, Hellmuth JC, Cui S, et al. (2009) 5′-triphosphate RNA requires base-paired structures to activate antiviral signaling via RIG-I. Proc Natl Acad Sci U S A 106: 12067–12072.
7. Rehwinkel J, Tan CP, Goubau D, Schulz O, Pichlmair A, et al. (2010) RIG-I detects viral genomic RNA during negative-strand RNA virus infection. Cell 140: 397–408.
8. Zhong B, Yang Y, Li S, Wang YY, Li Y, et al. (2008) The adaptor protein MITA links virus-sensing receptors to IRF3 transcription factor activation. Immunity 29: 538–550.
9. Sun W, Li Y, Chen L, Chen H, You F, et al. (2009) ERIS, an ER IFN stimulator, activates innate immune signaling through dimerization. Proc Natl Acad Sci U S A 106: 8653–8658.
10. Jin L, Waterman PM, Jonscher KR, Short CM, Reisdorph NA, et al. (2008) MPYS, a novel membrane tetraspanner, is associated with major histocompatibility complex class II and mediates transduction of apoptotic signals. Mol Cell Biol 28: 5014–5026.
11. Ishikawa H, Barber GN (2008) STING is an endoplasmic reticulum adaptor that facilitates innate immune signalling. Nature 455: 674–678.
12. Ishikawa H, Ma Z, Barber GN (2009) STING regulates intracellular DNA-mediated, type I interferon-dependent innate immunity. Nature 461: 788–792.
13. Perlman S, Netland J (2009) Coronaviruses post-SARS: update on replication and pathogenesis. Nat Rev Microbiol 7: 439–450.
14. Clementz MA, Chen Z, Banach BS, Wang Y, Sun L, et al. (2010) Deubiquitinating and interferon antagonism activities of coronavirus papain-like proteases. J Virol 84: 4619–4629.
15. Spiegel M, Pichlmair A, Martinez-Sobrido L, Cros J, Garcia-Sastre A, et al. (2005) Inhibition of Beta interferon induction by severe acute respiratory syndrome coronavirus suggests a two-step model for activation of interferon regulatory factor 3. J Virol 79: 2079–2086.
16. Zhou H, Perlman S (2006) Mouse Hepatitis Virus Does Not Induce Beta Interferon Synthesis and Does Not Inhibit Its Induction by Double-Stranded RNA. J Virol 81: 568–574.
17. Devaraj SG, Wang N, Chen Z, Tseng M, Barretto N, et al. (2007) Regulation of IRF-3-dependent Innate Immunity by the Papain-like Protease Domain of the Severe Acute Respiratory Syndrome Coronavirus. J Biol Chem 282: 32208–32221.
18. Versteeg GA, Bredenbeek PJ, van den Worm SH, Spaan WJ (2007) Group 2 coronaviruses prevent immediate early interferon induction by protection of viral RNA from host cell recognition. Virology 361: 18–26.
19. Cervantes-Barragan L, Zust R, Weber F, Spiegel M, Lang KS, et al. (2007) Control of coronavirus infection through plasmacytoid dendritic-cell-derived type I interferon. Blood 109: 1131–1137.
20. Roth-Cross JK, Bender SJ, Weiss SR (2008) Murine coronavirus mouse hepatitis virus is recognized by MDA5 and induces type I interferon in brain macrophages/microglia. J Virol 82: 9829–9838.
21. Li J, Liu Y, Zhang X (2010) Murine coronavirus induces type I interferon in oligodendrocytes through recognition by RIG-I and MDA5. J Virol 84: 6472–6482.
22. Sheahan T, Morrison TE, Funkhouser W, Uematsu S, Akira S, et al. (2008) MyD88 is required for protection from lethal infection with a mouse-adapted SARS-CoV. PLoS Pathog 4: e1000240.
23. Zhao J, Zhao J, Perlman S (2010) T cell responses are required for protection from clinical disease and for virus clearance in severe acute respiratory syndrome coronavirus-infected mice. J Virol 84: 9318–9325.
24. Rose KM, Elliott R, Martinez-Sobrido L, Garcia-Sastre A, Weiss SR (2010) Murine coronavirus delays expression of a subset of interferon-stimulated genes. J Virol 84: 5656–5669.

25. Gosert R, Kanjanahaluethai A, Egger D, Bienz K, Baker SC (2002) RNA replication of mouse hepatitis virus takes place at double-membrane vesicles. J Virol 76: 3697–3708.
26. Knoops K, Kikkert M, Worm SH, Zeverhover-Dobbe JC, van der Meer Y, et al. (2008) SARS-coronavirus replication is supported by a reticulovesicular network of modified endoplasmic reticulum. PLoS Biol 6: e226.
27. Narayanan K, Huang C, Lokugamage K, Kamitani W, Ikegami T, et al. (2008) Severe acute respiratory syndrome coronavirus nsp1 suppresses host gene expression, including that of type I interferon, in infected cells. J Virol 82: 4471–4479.
28. Lu X, Pan J, Tao J, Guo D (2010) SARS-CoV nucleocapsid protein antagonizes IFN-β response by targeting initial step of IFN-β induction pathway, and its C-terminal region is critical for the antagonism. Virus Genes 42(1): 37–45.
29. Siu KL, Kok KH, Ng MH, Poon VK, Yuen KY, et al. (2009) Severe Acute Respiratory Syndrome Coronavirus M Protein Inhibits Type I Interferon Production by Impeding the Formation of TRAF3.TANK.TBK1/IKKε Complex. J Biol Chem 284: 16202–16209.
30. Kopecky-Bromberg SA, Martinez-Sobrido L, Frieman M, Baric RA, Palese P (2007) Severe acute respiratory syndrome coronavirus open reading frame (ORF) 3b, ORF 6, and nucleocapsid proteins function as interferon antagonists. J Virol 81: 548–557.
31. van der Hoek L, Sure K, Ihorst G, Stang A, Pyrc K, et al. (2005) Croup Is Associated with the Novel Coronavirus NL63. PLoS Med 2: e240.
32. Frieman M, Ratia K, Johnston RE, Mesecar AD, Baric RS (2009) Severe acute respiratory syndrome coronavirus papain-like protease ubiquitin-like domain and catalytic domain regulate antagonism of IRF3 and NF-kappaB signaling. J Virol 83: 6689–6705.
33. Lindner HA, Fotouhi-Ardakani N, Lytvyn V, Lachance P, Sulea T, et al. (2005) The papain-like protease from the severe acute respiratory syndrome coronavirus is a deubiquitinating enzyme. J Virol 79: 15199–15208.
34. Ratia K, Saikatendu KS, Santarsiero BD, Barretto N, Baker SC, et al. (2006) Severe acute respiratory syndrome coronavirus papain-like protease: structure of a viral deubiquitinating enzyme. Proc Natl Acad Sci USA 103: 5717–5722.
35. Chen Z, Wang Y, Ratia K, Mesecar AD, Wilkinson KD, et al. (2007) Proteolytic processing and deubiquitinating activity of papain-like proteases of human coronavirus NL63. J Virol 81: 6007–6018.
36. Andersen J, VanScoy S, Cheng TF, Gomez D, Reich NC (2008) IRF-3-dependent and augmented target genes during viral infection. Genes Immun 9: 168–175.
37. Grandvaux N, Servant MJ, tenOever B, Sen GC, Balachandran S, et al. (2002) Transcriptional profiling of interferon regulatory factor 3 target genes: direct involvement in the regulation of interferon-stimulated genes. J Virol 76: 5532–5539.
38. Banach BS, Orenstein JM, Fox LM, Randell SH, Rowley AH, et al. (2009) Human Airway Epithelial Cell Culture to Identify New Respiratory Viruses: Coronavirus NL63 as a Model. J Virol Methods 156: 19–26.
39. Seth RB, Sun L, Chen ZJ (2006) Antiviral innate immunity pathways. Cell Res 16: 141–147.
40. Bibeau-Poirier A, Servant MJ (2008) Roles of ubiquitination in pattern-recognition receptors and type I interferon receptor signaling. Cytokine 43: 359–367.
41. Bhoj VG, Chen ZJ (2009) Ubiquitylation in innate and adaptive immunity. Nature 458: 430–437.
42. Isaacson MK, Ploegh HL (2009) Ubiquitination, ubiquitin-like modifiers, and deubiquitination in viral infection. Cell Host Microbe 5: 559–570.
43. Xia ZP, Sun L, Chen X, Pineda G, Jiang X, et al. (2009) Direct Activation of Protein Kinases by Unanchored Polyubiquitin Chains. Nature 461: 114–119.
44. Zeng W, Sun L, Jiang X, Chen X, Hou F, et al. (2010) Reconstitution of the RIG-I pathway reveals a signaling role of unanchored polyubiquitin chains in innate immunity. Cell 141: 315–330.
45. Bowie AG, Unterholzner L (2008) Viral evasion and subversion of pattern-recognition receptor signalling. Nat Rev Immunol 8: 911–922.
46. Meylan E, Curran J, Hofmann K, Moradpour D, Binder M, et al. (2005) Cardif is an adaptor protein in the RIG-I antiviral pathway and is targeted by hepatitis C virus. Nature 437: 1167–1172.
47. Loo YM, Owen DM, Li K, Erickson AK, Johnson CL, et al. (2006) Viral and therapeutic control of IFN-beta promoter stimulator 1 during hepatitis C virus infection. Proc Natl Acad Sci U S A 103: 6001–6006.
48. Lin R, Lacoste J, Nakhaei P, Sun Q, Yang L, et al. (2006) Dissociation of a MAVS/IPS-1/VISA/Cardif-IKKepsilon molecular complex from the mitochondrial outer membrane by hepatitis C virus NS3-4A proteolytic cleavage. J Virol 80: 6072–6083.
49. Chen Z, Benureau Y, Rijnbrand R, Yi J, Wang T, et al. (2007) GB virus B disrupts RIG-I signaling by NS3/4A-mediated cleavage of the adaptor protein MAVS. J Virol 81: 964–976.
50. Yang Y, Liang Y, Qu L, Chen Z, Yi M, et al. (2007) Disruption of innate immunity due to mitochondrial targeting of a picornaviral protease precursor. Proc Natl Acad Sci U S A 104: 7253–7258.
51. Li XD, Sun L, Seth RB, Pineda G, Chen ZJ (2005) Hepatitis C virus protease NS3/4A cleaves mitochondrial antiviral signaling protein off the mitochondria to evade innate immunity. Proc Natl Acad Sci U S A 102: 17717–17722.
52. Ratia K, Pegan S, Takayama J, Sleeman K, Coughlin M, et al. (2008) A noncovalent class of papain-like protease/deubiquitinase inhibitors blocks SARS virus replication. Proc Natl Acad Sci U S A 105: 16119–16124.
53. Friedman CS, O'Donnell MA, Legarda-Addison D, Ng A, Cárdenas WB, et al. (2008) The tumour suppressor CYLD is a negative regulator of RIG-I-mediated antiviral response. EMBO Rep 9: 930–936.
54. Zhang M, Wu X, Lee AJ, Jin W, Chang M, et al. (2008) Regulation of IkappaB kinase-related kinases and antiviral responses by tumor suppressor CYLD. J Biol Chem 283: 18621–18626.
55. Kayagaki N, Phung Q, Chan S, Chaudhari R, Quan C, et al. (2007) DUBA: a deubiquitinase that regulates type I interferon production. Science 318: 1628–1632.
56. Coornaert B, Carpentier I, Beyaert R (2009) A20: central gatekeeper in inflammation and immunity. J Biol Chem 284: 8217–8221.
57. Shembade N, Ma A, Harhaj EW (2010) Inhibition of NF-kappaB signaling by A20 through disruption of ubiquitin enzyme complexes. Science 327: 1135–1139.
58. Wertz IE, O'Rourke KM, Zhou H, Eby M, Aravind L, et al. (2004) De-ubiquitination and ubiquitin ligase domains of A20 downregulate NF-kappaB signalling. Nature 430: 694–699.
59. Stertz S, Reichelt M, Spiegel M, Kuri T, Martínez-Sobrido L, et al. (2007) The intracellular sites of early replication and budding of SARS-coronavirus. Virology 361: 304–315.

OPEN ACCESS Freely available online

PLoS one

Host Genetics and Chlamydia Disease: Prediction and Validation of Disease Severity Mechanisms

Isao Miyairi[1,2,6]*, Jesse Ziebarth[1], Jonathan D. Laxton[1], Xiaofei Wang[1], Nico van Rooijen[4], Robert W. Williams[3], Lu Lu[3,5], Gerald I. Byrne[1], Yan Cui[1]*

1 Department of Microbiology, Immunology & Biochemistry, University of Tennessee Health Science Center, Memphis, Tennessee, United States of America, **2** Department of Pediatrics, University of Tennessee Health Science Center, Memphis, Tennessee, United States of America, **3** Department of Anatomy and Neurobiology, University of Tennessee Health Science Center, Memphis, Tennessee, United States of America, **4** Department of Molecular Cell Biology,Vrije Universiteit Medical Center, Amsterdam, The Netherlands, **5** Jiangsu Key Laboratory of Neuroregeneration, Nantong University, Nantong, China, **6** Division of Infectious Diseases, National Center for Child Health and Development, Tokyo, Japan

Abstract

Genetic mapping studies may provide association between sequence variants and disease susceptibility that can, with further experimental and computational analysis, lead to discovery of causal mechanisms and effective intervention. We have previously demonstrated that polymorphisms in immunity-related GTPases (IRG) confer a significant difference in susceptibility to *Chlamydia psittaci* infection in BXD recombinant mice. Here we combine genetic mapping and network modeling to identify causal pathways underlying this association. We infected a large panel of BXD strains with *C. psittaci* and assessed host genotype, IRG protein polymorphisms, pathogen load, expression of 32 cytokines, inflammatory cell populations, and weight change. Proinflammatory cytokines correlated with each other and were controlled by a novel genetic locus on chromosome 1, but did not affect disease status, as quantified by weight change 6 days after infection In contrast, weight change correlated strongly with levels of inflammatory cell populations and pathogen load that were controlled by an IRG encoding genetic locus (*Ctrq3*) on chromosome 11. These data provided content to generate a predictive model of infection using a Bayesian framework incorporating genotypes, immune system parameters, and weight change as a measure of disease severity. Two predictions derived from the model were tested and confirmed in a second round of experiments. First, strains with the susceptible IRG haplotype lost weight as a function of pathogen load whereas strains with the resistant haplotype were almost completely unaffected over a very wide range of pathogen load. Second, we predicted that macrophage activation by *Ctrq3* would be central in conferring pathogen tolerance. We demonstrated that macrophage depletion in strains with the resistant haplotype led to neutrophil influx and greater weight loss despite a lower pathogen burden. Our results show that genetic mapping and network modeling can be combined to identify causal pathways underlying chlamydial disease susceptibility.

Citation: Miyairi I, Ziebarth J, Laxton JD, Wang X, van Rooijen N, et al. (2012) Host Genetics and Chlamydia Disease: Prediction and Validation of Disease Severity Mechanisms. PLoS ONE 7(3): e33781. doi:10.1371/journal.pone.0033781

Editor: Bernhard Kaltenboeck, Auburn University, United States of America

Received October 27, 2011; **Accepted** February 17, 2012; **Published** March 16, 2012

Funding: This work was funded by AI081050 (IM, YC, LL), 09GBIA2050135 (IM), Children's Infection and Defense Center Grant (IM), BAA08-1 (GIB, IM), AI19782 (GIB), AI30040 (GIB). The funders had no role in study design, data collection and analysis, decision to publish, or preparation of the manuscript.

Competing Interests: The authors have declared that no competing interests exist.

* E-mail: miyairi-i@ncchd.go.jp (IM); ycui2@uthsc.edu (YC)

Introduction

The genus *Chlamydia* comprises a number of species of highly related obligate intracellular prokaryotic pathogens that cause clinical disease in humans ranging from blinding trachoma [1] and sexually transmitted infection by *Chlamydia trachomatis* [2], community acquired pneumonia by *Chlamydia pneumoniae* [3] and life-threatening respiratory and systemic zoonosis by *Chlamydia psittaci* [4]. In a previous study, we determined that a known QTL on chromosome 11 (*Ctrq3*) [5,6] containing two polymorphic innate immune genes (*Irgm2* and *Irgb10*) in the family of immunity-related GTPases (IRG) were responsible for the innate difference in susceptibility to a systemic infection to *C. psittaci* among the BXD recombinant inbred strains [7]. Each member of this mouse reference strain set inherits a unique and approximately equal fraction of their genomes from two fully inbred progenitors—strain C57BL/6J (B6 or B) and DBA/2J (D2 or D). These two parental strains differ at roughly 5 million sites across the genome. The set of 80 BXD strains is being used for systematic multiscalar genetic studies of host-pathogen interactions [8,9,10]. This large set of genetically related strains can provide comparatively high precision mapping, with a resolution of 1–2 Mb in several cases [7,11]. Characterization of the disease susceptibility differences between the B6 and D2 parental strains revealed significant differences in *C. psittaci* load, inflammatory responses, and cytokine profiles. While the IRGs have been shown to control *Chlamydia* load [6,7,12], alternative immunomodulatory functions of these genes have also been reported [13,14,15] making it unclear if IRGs influence disease outcome by regulating pathogen load or by influencing other immunomodulatory functions [16].

Recent advances in high-throughput genomic technologies and computational methods allow us to formulate and test genetic network models without explicit data on molecular function. Translating large-scale genomic data into network models with

predictive power is a challenging task. The most valid approach is to systematically evaluate the possible hypothetical network models against data and then select the most probable models for experimental validation. The probability of a genetic network model conditioned on the data can be calculated using Bayesian network methods. A Bayesian network is a graphic probabilistic model representing the dependence structure among multiple interacting variables [17,18,19]. The probabilistic modelling provides a natural treatment for the stochastic aspects of biological processes and noisy measurements [20]. Bayesian networks can be used to integrate prior knowledge and new data to capture and express causal relationships [21,22,23].

We combined forward genetics and Bayesian network analysis to model the biological pathway of how *Ctrq3* or polymorphisms in immunity-related GTPases (IRGs) confer susceptibility and resistance to *Chlamydia* infection in strains of mice with different genetic backgrounds. We then predicted how individual mice would respond to different intervention and validated these predictions. The model predicted that *Ctrq3* confer protection against disease through macrophage activation, which then controls pathogen load and neutrophil influx. The factor with the greatest impact on disease severity, as quantified by weight change in strains infected with *Chlamydia*, was predicted to be neutrophil influx rather than pathogen load. We validated these predictions experimentally. Thus, our work provides an experimentally validated model for an immune-regulatory function of the IRG containing *Ctrq3* locus in contributing to the control of systemic *C. psittaci* infection.

Results

Immune responses and disease severity to *Chlamydia psittaci* infection is controlled by two major genetic loci

We infected the C57BL/6J parental strain and 40 BXD strains intraperitoneally, and measured peak *C. psittaci* load, levels of macrophages and neutrophils in the peritoneal cavity, 32 cytokines on days 3 and 6; and disease status as quantified by the weight change from the day of infection. Strains exhibited a spectrum of disease ranging from 30% weight loss to 10% weight gain over 6 days. Significant variation in cytokine protein expression was detected for 17 of 32 cytokines (all results will be deposited and will be accessible in GeneNetwork, www.genenetwork.org). We confirmed that the previously mapped and cloned *Ctrq3* locus on chromosome 11 is a major controller of weight change, macrophage activation status (MAS), level of neutrophil recruitment, and *C. psittaci* load on day 6 (Figure 1). A novel secondary locus was mapped to distal Chr 1 at ~190 Mb. This locus modulates levels of several key cytokines—GM-CSF, IL1a, MIP1a, MIP1b, MIP2—but has no effect on disease severity as measured by weight changes (Figure 2). To further investigate the influence of the genetic polymorphisms at *Ctrq3*, we analyzed the expression pattern of the IRGM2 protein in the peritoneal lavage specimens from infected BXD strains and found that it had two distinct band sizes that are directly correlated with the *Ctrq3* genotype [7].

Correlation network analysis reveals the immune phenotypes associated with disease severity

We constructed a correlation network, including cytokines, genotypes, immune parameters and disease phenotypes (Figure 3). The network nodes clustered into two groups. The first group correlated tightly with the *Ctrq3* genotype, IRGM2 expression pattern and several disease-related parameters, including weight change, macrophage activation status (MAS), pathogen load, and neutrophil recruitment. A single cytokine, G-CSF, had a high correlation with weight change and neutrophil level, but was not controlled by *Ctrq3* (Figure 1E. no significant QTL). The second group comprised the cytokines, many of which are highly correlated with each other, and the genotype at rs13476293, a marker located at ~190 Mb on Chr 1, but not directly with disease-related parameters.

Bayesian network model identifies the central role of macrophages in the disease pathway

We constructed a Bayesian network model to identify casual pathways through which genotype at *Ctrq3* influences disease outcome after infection with *C. psittaci* (Figure 4). The Bayesian network included variables that were highly correlated with weight change and influenced by the genotype at *Ctrq3*: IRGM2 expression pattern, macrophage activation status, neutrophils, and pathogen load. Because of the perfect correlation between the *Ctrq3* genotype and IRGM2 expression pattern, these variables were combined into a single node. In the most likely model structure, the genotype at *Ctrq3* was the immediate parent of all of the other variables in the model, signifying that each of these variables is directly influenced by the genotype. However, the model also suggests that *Ctrq3* genotype was not sufficient in explaining these variables, as there were additional conditional dependencies in the model structure. Weight change, for example, was directly influenced by neutrophil recruitment and macrophage activation status (MAS) in addition to genotype at *Ctrq3*, indicating that the levels of neutrophils and MAS influences weight change independent of the *Ctrq3* genotype. The model also suggested that macrophage activation influences weight change via regulation of neutrophil recruitment but not by pathogen load restriction.

Macrophage and neutrophil influx levels defines disease severity

We used the Bayesian network model to investigate the effect of depletion of macrophages on neutrophil influx, *C. psittaci* load, and weight change (Figure 5 network C and D). To discretize the predictions of the model, a threshold was determined by averaging the mean value of strains with a B genotype and the mean value of strains with a D genotype for the original data sample. Then, the probability that the predicted value for each variable was greater than (High) or less than (Low) this threshold was calculated from the conditional Gaussian distributions learned from the network for the original data and after macrophage depletion (Methods). Nodes with a yellow background have been assigned the value to represent data for only a given genotype and status of intervention on MAS. The magnitude of these changes is expected to be much more pronounced in strains with a B genotype at *Ctrq3* than in strains with a D genotype at this locus. (Figure 5 and Figure S2) Strains with the D genotype at *Ctrq3* typically have innately low macrophage activation, and as a result the model predicts only slight changes in the levels of neutrophils, pathogen load, and weight after depleting macrophages.

We tested these predictions by performing chemical depletion of macrophages with clodronate before infecting B6 and D2 strains with *C. psittaci*. The experiments validated many of the model's predictions (Figure 6). In the D2 strain, depletion of macrophages increased neutrophil influx, *C. psittaci* load, and induced a more rapid decline in weight and mice were therefore euthanized on day 4 post infection. Pathogen load in the liver was greater in macrophage depleted mice by nearly 2 logs (PBS control: 1.21×10^5 IFU/gram, Clodronate treated; 9.37×10^6 IFU/gram, $p = 0.03$). As predicted, in the resistant B6 strain, depletion of

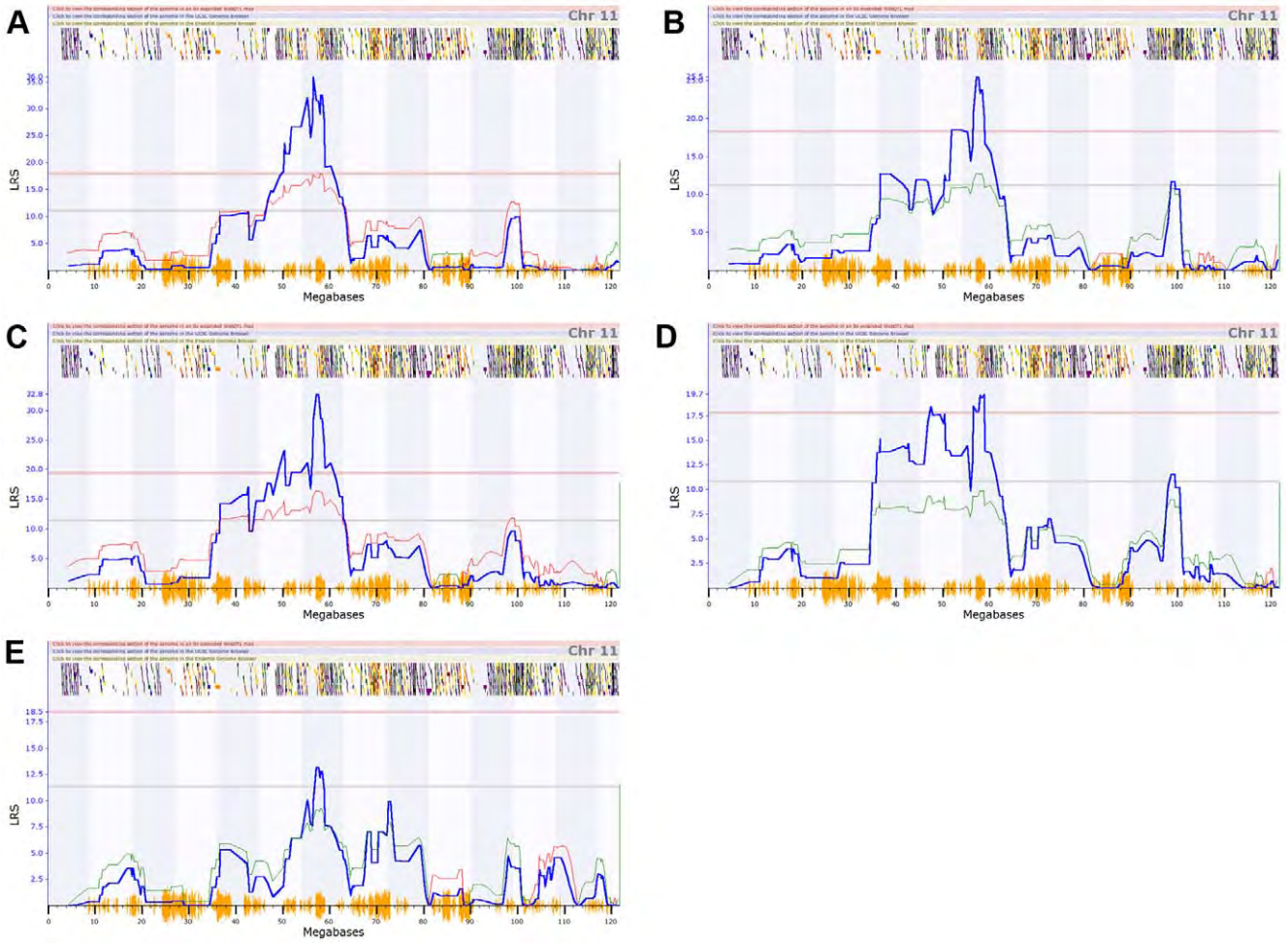

Figure 1. Association of the *Ctrq3* locus with immune parameters and disease status. QTL mapping results for (A) day 6 weight, (B) neutrophils, (C) macrophage activation status, (D) *C. psittaci* load, and (E) G-CSF on chromosome 11. *Ctrq3* is located near 58 Mb on chr 11. Significant (genome-wide adjusted $p<0.05$) and suggestive (adjusted $p<0.63$) QTLs are indicated by the solid red and grey lines, respectively. Blue lines indicate the likelihood-ratio statistic (LRS) that the phenotype is associated with the genomic locus. The colored lines following the trend of the LRS show the additive effect of the influence of the locus, with red lines indicating that D alleles increase trait values, while green alleles indicate that B alleles increase trait values.
doi:10.1371/journal.pone.0033781.g001

macrophages increased neutrophils and exacerbated the weight loss. These mice were moribund 5 days post-infection. Pathogen load in the liver was similar in B6 irrespective of whether macrophages were depleted or not (PBS control: 4.26×10^6 IFU/gram, Clodronate treated; 3.81×10^6 IFU/gram, $p=0.06$) but their peritoneal pathogen load was decreased after depleting macrophages, suggesting that pathogen load restriction may not be entirely responsible for controlling disease severity.

Ctrq3 confers genetic resistance and tolerance to Chlamydia

Several reports have documented that IRGs reduce pathogen burden in vitro and in vivo, which is expected to influence disease severity [6,7,12,24]. To investigate the possibility that the status of the *Ctrq3* genotype switches disease modality, we performed the Bayesian analysis for strains with the B genotype at the *Ctrq3* locus separately from strains with the D genotype. The influence of load on weight change was much stronger for strains with the susceptible D genotype than strains with the resistant B genotype (described further in Methods). Because of the genotype-specific switching between pathogen load and weight change in the model, we expanded this analysis to 197 BXD mice and correlated the weight loss with pathogen load in individual mice according to the genotype at the *Ctrq3* locus (Figure 7). Overall, mice with the B genotype had lower pathogen load compared to mice with a D genotype, although a considerable overlap existed. The mice with the B genotype were tolerant of increases in pathogen burden whereas mice with D genotype lost more weight with increases in pathogen burden as demonstrated by the differences in the slope of the load to weight linear regression lines ($p=0.02$).

Discussion

Individualized medicine requires the capability of predicting an individual's susceptibility to diseases and response to medical treatments, based on genetic profile. Individual differences in disease susceptibility and response to therapeutic interventions are complex phenotypes modulated by genetic factors. We formulated an approach using Bayesian networks to model the pathways through which gene variants operate on phenotypes. Results of our study demonstrate experimental validation of the combined

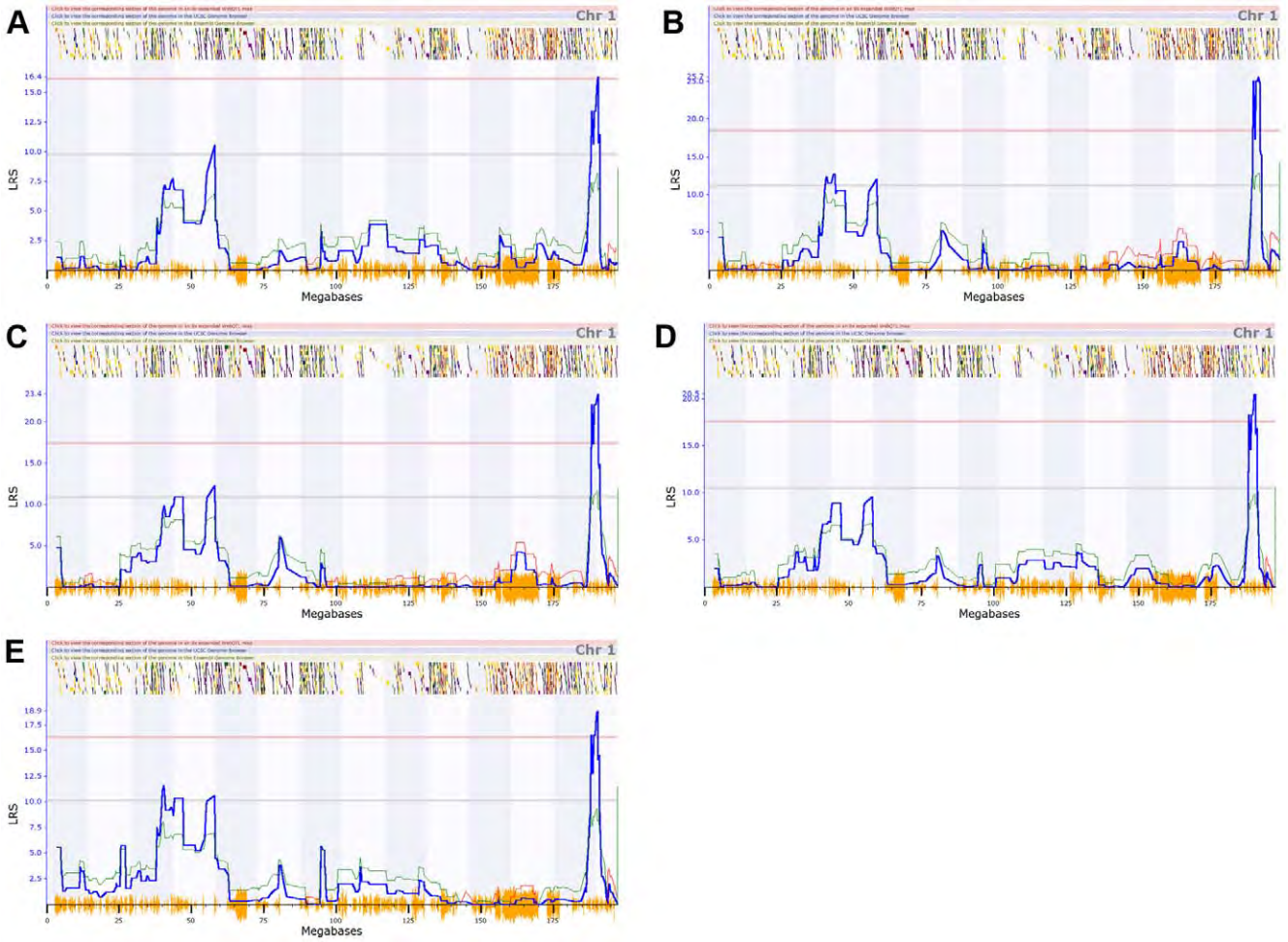

Figure 2. A QTL on chromosome 1 regulating cytokines. QTL mapping results for (A) GM-CSF, (B) IL-1a, (C) MIP-1a, (D) MIP-1b, and (E) MIP-2 on chromosome 1. Significant (genome-wide adjusted $p<0.05$) and suggestive (adjusted $p<0.63$) QTLs are indicated by the solid red and grey lines, respectively. Blue lines indicate the likelihood-ratio statistic (LRS) that the phenotype is associated with the genomic locus. The colored lines following the trend of the LRS show the additive effect of the influence of the locus, with red lines indicating that D alleles increase trait values, while green alleles indicate that B alleles increase trait values.
doi:10.1371/journal.pone.0033781.g002

systems genetics and Bayesian network approaches to immune pathway modeling and disease prediction. This approach provides a way to develop models for designing genetic association studies that can define causal pathways with the predictive power required in individualized medicine.

We had previously demonstrated that *Ctrq3* controls systemic *C. psittaci* disease outcome and found an association with IRG polymorphisms. While IRGs have cell autonomous functions of pathogen restriction, the immunological pathway that links this genotype to phenotype has not been defined. It has recently been reported that infected hosts employ two different strategies to defend themselves against pathogens—resistance and tolerance [25,26,27]. Resistance is defined as the ability to limit pathogen burden, whereas tolerance is defined as the ability to limit the damage caused by a given pathogen burden [28,29]. While most studies on genetic susceptibility to infectious diseases implicate resistance as a mechanism of host protection, there are several examples of genetic tolerance to infection in animal models [29,30,31].

In this study, we predicted that *Ctrq3* conferred resistance but with relatively little impact on weight change. We also predicted an expanded role for *Ctrq3* that included macrophage activation and weight change. Indeed mice with a B6 genotype at the *Ctrq3* locus tended to have a lower pathogen load than mice with D2 genotype and thus were more resistant. However, there was significant variability in the pathogen load within mice with the same genotype suggesting the presence of other factors that affect resistance. The mechanism of resistance by *Ctrq3* is likely to be due to the cell autonomous bactericidal functions of the B6 derived *Irgb10* and *Irgm2* genes given results of our previous ex vivo siRNA experiments [5,6,7]. On the other hand, we found that mice with a B6 genotype at the *Ctrq3* locus can maintain body weight over a wide range of pathogen load and thus have tolerance to *C. psittaci* infection. In contrast, mice with a D2 genotype lost weight as a function of increased pathogen burden and were thus less tolerant. The molecular basis of tolerance is still unclear.

An obvious limitation of our model is that we are assessing the function of the 2 MB *Ctrq3* locus. This locus encodes three IRGs (*Irgb10*, *Irgm2*, and *Irgm3*), 18 other genes, as well as non-coding regions with unknown functions. While IRGs remain a primary candidate given its association with immunoregulatory functions [13,14,15,16,32,33], it is possible that resistance and tolerance is

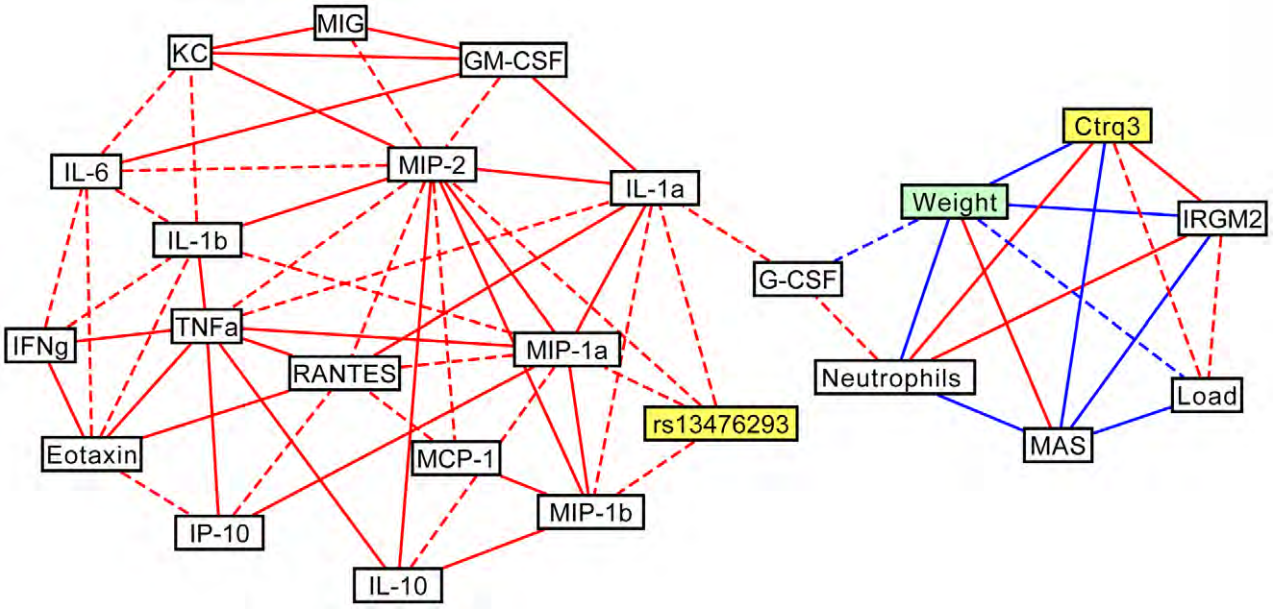

Figure 3. The correlation network of immune parameters during Chlamydia infection in BXD mice. Correlation network linking BXD genotypes (*Ctrq3* and rs13476293), *C. psittaci* load, inflammatory responses, cytokine profiles, IRGM2 protein expression pattern, and weight change after *C. psittaci* infection in BXD strains. Positive (red) and negative (blue) correlations between variables with magnitudes of Pearson's correlation coefficient greater than 0.6 (dashed lines) and 0.7 (solid lines) are shown.
doi:10.1371/journal.pone.0033781.g003

conveyed by one or more of the other genes in this interval. Furthermore, the exact nature of the B6 and D2 Irgm2 alleles (e.g. "wildtype," loss-of-function, hypomorph, constitutively active, etc) is unclear and warrant additional biological validation.

While the mechanism of tolerance is unclear, our model suggests that mice that do not recruit activated macrophages to the site of infection have an increased number of recruited neutrophils and more severe disease as evidenced by greater weight loss. Specifically, Bayesian analysis predicted that mice with a D genotype at the *Ctrq3* locus would lose less weight if neutrophils were depleted (day 6 to day 0 weight ratio: 0.83 for mice without neutrophil depletion and 0.89 with neutrophils depleted) without any change in pathogen load. This prediction was consistent with our previous observations where *Cxcr2* knockout mice that cannot recruit neutrophils to the site of infection, survived challenge without any detectible changes in pathogen load. In contrast, the BALB/c wild type strain succumbed to infection with significant neutrophil recruitment in a manner similar to the D2 strain [7]. We speculate that in our model, loss of tolerance leads to uncontrolled inflammation and severe disease high-lighted by neutrophil influx.

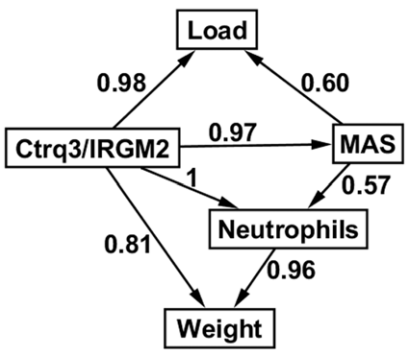

Figure 4. Structure of Bayesian network (BN) model of *C. psittaci* infection. The number next to each directed arc of the BN indicates the confidence (posterior probability) in the arc after model averaging as described in the Methods.
doi:10.1371/journal.pone.0033781.g004

Interestingly, we found that macrophage depleted B6 mice have a reduced number of *C. psittaci* in the infected peritoneal cavity; whereas macrophage depleted D2 mice had a greater number. We also found that after macrophage depletion, *C. psittaci* load in the liver of D2 mice increased by 2 logs whereas loads were similar in the liver of B6 mice. We speculate that in B6 mice, loss of a growth niche led to a decrease in pathogen load, whereas the apparent increase in pathogen load in the peritoneal cavity in D2 mice is being supported by an increase in *C. psittaci* growth in the surrounding tissues. While this indicates there may be a difference in tissue/cell tropism between B6 and D2 mice, the underlying mechanism is unknown at this point.

There are clear limitations of our model and approach. First, we are limited by the variables we chose to screen, which did not account for various other cell types, cytokines, physiological parameters, etc. Second, we are limited by the dynamic process of infectious diseases, which include the important variable of time, where our longitudinal analyses were limited (<1 week) due to the severity of disease in D2 mice. Third, we are limited by the nature of the intervention we can employ. In our model, we found that macrophage activation, which occurs gradually over the course of infection, was an important variable that determines disease outcome. In our validation experiment, we eliminated macrophages prior to infection in order to simulate the extreme end of this variable, which may have led to activation of alternative pathways or immune cells. Despite these limitations, our results demonstrate a proof of principal model of how genetic mapping and network modeling can be combined to identify causal pathways underlying infectious disease susceptibility.

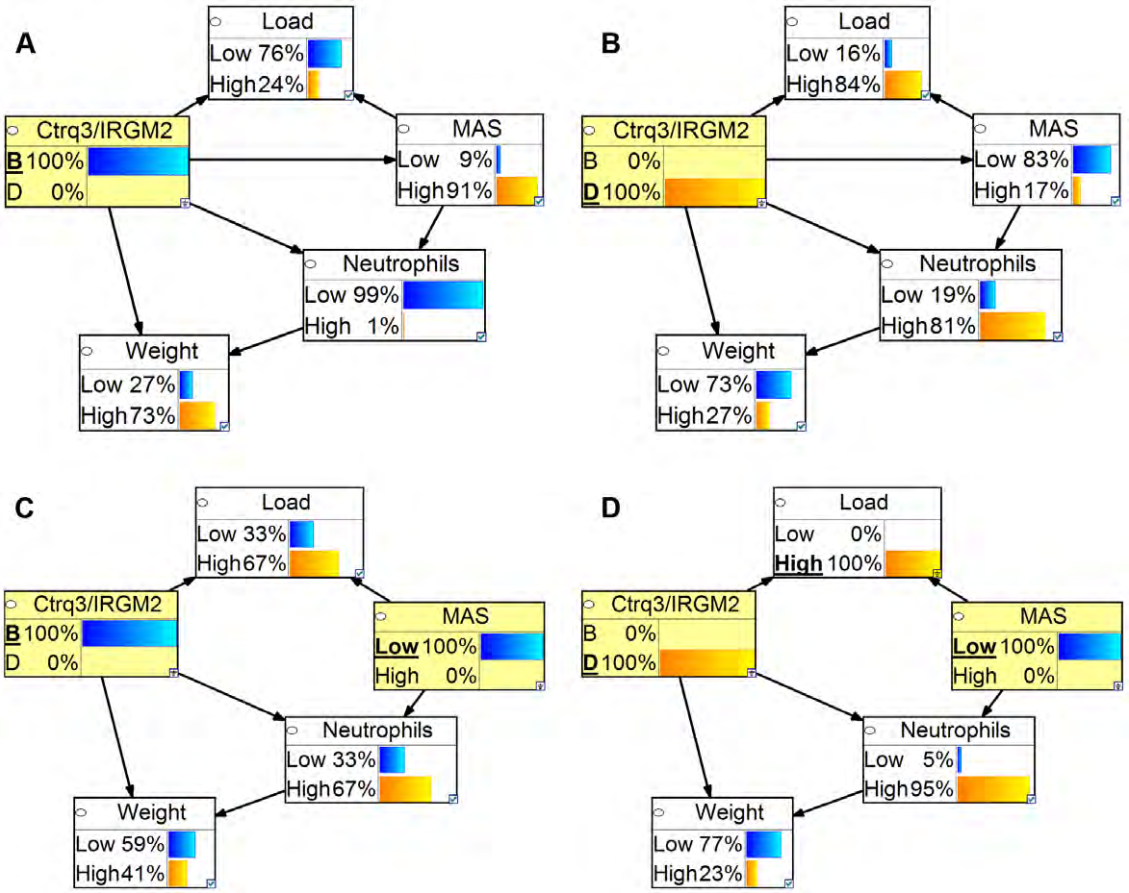

Figure 5. Predictions of the BN as a function of genotype and macrophage intervention. (A and B) Discretized p of the BN as a function of genotype at *Ctrq3*. BXD strains with the susceptible, D, genotype at the IRG locus tend to have lower MAS and weights and higher levels of neutrophils and pathogen load. (C and D) Discretized p effect of interventional depletion of macrophages on the values of variables in the BN.
doi:10.1371/journal.pone.0033781.g005

Materials and Methods

Ethics Statement

This study was carried out in strict accordance with the recommendations in the Guide for the Care and Use of Laboratory Animals of the National Institutes of Health. The protocol (internal protocol number 1709R1) was approved by the Animal Care and Use Committee of the University of Tennessee Health Science Center (PHS assurance# - A-3325-01). No surgical procedures were performed. All efforts were made to minimize suffering.

Infection and sample collection

Chlamydia psittaci infection: *C. psittaci* 6BC was propagated in L cells, titrated and stored at −80C°. Intraperitoneal infection with *C. psittaci* 6BC (10^4 IFU) was performed using the same stock source to minimize variations across experiments. 8–16 week old male mice (C57BL/6J, and 40 BXD strains) were infected in groups of 2 mice/strain. Infected mice were monitored daily for weight changes. On days 3 or 6-post infection, mice were euthanized to obtain peritoneal lavage samples for pathogen load, flow cytometry, and cytokine analysis. Additional mice, totaling 197 mice representing 56 BXD strains, were infected with *C. psittaci* 6BC (10^4 IFU) and monitored for weight changes and euthanized on day 6 for IFU analysis.

Assessment of immune phenotypes

***Chlamydia psittaci* load.** Titration was performed by a cell culture based IFU assay for day 6 samples as previously described [7]. DNA was extracted from 1 ml of peritoneal lavage fluid from day 3 and *C. psittaci* load was measured as a ratio of *C. psittaci* ompA DNA/host GAPDH by quantitative DNA PCR.

Flow cytometry. Standard methods were used as described previously [7]. Briefly, murine peritoneal exudates were blocked with Fc block and incubated with fluorochrome-conjugated antibodies. The following antibodies were used: Macrophage marker; F4/80-APC, Neutrophil marker; Ly6G (clone IA8)-PE, and MHC class II marker; IA/IE-PE. Data was expressed as percent of macrophages or neutrophils in the entire population. MHC class II expression was used as a marker for macrophage activation status and data was expressed as percent of F4/80 positive cells that were also positive for IA/IE.

Cytokine analysis. Peritoneal lavage supernatants were analyzed using the Luminex based Mouse 32-plex kit to analyze levels of 32 cytokines (CATALOG).

Western blot analysis. Peritoneal lavage specimens were analyzed by Western blot analysis using standard methods with GTPI antibody (M-14) Santa Cruz (sc-11088) and secondary antibody using Goat true blot (eBioscience 18-8814-31).

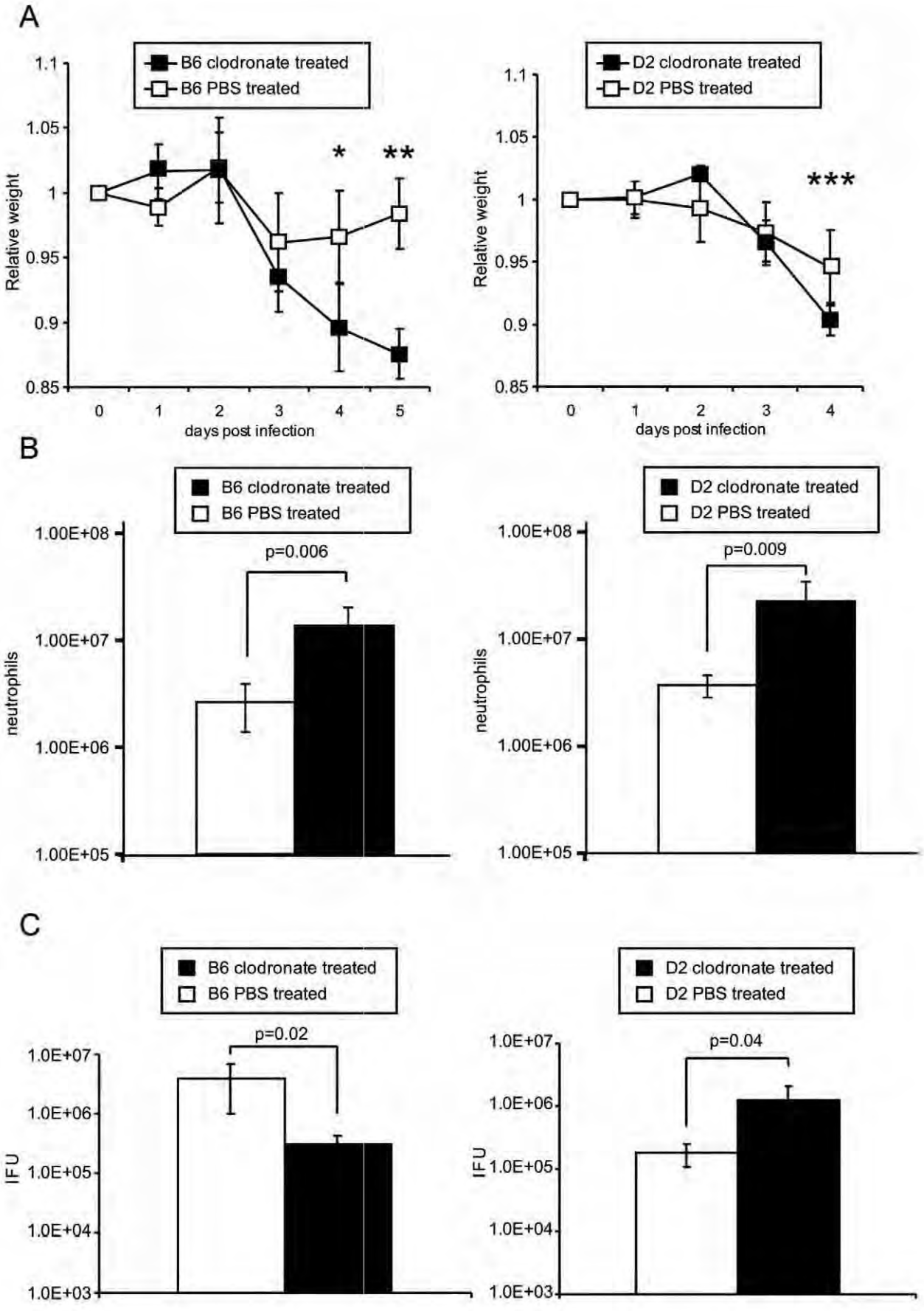
A
B6 clodronate treated
B6 PBS treated
Relative weight
days post infection
*
**
D2 clodronate treated
D2 PBS treated
***
B
neutrophils
p=0.006
p=0.009
C
IFU
p=0.02
p=0.04

Figure 6. Impact of macrophage depletion on the course of *C. psittaci* infection in B6 and D2 strains. B6 and D2 mice received either liposome clodronate or liposome PBS iv (day −1 post infection) and i.p. (day −1, 1, and 3 post infection) and infected with *C. psittaci* 10^4 IFU intraperitoneally (N = 5/group). Mice were monitored daily for weight (A) and appearance. Data points where differences in weight met statistical significance are indicated in asterix (* p = 0.003, ** p = 3.7×10E-5, p = 0.04). Clodronate treated D2 strain became moribund on day 4 and B6 on day 5 post infection and were euthanized. Brackets and p values are provided to indicate differences in, number of neutrophils (B), and *C. psittaci* load (C) between clodronate (black) and liposome (white) treated mice for both B6 and D2 strains. Data is representative of two experiments.
doi:10.1371/journal.pone.0033781.g006

Data analysis

QTL mapping. Quantitative trait locus (QTL) mapping was performed for 17 cytokine profiles that exhibited variation across strains; immune responses including levels of neutrophils, macrophages, and macrophage activation status (MAS); and weight change of BXD strain infection with *C. psittaci* with the GeneNetwork (www.genenetwork.org). Single marker regression was performed across the entire mouse chromosome at 3795 markers typed across BXD strains. A likelihood ratio statistic (LRS) was calculated at each marker comparing the hypothesis that the marker is associated with the phenotype with the null hypothesis that there is no association between marker and phenotype. Genome-wide significance was determined by performing 1000 permutations. Two significant (genome-wide p-value<0.05) QTLs were found: one QTL was located near 55 Mb on chromosome 11 and was associated with weight change, MAS, pathogen load, and neutrophil levels (Figure 1), while the other significant QTL was located on chromosome 1 near 190 Mb and was associated with several cytokines (Figure 2).

Bayesian network modeling. Structural learning of the Bayesian network was performed using the R package *deal* (http://cran.r-project.org/web/packages/deal/index.html). The network was constructed from data for C57BL/6J and 40 BXD strains using one discrete node, representing the *Ctrq3* genotype and IRGM2 protein expression pattern, and four continuous nodes (neutrophils, *C. psittaci* load, macrophage activation status, and the ratio of the weight of the mice 6 days after infection to the weight before infection), which were modeled with conditional Gaussian distributions. The Bayesian network score [34], which is basically a version of the BDe scoring metric [35] extended to include

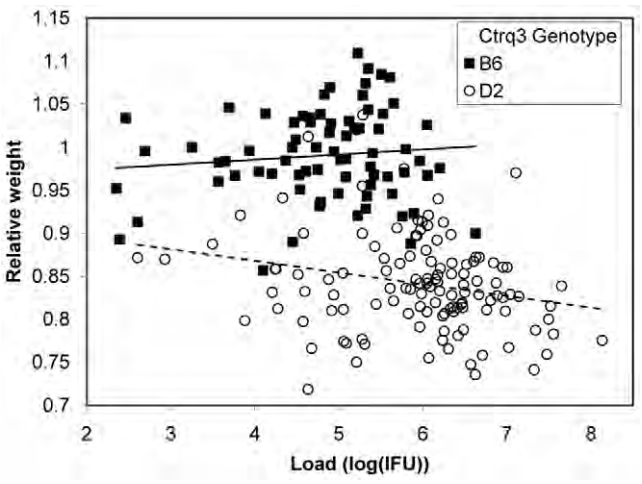

Figure 7. Genetic resistance and tolerance to Chlamydia infection in mice. Plot of weight change as a function of IFU for 197 BXD mice infected with *C. psittaci*. Mice with the susceptible D genotype at the *Ctrq3* (open symbols) lose weight as pathogen load increases, while mice with the resistant B genotype at the *Ctrq3* marker (filled circles) do not. The slopes of the linear regression lines for the B (solid line) and D (dashed line) data are significantly different (p = 0.02).
doi:10.1371/journal.pone.0033781.g007

conditional Gaussian distributions, was calculated in *deal* for all, except those that violated two restrictions. First, potential models in which the genotype node was the child of any other nodes in the network were not considered. This restriction does not require that the genotype node be the parent of the other nodes, as model structures in which continuous nodes were independent of genotype were allowed. Second, the weight node could not be the parent of any other node. The Bayesian score metric inherently handles the problem of over fitting data to complex models [36]. However, selecting a single best network model and ignoring all other models may still lead to over-fitting the data. Model averaging can be used to reduce this risk [37]. An indicator function f is defined as: if a network G learned from data D has the feature (here a feature is a directed edge representing a regulatory relationship), $f(G)=1$, otherwise, $f(G)=0$. The posterior probability of a feature is $P(f(G)|D)=\sum_G f(G)P(G|D)$. This probability reflects our confidence in the feature f. We calculated the posterior probability of features by averaging over all possible models, with the restrictions noted above. All features with a posterior probability greater than 0.5 were included in the network.

The reproducibility of the structure learning method was investigated with the use of simulated data. Briefly, the model learned for the original network was used to generate simulated data sets. Then, the structure learning method was repeated with the simulated data sets and the network structures learned from the simulated data sets were compared to the structure of the original network. A high correspondence between the simulated structures and the original structure indicates that the size of the original data set was sufficient to learn the structure of the network. To create the simulated data, parameter learning of the network was performed with the maximum likelihood estimator provided in the Bayes Net Toolbox [38], available for download at: http://code.google.com/p/bnt/. Before the parameters of the network were learned, the data for the four continuous nodes was normalized to have a mean of 0 and standard deviation of 1. 1000 simulated data sets with 41 samples were then generated with the sample_bnet function of the Bayes Net Toolbox. The structure learning method used to learn the original network was then used for each of the simulated data sets. The edges in the original network were highly reproduced in the simulated data (Figure S1).

Prediction of effects of macrophage depletion. We predicted the effects of intervention using a hybrid Bayesian network including both the discrete genotype node and continuous nodes modeled with conditional Gaussian distributions with the Bayes Net Toolbox. The parameters of the network were learned with a maximum likelihood approach. Macrophage depletion is an external intervention to the model. The intervention sets the value of the MAS node and relieves it from the influence of its parent node. Therefore, prediction was performed by removing the link *Ctrq3*/IRGM2→MAS and setting macrophage activation status to the minimum value observed in the data used for parameter learning [action *do* (MAS = MIN), where MIN = 0,032 is the minimum observed MAS value]. The probabilistic inference was executed using the Bayes Net Toolbox. The effects of macrophage depletion on the parameters of the conditional Gaussian

distributions for each node are compared in Table S1 and Figure S2. Depletion of macrophages causes increases in the levels of neutrophils and pathogen load and decreased weight. The magnitude of these changes is larger for mice with the D genotype at *Ctrq3*.

Bayesian network cross-validation. Leave-one-out cross validation was also used to test the performance of the hybrid Bayesian network. For each test strain, parameter learning of the remaining 40 strains and inference was performed with the Bayes Net Toolbox with the methods mentioned above. To evaluate the quality of the continuous predictions, we used the Q^2 parameter [39], which is given by:

$$Q^2 = 1 - \frac{\sum (y_i - \hat{y}_i)^2}{\sum (y_i - \bar{y})^2}$$

where y_i is the value of the ith sample, $\hat{y}_i$ is the predicted value of the ith sample, and $\bar{y}$ is the sample mean. The values of Q^2 for MAS, neutrophil level, pathogen load, and weight were 0.51, 0.59, 0.45, and 0.68, respectively. Additionally, we discretized the original data and the predictions from the leave-one-out-cross validation for each strain and used this discretized data to test the accuracy of the predictions. A threshold for each of the continuous variables was determined by averaging the mean value of the original data for all strains with the B genotype and the mean value for all strains with the D genotype. Then, the continuous variables for the original data and the predictions were classified as being either High or Low through comparison with these threshold values for each strain. The accuracy was then determined by dividing the number of predictions that matched the original data by the total number of strains. For MAS, neutrophil level, pathogen load, and weight, the accuracy was accuracy 85%, 93%, 80%, and 88%, respectively.

Strain dependent influence of pathogen load on weight change after infection: To test if the arc from pathogen load to weight ratio was genotype dependent, the data for mice with B and D genotypes at the *Ctrq3* locus were separated. As each data set only contained data from strains with one genotype, the genotype node was removed from the network, and the structure of the network, using model averaging of an exhaustive search of possible structures with *deal*, was learned for both the B and D data. For strains with the D genotype, a directed edge from pathogen load to weight ratio had a posterior probability of 0.64, while the same edge for strains with the B genotype had a posterior probability of only 0.16, indicating that weight change was dependent on *C. psittaci* load only for strains with the susceptible D genotype. This conclusion was confirmed by grouping the pathogen load and weight ratio for a total of 197 mice into B and D groups using the genotype at *Ctrq3*. Slopes of the linear regression lines of pathogen load vs. weight ratio for each group were calculated and compared using the analysis of covariance tool in Matlab 7.8 (R2009a). The slopes of the lines were significantly different with a p-value of 0.02.

Validation experiments

B6 and *D2* mice were each grouped into two groups (N = 5) that received clodronate containing liposome or PBS containing liposome injections on day −1, 1, 3, 5 (day −1: 200 uL iv, 200 uL i.p., day 1, 3, 5: 200 uL i.p.) [40]. All mice were infected on day 0 with *C. psittaci* 6BC at 10^4 IFU i.p. and monitored daily for weight changes. On day 6 post infection, mice were euthanized and peritoneal lavage was obtained. The peritoneal lavage was processed for pathogen load, cell population (number of neutrophils and macrophages) and macrophage activation status by flow cytometry as described before. The total number of cells in the lavage was enumerated by cytometer and total numbers of neutrophils were calculated.

Supporting Information

Figure S1 Reproducibility of network structures. The number next to each edge is the fraction of times that the edge was present in the structure of 1000 simulated data sets. The simulated data sets were generated from the parameters of the original network and contained 41 samples, the same number of samples as in the original data set. The structure learning method used for the simulated data sets was the same as that used for the original network. No edges not present in the original network occurred in more than 0.29 of the simulated data sets.
(TIF)

Figure S2 Effect of macrophage depletion on predictions of continuous data by Bayesian network. Probability density functions for Gaussian distributions describing the predicted values of macrophage activation status (A), pathogen load (B), neutrophils (C), and weight (D) in normal mice (solid lines) and in mice with depleted macrophages after treatment with clodronate (dashed lines). The effect of macrophage depletion has a much larger effect on predictions for mice with the resistant B6 genotype (blue lines) than with the susceptible D2 genotype (orange lines).
(TIF)

Table S1 Mean values of Bayesian network predictions as a function of genotype and macrophage intervention.
(DOC)

Author Contributions

Conceived and designed the experiments: IM JZ YC. Performed the experiments: IM JZ JDL XW YC. Analyzed the data: IM JZ YC GIB. Contributed reagents/materials/analysis tools: LL RWW NvR. Wrote the paper: IM JZ YC GIB RWW.

References

1. Burton MJ, Mabey DC (2009) The global burden of trachoma: a review. PLoS Negl Trop Dis 3: e460.
2. Centers for Disease Control and Prevention (2009) Chlamydia Prevalence Monitoring Project Annual Report 2007. Atlanta, GA.
3. Hammerschlag M, Kohlhoff S, Apfalter P (2009) Chlamydophila (Chlamydia) pneumoniae. In: Mandell G, Bennett J, Dolin R, eds. Mandell, Douglan, and Bennett's Principles and Practice of Infectious Diseases. 7th ed. Philadelphia, PA: Churchill Livingstone.
4. Beeckman DS, Vanrompay DC (2009) Zoonotic Chlamydophila psittaci infections from a clinical perspective. Clin Microbiol Infect 15: 11–17.
5. Bernstein-Hanley I, Balsara ZR, Ulmer W, Coers J, Starnbach MN, et al. (2006) Genetic analysis of susceptibility to Chlamydia trachomatis in mouse. Genes Immun 7: 122–129.
6. Bernstein-Hanley I, Coers J, Balsara ZR, Taylor GA, Starnbach MN, et al. (2006) The p47 GTPases Igtp and Irgb10 map to the Chlamydia trachomatis susceptibility locus Ctrq-3 and mediate cellular resistance in mice. Proc Natl Acad Sci U S A 103: 14092–14097.
7. Miyairi I, Tatireddigari VR, Mahdi OS, Rose LA, Belland RJ, et al. (2007) The p47 GTPases Iigp2 and Irgb10 regulate innate immunity and inflammation to murine Chlamydia psittaci infection. J Immunol 179: 1814–1824.
8. Boon AC, deBeauchamp J, Hollmann A, Luke J, Kotb M, et al. (2009) Host genetic variation affects resistance to infection with a highly pathogenic H5N1 influenza A virus in mice. J Virol 83: 10417–10426.
9. Abdeltawab NF, Aziz RK, Kansal R, Rowe SL, Su Y, et al. (2008) An unbiased systems genetics approach to mapping genetic loci modulating susceptibility to severe streptococcal sepsis. PLoS Pathog 4: e1000042.

10. Kotb M, Fathey N, Aziz R, Rowe S, Williams RW, et al. (2008) Unbiased forward genetics and systems biology approaches to understanding how gene-environment interactions work to predict susceptibility and outcomes of infections. Novartis Found Symp 293: 156–165; discussion 165–157, 181–153.
11. Mozhui K, Ciobanu DC, Schikorski T, Wang X, Lu L, et al. (2008) Dissection of a QTL hotspot on mouse distal chromosome 1 that modulates neurobehavioral phenotypes and gene expression. PLoS Genet 4: e1000260.
12. Nelson DE, Virok DP, Wood H, Roshick C, Johnson RM, et al. (2005) Chlamydial IFN-gamma immune evasion is linked to host infection tropism. Proc Natl Acad Sci U S A 102: 10658–10663.
13. Taylor GA (2007) IRG proteins: key mediators of interferon-regulated host resistance to intracellular pathogens. Cell Microbiol 9: 1099–1107.
14. Howard J (2008) The IRG proteins: a function in search of a mechanism. Immunobiology 213: 367–375.
15. Feng CG, Collazo-Custodio CM, Eckhaus M, Hieny S, Belkaid Y, et al. (2004) Mice deficient in LRG-47 display increased susceptibility to mycobacterial infection associated with the induction of lymphopenia. J Immunol 172: 1163–1168.
16. Hunn JP, Howard JC (2010) The mouse resistance protein Irgm1 (LRG-47): a regulator or an effector of pathogen defense? PLoS Pathog 6: e1001008.
17. Pearl J (1988) Probabilistic Reasoning in Intelligent Systems. California: Morgan Kaufmann Publishers.
18. Pearl J (2000) Causality: Models, Reasoning, and Inference. Cambridge, UK: Cambridge University Press.
19. Neapolitan RE (2003) Learning Bayesian Networks. Upper Saddle River: Prentice Hall.
20. de Jong H (2002) Modeling and Simulation of Genetic Regulatory Systems: A Literature Review. Journal of Computational Biology 9: 67–103.
21. Needham CJ, Bradford JR, Bulpitt AJ, Westhead DR (2007) A Primer on Learning in Bayesian Networks for Computational Biology. PLoS Computational Biology 3: e129.
22. Rockman MV (2008) Reverse engineering the genotype-phenotype map with natural genetic variation. Nature 456: 738.
23. Friedman N (2004) Inferring cellular networks using probabilistic graphical models. Science 303: 799–805.
24. MacMicking JD, Taylor GA, McKinney JD (2003) Immune control of tuberculosis by IFN-gamma-inducible LRG-47. Science 302: 654–659.
25. Raberg L, Sim D, Read AF (2007) Disentangling genetic variation for resistance and tolerance to infectious diseases in animals. Science 318: 812–814.
26. Best A, White A, Boots M (2008) Maintenance of host variation in tolerance to pathogens and parasites. Proc Natl Acad Sci U S A 105: 20786–20791.
27. Schneider DS, Ayres JS (2008) Two ways to survive infection: what resistance and tolerance can teach us about treating infectious diseases. Nat Rev Immunol 8: 889–895.
28. Medzhitov R (2009) Damage control in host-pathogen interactions. Proc Natl Acad Sci U S A 106: 15525–15526.
29. Seixas E, Gozzelino R, Chora A, Ferreira A, Silva G, et al. (2009) Heme oxygenase-1 affords protection against noncerebral forms of severe malaria. Proc Natl Acad Sci U S A 106: 15837–15842.
30. Ayres JS, Schneider DS (2008) A signaling protease required for melanization in Drosophila affects resistance and tolerance of infections. PLoS Biol 6: 2764–2773.
31. Ayres JS, Schneider DS (2009) The role of anorexia in resistance and tolerance to infections in Drosophila. PLoS Biol 7: e1000150.
32. Feng CG, Zheng L, Jankovic D, Bafica A, Cannons JL, et al. (2008) The immunity-related GTPase Irgm1 promotes the expansion of activated CD4+ T cell populations by preventing interferon-gamma-induced cell death. Nat Immunol 9: 1279–1287.
33. Bafica A, Feng CG, Santiago HC, Aliberti J, Cheever A, et al. (2007) The IFN-inducible GTPase LRG47 (Irgm1) negatively regulates TLR4-triggered proinflammatory cytokine production and prevents endotoxemia. J Immunol 179: 5514–5522.
34. Bottcher S (2001) Learning Bayesian networks with mixed variables Artificial Intelligence and Statistics, Key West, Florida. pp 149–156.
35. Heckerman D, Geiger D, Chickerling D (1995) Learning Baysian networks: The combination of knowledge and statistical data. Machine Learning: Microsoft Research. pp 197–243.
36. Pe'er D (2005) Bayesian network analysis of signaling networks: a primer. Sci STKE 2005: pl4.
37. Hartemink AJ, Gifford DK, Jaakkola TS, Young RA (2001) Using graphical models and genomic expression data to statistically validate models of genetic regulatory networks. Pac Symp Biocomput. pp 422–433.
38. Murphy KP (2001) The Bayes Net Toolbox for Matlab. Computing Science and Statistics 2001.
39. Hawkins DM, Basak SC, Mills D (2003) Assessing model fit by cross-validation. J Chem Inf Comput Sci 43: 579–586.
40. Van Rooijen N, Sanders A (1994) Liposome mediated depletion of macrophages: mechanism of action, preparation of liposomes and applications. J Immunol Methods 174: 83–93.

OPEN ACCESS Freely available online

PLoS one

Visualization of Murine Intranasal Dosing Efficiency Using Luminescent *Francisella tularensis*: Effect of Instillation Volume and Form of Anesthesia

Mark A. Miller[1]*, Jennifer M. Stabenow[1], Jyothi Parvathareddy[1], Andrew J. Wodowski[1], Thomas P. Fabrizio[1,2], Xiaowen R. Bina[1], Lillian Zalduondo[1], James E. Bina[1]

1 The University of Tennessee Health Science Center, Memphis, Tennessee, United States of America, **2** St Jude Children's Research Hospital, Memphis, Tennessee, United States of America

Abstract

Intranasal instillation is a widely used procedure for pneumonic delivery of drugs, vaccine candidates, or infectious agents into the respiratory tract of research mice. However, there is a paucity of published literature describing the efficiency of this delivery technique. In this report we have used the murine model of tularemia, with *Francisella tularensis* live vaccine strain (FTLVS) infection, to evaluate the efficiency of pneumonic delivery via intranasal dosing performed either with differing instillation volumes or different types of anesthesia. FTLVS was rendered luminescent via transformation with a reporter plasmid that constitutively expressed the *Photorhabdus luminescens lux* operon from a *Francisella* promoter. We then used an IVIS Spectrum whole animal imaging system to visualize FT dissemination at various time points following intranasal instillation. We found that instillation of FT in a dose volume of 10 µl routinely resulted in infection of the upper airways but failed to initiate infection of the pulmonary compartment. Efficient delivery of FT into the lungs via intranasal instillation required a dose volume of 50 µl or more. These studies also demonstrated that intranasal instillation was significantly more efficient for pneumonic delivery of FTLVS in mice that had been anesthetized with inhaled (isoflurane) vs. parenteral (ketamine/xylazine) anesthesia. The collective results underscore the need for researchers to consider both the dose volume and the anesthesia type when either performing pneumonic delivery via intranasal instillation, or when comparing studies that employed this technique.

Citation: Miller MA, Stabenow JM, Parvathareddy J, Wodowski AJ, Fabrizio TP, et al. (2012) Visualization of Murine Intranasal Dosing Efficiency Using Luminescent *Francisella tularensis*: Effect of Instillation Volume and Form of Anesthesia. PLoS ONE 7(2): e31359. doi:10.1371/journal.pone.0031359

Editor: Deepak Kaushal, Tulane University, United States of America

Received September 2, 2011; **Accepted** January 6, 2012; **Published** February 24, 2012

Funding: This project was supported by National Institutes of Health (NIH) grant #U54 AI057157 from the Southeastern Regional Center of Excellence for Emerging Infections and Biodefense (www.serceb.org/), by NIH (www.niaid.nih.gov/) grants AI074582 and AI079482 (to JEB) and AI061260 (to MAM), and by Department of Defense Army grant W81XHW-05-1-0227 (usacehr.amedd.army.mil/). The funders had no role in study design, data collection and analysis, decision to publish, or preparation of the manuscript.

Competing Interests: The authors have declared that no competing interests exist.

* E-mail: mamiller@uthsc.edu

Introduction

Intranasal instillation is currently the most widely used method for delivery of drugs, vaccines, or pathogen challenges targeted for either the upper respiratory tract (URT) or lungs of research mice. Intubation is an alternative method [1,2,3,4,5,6,7] that allows for very efficient delivery of materials into the lungs, but the procedure is technically much more demanding and more time-consuming than intranasal administration. In addition, intubation includes a much higher risk of injury to the animal that could compromise the study. Aerosol administration via a nebulizer-based device [8,9,10,11] also offers very efficient delivery of materials to the lungs with little risk of injury to the animal; however, this method is technically demanding and requires expensive equipment that is not widely available. Moreover, the use of aerosol generators for studies involving dangerous pathogens involves safety issues for research personnel that do not exist when using the intranasal delivery method. In light of these factors, it seems certain that intranasal administration will continue to be the most popular method for pneumonic instillation for the foreseeable future. Surprisingly, there is a paucity of published literature describing the efficiency of intranasal instillation of drugs, vaccines, or infectious agents. Therefore, an analysis of the efficiency of pneumonic delivery via intranasal instillation that would allow for standardization of the two most critical variables associated with this technique, namely dose volume and type of anesthesia, would be of great benefit to researchers working with murine models.

Francisella tularensis (FT) is a gram-negative facultative intracellular bacterium that causes a high morbidity/mortality zoonotic disease known as tularemia. FT is one of the most virulent bacterial pathogens in humans, as evidenced by its published LD_{50} of less then 10 CFU [12,13]. Because of its high infectivity and the relative ease with which if can be disseminated via the aerosol route, FT is considered to have high potential for use as a biological weapon. The *Francisellaceae* family of bacteria has a single genus, *Francisella*, which has been divided into two species: *Francisella philomiragia* (a muskrat pathogen) and *Francisella tularensis*. *F. tularensis* has been further subdivided into four subspecies: *tularensis* (type A), *holarctica* (type B), *novicida*, and *mediasiatica* [14]. Of these, only subsp. *tularensis* and subsp. *holarctica* cause disease in humans [15]. The live vaccine strain (LVS) of FT (FTLVS) is an

attenuated *F. holarctica* strain that was developed as a vaccine candidate in the former Soviet Union [16]. While FTLVS is highly attenuated in humans, it remains virulent in mice and causes a tularemic disease syndrome similar to that observed in humans [17].

Technological advances in small animal imaging have made it possible to monitor in real-time the growth and dissemination of fluorescent or bioluminescent bacteria in individual animals over the entire course of infection, offering a powerful alternative to traditional methodologies. Bioluminescence has proven to be particularly useful for this application. We recently created a novel bioluminescence reporter vector (pXB173-lux) that encodes the *P. luminescens* lux operon downstream of the FT P*gro* promoter. The lux operon contains genes that are required for production of both luciferase and luciferin, and transformation of FTLVS with this vector causes the bacteria to constitutively produce light during *in vitro* or *in vivo* growth [18]. In this report, we employed an IVIS Spectrum whole-animal live imaging system, coupled with bacterial load determinations, to evaluate in real-time the efficiency of intranasal instillation for initiation of lower respiratory tract (LRT) infections in mice. The results presented here provide striking visual evidence that both the instillation volume and the type of anesthesia used during instillation have a significant impact on the efficiency of pulmonary delivery of FTLVS.

Results

To evaluate the efficiency of intranasal administration for delivery of FT to the lungs, BALB/c mice (5/group) were anesthetized with inhaled isoflurane and then challenged with 1×10^6 CFU of FTLVS bearing a luminescent reporter vector (pXB173-lux, **Figure 1**, see [18]) in a total volume (PBS) of either 10 µl, 20 µl, 50 µl, or 100 µl. Each mouse was subjected to live whole animal luminescent imaging using an IVIS Spectrum imaging system beginning 24 hours post-challenge (**Figure 2A**). The imaging studies revealed a clear difference in luminescent signal from the lungs that correlated with the dose volume used for intranasal instillation. While very little luminescent signal was observed emanating from the lungs of mice challenged using a 10 µl or 20 µl dose, the mice that were dosed using the larger instillation volumes (50 µl or 100 µl) displayed significantly higher levels of luminescent signal. These findings were confirmed by sacrificing the mice immediately after imaging was completed to determine the bacterial burdens in the lungs using standard dilution plating techniques (**Figure 2B**).

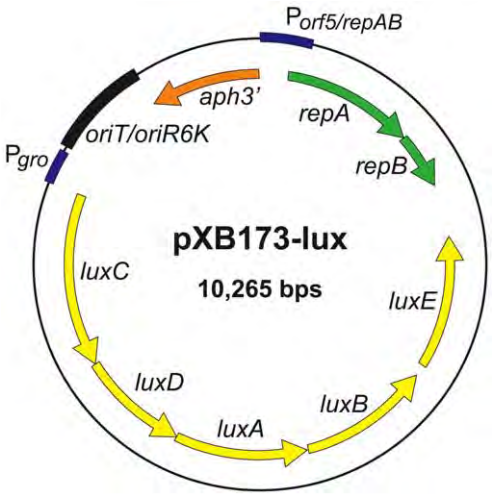

Figure 1. Genetic Map of pXB173-lux. pXB173-lux constitutively expresses the *Photorhabdus luminescens* luciferace (*lux AB*) and luciferase substrate (*luxCDE*) from the *Francisella groE* promoter. This vector also encodes a selectable marker for kanamycin resistance (*aph3'*).
doi:10.1371/journal.pone.0031359.g001

To determine the impact of dose volume-dependent challenge efficiencies on the course of experimental tularemic disease, we performed a kinetic IVIS imaging analysis of BALB/c mice (3/group) were anesthetized with inhaled isoflurane and then challenged with 1×10^6 FTLVS-lux using a range of instillation volumes (10 µl, 20 µl, 50 µl, or 100 µl). Each mouse was subjected to live whole-animal luminescent imaging at 24 hr intervals post infection. These imaging studies revealed striking differences in both the rate and tissue specificity of FT dissemination (**Figure 3A**). At the 24-hour time point, the luminescence emanating from the lungs of challenged mice confirmed that the larger instillation volumes more efficiently delivered bacteria into the lungs. By 48 hrs post-challenge, luminescent signatures were detected in or around the upper airways of all of the animals. In the mice that were challenged using a 10 µl volume, the luminescent signature remained confined to the upper airways over the entire timecourse, suggesting that the bacteria never disseminated from the upper airways to the lungs, liver or spleen. In contrast, the luminescent signatures observed in the lungs of mice challenged using instillation volumes of 20 µl, 50 µl, and 100 µl increased in intensity over the timecourse. Moreover, the infection appeared to disseminate from the lungs to the liver and spleen in each of these experimental groups, and the rate of dissemination increased with increasing instillation volume used to administer intranasal challenge. Each mouse was also weighed daily as an assessment of disease state. Weight retention results confirmed that the dose volume used for intranasal instillation had a significant impact on the course of tularemic disease (**Figure 3B**). A significant difference ($p<0.05$) in weight retention between mice that were dosed using a volume of 10 µl vs. 100 µl was observed as early as 2 days post-infection, and by day 4 post-infection there was a highly significant difference ($p<0.001$) between the 10 µl volume group and each of the other experimental groups.

To examine the efficiency of intranasal dosing for pneumonic delivery under differing forms of anesthesia, BALB/c mice (5/group) that had been anesthetized with either parenteral (ketamine/xylazine) or inhaled (isoflurane) anesthesia were challenged with FTLVS-lux in an instillation volume of either 50 µl or 100 µl. IVIS imaging studies and lung bacterial burden determinations were performed 24 hrs post-infection (**Figure 4**). The intensity of luminescence emanating from the lungs of mice challenged under inhaled anesthesia was more intense than observed in mice anesthetized with parenterally-administered ketamine/xylazine. The bacterial burden in the lungs was then determined via dilution plating. Mice that were anesthetized using inhaled isoflurane had significantly higher bacterial burdens in their lungs than mice that had been anesthetized with parenteral ketamine/xylazine (**Figure 4**), confirming the IVIS imaging results.

Discussion

Intranasal instillation is the most widely used method for delivery of drugs, vaccines, and/or infectious agents into the respiratory tract of research mice. However, over the years there have only been a handful of published studies designed to analyse the efficiency of intranasal dosing. The primary variables that should be considered when employing this technique are: i) type of diluent used as vehicle for instillation, ii) physical positioning of the

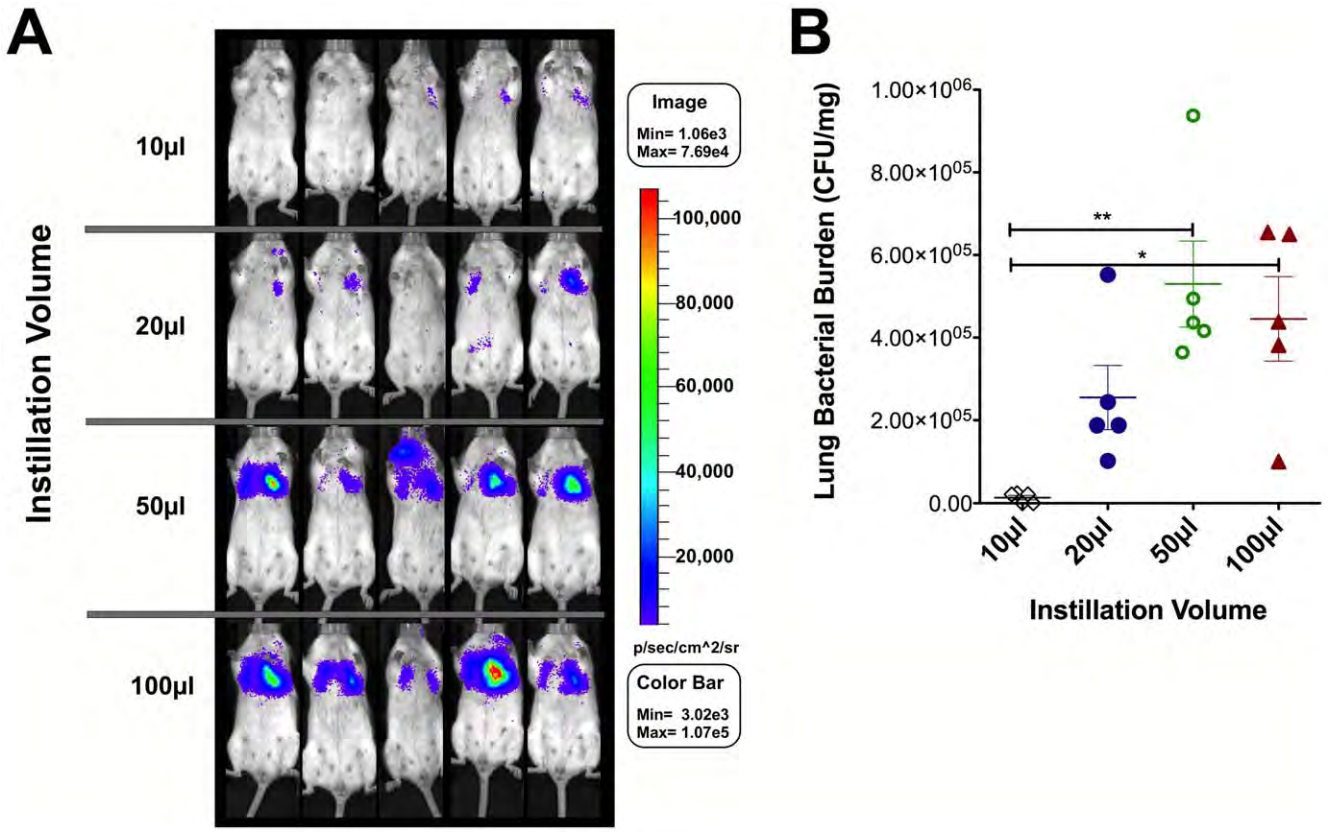

Figure 2. Correlation between whole animal *in vivo* imaging with viable bacterial counts 24 hours after challenge. BALB/c mice (5/group) were challenged with 1×10^6 CFU of FTLVS bearing the pXB173-lux reporter plasmid via the intranasal route in a total bolus volume of either 10 µl, 20 µl, 50 µl, or 100 µl. **Panel A**: Dissemination of FTLVS was then monitored 24 hrs later using an IVIS Spectrum whole animal imaging system. Images were collected at the indicated time points post-infection and were normalized to reflect photons per second per cm^2/sr. (**Panel B**): Lungs were collected after imaging was completed for bacterial burden determination via dilution plating. Statistical analyses were performed via one-way ANOVA using a Bonferroni multiple comparisons posttest. Statistically significant differences are indicated as follows: $p<0.05$ (*) and $p<0.01$ (**).
doi:10.1371/journal.pone.0031359.g002

mouse during and after instillation, iii) instillation volume, and iv) the type of anesthesia used during instillation. Two of these variables, namely instillation vehicle and physical positioning of the mouse, were not considered in this report. Previously published findings revealed that aqueous diluents were preferable for intranasal instillation [19], therefore, PBS was used as the vehicle for all of the experiments described herein. Moreover, there have been several published studies in which positioning of the mouse during intranasal instillation was considered, and while some of the findings indicated that supine positioning was best for promoting delivery of inocula to the lungs [19], other findings suggested that positioning of the mouse did not have a significant impact on pneumonic delivery efficiency [20]. Therefore, for all of the studies reported here, mice were held in a tilted supine position with their heads elevated to between 60 and 75 degrees above their feet during and after (for approximately 1 minute) instillation.

Dose volume is the best characterized variable associated with intranasal instillation. Published studies have evaluated instillation volumes between 2 µl [21] and 100 µl [22]. Several reports used either dyes or radioactive tracers to investigate the relative efficiencies of various instillation volumes. Visweswaraiah and colleagues performed instillations with Evan's blue dye to evaluate the efficiency of lung delivery using instillation volumes between 5 µl and 50 µl [23] and found that lower instillation volumes resulted in retention of the inoculum in the URT while delivery of dye to the lungs was accomplished only with the larger bolus volumes. A similar study using a radioactive tracer (^{99m}Tc-SC) also concluded that instillation in a total volume of 5 µl resulted in retention of the tracer in the URT with no detectable delivery to the lungs [20]. This study also concluded that 35 µl was the optimal instillation volume for delivery of tracer into the lungs. Eyles and colleagues performed instillations of radiolabeled microspheres in either 10 µl or 50 µl volumes and found that the radioactive microspheres accumulated in the URT when delivered in the lower volume while approximately 50% of the microspheres were delivered to the lungs when administered in the larger volume [24]. Because we could find no studies in which efficiency of pneumonic delivery via intranasal instillation was tested using a bacterial agent, we performed a series of intranasal instillation studies using luminescent FTLVS. Our findings were consistent with those employing dyes or radioactive tracers and confirmed that instillation in small volumes (10 µl) resulted in delivery of FTLVS only to the URT while instillation in larger volumes (50–100 µl) resulted in delivery of luminescent bacteria to the lungs.

The use of anesthesia and the type of anesthesia used during intranasal instillation is another variable that could have a significant impact on its efficiency for delivery of inocula to the lungs. It has been previously shown that delivery of materials to the lungs via this technique is significantly more effective when instillation of mice is performed under anesthesia during the

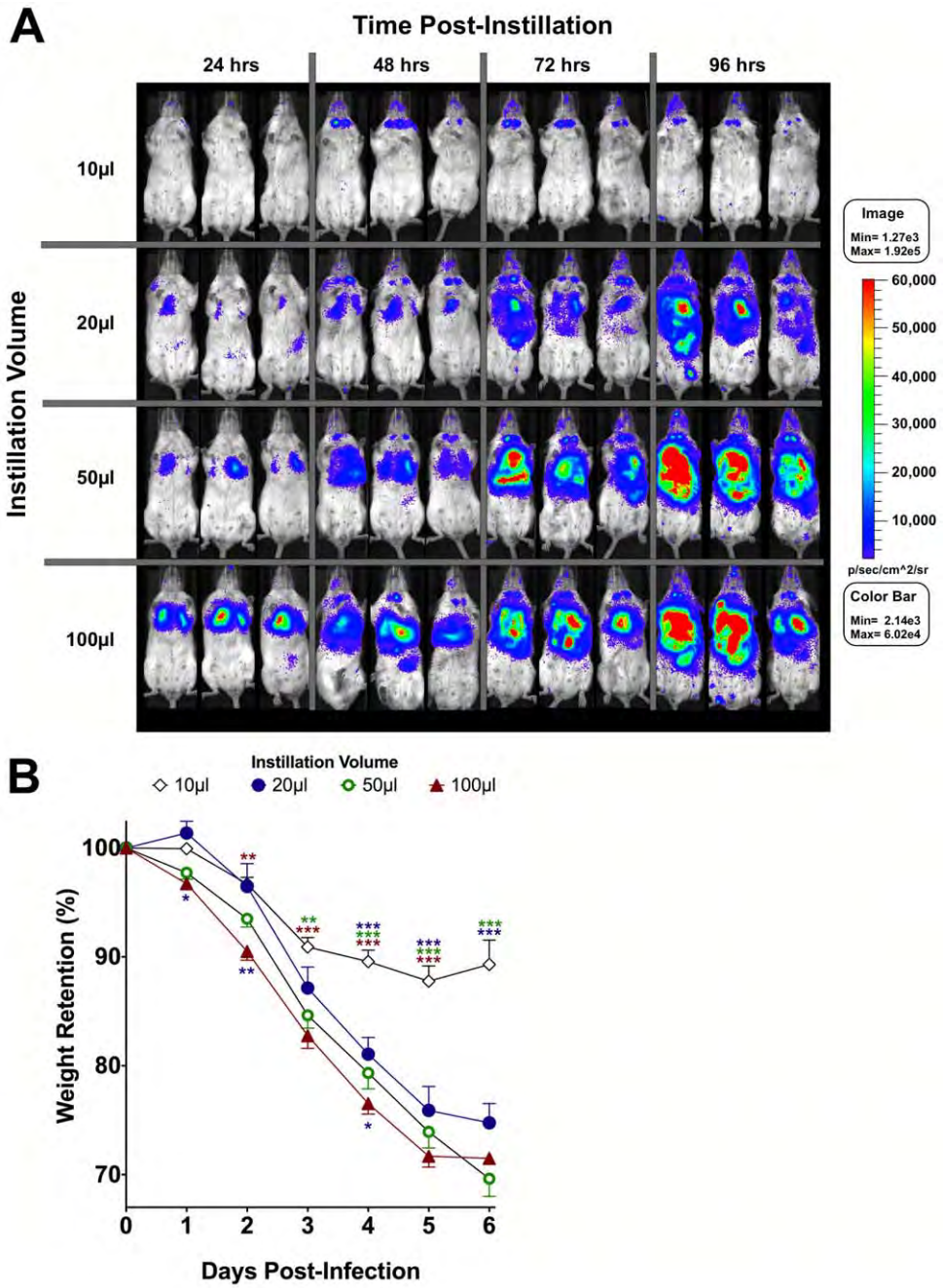

Figure 3. Kinetic *in vivo* localization of luminescent FTLVS following intranasal dosing in titrated volumes of inocula. BALB/c mice (3/group) were challenged via the intranasal route with 1×10^6 CFU of FTLVS-lux suspended in a volume of 10 µl, 20 µl, 50 µl, or 100 µl of sterile PBS. **Panel A**: All mice were then subjected to whole animal imaging using an IVIS Spectrum Imaging system at the indicated time points. Scaling intensity of all images was normalized and data are reported as photons/sec/cm^2/sr. **Panel B**: All mice were weighed daily as a measure of disease-state. Statistical analysis was performed via 2-way ANOVA with Bonferroni post-tests. Significant differences between the 10 µl instillation volume group and all other groups are indicated toward the top of the graph and are color-coded. Significant differences between the 100 µl instillation volume group and either the 20 µl or 50 µl dose volume groups are indicated toward the bottom of the graph and are color-coded. The calculated p values are indicated as follows: $p<0.05$ (*), $p<0.01$ (**), and $p<0.001$ (***).
doi:10.1371/journal.pone.0031359.g003

procedure [19,20,23]. In fact, one of these studies showed that when intranasal instillation is performed on unanesthetized mice, much of the instilled material was delivered to the gastrointestinal tract suggesting that alert mice tend to swallow a significant portion of the inoculum [23]. In light of these findings, and likely because intranasal instillation is technically much easier to perform on anesthetized mice, the majority of researchers using this technique routinely anesthetize mice prior to the procedure. Therefore, it is surprising that there has only been one other published study that examined the effects of different types of anesthesia (parenteral vs. inhaled) on the efficiency of this procedure for delivery of materials to the lower respiratory tract (LRT) [20].

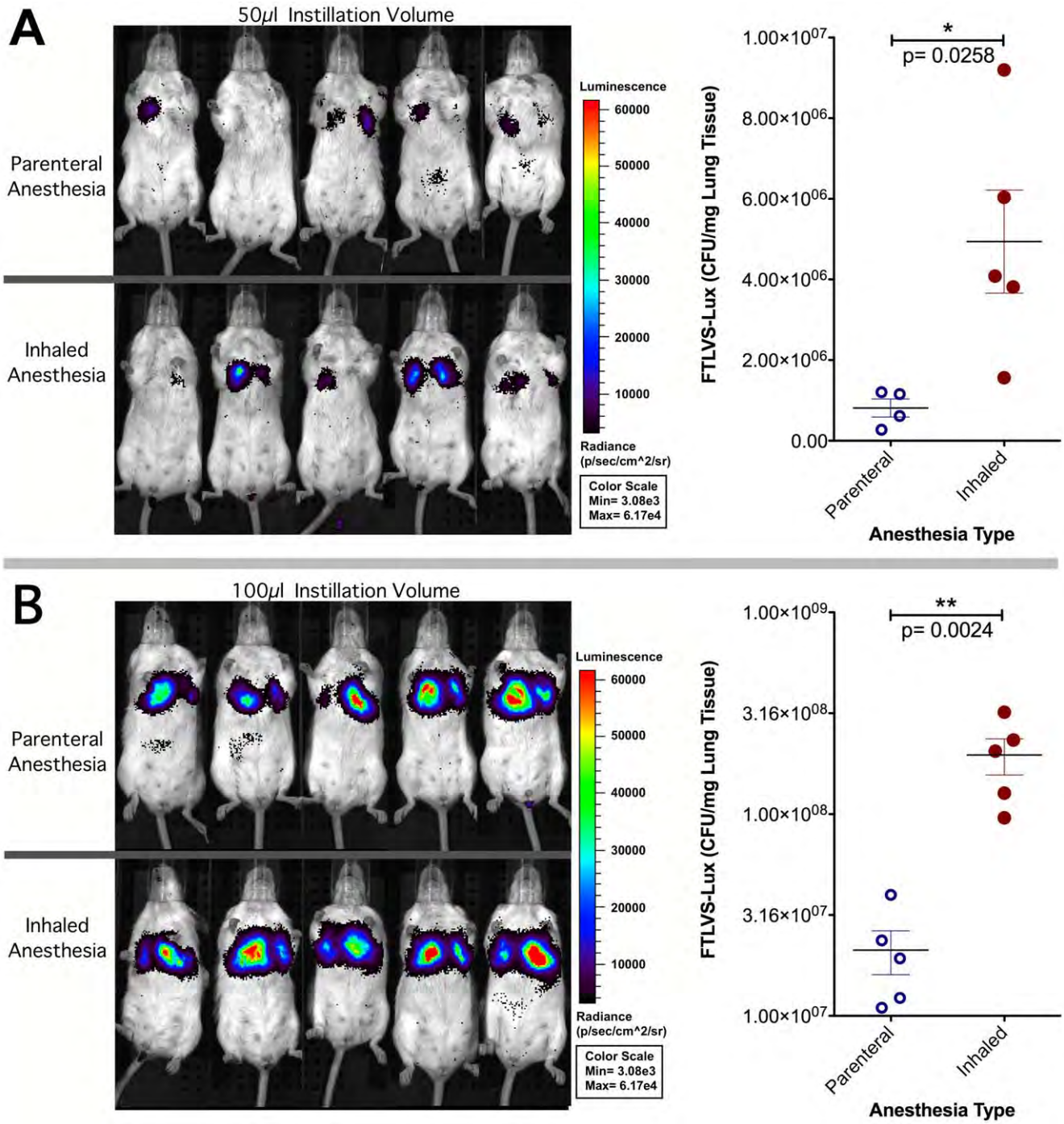

Figure 4. Pulmonary delivery of FTLVS-lux was more efficient under inhaled vs. parenteral anesthesia. BALB/c mice (5/group) were anesthetized using either inhaled isoflurane or parenterally-administered ketamine/xylazine and then challenged with either 1×10^5 CFU FTLVS-lux in a volume of 50 µl (**Panel A**) or 1×10^6 CFU FTLVS-lux in a volume of 100 µl (**Panel B**). Dissemination of FTLVS was monitored 24 hrs later using an IVIS Spectrum whole animal imaging system. Lungs were collected after imaging was completed for bacterial burden determination via dilution plating. All IVIS images were normalized to reflect photons per second per cm^2/sr. Statistical analyses were performed using the student t test.
doi:10.1371/journal.pone.0031359.g004

Because isoflurane and ketamine/xylazine are commonly used for anesthesia in rodent-based research [25], we performed a direct comparison of the efficiency of pneumonic delivery of FTLVS-lux via intranasal instillation under these two types of anesthesia. In light of our general observation that mice anesthetized using parenteral-administered ketamine/xylazine maintain a steadier breathing pattern than mice anesthetized for relatively short periods using inhaled isoflurane, we hypothesized that intranasal instillation would be more efficient for pulmonary delivery of bacteria in mice that had been anesthetized with ketamine/xylazine. To our surprise, delivery of bacteria to the lungs was significantly more efficient when instillation was

performed under inhaled anesthesia. These results lead us to speculate that the irregular Cheyne-Stokes type respiratory pattern that is typically observed following removal of mice from an induction chamber with inhaled anesthesia causes transient hypoxia which results in deeper inhalation of larger volumes of inoculum per breath, facilitating more efficient delivery of the material to the LRT. In contrast, mice that receive injectable anesthesia breathe in a more-regular and more-shallow pattern, resulting in a more-even coating of the URT surface with the inoculum. Because the inoculum is more distributed along the mucosal surface of the URT and the breathing pattern of the mice is more shallow and regular, the inoculum is not delivered as efficiently to the LRT. Our findings are in contrast to those from the other published study that performed a comparison of inhaled vs. parenteral anesthesia and concluded that the efficiency of pulmonary delivery of intranasally instilled materials was not impacted by the type of anesthesia [20].

It is relatively well established [20,23,24,26,27] that intranasal instillation for the purpose of URT delivery requires a low administration volume ($\leq$10 µl). However, no consensus has been reached with respect to dose volume for delivery to the LRT. A random survey of very recently published papers in which intranasal instillation was employed for delivery of infectious agents (bacterial and fungal pathogens) to the lungs of mice revealed that researchers used a wide range of dose volumes in combination with a variety of anesthesia types as follows: i) 20 µl instillation volume under pentobarbital [28] or ketamine/xylazine anesthesia [29,30,31,32,33], ii) 25 µl instillation volume under either pentobarbital [34] or ketamine/xylazine anesthesia [35], iii) 30 µl instillation volume under ketamine/xylazine anesthesia [36], iv) 35 µl instillation volume under ketamine/xylazine anesthesia [37], v) 40 µl instillation volume under isoflurane anesthesia [38], vi) 50 µl instillation volume under either ketamine/xylazine [39], isoflurane [40,41,42,43,44], halothane [45,46], and vii) 100 µl instillation volume under isoflurane anesthesia [47]. Moreover, a number of recent papers either supplied information regarding the dose volume used without indicating the type of anesthesia [48,49], indicated the anesthesia used but failed to indicate the dose volume [50,51], or supplied no information regarding either the dose volume or anesthesia [52,53,54] used for intranasal instillation.

The findings presented here have clearly shown that the efficiency of pneumonic delivery via intranasal instillation is significantly impacted by the volume of the inoculum as well as by the type of anesthesia used during the procedure. These findings underscore the importance of considering both variables when comparing the experimental results between studies that involved intranasal instillation for the purpose of delivering infectious agents or other materials to the lungs. Therefore, it is critical that a complete description of the methods used to anesthetize and inoculate mice via intranasal instillation be supplied in any study that employs this technique. Further studies are needed to determine whether "high-volume" intranasal instillation has any deleterious effects on research mice. The reference book entitled "The Mouse in Biomedical Research" states that intranasal instillation in volumes greater than 20 µl can result in suffocation and death of research mice [55]. While our findings do not support this conclusion, we have noted brief respiratory distress in mice that have received intranasal instillation volumes $\geq$50 µl. Therefore, studies designed to evaluate respiratory function before, during, and after intranasal instillation with a range of instillation volumes are warranted. We are also initiating studies that will determine whether instillation in larger volumes alters the microenvironment of the lung enough to alter pneumonic disease progression.

Materials and Methods

Bacterial Strains and Growth Conditions

F. tularensis strain LVS (live vaccine strain) was obtained from the Centers for Disease Control and Prevention (CDC, Atlanta, GA). *F. tularensis* was cultured in modified Mueller Hinton broth (MMH broth supplemented with 10 g/L tryptone, 0.1% glucose, 0.025% ferrous pyrophosphate, 0.1% L-cysteine, and 2.5% calf serum) or on MMH agar (supplemented with 5% calf serum and 1% IsoVitalex). FTLVS was transformed with the luminescence reporter plasmid (pXB173-lux) as described previously [18]. Kanamycin (km) was used at 10 µg/mL to maintain selection for FTLVS bearing the lux-reporter plasmid. We received authorization from the CDC, the Department of Health and Human Services, and from the University of Tennessee Health Science Center (UTHSC) Institutional Biosafety Committee for the use of *aph3′* in FT.

Mice

Female BALB/c mice were purchased from either Jackson Laboratories or Charles River Laboratories. Mice were age-matched and used between 8 and 16 weeks of age. Mice were housed in an AALAC accredited facility in microisolator cages with food and water available *ad libitum*. All experimental protocols were reviewed and approved by the UTHSC IACUC.

Anesthesia and Intranasal Instillation

Prior to instillation, mice were anesthetized using either inhaled (isoflurane) or parenteral (ketamine/xylazine) anesthesia. Isoflurane was delivered using a SurgiVet® Vaporstick small animal anesthesia machine equipped with a Classic T3™ isoflurane vaporizer (Smith Medical, Dublin, OH) and mice were exposed to 2.5% isoflurane delivered in O_2 (2 L/min) within a 1 liter induction chamber until a state of areflexia was reached. Ketamine (KetaVed, VEDCO, St. Joseph, MO; 9 mg/10 g body weight) and xylazine (AnaSed, Lloyd Laboratories, Shenandoah, IA; 1 mg/g body weight) were administered intraperitoneally and mice were challenged once a stable plane of anesthesia was reached. Intranasal administration of each challenge dose was performed by pipetting approximately half of the designated volume of PBS (containing the indicated number of FTLVS) onto the outer edge of each nare of the mice. Mice receiving isoflurane anesthesia were removed from the induction chamber and instillation was performed immediately; no supplemental anesthesia or oxygen was administered following removal from the induction chamber.

Whole-Animal Luminescent Imaging

The photon emissions from mice that had been infected with FTLVS-lux were measured using an IVIS Spectrum whole live-animal imaging system (Caliper Life Sciences, Hopkinton, MA). Mice were anesthetized with isoflurane using a precision vaporizer and oxygen before and during imaging. Images were collected using medium binning with an F-stop of 1, and the maximum exposure time was 5 minutes. The luminescent signals for all images in any individual study were normalized and reported as photons/second/cm^2/sr.

Bacterial Burden Determination

Lungs of challenged mice were removed aseptically and homogenized (using a closed tissue grinder system, Fisher Scientific, Pittsburgh, PA) in one ml of sterile PBS, and the final volume was adjusted to 1.25 ml with PBS. To disrupt cells (releasing FT), 0.25 ml disruption buffer (2.5% saponin, 15%

BSA, in PBS) was added with light vortexing. Appropriate dilutions of each sample were then plated in duplicate using an Eddy Jet spiral plater (Neutec Group Inc., Farmingdale, NY) on MMH agar plates and incubated at 37°C for 48–72 hours. Colonies were counted using a Flash & Go automated colony counter (Neutec Group Inc.).

Statistical Methodology

Statistical analyses of each figure were performed using GraphPad Prism software (GraphPad Software, La Jolla, CA). The specific statistical method used for each dataset is described in the figure legends.

Acknowledgments

The authors wish to thank Ms. Janice Collum and Mr. Timothy Higgins for technical support.

Author Contributions

Conceived and designed the experiments: MAM JMS JEB. Performed the experiments: MAM JMS JP AJW TPF XRB LZ JEB. Analyzed the data: MAM. Contributed reagents/materials/analysis tools: XRB. Wrote the paper: MAM JMS.

References

1. MacDonald KD, Chang HY, Mitzner W (2009) An improved simple method of mouse lung intubation. J Appl Physiol 106: 984–987.
2. Hamacher J, Arras M, Bootz F, Weiss M, Schramm R, et al. (2008) Microscopic wire guide-based orotracheal mouse intubation: description, evaluation and comparison with transillumination. Lab Anim 42: 222–230.
3. Spoelstra EN, Ince C, Koeman A, Emons VM, Brouwer LA, et al. (2007) A novel and simple method for endotracheal intubation of mice. Lab Anim 41: 128–135.
4. Rivera B, Miller S, Brown E, Price R (2005) A novel method for endotracheal intubation of mice and rats used in imaging studies. Contemp Top Lab Anim Sci 44: 52–55.
5. Vergari A, Polito A, Musumeci M, Palazzesi S, Marano G (2003) Video-assisted orotracheal intubation in mice. Lab Anim 37: 204–206.
6. Schook LB, Carrick L, Jr., Berk RS (1977) Experimental pulmonary infection of mice by tracheal intubation of Pseudomonas aeruginosa: the use of antineoplastic agents to overcome natural resistance. Can J Microbiol 23: 823–826.
7. Su X, Looney M, Robriquet L, Fang X, Matthay MA (2004) Direct visual instillation as a method for efficient delivery of fluid into the distal airspaces of anesthetized mice. Exp Lung Res 30: 479–493.
8. Onischuk AA, Tolstikova TG, Sorokina IV, Zhukova NA, Baklanov AM, et al. (2009) Analgesic effect from Ibuprofen nanoparticles inhaled by male mice. J Aerosol Med Pulm Drug Deliv 22: 245–253.
9. Thomas RJ, Webber D, Sellors W, Collinge A, Frost A, et al. (2008) Characterization and deposition of respirable large- and small-particle bioaerosols. Appl Environ Microbiol 74: 6437–6443.
10. Hrvacic B, Bosnjak B, Tudja M, Mesic M, Mercep M (2006) Applicability of an ultrasonic nebulization system for the airways delivery of beclomethasone dipropionate in a murine model of asthma. Pharm Res 23: 1765–1775.
11. Allen SD, Sorensen KN, Nejdl MJ, Durrant C, Proffit RT (1994) Prophylactic efficacy of aerosolized liposomal (AmBisome) and non-liposomal (Fungizone) amphotericin B in murine pulmonary aspergillosis. J Antimicrob Chemother 34: 1001–1013.
12. Saslaw S, Eigelsbach HT, Prior JA, Wilson HE, Carhart S (1961) Tularemia vaccine study. II. Respiratory challenge. Archives of internal medicine 107: 702–714.
13. Saslaw S, Eigelsbach HT, Wilson HE, Prior JA, Carhart S (1961) Tularemia vaccine study. I. Intracutaneous challenge. Archives of internal medicine 107: 689–701.
14. Dennis DT, Inglesby TV, Henderson DA, Bartlett JG, Ascher MS, et al. (2001) Tularemia as a biological weapon: medical and public health management. JAMA : the journal of the American Medical Association 285: 2763–2773.
15. Twine S, Bystrom M, Chen W, Forsman M, Golovliov I, et al. (2005) A mutant of Francisella tularensis strain SCHU S4 lacking the ability to express a 58-kilodalton protein is attenuated for virulence and is an effective live vaccine. Infection and immunity 73: 8345–8352.
16. Eigelsbach HT, Downs CM (1961) Prophylactic effectiveness of live and killed tularemia vaccines. I. Production of vaccine and evaluation in the white mouse and guinea pig. Journal of immunology 87: 415–425.
17. Elkins KL, Cowley SC, Bosio CM (2003) Innate and adaptive immune responses to an intracellular bacterium, Francisella tularensis live vaccine strain. Microbes and infection/Institut Pasteur 5: 135–142.
18. Bina XR, Miller MA, Bina JE (2010) Construction of a bioluminescence reporter plasmid for Francisella tularensis. Plasmid 64: 156–161.
19. Ebino K, Lemus R, Karol MH (1999) The importance of the diluent for airway transport of toluene diisocyanate following intranasal dosing of mice. Inhal Toxicol 11: 171–185.
20. Southam DS, Dolovich M, O'Byrne PM, Inman MD (2002) Distribution of intranasal instillations in mice: effects of volume, time, body position, and anesthesia. Am J Physiol Lung Cell Mol Physiol 282: L833–839.
21. Matsuo K, Iwasaki T, Asanuma H, Yoshikawa T, Chen Z, et al. (2000) Cytokine mRNAs in the nasal-associated lymphoid tissue during influenza virus infection and nasal vaccination. Vaccine 18: 1344–1350.
22. Chapoval SP, Nabozny GH, Marietta EV, Raymond EL, Krco CJ, et al. (1999) Short ragweed allergen induces eosinophilic lung disease in HLA-DQ transgenic mice. J Clin Invest 103: 1707–1717.
23. Visweswaraiah A, Novotny LA, Hjemdahl-Monsen EJ, Bakaletz LO, Thanavala Y (2002) Tracking the tissue distribution of marker dye following intranasal delivery in mice and chinchillas: a multifactorial analysis of parameters affecting nasal retention. Vaccine 20: 3209–3220.
24. Eyles JE, Spiers ID, Williamson ED, Alpar HO (2001) Tissue distribution of radioactivity following intranasal administration of radioactive microspheres. J Pharm Pharmacol 53: 601–607.
25. Flecknell P (2009) Laboratory Animal Anesthesia. London, UK: Academic Press.
26. Stabenow J, Buller RM, Schriewer J, West C, Sagartz JE, et al. (2010) A mouse model of lethal infection for evaluating prophylactics and therapeutics against Monkeypox virus. Journal of virology 84: 3909–3920.
27. Smee DF, Gowen BB, Wandersee MK, Wong MH, Skirpstunas RT, et al. (2008) Differential pathogenesis of cowpox virus intranasal infections in mice induced by low and high inoculum volumes and effects of cidofovir treatment. Int J Antimicrob Agents 31: 352–359.
28. Lange M, Hamahata A, Traber DL, Nakano Y, Traber LD, et al. (2011) Specific inhibition of nitric oxide synthases at different time points in a murine model of pulmonary sepsis. Biochemical and biophysical research communications 404: 877–881.
29. Rouf R, Karaba SM, Dao J, Cianciotto NP (2011) Stenotrophomonas maltophilia strains replicate and persist in the murine lung, but to significantly different degrees. Microbiology 157: 2133–2142.
30. Margolis DA, Viriyakosol S, Fierer J, Kirkland TN (2011) The role of reactive oxygen intermediates in experimental coccidioidomycois in mice. BMC microbiology 11: 71.
31. Mares CA, Sharma J, Ojeda SS, Li Q, Campos JA, et al. (2010) Attenuated response of aged mice to respiratory Francisella novicida is characterized by reduced cell death and absence of subsequent hypercytokinemia. PLoS One 5: e14088.
32. Kamei A, Coutinho-Sledge YS, Goldberg JB, Priebe GP, Pier GB (2011) Mucosal vaccination with a multivalent, live-attenuated vaccine induces multifactorial immunity against Pseudomonas aeruginosa acute lung infection. Infection and immunity 79: 1289–1299.
33. He X, Nair A, Mekasha S, Alroy J, O'Connell CM, et al. (2011) Enhanced virulence of Chlamydia muridarum respiratory infections in the absence of TLR2 activation. PLoS One 6: e20846.
34. Balogh EP, Faludi I, Virok DP, Endresz V, Burian K (2011) Chlamydophila pneumoniae induces production of the defensin-like MIG/CXCL9, which has in vitro antichlamydial activity. International journal of medical microbiology : IJMM 301: 252–259.
35. Pore D, Mahata N, Pal A, Chakrabarti MK (2011) Outer Membrane Protein A (OmpA) of Shigella flexneri 2a, Induces Protective Immune Response in a Mouse Model. PLoS One 6: e22663.
36. Ezoe H, Akeda Y, Piao Z, Aoshi T, Koyama S, et al. (2011) Intranasal vaccination with pneumococcal surface protein A plus poly(I:C) protects against secondary pneumococcal pneumonia in mice. Vaccine 29: 1754–1761.
37. Surendran N, Sriranganathan N, Lawler H, Boyle SM, Hiltbold EM, et al. (2011) Efficacy of vaccination strategies against intranasal challenge with Brucella abortus in BALB/c mice. Vaccine 29: 2749–2755.
38. Weber SE, Tian H, Pirofski LA (2011) CD8+ cells enhance resistance to pulmonary serotype 3 Streptococcus pneumoniae infection in mice. Journal of immunology 186: 432–442.
39. Zhao L, Kuolee R, Harris G, Tram K, Yan H, et al. (2011) c-di-GMP protects against intranasal Acinetobacter baumannii infection in mice by chemokine induction and enhanced neutrophil recruitment. International immunopharmacology 11: 1378–1383.
40. Van Den Boogaard FE, Brands X, Schultz MJ, Levi M, Roelofs JJ, et al. (2011) Recombinant human tissue factor pathway inhibitor exerts anticoagulant, anti-inflammatory and antimicrobial effects in murine pneumococcal pneumonia. Journal of thrombosis and haemostasis : JTH 9: 122–132.

41. McNeela EA, Burke A, Neill DR, Baxter C, Fernandes VE, et al. (2010) Pneumolysin activates the NLRP3 inflammasome and promotes proinflammatory cytokines independently of TLR4. PLoS pathogens 6: e1001191.
42. Lee LN, Ronan EO, de Lara C, Franken KL, Ottenhoff TH, et al. (2011) CXCR6 Is a Marker for Protective Antigen-Specific Cells in the Lungs after Intranasal Immunization against Mycobacterium tuberculosis. Infection and immunity 79: 3328–3337.
43. Hoogendijk AJ, Diks SH, van der Poll T, Peppelenbosch MP, Wieland CW (2011) Kinase activity profiling of pneumococcal pneumonia. PLoS One 6: e18519.
44. Ayala VI, Teijaro JR, Farber DL, Dorsey SG, Carbonetti NH (2011) Bordetella pertussis infection exacerbates influenza virus infection through pertussis toxin-mediated suppression of innate immunity. PLoS One 6: e19016.
45. Gabryszewski SJ, Bachar O, Dyer KD, Percopo CM, Killoran KE, et al. (2011) Lactobacillus-mediated priming of the respiratory mucosa protects against lethal pneumovirus infection. Journal of immunology 186: 1151–1161.
46. Kadioglu A, De Filippo K, Bangert M, Fernandes VE, Richards L, et al. (2011) The integrins Mac-1 and alpha4beta1 perform crucial roles in neutrophil and T cell recruitment to lungs during Streptococcus pneumoniae infection. Journal of immunology 186: 5907–5915.
47. Mendez MP, Monroy YK, Du M, Preston AM, Tolle L, et al. (2011) Overexpression of sICAM-1 in the alveolar epithelial space results in an exaggerated inflammatory response and early death in Gram negative pneumonia. Respiratory research 12: 12.
48. Asensio CJ, Gaillard ME, Moreno G, Bottero D, Zurita E, et al. (2011) Outer membrane vesicles obtained from Bordetella pertussis Tohama expressing the lipid A deacylase PagL as a novel acellular vaccine candidate. Vaccine 29: 1649–1656.
49. KuoLee R, Harris G, Conlan JW, Chen W (2011) Role of neutrophils and NADPH phagocyte oxidase in host defense against respiratory infection with virulent Francisella tularensis in mice. Microbes and infection/Institut Pasteur 13: 447–456.
50. Mijares LA, Wangdi T, Sokol C, Homer R, Medzhitov R, et al. (2011) Airway epithelial MyD88 restores control of Pseudomonas aeruginosa murine infection via an IL-1-dependent pathway. Journal of immunology 186: 7080–7088.
51. Hilliard JJ, Melton JL, Hall L, Abbanat D, Fernandez J, et al. (2011) Comparative effects of carbapenems on bacterial load and host immune response in a Klebsiella pneumoniae murine pneumonia model. Antimicrobial agents and chemotherapy 55: 836–844.
52. Gonzalez A, Hung CY, Cole GT (2011) Nitric oxide synthase activity has limited influence on the control of Coccidioides infection in mice. Microbial pathogenesis 51: 161–168.
53. Easton A, Haque A, Chu K, Patel N, Lukaszewski RA, et al. (2011) Combining vaccination and postexposure CpG therapy provides optimal protection against lethal sepsis in a biodefense model of human melioidosis. The Journal of infectious diseases 204: 636–644.
54. Cheng C, Cruz-Fisher MI, Tifrea D, Pal S, Wizel B, et al. (2011) Induction of protection in mice against a respiratory challenge by a vaccine formulated with the Chlamydia major outer membrane protein adjuvanted with IC31(R). Vaccine 29: 2437–2443.
55. Fox JG, Davisson MT, Quimby FW, Barthold SW, Newcomer CE, et al. (2007) The Mouse in Biomedical Research. 2nd ed London, UK: Academic Press.

CHLAMYDIAL PERSISTENCE REDUX

Gerald I. Byrne and Wandy L. Beatty

12

INTRODUCTION

In the third edition of the Wilson et al. text on bacterial pathogenesis (Wilson et al., 2011) the authors make a point of explaining that a major reason for bacteria to be in the public health spotlight in the 21st century is their capacity to develop resistance to antibiotics, to acquire genes from other bacteria and thereby accrue new virulence traits, or to emerge as opportunistic pathogens due to host abatement to combat innocuous microbes. These arguments are in fact true for many infectious disease pathogens, but they categorically do not apply to chlamydiae. The genus *Chlamydia* is essentially pathogenic by definition (it has no other niche but the eukaryotic host to exploit) and virtually ubiquitous; yet it fits none of the criteria deemed to be essential for success as an infectious disease agent these days.

First, at present antibiotic resistance is not a major issue with chlamydiae. It is true that a tetracycline resistance cassette has been identified in the genome of some isolates of *Chlamydia suis*, a porcine pathogen that is constantly exposed to tetracycline in hog feed; but this finding has not emerged as a problem in hogs, let alone other species. Certainly we should be ever vigilant for emergent drug resistance against both human and animal infections, since the repertoire of effective classes of drugs against chlamydiae is limited. But other than for porcine infections, the reasons that chronic chlamydial infections are difficult to effectively manage are not related to the development of true genetic resistance, but rather to a drug tolerant phenotype. By and large, human isolates have remained fully susceptible to tetracyclines, erythromycin, and azalides.

Second, the *Chlamydiaceae* are not very genetically diverse. All members of the *Chlamydiaceae* have very similar genomes (reviewed in chapter 2, "Deep and wide: comparative genomics of *Chlamydia*"). They code for roughly 1,000 proteins, and most of the same genes are not only present in all strains but also preserved in the same order in the genome. This fact argues strongly that transfer of genes to chlamydiae from other bacteria does not occur with any degree of frequency. Even development of experimental gene transfer systems for chlamydiae has been problematical (reviewed in chapter 15, "Chlamydial genetics: decades of efforts,

Gerald I. Byrne, Department of Microbiology, Immunology, and Biochemistry, University of Tennessee Health Science Center, Memphis, TN 38163. *Wandy L. Beatty*, Department of Molecular Microbiology, Washington University at St. Louis, St. Louis, MO 63110.

Intracellular Pathogens I: Chlamydiales
Edited by Ming Tan and Patrik M. Bavoil © 2012 ASM Press, Washington, DC
10.1128/9781555817329.ch12

very recent successes"). This research specialty field has been fraught with stops and starts, with hopeful signs followed by long periods of silence. A tractable gene transfer system has not been developed to study chlamydial virulence and pathogenesis. Thus, exchange of genes is something chlamydiae neither do on their own nor can be coerced to do experimentally under idealized laboratory conditions.

Finally, the chlamydiae are anything but opportunistic. Some of the earliest recorded accurate descriptions of an infectious disease are a hieroglyphic description of remedies for trachoma from an ancient Egyptian text written some 3,400 years ago (Stern, 1875) and a written comment about eye disease from the Chang dynasty in China from more than 3,000 years ago (Taylor, 2008). *Chlamydia* continues to be a serious reproductive health problem for women globally despite quantum-like improvements in screening and treatment. In the United States, *Chlamydia trachomatis* is the most frequently reported bacterial infectious disease, period; and similar reporting frequencies are seen everywhere around the world. *Chlamydia* spp. continue to cause problems both in domesticated animals and in sylvatic populations (e.g., koalas).

How is it that *Chlamydia*, a bacterial genus that has none of the features associated with textbook traits for success as a pathogen, has been successfully causing disease in eukaryotes for the past 700 million years or so (Horn et al., 2004)? Obviously the chlamydiae have found another way. The relationships that chlamydiae have evolved with their eukaryotic hosts, in terms of both successfully invading epithelial or mononuclear phagocytic cells and dealing with the innate and acquired immune response generated in their presence, are key elements in understanding the success that chlamydiae enjoy. We have made dramatic strides in the postgenomic era in understanding what chlamydiae can and cannot do biochemically and metabolically and how the host responds to the presence of these pathogens. However, a still unresolved question is whether the encounter of chlamydiae with the host involves what has come to be known as persistence, which has been defined as a reversible interruption in the productive intracellular chlamydial growth cycle that is mediated by environmental factors (Fig. 1). It is the purpose of this chapter to define what we do and do not know about chlamydial persistence with the goal of determining the extent of the role that persistence plays in chlamydial disease (if at all) and what we should be doing to better understand this chlamydial attribute.

PERSISTENCE AS A FUNCTION OF MICROBIAL PATHOGENESIS: WHAT DO OTHER MICROBIAL PATHOGENS DO, AND ARE THERE ANALOGIES FOR CHLAMYDIAE?

One of the problems encountered in the study of chlamydiae is that often the basic biology of the pathogen, worked out in cell culture systems, is then applied to speculate about actual disease pathogenesis, without knowing if there are strong in vivo correlates to cell culture observations. In contrast, there are a number of important microbial pathogens that clearly have a persistent, dormant, or latent stage associated with disease. These infections may serve as examples of well-characterized persistence phenotypes associated with disease. For the pathogens described below, persistence was first documented as a feature of the disease, and this was followed by characterization of persistence mechanisms, which is just the opposite of how the problem of persistence has been developed in the case of *Chlamydia*.

Vivax Malaria

Malaria is arguably the most significant infectious disease on the planet. Although four species of *Plasmodium* cause infections in people (*P. falciparum*, *P. vivax*, *P. malariae*, and *P. ovale*), two dominate: *P. falciparum* and *P. vivax*. *P. falciparum*, which causes a form of malaria called malignant tertian malaria, is considered a major killer due to its capacity to modify the surface of infected erythrocytes such that they stick to each other and to the endothelial cells lining vessels and capillaries.

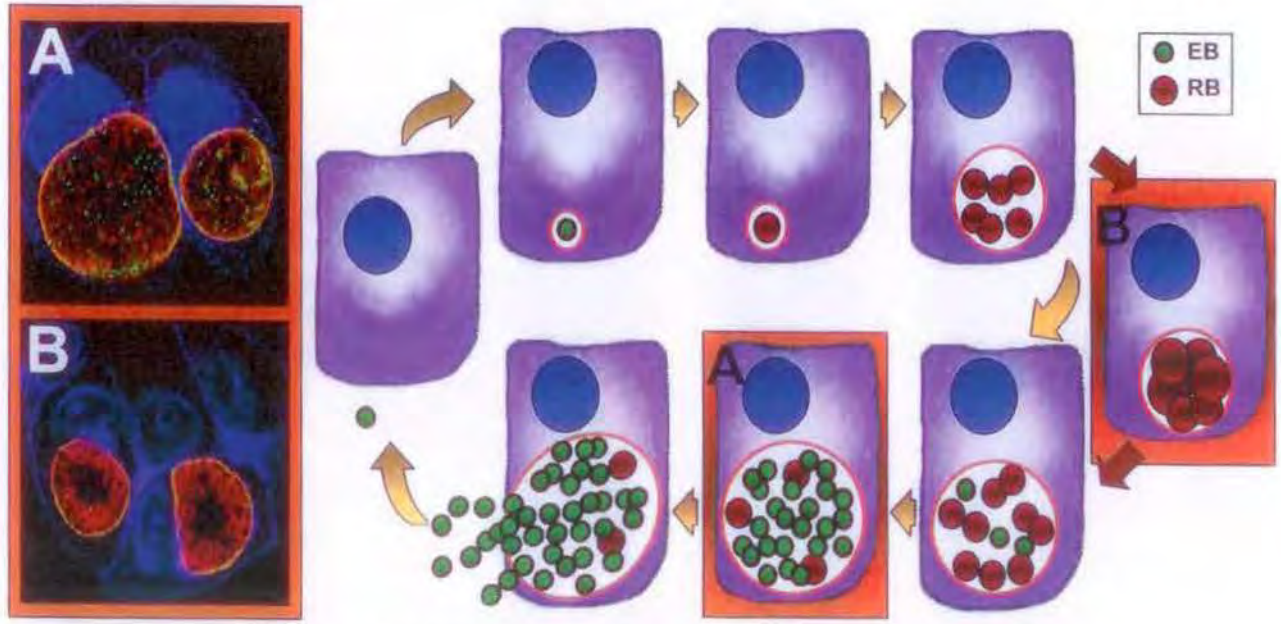

FIGURE 1 Schematic diagram of the chlamydial developmental cycle. Red arrows indicate altered intracellular chlamydial development mediated by environmental factors. (A) Immunofluorescence images and schematic show mature *C. trachomatis* serovar B inclusions with elementary bodies (EBs) in green (anti-OmcB), reticulate bodies (RBs) in red (anti-major outer membrane protein), and the inclusion membrane in orange (anti-incG). (B) Persistence in vitro in response to IFN-γ results in enlarged, aberrant RBs that can be maintained in this state for extended periods of time, with subsequent reversion to normal intracellular development. doi:10.1128/9781555817329.ch12.f1

This sequestration of infected erythrocytes has numerous consequences important for both diagnosis (e.g., only ring stages are found in the circulation) and pathogenesis, as blockage of capillaries causes ischemic consequences. The most serious capillary blockage complication is cerebral malaria, the principal immediate cause of malaria mortality in children. But vivax malaria also can have severe consequences, often disproportional to the level of parasitemia, which is generally less than for *P. falciparum* due to the *P. vivax* preference for young erythrocytes. *P. vivax* and *P. ovale* also have the unusual capacity to cause a clinical relapse months to years after the initial illness has cleared, even though the individual has left the area of endemicity and is not at risk of becoming reinfected. Although all plasmodia are intracellular pathogens of erythrocytes, they must go through an obligatory stage in the liver before merozoites are released into the circulation. This preerythrocytic stage is a one-time-only portion of the infectious cycle for falciparum malaria, but an added developmental form is produced by *P. vivax* and *P. ovale*, called the hypnozoite, that remains within hepatic cells in a nongrowing dormant state. This form of the parasite can reactivate to produce red blood cell-invading merozoites from weeks to months and even years after the initial circulating parasitemia has been cleared or treated. Although the nature of the hypnozoite remains mysterious, recent findings (Wells et al., 2010; Imwong et al., 2007; Chen et al., 2007) demonstrate that these "dormant" forms are clonal and are frequently genetic variants of the original infecting strain. The existence of hypnozoites not only is well founded in the clinical literature but also has practical ramifications for malaria management because additional therapeutics are required to eradicate the liver-bound hypnozoites.

WHAT ABOUT CHLAMYDIAE?

Vivax malaria represents a classic example of persistence of a unique developmental form that can emerge at a later time and cause disease. Are there data to suggest that something similar exists for chlamydiae? It is important to recognize that the first consideration should be whether or not clinical conditions or indications suggest the presence of a dormant persistent form similar to the *P. vivax* hypnozoite. For example, there are a smattering of reports describing individuals with reactivation of ocular disease years after they have left regions of the world where trachoma is endemic (reviewed by Taylor [2008]). One might predict that if a dormant form of *C. trachomatis* could reactivate and cause trachoma, this type of presentation would be frequently reported; but it is not. In sharp contrast, everyone who is infected with vivax malaria runs the risk of reactivated infections. The hypnozoite is part of the *P. vivax* developmental process within the mammalian host; but there is little evidence that there is an analogous dormant but reactivatable stage of chlamydial infection.

Interestingly, there may be a developmental form of *Chlamydia*, at least for *Chlamydia psittaci*, that resembles a hypnozoite. This is the "cryptic" form originally described by Moulder in the late 1970s (Moulder et al., 1980) in a mouse fibroblast cell culture model, which has been completely understudied since. Cryptic chlamydiae emerge after the developmental cycle is complete and the host cell population experiences "wipeout." That is to say, virtually all of the host cells in the cell culture population support a productive infection and are then destroyed, releasing infectious elementary bodies (EBs). However, if one saves the flasks and adds fresh medium that is allowed to incubate, a new population of host cells will emerge in about 2 weeks. Interestingly, these cells are not capable of being reinfected by the same strain that yielded the initial wipeout. This might very well be because the surviving host cells are variants that no longer take up the invading strain; but the curious finding that Moulder noticed was that if the incubation time is extended for another 2 weeks or so without the reinfection step, the cells eventually become infected with chlamydiae again and another wipeout soon follows. The conclusion drawn from these

studies was that the surviving host cells harbor cryptic chlamydiae, which initiate a new round of productive infection under favorable environmental conditions. The search for cryptic chlamydiae during the initial stages of host cell regrowth proved futile, and therefore the cryptic form of the pathogen was proposed by inference. These interesting observations have never been properly followed up and are worthy of reexamination.

Are there cryptic chlamydiae that emerge during a natural infection and act in a manner similar to that of hypnozoites? Unfortunately, the appropriate in vivo investigation has not been done. An important lesson that can be drawn from these studies is that it may be dangerous to base any type of disease property exclusively on in vitro findings, but unfortunately this has been done time and time again for *Chlamydia*. The case of cryptic chlamydiae may simply represent a cell culture-based mechanism for survival of the pathogen. If cryptic chlamydiae exist in nature, they might be unique to *C. psittaci* and related species (Moulder never found the equivalent in *C. trachomatis* infections [Lee and Moulder, 1981]). Therefore, reactivation of bird infections, genital infections in sheep, or intestinal infections in swine might be a good method to look for these enigmatic chlamydial developmental forms with unique properties.

Toxoplasmosis

Toxoplasma gondii is an obligate intracellular protozoan parasite that is acquired by eating undercooked meat (mainly pork and lamb, but also beef) containing *Toxoplasma* cysts or by ingesting mature oocysts associated with cat feces, felines being the definitive host for *T. gondii* (Montoya and Liesenfeld, 2004). Congenital transmission places the fetus at risk for serious disease as the parasite can enter the fetal circulation by infection of the placenta when maternal primary disease occurs during gestation. Infection also can occur as a result of organ transplant from an asymptomatic, seropositive donor to a seronegative recipient. This is because once the acute stage of the disease has resolved (often asymptomatic in immunocompetent individuals), the infection goes into a persistent phase characterized by the presence of slow-growing forms, contained within an intracellular cyst-like structure. These developmental forms are called bradyzoites to distinguish them from the fast-growing tachyzoites that characterize acute infections. This latent or persistent stage of *T. gondii* development is a critical component in the pathogenesis and transmission of this parasite. The significance of the bradyzoite form of the parasite became apparent when it was recognized that transmission frequently occurs via ingestion of contaminated meat (reviewed by Sullivan et al. [2009]), but the clinical significance of tissue cysts was not recognized until immunosuppression became more frequent as a result of organ transplantation or cancer therapy. Then, when AIDS emerged as a major new immunosuppressive disease, reactivated toxoplasmosis became one of the most frequently encountered opportunistic infections in AIDS patients with low $CD4^+$ cell counts (Sullivan et al., 2009; Weiss and Kim, 2000).

WHAT ABOUT CHLAMYDIAE?

There are many analogies between *Toxoplasma* and *Chlamydia*, as these two intracellular pathogens represent remarkable examples of convergent evolution of very different life forms. *Toxoplasma* and *Chlamydia* both invade a variety of host cell types, ranging from epithelial cells to mononuclear phagocytes. They both reside within the confines of a cytoplasmic vesicle termed the parasitophorous vacuole in the case of *Toxoplasma* and the inclusion in the case of *Chlamydia*. They both initiate a sequence of events that probably starts during the uptake process to prevent lysosomes from fusing with the pathogen-containing cytoplasmic vesicle, thus sequestering themselves from host cell-specific antimicrobial factors. They both cause extensive remodeling of vesicle membranes and initiate reprogramming events that alter host cell physiology to the benefit of the pathogen.

Given the similarities of their intracellular niches, it may not be too surprising that

intracellular growth of both of these pathogens can be curtailed by similar immune mechanisms. Both are affected by intracellular starvation conditions imposed by induction of a tryptophan-decyclizing enzyme IDO (indoleamine 2,3 dioxygenase), which is induced in the presence of the immune-regulated cytokine gamma interferon (IFN-γ) (Byrne et al., 1986; Pfefferkorn et al., 1986). This may not be completely unique to *Chlamydia* and *Toxoplasma* (for example, see Peng and Monack, 2010), yet it represents a nutrient starvation-based mechanism to slow intracellular growth without pathogen eradication. The idea that the induction of IDO by the host cell, through the innate or acquired immune response, and the reversible inhibition of intracellular growth contribute to the development of *Toxoplasma* bradyzoites and development of slow-growing aberrant chlamydial forms is a compelling model for the development of persistence. Unfortunately this model is also overly simplistic. Bradyzoite development in *Toxoplasma* is by no means fully understood but is thought to be a stress response regulated by a multilayered cascade of steps that involves production of an intracellular protective "cyst" coat around the parasitophorous vacuole, a shutdown of general protein synthesis, and interference with replication (Montoya and Liesenfeld, 2004; Sullivan et al., 2009; Weiss and Kim, 2000). It is also known that the likelihood of bradyzoite formation is to some extent strain-dependent, with slower-growing, less virulent strains being more adept at shifting from the tachyzoite to the bradyzoite stage (Soete et al., 1994; Howe and Sibley, 1995). Depletion of intracellular tryptophan via IDO may contribute to this morphogenesis, but the reversible shift between a tachyzoite and a bradyzoite is thought to be stochastic, with intact immunity better able to control the tachyzoite stage.

The details of cell culture models of chlamydial persistence have been reviewed extensively (for examples, see Beatty et al., 1994; Hogan et al., 2004; Wyrick, 2010; and Schoborg, 2011), and correlations to in vivo conditions have been developed (Hogan et al., 2004). The overall process involves virtually complete absence of intracellular replication, the appearance of greatly enlarged aberrant reticulate body (RB) forms, and dramatic reprogramming of protein expression patterns. There are some data to support altered transcriptional patterns (Mathews et al., 2001; Gerard et al., 2004; Goellner et al., 2006; Maurer et al., 2007), disconnected transcription and translation (Ouellette et al., 2006), and regulated gene expression via noncoding small RNAs during cell culture-induced chlamydial persistence (AbdelRahman et al., 2011). However, little is known about structural changes to the inclusion membrane, and there are no reports of clinical complications stemming from chlamydial reactivation in immunocompromised individuals. In fact, in most natural animal infections in which persistence has been documented, the persistent state is associated with asymptomatic infection (Pospischil et al., 2009; Reinhold et al., 2010, 2011). A notable exception may be persistence of chlamydiae in ewes subsequent to infectious abortion, where the persistence of the pathogen is thought to contribute to diminished reproductive capacity and genital tract pathology (Papp and Shewen, 1996, 1997). Thus, although stress-induced (through nutrient deprivation, temperature shifts, or changes in host cell physiology as a result of immune-regulated cytokines), slow-growing developmental forms of *Toxoplasma* and *Chlamydia* share common features, the bradyzoite-containing *Toxoplasma* cyst and the aberrant RB-containing inclusion are clearly not equivalent. The *Toxoplasma* cyst is the main reason why *Toxoplasma* infections are incurable. Cysts survive passage through the stomach, are impervious to host immunity and drug treatments, and allow the parasite to persist benignly. Yet bradyzoites remain infectious and are capable of reactivating and being efficiently transmitted. In contrast, aberrant RBs observed in the cell culture model of chlamydial persistence have not been shown to reactivate in the context of chlamydial disease. If persistence were a major feature of

chlamydial genital tract disease, associations between reactivated infections and immune suppression should be evident. This is not the case in general, although there is at least one report showing that HIV-infected sex workers with depleted $CD4^+$ T cells have a higher risk of pelvic inflammatory disease (Kimani et al., 1996). It may be that the interaction between chlamydiae and their host is more subtle, but compelling arguments for in vivo persistence in human chlamydial diseases have not been made. In addition, there remains an unexplained gap between in vitro descriptions of persistence and clinical disease syndromes, and more details are needed about the growth state of persistent chlamydiae in vivo and its pathologic consequences on the host.

Syphilis

Treponema pallidum is a human-specific microaerophilic spirochete that causes syphilis. Since the mid-19th century, this sexually transmitted infection has been recognized to progress through three distinct stages, referred to as primary, secondary, and tertiary syphilis (reviewed by Singh and Romanowski [1999]). Syphilis is one of the best-described infectious diseases, with a long history of academic and practical interest, including the infamous self-infection study carried out by the well-intentioned 18th century British physician John Hunter, who set out to demonstrate that the signs and symptoms of what turned out to be a mixed infection by *N. gonorrhoeae* and *T. pallidum* were caused by *N. gonorrhoeae* (Hunter, 1818). This experiment seems to be a little like testing the laws of gravity by jumping off a bridge to assess the effects of acceleration. The foolhardy nature of the investigation was made worse by the fact that Dr. Hunter was wrong. The good doctor suffered not only from gonococcal infection but also from syphilis, an unfortunate segue since syphilis was an incurable disease with life-threatening complications at that time (Singh and Romanowski, 1999; Baughn and Musher, 2005; LaFond and Lukehart, 2006). Other 18th and 19th century investigators completed their studies without delusions of grandeur. Philippe Ricord is credited with the first accurate account of primary, secondary, and tertiary syphilis in 1837, a time that predated popularization of the germ theory of disease by such luminaries as Robert Koch, Louis Pasteur, and Rudolf Virchow (reviewed by Baughn and Musher [2005]).

Syphilis is a multistage disease. The progression of syphilis, from the primary lesion through the tertiary stages of disease, is an extremely well-studied example of the natural history of a chronic infection. The primary lesion appears within 2 or 3 weeks of sexual exposure to an infected individual. It initially appears as a red, painless papule that progresses to an ulcerative chancre, which is loaded with treponemes and often has an exudate and an indurated margin. The primary lesion occurs most frequently in the genital, perianal, anal, or oral area as a reflection of recent sexual activity. At this early stage of the infection the organisms have already disseminated throughout the body via the lymphatics and the bloodstream, although it is not yet clinically apparent. Unless present in an obviously visible location, primary lesions often go unnoticed and will spontaneously heal within a month or two without treatment.

Despite the disappearance of the primary lesion, the infection may not have been cleared, and 25% of patients with untreated primary syphilis will develop secondary syphilis. The lesions of secondary syphilis result from hematogenous dissemination of treponemes from the primary chancre. Generally, secondary lesions appear 2 to 3 months after the initial appearance of the primary lesion and manifest as a variety of skin rashes containing transmissible treponemes. The general sequence is for a macular rash to erupt into papular lesions. Secondary syphilis is basically a systemic disease that also includes a variety of nonspecific complaints that accompany the dermatologic manifestations. Although the presence of treponemes in secondary lesions is plentiful, as demonstrated by dark-field microscopy or nucleic acid detection methods, the lesions spontaneously resolve within 1 or 2 months.

The next stage in the progression of disease is latency, characterized by continuous seroreactivity in the absence of symptoms. Sometimes reactivation of secondary syphilis can occur during this time, usually within 1 year of the initial secondary episode. If latency continues for more than a year, this is referred to as late latent syphilis. Individuals who have late latent syphilis are refractory to reinfection. However, following successful treatment, patients are susceptible to reinfection.

Tertiary syphilis, although mainly of historic importance, represents an excellent example of how progressive inflammation may manifest decades after the initial infection. As early as 2 years after primary infection, granulomatous nodular lesions may develop in the skin, bone, or other tissue. These are referred to as gummas. *T. pallidum* can be identified in these lesions, and the lesions resolve when antibiotics are administered (LaFond and Lukehart, 2006). Cardiovascular and late neurologic complications can develop 20 to 30 years after exposure. Historically, cardiovascular syphilis was responsible for the majority of deaths due to this infection. Late neurologic complications lead to personality disorder (e.g., delusions of grandeur—get it now!), impaired movement (general paresis), and muscle weakness resulting from nerve damage (tabes dorsalis). The presence of the pathogen has only rarely been identified in tertiary syphilis, but PCR methods have been used to demonstrate the presence of the organism in cardiovascular disease (O'Regan et al., 2002).

T. pallidum may be one of only a very few bacterial pathogens that is more difficult to work with than *Chlamydia*. We are more than 100 years removed from the initial specific identification of *T. pallidum* as an important human pathogen, and it still has not been routinely cultivated except by inoculation into experimental animals (reviewed by LaFond and Lukehart [2006]). The organism is virtually impossible to keep alive in vitro. However, in an in vivo infection, it rapidly disseminates from the skin via lymphatic and bloodstream invasion. Within an infected individual, it replicates and survives for lengthy periods of time, initiating an inflammatory cascade that may have dire consequences for the host in the absence of any well-established traditional virulence factors. It is almost entirely unclear how this pathogen has been so successful in the human host, although it is likely that a small proportion of infecting pathogens resist macrophage ingestion and killing. It is this subpopulation that survives subsequent to secondary stages of disease, maintains treponemal latency, and ultimately contributes to the development of tertiary syphilis. There are indications that a family of treponemal outer envelope proteins (Tprs) may undergo antigenic variation via gene conversion mechanisms and that expression of different Tpr variants are important in changes the pathogen undergoes in surviving through to latency and tertiary stages of disease (LaFond and Lukehart, 2006).

WHAT ABOUT CHLAMYDIAE?

Syphilis is the ultimate example of a chronic clinical syndrome (primary, secondary, latency, and tertiary phases) that was well described before anything was known about the properties of the pathogen that might contribute to the disease process. Even today, very little mechanistically is known about how *T. pallidum* orchestrates progression from a primary chancre to tertiary disease. Perhaps the stages of trachoma come closest to mimicking the distinct stages of syphilis, but for trachoma, the pathologic changes that accompany disease progression are very different from those seen with syphilis. The presence of the pathogen is required for each stage of syphilis. For trachoma, it is clear that follicular scarring, a process that occurs relatively early in the pathogenesis of disease, sets the stage for eyelid deformities, trichiasis, and corneal abrasion. Blinding trachoma is a direct function of mechanical malfunctions of the eyelid and eyelashes that may be exacerbated by events unrelated to chlamydial infection per se but are rather a function of other infections or even irritants like sand or grit. Certainly there is nothing described in the pathogenesis of trachoma that would suggest

either dissemination or long-term persistence of the pathogen. Trachoma is best thought of as an acute conjunctival infection of the very young, where repeated exposures lead to follicular scarring resulting in mechanical deformities that culminate in abrasions of the cornea and may lead to blindness. If ocular *C. trachomatis* infection does persist, it is rare, because literally millions of exposed individuals leave regions of endemicity for trachoma, yet reports of positive cultures in individuals having lived for years afterwards in regions of nonendemicity are few; and even in these cases aberrant forms (persistence) have not been identified.

It is known that some women who recover from chlamydial genital tract infections may harbor the organism for more than a year (McCormack et al., 1979; Oriel and Ridgway, 1982b). However, in these cases it is always difficult to sort out reinfection from persistent infections; and, as of yet, there is no clear chlamydial persistence phenotype that is associated with chronically infected women. In addition, unlike syphilis, a distinct clinical syndrome that requires long-term persistence from a primary infection for chlamydial genital tract infection has not been described.

Infections caused by *Chlamydia pneumoniae* may have disseminating chronic manifestations (Watson and Alp, 2008), and these conditions (e.g., heart disease and atopic asthma) implicate the presence of persisting forms of the pathogen, especially in either macrophages, endothelial cells, or smooth muscle cells in atherosclerotic plaque of the coronary arteries (Watson and Alp, 2008; Mahoney and Coombes, 2001). *C. pneumoniae* has been identified, although rarely cultivated, in atheromas (Watson and Alp, 2008; Mahoney and Coombes, 2001), although these findings have been disputed (Regan et al., 2002; Ieven and Hoymans, 2005). If these organisms causally contribute to heart disease, then the microbiology of the disease must be very different from that of chronic syphilis since secondary and tertiary stages of syphilis respond to antibiotics, while, at least for treatment of heart disease patients, antibiotics effective against chlamydiae do not prevent secondary events (collated by Song et al. [2008]). A role for *C. pneumoniae* in other chronic diseases, such as nonatopic asthma or neurologic diseases, has not been studied in a prospective manner and remains highly speculative at this time both in terms of a true role for chlamydiae and for the presence of persistent chlamydiae.

On the other hand, veterinary chlamydial infections, including *C. suis* infections of swine, *C. psittaci* infections of birds, or *Chlamydia abortus* and *Chlamydia pecorum* infection of livestock may have true persistent components. For example, the presence of classic aberrant chlamydial developmental forms (Fig. 2) has been documented in the gastrointestinal tract of pigs that have *C. suis* infection (Pospischil et al., 2009), and short-term antibiotic treatment of infected animals is not effective in eliminating subclinical infection (Reinhold et al., 2011). Evidence for the development of antibiotic resistance to tetracyclines via acquisition of resistance gene cassettes has been reported for *C. suis* (Lenart et al., 2001). Is it possible that one of the consequences of the presence of persistent forms is competence for genetic exchange? *C. abortus*, a sexually acquired infection in sheep, is a major cause of infectious abortion. Chronic chlamydial infection of the reproductive tract of ewes that experience pregnancy failure has been reported to limit the breeding life of affected ewes and eventually results in upper genital tract pathology (Papp and Shewen, 1997). It is unfortunate that a detailed characterization of the nature of chlamydial development in chronically infected ewes has not been done. Are these persistent infections, and is there an equivalent in the upper genital tract of women who harbor *C. trachomatis*?

Are there chlamydial attributes that are similar to those perceived to be important in the development of syphilis latency? The chlamydial Pmp family of proteins may share features with the *T. pallidum* Tpr family. It is known that some chlamydial Pmp family members are surface expressed and may be developmentally regulated. Pmp expression in vivo has been

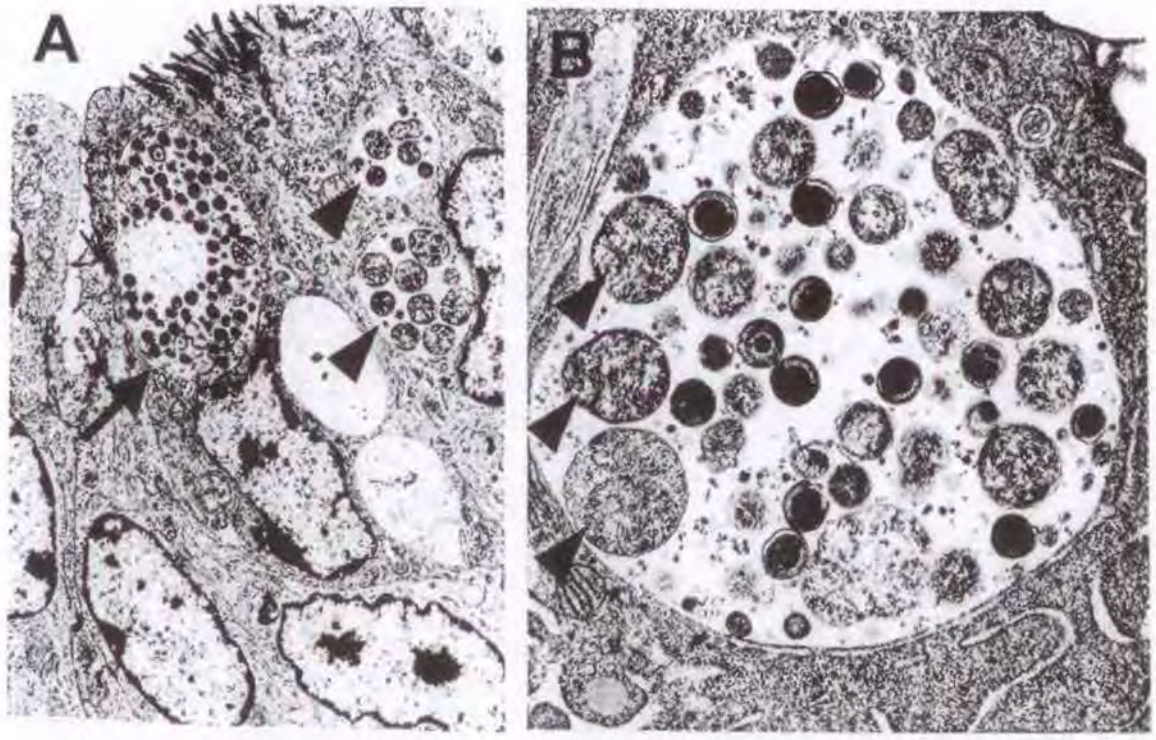

FIGURE 2 Chlamydial inclusions in intestinal enterocytes of naturally infected swine. (A) Lower-magnification electron micrograph showing both a typical inclusion (indicated by arrow) with an abundance of dense EBs and inclusions containing somewhat enlarged RBs (arrowheads). (B) Higher-magnification electron micrograph showing an inclusion containing typical EBs and RBs, in addition to enlarged, aberrant RBs (arrowheads). It is interesting that both normal and abnormal developmental forms are seen, as if persistence is a stochastic event for *C. suis* infecting the pig intestine. Images generously provided by Andreas Pospischil, University of Zurich. doi: 10.1128/9781555817329.ch12.f2

investigated by assessing immune responses to these proteins (Tan et al., 2009). In vivo studies are needed to determine if subsets of chlamydial Pmps are associated with acute versus chronic disease.

Tuberculosis

Tuberculosis is a chronic disease caused by the bacterium *Mycobacterium tuberculosis*. Recognition of asymptomatic carriage punctuated by episodes of active infection is very well described in the literature, with a rich history of both clinical and basic investigations. Control of tuberculosis is a function of the immune response and the development of granulomas, generally in the lung, consisting of a necrotic core surrounded by immune effector cells. Tubercle bacilli are often found in the necrotic core, existing under highly hypoxic conditions (Chao and Rubin, 2010). Reactivation of disease is a result of interference with the immune response. Identification of immune mechanisms that control primary infection and prevent reactivation is an area of intense investigation (Lin and Flynn, 2010). Studies of the natural history of tuberculosis and the cell and molecular biology of the pathogen have provided us not only with a fundamentally precise understanding of disease progression but also with an excellent lexicon of terms that help to precisely define disease status and characterizations of the pathogen in ways that help understand shifts in disease state. For example, according to Chao and Rubin (Chao and Rubin, 2010) latency and reactivation reflect disease states, whereas dormancy and resuscitation reflect pathogen phenotypes. Latency is defined as "a state of asymptomatic infection characterized by low bacterial counts and a lack of clinical signs of disease." Reactivation is defined as "the transition from asymptomatic *M. tuberculosis* infection to visible signs of active disease." Dormancy is defined as "a state of nonreplication that is characterized by long-term viability despite metabolic down-regulation." Resuscitation is defined as "a metabolic transformation from a relatively inert, nonreplicating state into an actively dividing state." According to these definitions, pathogen dormancy correlates with latency and pathogen resuscitation correlates with reactivation.

Tuberculosis researchers have successfully exploited molecular genetic techniques to understand conditions that elicit pathogen dormancy. Knowledge of how *M. tuberculosis* modulates gene expression and metabolism to enter and exit the nonreplicating dormant state has then been applied to develop in vivo models of latency and reactivation. Environmental factors that trigger dormancy include starvation for nutrients and hypoxia (Chao and Rubin, 2010; Shleeva et al., 2004; Wayne and Sohaskey, 2001). When these stress-related conditions are applied to *M. tuberculosis*, striking metabolic reprogramming occurs, including upregulation of stress response genes and downregulation of many central metabolism genes. Microarray studies have provided evidence for a hypoxic regulon called *dos* (an acronym for dormancy survival) (Voskuil et al., 2004). The *dos* regulon includes activation of genes needed for catabolism of novel carbon sources, including fatty acids and cholesterol (Chao and Rubin, 2010). Mutants unable to control the *dos* regulon do not resuscitate from hypoxia normally (Kumar et al., 2007) and have a defect in a two-component signaling system regulator called DosR (also known as DevR). Activity controlled by *dos* eventually matures into a longer-term hypoxia response controlled by a stress-related sigma factor (Rustad et al., 2008). Some of the *dos*-regulated genes are thought to restrain virulence by slowing down bacterial growth. DosR-mediated events also may confer phenotypic resistance to antibiotics via toxin-antitoxin mechanisms that involve rapid mRNA degradation when the levels of the toxin gene product exceed those of the antitoxin (Ramage et al., 2009).

Resuscitation from dormancy involves upregulation of enzymes that alter peptidoglycan structure. It is known that dormancy results in a peptidoglycan structure that is cross-linked differently from that found in vegetative cells.

It is thought that this creates a more stable cell wall for dormant-phase organisms. Switching to the vegetative form of peptidoglycan produces a muropeptide ligand that initiates a signal transduction cascade, which leads to metabolic upregulation and thereby facilitates resuscitation (Chao and Rubin, 2010; Lavollay et al., 2008).

It is very clear that *M. tuberculosis* reactivates from a latent state and that this results in episodes of active disease. The roles of in vitro-defined dormancy and resuscitation have not yet been proven to be the mechanisms that account for latency/reactivation disease states of tuberculosis. However, the investigation of programmed changes in the pathogen's growth status is a logical strategy toward understanding active versus latent tuberculosis, as it involves the pathogen responding to environmental cues that ultimately reflect changes in the immune status of the host.

WHAT ABOUT CHLAMYDIAE?

Clinical data for chlamydial infections do not provide strong support for alternation between active and latent states, except perhaps for *C. psittaci* infections in birds under highly stressed conditions in the abattoir, which may cause reactivation of latent gastrointestinal infection. This potentially interesting example of reactivation has not been systematically studied, and very little is known about either the status of the host or the status of the pathogen under conditions of latency or reactivation for avian infections.

An alternative possibility is that active chlamydial infection may irreversibly transition into latent disease without any possibility of reactivation. Perhaps female genital tract infections best exemplify this scenario. Active chlamydial infection must occur in the lower genital tract. It is there that chlamydiae are required to complete a productive infectious cycle (EB → RB → EB) to be effectively transmitted. In contrast, transmission is never associated with upper genital tract disease, and therefore the necessity of completing the developmental cycle to yield infectious EB populations is not an essential component of chlamydial infection of the upper genital tract. Thus, latency in the form of persistence or development of other metabolically dormant phenotypes would not compromise transmissibility, since the upper genital tract is, in effect, a dead-end locale.

The problem with this scenario is that data have not been obtained to determine if RBs, cryptic chlamydiae, or noninfectious aberrant forms are enriched in upper genital tract disease. But can we take some cues from the work done in tuberculosis research to assess pathogen phenotypes that are programmed according to environmental modulation to gain insights into the pathogenesis of chlamydial genital tract infections in women? It turns out that much like what has been seen in studies on *M. tuberculosis* dormancy in vitro, chlamydiae may have a way of regulating a productive versus a nonproductive growth status. Indeed the development of acquired immunity in the form of Th1-dependent immune-regulated cytokines induces changes in the physiology of the infected host cell known to elicit persistent chlamydial growth in vitro. We come once again to the IFN-γ-mediated induction of IDO, the intracellular degradation of tryptophan, and its effects on chlamydial growth (Beatty et al., 1994). The development of aberrant chlamydial growth under these conditions, all done in cell culture models, provides a potentially physiologically relevant mechanism for the induction of chlamydial latency. The relevance of this model of chlamydial persistence was bolstered by chlamydial proteome studies (Shaw et al., 2000) and genome-sequencing studies (Caldwell et al., 2003). These studies demonstrated that (i) *C. trachomatis* has a partial tryptophan operon that is activated under conditions of tryptophan starvation and (ii) the required substrate for the production of tryptophan, a required amino acid, is indole (Wood et al., 2003). Neither chlamydiae nor the mammalian host can make indole, but intriguingly, members of the vaginal microbiota are very often indole producers. With these findings, in vitro observations made without in vivo correlations begin to make sense.

Now we have a scenario where chlamydiae have evolved a mechanism that utilizes the polymicrobial environment in the lower genital tract to overcome tryptophan starvation induced by the host immune response. This mechanism involves the ability of chlamydiae to sense tryptophan availability through the requirement of this amino acid as a corepressor for the transcriptional regulator TrpR. When tryptophan is readily available, TrpR represses expression of the enzyme tryptophan synthase from the partial tryptophan operon of genital *C. trachomatis* (Carlson et al., 2006; Akers and Tan, 2006). However, when the host cell induces IDO and degrades tryptophan to inhibit chlamydial growth, the absence of tryptophan prevents TrpR from functioning as a repressor and allows tryptophan synthase to be expressed. Indole, provided by the polymicrobial environment of the lower genital tract, can then be used as a substrate for production of tryptophan, allowing normal chlamydial growth and generation of infectious progeny. In the upper genital tract, however, other microbial flora may not be present and chlamydiae may be unable to overcome IDO-induced tryptophan starvation. But this is of little importance to the chlamydiae that reside in this locale, since a productive infection in the upper genital tract is not important for transmission. These differences in the pathogen phenotype at different sites in the female reproductive tract may explain some fundamental features of chlamydial genital disease: productive infection in the lower genital tract leads to spread, while a nonproductive persistent infection may lead to smoldering inflammation, which is a hallmark of chlamydial upper genital tract disease in women.

This is a compelling story that builds on cell culture systems of immune effector functions, the development of chlamydial persistence in vitro, and chlamydial genomic and gene regulation studies. Indeed, the implication that the evolution of this genital tract pathogen involves the need to acquire tryptophan in a way that engages polymicrobial involvement is often overlooked in infectious disease research. But let us step back from this hypothetical example of how chlamydial genital tract disease in women may occur and consider what is actually known. We speculate about the role of immunoregulated cytokines in altering chlamydial growth to induce persistence. All data about this part of the story are from cell culture systems, and in vivo correlates have not been established. We discuss the inducible partial tryptophan operon and indole requirements as if this is what actually is occurring in vivo, but correlates between indole-producing microbiota and chlamydial EB production as defined by infectivity assays have not been obtained. We consider the differences in indole-producing microbiotas between upper and lower tract compartments, but this remains speculative; and we conclude that persistent forms may account for the insidious inflammation associated with upper genital tract disease in women, but we have not identified persistent infections as contributing factors to chlamydial genital tract disease in women. The problem is not that the hypotheses concerning chlamydial persistence and disease status are not attractive but that required in vivo data are lacking. If nonproductive, long-lasting chlamydial phenotypes are residing in cells of the upper genital tract of women with chlamydial disease, then these forms must be identified either in an appropriate animal model or in specimens taken from patients. If conversion from productive to nonproductive, persistent infections is impacted by the genital tract microbiota and its capacity to produce indole, then investigation of the metabolome of the genital microbiota in women and the status of chlamydial infections should be done. These studies are necessary to support or refute the role of persistent infections in chlamydial disease.

Typhoid Fever

Typhoid fever is a systemic infection caused by *Salmonella enterica* serovar Typhi and acquired via the oral route (Monack et al., 2004b). Infection is characterized by inflammation in the small intestine at Peyer's patches. This intestinal compartment, comprised of lymph

nodules designed to provide antigen sampling for macrophages, dendritic cells, and T and B lymphocytes, is the site of *Salmonella* serovar Typhi dissemination, where phagocytes are infected within the lamina propria. Infected phagocytes gain access to the lymphatics and bloodstream, resulting in spread of the infection to the liver, spleen, gall bladder, and bone marrow. Some individuals become lifelong carriers, periodically shed *Salmonella* Typhi in their stools, and are therefore important reservoirs of infection (Sinnott and Teall, 1987). The carrier state is characterized by a robust immune response to serovar Typhi and the absence of disease symptoms. Studies of persistent *Salmonella* disease in mice indicate that persistence is a function of the capacity of the pathogen to survive in macrophages (Monack et al., 2004a), and at least for nontyphoidal salmonellae, macrophage persistence contributes to increased disease severity in AIDS patients (Gordon, 2008). It is also known that macrophage persistence requires the SPI1 and SPI2 type three secretion (T3S) systems and effector gene products that help resist the effects of antimicrobial peptides and phagocyte oxidases and other antimicrobial effects (Monack et al., 2004b; Hensel, 2000).

WHAT ABOUT CHLAMYDIAE?

Persistent salmonellae reside in monocytes and macrophages. There are reports of chlamydiae existing as persistent, aberrant RBs in macrophages in the joints of patients with reactive arthritis (Carter and Hudson, 2010), but the characteristics of the pathogen within infected joints have not been established. Reactive arthritis is an illness characterized by joint inflammation occurring shortly after gastroenteritis caused by gram-negative bacteria or genital infections caused by *C. trachomatis* (Townes, 2010).

Members of the genus *Salmonella* are able to effect changes in host cell function after infection by virtue of their T3S system, which is designed to deliver pathogen-produced effectors into membrane structures and cytoplasm of the host cell. *Chlamydia*, like *Salmonella*, possesses a T3S system, and secreted effectors have been shown to modulate host cell function (Hower et al., 2009; Mitel et al., 2010). One important criterion for long-term persistence is the ability to maintain a stable relationship with the infected host cell over a long term. Intracellular chlamydiae are reported to program infected host cell physiology to actively elicit an antiapoptotic state, especially under conditions of nonproductive, persistent growth (Byrne and Ojcius, 2004). This activity may involve the secretion of chlamydial effector molecules into the host cell cytoplasm via T3S. It is not known if this mechanism of host cell reprogramming occurs in vivo or if it in any way contributes to the development or maintenance of chronic chlamydial infections, but it is a feature shared with *Salmonella*, a well-known cause of persistent disease.

WHAT IN VIVO CONDITIONS FALL UNDER THE RUBRIC OF CHLAMYDIAL PERSISTENCE?

Chlamydial infections of animals, including birds, sheep, swine, and bovines are common, often subclinical and chronic, and are reported to have a measureable adverse impact on the health and well-being of economically important livestock (Pospischil et al., 2009; Reinhold et al., 2010, 2011; Papp and Shewen, 1996, 1997). Unfortunately, very little is known about the growth status of the pathogen in these chronic infections. Work on *C. suis* infections in swine has clearly demonstrated the presence of chlamydial inclusions containing morphotypes that have features in common with classical cell culture-based chlamydial persistence (Pospischil et al., 2009). This provides a rationale for study of veterinary chlamydial infections to gain a perspective on how modulation of pathogen function and productive versus persistent infection may relate to the problem of chronic chlamydial disease. Roger Rank and colleagues (see chapter 13, "In vivo chlamydial infection") have shown that *C. muridarum* infection of mice depleted of neutrophils promotes the development of the aberrant chlamydial phenotype and that Nu/

Nu nude mice maintain long-term chronic *C. trachomatis* infections. Study of these models should be exploited more fully.

For human chlamydial infections, postgonococcal urethritis may provide an example of clinical persistence. Postgonococcal urethritis is defined as a persistent or recurrent sexually acquired urethral infection occurring in men who had been successfully treated for gonorrhea with beta-lactam antibiotics (Oriel and Ridgway, 1982a). Most of these patients were found to be positive for *Chlamydia*. This syndrome is now of historical significance because antichlamydial antibiotics are now routinely added to the treatment of gonococcal infections. However, when intracellular chlamydiae are exposed to penicillin or other beta-lactam antibiotics in vitro, they stop dividing and display the large aberrant phenotype associated with cell culture persistence (Matsumoto and Manire, 1970). While aberrant chlamydial forms have not been identified in postgonococcal urethritis, the detection of chlamydiae after treatment with beta-lactam antibiotics suggests that *C. trachomatis* may persist in the human host and reactivate to cause disease. This is not an insignificant observation, although it is curious that the best example of chlamydial persistence in human disease arises from an exogenous source of persistence induction (penicillin) rather than as a result of a pathogen-driven mechanism.

Curiously, there were no reports of the equivalent of post-gonococcal-treatment disease in women when it was established that *C. trachomatis* caused postgonococcal urethritis in the 1970s (Richmond et al., 1972). At that time there were reports to indicate that chlamydial cervicitis could persist for more than a year in untreated women who denied having had intercourse since their initially positive examination (McCormack et al., 1979). Geisler recently commented on the practical and ethical issues associated with human natural history of infection studies (Geisler, 2010). It is difficult to know with certainty the time at which initial exposure to the pathogen occurs or whether reinfections play a role. Most importantly, once the pathogen is identified, treatment, if available, must begin. In the absence of natural history studies, but with reasonable indications that persistence is important in upper genital tract disease in women, it is of critical importance to establish reliable biomarkers to help characterize the presence of chronic chlamydiae with a high degree of specificity and sensitivity.

WHERE DO WE GO FROM HERE?

We began this chapter by suggesting that chlamydiae were different from other pathogens. This chapter has posed the question of how similar or different chlamydiae are from other microbial pathogens that are also different from run-of-the-mill pathogens. All comparative examples chosen represent pathogens well established in causing persistent, chronic, or latent disease (Fig. 3). The pathogens selected for comparison here were chosen because we thought they provided excellent examples of chronic disease that have correlates with chlamydiae as assessed by cell culture models. But this list is by no means complete, and we may not even have chosen the best examples. Why not take the time to make your own list and see how chlamydiae are similar to or different from the pathogens that you select. It is fun—and educational!

Evidence suggests that chlamydiae also are different from the group of persistent pathogens described here, although they share features with many of them. There are very few examples of chlamydial infections that cause reactivation of infection in ways that have been described for vivax malaria, toxoplasmosis, or tuberculosis, except when the conditions for persistence are established exogenously, such as via induction of the persistence phenotype by administration of penicillin, setting the stage for postgonococcal urethritis, but apparently (and curiously) with no recognized equivalent in women. Similarly, chlamydial infections do not appear to progress through defined stages of primary, secondary, and tertiary disease in a manner similar to *T. pallidum* infection and syphilis, where stealth in avoiding immune

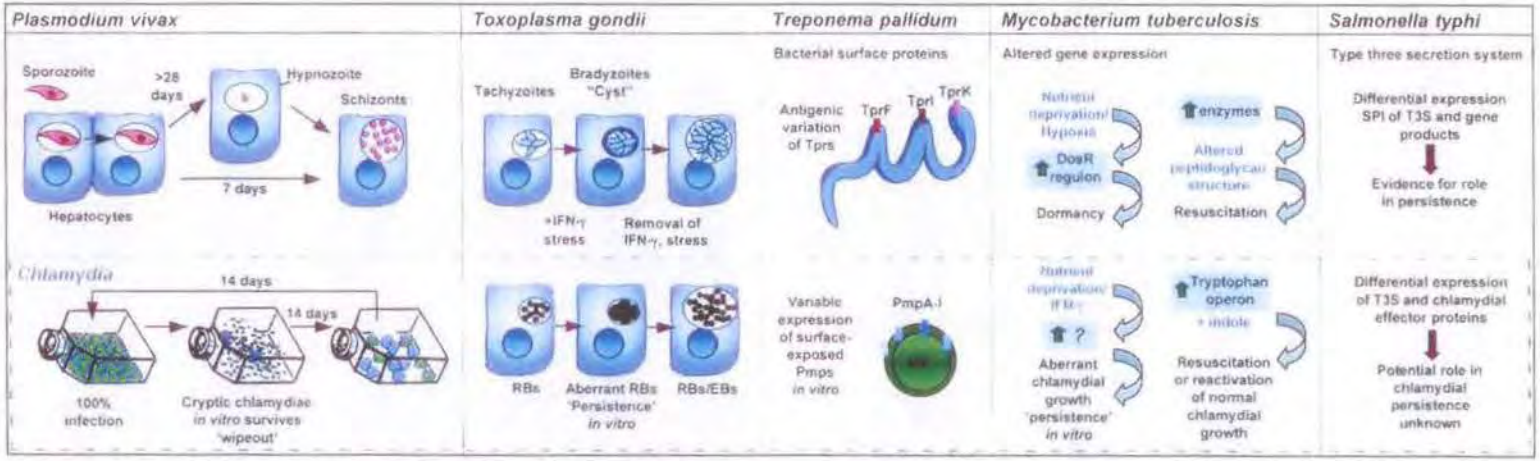

FIGURE 3 Factors contributing to persistence of other microorganisms and potential correlates in *Chlamydia*. Attributes of other microorganisms are shown in upper panels, and potential correlates in *Chlamydia* are shown in the corresponding lower panels. Please see the text for details.

doi:10.1128/9781555817329.ch12.f3

elimination from an extracellular residence must be paramount.

Established examples of chronic chlamydial infections may share similarities with typhoid fever. The carrier state in typhoid fever is basically that of an asymptomatic shedder. This condition seems similar to chlamydial infections reported in swine and other livestock. In these cases, severe acute infections (e.g., infectious abortion) mature into chronic relationships between the microbe and the host with debatable pathogenic potential (Pospischil et al., 2009; Reinhold et al., 2011; Papp and Shewen, 1997). There are a number of available animal models that could be developed to study chronic chlamydial infections using natural infection models. These include studies of *C. suis* in pigs (Pospischil et al., 2009) and *C. abortus* in sheep (Papp and Shewen, 1996, 1997). Development of these models is likely to provide direct information relevant to swine and sheep infectious diseases and may provide insight relevant to human chlamydial infections. At the very least, we will learn how animal-infecting *Chlamydia* strains and diseases of livestock are similar to, or different from, human chlamydial strains and chlamydial diseases of humans.

But is there more to the relationship between chlamydiae and their hosts than currently meets the eye? Chimera is an interesting word. Sometimes it refers to something that is real and very abnormal, but usually it conceptualizes a creation in one's mind, a figment of the imagination, a phantom from lost worlds—not an everyday reality. Antonyms for chimera include on the one hand terms like reality and truth but on the other hand terms like normal, ordinary, and regular. The mythological fire-breathing monster with a lion's head, a goat's body, and a serpent's tail is the most common vision of a chimera; clearly a creature of dreams (or nightmares). But what of a microbial pathogen with the dormancy potential of *P. vivax*, the capacity to survive an immune response like *T. gondii* and *M. tuberculosis*, and a tendency toward asymptomatic carriage like *Salmonella* but with the potential for causing long-term consequences like *T. pallidum*? Is this a chimera or the definition of a highly successful, well-adapted pathogen that has found a novel way to survive within its host? Is this the definition of *Chlamydia*?

A major question continues to be where human *C. trachomatis* infections fit in the spectrum of acute versus chronic infection. Chronic stages of blinding trachoma represent a mechanical disorder where the pathogen is irrelevant once the lid distortion process begins. Reactive arthritis is clearly a chronic disease in which chlamydiae may be involved, and the story of *C. pneumoniae* and heart disease is well known. Urethritis and cervicitis may evolve into more chronic conditions, but natural history studies are difficult to conduct and relevant animal models are not well established vis-à-vis persistence. Upper genital tract disease in women may reflect chronic disease, but sorting through the process in the natural host is not practical or ethical. Animal models may be useful tools to better understand chlamydial persistence in the upper genital tract, but in vivo approaches have provided only limited information, thus far.

Systems biology studies are needed to address key questions that will link details regarding pathogen phenotypes and the development of chronic disease. In developing these types of strategies, it will be important first to carefully select an appropriate, tractable model host that reflects conditions relevant to the experimental questions under investigation. Mouse models probably represent the most valuable available tool because these animals can be genetically modified to suit the type of infection under investigation. The mouse as host may not be the only experimental system likely to yield a body of systems biology data; but it is relevant and highly tractable in that production of designer mouse strains featuring traits specific for best mimicking human disease is feasible, and data sets using mice lend themselves readily to bioinformatic and systems biology approaches. When "omics" tools are applied to the study of chlamydial disease, the problem of persistence and chlamydial disease severity may finally

mature to the point where reliable biomarkers are discovered that will enable translation to human infections in ways that will help us to better understand the true role of chronic infections in the repertoire of important human diseases that are caused by chlamydiae.

ACKNOWLEDGMENTS

We thank Patrik Bavoil, Ming Tan, Andreas Pospischil, Roger Rank, and Byron Batteiger for critically reviewing the text. Their suggestions have made the chapter better. Lingering deficiencies are the fault of the authors. This work was supported by PHS grant AI19782 (GIB) and Department of Defense award W81XWH-09-0391 (GIB).

REFERENCES

AbdelRahman, Y. M., L. A. Rose, and R. J. Belland. 2011. Developmental expression on non-coding RNAs in *Chlamydia trachomatis* during normal and persistent growth. *Nucleic Acids Res.* **39:**1843–1854.

Akers, J. C., and M. Tan. 2006. Molecular mechanism of tryptophan-dependent transcriptional regulation in *Chlamydia trachomatis*. *J. Bacteriol.* **188:**4236–4243.

Baughn, R. E., and D. M. Musher. 2005. Secondary syphylitic lesions. *Clin. Microbiol. Rev.* **18:**205–216.

Beatty, W. L., R. P. Morrison, and G. I. Byrne. 1994. Persistent chlamydiae: from cell culture to a paradigm for chlamydial pathogenesis. *Microbiol. Rev.* **58:**686–699.

Byrne, G. I., L. K. Lehmann, and G. L. Landry. 1986. Induction of tryptophan catabolism is the mechanism for gamma-interferon-mediated inhibition of intracellular *Chlamydia psittaci* replication in T24 cells. *Infect. Immun.* **53:**347–351.

Byrne, G. I., and D. Ojcius. 2004. *Chlamydia* and apoptosis: life and death decisions of an intracellular pathogen. *Nat. Rev. Microbiol.* **2:**802–808.

Caldwell, H. D., H. Wood, D. Crane, R. Bailey, R. B. Jones, D. Mabey, I. MacLean, Z. Mohammed, R. Peeling, C. Roshick, J. Schachter, A. W. Solomon, W. E. Stamm, R. L. Suchland, L. Taylor, S. K. West, T. C. Quinn, R. J. Belland, and G. McClarty. 2003. Polymorphisms in *Chlamydia trachomatis* tryptophan synthase genes differentiate between genital and ocular isolates. *J. Clin. Investig.* **111:**1757–1769.

Carlson. J. H., H. Wood, C. Roshick, H. D. Caldwell, and G. McClarty. 2006. *In vivo* and *in vitro* studies of *C. trachomatis* TrpR:DNA interactions. *Mol. Microbiol.* **59:**1678–1691.

Carter, J. D., and A. P. Hudson. 2010. The evolving story of *Chlamydia*-induced reactive arthritis. *Curr. Opin. Rheumatol.* **22:**424–430.

Chao, M. C., and E. J. Rubin. 2010. Letting sleeping *dos* lie: does dormancy play a role in tuberculosis? *Annu. Rev. Microbiol.* **64:**293–311.

Chen, N., A. Auliff, K. Riekmann, M. Gatton, and Q. Cheng. 2007. Relapses of *Plasmodium vivax* result from clonal hypnozoites activated at predetermined intervals. *J. Infect. Dis.* **195:**934–941.

Geisler, W. M. 2010. Duration of untreated, uncomplicated *Chlamydia trachomatis* genital infection and factors associated with chlamydia resolution: a review of human studies. *J. Infect. Dis.* **201**(S2): S104–S113.

Gerard, H., J. Whittum-Hudson, H. R. Schumacher, and A. Hudson. 2004. Differential expression of three *C. trachomatis* hsp-60-encoding genes in active vs persistent infections. *Microb. Pathog.* **36:**35–39.

Goellner, S., E. Schubert, E. Lieber-Tenorio, H. Hotzel, H. P. Saluz, and K. Sache. 2006. Transcriptional response patterns of *Chlamydophila psittaci* in different in vitro models of persistent infection. *Infect. Immun.* **74:**4801–4808.

Gordon, M. A. 2008. *Salmonella* infections in immunocompromised adults. *J. Infect.* **56:**413–422.

Hensel, M. 2000. *Salmonella* pathogenicity island 2. *Mol. Microbiol.* **36:**1015–1023.

Hogan, R. J., S. A. Mathews, S. Mukhopadhyay, J. T. Summersgill, and P. Timms. 2004. Chlamydial persistence: beyond the basic paradigm. *Infect. Immun.* **72:**1843–1855.

Horn, M., A. Collingro, S. Schmitz-Esser, C. L. Beier, U. Purkhold, B. Fartmann, P. Brandt, G. J. Nyakatura, M. Droege, D. Frishman, T. Rattei, H.-W. Mewes, and M. Wagner. 2004. Illuminating the evolutionary history of *Chlamydia*. *Science* **304:**728–730.

Howe, D. K., and D. L. Sibley. 1995. *Toxoplasma gondii* comprises three clonal lineages: correlation of parasite genotype with human disease. *J. Infect. Dis.* **172:**1561–1566.

Hower, S., K. Wolf, and K. Fields. 2009. Evidence that CT694 is a novel *Chlamydia trachomatis* T3S substrate capable of functioning during invasion or early cycle development. *Mol. Microbiol.* **72:**1423–1437.

Hunter, J. 1818. *Treatise on Venereal Disease*, 2nd ed. Sherwood, Neely, and Jones, London, United Kingdom.

Ieven, M. M., and V. Y. Hoymans. 2005. Involvement of *Chlamydia pneumoniae* in atherosclerosis: more evidence for lack of evidence. *J. Clin. Microbiol.* **43:**19–24.

Imwong, M., G. Snounou, S. Pukrittayakamee, N. Tanomsing, J. R. Kim, A. Nandy, J. P. Guthmann, F. Nosten, J. Carlton, S. Looareesuwan, S. Nair, D. Sudimack, N. P. J.

Day, T. J. C. Anderson, and N. J. White. 2007. Relapses of *Plasmodium vivax* infection usually result from activation of heterologous hypnozoites. *J. Infect. Dis.* **195:**927–933.

Kimani, J., I. W. Maclean, J. J. Bwayo, K. MacDonald, J. Oyugi, G. M. Maitha, R. W. Peeling, M. Cheang, N. J. D. Nagelkerke, F. A. Plummer, and R. C. Brunham. 1996. Risk factors for *Chlamydia trachomatis* pelvic inflammatory disease among sex workers in Nairobi, Kenya. *J. Infect. Dis.* **173:**1437–1444.

Kumar, A., J. C. Toleda, R. P. Patel, J. R. Lancaster, Jr., and A. J. Steyn. 2007. *Mycobacterium tuberculosis* DosS is a redo sensor and DosT is a hypoxia sensor. *Proc. Natl. Acad. Sci. USA* **104:**11568–11574.

LaFond, R. E., and S. A. Lukehart. 2006. Biological basis for syphilis. *Clin. Microbiol. Rev.* **19:**29–49.

Lavollay, M., M. Arthur, M. Fourgeaud, L. Dubost, A. M. N. Veziris, D. Blanot, L. Gutmann, and J.-L. Mainardi. 2008. The peptidoglycan of stationary phase *Mycobacterium tuberculosis* predominantly contains cross-links generated by L,D-transpeptidation. *J. Bacteriol.* **190:**4360–4366.

Lee, C. K., and J. W. Moulder. 1981. Persistent infection of mouse fibroblasts (McCoy cells) with a trachoma strain of *Chlamydia trachomatis*. *Infect. Immun.* **32:**822–829.

Lenart, J., A. A. Anderson, and D. D. Rockey. 2001. Growth and development of tetracycline-resistant *Chlamydia suis*. *Antimicrob. Agents Chemother.* **42:**2198–2203.

Lin, P. L., and J. L. Flynn. 2010. Understanding latent tuberculosis: a moving target. *J. Immunol.* **185:**15–22.

Mahoney, J. B., and B. K. Coombes. 2001. *Chlamydia pneumoniae* and atherosclerosis: does the evidence support a causal or contributory role? *FEMS Microbiol. Lett.* **197:**1–9.

Mathews, S., C. George, C. Flegg, D. Stenzel, and P. Timms. 2001. Differential expression of *ompA, ompB, pyk, nlpD* and Cpn0585 genes between normal and interferon-gamma treated cultures of *Chlamydia pneumoniae*. *Microb. Pathog.* **30:**337–345.

Matsumoto, A., and G. P. Manire. 1970. Electron microscopic observations on the effect of penicillin on the morphology of *Chlamydia psittaci*. *J. Bacteriol.* **101:**278–285.

Maurer, A. P., A. Mehlitz, H. J. Mollenkopf, and T. F. Meyer. 2007. Gene expression profiles of *Chlamydophila pneumoniae* during the developmental cycle and iron-depleted mediated persistence. *PLoS Pathog.* **3:**e83.

McCormack, W. M., S. Alpert, D. E. McComb, R. L. Nichols, Z. Semine, and S. H. Zinner. 1979. Fifteen-month follow-up study of women infected with *C. trachomatis*. *N. Engl. J. Med.* **300:**123–125.

Mitel, S., N. J. Miller, E. R. Fischer, and T. Hackstadt. 2010. Specific chlamydial inclusion membrane proteins associated with active Src family kinases in microdomains that interact with the host microtubule network. *Cell. Microbiol.* **12:**1235–1249.

Monack, D. M., D. M. Bouley, and S. Falkow. 2004a. *Salmonella typhimurium* persists within macrophages in the mesenteric lymph nodes of chronically infected Nramp1+/+ mice and can be reactivated by IFN-γ neutralization. *J. Exp. Med.* **199:**231–241.

Monack, D. M., A. Mueller, and S. Falkow. 2004b. Persistent bacterial infections: the interface of the pathogen and the host immune system. *Nat. Rev. Microbiol.* **2:**747–765.

Montoya, J. G., and O. Liesenfeld. 2004. Toxoplasmosis. *Lancet* **363:**1965–1976.

Moulder, J. W., N. J. Levy, and L. P. Shulman. 1980. Persistent infection of mouse fibroblasts (L cells) with *Chlamydia psittaci*: evidence for a cryptic chlamydial form. *Infect. Immun.* **30:**874–883.

O'Regan, A. W., C. Castro, S. A. Lukehart, J. M. Kasznica, P. A. Rice, and M. F. Joyce-Brady. 2002. Barking up the wrong tree? Use of polymerase chain reaction to diagnose syphylitic aortitis. *Thorax* **57:**917–918.

Oriel, J. D., and G. L. Ridgway. 1982. Genital infection by *Chlamydia trachomatis*. *Ciba Topics Infect. Dis.* **2:**41–52.

Oriel, J. D., and G. L. Ridgway. 1982. Genital infection by *Chlamydia trachomatis*. *Ciba Top. Infect. Dis.* **2:**53–67.

Ouellette, S. P., T. P. Hatch, Y. M. AbdelRahman, L. A. Rose, R. J. Belland, and G. I. Byrne. 2006. Global transcriptional up-regulation in the absence of increased translation in *Chlamydia* during IFN-γ-mediated host cell tryptophan starvation. *Mol. Microbiol.* **62:**1387–1401.

Papp, J. R., and P. E. Shewen. 1996. Localization of chronic *Chlamydia psittaci* infection in the reproductive tract of sheep. *J. Infect. Dis.* **174:**1296–1302.

Papp, J. R., and P. E. Shewen. 1997. *Chlamydia psittaci* infection in sheep: a paradigm for human reproductive tract infection. *J. Reprod. Immunol.* **34:**185–202.

Peng, K., and D. M. Monack. 2010. Indoleamine 2,3-dioxygenase 1 is a lung-specific innate immune defense mechanism that inhibits growth of *Francisella tularensis* tryptophan auxotrophs. *Infect. Immun.* **78:**2723–2733.

Pfefferkorn, E. R., M. Eckel, and S. Rebhun. 1986. Interferon-gamma suppresses the growth of *Toxoplasma gondii* in human fibroblasts through starvation for tryptophan. *Mol. Biochem. Parasitol.* **20:**215–224.

Pospischil, A., N. Borel, E. H. Chowdury, and F. Guscetti. 2009. Aberrant chlamydial developmental forms in the gastrointestinal tract of pigs

spontaneously and experimentally infected with *Chlamydia suis*. *Vet. Microbiol.* **135**:147–156.

Ramage, H. R., L. E. Connolly, and J. S. Cox. 2009. Comprehensive functional analysis of *Mycobacterium tuberculosis* toxin-antitoxin systems: implications for pathogenesis, stress responses, and evolution. *PLoS Genet.* **5**:e1000767.

Regan, M. J., B. J. Wood, Y. H. Hsieh, M. L. Theodore, T. C. Quinn, D. B. Hellman, R. Green, C. A. Gaydos, and J. H. Stone. 2002. Temporal arteritis and *Chlamydia pneumoniae*. Failure to detect the organism by polymerase chain reaction in ninety cases and ninety controls. *Arthritis Rheum.* **46**:1056–1060.

Reinhold, P., E. Liebler-Tenorio, S. Sattler, and K. Sachse. 2011. Recurrence of *Chlamydia suis* infection in pigs after short-term antimicrobial treatment. *Vet. J.* **187**:405–407.

Reinhold, P., K. Sachse, and B. Kaltenboeck. 2011. *Chlamydiaceae* in cattle: commensals, trigger organisms, or pathogens? *Vet. J.* **189**:257–267. doi:10.1016/j.tvjl.2010.09.003.

Richmond, S. J., A. L. Hilton, and S. K. R. Clarke. 1972. Chlamydial infection. Role of *Chlamydia* sub-group A in non-gonococcal and post-gonococcal urethritis. *Br. J. Vener. Dis.* **48**:437–444.

Rustad, T. R., M. I. Harrell, R. Liao, and D. R. Sherman. 2008. The enduring hypoxic response of *Mycobacterium tuberculosis*. *PLoS One* **3**:e1502.

Schoborg, R. V. 2011. *Chlamydia* persistence—a tool to dissect *Chlamydia*-host cell interactions. *Microbes Infect.* **13**:649–662.

Shaw, A. C., G. Christiansen, P. Roepstorff, and S. Birkelund. 2000. Genetic differences in the *Chlamydia trachomatis* tryptophan synthase a-subunit can explain variations in serovar pathogenesis. *Microbes Infect.* **2**:581–592.

Shleeva, M. O., G. V. Mukamolova, M. Young, H. D. Williams, and A. S. Kaprelyants. 2004. Formation of "non-culturable" cells of *Mycobacterium smegmatis* in stationary phase in response to growth under suboptimal conditions and their Rpf-mediated resuscitation. *Microbiology* **150**:1687–1697.

Singh, A. E., and B. Romanowski. 1999. Syphilis: review with emphasis on clinical, epidemiologic, and some biologic features. *Clin. Microbiol. Rev.* **12**:187–209.

Sinnott, C. R., and A. J. Teall. 1987. Persistent gallbladder carriage of *Salmonella typhi*. *Lancet* **i**:976.

Soete, M., D. Camus, and J. F. Dubremetz. 1994. Experimental induction of bradyzoite-specific antigen expression and cyst formation by the RH strain of *Toxoplasma gondii* in vitro. *Exp. Parasitol.* **78**:361–370.

Song, Z., P. Brassard, and J. M. Brophy. 2008. A meta-analysis of antibiotic use for the secondary prevention of cardiovascular diseases. *Can. J. Cardiol.* **24**:391–395.

Stern, L. C. 1875. *Papyros Ebers: Das hermetische Buch uber die Arzeneimittel der alten Agypter in hieratischer Schrift, herausgegeben mit Inhaltsangabe und Einleitung versehen von Georg Ebers, mit Heiroglyphisch-Lateinischem Glosser von Ludwig Stern, mit Unterstutzung des Koniglich Sachsischen Cultusministerium*, 2. G Ebers ed., Leipzig, Germany.

Sullivan, W. J., Jr., A. T. Smith, and B. R. Joyce. 2009. Understanding mechanisms of differentiation and a role in the pathogenesis of *Toxoplasma gondii*: a review. *Mem. Inst. Oswaldo Cruz* **104**:155–161.

Tan, C., R.-C. Hsia, H. Shou, C. Haggerty, C. Gaydos, D. Dean, A. Scurlock, D. P. Wilson, and P. M. Bavoil. 2009. *Chlamydia trachomatis*-infected patients display variable antibody profiles against the nine-member polymorphic membrane protein family. *Infect. Immun.* **77**:3218–3226.

Taylor, H. R. 2008. *Trachoma, a Blinding Scourge from the Bronze Age to the Twenty-First Century*. Haddington Press, South Yarra, Australia.

Townes, J. M. 2010. Reactive arthritis after enteric infections in the United States: the problem of definition. *Clin. Infect. Dis.* **50**:247–254.

Voskuil, M. I., K. C. Visconti, and G. K. Schoolnik. 2004. *Mycobacterium tuberculosis* gene expression during adaptation to stationary phase and low-oxygen dormancy. *Tuberculosis* **84**:218–227.

Watson, C., and N. J. Alp. 2008. Role of *Chlamydia pneumoniae* in atherosclerosis. *Clin. Sci.* **114**:509–531.

Wayne, L. G., and C. D. Sohaskey. 2001. Nonreplicating persistence of *Mycobacterium tuberculosis*. *Annu. Rev. Microbiol.* **55**:139–163.

Weiss, L. M., and K. Kim. 2000. The development and biology of bradyzoites of *Toxoplasma gondii*. *Front. Biosci.* **5**:391–405.

Wells, T. N. C., J. N. Burrows, and J. K. Baird. 2010. Targeting the hypnozoite reservoir of *Plasmodium vivax*: the hidden obstacle to malaria elimination. *Trends Parasitol.* **26**:145–151.

Wilson, B. A., A. A. Salyers, D. D. Whitt, and M. E. Winkler. 2011. *Bacterial Pathogenesis: a Molecular Approach*, 3rd ed. ASM Press, Washington, DC.

Wood, H., C. Fehlner-Gardner, J. Berry, E. Fischer, B. Graham, T. Hackstadt, C. Roshick, and G. McClarty. 2003. Regulation of tryptophan synthase gene expression in *Chlamydia trachomatis*. *Mol. Microbiol.* **49**:1347–1359.

Wyrick, P. B. 2010. *Chlamydia* persistence *in vitro*: an overview. *J. Infect. Dis.* **201**(S2):S88–S95.

Link between intraphagosomal biotin and rapid phagosomal escape in *Francisella*

Brooke A. Napier[a,b], Lena Meyer[c], James E. Bina[d], Mark A. Miller[e], Anders Sjöstedt[c], and David S. Weiss[a,b,f,1]

[a]Department of Microbiology and Immunology, [b]Emory Vaccine Center, and [f]Division of Infectious Diseases, Department of Medicine, Emory University School of Medicine, Atlanta, GA 30329; [c]Department of Clinical Microbiology and Laboratory for Molecular Infection Medicine Sweden (MIMS), Umeå University, SE-901 85 Umeå, Sweden; [d]Department of Microbiology and Molecular Genetics, University of Pittsburgh School of Medicine, Pittsburgh, PA 15219; and [e]Department of Microbiology, Immunology, and Biochemistry, University of Tennessee Health Science Center, Memphis, TN 38163

Edited by Ralph R. Isberg, Howard Hughes Medical Institute, Tufts University School of Medicine, Boston, MA, and approved September 13, 2012 (received for review April 25, 2012)

Cytosolic bacterial pathogens require extensive metabolic adaptations within the host to replicate intracellularly and cause disease. In phagocytic cells such as macrophages, these pathogens must respond rapidly to nutrient limitation within the harsh environment of the phagosome. Many cytosolic pathogens escape the phagosome quickly (15–60 min) and thereby subvert this host defense, reaching the cytosol where they can replicate. Although a great deal of research has focused on strategies used by bacteria to resist antimicrobial phagosomal defenses and transiently pass through this compartment, the metabolic requirements of bacteria in the phagosome are largely uncharacterized. We previously identified a *Francisella* protein, FTN_0818, as being essential for intracellular replication and involved in virulence in vivo. We now show that FTN_0818 is involved in biotin biosynthesis and required for rapid escape from the *Francisella*-containing phagosome (FCP). Addition of biotin complemented the phagosomal escape defect of the *FTN_0818* mutant, demonstrating that biotin is critical for promoting rapid escape during the short time that the bacteria are in the phagosome. Biotin also rescued the attenuation of the *FTN_0818* mutant during infection in vitro and in vivo, highlighting the importance of this process. The key role of biotin in phagosomal escape implies biotin may be a limiting factor during infection. We demonstrate that a bacterial metabolite is required for phagosomal escape of an intracellular pathogen, providing insight into the link between bacterial metabolism and virulence, likely serving as a paradigm for other cytosolic pathogens.

Subversion of the hostile phagosomal environment is required for the survival of intracellular bacteria. Although bacterial strategies to resist antimicrobial phagosomal defenses have been studied in great detail (1, 2), the ways in which bacteria counter phagosomal nutrient limitation are largely unknown. This is especially true for cytosolic pathogens that are often in the phagosome for a very limited time (15–60 min), before escaping this compartment to reach their replicative niche in the cytoplasm. During this brief and dynamic time, it is unclear if cytosolic pathogens require sequestration of nutrients or synthesis of de novo metabolites to promote their virulence strategies and escape the toxic phagosome.

Francisella tularensis is a cytosolic intracellular Gram-negative bacterial pathogen that uses a multitude of mechanisms to evade phagosomal host defenses (3). This pathogen is highly virulent and causes the potentially fatal disease tularemia. *Francisella novicida* U112 and *Francisella holarctica* LVS (live vaccine strain) are less virulent yet highly related strains that are often used as models to study *F. tularensis*. Like other cytosolic bacterial pathogens, after initial contact with the host macrophage, *Francisella* spp. are taken up into a phagosome and rapidly escape (30–60 min) this compartment to reach and replicate within the cytosol (3–5). The mechanism by which *Francisella* escapes the *Francisella*-containing phagosome (FCP) is unknown; however, this process requires expression of the *Francisella* pathogenicity island (FPI), a cluster of 17 genes encoding a putative type VI secretion system (T6SS) (6–8).

We previously identified FTN_0818, a hypothetical protein with no known function, as one of the most critical genes for *F. novicida* replication in mouse macrophages (9). We also identified FTN_0818 as being required for infection of mice using an unbiased genome-wide, in vivo negative selection screen (10), a finding later supported by another group as well (11). FTN_0818 was also identified in an intracellular replication screen in arthropod-derived cells (12). Here, we characterize FTN_0818 and highlight an adaptation of *Francisella* to the FCP by linking intraphagosomal metabolic requirements with rapid escape from this compartment.

Our studies demonstrate that FTN_0818 is required for growth in nutrient-limiting environments, and by use of a phenotypic microarray, we identified the enzymatic cofactor biotin as being able to fully complement the growth defect of the *FTN_0818* mutant. The addition of exogenous biotin alleviated the requirement of FTN_0818 for rapid FCP escape, intracellular replication, and pathogenesis in mice. Our data suggest that biotin may be a limiting factor that, when absent, restricts cytosolic pathogens to the phagosome, blocking their escape and preventing them from reaching their replicative niche in the cytoplasm. We show that bacterial metabolism within the phagosome is vital for rapid phagosomal escape and likely serves as a paradigm for other cytosolic bacterial pathogens.

Results

FTN_0818 Is Required for Rapid Escape from the FCP and Intracellular Replication. The screens that identified FTN_0818 as being required for *Francisella* virulence used transposon insertion mutants that can have defects in genes other than the one targeted. We therefore wanted to validate the identification of *FTN_0818* and constructed a clean deletion mutant in *F. novicida* (*ΔFTN_0818*). We infected macrophages and found that at 7.5 h postinfection (pi), wild-type (WT) bacteria replicated almost 10-fold, whereas *ΔFTN_0818* was unable to replicate (Fig. S1). To ensure that this phenotype was attributable solely to deletion of *FTN_0818* and not an unknown second-site mutation, we complemented the deletion strain with a WT copy of *FTN_0818*. The complemented strain replicated to levels similar to the WT (Fig. S1). These data confirm that *FTN_0818* is indeed required for *F. novicida* replication in macrophages.

Several steps are required for *Francisella* replication in macrophages including passage through the highly nutrient-limiting FCP (13), and we set out to determine at which step *ΔFTN_0818* was

Author contributions: B.A.N., L.M., and D.S.W. designed research; B.A.N., L.M., J.E.B., and M.A.M. performed research; B.A.N. contributed new reagents/analytic tools; B.A.N., L.M., A.S., and D.S.W. analyzed data; and B.A.N., L.M., and D.S.W. wrote the paper.

The authors declare no conflict of interest.

This article is a PNAS Direct Submission.

[1]To whom correspondence should be addressed. E-mail: david.weiss@emory.edu.

This article contains supporting information online at www.pnas.org/lookup/suppl/doi:10.1073/pnas.1206411109/-/DCSupplemental.

defective. To test whether Δ*FTN_0818* had a deficiency in entry, we infected macrophages and determined the levels of intracellular colony-forming units at 30 min pi, before any bacterial replication occurs. WT, Δ*FTN_0818*, and the complemented strain were present at similar levels (Fig. 1*A*), demonstrating that FTN_0818 is not required for initial uptake of *F. novicida* by macrophages.

Escape from the FCP is essential for *Francisella* to evade this nonpermissive environment to successfully replicate in the cytosol (4), and this process requires the expression of *Francisella* pathogenicity island (FPI) genes. We, therefore, measured the expression of the FPI gene *iglA* during macrophage infection with either the WT or Δ*FTN_0818* strain. At 30 min pi, *iglA* expression in the Δ*FTN_0818* mutant was significantly lower than that in the WT strain, although its expression increased by 4 h pi (Fig. 1*B*). The kinetics of FCP escape correlated with this *iglA* expression defect. At 30 min pi, both WT and *ΔFTN_0818* were almost exclusively (>95%) within phagosomes (Fig. 1*E* and Fig. S2). At 3 h pi, WT had largely escaped as >95% of the bacteria were cytosolic (Fig. 1 *C* and *E*), whereas *ΔFTN_0818* was still almost completely retained within the FCP (Fig. 1 *D* and *E*). However, *ΔFTN_0818* escaped the FCP at 6 h pi after *iglA* expression increased in this strain (Fig. 1*E*). These results indicate that FTN_0818 is required for WT expression of an FPI gene early in infection and subsequent rapid escape from the FCP, correlating with the severe growth defect of the Δ*FTN_0818* mutant during macrophage infection.

FTN_0818 Plays a Role in Biotin Metabolism. Because FTN_0818 is required for regulation of *iglA* in the nutrient-limiting FCP, a process critical for escape from this compartment (Fig. 1*B*), and recent literature has emphasized the importance of the metabolic state of *Francisella* for virulence (14), we hypothesized that FTN_0818 may play a role in the acquisition of nutrients or production of metabolites. To determine whether FTN_0818 might be involved in these processes, we compared the growth of *ΔFTN_0818* in rich [tryptic soy broth (TSB)] and defined minimal medium [Chamberlain's medium (CHB; Table S1)] (15). We found that *ΔFTN_0818* replicated to WT levels in TSB (Fig. S3*A*); however, it exhibited a severe growth defect in CHB in comparison with the WT and complemented strains (Fig. S3*B*). These data demonstrate that FTN_0818 is specifically required for growth in a nutrient-limiting environment (13), suggesting that it may contribute to the acquisition and/or biosynthesis of nutrients that are required for growth in these conditions.

To determine whether a specific metabolite could complement the growth defect of Δ*FTN_0818* in minimal media, we used a Biolog Phenotypic Microarray. As expected, the WT strain grew well in minimal medium (modified CHB), whereas the *FTN_0818* mutant did not (Fig. S4). Only biotin was able to complement growth of the *FTN_0818* mutant (Fig. S4). We further validated these results, showing that biotin complemented *ΔFTN_0818* growth in CHB (Fig. 2*A*). These data suggest that the *FTN_0818* mutant has insufficient levels of biotin and that FTN_0818 is involved in the acquisition or synthesis of biotin in *F. novicida*.

Biotin is required for numerous metabolic pathways and is covalently attached (biotinylation) to proteins to facilitate their activity. Therefore, one method for quantifying biotin levels in bacteria is to measure the level of biotinylated proteins. Using immunoprecipitation with streptavidin, we quantified the total concentration of biotinylated proteins and detected much lower levels in the *FTN_0818* mutant compared with WT (Fig. 2*B*). Furthermore, exogenous addition of biotin to CHB restored the levels of biotinylated proteins in *ΔFTN_0818* to those of the WT.

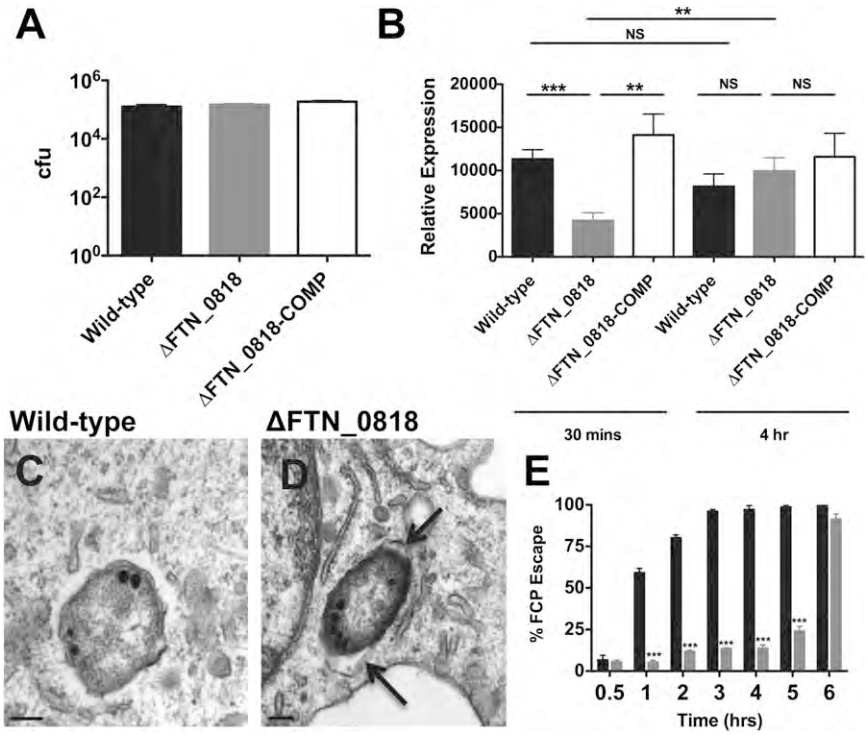

Fig. 1. FTN_0818 is required for rapid phagosomal escape. (*A* and *B*) Macrophages were infected with the indicated strains, and colony-forming units were quantified at 30 min pi (*A*) or qRT-PCR was used to measure the expression of *iglA* and normalized to the expression of *uvrD* at 30 min and 4 h pi (*B*). (*C* and *D*) Transmission electron microscopy of infected macrophages at 3 h pi (arrows, intact FCP). (*E*) Phagosomal escape of WT (black) and *ΔFTN_0818* (gray) was quantified 30 min to 6 h pi. One hundred bacteria per condition were viewed and the percentage of phagosomal escape was determined for three independent experiments. *$P < 0.05$; **$P < 0.001$; ***$P < 0.0001$.

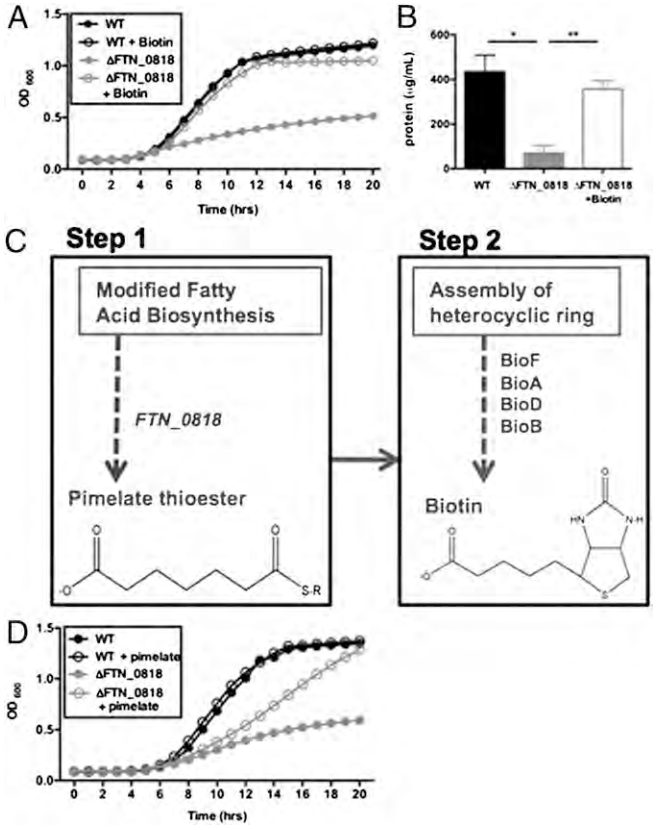

Fig. 2. Biotin complements the Δ*FTN_0818* growth defect in minimal media. (*A*) WT and Δ*FTN_0818* were grown in CHB with or without biotin and the OD_{600} was measured every hour. (*B*) The concentration of biotinylated proteins in whole cell lysates of all strains was quantified after immunoprecipitation with anti-biotin antibodies. $*P < 0.05$; $**P < 0.001$. (*C*) Schematic of the biotin biosynthesis pathway with the proposed placement of FTN_0818 (steps before the generation of pimelate have not been defined in *Francisella*). (*D*) WT and Δ*FTN_0818* were grown in CHB with or without pimelate and the OD_{600} was measured every hour.

Therefore, these data further suggest that the *FTN_0818* mutant has a biotin deficiency.

Biotin biosynthesis in *E. coli* consists of two major steps: the well-characterized latter step involves the synthesis of two fused heterocyclic rings on a valeryl side chain, and the first step is dedicated to the acquisition of a pimelate moiety, which is required to generate the aforementioned valeryl side chain (Fig. 2*C*) (16). To gain an indication of where FTN_0818 is required in the pathway, we tested whether pimelate could complement the growth defect of Δ*FTN_0818* in CHB. Interestingly, when pimelate was added to CHB, it rescued the Δ*FTN_0818* growth defect with a minor delay (Fig. 2*D*). These data suggest that FTN_0818 is required for the production of pimelate and subsequent biotin biosynthesis.

Biotin Alleviates the Requirement of FTN_0818 for Phagosomal Escape and Replication in Macrophages. We next tested whether exogenous biotin could also rescue the intracellular defects of the Δ*FTN_0818* mutant. At 30 min pi, exogenous biotin complemented *iglA* expression in the Δ*FTN_0818* mutant (Fig. 3*A*). We used immunofluorescence microscopy to determine whether FCP escape kinetics correlated with the rescue of *iglA* expression in the presence of biotin. We observed that Δ*FTN_0818* had a phagosomal escape defect (Fig. 3 *B–G* and *K*), similar to our previous results using electron microscopy (Fig. 1 *C–E*). At 30 min pi, biotin-supplemented Δ*FTN_0818* localized to the FCP (Fig. 3*K*). However, at 2 h pi, this strain was within the cytosol (Fig. 3 *H–K*), similar to WT. These data clearly demonstrate that biotin is required for the rapid escape of *Francisella* from the FCP.

Because biotin rescued *iglA* gene expression and subsequent escape of the *FTN_0818* mutant, and escape is required for intracellular replication, we tested whether biotin could also rescue replication. During macrophage infection, the WT strain replicated nearly 30-fold, whereas Δ*FTN_0818* exhibited a severe replication defect (Fig. 3*L*), in agreement with our previous data (Fig. S1). However, when biotin was added to the macrophages at the time of infection, the Δ*FTN_0818* replication defect was significantly complemented (Fig. 3*L*). We further tested whether pretreatment with biotin before infection would rescue the intracellular growth defect of the *FTN_0818* mutant, or whether biotin had to be present during the infection. Δ*FTN_0818* grown in CHB supplemented with biotin overnight, but without exogenous biotin during infection, was unable to replicate in macrophages (Fig. S5). This demonstrates that biotin must be present at the time of infection to facilitate replication. These data show that biotin is required to promote escape when the bacteria are present within the FCP.

FTN_0818 Is Required for FCP Escape in Multiple *Francisella* Species. To determine whether the role of FTN_0818 was conserved in other *Francisella* species, we first generated a deletion mutant lacking the *FTN_0818* ortholog, *FTT_0941* (99% amino acid identity), in the human pathogenic *Francisella tularensis* strain SchuS4. Similar to our findings with *F. novicida*, the *FTT_0941* mutant in *F. tularensis* had a defect in escape from the FCP (Fig. S6). However, when biotin was added to the media, the *FTT_0941* mutant escaped with WT kinetics (Fig. S6). We also generated and tested a mutant in the live vaccine strain (LVS), a derivative of highly pathogenic *F. holarctica*. We found that the *FTN_0818* ortholog, *FTL_1266* (99% amino acid identity), was also required for LVS escape from the phagosome, as well as growth in minimal media, and that these phenotypes were complemented by biotin (Fig. S7 *A–D*). Furthermore, *FTL_1266* was also required for replication in macrophages (Fig. S7*E*), in agreement with the role of *FTN_0818* in *F. novicida*. Together, these data highlight the conserved role of FTN_0818 in multiple *Francisella* species.

FTN_0818 Is Necessary for Pathogenesis in Mice, and This Requirement Is Alleviated by Biotin. We and others identified FTN_0818 as being required for *Francisella* virulence in mice using in vivo screens (10, 11). To validate these findings, we performed competition experiments in which a 1:1 mixture of the WT and Δ*FTN_0818* or the complemented strain was used to infect mice. Forty-eight hours pi, Δ*FTN_0818* levels were 1–2 logs lower in spleens compared with WT (Fig. 4*A*). In contrast, the complemented strain colonized the spleen of mice similarly to WT bacteria (Fig. 4*A*). We also infected mice with the WT or Δ*FTN_0818* strain separately and determined that Δ*FTN_0818* was attenuated 100-fold in the spleen (Fig. 4*B*) and almost 10-fold in the skin (Fig. 4*C*), compared with WT. In agreement, the FTN_0818 ortholog, FTL_1266, was required to reach WT LVS levels in spleens 48 h pi (Fig. S7*F*). Together, these results demonstrate the requirement of FTN_0818 for *Francisella* virulence in vivo.

To determine whether exogenous biotin could rescue the attenuation of the *FTN_0818* mutant during in vivo infection, as we observed during macrophage infection, we added biotin to the inoculum. Δ*FTN_0818* without biotin was attenuated nearly 10-fold compared with WT in the skin at the site of infection, whereas when biotin was added, Δ*FTN_0818* was present at WT levels (Fig. 4*D*). Furthermore, addition of biotin resulted in rescue to levels similar as genetic complementation, as observed with the complemented strain (Fig. 4*D*). These results confirm that FTN_0818 is required for virulence in mice and that biotin can

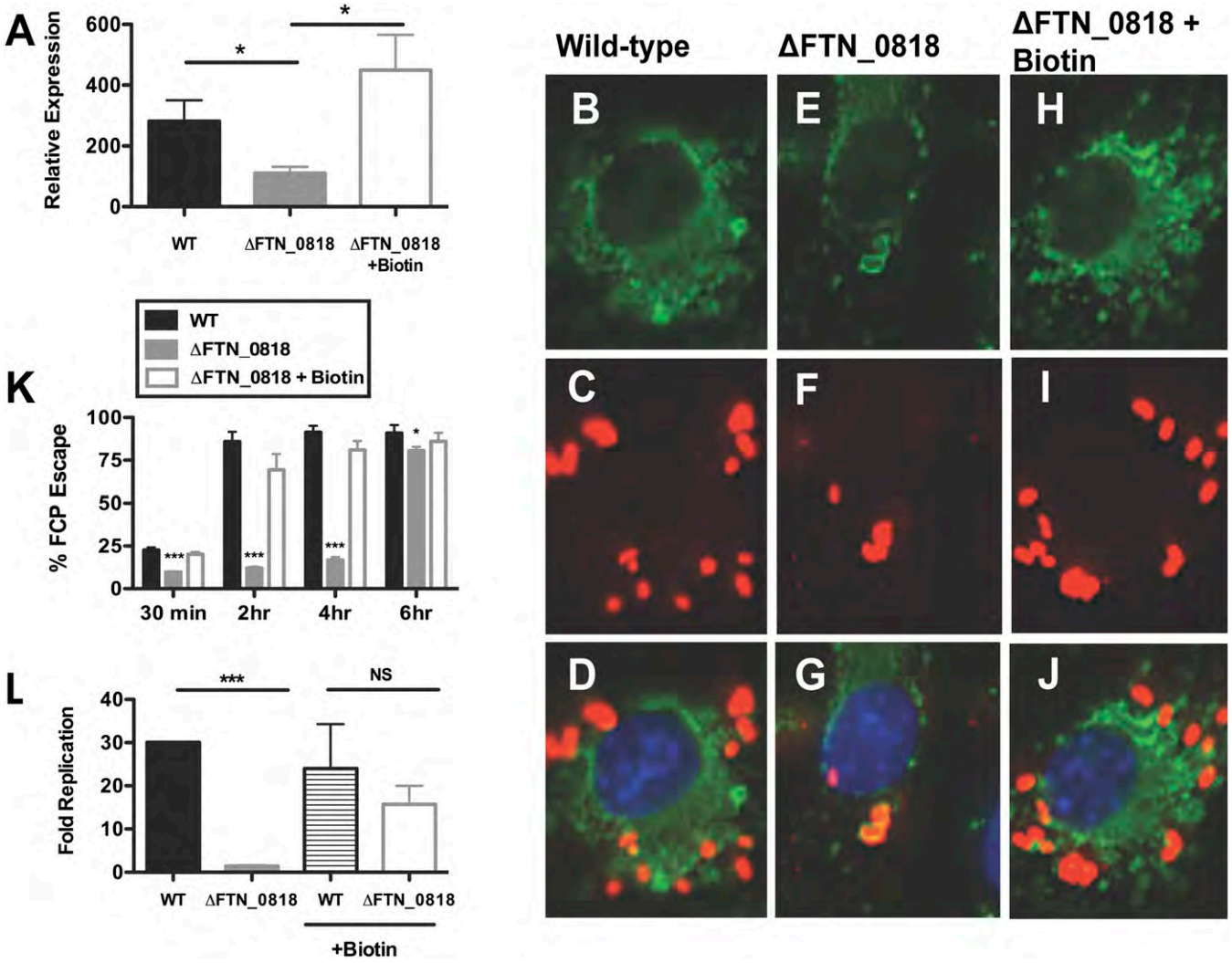

Fig. 3. Biotin rescues rapid phagosomal escape and the *ΔFTN_0818* replication defect in macrophages. (*A–J*) Macrophages were infected, and qRT-PCR was used to measure the expression of *iglA* and normalized to the expression of *uvrD* at 30 min pi (*$P < 0.05$) (*A*) and immunofluorescence microscopy was used to determine escape kinetics of WT (*B–D*), *ΔFTN_0818* (*E–G*), and *ΔFTN_0818* supplemented with biotin (*H–J*) 2 h pi (FITC-stained LAMP-1, green; anti-*Francisella*, red; DAPI, blue). (*K*) Two hundred bacteria were counted per sample, and colocalization with lysosomal-associated membrane protein 1 (LAMP-1) was used as a marker for phagosomal localization. *$P < 0.05$; ***$P < 0.0001$. (*L*) Macrophages were infected with WT or *ΔFTN_0818* strains in media with or without biotin. Colony-forming units were quantified 30 min and 6 h pi, and fold replication was calculated.

alleviate this requirement. Taken together, we have characterized a metabolic protein that links the requirement for biotin in the phagosome with rapid phagosomal escape and virulence in vivo.

Discussion

Evasion of the harsh phagosomal environment is imperative for the survival of intracellular bacterial pathogens. We have characterized a metabolic protein, FTN_0818, revealing a unique link between metabolism and rapid escape from the FCP during *F. novicida* infection of macrophages. Exogenous biotin overrode the requirement of FTN_0818 for rapid phagosomal escape, replication in macrophages, and in vivo pathogenesis. Pretreatment with biotin before infection of macrophages was unable to complement the mutant strain. However, when the mutant was microinjected with biotin into the host cytosol (bypassing the phagosome), or when biotin was added at 6 h (after the mutant escaped the phagosome), the mutant's replication defect was rescued (Fig. S8 *A* and *B*). This suggests that *Francisella* requires biotin in the FCP to promote rapid escape and in the cytosol for intracellular replication. These data contribute to current literature highlighting the link between *Francisella* metabolism and virulence (3). Specifically, it has been shown that utilization of glutathione as a cysteine source is required for intracellular replication (14). Similarly, utilization of uracil has been shown to be required for inhibition of the neutrophil respiratory burst (17). It would be interesting to delineate the full metabolic requirements of *Francisella* within host cells and, specifically, to determine how these control phagosomal escape and other virulence traits.

In support of our current data, biotin biosynthetic genes have been identified as being important for *Francisella* replication in vitro and in vivo (9, 10, 18). In addition, Wehrly et al. previously published a transcriptional profile of *F. tularensis* within the macrophage and identified *bioB*, a gene required for step 2 (Fig. 2*C*) of biotin biosynthesis, as being up-regulated (19). Additionally, Asare and Abu Kwaik published a screen for mutants with defects in phagosomal escape and identified *birA*, a biotin associated gene (18). Taken together, these data provide additional evidence that biotin, and biotin-associated genes, play important roles during intracellular infection by *Francisella*.

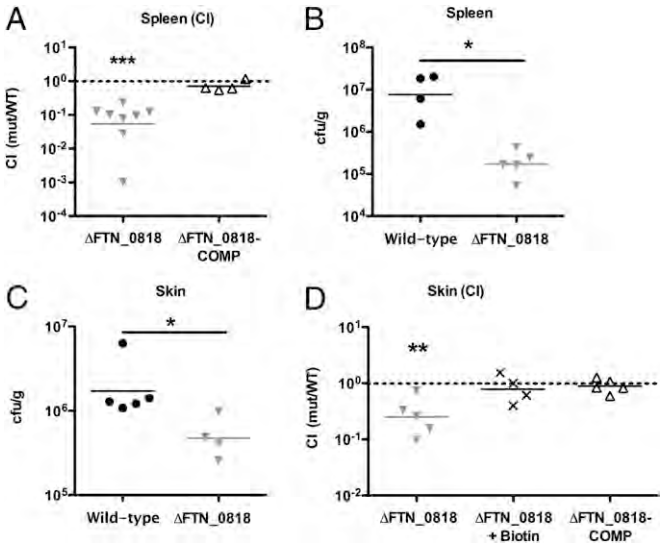

Fig. 4. Biotin rescues the Δ*FTN_0818* virulence defect in vivo. (*A*) Mice were infected s.c. with a 1:1 mixture of WT with the *ΔFTN_0818* or the *ΔFTN_0818* complemented strain (ΔFTN_0818-COMP). At 48 h pi, spleens were harvested to quantify bacterial levels, and the CI was calculated. (*B* and *C*) Mice were s.c. infected with 10^6 cfu of WT or *ΔFTN_0818*. At 48 h pi, the spleen (*B*) and skin at the site of infection (*C*) were harvested and bacterial levels quantified. (*D*) A competition assay was performed with WT and *ΔFTN_0818* in the absence of biotin or WT and the *ΔFTN_0818* complemented strain in the presence of biotin. At 24 h pi, the skin at the site of infection was harvested to quantify bacterial levels, and the CI was calculated. **P* < 0.05; ***P* < 0.001; ****P* < 0.0001.

Bioinformatic analysis revealed that FTN_0818 shares high sequence similarity with the hormone-sensitive lipase (HSL) superfamily of proteins. Mammalian HSL family proteins hydrolyze triacylglycerols for release into the circulation to provide energy for other tissues (20). They are also the rate-limiting enzyme in the mobilization of free fatty acids and are, therefore, critical for lipid metabolism and energy homeostasis (21, 22). Interestingly, most HSL family proteins characterized in *Mycobacterium tuberculosis* are also required for utilization of stored triacylglycerols under starvation conditions (23). Alignment of the amino acid sequence of FTN_0818 with human HSL, rat HSL, and the *M. tuberculosis* HSL family proteins LipN and LipY revealed two regions that contained conserved active site residues (Fig. 5*A*) (22, 23). Additionally, these HSL family proteins have between 21–31% identity and 35–46% similarity with FTN_0818 (Fig. 5*B*). The first region (FTN_0818, amino acids 77–158) contains the characteristic HGGG motif present in most HSL family proteins and the GDSAGGNL motif that includes the catalytic serine residue (Fig. 5*A*) (24). The second region (FTN_0818, amino acids 247–278) includes the conserved aspartate and histidine catalytic residues (Fig. 5*A*) (24). These data show that critical catalytic residues conserved in HSL family proteins are present in FTN_0818 and suggest that this protein may act as an HSL.

Interestingly, we showed that when the putative catalytic serine (S151) in FTN_0818 was mutated to an alanine residue, *Francisella* could no longer grow in minimal media (this phenotype was rescued by exogenous biotin) (Fig. S9*A*). This was not attributable to a decrease in the level of expression of the point mutant compared with WT FTN_0818 (Fig. S9*B*). Furthermore, disruption of this catalytic residue led to retention of *Francisella* within the FCP (which could be rescued by the addition of biotin) (Fig. S9*C*), and inhibition of replication in macrophages and during in vivo infection (Fig. S9 *D* and *E*). These data provide further support for the hypothesis that FTN_0818 is an HSL family protein.

The role of FTN_0818 in biotin metabolism and its homology to HSL family lipases raises the question of how fatty acid metabolism might contribute to biotin biosynthesis. The link between fatty acid metabolism and biotin biosynthesis has long been unclear but recent insights have been made. Recently, Lin et al. demonstrated that pimelate is the product of a modified fatty acid synthesis pathway in *E. coli* (Fig. 2*C*) (16, 25). The fact that (*i*) fatty acid metabolism has been shown to play an important role in generating the pimelate intermediate required for biotin biosynthesis, (*ii*) FTN_0818 has homology to the HSL family of lipases that cleave triacylglycerols, (*iii*) the FTN_0818 catalytic serine point mutant abolishes function of the protein, and (*iv*) pimelate and biotin rescue the growth defect of the *FTN_0818* mutant, together, strongly suggest that FTN_0818 is an HSL family member that acts early in the biotin metabolic pathway to liberate free fatty acids for biotin biosynthesis.

Taken together, the work presented here strongly suggests that biotin availability may be a limiting factor for *Francisella* spp., and likely other bacterial pathogens, during infection. Biotin has been reported as being required for *Mycobacterium tuberculosis* virulence in mice and *Vibrio cholera* colonization of the mouse intestine, both through unknown mechanisms (26–28). In addition, several antimicrobials target the biotin pathway by causing the degradation of biotin or biotin precursors including amiclenomycin, actithiazic acid, and the biotin analog α-dehydrobiotin (29–31), further demonstrating the importance of biotin during infection, as well as the therapeutic utility of limiting biotin availability to pathogens.

Our data show that biotin is required in the phagosome to promote rapid escape, suggesting that biotin is limiting in this compartment. Iron is also limiting in the phagosome and numerous host factors such as transferrin play a critical role in the control of

A

Region 1:

```
hHSL      650 HGGG 653   723 GDSAGGNL 731
rHSL      648 HGGG 651   721 GDSAGGNL 729
LipN      140 HGGG 143   214 GDSAGGNL 222
LipY      238 HGGA 241   207 GDSAGGNL 215
FTN_0818   77 HGGG 80    150 GDSAGGNL 158
              ***            **γ*****
```

Region 2:

```
hHSL      994 DPMLDDSVMLARRLRNLGQPVTLRVVEDLPHGF 1027
rHSL     1003 DPMLDDSVMFARRLKDLGQPVTLKVVEDLPHGF 1036
LipN      160 DPLRDEGESYAKALRAAGTAVDLRYLGSLTHGF 193
LipY      141 DPLAQQAVVLEHTAVVQGAPFSFVLAPWQIHDW 174
FTN_0818  247 DILIDGIYAYEEKLKQQGTYVETYYDDEMFHGF 278
              γ                  *           γ
```

B

Protein	e- value	% Similarity	% Identity
hHSL	3e-11	46	26.5
rHSL	9e-14	45	26.5
LipN	9e-36	46	31
LipY	8e-4	35	21

Fig. 5. FTN_0818 is a putative HSL family protein. (*A*) CLUSTAL multisequence alignment including mammalian HSL proteins (human, GenBank accession no. NP_055348.2; rat, GenBank accession no. NP_036991.1) and the *Mycobacterium tuberculosis* HSL family proteins LipY (GenBank accession no. YP_177924.1) and LipN (GenBank accession no. CAB05441.1), in two regions, including the conserved residues (γ) of the catalytic triad (serine, red; aspartic acid, green; histidine, blue) and HSL family protein amino acid motif HGGG (purple). (*B*) Percentage identity, percentage similarity, and e value of HSL family proteins to FTN_0818.

infection by depleting phagosomal iron. Similarly, the host innate immune system has been shown to target biotin. Chicken embryo fibroblasts and yolk-sac macrophages induce the production of avidin, which binds and sequesters biotin in response to *Escherichia coli* infection, treatment with lipopolysaccharide (LPS), or interleukin-6 (32, 33). These data suggest that sequestration of biotin may be a form of nutritional immunity by the host innate immune system and support the idea that biotin might be a critical and limited commodity during infection. Sequestration of biotin could restrict cytosolic pathogens to the phagosome, blocking their escape and preventing them from reaching their replicative niche in the cytoplasm. Understanding more about how specific bacterial metabolites are generated and how the host attempts to sequester these compounds could provide insight into host-pathogen interactions and may reveal targets for the development of antimicrobials to inhibit bacteria at an early step in pathogenesis and combat infection.

Materials and Methods

WT *F. novicida* strain U112 and *F. holarctica* LVS growth conditions were described previously (9), and *F. tularensis* (SchuS4) growth conditions are described in *SI Materials and Methods*. Details of the construction of mutant/complemented strains and growth curve protocols are in *SI Materials and Methods*. Macrophage preparation and infections described in *SI Materials and Methods*. RNA was collected during macrophage infections as described previously (9). Quantitative (q)RT-PCR (real-time PCR) was performed with the Power SYBR Green RNA-to-C_T 1-Step Kit (Applied Biosystems) and primers (Table S2) using the StepOnePlus Real-time PCR System (Applied Biosystems). Immunoprecipitation and microscopy complete descriptions found in *SI Materials and Methods*. For mouse infections, female C57BL/6 mice (6–8 wk) (Jackson Laboratory) were housed under specific pathogen-free housing at Emory University. Experimental studies were performed in accordance with the Institutional Animal Care and Use Committee guidelines. Competitive index (CI) [(mutant output/WT output)/(mutant input/WT input)] and infections with single strains were carried out as described previously (9). Statistical analysis for CI experiments was as described previously (10). Macrophage experiments were analyzed by using the Student's unpaired *t* test (in escape experiments, average percentage escape per strain for three independent experiments were compared).

ACKNOWLEDGMENTS. We thank Colin Manoil and Beth Ramage for help with the Biolog array; Patrik Rydén (Umeå University) for statistical analysis of the microinjection data; and Hong Yi for help with electron microscopy (Emory Robert P. Apkarian Integrated EM Core). This work was supported by National Institutes of Health Grant U54 AI057157 [from the Southeast Regional Center of Excellence for Emerging Infections and Biodefense (SERCEB)].

1. Skeiky YA, Sadoff JC (2006) Advances in tuberculosis vaccine strategies. *Nat Rev Microbiol* 4(6):469–476.
2. Flannagan RS, Cosío G, Grinstein S (2009) Antimicrobial mechanisms of phagocytes and bacterial evasion strategies. *Nat Rev Microbiol* 7(5):355–366.
3. Meibom KL, Charbit A (2010) Francisella tularensis metabolism and its relation to virulence. *Front Microbiol* 1:140.
4. Golovliov I, Baranov V, Krocova Z, Kovarova H, Sjöstedt A (2003) An attenuated strain of the facultative intracellular bacterium Francisella tularensis can escape the phagosome of monocytic cells. *Infect Immun* 71(10):5940–5950.
5. Chong A, Celli J (2010) The francisella intracellular life cycle: Toward molecular mechanisms of intracellular survival and proliferation. *Front Microbiol* 1:138.
6. de Bruin OM, et al. (2011) The biochemical properties of the Francisella pathogenicity island (FPI)-encoded proteins IglA, IglB, IglC, PdpB and DotU suggest roles in type VI secretion. *Microbiology* 157(Pt 12):3483–3491.
7. Barker JR, et al. (2009) The Francisella tularensis pathogenicity island encodes a secretion system that is required for phagosome escape and virulence. *Mol Microbiol* 74 (6):1459–1470.
8. Meibom KL, Charbit A (2010) The unraveling panoply of Francisella tularensis virulence attributes. *Curr Opin Microbiol* 13(1):11–17.
9. Llewellyn AC, Jones CL, Napier BA, Bina JE, Weiss DS (2011) Macrophage replication screen identifies a novel Francisella hydroperoxide resistance protein involved in virulence. *PLoS ONE* 6(9):e24201.
10. Weiss DS, et al. (2007) In vivo negative selection screen identifies genes required for Francisella virulence. *Proc Natl Acad Sci USA* 104(14):6037–6042.
11. Su J, et al. (2007) Genome-wide identification of Francisella tularensis virulence determinants. *Infect Immun* 75(6):3089–3101.
12. Asare R, Akimana C, Jones S, Abu Kwaik Y (2010) Molecular bases of proliferation of Francisella tularensis in arthropod vectors. *Environ Microbiol* 12(9):2587–2612.
13. Headley VL, Payne SM (1990) Differential protein expression by Shigella flexneri in intracellular and extracellular environments. *Proc Natl Acad Sci USA* 87(11):4179–4183.
14. Alkhuder K, Meibom KL, Dubail I, Dupuis M, Charbit A (2009) Glutathione provides a source of cysteine essential for intracellular multiplication of Francisella tularensis. *PLoS Pathog* 5(1):e1000284.
15. Chamberlain RE (1965) Evaluation of live tularemia vaccine prepared in a chemically defined medium. *Appl Microbiol* 13:232–235.
16. Lin S, Cronan JE (2011) Closing in on complete pathways of biotin biosynthesis. *Mol Biosyst* 7(6):1811–1821.
17. Schulert GS, et al. (2009) Francisella tularensis genes required for inhibition of the neutrophil respiratory burst and intramacrophage growth identified by random transposon mutagenesis of strain LVS. *Infect Immun* 77(4):1324–1336.
18. Asare R, Abu Kwaik Y (2010) Molecular complexity orchestrates modulation of phagosome biogenesis and escape to the cytosol of macrophages by Francisella tularensis. *Environ Microbiol* 12(9):2559–2586.
19. Wehrly TD, et al. (2009) Intracellular biology and virulence determinants of Francisella tularensis revealed by transcriptional profiling inside macrophages. *Cell Microbiol* 11 (7):1128–1150.
20. Yeaman SJ (2004) Hormone-sensitive lipase—new roles for an old enzyme. *Biochem J* 379(Pt 1):11–22.
21. Osterlund T (2001) Structure-function relationships of hormone-sensitive lipase. *Eur J Biochem* 268(7):1899–1907.
22. Shen WJ, Sridhar K, Bernlohr DA, Kraemer FB (1999) Interaction of rat hormone-sensitive lipase with adipocyte lipid-binding protein. *Proc Natl Acad Sci USA* 96(10): 5528–5532.
23. Deb C, et al. (2006) A novel lipase belonging to the hormone-sensitive lipase family induced under starvation to utilize stored triacylglycerol in Mycobacterium tuberculosis. *J Biol Chem* 281(7):3866–3875.
24. Kanaya S, Koyanagi T, Kanaya E (1998) An esterase from Escherichia coli with a sequence similarity to hormone-sensitive lipase. *Biochem J* 332(Pt 1):75–80.
25. Lin S, Hanson RE, Cronan JE (2010) Biotin synthesis begins by hijacking the fatty acid synthetic pathway. *Nat Chem Biol* 6(9):682–688.
26. Sassetti CM, Rubin EJ (2003) Genetic requirements for mycobacterial survival during infection. *Proc Natl Acad Sci USA* 100(22):12989–12994.
27. Salaemae W, Azhar A, Booker GW, Polyak SW (2011) Biotin biosynthesis in Mycobacterium tuberculosis: Physiology, biochemistry and molecular intervention. *Protein Cell* 2(9):691–695.
28. Chiang SL, Mekalanos JJ (1998) Use of signature-tagged transposon mutagenesis to identify Vibrio cholerae genes critical for colonization. *Mol Microbiol* 27(4):797–805.
29. Kitahara T, Hotta K, Yoshida M, Okami Y (1975) Biological studies of amiclenomycin. *J Antibiot (Tokyo)* 28(3):215–221.
30. Eisenberg MA, Hsiung SC (1982) Mode of action of the biotin antimetabolites actithiazic acid and alpha-methyldethiobiotin. *Antimicrob Agents Chemother* 21(1):5–10.
31. Piffeteau A, Dufour MN, Zamboni M, Gaudry M, Marquet A (1980) Mechanism of the antibiotic action of alpha-dehydrobiotin. *Biochemistry* 19(13):3069–3073.
32. Elo HA, Korpela J (1984) The occurrence and production of avidin: A new conception of the high-affinity biotin-binding protein. *Comp Biochem Physiol B* 78(1):15–20.
33. Zerega B, et al. (2001) Avidin expression during chick chondrocyte and myoblast development in vitro and in vivo: Regulation of cell proliferation. *J Cell Sci* 114(Pt 8): 1473–1482.

Molecular Microbiology (2012) 86(3), 611–627 ■
doi:10.1111/mmi.12004
First published online 11 September 2012

NaxD is a deacetylase required for lipid A modification and *Francisella* pathogenesis

Anna C. Llewellyn,[1,2] Jinshi Zhao,[3] Feng Song,[3] Jyothi Parvathareddy,[4] Qian Xu,[5] Brooke A. Napier,[1,2] Hamed Laroui,[6] Didier Merlin,[6,7] James E. Bina,[8] Peggy A. Cotter,[5] Mark A. Miller,[4] Christian R. H. Raetz[3] and David S. Weiss[2,9]*

[1]*Department of Microbiology and Immunology, Microbiology and Molecular Genetics Program, Emory University, Atlanta, GA, USA.*
[2]*Emory Vaccine Center, Emory University, Atlanta, GA, USA.*
[3]*Department of Biochemistry, Duke University Medical Center, Durham, NC, USA.*
[4]*Department of Microbiology, Immunology, and Biochemistry, The University of Tennessee Health Science Center, Memphis, TN, USA.*
[5]*Department of Microbiology and Immunology, School of Medicine, University of North Carolina at Chapel Hill, Chapel Hill, NC, USA.*
[6]*Department of Biology, Center for Diagnostics and Therapeutics, Georgia State University, Atlanta, GA, USA.*
[7]*Veterans Affairs Medical Center, Decatur, GA, USA.*
[8]*Department of Microbiology and Molecular Genetics, University of Pittsburgh School of Medicine, Pittsburgh, PA, USA.*
[9]*Division of Infectious Diseases, Department of Medicine, Emory University, Atlanta, GA, USA.*

Summary

Modification of specific Gram-negative bacterial cell envelope components, such as capsule, O-antigen and lipid A, are often essential for the successful establishment of infection. *Francisella* species express lipid A molecules with unique characteristics involved in circumventing host defences, which significantly contribute to their virulence. In this study, we show that NaxD, a member of the highly conserved YdjC superfamily, is a deacetylase required for an important modification of the outer membrane component lipid A in *Francisella*. Mass spectrometry analysis revealed that NaxD is essential for the modification of a lipid A phosphate with galactosamine in *Francisella novicida*, a model organism for the study of highly virulent *Francisella tularensis*. Significantly, enzymatic assays confirmed that this protein is necessary for deacetylation of its substrate. In addition, NaxD was involved in resistance to the antimicrobial peptide polymyxin B and critical for replication in macrophages and *in vivo* virulence. Importantly, this protein is also required for lipid A modification in *F. tularensis* as well as *Bordetella bronchiseptica*. Since NaxD homologues are conserved among many Gram-negative pathogens, this work has broad implications for our understanding of host subversion mechanisms of other virulent bacteria.

Accepted 17 August, 2012. *For correspondence. E-mail david.weiss@emory.edu; Tel. (+1) 404 727 8214; Fax (+1) 404 727 8199.

Introduction

Mammalian host defences include multiple pathways for recognition of, and action against, Gram-negative bacterial cell wall components including capsule, O-antigen and lipid A. Accordingly, many such pathogens have evolved modifications of these structural elements in order to evade host responses. The lipid A molecules of *Francisella* species have multiple unique modifications, although the details of the pathways involved in generating these alterations are still being elucidated.

Francisella tularensis is a Gram-negative intracellular pathogen and the causative agent of tularaemia. Due to its extreme infectivity, high morbidity and mortality rates, history of weaponization, and ease of aerosolization and dissemination, it is considered a category A select agent (potential bioweapon) by the Centers for Disease Control and Prevention (CDC) (Darling *et al*., 2002). *Francisella novicida* is a less virulent species that rarely causes disease in humans but is frequently used as a laboratory model as it causes a tularaemia-like disease in mice, is easily genetically manipulated, and is known to use many of the same virulence determinants as *F. tularensis* (Titball and Petrosino, 2007). These include the *Francisella* pathogenicity island (FPI), which is thought to encode a putative type VI secretion system, oxidative stress resistance proteins, siderophores, and outer membrane lipid A modifications that enable the bacteria to evade recognition and

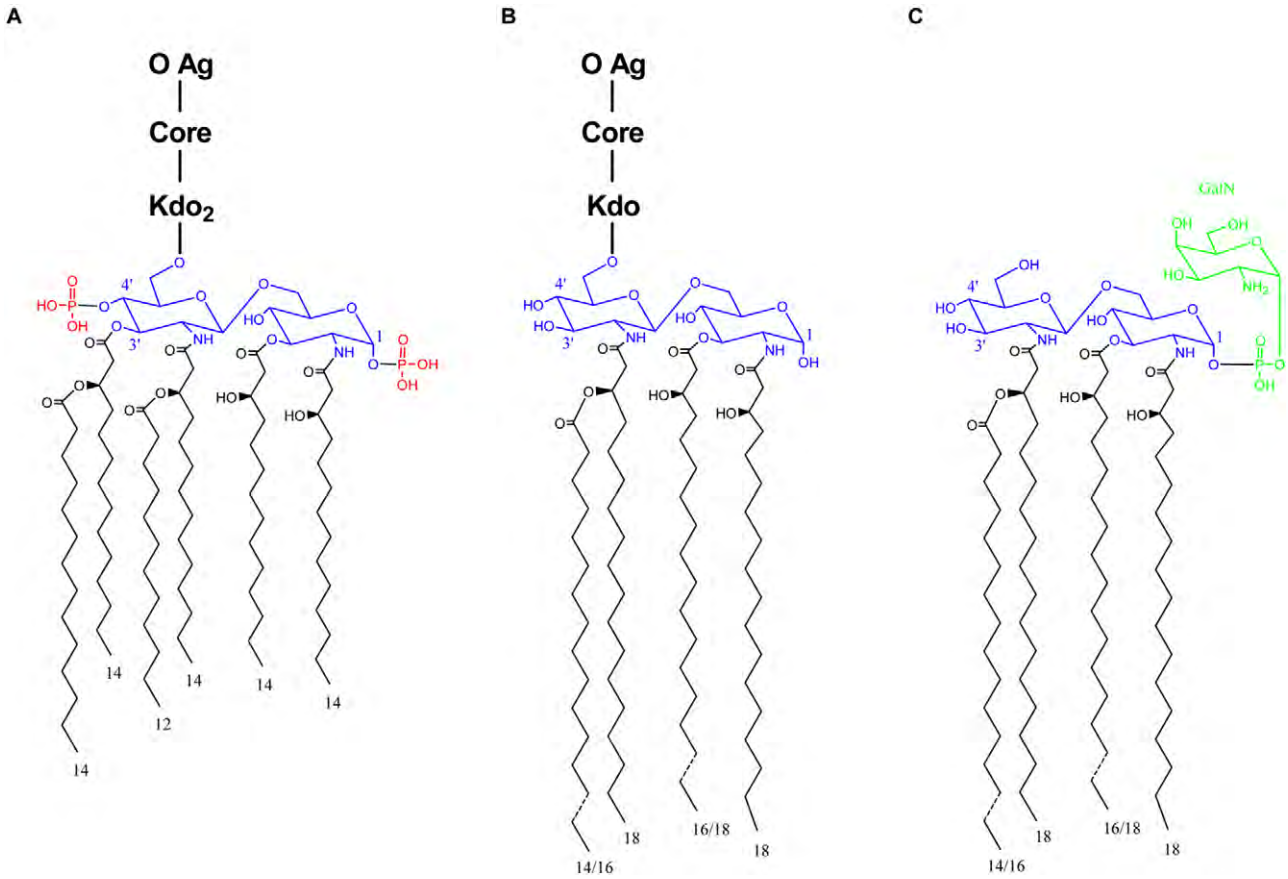

Fig. 1. *E. coli* and *Francisella* LPS and lipid A structures. Structures of (A) *E. coli* LPS, (B) complete LPS from *Francisella* species and (C) 'free' lipid A of *Francisella* species are compared. (A, B) O-antigen (O Ag), core sugars (Core) and the specific core sugar Kdo (Kdo) are indicated. For all structures, lipid A backbone disaccharides are highlighted in blue and acyl chains are represented in black with numbers denoting length. *E. coli* lipid A 4′ and 1 position phosphate groups (missing from the lipid A of complete *Francisella* LPS) are highlighted in red. Unlike the lipid A component of complete *Francisella* LPS, *Francisella* free lipid A includes a phosphate modified with galactosamine at the 1 position (highlighted in green).

damage by host phagocytes (Bakshi *et al*., 2006; Gunn and Ernst, 2007; Nano and Schmerk, 2007; Ramakrishnan *et al*., 2008; Honn *et al*., 2012).

Francisella LPS has a unique lipid A moiety that is distinct from canonical lipid A structures of other Gram-negative pathogens. For example, compared with the hexa-acylated lipid A expressed by *Escherichia coli*, *Francisella* lipid A features only four acyl chains that are longer than those of *E. coli* by as many as six carbons (Raetz and Whitfield, 2002; Trent, 2004; Raetz *et al*., 2009) (Fig. 1A and B). In addition, *Francisella* LPS lacks both the 4′ and 1 position distal phosphates (Raetz *et al*., 2009). Also unique to *Francisella* species, 70% of the total lipid A in the outer membrane exists in a 'free' form that lacks the traditional Kdo, core and O-antigen polysaccharides of complete LPS (Wang *et al*., 2006; Zhao and Raetz, 2010) (Fig. 1C). Unlike the lipid A of complete LPS, free lipid A retains the 1 position phosphate that is further modified with a galactosamine residue.

As highly successful intracellular pathogens, *Francisella* species are able to utilize multiple phagocytic and non-phagocytic cell types for replication (Fujita *et al*., 1993; Qin and Mann, 2006; Hall *et al*., 2007; 2008; Schulert *et al*., 2009). Entry into host macrophages often occurs by a novel process involving the formation of unusually large and asymmetrical pseudopod loops (Clemens and Horwitz, 2007). One to 3 h after uptake by phagocytes, *Francisella* species escape the phagosome before replicating within the host cytosol. However, many of the details of *Francisella*'s intracellular life cycle are still unknown (Clemens and Horwitz, 2007).

Although much progress has been made in understanding *Francisella* virulence mechanisms, there are still many questions regarding how this pathogen is able to so effectively replicate within host cells and cause disease. To begin to answer these questions, we performed a genome-wide *in vivo* negative selection screen to identify genes required for pathogenesis (Weiss *et al*., 2007).

A

NaxD and select YdjC Superfamily members

	Length	% Identity	% Similarity
F. novicida	**268**	-	-
F. tularensis	**268**	**98.5**	**98.9**
T. thermophilus	264	11.8	23.9
B. bronchiseptica	**367**	**18.3**	**30.5**
L. pneumophila	270	33.0	49.1
B. abortus	262	21.7	36.5
C. burnetii	273	34.4	47.9

B

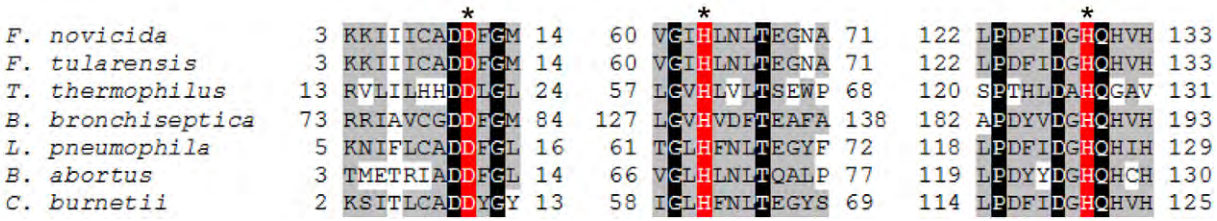

Fig. 2. NaxD is a member of the YdjC superfamily. The amino acid sequences of *F. novicida* and *F. tularensis* NaxD (FTN_0544 and FTT_0453 respectively) were aligned with YdjC superfamily proteins from *Thermus thermophilus* (TTHB029), *Bordetella bronchiseptica* (BB4267), *Legionella pneumophila* (lp12_2472), *Brucella abortus* (BAbS19_II01260) and *Coxiella burnetii* (CBU_0580) using CLUSTALO (http://www.ebi.ac.uk/Tools/msa/clustalo/).

A. The per cent amino acid identity and similarity to *F. novicida* NaxD are shown. Proteins in bold and highlighted in red are described in this manuscript.

B. Amino acids surrounding putative active-site residues are shown and numbers indicate their position in the sequence. Highlighting indicates conserved putative active-site residues (red, asterisk), identical (black) and similar (grey) residues.

Next, we conducted an intracellular replication screen to determine which of those genes were important specifically for replication in macrophages (Llewellyn *et al*., 2011). *FTN_0544* was identified in both of these screens. Although annotated as a hypothetical protein of unknown function in the NCBI database, FTN_0544 belongs to the YdjC superfamily of proteins. Interestingly, proteins belonging to this family are encoded by multiple Gram-negative pathogens including *Bordetella bronchiseptica*, *Brucella abortus*, *Coxiella burnetii* and *Legionella pneumophila*.

In this study, we show that FTN_0544 is a deacetylase involved in the galactosamine modification of *Francisella*'s unique free lipid A molecules. We have thus renamed this protein NaxD (*N*-acetylhexosamine deacetylase). Furthermore, we show that the action of NaxD is required for resistance to the cationic antimicrobial peptide polymyxin B, intracellular replication and virulence *in vivo*. Importantly, we have shown that the role of this protein is conserved in human pathogenic *F. tularensis*, as well as *B. bronchiseptica*. Since NaxD is highly conserved in numerous Gram-negative pathogens, this work has broad implications for the elucidation of mechanisms of pathogenesis in other virulent bacteria.

Results

NaxD is a member of the YdjC superfamily of proteins

Although *naxD* is annotated as encoding a hypothetical protein in the NCBI database, protein sequence analysis revealed that NaxD belongs to the YdjC superfamily. This family is highly conserved, with over 3000 entries in the NCBI database. Homologues of NaxD are encoded by numerous pathogens including *B. bronchiseptica*, *B. abortus*, *L. pneumophila* and *C. burnetii* (Fig. 2A). While a member of this family from *Bacillus stearothermophilus* had been putatively identified as a part of a cryptic cellobiose metabolism operon (Lai and Ingram, 1993), another member from *Thermus thermophilus*, TTHB029, has been shown to have structural similarity to a deacetylase from *Streptococcus pneumoniae* (Imagawa

et al., 2008). Structural analysis revealed a putative active site containing three potential catalytic residues (Imagawa *et al*., 2008). Importantly, these residues are conserved among YdjC superfamily proteins (Fig. 2B), suggesting that NaxD and other YdjC proteins may function as deacetylases.

NaxD is required for F. novicida *replication in macrophages and virulence* in vivo

We originally identified *naxD* as being required for virulence in an *in vivo* genome-wide negative selection screen (Weiss *et al*., 2007). In addition, we showed that this gene was required for intracellular proliferation in a macrophage replication screen (Llewellyn *et al*., 2011). Since both of these screens utilized transposon mutants, we wanted to ensure that the observed phenotypes resulted from disruption of *naxD* and not unintended secondary mutations. To do this, we generated an *F. novicida naxD* deletion mutant and a complemented strain. The *naxD* mutant exhibited wild-type growth kinetics in both rich and minimal media (Fig. S1). Macrophage replication experiments revealed that the *naxD* mutant was unable to replicate in either RAW264.7 macrophages or primary murine bone marrow-derived macrophages (BMM) (Fig. 3A and B). In fact, the level of attenuation of the *naxD* mutant was similar to that of a previously characterized strain lacking a functional copy of the gene encoding the virulence factor MglA, which is known to persist but not replicate in macrophages (Baron and Nano, 1998). In addition, the *naxD* complemented strain replicated to levels similar to wild-type. Given that *Francisella* must escape the phagosome in order to replicate, we used fluorescence microscopy to measure escape kinetics via colocalization of intracellular bacteria with the phagosomal marker LAMP-1 (Fig. S2). These experiments demonstrated that wild-type and *naxD* mutant *F. novicida* escaped the phagosomes of BMM with similar kinetics, indicating that the mutant's attenuation in macrophages is not due to a deficiency in phagosomal escape (Fig. S2). Overall, these results show that NaxD is required for intracellular proliferation but not for phagosomal escape.

While our *in vivo* negative selection screen identified *naxD* as being important for virulence, it did not provide quantitative data regarding the degree of attenuation of a *naxD* mutant. To determine this, we performed competition experiments. Briefly, mice were infected with a 1:1 ratio of wild-type *F. novicida* and either the *naxD* deletion mutant or complemented strain. Forty-eight hours post infection, the *naxD* mutant displayed an approximate 2.5 log attenuation in the skin and a nearly 5 log attenuation in both the liver and spleen compared with wild-type (Fig. 3C). All mutant phenotypes were restored to wild-type levels in the complemented strain (Fig. 3C). To determine the consequence of the *naxD* mutant's virulence defect, we infected mice with either the wild-type or mutant strain and monitored survival. While mice infected with wild-type bacteria were moribund by 4 days after infection, the mutant did not kill mice up to 28 days post infection (Fig. 3D). Taken together, these data show that *naxD* is required for both replication in host macrophages and virulence *in vivo*.

NaxD is involved in altering surface charge and resistance to polymyxin B

After validating the importance of NaxD in *F. novicida* infection of macrophages and mice, our next aim was to determine the role of this protein in pathogenesis. To further characterize the phenotypes of the *naxD* mutant, we subjected both wild-type and the deletion mutant to different antimicrobials and compared the survival of each strain. While the wild-type was unaffected at the concentrations tested, the mutant displayed dose-dependent sensitivity to the cationic antimicrobial peptide polymyxin B (Fig. 4A), which acts on Gram-negative bacteria by binding to the negatively charged lipid A component of LPS (Morrison and Jacobs, 1976). Conversely, the mutant showed increased resistance to the anionic detergent SDS (Fig. 4B) and displayed wild-type levels of sensitivity to the non-ionic detergent Triton X-100 (Fig. 4C). The altered response of the mutant to charged antimicrobials that act on the cell membrane suggested that NaxD might be involved in altering the net charge of the bacterial surface. To test this hypothesis, we measured the zeta electrokinetic potential of each strain, which gives an indirect reading of the bacterial surface charge. We determined that the mutant exhibited approximately a twofold decrease in zeta potential compared with wild-type bacteria (Fig. 4D), indicating that NaxD is involved in increasing the charge of the bacterial surface. Taken together, the *naxD* mutant's decreased surface charge and increased sensitivity to cationic polymyxin B, which targets negatively charged lipid A, suggested that NaxD could be required for a modification to lipid A that alters its charge.

NaxD is required for lipid A modification with galactosamine

In order to determine if NaxD is involved in lipid A modification, we analysed the lipid fractions of the wild-type and mutant strains using liquid chromatography electrospray ionization mass spectrometry (LC-ESI/MS). As mentioned previously, the majority of *Francisella* lipid A exists as free lipid A (Vinogradov *et al*., 2002; Wang *et al*., 2006). ESI/MS analysis via direct infusion of wild-type *F. novicida* free lipid A revealed an anticipated peak at *m*/*z*

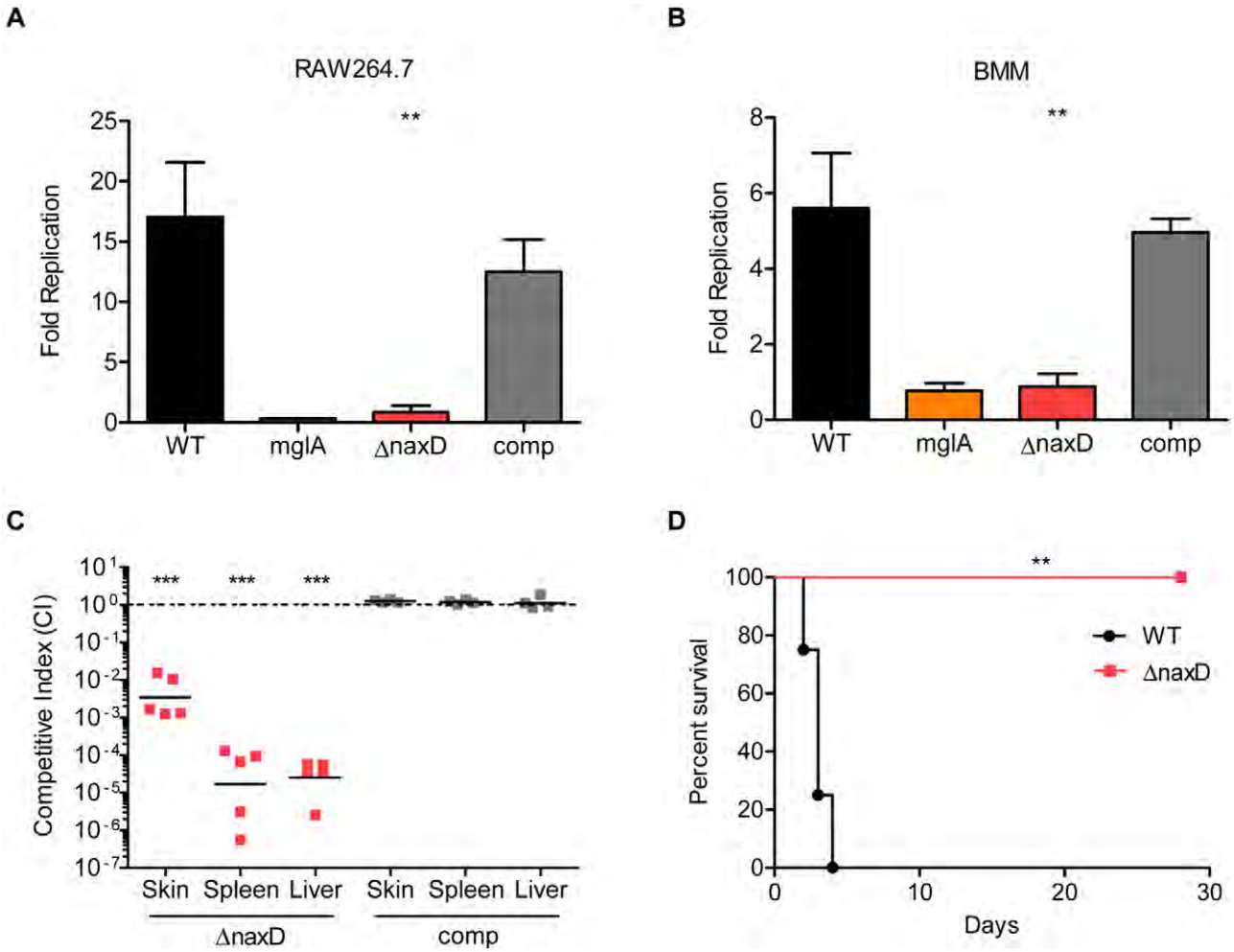

Fig. 3. NaxD is required for replication in murine macrophages and mice.
A and B. (A) RAW264.7 or (B) primary murine bone marrow-derived macrophages (BMM) were infected with a 20:1 moi of wild-type *F. novicida* (WT), the *mglA* mutant (mglA), the *naxD* deletion strain (ΔnaxD) or the complemented strain (comp). Colony-forming units from lysates 30 min post infection were compared with those from (A) 24 or (B) 6 h post infection to determine fold intracellular replication ($n = 3$ biological replicates).
C. Mice were subcutaneously infected with a 1:1 mixture of 10^5 cfu each of wild-type and ΔnaxD (red) or wild-type and the complemented strain (grey). Forty-eight hours after infection, organs were harvested, cfu enumerated and the competitive index (CI) calculated for the skin at the site of infection, spleen and liver. CI = (cfu mutant output/cfu WT output)/(cfu mutant input/cfu WT input). Bars represent the geometric mean CI values from each group of mice ($n = 5$ mice). CI values below 1 (dashed line) indicate attenuation of the mutant strain.
D. Mice were subcutaneously infected with 2×10^7 cfu of either wild-type or ΔnaxD and sacrificed if they appeared moribund ($n = 4$ mice).
In (A) and (B), bars represent the average and error bars represent the standard deviation of three biological replicates from one experiment. Data shown in all panels are representative of at least three independent experiments. Asterisks indicate significance as compared with wild-type (A, B, D) or compared with 1 (C). $^{**}P < 0.005$, $^{***}P < 0.0005$.

1665.22 (Fig. 5A) (Phillips *et al*., 2004; Wang *et al*., 2006), while the *naxD* mutant lipid A exhibited a peak at *m/z* 1504.15 (Fig. 5B). Interestingly, this shift corresponds to the molecular weight of galactosamine, and wild-type *Francisella* free lipid A is modified with a galactosamine at the 1 position phosphate (Phillips *et al*., 2004; Wang *et al*., 2006; 2009; Schilling *et al*., 2007; Shaffer *et al*., 2007; Kanistanon *et al*., 2008; Kalhorn *et al*., 2009; Song *et al*., 2009; Soni *et al*., 2010; Beasley *et al*., 2012). The absence of the galactosamine moiety on the free lipid A of the mutant would result in an exposed, negatively charged phosphate group, which correlates with the decreased surface charge of the mutant strain (Fig. 4D) (Phillips *et al*., 2004; Wang *et al*., 2006).

To determine why the *naxD* deletion mutant lacks galactosamine and where NaxD might act in the lipid A biosynthetic pathway, we measured the presence and quantities of precursor molecules required for the galactosamine modification. Galactosamine is added to *Francisella* free lipid A from undecaprenyl phosphate-galactosamine (undecaprenyl phosphate-GalN) (Song *et al*., 2009), a complex of the sugar with a lipid carrier

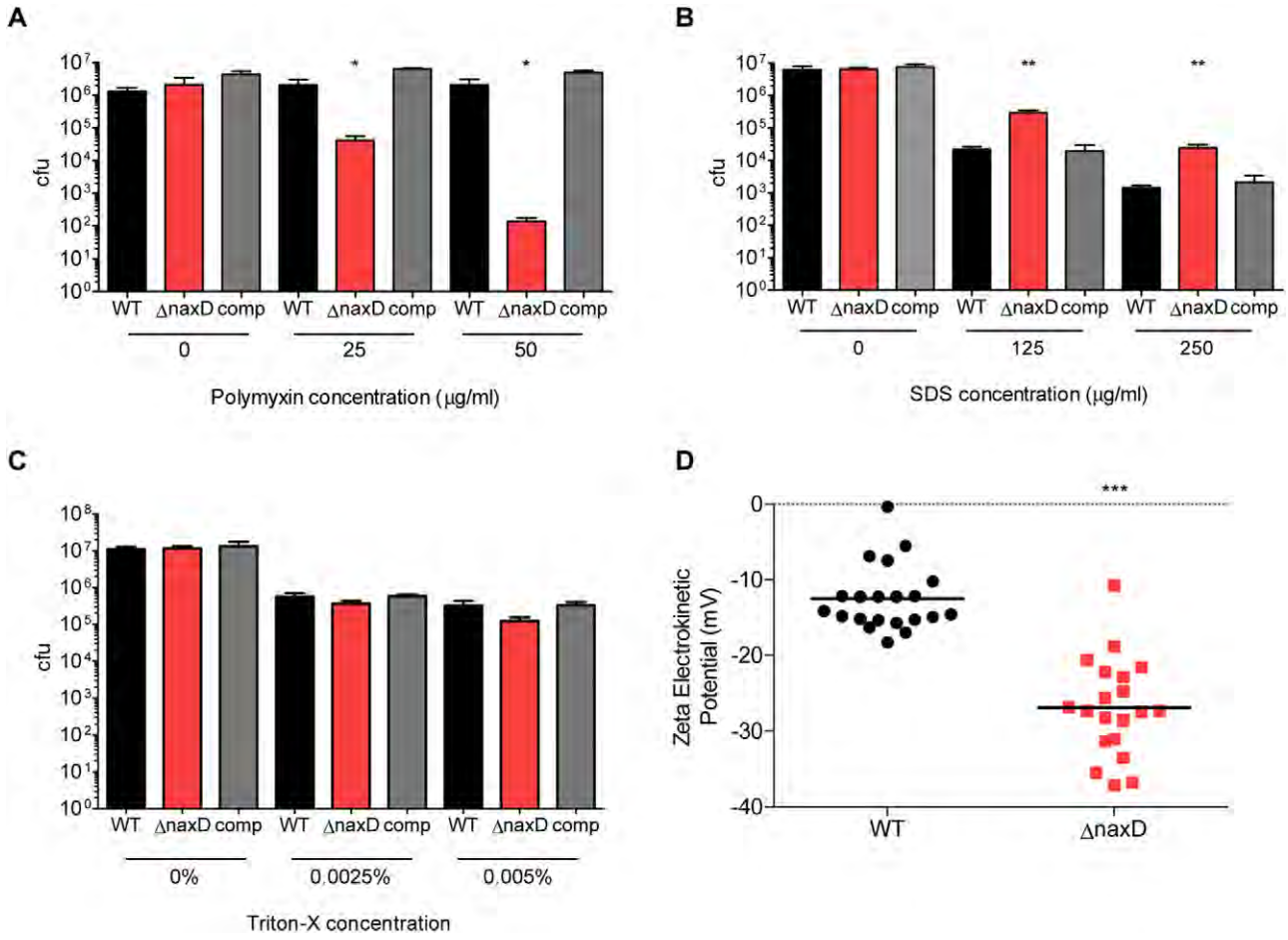

Fig. 4. NaxD is involved in resistance to cationic antimicrobials and alteration of bacterial surface charge.
A–C. Wild-type *F. novicida* (WT), the *naxD* deletion mutant (ΔnaxD) or the complemented strain (comp) were incubated with the indicated concentrations of (A) polymyxin B, (B) SDS or (C) Triton X-100 for 6 h. Cultures were then serially diluted and plated for cfu ($n = 3$ biological replicates).
D. The zeta potential of wild-type and ΔnaxD was measured ($n = 10$ technical replicates) and the results of three independent experiments were combined for statistical analysis.
In (A)–(C), bars represent the average and error bars represent the standard deviation of three biological replicates from one experiment. Data shown are representative of at least three independent experiments. Asterisks indicate significance as compared with wild-type. *$P < 0.05$, **$P < 0.005$, ***$P < 0.0005$.

molecule. Analysis of the wild-type lipid fraction revealed a singly charged peak corresponding to undecaprenyl phosphate-GalN at *m/z* 1006.76 (Fig. 5C). However, this glycolipid was not present in the mutant strain (Fig. 5D). Instead, the mutant exhibited a peak at *m/z* 1048.79, corresponding to undecaprenyl phosphate-*N*-acetylgalactosamine (undecaprenyl phosphate-GalNAc), the acetylated precursor of undecaprenyl phosphate-GalN (Fig. 5D and E). Conversely, this acetylated precursor was not detected in the wild-type lipid fraction (Fig. 5C). Taken together, these data show that NaxD is required for deacetylation of undecaprenyl phosphate-GalNAc and that the absence of this deacetylation event prevents the galactosamine modification to *F. novicida* free lipid A.

NaxD is necessary for deacetylation of undecaprenyl phosphate-GalNAc

After MS analysis revealed NaxD was involved in deacetylation of undecaprenyl phosphate-GalNAc, we set out to determine whether NaxD was directly responsible for this reaction. First, using a strain in which NaxD was labelled with an 8× histidine tag, we found that NaxD localizes to the *F. novicida* membrane fraction (Fig. S4). To determine if NaxD could deacetylate undecaprenyl phosphate-GalNAc in the membrane, we harvested crude membrane fractions from either wild-type or mutant strains and incubated them with synthetic undecaprenyl phosphate-GalNAc. The lipids were extracted from each reaction and analysed using LC-ESI/MS. For both

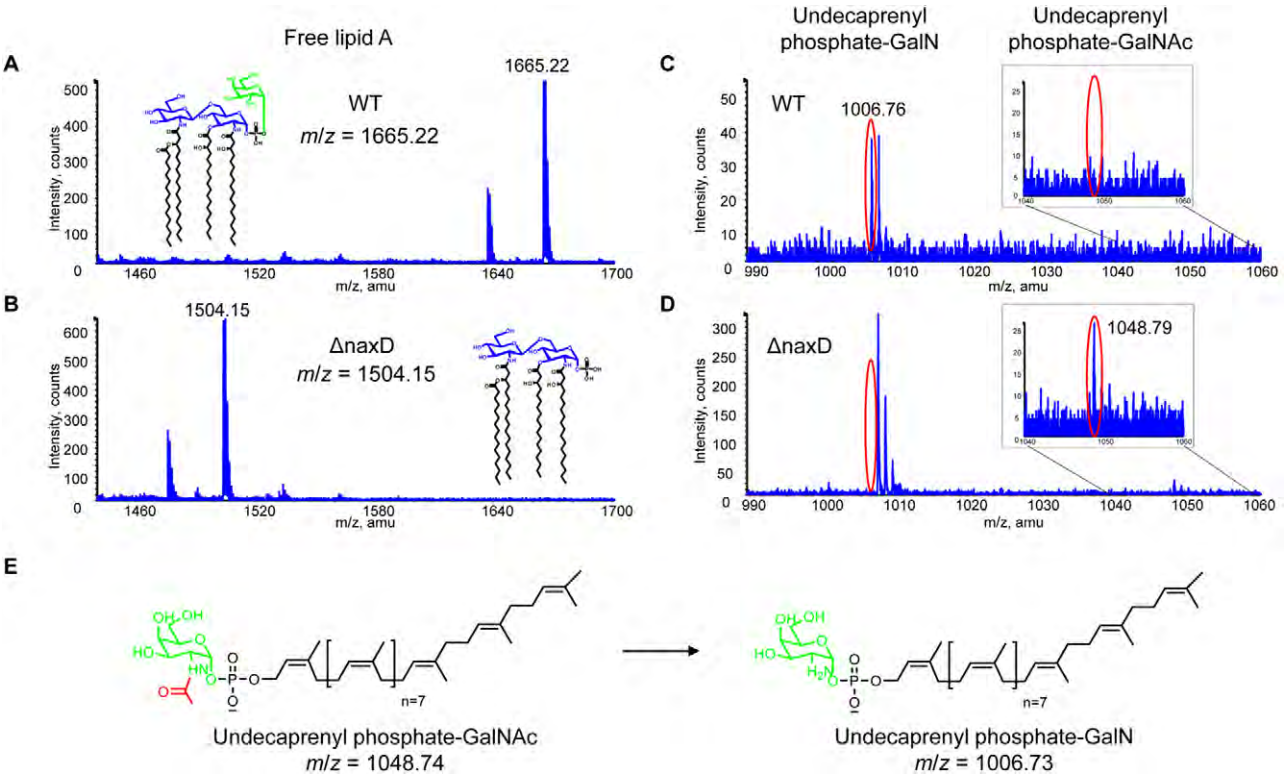

Fig. 5. NaxD is required for the galactosamine modification of *F. novicida* free lipid A.
A–D. Total lipids were extracted from (A, C) wild-type *F. novicida* (WT) and (B, D) *naxD* mutant (ΔnaxD) strains in mid-log phase and (A, B) free lipid A, (C, D) undecaprenyl phosphate-*N*-acetylgalactosamine (GalNAc), and undecaprenyl phosphate-galactosamine (GalN) were analysed by ESI/MS in negative ion mode via direct infusion.
E. A schematic for the deacetylation of undecaprenyl phosphate-GalNAc (expected *m/z* = 1048.74) to undecaprenyl phosphate-GalN (expected *m/z* = 1006.73) is shown.
(A, E) Galactosamine is highlighted in green and (E) the acetyl group is highlighted in red.

wild-type and mutant, the substrate peak (undecaprenyl phosphate-GalNAc, expected *m/z* 1048.74) was present at time zero (Fig. 6). After a 5 h incubation, deacetylation of undecaprenyl phosphate-GalNAc was observed in the wild-type reaction, since a peak consistent with undecaprenyl phosphate-GalN was detected (Fig. 6A). In contrast, no product peak was observed in the mutant reaction (Fig. 6B). These results showed that NaxD in the membrane fraction was necessary for undecaprenyl phosphate-GalNAc deacetylation.

To determine if NaxD was responsible for this enzymatic activity, we overexpressed *naxD* in *E. coli*, which does not encode a NaxD homologue, does not synthesize undecaprenyl phosphate-GalNAc or undecaprenyl phosphate-GalN, and does not modify its lipid A with galactosamine. We demonstrated that NaxD localized to the *E. coli* membrane fraction (Fig. S5), isolated membranes from strains that were transformed with either an empty vector control or the *naxD* expression plasmid, and assayed for enzymatic activity as described for *F. novicida* above. LC-ESI/MS analysis revealed that there was no deacetylated product (expected *m/z* 1006.73) detected for the reactions using a whole-cell lysate from the *E. coli* empty vector control strain (Fig. 7A) or with the soluble fraction from *E. coli* expressing *naxD* (Fig. 7B). However, the deacetylated product, undecaprenyl phosphate-GalN, was detected in assays that contained the membrane fraction from *E. coli* expressing NaxD (Fig. 7C). Together, these results using membrane fractions from *F. novicida* and *E. coli* respectively demonstrate that NaxD is necessary and suggest that it is sufficient for deacetylation of undecaprenyl phosphate-GalNAc.

The NaxD orthologue in F. tularensis *is required for lipid A modification and virulence*

The NaxD orthologue from human pathogenic *F. tularensis*, FTT_0453, retains 99% amino acid identity with *F. novicida* NaxD (Fig. 2A). In order to ascertain if NaxD function is conserved in *F. tularensis*, we generated a *FTT_0453* (*naxD*) deletion mutant in strain SchuS4. LC-ESI/MS analysis of wild-type *F. tularensis* free lipid A

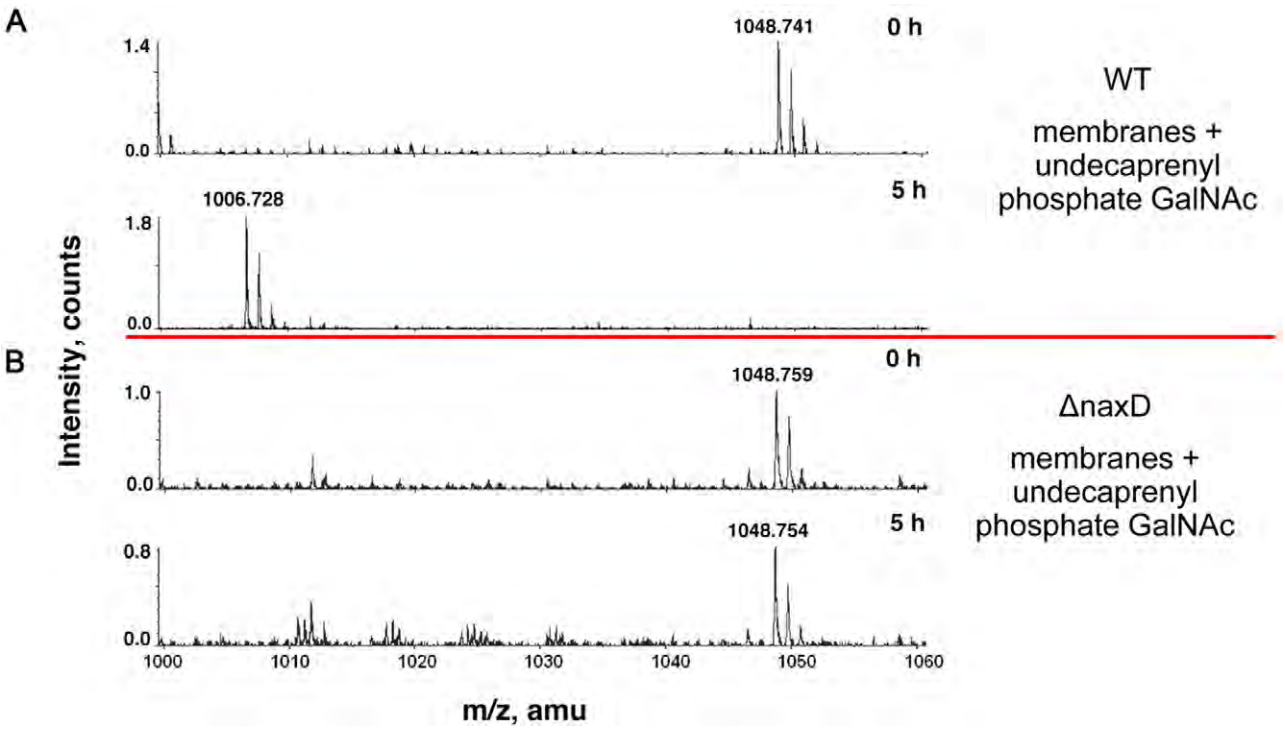

Fig. 6. NaxD is necessary for deacetylation of undecaprenyl phosphate-*N*-acetylgalactosamine. Deacetylase activity assays using synthesized undecaprenyl phosphate-*N*-acetylgalactosamine (GalNAc) and (A) 0.5 mg ml^{-1} *F. novicida* wild-type (WT) membrane fraction or (B) *F. novicida naxD* mutant (ΔnaxD) membrane fraction were incubated at 30°C for the indicated times and then analysed using LC-ESI/MS in negative ion mode.

revealed the *m/z* 1665.21 peak that corresponds to *Francisella* lipid A modified with galactosamine (Fig. 8A), although this species was not detected in the mutant. Instead, the *naxD* mutant displayed a peak at *m/z* 1504.13 that corresponds to lipid A without galactosamine (Fig. 8B). This demonstrates the conserved role of NaxD in lipid A modification in highly virulent *F. tularensis*.

Next we tested the functional role of *F. tularensis* NaxD in polymyxin B resistance, intracellular replication and *in vivo* survival. The *naxD* deletion mutant displayed an increased susceptibility to polymyxin B as compared with wild-type (Fig. 8C). Given that *F. tularensis* is a virulent human pathogen, we wanted to determine the importance of NaxD function during infection of human cells. Indeed, we observed a severe defect in replication of the *naxD* deletion mutant compared with wild-type *F. tularensis* 24 h after infection of human THP-1 macrophage-like cells (Fig. 8D). In addition, similar to the *F. novicida naxD* mutant (Fig. 3B), the *F. tularensis naxD* deletion mutant was unable to proliferate in primary murine BMM (Fig. S3). Importantly, NaxD was also required for replication in mice, since 48 h after subcutaneous infection, wild-type *F. tularensis* was recovered at a level 2.5 logs higher in the spleen of mice (Fig. 8E) and nearly 1.5 logs higher in the liver than the mutant strain (Fig. 8F). These data show that NaxD function is conserved in human pathogenic *F. tularensis*, in which it is required for the addition of galactosamine to free lipid A and is required for resistance to the cationic antimicrobial peptide polymyxin B, replication within human cells and virulence in mice.

Conserved role of the NaxD homologue in Bordetella bronchiseptica

Given that the YdjC superfamily of proteins is conserved among many virulent bacteria, we wanted to determine if a NaxD homologue from a different pathogen shared a similar function in lipid A modification. To test this, we generated a *B. bronchiseptica* deletion mutant lacking the gene encoding the NaxD homologue BB4267 (Fig. 2). *B. bronchiseptica* is a Gram-negative bacterium that colonizes mammalian respiratory tracts and is considered a primary pathogen of domestic animals such as dogs, cats, rabbits and pigs, but can also establish chronic infections in immunocompromised humans (Egberink *et al*., 2009). Lipid A from this pathogen has two phosphate groups that are known to be modified with glucosamine, a stereoisomer of galactosamine (Tirsoaga *et al*., 2007; Marr *et al*., 2008; Basheer *et al*., 2011). Although BB4267 is nearly 100 amino acids larger than NaxD, the majority of the

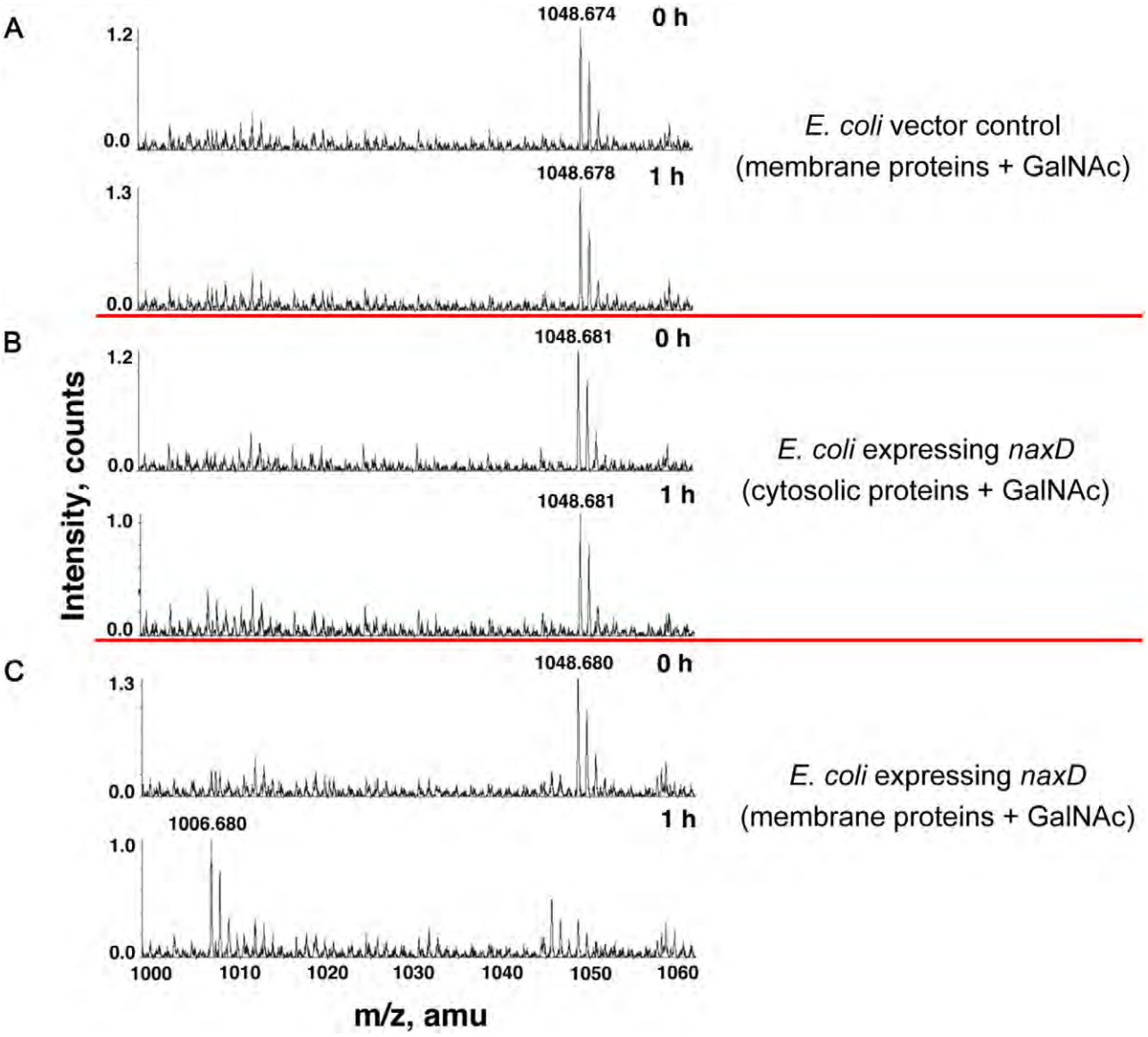

Fig. 7. NaxD is required for deacetylation of undecaprenyl phosphate-*N*-acetylgalactosamine when exogenously expressed in *E. coli*. Deacetylase activity assays using synthesized undecaprenyl phosphate-*N*-acetylgalactosamine (GalNAc) and (A) whole-cell lysate from *E. coli* with an empty vector, (B) the soluble fraction from *E. coli* expressing *naxD*, or (C) the membrane fraction from *E. coli* expressing *naxD* were incubated at 30°C for the indicated times and then analysed using LC-ESI/MS in negative ion mode.

protein is comprised of the YdjC superfamily domain, including the conserved putative active-site residues, which suggests conserved function (Fig. 2B).

Indeed, LC-ESI/MS analysis of the wild-type lipid fractions revealed a doubly charged lipid A peak at *m/z* 1072.70 that corresponds to lipid A with glucosamine modifications at both the 4′ and 1 position phosphates (Fig. 9A). This peak was absent in the mutant fractions, which instead displayed a doubly charged peak at *m/z* 911.64, corresponding to the lipid A molecule missing both glucosamine modifications (Fig. 9B). These data show that the NaxD homologue BB4267, like NaxD in *Francisella*, is required for the modification of lipid A phosphates with hexosamine sugars.

Similar to the addition of galactosamine to *Francisella* lipid A, the modification of *B. bronchiseptica* lipid A with glucosamine requires the deacetylation of undecaprenyl phosphate-*N*-acetylglucosamine (undecaprenyl phosphate-GlcNAc) to form undecaprenyl phosphate-glucosamine (undecaprenyl phosphate-GlcN). LC-ESI/MS from the lipid fraction of the wild-type strain showed a singly charged peak at *m/z* 1006.85, corresponding to undecaprenyl phosphate-GlcN (Fig. 9C). In contrast, the *bb4267* mutant displayed a peak at *m/z* 1048.88, corresponding to

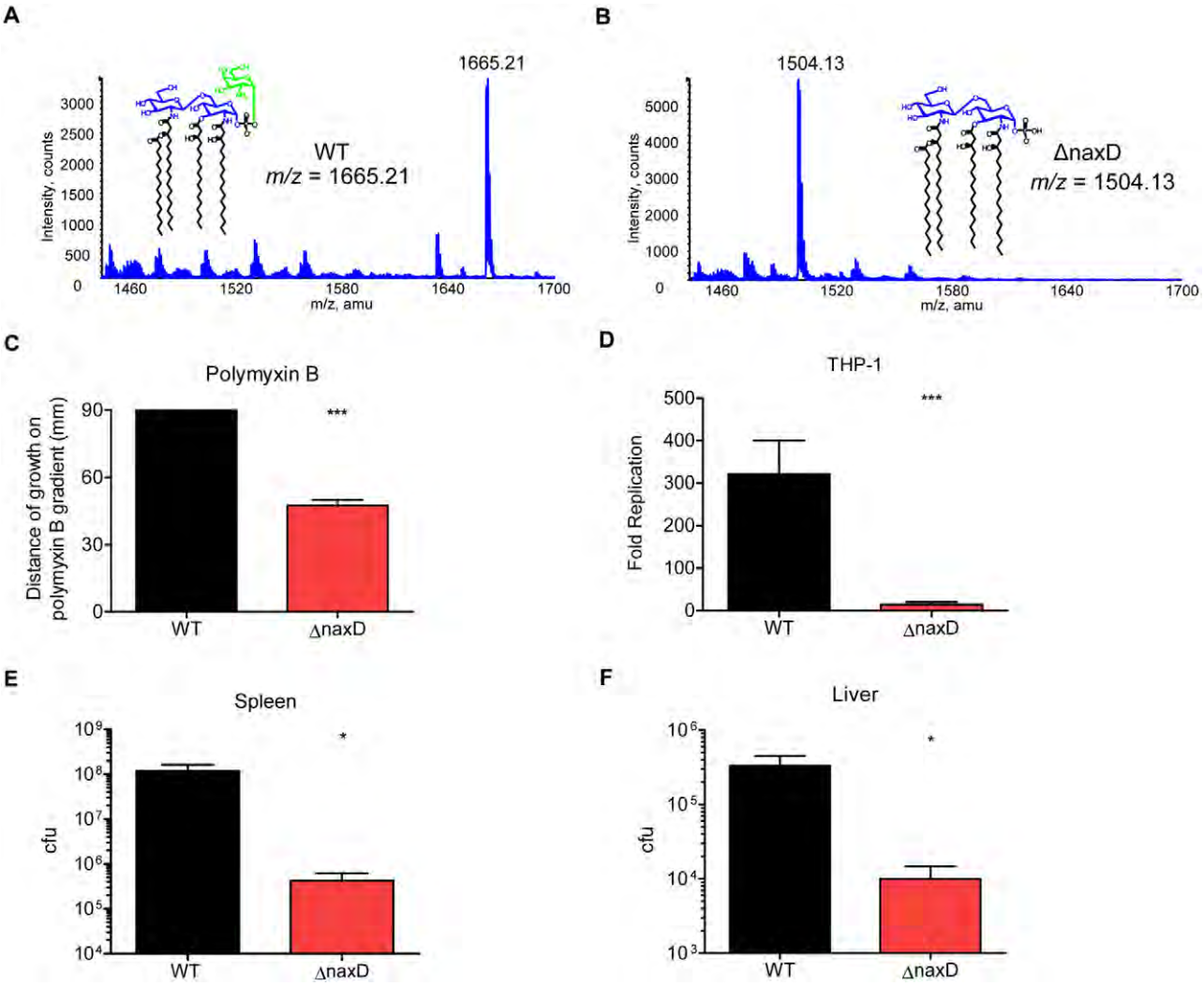

Fig. 8. NaxD function is conserved in human pathogenic *F. tularensis*.
A and B. Total lipids were extracted from (A) wild-type *F. tularensis* and (B) the ΔnaxD strain in mid-log phase and lipid A composition was analysed by LC-ESI/MS. (A) Galactosamine is highlighted in green.
C. The distance of growth of wild-type or ΔnaxD along a 0–2 mg ml^{-1} gradient of polymyxin B was measured ($n = 3$ biological replicates).
D. Human PMA-differentiated THP-1 macrophage-like cells were infected with either wild-type *F. tularensis* (WT) or the *naxD* deletion mutant (ΔnaxD) at a 50:1 moi. Colony-forming units recovered from macrophages lysed 24 h after infection were compared with cfu recovered at 2 h post infection to calculate fold replication ($n = 3$ biological replicates).
E and F. Mice were subcutaneously infected with 50 cfu of either wild-type or ΔnaxD and 48 h after infection, organs were harvested and plated and cfu were enumerated for the (E) spleen and (F) liver ($n = 5$ mice).
In (C) and (D), bars represent the average and error bars represent the standard deviation of three biological replicates from one experiment. Data shown in (C)–(F) are representative of at least three independent experiments. Asterisks indicate significance as compared with wild-type. *$P < 0.05$, ***$P < 0.0005$.

undecaprenyl phosphate-GlcNAc (Fig. 9D), which was undetectable in the wild-type. This demonstrates that, similar to NaxD function in *Francisella*, BB4267 is required for a deacetylation reaction in *B. bronchiseptica*. To test the functional relevance of the lipid A modification with glucosamine, we measured the polymyxin B sensitivity of the wild-type and mutant strains and found that the *bb4267* mutant exhibited a dose-dependent increase in susceptibility to polymyxin B as compared with wild-type (Fig. 9E). These data confirm that the function of NaxD is conserved among multiple Gram-negative pathogens.

Discussion

Using *in vivo* negative selection (Weiss *et al*., 2007) and intramacrophage replication (Llewellyn *et al*., 2011) screens, we have recently identified NaxD as an important virulence factor of *Francisella*. Here we have

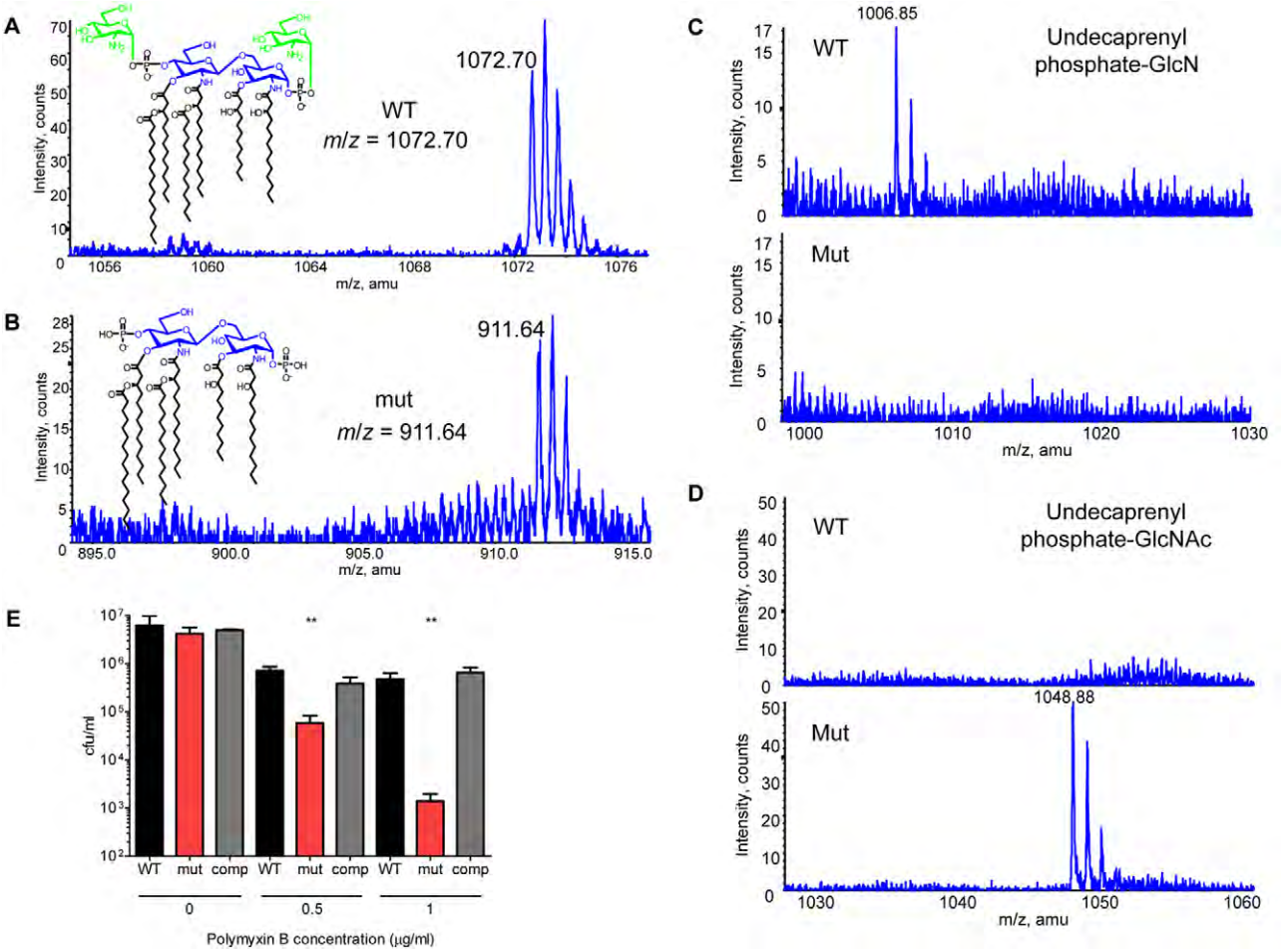

Fig. 9. Conserved role of the *Bordetella bronchiseptica* NaxD homologue in lipid A modification.
A–D. Total lipids were extracted from wild-type (WT) and *naxD* homologue mutant (mut) strains of *B. bronchiseptica* in mid-log phase and (A, B) lipid A, (C) undecaprenyl phosphate-glucosamine (GlcN) and (D) undecaprenyl phosphate-*N*-acetylglucosamine (GlcNAc) analysed by LC-ESI/MS. In (A), glucosamine groups are highlighted in green.
E. WT, mut or the complemented strain (comp) were incubated with the indicated concentrations of polymyxin B for 6 h and cfu were enumerated ($n = 3$ biological replicates). Bars represent the average and error bars represent the standard deviation of three biological replicates from one experiment. Data shown are representative of at least three independent experiments. Asterisks indicate significance as compared with wild-type. $^{**}P < 0.005$.

extended those findings by showing that this member of the YdjC protein superfamily is a deacetylase that is required for lipid A modifications that render bacteria more resistant to killing by the cationic antimicrobial peptide polymyxin B. Given our findings that the *B. bronchiseptica* NaxD homologue is also required for lipid A modification, this report suggests that NaxD/YdjC proteins are likely to have an important role in the pathogenesis of other virulent Gram-negative bacteria.

This work contributes to a greater understanding of the mechanisms by which *Francisella* is able to so effectively evade killing by antimicrobial peptides compared with other Gram-negative pathogens (Ishimoto *et al*., 2006; Mohapatra *et al*., 2007). For example, *Francisella* is nearly 1000× more resistant to polymyxin B than *E. coli* (Mohapatra *et al*., 2007). Because polymyxin B is known to bind Gram-negative lipid A, it is interesting that the majority of the exposed surface of the *Francisella* outer membrane consists of free lipid A (Zhao and Raetz, 2010). To our knowledge, *Francisella* is the only Gram-negative pathogen shown to exhibit this sort of unique outer membrane composition. Mutants that lack the galactosamine modification on free lipid A have an exposed phosphate at the 1 position (Phillips *et al*., 2004; Bina *et al*., 2006; Schilling *et al*., 2007; Shaffer *et al*., 2007; Kanistanon *et al*., 2008; Kalhorn *et al*., 2009; Song *et al*., 2009; Wang *et al*., 2009; Soni *et al*., 2010; Beasley *et al*., 2012), significantly altering the charge and likely the topography of the majority of the outer leaflet of the outer membrane. Interestingly, the small percentage of lipid A that is part of complete LPS lacks the 1 position phosphate and, therefore, the galactosamine modification as well (Zhao and Raetz, 2010). It is

not clear why *Francisella* produces such a large amount of lipid A without O-antigen, given that O-antigen is critical for virulence (Sandstrom *et al*., 1988; Sorokin *et al*., 1996; Clay *et al*., 2008). However, since the majority of *Francisella*'s outer membrane is composed of free lipid A, it is intuitive that the galactosamine modification to this moiety would be critical in resistance to host stresses, similar to the importance of modifications to complete LPS in other bacteria (Wang and Quinn, 2010). Indeed, given that this modification is important for resistance to polymyxin B, replication in macrophages, and during *in vivo* infection, it likely contributes to *Francisella* resistance to host cationic antimicrobial peptides such as cathelicidins, defensins and ubiquicidin (Weiss *et al*., 2007; Kanistanon *et al*., 2008; Flannagan *et al*., 2009; Llewellyn *et al*., 2011). Future work will aim to elucidate whether there are advantages conferred by the novel cell surface component free lipid A, e.g. whether free lipid A promotes enhanced resistance to host antimicrobials compared with full LPS.

The Gram-negative pathogen *B. bronchiseptica* has been shown to express lipid A species that have one or both phosphates modified with glucosamine, a stereoisomer of galactosamine (Tirsoaga *et al*., 2007; Marr *et al*., 2008; Basheer *et al*., 2011). Like galactosamine, addition of glucosamine neutralizes the negative charge of lipid A phosphates (Marr *et al*., 2008). In this study we show that the *B. bronchiseptica* NaxD homologue BB4267 is required for the glucosamine modification of lipid A phosphates and specifically is necessary for the deacetylation of undecaprenyl phosphate-*N*-acetylglucosamine. Similar to the *Francisella* galactosamine modification, we show that this glucosamine modification is important for resistance to the lipid A-binding cationic antimicrobial peptide polymyxin B. While no bacteria other than *Francisella* species have been reported to utilize free lipid A, our *B. bronchiseptica* data indicate that NaxD homologues could be involved in modifying the lipid A component of complete LPS of other Gram-negative pathogens.

This study has generated new insight into *Francisella* pathogenesis and lipid A biosynthesis as well as the function of YdjC superfamily proteins. Significantly, this study has broad implications for host–pathogen interactions of other highly virulent NaxD homologue-encoding Gram-negative bacteria, particularly intracellular pathogens such as *B. abortus*, *L. pneumophila* and *C. burnetii*. Future studies on the role of this family of proteins will likely further illuminate the virulence mechanisms of other NaxD homologue-encoding pathogenic bacteria.

Experimental procedures

Bacterial strains and growth conditions

Wild-type *F. novicida* strain U112 and a previously described *mglA* point mutant, GB2 (Baron and Nano, 1998), were a generous gift from Dr Denise Monack (Stanford University, Stanford, CA). These strains, the *naxD* deletion mutant and the *naxD* complemented strain were grown at 37°C on a rolling drum in tryptic soy broth (TSB; Difco/BD, Sparks, MD) supplemented with 0.02% L-cysteine (Sigma-Aldrich, St. Louis, MO). *F. novicida* was plated for colony-forming units (cfu) on tryptic soy agar (TSA; Difco/BD) and supplemented with 0.01% L-cysteine, with the exception of bacteria from mouse experiments, which were plated on modified Mueller Hinton (mMH) agar plates (Difco/BD) supplemented with 0.025% ferric pyrophosphate (Sigma-Aldrich), 0.1% glucose (Sigma-Aldrich) and 0.01% L-cysteine. When appropriate, kanamycin (Fisher Scientific, Fair Lawn, NJ) was added to media at a concentration of 30 μg ml^{-1}. *F. tularensis* strains were grown in mMH broth or on Brain Heart Infusion (BHI) agar (BHI supplemented with 50 μg ml^{-1} haemin, 1.4% agar (w/v) and 1% (v/v) IsoVitalex (BBL, Cockeysville, MD). Counter selection for resolution of *F. tularensis FTT0453* deletion plasmid co-integrants was performed on cysteine heart agar containing 5% sucrose. Kanamycin was added to the plates when necessary at 10 μg ml^{-1} for *F. tularensis*. *B. bronchiseptica* wild-type strain RB50, the *bb4267* deletion mutant and the *bb4267* complemented strain were grown under similar conditions as *F. novicida*, except using Stainer-Scholte broth supplemented with nicotinic acid, glutathione and ascorbic acid as previously described (Hulbert and Cotter, 2009), or Bordet-Gengou blood agar plates (Remel, Lenexa, KS). When appropriate, streptomycin (Fisher Scientific) and kanamycin were added at concentrations of 25 μg ml^{-1} and 50 μg ml^{-1} respectively.

Mutagenesis and complementation

To generate the *naxD* deletion mutant in *F. novicida*, PCR was used to amplify flanking DNA regions upstream and downstream of the gene of interest. A kanamycin resistance cassette was sewn in between these flanking regions using overlapping PCR reactions. The final linear PCR product was then gel purified and transformed into chemically competent wild-type strain U112 as previously described (Anthony *et al*., 1991). The primers used to create the kanamycin-resistant deletion mutant contained FRT sites flanking the kanamycin resistance cassette, which allowed a clean deletion of each mutant to be made using the plasmid pFFlp encoding the Flp-recombinase as previously described (Gallagher *et al*., 2008). A construct for the complementation of the mutant was generated by overlapping PCR using PCR-amplified fragments of the wild-type gene of interest, upstream and downstream flanking regions, and a kanamycin resistance cassette. These constructs were then transformed into the chemically competent *naxD* clean deletion mutant. Verification of allelic replacement in the mutant and complemented strains was performed using check primers in PCR reactions on purified genomic DNA from each strain. PCR products of the correct size were subsequently sequenced (MWG Operon, Huntsville, AL) for final verification of allelic replacement. PCR constructs for *F. tularensis* mutagenesis were amplified as for *F. novicida* and then cloned into plasmid pXB186 containing a kanamycin resistance cassette and the *sacB* counter-selectable marker (making plasmid pΔFTT0453). To generate the *FTT0453* deletion mutant, the

deletion plasmid was introduced by electroporation into electrocompetent *F. tularensis* SchuS4. Electrocompetent cells were prepared on the day of the transformation as described in the supplemental experimental procedures. The resulting clones were screened by PCR for the *FTT0453* deletion. To generate the *B. bronchiseptica bb4267* deletion mutant, linear PCR deletion constructs were amplified as described above for *F. novicida*. This *bb4267*-deleting fragment was cloned into the *Bordetella* allelic exchange plasmid pSS4245. The resulting plasmid was then transformed into wild-type *B. bronchiseptica* strain RB50, following procedures described previously (Inatsuka *et al*., 2010). The loss of *bb4267* was confirmed by PCR and subsequent enzymatic digestions. To generate the complementation plasmid, the two external primers used to produce the *bb4267*-deleting fragment were employed and this complementing fragment was cloned into pUC18-Mini-TN7 plasmid that has a Tn*7* integration sequence, which, along with a helper plasmid pTNS3, was mated into the deletion strain via tri-parental mating (Choi *et al*., 2005) to generate the complemented strain. All primers and plasmids used in this study are listed in Table S1.

Antimicrobial assays

The antimicrobial peptide polymyxin B (USB, Cleveland, OH) was dissolved in peptide buffer (0.01% acetic acid, 0.2% BSA) and then serially diluted in the same buffer to desired concentrations. The detergents sodium-dodecyl-sulphate (SDS; Fisher Scientific) and Triton X-100 (Fisher Scientific) were serially diluted in 25% TSB. Overnight cultures of bacteria were diluted to 1×10^7 cfu ml^{-1} in 25% TSB. Ninety microlitres of diluted cultures were then added to 96-well plates containing 10 µl of the appropriate antimicrobial. Plates were incubated at 37°C on shaking platforms for 6 h. Cultures were then serially diluted and plated to enumerate cfu. *F. tularensis* antimicrobial susceptibility was determined by the gradient agar plate method as previously described (Szybalski and Bryson, 1952; Bina *et al*., 2006; 2008). Briefly, 35 ml of BHI-chocolate agar (without polymyxin B) was poured into a square Petri dish and allowed to solidify as a wedge by elevating one side of the plate. After the agar solidified, 35 ml of BHI-chocolate agar containing polymyxin B at 2 mg ml^{-1} was added to the levelled plate and allowed to solidify. Theses plates were inoculated with overnight mMH broth cultures of each respective strain and incubated at 37°C for 2 days when the length of growth along the polymyxin B gradient was recorded. The gradient agar plate tests were performed a minimum of three times and representative results are presented.

Zeta electrokinetic potential

Overnight cultures of bacteria were subcultured and grown to $OD_{600} = 1.0$. The bacteria were then pelleted (10 000 *g*, 3 min) and resuspended at a 5× concentration in 20 mM potassium chloride. Twenty microlitres of the concentrated bacteria were added to 3.2 ml of 20 mM potassium chloride in the zeta potential electrokinetic cuvette from Brookhaven Instruments Corporation (BIC, Holtsville, NY). The bacterial sizes and zeta electrokinetic potentials were measured using the 90Plus size and zeta potential analyser (BIC). Data were analysed using BIC Zeta Potential Analyser Software Version 5.20, which takes into account the size of the bacteria when calculating the zeta potential.

Macrophages

RAW264.7 murine macrophages (ATCC, Manassas, VA) were cultured in Dulbecco's modified Eagle's medium (high glucose, L-glutamine; DMEM; Lonza, Walkersville, MD) supplemented with 10% heat-inactivated fetal calf serum (FCS; HyClone, Logan, UT). Bone marrow-derived macrophages (BMM) were isolated from wild-type C57BL/6 mice and cultured as described previously (Schaible and Kaufmann, 2002) in DMEM supplemented with 10% heat-inactivated FCS and 10% macrophage colony-stimulating factor (M-CSF)-conditioned medium (collected from M-CSF-producing L929 cells). THP-1 monocyte-like cells (ATCC) were cultured in RPMI (Lonza) with 10% heat-inactivated fetal calf serum (HyClone). Macrophages were incubated before and during infection at 37°C with 5% CO_2.

Macrophage infections

RAW264.7 macrophages were seeded in 24-well plates at 5×10^5 cells per well and incubated overnight. The following day, overnight cultures of the indicated strains were pelleted (10 000 *g*, 3 min) and resuspended in DMEM/10% FCS. After removal of the overnight media, the macrophages were infected with bacteria at an moi of 20:1 (bacteria to macrophage), centrifuged for 15 min at 900 *g*, and then incubated for 30 min. Next, the macrophages were washed twice with warm DMEM and then incubated in DMEM/10% FCS with 10 µg ml^{-1} gentamicin. At 30 min and 24 h post infection, the macrophages were washed twice and then lysed with 1% saponin in phosphate-buffered saline (PBS). Macrophage lysates were serially diluted and plated on mMH agar, the resulting cfu were enumerated and the fold replication of each strain was determined. The same protocol as above was followed for the BMM infections with the following alterations: 3×10^5 BMM were plated per well, DMEM/10% FCS/10% M-CSF was used throughout, and the final time point was 6 h instead of 24 h. The difference in time point was due to the fact that *F. novicida* triggers inflammatory mediated cell death in BMM (Mariathasan *et al*., 2005). Therefore, bacterial replication was measured at 6 h post infection to minimize loss of bacterial counts as a consequence of the host cell death response. It is likely that we did not observe this early cell death in RAW264.7 macrophages because this cell line is known to be deficient in ASC/caspase-1 inflammasome-mediated cell death (Pelegrin *et al*., 2008). For *F. tularensis* experiments, THP-1 cells or BMM were seeded into 24-well tissue culture plates (3×10^5 cells per well) in a total volume of 1 ml of culture medium. THP-1 cells were treated with 200 nM phorbol 12-myristate 13-acetate (PMA) immediately after cells were plated. The cells were infected 24 h later with the indicated strains at an moi of 50:1 bacteria to macrophage. Fifty micrograms per millilitre of gentamicin was added 2 h later to kill any remaining extracellular bacteria. At

2 or 24 h after infection, wells were washed twice with PBS, lysed, and then bacteria were enumerated by dilution plating in duplicate using an IUL Eddy Jet Spiral plater and a Flash and Go automated colony counter (Neutec Group, Farmingdale, NY).

Mice

For *F. novicida* experiments, female C57BL/6 mice (Jackson Laboratory, Bar Harbor, ME) between 7 and 10 weeks of age were kept under specific pathogen-free conditions in filter-top cages at Emory University and provided with sterile food and water *ad libitum*. Experimental studies were performed in accordance with the Emory University Institutional Animal Care and Use Committee (IACUC) guidelines. For *F. tularensis* experiments, C57BL/6 mice were purchased from Charles River Laboratories. Mice were age-matched and used between 7 and 10 weeks of age. Mice were housed in sealed Allentown caging and HEPA-filtered cage racks with food and water *ad libitum*. All experimental protocols were reviewed and approved by the University of Tennessee Health Science Center IACUC.

Mouse experiments

For competition experiments, mice were inoculated subcutaneously with a 1:1 ratio of kanamycin-resistant deletion mutant and kanamycin-sensitive wild-type *F. novicida* for a total of 2×10^5 cfu in 50 µl of sterile PBS. After 48 h, the mice were sacrificed and the spleen, liver and skin at the site of infection were harvested, homogenized, plated for cfu on MH plates with and without kanamycin, and then incubated overnight at 37°C. Competitive index (CI) values were determined using the formula: (cfu mutant output/cfu WT output)/(cfu mutant input/cfu WT input). For survival experiments, mice were infected subcutaneously with 2×10^5 cfu of either the deletion mutant or wild-type strain in 50 µl of sterile PBS and then monitored for signs of illness and sacrificed if they appeared moribund.

For *F. tularensis* infection experiments, mice were challenged subcutaneously with 50 cfu in 100 µl of sterile PBS. All procedures were performed under BSL3 containment according to standard operating procedures that have been fully vetted by the UTHSC Committee On Biocontainment and Restricted Entities (COBRE). Spleens, livers and lungs of challenged mice were homogenized with a disposable tissue homogenizer in 1 ml of sterile PBS and then 0.25 ml disruption buffer (2.5% saponin, 15% BSA, in PBS) was added with light vortexing. Appropriate dilutions of each sample were then plated in duplicate using an Eddy Jet spiral plater on mMH agar plates supplemented with 5% calf serum and incubated at 37°C for 48–72 h. Colonies were counted using a Flash & Go automated colony counter.

Preparation of total lipids

Overnight cultures of *F. novicida* U112 wild-type or *naxD* mutant strains were subcultured to $OD_{600} = 0.02$ and grown at 37°C in TSB supplemented with L-cysteine until the $OD_{600} = 1.0$. The cells were collected by centrifugation (5000 *g*, 20 min) and washed with PBS. The cell pellets were resuspended in a single-phase Bligh-Dyer mixture (Bligh and Dyer, 1959) consisting of chloroform, methanol and water (1:2:0.8, v/v), incubated at room temperature for 60 min, and centrifuged (10 000 *g*, 20 min) to remove insoluble debris. The supernatant was converted to a two-phase Bligh-Dyer system by adding chloroform and water to generate a mixture consisting of chloroform, methanol and water (2:2:1.8, v/v). The two phases of Bligh-Dyer system were separated under centrifugation and the lower phase was dried by rotary evaporation and under a stream of nitrogen. The total lipids were analysed using thin-layer chromatography (TLC) and LC-ESI/MS. The TLC plate was developed using the solvent chloroform, methanol, pyridine, acetic acid and water (25:10:5:4:3, v/v). Lipids were detected by spraying 10% of sulphuric acid in ethanol and charring at 300°C.

Negative ion mode electrospray ionization (ESI) mass spectrometry (MS) and MS/MS analysis

All ESI/MS and MS/MS spectra were acquired on a QSTAR XL quadrupole time-of-flight tandem mass spectrometer (Applied Biosystems, Foster City, CA) equipped with an ESI source. Lipid A samples were dissolved in chloroform and methanol (2:1, v/v) containing 1% piperidine and subjected to ESI/MS in the negative ion mode via direct infusion (Garrett and Yost, 2006; Guan *et al*., 2007; Wang *et al*., 2009). Nitrogen was used as the collision gas for MS/MS experiments (Garrett and Yost, 2006; Guan *et al*., 2007; Wang *et al*., 2009). Data acquisition and analysis were performed using the instrument's Analyst QS software.

Liquid chromatography/mass spectrometry (LC/MS)

LC/MS of lipids was performed using a Shimadzu LC system (comprising a solvent degasser, two LC-10A pumps and an SCL-10A system controller) coupled to a QSTAR XL quadrupole time-of-flight tandem mass spectrometer (as above). LC was performed at a flow rate of 200 µl min^{-1} with a linear gradient as follows: 100% mobile phase A was held isocratically for 2 min and then linearly increased to 100% mobile phase B over 14 min and held at 100% B for 4 min. Mobile phase A consisted of methanol/acetonitrile/aqueous 1 mM ammonium acetate (60:20:20, v/v/v). Mobile phase B consisted of 100% ethanol containing 1 mM ammonium acetate. A Zorbax SB-C8 reversed-phase column (5 m, 2.1×50 mm) was obtained from Agilent (Palo Alto, CA). The postcolumn splitter diverted ~ 10% of the LC flow to the ESI source of the mass spectrometer.

Membrane fractionation

Fifty millilitres of *F. novicida* strains were harvested at $OD_{600} = 1.0$ by centrifugation for 20 min at 5000 *g* at 4°C. Cell pellets were washed with 50 mM K + HEPES, pH 7.5, resuspended in 5 ml of the same buffer and passed through a French pressure cell at 18 000 p.s.i. Unbroken cells were then removed by centrifugation at 10 000 *g* for 20 min at 4°C. Membrane fractions were pelleted from whole-cell lysates by

ultracentrifugation at 200 000 *g* for 2 h at 4°C. *F. novicida* fractionation and protein localization were verified using Western blotting (see supplemental experimental procedures). For *E. coli*, fractions were prepared similarly with the following exceptions: *E. coli* C41 (DE3) strains transformed with the empty vector or vector encoding *naxD* were grown in LB broth (1% tryptone, 0.5% yeast extract and 1% NaCl) with 100 μg ml^{-1} ampicillin and were induced using 1 mM IPTG when cell density reached OD_{600} = 0.8, then harvested when the OD_{600} = 2.0. NaxD protein expression was analysed using 12% SDS-PAGE gel and Coomassie staining.

Undecaprenyl phosphate-GalNAc deacetylase assay

These assays measured the deacetylase activity of proteins from the *F. novicida* wild-type or *naxD* mutant membrane fractions, whole-cell lysate of *E. coli* transformed with the empty vector, and the membrane and cytosolic fractions of *E. coli* transformed with vector encoding *naxD* (grown under inducing conditions). The 100 μl reaction mixture included 50 μg ml^{-1} protein from the bacterial fractions, 4.0 μM synthesized undecaprenyl phosphate-GalNAc (Song *et al*., 2009), 1 mM $MnCl_2$, 150 mM KCl, 1.0 mg ml^{-1} BSA, 0.1% Triton X-100 and 50 mM HEPES (pH 7.5) and was incubated at 30°C. A 20 μl sample was removed at 0 and 5 h for *F. novicida* and 0 and 1 h for *E. coli*. Samples were converted to a two-phase Bligh-Dyer system by the addition of chloroform and methanol. After centrifugation, the lower phase was dried under nitrogen and analysed using LC-ESI/MS.

Statistical analysis

All macrophage replication, single infection, killing assay and zeta potential data were analysed for significance using the unpaired Student's *t*-test. For zeta potential, values beyond three standard deviations of the mean were excluded as outliers. The CI values from the mouse competition experiments were analysed with the one-sample Student's *t*-test and compared with 1. The mouse survival infection data were analysed for significance using the Gehan–Breslow–Wilcoxon test.

Acknowledgements

We dedicate this manuscript *in memoriam* of our friend, mentor, collaborator and renowned LPS biosynthesis expert Christian R. H. Raetz. We thank Larry Gallagher and Colin Manoil (University of Washington) for generously providing the pFFlp plasmid. In addition, we thank William Shafer, Thomas Henry, Brooke Napier and Tim Sampson for critical reading of this manuscript. The project described was supported by NIH Grant U54-AI057157 from the Southeastern Regional Center of Excellence for Emerging Infections and Biodefense. Its contents are solely the responsibility of the authors and do not necessarily represent the official views of the NIH.

References

Anthony, L.S., Gu, M.Z., Cowley, S.C., Leung, W.W., and Nano, F.E. (1991) Transformation and allelic replacement in *Francisella* spp. *J Gen Microbiol* **137:** 2697–2703.

Bakshi, C.S., Malik, M., Regan, K., Melendez, J.A., Metzger, D.W., Pavlov, V.M., and Sellati, T.J. (2006) Superoxide dismutase B gene (*sodB*)-deficient mutants of *Francisella tularensis* demonstrate hypersensitivity to oxidative stress and attenuated virulence. *J Bacteriol* **188:** 6443–6448.

Baron, G.S., and Nano, F.E. (1998) MglA and MglB are required for the intramacrophage growth of *Francisella novicida*. *Mol Microbiol* **29:** 247–259.

Basheer, S.M., Guiso, N., Tirsoaga, A., Caroff, M., and Novikov, A. (2011) Structural modifications occurring in lipid A of *Bordetella bronchiseptica* clinical isolates as demonstrated by matrix-assisted laser desorption/ionization time-of-flight mass spectrometry. *Rapid Commun Mass Spectrom* **25:** 1075–1081.

Beasley, A.S., Cotter, R.J., Vogel, S.N., Inzana, T.J., Qureshi, A.A., and Qureshi, N. (2012) A variety of novel lipid A structures obtained from *Francisella tularensis* live vaccine strain. *Innate Immun* **18:** 268–278.

Bina, X.R., Wang, C., Miller, M.A., and Bina, J.E. (2006) The Bla2 beta-lactamase from the live-vaccine strain of *Francisella tularensis* encodes a functional protein that is only active against penicillin-class beta-lactam antibiotics. *Arch Microbiol* **186:** 219–228.

Bina, X.R., Lavine, C.L., Miller, M.A., and Bina, J.E. (2008) The AcrAB RND efflux system from the live vaccine strain of *Francisella tularensis* is a multiple drug efflux system that is required for virulence in mice. *FEMS Microbiol Lett* **279:** 226–233.

Bligh, E.G., and Dyer, W.J. (1959) A rapid method of total lipid extraction and purification. *Can J Biochem Physiol* **37:** 911–917.

Choi, K.H., Gaynor, J.B., White, K.G., Lopez, C., Bosio, C.M., Karkhoff-Schweizer, R.R., and Schweizer, H.P. (2005) A Tn7-based broad-range bacterial cloning and expression system. *Nat Methods* **2:** 443–448.

Clay, C.D., Soni, S., Gunn, J.S., and Schlesinger, L.S. (2008) Evasion of complement-mediated lysis and complement C3 deposition are regulated by *Francisella tularensis* lipopolysaccharide O antigen. *J Immunol* **181:** 5568–5578.

Clemens, D.L., and Horwitz, M.A. (2007) Uptake and intracellular fate of *Francisella tularensis* in human macrophages. *Ann N Y Acad Sci* **1105:** 160–186.

Darling, R.G., Catlett, C.L., Huebner, K.D., and Jarrett, D.G. (2002) Threats in bioterrorism. I: CDC category A agents. *Emerg Med Clin North Am* **20:** 273–309.

Egberink, H., Addie, D., Belak, S., Boucraut-Baralon, C., Frymus, T., Gruffydd-Jones, T., *et al*. (2009) *Bordetella bronchiseptica* infection in cats. ABCD guidelines on prevention and management. *J Feline Med Surg* **11:** 610–614.

Flannagan, R.S., Cosio, G., and Grinstein, S. (2009) Antimicrobial mechanisms of phagocytes and bacterial evasion strategies. *Nat Rev Microbiol* **7:** 355–366.

Fujita, H., Watanabe, Y., Sato, T., Ohara, Y., and Homma, M. (1993) The entry and intracellular multiplication of *Francisella tularensis* in cultured cells: its correlation with virulence in experimental mice. *Microbiol Immunol* **37:** 837–842.

Gallagher, L.A., McKevitt, M., Ramage, E.R., and Manoil, C. (2008) Genetic dissection of the *Francisella novicida* restriction barrier. *J Bacteriol* **190:** 7830–7837.

Garrett, T.J., and Yost, R.A. (2006) Analysis of intact tissue by

intermediate-pressure MALDI on a linear ion trap mass spectrometer. *Anal Chem* **78:** 2465–2469.
Guan, F., Uboh, C.E., Soma, L.R., Birks, E., Chen, J., Mitchell, J., *et al*. (2007) LC-MS/MS method for confirmation of recombinant human erythropoietin and darbepoetin alpha in equine plasma. *Anal Chem* **79:** 4627–4635.
Gunn, J.S., and Ernst, R.K. (2007) The structure and function of *Francisella* lipopolysaccharide. *Ann N Y Acad Sci* **1105:** 202–218.
Hall, J.D., Craven, R.R., Fuller, J.R., Pickles, R.J., and Kawula, T.H. (2007) *Francisella tularensis* replicates within alveolar type II epithelial cells *in vitro* and *in vivo* following inhalation. *Infect Immun* **75:** 1034–1039.
Hall, J.D., Woolard, M.D., Gunn, B.M., Craven, R.R., Taft-Benz, S., Frelinger, J.A., and Kawula, T.H. (2008) Infected-host-cell repertoire and cellular response in the lung following inhalation of *Francisella tularensis* Schu S4, LVS, or U112. *Infect Immun* **76:** 5843–5852.
Honn, M., Lindgren, H., and Sjostedt, A. (2012) The role of MglA for adaptation to oxidative stress of *Francisella tularensis* LVS. *BMC Microbiol* **12:** 14.
Hulbert, R.R., and Cotter, P.A. (2009) Laboratory Maintenance of *Bordetella pertussis*. *Curr Protoc Microbiol* **Chapter 4:** Unit 4B 1.
Imagawa, T., Iino, H., Kanagawa, M., Ebihara, A., Kuramitsu, S., and Tsuge, H. (2008) Crystal structure of the YdjC-family protein TTHB029 from *Thermus thermophilus* HB8: structural relationship with peptidoglycan N-acetylglucosamine deacetylase. *Biochem Biophys Res Commun* **367:** 535–541.
Inatsuka, C.S., Xu, Q., Vujkovic-Cvijin, I., Wong, S., Stibitz, S., Miller, J.F., and Cotter, P.A. (2010) Pertactin is required for *Bordetella* species to resist neutrophil-mediated clearance. *Infect Immun* **78:** 2901–2909.
Ishimoto, H., Mukae, H., Date, Y., Shimbara, T., Mondal, M.S., Ashitani, J., *et al*. (2006) Identification of hBD-3 in respiratory tract and serum: the increase in pneumonia. *Eur Respir J* **27:** 253–260.
Kalhorn, T.F., Kiavand, A., Cohen, I.E., Nelson, A.K., and Ernst, R.K. (2009) A sensitive liquid chromatography/mass spectrometry-based assay for quantitation of amino-containing moieties in lipid A. *Rapid Commun Mass Spectrom* **23:** 433–442.
Kanistanon, D., Hajjar, A.M., Pelletier, M.R., Gallagher, L.A., Kalhorn, T., Shaffer, S.A., *et al*. (2008) A *Francisella* mutant in lipid A carbohydrate modification elicits protective immunity. *PLoS Pathog* **4:** e24.
Lai, X., and Ingram, L.O. (1993) Cloning and sequencing of a cellobiose phosphotransferase system operon from *Bacillus stearothermophilus* XL-65-6 and functional expression in *Escherichia coli*. *J Bacteriol* **175:** 6441–6450.
Llewellyn, A.C., Jones, C.L., Napier, B.A., Bina, J.E., and Weiss, D.S. (2011) Macrophage replication screen identifies a novel *Francisella* hydroperoxide resistance protein involved in virulence. *PLoS ONE* **6:** e24201.
Mariathasan, S., Weiss, D.S., Dixit, V.M., and Monack, D.M. (2005) Innate immunity against *Francisella tularensis* is dependent on the ASC/caspase-1 axis. *J Exp Med* **202:** 1043–1049.
Marr, N., Tirsoaga, A., Blanot, D., Fernandez, R., and Caroff, M. (2008) Glucosamine found as a substituent of both phosphate groups in *Bordetella* lipid A backbones: role of a BvgAS-activated ArnT ortholog. *J Bacteriol* **190:** 4281–4290.
Mohapatra, N.P., Soni, S., Bell, B.L., Warren, R., Ernst, R.K., Muszynski, A., *et al*. (2007) Identification of an orphan response regulator required for the virulence of *Francisella* spp. and transcription of pathogenicity island genes. *Infect Immun* **75:** 3305–3314.
Morrison, D.C., and Jacobs, D.M. (1976) Binding of polymyxin B to the lipid A portion of bacterial lipopolysaccharides. *Immunochemistry* **13:** 813–818.
Nano, F.E., and Schmerk, C. (2007) The *Francisella* pathogenicity island. *Ann N Y Acad Sci* **1105:** 122–137.
Pelegrin, P., Barroso-Gutierrez, C., and Surprenant, A. (2008) P2X7 receptor differentially couples to distinct release pathways for IL-1beta in mouse macrophage. *J Immunol* **180:** 7147–7157.
Phillips, N.J., Schilling, B., McLendon, M.K., Apicella, M.A., and Gibson, B.W. (2004) Novel modification of lipid A of *Francisella tularensis*. *Infect Immun* **72:** 5340–5348.
Qin, A., and Mann, B.J. (2006) Identification of transposon insertion mutants of *Francisella tularensis tularensis* strain Schu S4 deficient in intracellular replication in the hepatic cell line HepG2. *BMC Microbiol* **6:** 69.
Raetz, C.R., and Whitfield, C. (2002) Lipopolysaccharide endotoxins. *Annu Rev Biochem* **71:** 635–700.
Raetz, C.R., Guan, Z., Ingram, B.O., Six, D.A., Song, F., Wang, X., and Zhao, J. (2009) Discovery of new biosynthetic pathways: the lipid A story. *J Lipid Res* **50** (Suppl.): S103–S108.
Ramakrishnan, G., Meeker, A., and Dragulev, B. (2008) *fslE* is necessary for siderophore-mediated iron acquisition in *Francisella tularensis* Schu S4. *J Bacteriol* **190:** 5353–5361.
Sandstrom, G., Lofgren, S., and Tarnvik, A. (1988) A capsule-deficient mutant of *Francisella tularensis* LVS exhibits enhanced sensitivity to killing by serum but diminished sensitivity to killing by polymorphonuclear leukocytes. *Infect Immun* **56:** 1194–1202.
Schaible, U.E., and Kaufmann, S.H.E. (2002) Studying trafficking of intracellular pathogens in antigen-presenting cells. *Methods Microbiol* **31:** 343–360.
Schilling, B., McLendon, M.K., Phillips, N.J., Apicella, M.A., and Gibson, B.W. (2007) Characterization of lipid A acylation patterns in *Francisella tularensis*, *Francisella novicida*, and *Francisella philomiragia* using multiple-stage mass spectrometry and matrix-assisted laser desorption/ionization on an intermediate vacuum source linear ion trap. *Anal Chem* **79:** 1034–1042.
Schulert, G.S., McCaffrey, R.L., Buchan, B.W., Lindemann, S.R., Hollenback, C., Jones, B.D., and Allen, L.A. (2009) *Francisella tularensis* genes required for inhibition of the neutrophil respiratory burst and intramacrophage growth identified by random transposon mutagenesis of strain LVS. *Infect Immun* **77:** 1324–1336.
Shaffer, S.A., Harvey, M.D., Goodlett, D.R., and Ernst, R.K. (2007) Structural heterogeneity and environmentally regulated remodeling of *Francisella tularensis* subspecies novicida lipid A characterized by tandem mass spectrometry. *J Am Soc Mass Spectrom* **18:** 1080–1092.
Song, F., Guan, Z., and Raetz, C.R. (2009) Biosynthesis of undecaprenyl phosphate-galactosamine and undecaprenyl

phosphate-glucose in *Francisella novicida*. *Biochemistry* **48:** 1173–1182.
Soni, S., Ernst, R.K., Muszynski, A., Mohapatra, N.P., Perry, M.B., Vinogradov, E., *et al*. (2010) *Francisella tularensis* blue-gray phase variation involves structural modifications of lipopolysaccharide o-antigen, core and lipid a and affects intramacrophage survival and vaccine efficacy. *Front Microbiol* **1:** 129.
Sorokin, V.M., Pavlovich, N.V., and Prozorova, L.A. (1996) *Francisella tularensis* resistance to bactericidal action of normal human serum. *FEMS Immunol Med Microbiol* **13:** 249–252.
Szybalski, W., and Bryson, V. (1952) Genetic studies on microbial cross resistance to toxic agents. I. Cross resistance of *Escherichia coli* to fifteen antibiotics. *J Bacteriol* **64:** 489–499.
Tirsoaga, A., El Hamidi, A., Perry, M.B., Caroff, M., and Novikov, A. (2007) A rapid, small-scale procedure for the structural characterization of lipid A applied to *Citrobacter* and *Bordetella* strains: discovery of a new structural element. *J Lipid Res* **48:** 2419–2427.
Titball, R.W., and Petrosino, J.F. (2007) *Francisella tularensis* genomics and proteomics. *Ann N Y Acad Sci* **1105:** 98–121.
Trent, M.S. (2004) Biosynthesis, transport, and modification of lipid A. *Biochem Cell Biol* **82:** 71–86.
Vinogradov, E., Perry, M.B., and Conlan, J.W. (2002) Structural analysis of *Francisella tularensis* lipopolysaccharide. *Eur J Biochem* **269:** 6112–6118.
Wang, X., and Quinn, P.J. (2010) Lipopolysaccharide: biosynthetic pathway and structure modification. *Prog Lipid Res* **49:** 97–107.
Wang, X., Ribeiro, A.A., Guan, Z., McGrath, S.C., Cotter, R.J., and Raetz, C.R. (2006) Structure and biosynthesis of free lipid A molecules that replace lipopolysaccharide in *Francisella tularensis* subsp. *novicida*. *Biochemistry* **45:** 14427–14440.
Wang, X., Ribeiro, A.A., Guan, Z., and Raetz, C.R. (2009) Identification of undecaprenyl phosphate-beta-D-galactosamine in *Francisella novicida* and its function in lipid A modification. *Biochemistry* **48:** 1162–1172.
Weiss, D.S., Brotcke, A., Henry, T., Margolis, J.J., Chan, K., and Monack, D.M. (2007) In vivo negative selection screen identifies genes required for *Francisella* virulence. *Proc Natl Acad Sci USA* **104:** 6037–6042.
Zhao, J., and Raetz, C.R. (2010) A two-component Kdo hydrolase in the inner membrane of *Francisella novicida*. *Mol Microbiol* **78:** 820–836.

Supporting information

Additional supporting information may be found in the online version of this article.

Please note: Wiley-Blackwell are not responsible for the content or functionality of any supporting materials supplied by the authors. Any queries (other than missing material) should be directed to the corresponding author for the article.

BMC Genomics

RESEARCH ARTICLE Open Access

Distinct gene loci control the host response to influenza H1N1 virus infection in a time-dependent manner

Tatiana Nedelko[1], Heike Kollmus[1], Frank Klawonn[2,3], Sabine Spijker[5], Lu Lu[4,6], Manuela Heßman[1,7], Rudi Alberts[1], Robert W. Williams[5] and Klaus Schughart[1*]

Abstract

Background: There is strong but mostly circumstantial evidence that genetic factors modulate the severity of influenza infection in humans. Using genetically diverse but fully inbred strains of mice it has been shown that host sequence variants have a strong influence on the severity of influenza A disease progression. In particular, C57BL/6J, the most widely used mouse strain in biomedical research, is comparatively resistant. In contrast, DBA/2J is highly susceptible.

Results: To map regions of the genome responsible for differences in influenza susceptibility, we infected a family of 53 BXD-type lines derived from a cross between C57BL/6J and DBA/2J strains with influenza A virus (PR8, H1N1). We monitored body weight, survival, and mean time to death for 13 days after infection. *Qivr5* (quantitative trait for influenza virus resistance on chromosome 5) was the largest and most significant QTL for weight loss. The effect of *Qivr5* was detectable on day 2 post infection, but was most pronounced on days 5 and 6. Survival rate mapped to *Qivr5*, but additionally revealed a second significant locus on chromosome 19 (*Qivr19*). Analysis of mean time to death affirmed both *Qivr5* and *Qivr19*. In addition, we observed several regions of the genome with suggestive linkage. There are potentially complex combinatorial interactions of the parental alleles among loci. Analysis of multiple gene expression data sets and sequence variants in these strains highlights about 30 strong candidate genes across all loci that may control influenza A susceptibility and resistance.

Conclusions: We have mapped influenza susceptibility loci to chromosomes 2, 5, 16, 17, and 19. Body weight and survival loci have a time-dependent profile that presumably reflects the temporal dynamic of the response to infection. We highlight candidate genes in the respective intervals and review their possible biological function during infection.

Background

Influenza A virus represents a major health threat to humans. The 1918 H1N1 pandemic caused at about 30 to 50 million deaths [1]. Seasonal influenza epidemics cause high economic loss, morbidity and deaths every year [2]. The course and outcome of an influenza A virus infection is influenced by viral and host factors. Host risk factors, like obesity or pregnancy, became evident during the recent swine flu pandemics [3,4]. Furthermore, genetic factors in humans associated with a higher susceptibility to influenza infections and severe disease outcome have been suspected for the 1918 pandemics, as well as the H5N1 human infections [5-7]. Recently, the importance of *IFITM3* as a crucial factor for host susceptibility has been demonstrated in mice and humans [8].

The importance of host factors to host susceptibility and resistance has been demonstrated clearly in animal models. We and others have shown in mouse infection models that the susceptibility of the host to influenza A infection strongly depends on the genetic background [9-17]. In particular, DBA/2J mice are highly susceptible to many influenza A virus subtypes, including those that

* Correspondence: kls@helmholtz-hzi.de
[1]Department of Infection Genetics, Helmholtz Centre for Infection Research and University of Veterinary Medicine Hannover, 38124, Braunschweig, Germany
Full list of author information is available at the end of the article

were directly derived from human isolates without prior adaptation to the mouse [9,13,16-18]. In contrast, C57BL/6J mice are more resistant. After infection with mouse-adapted H1N1 (PR8M virus), DBA/2J mice loss weight very rapidly and die within 5–7 days post infection (p.i.), whereas C57BL/6J mice loss weight until days 6–8 after infection and regain their initial weight by 14 days p.i. [9,18]. Viral load in the lungs of DBA/2J infected mice is much higher and lung pathology is very severe compared to infected C57BL/6J mice. Also, the production of chemokines and cytokines is much higher in DBA/2J mice [9,18].

However, the genomic regions that are responsible for the differential response after infection with H1N1 have not been determined. Therefore, we used a large family of BXD type recombinant inbred strains generated by crossing C57BL/6J (resistant) to DBA/2J (susceptible) to map genetic loci that modulate disease severity. The BXD genetic reference population (GRP) is made up of a set of progeny strains, each with a defined and fixed genetic architecture. It is one of the largest families of strains, consisting of about 80 fully inbred strains [19,20] available from the Jackson Laboratory and a new set of 80 additional lines that are still in production at the University of Tennessee. Individuals within each single strain are essentially isogenic (except for the sex chromosomes) and genotypes for the entire family, including most of the new strains, are known [21]. Genetic variation among this family has be exploited extensively in the past to systematically study the genetics of many traits (for examples of phenotypes see the GeneNetwork database [22]).

Here, we infected over 50 of the BXD strains with influenza A H1N1 virus and monitored body weight, survival, and mean time to death for the following 13 days post infection. We identified two significant and several suggestive loci peaks for all three traits. All showed a time-dependent appearance. Data mining of the intervals revealed several candidate genes, several of which may be important for the host response to influenza A virus infection.

Results

Susceptibility to influenza A virus after experimental infection of BXD mouse strains is highly variable

We infected 53 recombinant inbred strains of the BXD population plus the parental strains C57BL/6J, DBA/2J and B6D2F1 mice with mouse-adapted H1N1 virus (PR8M, H1N1 [18]) and followed body weight and survival over the next 13 days. Mice that lost more than 25% of their starting weight were sacrificed and also recorded as dead. After infection, body weight changes were highly variable between the BXD strains over the period of 13 days post infection (Figure 1, Additional file 1: Table S1). Similarly, survival rates (Additional file 2: Figure S1A, B) and mean time to death (MTTD; Additional file 2: Figure S1C) were highly variable between the different BXD strains. Furthermore, the trait percent survival showed a strain-dependent progression over time.

For body weight loss and survival, three different phenotypic response groups can be defined (Figure 1). In the first (Figure 1A), all infected mice within a strain survived, in the second (Figure 1B) a majority but not all individuals within a strain survived, and in the third group (Figure 1C), a majority died. Most remarkably, in the first group four strains—BXD9, BXD13, BXD43, BXD97—were highly resistant indicating that the infection may not cause any major pathology (Figure 1A). In contrast, BXD28 belonging to the third group, lost body weight much more rapidly than even the highly susceptible DBA/2J parent (Figure 1C). These results illustrate a large variation of responses within the BXD family.

By day 7 p.i., all infected mice had succumbed to infection in 11 strains, whereas 14 others exhibited more limited mortality (Additional file 2: Figure S1A). The incidence of mortality increased in some strains from day 8 p.i. through day 11 but not thereafter (Additional file 2: Figure S1B). For the MTTD phenotype, 17 strains showed no mortality after infection, similar to the resistant C57BL/6J parent. Three strains—BXD28, BXD18, BXD103—exhibited a MTTD that was even shorter than for the susceptible DBA/2J parent (Additional file 2: Figure S1C). Although this study was conducted over a period of approximately three years, and although mice were received from different sources and different experimenters performed the infection experiments, we did not note any significant influence of these potential confounds and cofactors.

Principal Component Analysis (PCA) of strain mean body weight loss from day 1 until day 7 was carried out to reduce the number and redundancy of related measurements, as well as to evaluate whether this set of measurements can be broken down into statistically and genetically independent processes. This analysis revealed one major component, PC1 that explains most of the weight loss among strains (more than 80%, see Additional file 3: Figure S2). This component corresponds to differences in loss from day 3 to 7 p.i. (Figure 2). In contrast, PC2 accounts for only about 10% of the variance in weight loss (Additional file 3: Figure S2). This component corresponds only to very early weight loss after virus inoculation, on days 1 and 2 p.i.(Figure 2), well before any appreciable virus replication has occurred. Thus, PC2 is highly likely to be a technical, but still interesting effect associated with the stressful procedure of intranasal inoculation and full anesthesia. PC1 most likely reflects the biologically relevant variation among strains in response to viral replication.

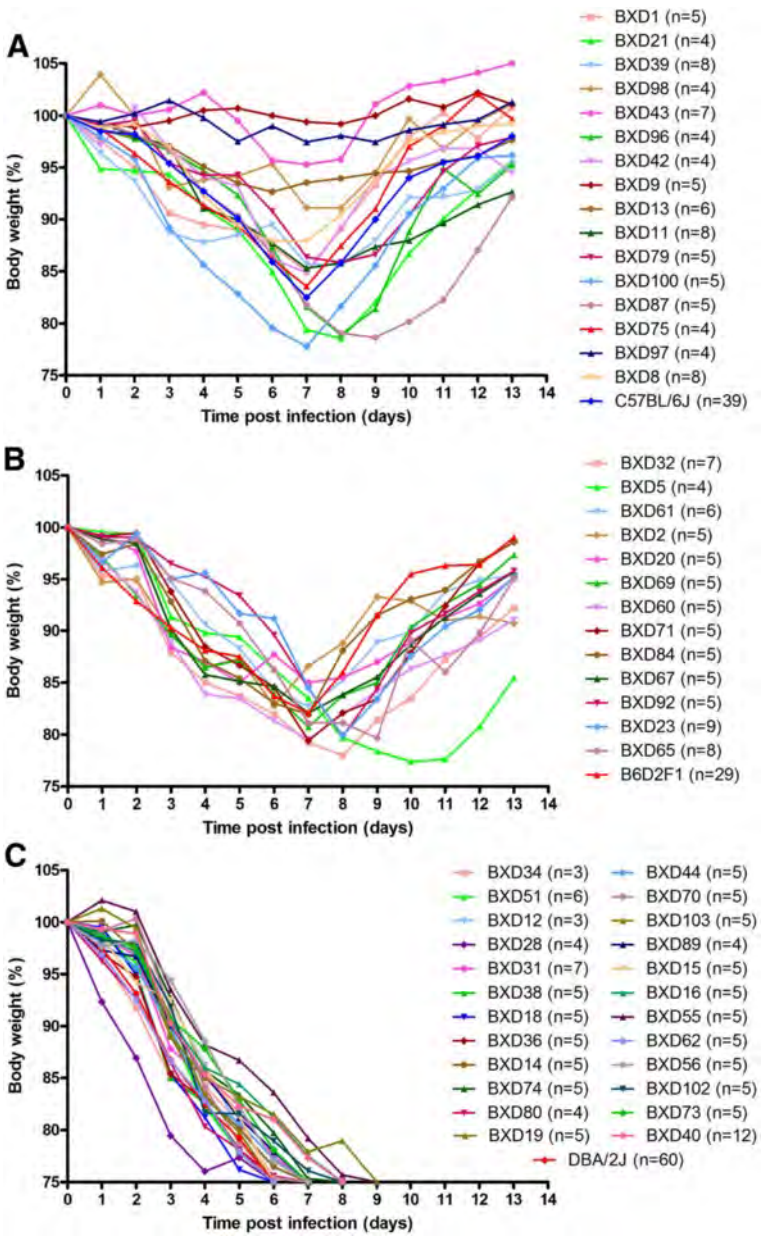

Figure 1 BXD strains exhibit variable kinetics of weight loss and survival after infection with Influenza A virus. Mice from 53 BXD and parental strains were infected intra-nasally with 2×10^3 FFU of PR8 virus. Weight loss and survival of infected mice was followed over a period of 13 days. Mortality includes mice that were sacrificed because they had lost more than 25% of body weight. Three phenotypic groups can be distinguished: in the first group (**A**), all infected mice within a given BXD strain survived, in the second group (**B**) less than 50% of infected mice within a given BXD strain died, in the third group (**C**), more than 50% of infected mice within a given BXD strain died. From the weight loss curve of the second and third group it also becomes obvious that non-surviving mice were all approaching the 75% body weight loss endpoint before dying.

Analysis of body weight loss revealed a significant QTL on chromosome 5 and several suggestive QTLs with time-dependent effects

We mapped body weight loss following infection day by day. For purposes of analysis, body weights of mice that had died or that were euthanized were assigned a weight equal to 75% of their initial weight. It should be noted that mice which died continuously lost weight and were close to 75% body weight loss before they were found dead (Figure 1B, C). After day 7, surviving mice started to gain weight (Figure 1A, B). For this reason, we limited our analyses of body weight traits to the period of day 1 to day 7 p.i. in order to avoid mixing data from dead with recovering mice. Interval mapping of body weight

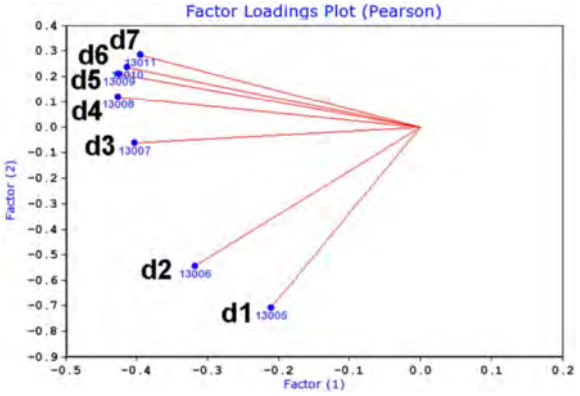

Figure 2 Principal component analysis of all body weight traits reveals two distinct groups. PCA loading plot of principal components PC1 and PC2 (Supplement Figure 2) for body weight traits form day 1 to day 7 p.i. shows two distinct groups. The variation of body weight loss at day 3 to day 7 (ID 13007 to ID 13011) are mainly represented by factor 1. On the other hand, variation of body weight loss at day 1 (ID 13005) and 2 (ID 13006) are most likely explained by factor 2.

loss detected a significant time-dependent locus on chromosome 5 that we named '*QTL for influenza virus resistance on chromosome 5*' (*Qivr5)* adopting the nomenclature proposed by [12]. This QTL exhibited genome-wide significance on days 5 (LRS: 19.0, effect size: 30%) and 6 (LRS: 19.4, effect size: 31%, Figure 3). However, the effect of *Qivr5*, although weaker, can also be detected on days 2, 3, and 4 and 7 (Figure 3). Most interestingly; the resistance allele at *Qivr5* is inherited from the nominally sensitive DBA/2J parental strain, illustrating the genetic complexity of the influenza response. Suggestive loci (LRS values between 10 and 15) map to chromosomes 2, 6, 9, proximal and distal 16, and chromosome 17. The effect of these loci was also time-dependent (Figure 3A-G).

Another suggestive QTL peak was found on chromosome 10 on day 1 (LRS: 14.1, effect size: 23%, Figure 3A). Its effect is lower at day 2 and not apparent at later days. These observations are in accordance with the PCA (Figure 2) that reveals two separate time-dependent influences on body weight variance among strains. The QTL appeared at an early time point after infection, when virus replication has just begun and strong inflammatory host responses are not yet evident [9,18,23]. These observations indicate that the effect is most likely related to the experimental protocol, namely the stress to anesthesia and intra-nasal application as well as treatment recovery. Treatment-dependent QTLs were described previously [24]. It is worth to note that mock-infection of the parental DBA/2J and C57BL/6J mice did not lead to a lasting body weight loss over a longer time interval except for a slight drop in body weight on day 1 p.i. (Additional file 4: Figure S3).

We also performed a QTL analysis for the PC1 and PC2 described above. PC1 detects a significant QTL on chromosome 5 (LRS: 19, effect size: 30%, Figure 4A) as well as suggestive QTL peaks on proximal chromosome 16 and on chromosome 17 (Figure 4A). Thus, the PC1 confirmed the significant QTL on chromosome 5 found with the daily body weight loss traits. Interval mapping of PC2 detected no significant QTL and one suggestive QTL on chromosome 13 (Figure 4B) which was not seen in any other trait.

Survival rate and mean time to death traits confirmed the QTL on chromosome 5 and detected another significant QTL on chromosome 19

The analysis of survival rate traits on days 7, 8 and 11 p.i. revealed significant peaks on chromosomes 5 and 19 and suggestive peaks on chromosomes 1, 2, 3, 10, 16 and 17 (Figure 5A-C). The effects of these QTLs were again time-dependent. *Qivr5* was significant at day 7 (LRS: 24.8, effect size: 37%) and day 8 p.i. (LRS: 19.7, effect size: 31% Figure 5A, B) and its effect was still evident from day 9 until 11 p.i. (Additional file 5: Figure S4 and Figure 5C). Similarly, another significant QTL with time-dependent effects was observed on chromosome 19 (*Qivr19*) at day 8 (LRS: 19.4; effect size: 29%) that could also be detected at day 7 and days 9–11 (Figure 5A-C and Additional file 5: Figure S4). *Qivr5* and *Qivr19* resulted from a positive influence of DBA/2J on survival, whereas *Qivr16* (distal locus) and *Qivr17-2* resulted from a positive influence of C57BL/6J alleles to increase survival. Furthermore, MTTD analysis confirmed *Qivr5* as a significant QTL (LRS: 20.5, effect size: 32%), and *Qivr19* was almost significant for this trait (Figure 5D). In addition, suggestive QTLs were found on chromosomes 2 and 17 for the MTTD trait.

In conclusion, survival and MTTD traits confirmed the significant QTL on chromosome 5, revealed an additional significant QTL on chromosome 19 and several suggestive QTLs. All QTLs showed a time-dependent effect.

Composite interval and pair-scan mapping indicates various interactions of QTLs

The strongest QTLs map to chromosomes 5 and 19. We therefore performed composite interval mapping in which the contributions of these strong QTLs were factored out to reveal possible secondary QTLs. When we controlled for *Qivr19*, the linkage to distal chromosome 16 increased and became nearly significant for both survival at day 8 and MTTD (Figure 6A, B). The linkage to chromosome 2 increased slightly. However, control for the contribution of *Qivr5* did not reveal any additional loci linked to survival or MTTD traits (Figure 6C, D).

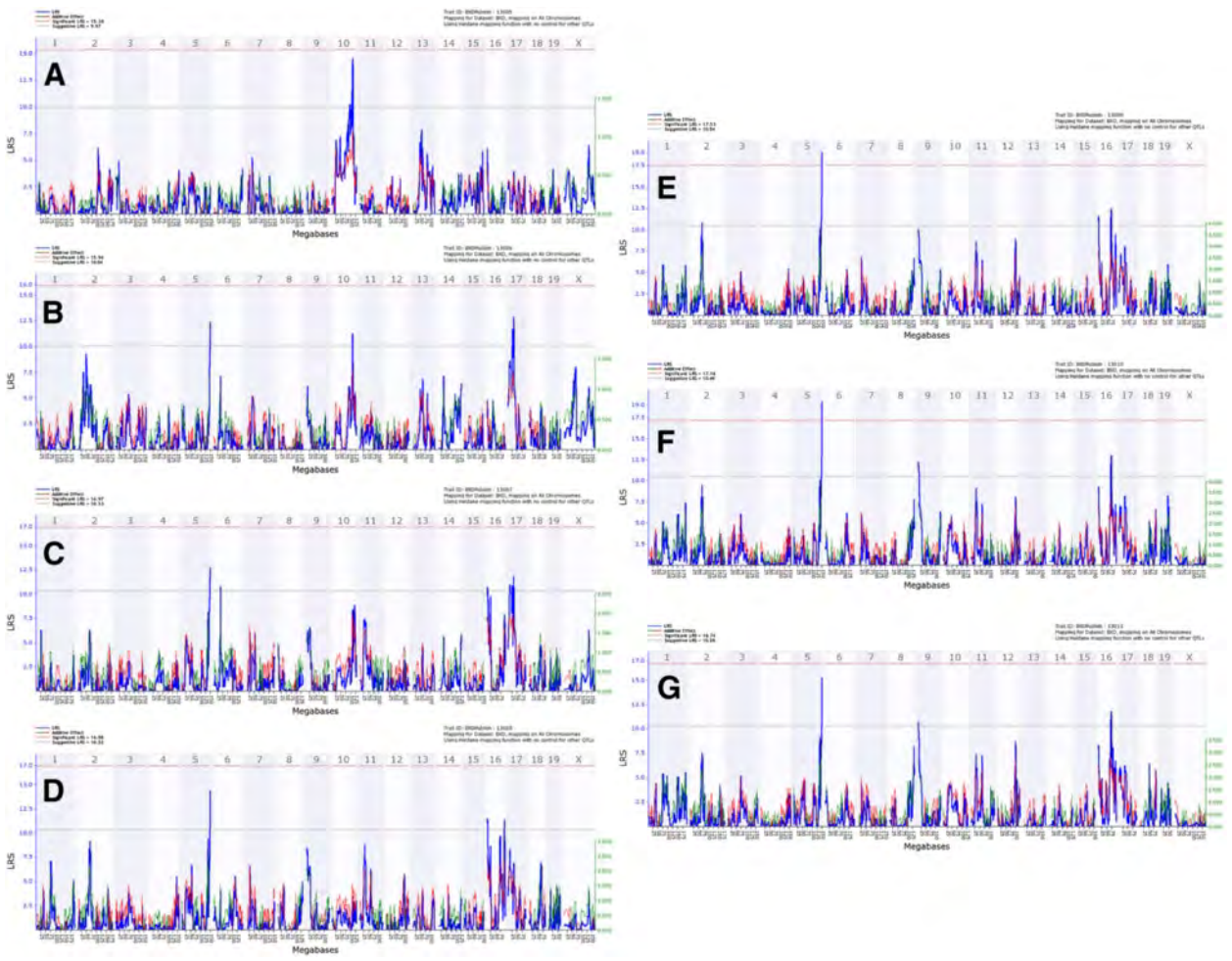

Figure 3 Genome-wide linkage analysis for body weight loss after H1N1 infection identifies time-dependent QTLs. Analysis of body weight from day 1 (**A**), day 2 (**B**), day 3 (**C**), day 4 (**D**), day 5 (**E**), day 6 (**F**) and day 7 (**G**) after PR8 infection revealed time-dependent QTLs. A significant QTL is located on chromosome 5 and suggestive QTLs are observed on chromosomes 2, 6, 9, 10, 16 and 17. Dead or euthanized mice were included for the analysis by manually setting their body weight to 75%. Interval mapping is shown across the entire genome as blue line representing the LRS scores; green line: DBA/2J alleles increase trait values; red line: C57BL/6J alleles increase trait values. Upper x-axis shows mouse chromosomes, lower x-axis shows physical map in mega bases for each chromosome, y-axis represents LRS score. The horizontal lines mark the genome-wide significant thresholds at p<0.05 (red line) and suggestive thresholds at p<0.37 (gray line).

Finally, we analyzed the joint additive effects of QTLs described above as well as possible epistatic interactions among these QTLs. When using a full two-locus model (Trait Variance = Q1 + Q2 + Q1 x Q2), we found two potential interactions between *Qivr5* and a new locus on chromosome 9 as well as between Qivr5 and *Qivr19*, respectively, for the survival trait at day 8 (Figure 7A). The inclusion of an interaction term increases the LRS by 23 (Additional file 6: Figure S5). For both *Qivr5* - chromosome 9 interaction (Figure 7B) and *Qivr5* – *Qivr19* interaction (Figure 7C), the allele combination DBA/2J / DBA/2J showed highest and the combination C57BL/6J / C57BL/6J lowest survival scores. All differences were highly significant.

Analysis of QTL regions identified several candidate genes that may contribute to host susceptibility or resistance

In total, the mapping studies revealed five QTLs on chromosomes 2, 5, distal 16, 17 and 19 (*Qivr2-2*, *Qivr5*, *Qivr16*, *Qivr17-2* and *Qivr19*) that did merit further analysis because they were consistently observed in at least two traits and exerted an effect on at least two different days p.i.

For the candidate gene searches, we defined the critical regions of the QTLs manually by considering peak height, its shoulder and bootstraps as guidance (Figure 8). We then investigated these *Qivr* intervals for potential candidate genes that may be causal for the studied traits

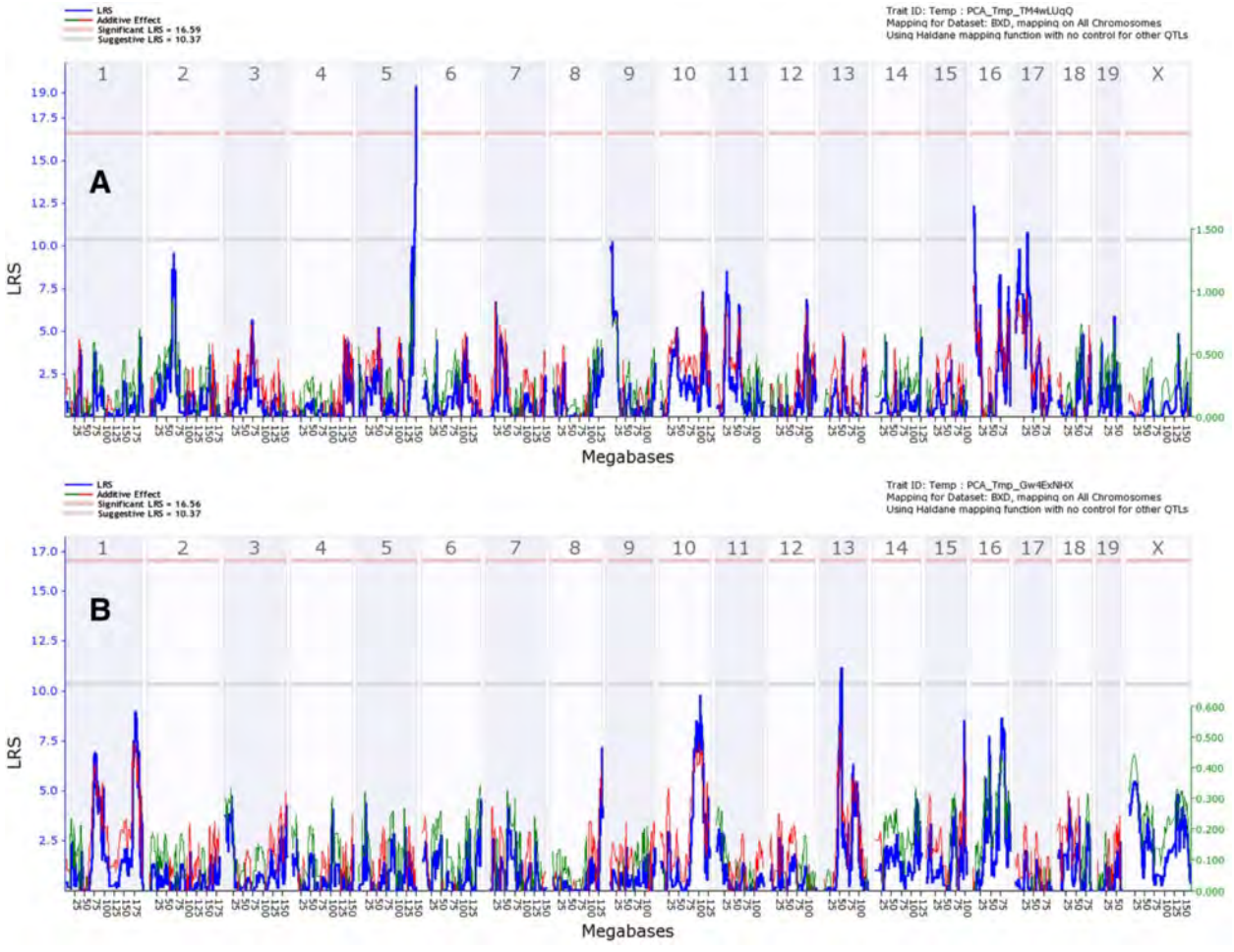

Figure 4 Genome-wide linkage scan for PC1 and PC2 body weight loss. Interval mapping of principle component PC1 (**A**) for body weight loss traits at day 1 to 7 after PR8 infection shows significant QTLs on chromosome 5 and suggestive QTLs on chromosomes 16 and 17. Interval mapping of PC2 (**B**) for body weight loss traits reveals no significant QTLs and a suggestive QTL on chromosome 13. Interval mapping is shown across the entire genome as blue line representing the LRS scores; green line: DBA/2J alleles increase trait values; red line: C57BL/6J alleles increase trait values. Upper x-axis shows mouse chromosomes, lower x-axis shows physical map in mega bases for each chromosome, y-axis represents LRS score. The horizontal lines mark the genome-wide significant thresholds at p<0.05 (red line) and suggestive thresholds at p<0.37 (gray line).

(Additional file 7: Figure S6). We first used the QTLminer tool in GeneNetwork [25] to identify all genes in the QTL intervals and to obtain associated GO terms. Next, we select all annotated genes within the QTL intervals that were expressed between day 1 and day 60 after infection of C57BL/6J mice with PR8M virus (the latter data set is derived from a separate study (Pommerenke et al., PLoS ONE, in press). Subsequently, these genes were further characterized for the following attributes: genes that were up- or up-regulated in infected lungs by at least 1.5-fold in C57BL/6J after PR8M infection, genes carrying an insertion or deletion or a non-synonymous nucleotide change in the open reading frame, genes exhibiting a cis-expression QTL in the lung [26], and genes that were differentially expressed by at least 1.5-fold in C57BL/6J and DBA/2J mice in infected lungs between day 1 and day 8 p.i. [23] and Pommerenke et al., PLoS ONE, in press). The strategy of the QTL mining is shown as flow chart in the Additional file 7: Figure S6, and the final results are presented in Table 1. Furthermore, the attributes of all genes located in the QTL regions are listed in detail in the Additional file 8: Table S2). Using these combined attributes, we identified 31 genes as the most likely candidates to regulate the traits controlled by *Qivr2-2*, *Qivr5*, *Qivr16*, *Qivr17-2* and *Qivr19* (listed in Table 2). These genes were further evaluated based on their known function from the literature and phenotypes in knock-out mouse mutants (see discussion).

Discussion

DBA/2J and C57BL/6J mice have been shown previously to differ largely in their susceptibility to H1N1

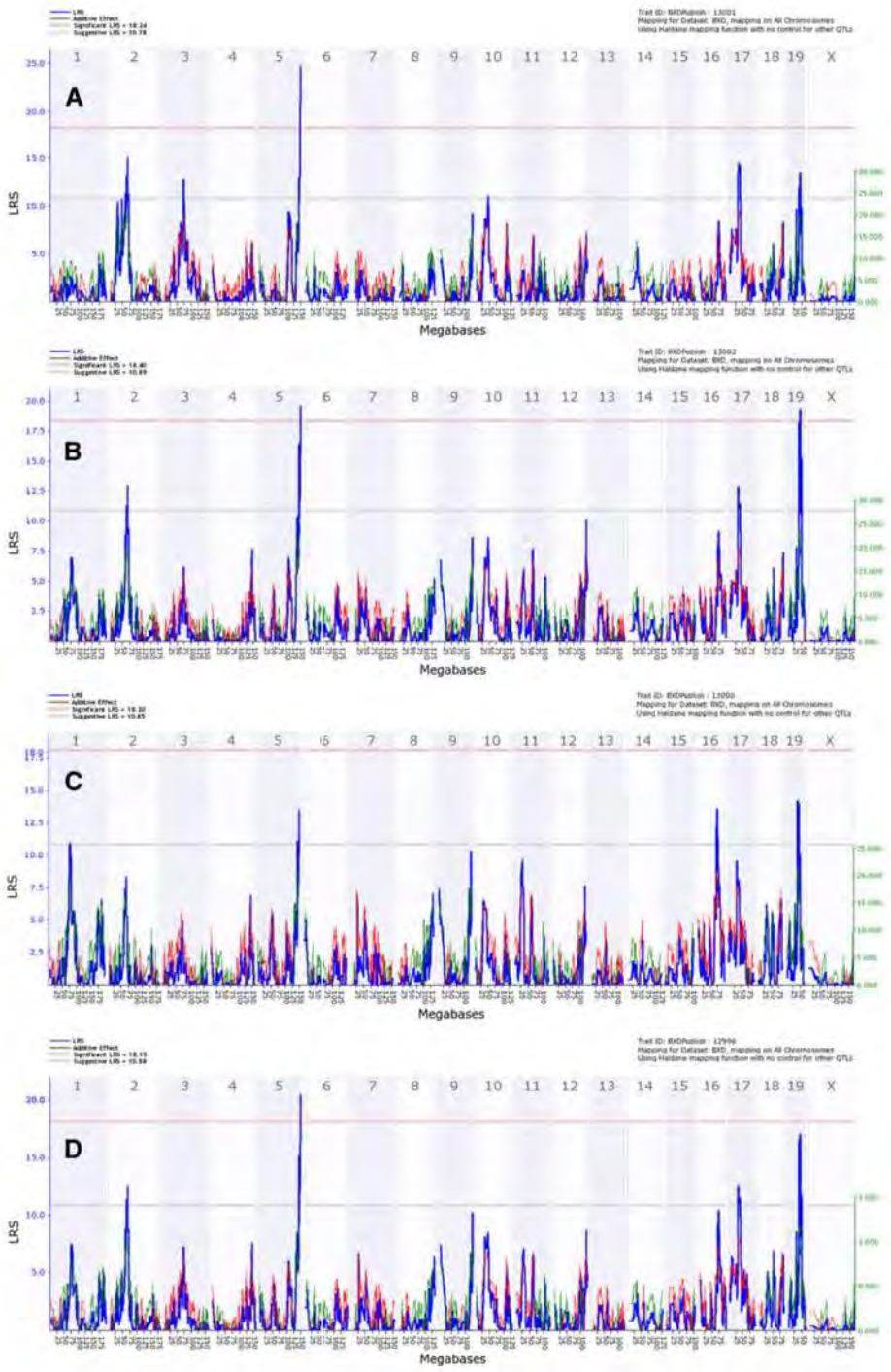

Figure 5 Genome-wide linkage scan for survival rate and mean time to death confirms QTLs on chromosomes 5 and 19. Interval mapping of survival rates (in %) after PR8 infection at day 7 (**A**), day 8 (**B**) and day 11 (**C**) show significant QTLs on chromosomes 5 and 19. Suggestive QTLs are observed on chromosomes 2, 3, 10, 16 and 17. Interval mapping using mean time to death confirmed the significant QTL on chromosome 5 and revealed suggestive QTLs on chromosomes 2, 17 and 19 (**D**). Interval mapping is shown across the entire genome as blue line representing the LRS scores; green line: DBA/2J alleles increase trait values; red line: C57BL/6J alleles increase trait values. Upper x-axis shows mouse chromosomes, lower x-axis shows physical map in mega bases for each chromosome, y-axis represents LRS score. The horizontal lines mark the genome-wide significant thresholds at $p<0.05$ (red line) and suggestive thresholds at $p<0.37$ (gray line).

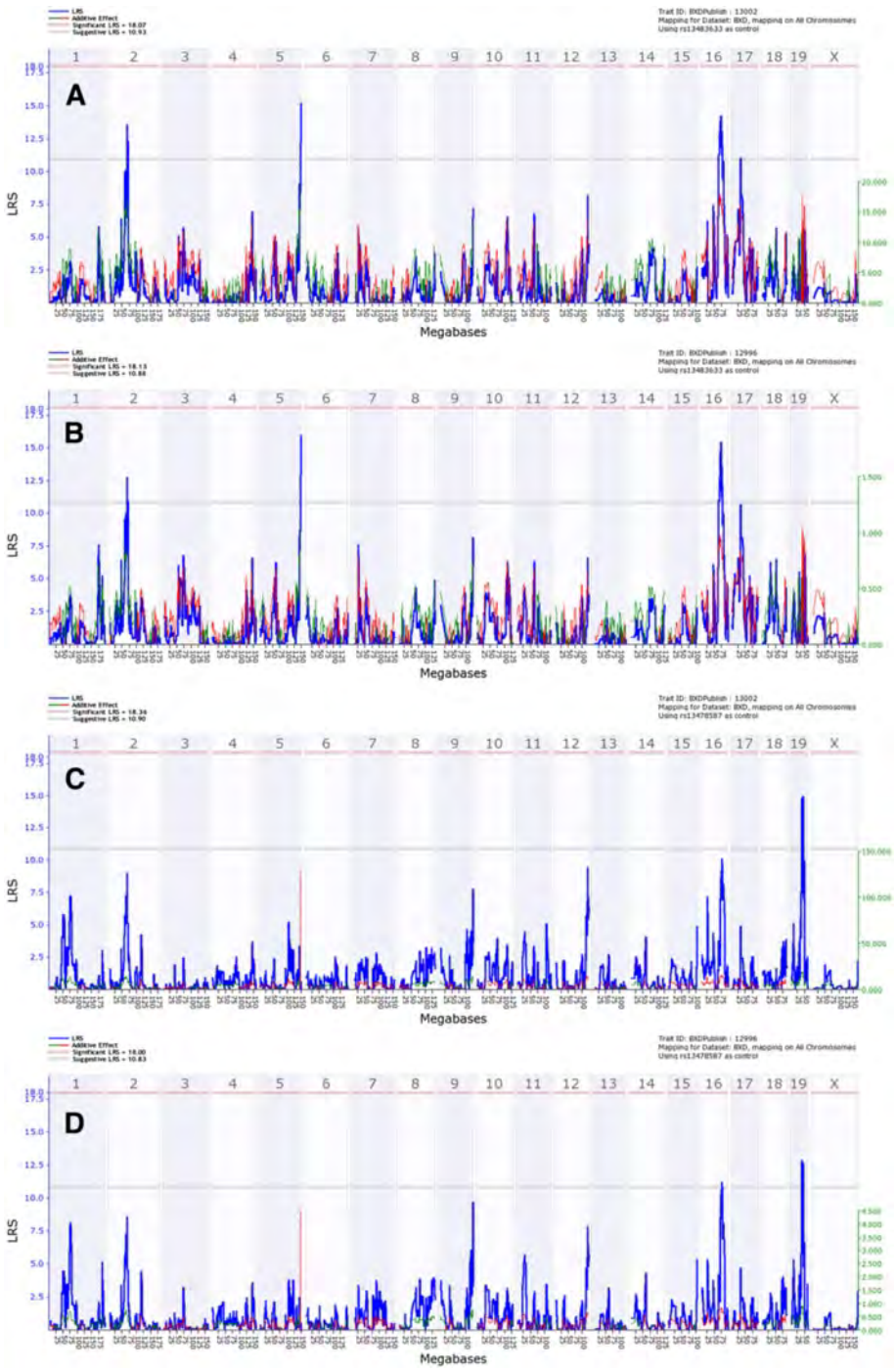

Figure 6 Composite interval mapping indicates interactions of QTLs on chromosomes 5 and 19. The influence of the markers rs13483633 on chromosome 19 (**A**, **B**) and rs13478587 on chromosome 5 (**C**, **D**) was factored out and the residual LRS were calculated. Two different traits, survival day 8 (A, C) and mean time of death (B, D) were tested by using the web tool of GeneNetwork. Interval mapping is shown across the entire genome as blue line representing the LRS scores; green line: DBA/2J alleles increase trait values; red line: C57BL/6J alleles increase trait values. Upper x-axis shows mouse chromosomes, lower x-axis shows physical map in mega bases for each chromosome, y-axis represents LRS score. The horizontal lines mark the genome-wide significant thresholds at $p<0.05$ (red line) and suggestive thresholds at $p<0.37$ (gray line).

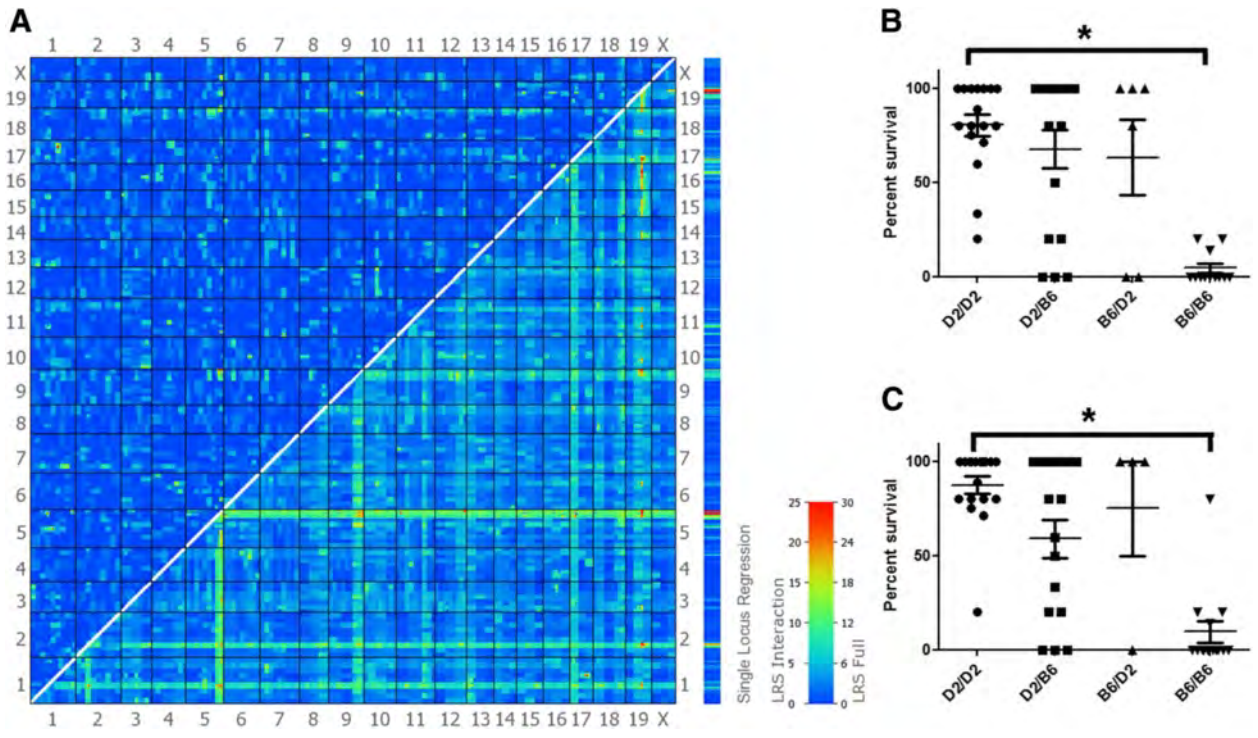

Figure 7 Interactions are observed between several QTLs. The graph displays pair-scan results for the trait percent survival at day 8 p.i. (ID13002) (**A**). The upper left half of the plot highlights any epistatic interactions, the lower right half provides a summary of LRS of the full model, representing cumulative effects of linear and non-linear terms based on the model 'Trait Variance = Q1 + Q2 + Q1 x Q2 '. Subsequently, BXD lines were grouped according to their allele combinations and trait values were compared between groups (**B**, **C**). The largest differences are indicated by asterisks. They are highly significant between the respective groups ($p < 0.0001$). For the various loci, trait values for the following markers were used: *Qivr5*: rs13478587, chromosome 9: rs6191976, *Qivr19*: rs13483633. Number of lines and p-values for *Qivr5* – chromosome 9: D2/D2: n = 17, D2/B6: n = 17, B6/D2: n = 6, B6/B6 n = 12; D2/D2 vs B6/B6: $p < 0.0001$, D2/B6 vs B6/B6: $p = 0.003$. Number of lines and p-values for *Qivr5* – *Qivr19*: D2/D2: n = 18, D2/B6: n = 16, B6/D2: n = 4, B6/B6: n = 14; p-values: D2/D2 vs B6/B6: $p < 0.0001$, D2/B6 vs B6/B6: $p = 0.0008$. Abbreviations: D2: DBA/2J, B6: C57BL/6J.

(PR8M) influenza A virus [9,18]. Here, we expanded these studies and utilized the BXD recombinant inbred set of mouse strains to map the genomic regions that are responsible for differences in these two mouse strains. We monitored three phenotypic traits, body weight over time, survival over time and mean time to death to identify quantitative trait for influenza resistance. Two significant QTLs, *Qivr5* and *Qivr19*, were found on chromosomes 5 and 19, respectively. Furthermore several suggestive QTLs, *Qivr2-2*, *Qivr16* and *Qivr17-2* were observed in at least two traits and at two days on chromosomes 2, 16 and 17, respectively. Composite mapping revealed an additional almost significant QTL at distal chromosome 16, *Qivr16*.

A similar analysis for host resistance to influenza has been performed previously after infecting 66 BXD strains with H5N1 influenza virus. This study reported three significant QTLs on chromosomes 2, 7, and 17 [12]. Thus, none of these significant QTLs overlaps with the QTLs identified in our analysis. Five of the strains that were resistant (all infected mice survived) in our study were also resistant in the study of [12] where a total of 14 strains were found to be resistant. Five strains that were highly susceptible in our study (100% of infected mice died) were also highly susceptible in the study by [12] of a total of 26 susceptible strains. Furthermore, five strains that were resistant in our study were susceptible in the study by [12]. Thus, there is also not much overlap between the two studies with respect of susceptible and resistant strains. The differences between the two studies are most likely explained by the use of two different influenza virus subtypes. The H1N1 virus from our study represents a subtype with a monobasic hemagglutinin (HA) cleavage site, whereas the H5N1 which was used in the study by Boon et al. is a subtype with a polybasic HA cleavage site. The cellular tropism of these two subtypes for virus replication and processing is quite different, because monobasic viruses are dependent on cell-specific proteases for the processing of the HA whereas polybasic subtypes can be processed by more ubiquitously expressed host proteases, *e.g.* [27-32]. Therefore, the contribution of host

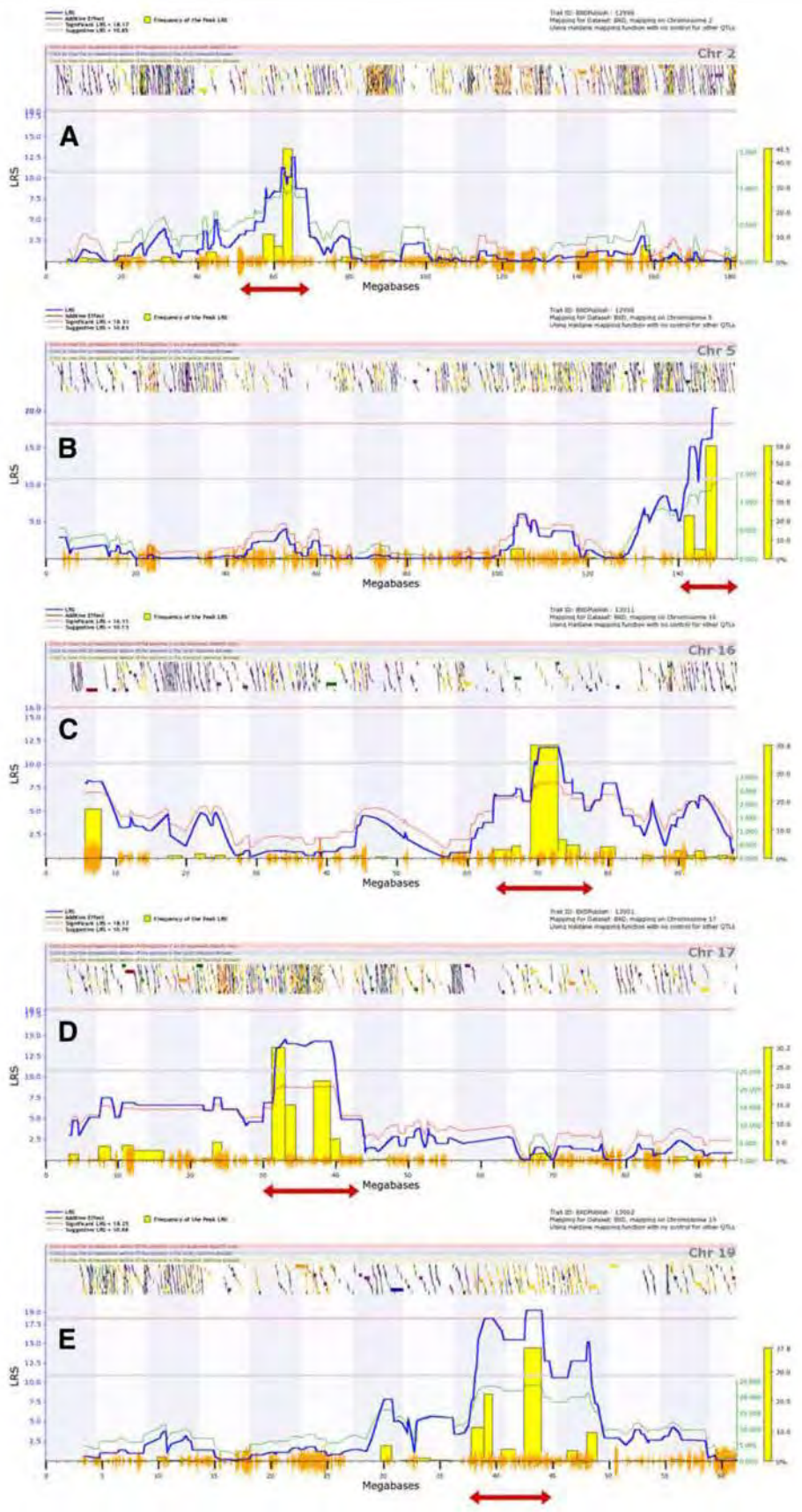

Figure 8 (See legend on next page.)

(See figure on previous page.)
Figure 8 Detailed maps of QTLs contributing to host susceptibility and resistance to PR8 influenza A infection. Interval mapping was performed for chromosomes 2 (**A**), 5 (**B**), 16 (**C**), 17 (**D**) and 19 (**E**). The critical intervals were selected based on the peak shapes and the bootstrap signals: *Qivr2-1* (56–68 Mb), *Qivr5* (140–153 Mb), *Qivr16* (64–78 Mb), *Qivr17-2* (30–44 Mb) and *Qivr19* (37–45 Mb). The *Qivr* intervals are delineated by red arrows. The yellow bars represent the frequencies of peak LRS using bootstrap analysis. The multicolored chatters along the top of the graph are hyperlinks to sites with additional genetic and sequence information. The orange chatter along the x-axis indicates the density of SNPs present in the BXD strains. Interval mapping is shown across the entire genome as blue line representing the LRS scores; green line: DBA/2J alleles increase trait values; red line: C57BL/6J alleles increase trait values. Upper x-axis shows mouse chromosomes, lower x-axis shows physical map in mega bases for each chromosome, y-axis represents LRS score. The horizontal lines mark the genome-wide significant thresholds at $p<0.05$ (red line) and suggestive thresholds at $p<0.37$ (gray line).

factors to susceptibility may be different between H1 and H5 containing virus subtypes.

Another study described the genetic mapping of susceptibility and resistance factors after infecting a panel of 29 AxB / BxA congenic strains with a mouse-adapted H3N2 influenza virus [33]. The AxB / BxA congenic strains were generated from a cross of susceptible A/J and resistant C57BL/6J parental mouse strains. The authors found three major QTLs on chromosomes 2, 6 and 17. The QTL on chromosome 17 overlaps with the *Qivr17-2* locus which we found in our study. Furthermore, the candidate gene *Pla2g7* that was identified in their study was also detected as candidate gene in our analysis (see below).

The influence of genetic factors determining the host response to H1N1 influenza virus infections was also examined in mice of the pre-Collaborative Cross collection [34]. In this study, gene expression levels in extreme responders were used to identify expression QTLs (eQTL). One gene that exhibited a cis-eQTL, *Sik1* (salt inducible kinase 1), was located in the *Qivr17-2* interval from our study, and we also identified it as potential quantitative trait gene (Table 2). This gene is associated with the GO terms 'negative regulation of transcription from RNA polymerase II promoter, regulation of cell differentiation, and protein kinase cascade'. However, no specific infection-related functions have been yet described for this gene.

One of the most interesting findings in our study was the time-dependent effect of QTLs which we observed in the body weight and survival traits. The peak QTLs for the two significant QTLs, *Qivr5* and *Qivr19*, were found at different times p.i., day 6 and day 8, respectively. In addition, the effects of both QTLs were not only evident at the times p.i. where they exerted the significant peak QTL signals but also several days before and after the peak. Furthermore, for the suggestive QTLs, also time-dependent effects were observed. These results suggest that the causal genes underlying different QTLs act at different time points of the host defense.

Most interestingly, *Qivr5* as well as *Qivr19* represent a positive influence on body weight, survival and MTTD from the DBA/2J haplotype, the susceptible strain. These findings indicate that genomic regions from the susceptible parent are able to increase resistance when combined with the resistant parental genome. We are now analyzing several BXD strains that were more resistant than the parental C57BL/6J mice in more detail. One possible mechanism to explain such an effect may be that an activator (secreted ligand or transcription factor) is expressed in susceptible DBA/2J mice but the corresponding target (receptor or regulated gene) is mutated. On the other hand, in C57BL/6J mice, the target but not the activator may be mutated. If the wild type alleles are now coming together in a BXD strain, the functional activator finds its functional target and thereby an increased resistance state is achieved.

Both composite and interaction mapping revealed many genetic interactions between C57BL/6J and DBA/2 J alleles. Thus, many genomic regions from the parental strains are able to contribute to the host response and this effect depends strongly on the allele combinations in the respective QTLs. These observations may be studied further in double congenic mouse lines.

We subsequently analyzed the five QTL intervals, *Qivr2*-2, *Qivr5*, *Qivr16*, *Qivr17-2* and *Qivr19* in more detail to identify genes that may be causal for resistance or susceptibility. In total, 830 genes are located in these intervals. We narrowed down the total number of genes to 31 candidates (Table 2) by using additional information, such as temporal expression after PRM8 infection (Pommerenke et al., PLoS ONE, in press), cis-eQTLs in non-infected lungs [26], differences in expression between DBA/2J and C57BL/6J [23], and sequence variants in the coding regions.

Qivr5 contains the candidate gene *Eif2ak1* (eukaryotic translation initiation factor 2 alpha kinase 1) that is a member of eIF2alpha kinases which have been associated with anti-viral host responses [35]. Boon et al. described another eIF2alpha kinase, *Eif2ak2* / *Pkr* (eukaryotic translation initiation factor 2-alpha kinase 2), in the *Qirv17* locus after infection with influenza H5N1 [12]. *Eif2ak2* plays a critical role in modulating immunoglobulin expression during RSV infection. In addition *Eif2ak2* knockout mouse mutants are more susceptible to influenza infections [36,37]. We have initiated the generation of a

Table 1 Candidate genes in mapped QTL intervals

Qivr	Interval	Allele increasing survival	No of genes in interval	No of genes expressed during infection (up-/down- regulated)	No of genes with Indels (FS in coding region)	No of genes with SNPs (non-synonymous codons / stop codons)	Cis-eQTLs in non-infected lung	Differentially expressed btw B6/D2
2-2	56-68 Mb	D2	72	24 (19)	-	4 / 0	6	3
5	140-153 Mb	D2	179	83 (57)	-	9 / 0	13	10
16	64-78 Mb	B6	52	12 (7)	1[a]	5 / 0	4	4
17-2	30-44 Mb	B6	370	158 (104)	1[b]	58 / 4[c-f]	32	40
19	37– 45 Mb	D2	161	51 (30)	1[g]	14 / 1[h]	11	4

Up- or down-regulated genes were defined as genes that exhibited at least a 1.5 difference change in expression levels in lungs of infected mice compared to the non-infected controls. Genes were defined as differentially expressed exhibiting at least a 1.5 difference in expression changes in infected lungs of C57BL/6J and DBA/2J. Genes with sequence variations: [a]*Robo1*, [b]*Lst1*, [c]*Brd2*, [d]*H2-Ab1*, [e]*H2-Bl*, [f]*Rpp21*, [g]*Tctn3*, [h]*Dhdpsl*. Abbreviations: FS: frame shift in coding region, SNP: single nucleotide polymorphism, cis-eQTL: cis regulated expression QTL, B6: C57BL/6J, D2: DBA/2J.

congenic mouse lines for the chromosome 5 interval to verify and further characterize the effect of this region for resistance to influenza infection.

Qivr2-2 contains two candidate genes, *Itgb6* (integrin beta 6) and *Ifih1* (interferon induced with helicase C domain 1), with known functions in the host defense to viral infections. *Itgb6* mouse knock-out mutants exhibit severe pneumonia and an increase in granulocyte recruitment to the lung [38]. The protease-activated receptor 1-mediated enhancement of *Itgb6*-dependent TGF-beta activation has been proposed to represent one mechanism by which activation of the coagulation cascade contributes to the development of acute lung injury [39]. The *Ifih1* gene is also known as MDA5 (Melanoma Differentiation-Associated protein 5). IFIH1 is part of the RIG-I-like receptor (RLR) family, which function as pattern recognition receptors and are activated upon binding of virus dsRNA [40]. IFIH1 functions as cytosolic receptor that leads to the selective activation of type I IFN genes and is indispensable for sustained expression of IFN in response to paramyxovirus infection [41,42]. *Ifih1* mutant knock-out mice exhibit an impaired response to different viral pathogens [43,44].

Qivr16 contains two potential genes with known functions in the host defense and lung function, *Robo1* (roundabout homolog 1 (Drosophila)) and *Nrip1* (nuclear receptor interacting protein 1). DBA/2J mice carry a frame shift mutation in the *Robo1* gene which might lead to an impaired function of the encoded protein. *Robo1* has been described to be involved in guidance and migration of axons, myoblasts, and leukocytes in vertebrates (*e.g.* [45-47]*)* but is also expressed in the developing lung [48]. *Robo1* knock-out mutants exhibit a delayed lung maturation and bronchial hyperplasia. The latter results suggest that *Robo1* may be involved in maintaining proper lung function and it may become essential when lung epithelium is destroyed during an influenza infection. *Nrip1/Rip140* functions as a co-activator for cytokine gene promoter activity via direct protein-protein interactions with the NFkappaB subunit RelA and histone acetylase cAMP-responsive element binding protein (CREB)-binding protein (CBP) [49]. It is involved in modulating pro-inflammatory responses in macrophages [50].

Qivr17-2 represents a positive influence of the C57BL/6 J genotype on body weight, survival and MTTD. This QTL is located in a gene-rich region which carries many genes that are involved in the host immune response, in particular the *H2* histocompatibility genes which are involved in antigen presentation [51]. Therefore, many candidate genes are found in the *Qivr17-2* region. The *Lst1* (leukocyte specific transcript 1) gene is of special interest because the DBA/2J allele mice carries a single nucleotide deletion in the first exon resulting in a frame shift of the open reading frame. This mutation most likely results in a non-functional Lst1 protein in DBA/2 J mice. We confirmed the presence of the deletion by sequencing the parental DBA/2J and some BXD strains carrying the DBA/2J allele. The wild type allele was confirmed in C57BL/6J mice and in some BXD strains carrying the C57BL/6J allele. In humans, *LST1* plays a role in the regulation of the immune response to inflammatory diseases such as rheumatoid arthritis, microbial infection or Rubella vaccine-induced immunity [52-55]. Also, *Lst1* is up-regulated after influenza A infection in C57BL/6J mice starting at day 2 and exhibits a strong peak of expression at day 8 p.i. Pommerenke et al., 2012 (Pommerenke, C., E. Wilk, B. Srivastava, A. Schulze, N. Novoselova, R. Geffers, and K. Schughart. 2012. Global transcriptome analysis in influenza-infected mouse lungs reveals the kinetics of innate and adaptive host immune responses. PLoS ONE. 7:e41169.). Thus, the expression profile and known functions of *Lst1* fit well with a possible critical role for the host defense to influenza A virus. We initiated the generation of knock-out mice to evaluate the role of *Lst1* in more detail. In addition, a second, most interesting candidate, *Pla2g7* (phospholipase A2, group VII (platelet-activating factor acetylhydrolase, plasma)) was identified in the *Qivr17-2* interval. In

Table 2 GO-terms and functions observed in knock-out mice of 31 potential candidates from QTL intervals

Qivr	Gene symbol	Gene description	Function	KO phenotype	Type polymorphism in ORF
Qivr2-2	*Itgb6*	integrin beta 6	Integrin-mediated signaling pathway, inflammatory response, cell-matrix adhesion	Baldness associated with macrophage infiltration of skin, exaggerated pulmonary inflammation, impaired mucosal mast cell response to nematode infection.	ns (1)
Qivr2-2	*Ifih1*	interferon induced with helicase C domain 1	Response to virus, innate immune response, regulation of apoptosis, RIG-I-like receptor signaling pathway	Increased virus-associated morbidity and mortality, decreased cytokine response to several viral infection.	ns (5)
Qivr5	*Eif3b*	eukaryotic translation initiation factor 3, subunit B	Translation, translation initiation	NA	ns (1)
Qivr5	*Sdk1*	sidekick homolog 1 (chicken)	Cell adhesion	NA	ns (1)
Qivr5	*Eif2ak1*	eukaryotic translation initiation factor 2 alpha kinase 1	Negative regulation of translation, response to stress, negative regulation of cell proliferation, regulation of eIF2 alpha phosphorylation by heme	Enlarged heart size, abnormal red blood cell development, morphology, physiology with macrocytic anemia.	ns (1)
Qivr5	*Rnf6*	ring finger protein (C3H2C3 type) 6	Ubiquitin-dependent protein catabolic process, positive regulation of transcription, DNA-dependent	NA	ns (2)
Qivr16	*Robo1*	roundabout homolog 1 (Drosophila)	Cell differentiation, axon guidance, chemotaxis	Neonatal death, aphagia, delayed lung maturation and bronchial hyperplasia.	insertion
Qivr16	*Nrip1*	Nuclear receptor interaacting protein 1	Regulation of transcription	Female infertility due to ovulation failure. Male and female mice are smaller than wild-type littermates.	ns (1)
Qivr16	*Usp25*	ubiquitin specific peptidase 25	Ubiquitin-dependent protein catabolic process	NA	ns (1)
Qivr17-1	*Cryaa*	crystallin, alpha A	Negative regulation of apoptosis, negative regulation of caspase activity, lens fiber cell morphogenesis	Small lenses that develop progressive opacity beginning in the nucleus.	no
Qivr17-2	*Snf1lk/Sik1*	SNF1-like kinase	Negative regulation of transcription from RNA polymerase II promoter, regulation of cell differentiation, protein kinase cascade	NA	no
Qivr17-2	*March2*	membrane-associated ring finger (C3HC4) 2	Endocytosis, biological process	NA	no
Qivr17-2	*Tapbp*	TAP binding protein	Antigen processing and presentation of exogenous peptide antigen via MHC class I, TAP-dependent; defense response	Reduced and thermolabile MHC class I surface expression due to impaired peptide loading with stabilizing peptides, impaired T cell selection, altered NK repertoire, lower CD8+ T cell numbers, impaired responses to select class I-restricted antigens.	ns (1)
Qivr17-2	*H2-Oa*	histocompatibility 2, O region alpha locus	Antigen processing and presentation of peptide or polysaccharide antigen via MHC class II, regulation of T cell differentiation, Graft-versus-host disease, viral myocarditis	Abnormal antigen presentation via MHC class II, enhanced selection of CD4+ single positive thymocytes. Mice homozygous for a different knock-out allele show increased serum IgG1 levels.	ns (1)

Table 2 GO-terms and functions observed in knock-out mice of 31 potential candidates from QTL intervals *(Continued)*

Qivr17-2	*H2-DMa*	histocompatibility 2, class II, locus DMa	Antigen processing and presentation of exogenous peptide antigen via MHC class II, positive regulation of T cell differentiation, positive regulation of immune response, Graft-versus-host disease, viral myocarditis	Impaired antigen presenting cell function, poor IgG responses to T-dependent antigens, reduced numbers of mature CD4+ T cells, increased susceptibility to Leishmania major infection.	ns (2)
Qivr17-2	*Tap2*	transporter 2, ATP-binding cassette, sub-family B (MDR/TAP)	Antigen processing and presentation of exogenous protein antigen via MHC class Ib, TAP-dependent; positive regulation of T cell mediated cytotoxicity, protection from natural killer cell mediated cytotoxicity	No CD8+ T cells, although numbers of CD4+ T cells and B cells are normal.	ns (6)
Qivr17-2	*H2-Ob*	histocompatibility 2, O region beta locus	Antigen processing and presentation of peptide or polysaccharide antigen via MHC class II, Graft-versus-host disease, viral myocarditis	NA	ns (7)
Qivr17-2	*H2-Ab1*	histocompatibility 2, class II antigen A, beta 1	Antigen processing and presentation of peptide or polysaccharide antigen via MHC class II, Graft-versus-host disease, viral myocarditis	Depletion of mature CD4+ T cells, deficiency in cell-mediated immune responses, increased susceptibility to viral infections.	ns (9) stop_L
Qivr17-2	*H2-Aa*	histocompatibility 2, class II antigen A, alpha	Antigen processing and presentation of exogenous peptide antigen via MHC class II, positive regulation of T cell differentiation, Graft-versus-host disease, viral myocarditis	Lack of cell surface expression of MHC class II molecules on macrophages, decreased CD4-positive T cell number, increased CD8-positive T cell number, thymus hyperplasia, enlarged lymph nodes, altered splenocyte response to staphylococcal enterotoxin B.	ns (10)
Qivr17-2	*Lst1*	leukocyte specific transcript 1	Negative regulation of lymphocyte proliferation, immune response, cell morphogenesis	NA	ns (1) deletion
Qivr17-2	*Gtf2h4*	general transcription factor II H, polypeptide 4	Regulation of transcription, DNA-dependent	NA	ns (3)
Qivr17-2	*H2-T23*	histocompatibility 2, T region locus 23	Antigen processing and presentation of peptide antigen via MHC class I, Graft-versus-host disease, viral myocarditis	$CD4^+$ T cells have enhanced responses after infection or immunization, are resistant to suppressor activity mediated by a subset of $CD8^+$ T cells, but are more susceptible to NK cell lysis.	ns (3)
Qivr17-2	*H2-Bl*	histocompatibility 2, blastocyst	Antigen processing and presentation	NA	ns (4) stop_L
Qivr17-2	*Rpp21*	ribonuclease P 21 subunit (human)	tRNA processing	NA	ns (1) stop_G
Qivr17-2	*Trim26*	tripartite motif protein 26	Biological process	NA	ns (1)
Qivr17-2	*Pla2g7*	phospholipase A2, group VII (platelet-activating factor acetylhydrolase, plasma)	Inflammatory response, lipid catabolic process	NA	ns (1)
Qivr17-2	*Cyp39a1*	cytochrome P450, family 39, subfamily a, polypeptide 1	Lipid metabolic process, oxidation reduction	NA	ns (2)
Qivr-19	*Sorbs1*	sorbin and SH3 domain containing 1	Transport, focal adhesion assembly, positive regulation of establishment of protein localization in plasma membrane	Decreased triglyceride levels, altered glucose homeostasis, decreased white blood cells and resistance to developing glucose intolerance induced by a high fat diet.	ns (6)
Qivr-19	*Tctn3*	tectonic family member 3	Apoptosis	NA	ns (1) insertion (2)

Table 2 GO-terms and functions observed in knock-out mice of 31 potential candidates from QTL intervals *(Continued)*

Qivr-19	*Hps1*	Hermansky-Pudlak syndrome 1 homolog (human)	Positive regulation of natural killer cell activation, secretion of lysosomal enzymes	Hypopigmentation and increased bleeding time. Impaired natural killer cell function, reduced secretion of kidney lysosomal enzymes, abnormal retinofugal neuronal projections characterize some alleles.	ns (6)
Qivr-19	*Dnmbp*	dynamin binding protein	Intracellular signaling cascade, regulation of Rho protein signal transduction	NA	ns (3)

The genotype of C57BL/6J was used as reference for the sequence polymorphisms. The knockout mutant phenotype was identified in the MGI Mouse Genome Database. Gene *Fign* (fidgetin) fulfilled most criteria but was found to be expressed only at late times p.i. (after day 14) and was therefore omitted from the candidate gene list. Abbreviations: KO: knockout mutant, NA: not analyzed, SNP: single nucleotide polymorphism, ns: non-synonymous codons, ORF: open reading frame, stop_G: stop codon gained, stop_L: stop codon lost.

humans, increased activities of certain variants of PLA2G7 were associated with early coronary atherosclerosis and with endothelial dysfunction, but the gene may also exert an anti-inflammatory function [56-60]. The *Pla2g7* gene was also identified as a potential candidate gene for susceptibility against infections with H3N2 influenza virus [33]. *Pla2g7* expression levels in susceptible A/J mice were higher than in resistant C57BL/6J mice after infection with H3N2 virus [33]. We also showed previously that *Pla2g7* exhibits a cis-eQTL between C57BL/6J and DBA/2J in non-infected lungs where the DBA/2J allele shows high levels of expression [26]. *Tnfrsf21* which was identified by [33] as potential candidate of *Qivr17-2* also exhibits a cis-eQTL in non-infected BXD mice [26] but was not found to be regulated in C57BL/6 mice after infection (data not published). *Tapbp* (TAP binding protein) plays a major role in the antigen processing and MHC class I presentation by stabilizing the TAP peptide transporter, *e.g.* [61-65]. Also, *Tap2* (transporter 2, ATP-binding cassette, sub-family B (MDR/TAP)) gene is involved in antigen processing and presentation [63,66]. *Gtf2h4* (general transcription factor II H, polypeptide 4) encodes a general transcription factor. Recruitment and activation of *Gtf2h4* represents a rate-limiting step for the emergence of HIV from latency and sequence variants have been associated with multiple sclerosis [67-69].

Within the *Qivr19* interval, only one gene, *Hps1* (Hermansky-Pudlak syndrome 1 homolog (human)), has been associated with the host responses to infection. Mice carrying a natural mutation in the *Hps1* gene showed an increased inflammatory response in alveolar macrophages after intranasal challenge with LPS [70].

The GeneNetwork database allows searching for other phenotypic traits that exhibit a genome-wide significant (LRS ≥ 18) within the *Qivr* intervals identified by our study. Two phenotypic traits, related to neuronal responses (trait ID 11285) and body weight changes (trait ID 12838), are located to the *Qivr16* locus. Also, the Qivr17-2 interval contained significant QTLs for other traits. Two traits are related to host infectious diseases, 'Ectromelia virus survival' (ID 12672) and 'Chlamydia psittaci (6BC) infection response' (ID 11025) and four traits are associated with immune cell responses (ID 10201, 10466, 10238, 10236). In addition two traits described seizure responses (ID 10388, 10507), and one trait has not been disclosed yet (ID 13920). Within the early time chromosome 10 interval, three other traits exhibit their most significant QTLs: '3a,5a-THDOC in blood plasma 3 days after cycle 5 of chronic intermittent air vapor' (ID13027) and two non-disclosed traits. The first trait may relate to stress responses in the central nervous system (ID 13292 and 13846).

Conclusions

The mapping of resistance and susceptibility loci in the BXD population revealed several new QTLs and potential gene candidates that may be critical for the host defense against influenza A virus infection. Body weight and survival QTLs showed a time-dependent profile indicating that the genetic factors in these QTLs are important for the host response in a temporal dynamic fashion. Five QTL regions were examined in detail, and we identified several possible candidate genes that may be critical for the host response to influenza A infections in humans.

Methods

Animals

The mouse inbred strains C57BL/6J, DBA/2J and B6D2F1 were delivered from Janvier, France. Recombinant inbred mouse strains BXD were purchased from three different sources: The Jackson Laboratory, the University of Tennessee Health Science Center (Memphis, TN) and from Harlan, The Netherlands. For the analysis, mice were transferred to the animal facility in Braunschweig and adapted for at least two weeks to the new environment before starting experiments. Animals were maintained under specific pathogen free conditions. All experiments in mice were approved by an external committee and according to the national guidelines of the animal welfare law in Germany

('Tierschutzgesetz in der Fassung der Bekanntmachung vom 18. Mai 2006 (BGBl. I S. 1206, 1313), das zuletzt durch Artikel 20 des Gesetzes vom 9. Dezember 2010 (BGBl. I S. 1934) geändert worden ist.'). The protocol used in these experiments has been reviewed by an ethics committee and approved by the 'Niedersächsisches Landesamt für Verbraucherschutz und Lebensmittelsicherheit, Oldenburg, Germany', according to the German animal welfare law (Permit Numbers: 33.42502/04-108/06, 33.9.42502-04-051/09).

Virus and infection of mice

The mouse-adapted influenza strain A/Puerto Rico/8/34 (H1N1; PR8M, [18] and references therein) was used for all infection studies. Stocks were prepared by infection of 10-day-old embryonated chicken eggs. After mice were anesthetized by intra-peritoneal injection of Ketamin-Xylazine solution in sterile NaCl (50 mg/ml Ketamine, Invesa Arzneimittel GmbH, Freiburg; 2% Xylazine, Bayer Health-Care, Leverkusen) with a dose adjusted to the individual body weight, mice were infected intranasally with 2×10^3 FFU of PR8M in 20 μl of sterile phosphate-buffered saline. Mice were assayed daily for body weight (determined as % of initial weight at day 0) and mortality during 13 days p.i. We used death as the end point for survival. Mice were sacrificed if body weight loss exceeded 25%. It should be noted that for mice that did not show any signs of body weight loss over the entire time period after infection, we do not have additional parameters to verify that they have indeed been infected. However, these cases were very few. In addition, we have ample experience with this infection method and the failure rate, for example with the DBA/2J strain, is less that 5%.

Data handling and statistical analysis

In total, 283 BXD mice and 127 mice from the parental strains or F1 generation were used for the infection experiments. In total 53 BXD strains were infected with an average of 5 mice per strain. We performed all primary calculations using simple features and functions of Microsoft Excel. Three sets of analysis were performed for the following variables: (1) body weight in percentage from starting weight (day 0) using the strain medians to exclude outliers; (2) survival by calculating the survival rate of each strain from day 7 to 13, (3) mean time to death in days. For statistical analyses, tests and visualization we used R, a free software environment for statistical computing and graphics (http://www.R-project.org). In order to test for batch effects or other co-factors, we visualized the data using multidimensional scaling based on the Sammon mapping method [71]. No clusters with respect to any of the co-factors age, weight at day 0, experimenter, time of infection, or source of mice could be found in the visualizations.

QTL mapping

QTL mapping was performed using the web-based complex trait analysis available on the GeneNetwork website (www.genenetwork.org) and the mapping module to analyze phenotypes in context of mouse genotypic differences. Interval mapping evaluates potential QTLs at regular intervals and estimates the significance at each location with a graphical representation of the likelihood ratio statistics (LRS) using 2000 permutation tests [19,22]. LRS values may be converted to LOD scores by dividing by 4.61. For the two locus model the following equation was used: $Var = Q1 + Q2 + Q1xQ2 + e$, where Var = the between-strain mean variance in the trait, $Q1$ and $Q2$ are makers tightly linked to the loci, $Q1XQ2$ is the 'additive-by-additive' epistatic interaction term, and e is the residual error. The original data sets can be obtained at www.genenetwork.org with the following identification numbers: body weight: 13005 to 13017; survival: 13000 to 13004 and mean time to death: 12996. We performed full genome scans for epistatic interactions using the pair-scan module that is implemented in GeneNetwork. This module exploits the direct global optimization algorithm developed by [72]. The code compares the fit (as measured by LRS scores) for a purely additive model, a purely epistatic model, and the full model. The code also implements a permutation test (n = 500) and this enabled us to estimate the empirical p value of the alternative models.

Candidate gene discovery

The QTL region analysis was initially performed using the QTLminer which has been implemented in GeneNetwork [25]. By using the automatic function of GeneNetwork we identified significant cis-QTLs with LRS higher than 18 at a genome-wide p-value of < 0.05. Additionally the genes mapped within the analyzed QTLs were surveyed by the National Center for Biotechnology Information (NCBI) Entrez Gene website (http://www.ncbi.nlm.nih.gov/sites/entrez?db=gene) and the Jackson Laboratory's MGI Mouse Genome Database project (http://www.informatics.jax.org/) to identify potential candidate genes. The GeneRIF database (http://www.ncbi.nlm.nih.gov/projects/GeneRIF/GeneRIFhelp.html) was used as a primary source to search for known gene functions and corresponding citations.

All sequence variants between B6 and D2 parental genomes (SNPs, indels) were extracted by using a comparative analysis that relies on approximately 100x whole genome shot gun of DBA/2J [73]. All of these sequence data are available at http://ucscbrowser.genenetwork.org/, the GeneNetwork Variant Browser (http://www.genenetwork.org/webqtl/main.py?FormID=snpBrowser), and the NCBI Short Read Archive (18 files

total, e.g., SRX037575, SRX013980, SRX013299, SRX012582, SRX012581, SRX012580); http://www.biomedcentral.com/1471-2105/11/S4/O7.

Additional files

Additional file 1: Table S1. Body weight loss from day 1 until day 7 for all strains showing the mean values, SEM per day and number of mice per strain analyzed.

Additional file 2: Figure S1. Differential susceptibility to influenza A infection among different BXD strains, parental strains and F1 generation. Rank-ordered strain distribution pattern illustrating the percentage of surviving mice per strain after influenza A infection for 53 BXD, parental DBA/2J and C57BL/6J strains and F1 (B6D2F1) mice for day 7 (A, trait ID: 13001) and day 8 (B, trait ID: 13002). Rank-ordered strain distribution pattern showing mean time to death for 53 BXD, parental DBA/2J and C57BL/6J strains and F1 (B6D2F1) mice (C, trait ID: 12996).

Additional file 3: Figure S2. Principal component analysis of all body weight traits. Percent contribution of principal components to the total variance for body weight traits from day 1 until day 7 p.i. PC1 contributes about 80% and PC2 about 10% to the total variance.

Additional file 4: Figure S3. Body weight changes in mock-infected C57BL/6J and DBA/2J mice. Female DBA/2J (n=4) and C57BL/6J (n=3) mice were intranasally inoculated with 25 μl PBS under anesthesia. Body weight changes for each group of treated mice at various days p.i. is shown with reference to the starting weight (% body weight). Data represent mean values +/- SEM.

Additional file 5: Figure S4. Genome-wide linkage analysis for survival after H1N1 infection at days 9 and 10 p.i. Analysis of survival from day 9 (A) and day 10 (B) after PR8 infection revealed suggestive QTLs on chromosomes 5, 16, 17 and 19. Interval mapping is shown across the entire genome as blue line representing the LRS scores; green line: DBA/2J alleles increase trait values; red line: C57BL/6J alleles increase trait values. Upper x-axis shows mouse chromosomes, lower x-axis shows physical map in mega bases for each chromosome, y-axis represents LRS score. The horizontal lines mark the genome-wide significant thresholds at p0.05 (red line) and suggestive thresholds at p0.37 (gray line).

Additional file 6: Figure S5. Pair Scan analysis of trait 13002. The table provides the breakdown of trait 13002 as an example for a pair scan analysis study that compares the fit of the alternative models. An analysis of this type can be regenerated rapidly on any of the traits presented in our manuscript.

Additional file 7: Figure S6. Scheme to identify potential candidate genes in the analyzed QTL intervals. The detailed steps are described in the main manuscript.

Additional file 8: Table S2. List of genes in the QTL intervals that were studied in detail. The QTLminer tool in GeneNetwork was to identify all genes in the QTL intervals and to obtain associated GO terms and KEGG pathways. All annotated genes within the QTL intervals that were expressed between day 1 and day 60 after infection of C57BL/6J mice with PR8M virus were further analyzed for the following attributes: genes that were up- or down-regulated in infected lungs after PR8M infection, genes carrying an insertion or deletion or a non-synonymous nucleotide change in the open reading frame, genes exhibiting a cis-expression QTL in the lung, and genes that were differentially expressed in C57BL/6J and DBA/2J mice in infected lungs between day 1 and day 8 p.i.
Abbreviations: FS: frame shift in coding region, SNP: single nucleotide polymorphism, cis-eQTL: cis-regulated expression QTL, B6: C57BL/6J, D2: DBA/2J, ns: non-synonymous codons, stop_G: stop codon gained, stop_L: stop codon lost, DEL: deletion, INS: insertion; ns (. . .): number of non-synonymous codons. Legends: Expression d0-d60, log2 ≥8 at any day during infection; No: log2 8; ?: no expression data available. Regulation during infection (d0-d60): + - up or down regulation, genes that exhibited at least a 2-fold difference in changes of the expression levels in lungs of infected mice compared to non-infected controls; (+)(-): up-or down-regulation, genes that exhibited at least a 1.5-fold difference in changes of the expression levels in lungs of infected mice compared to the non-infected controls; no: no regulation. SNP: ns (..) number of non-synonymous codons; STOP_L: Stop codon lost, STOP_G: Stop codon gained; no: no SNPs between B6 and D2. Indel: DEL: Deletion; INS: Insertion; no: no INDEL. cisQTL: yes (. . .): LRS value has to be greater than ≥18; no: no QTL or LRS 18. diff expressed (B6-D2) during infection: Genes were defined as differentially expressed (log2 ≥8) at any day in infected lungs of C57BL/6J and DBA/2J; + -: Genes were defined as differentially expressed exhibiting at least a 2.0 difference in changes of the expression levels in infected lungs of C57BL/6J and DBA/2J; (+)(-) differentially expressed: Genes were defined as differentially expressed exhibiting at least a 1.5 difference in changes of the expression levels in infected lungs of C57BL/6J and DBA/2J; no: no regulation or not expressed; Score: the different attributes were counted.

Competing interests
The authors declare that they have no competing interests.

Authors' contributions
TN, MH and KS conceived and designed the experiments. TN and MH infected the mice and collected the data. HK, RA, RW and KS performed and interpreted the QTL analysis. FK performed the analysis of environmental and experimental factors. SS and LL provided BXD mice for experimental studies. HK, RW and KS wrote the manuscript. All authors read and approved the final manuscript.

Authors' information
Tatiana Nedelko and Heike Kollmus contributed equally as first authors. Robert W. Williams and Klaus Schughart contributed equally as senior authors.

Acknowledgments
This work was supported by intra-mural grants from the Helmholtz-Association (Program Infection and Immunity) and a research grant FluResearchNet (No. 01KI07137) from the German Ministry of Education and Research to KS and the virtual institute 'GeNeSys' funded by the Helmholtz Association. The funders have no role in study design, data collection and analysis, decision to publish, or preparation of the manuscript. Mice for these experiments were maintained by the animal caretakers of the Central Animal Facilities at the HZI. We wish to thank Christin Fricke for excellent technical assistance.

Author details
[1]Department of Infection Genetics, Helmholtz Centre for Infection Research and University of Veterinary Medicine Hannover, 38124, Braunschweig, Germany. [2]Department of Bioinformatics and Statistics, Helmholtz Centre for Infection Research, Braunschweig, Germany. [3]Department of Computer Science, Ostfalia University of Applied Sciences, Wolfenbüttel, Germany. [4]Department of Anatomy and Neurobiology, University of Tennessee Health Science Center, Memphis, Tennessee, United States of America. [5]Department of Molecular and Cellular Neurobiology, Neuroscience Campus Amsterdam, Amsterdam, VU, the Netherlands. [6]Jiangsu Key Laboratory of Neuroregeneration, Nantong University, Nantong, China. [7]Nycomed GmbH, Institute for Pharmacology and Preclinical Drug Safety, Barsbuettel-Willinghusen, Germany.

Received: 10 April 2012 Accepted: 10 August 2012
Published: 20 August 2012

References
1. Johnson NP, Mueller J: **Updating the accounts: global mortality of the 1918–1920 "Spanish" influenza pandemic.** *Bull Hist Med* 2002, **76**(1):105–115.
2. Fauci AS: **Seasonal and pandemic influenza preparedness: science and countermeasures.** *J Infect Dis* 2006, **194**(Suppl 2):S73–76.
3. Scriven J, McEwen R, Mistry S, Green C, Osman H, Bailey M, Ellis C: **Swine flu: a Birmingham experience.** *Clin Med* 2009, **9**(6):534–538.
4. Yates L, Pierce M, Stephens S, Mill A, Spark P, Kurinczuk J, Valappil M, Brocklehurst P, Thomas S, Knight M: **Influenza A/H1N1v in pregnancy: an investigation of the characteristics and management of affected women**

and the relationship to pregnancy outcomes for mother and infant. *Health Technol Assess* 2010, **14**(34):109–182.
5. Albright FS, Orlando P, Pavia AT, Jackson GG, Cannon-Albright LA: **Evidence for a heritable predisposition to death due to influenza.** *J Infect Dis* 2008, **197**(1):18–24.
6. Gottfredsson M, Halldorsson BV, Jonsson S, Kristjansson M, Kristjansson K, Kristinsson KG, Love A, Blondal T, Viboud C, Thorvaldsson S, *et al*: **Lessons from the past: familial aggregation analysis of fatal pandemic influenza (Spanish flu) in Iceland in 1918.** *Proc Natl Acad Sci U S A* 2008, **105**(4):1303–1308.
7. Horby P, Sudoyo H, Viprakasit V, Fox A, Thai PQ, Yu H, Davila S, Hibberd M, Dunstan SJ, Monteerarat Y, *et al*: **What is the evidence of a role for host genetics in susceptibility to influenza A/H5N1?** *Epidemiol Infect* 2010, **138**(11):1–9.
8. Everitt AR, Clare S, Pertel T, John SP, Wash RS, Smith SE, Chin CR, Feeley EM, Sims JS, Adams DJ, *et al*: **IFITM3 restricts the morbidity and mortality associated with influenza.** *Nature* 2012, **484**(7395):519–523.
9. Srivastava B, Blazejewska P, Hessmann M, Bruder D, Geffers R, Mauel S, Gruber AD, Schughart K: **Host genetic background strongly influences the response to influenza a virus infections.** *PLoS ONE* 2009, **4**(3):e4857.
10. Trammell RA, Toth LA: **Genetic susceptibility and resistance to influenza infection and disease in humans and mice.** *Expert Rev Mol Diagn* 2008, **8**(4):515–529.
11. Ding M, Lu L, Toth LA: **Gene expression in lung and basal forebrain during influenza infection in mice.** *Genes Brain Behav* 2008, **7**(2):173–183.
12. Boon AC, DeBeauchamp J, Hollmann A, Luke J, Kotb M, Rowe S, Finkelstein D, Neale G, Lu L, Williams RW, *et al*: **Host genetic variation affects resistance to infection with a highly pathogenic H5N1 influenza A virus in mice.** *J Virol* 2009, **83**(20):10417–10426.
13. Boon AC, Debeauchamp J, Krauss S, Rubrum A, Webb AD, Webster RG, McElhaney J, Webby RJ: **Cross-reactive neutralizing antibodies directed against pandemic H1N1 2009 virus are protective in a highly sensitive DBA/2 influenza mouse model.** *J Virol* 2010, **84**(15):7662–7667.
14. Otte A, Sauter M, Alleva L, Baumgarte S, Klingel K, Gabriel G: **Differential host determinants contribute to the pathogenesis of 2009 pandemic H1N1 and human H5N1 influenza A viruses in experimental mouse models.** *Am J Pathol* 2011, **179**(1):230–239.
15. Boon AC, Finkelstein D, Zheng M, Liao G, Allard J, Klumpp K, Webster R, Peltz G, Webby RJ: **H5N1 influenza virus pathogenesis in genetically diverse mice is mediated at the level of viral load.** *MBio* 2011, **2**(5):pii: e00171–11.
16. Trammell RA: *Liberati TA*. Toth LA: Host genetic background and the innate inflammatory response of lung to influenza virus. Microbes Infect; 2011.
17. Pica N, Iyer A, Ramos I, Bouvier NM, Fernandez-Sesma A, Garcia-Sastre A, Lowen AC, Palese P, Steel J: **The DBA.2 mouse is susceptible to disease following infection with a broad, but limited, range of influenza A and B viruses.** *J Virol* 2011, **85**(23):5–12829.
18. Blazejewska P, Koscinski L, Viegas N, Anhlan D, Ludwig S, Schughart K: **Pathogenicity of different PR8 influenza A virus variants in mice is determined by both viral and host factors.** *Virology* 2011, **412**(1):36–45.
19. Peirce JL, Lu L, Gu J, Silver LM, Williams RW: **A new set of BXD recombinant inbred lines from advanced intercross populations in mice.** *BMC Genet* 2004, **5**:7.
20. Taylor BA, Wnek C, Kotlus BS, Roeme RN, MacTaggart T, Phillips SJ: **Genotyping new BXD recombinant inbred mouse strains and comparison of BXD and consensus maps.** *Mamm Genome* 1999, **10**(4):335–348.
21. Williams RW, Gu J, Qi S, Lu L: **The genetic structure of recombinant inbred mice: high-resolution consensus maps for complex trait analysis.** *Genome Biol* 2001, **2**(11):RESEARCH0046.
22. Chesler EJ, Lu L, Wang J, Williams RW, Manly KF: **WebQTL: rapid exploratory analysis of gene expression and genetic networks for brain and behavior.** *Nat Neurosci* 2004, **7**(5):485–486.
23. Alberts R, Srivastava B, Wu H, Viegas N, Geffers R, Klawonn F, Novoselova N, Do Valle TZ, Panthier JJ, Schughart K: **Gene expression changes in the host response between resistant and susceptible inbred mouse strains after influenza A infection.** *Microbes Infect* 2010, **12**(4):309–318.
24. Ziebarth JD, Cook MN, Wang X, Williams RW, Lu L, Cui Y: **Treatment- and population-dependent activity patterns of behavioral and expression QTLs.** *PLoS ONE* 2012, **7**(2):e31805.
25. Alberts R, Schughart K: **QTLminer: identifying genes regulating quantitative traits.** *BMC Bioinformatics* 2010, **11**:516.
26. Alberts R, Lu L, Williams RW, Schughart K: **Genome-wide analysis of the mouse lung transcriptome reveals novel molecular gene interaction networks and cell-specific expression signatures.** *Respir Res* 2011, **12**:61.
27. Zhirnov OP, Matrosovich TY, Matrosovich MN, Klenk HD: **Aprotinin, a protease inhibitor, suppresses proteolytic activation of pandemic H1N1v influenza virus.** *Antivir Chem Chemother* 2011, **21**(4):169–174.
28. Okumura Y, Takahashi E, Yano M, Ohuchi M, Daidoji T, Nakaya T, Bottcher E, Garten W, Klenk HD, Kido H: **Novel type II transmembrane serine proteases, MSPL and TMPRSS13, proteolytically activate membrane fusion activity of hemagglutinin of highly pathogenic avian influenza viruses and induce their multicycle replication.** *J Viro* 2010, **84**(10):5089–5096.
29. Bottcher-Friebertshauser E, Freuer C, Sielaff F, Schmidt S, Eickmann M, Uhlendorff J, Steinmetzer T, Klenk HD, Garten W: **Cleavage of influenza virus hemagglutinin by airway proteases TMPRSS2 and HAT differs in subcellular localization and susceptibility to protease inhibitors.** *J Virol* 2010, **84**(11):5605–5614.
30. Bertram S, Glowacka I, Blazejewska P, Soilleux E, Allen P, Danisch S, Steffen I, Choi SY, Park Y, Schneider H, *et al*: **TMPRSS2 and TMPRSS4 facilitate trypsin-independent spread of influenza virus in Caco-2 cells.** *J Virol* 2010, **84**(19):10016–10025.
31. Chaipan C, Kobasa D, Bertram S, Glowacka I, Steffen I, Tsegaye TS, Takeda M, Bugge TH, Kim S, Park Y, *et al*: **Proteolytic activation of the 1918 influenza virus hemagglutinin.** *J Virol* 2009, **83**(7):3200–3211.
32. Steinhauer DA: **Role of hemagglutinin cleavage for the pathogenicity of influenza virus.** *Virology* 1999, **258**(1):1–20.
33. Boivin GA, Pothlichet J, Skamene E, Brown EG, Loredo-Osti JC, Sladek R, Vidal SM: **Mapping of clinical and expression quantitative trait loci in a sex-dependent effect of host susceptibility to mouse-adapted influenza H3N2/HK/1/68.** *J Immunol* 2012, .
34. Bottomly D, Ferris MT, Aicher LD, Rosenzweig E, Whitmore A, Aylor DL, Haagmans BL, Gralinski LE, Bradel-Tretheway BG, Bryan JT, *et al*: **Expression quantitative trait Loci for extreme host response to influenza a in pre-collaborative cross mice.** *G3 (Bethesda)* 2012, **2**(2):213–221.
35. Krishnamoorthy J, Mounir Z, Raven JF, Koromilas AE: **The eIF2alpha kinases inhibit vesicular stomatitis virus replication independently of eIF2alpha phosphorylation.** *Cell Cycle* 2008, **7**(15):2346–2351.
36. Thakur SA, Zalinger Z, Johnson TR, Imani F: **PKR is a novel mediator of CD40 signaling and plays a critical role in modulating immunoglobulin expression during RSV infection.** *Clin Vaccine Immunol* 2011, **18**(12):2060–2066.
37. Bergmann M, Garcia-Sastre A, Carnero E, Pehamberger H, Wolff K, Palese P, Muster T: **Influenza virus NS1 protein counteracts PKR-mediated inhibition of replication.** *J Virol* 2000, **74**(13):6203–6206.
38. Ludlow A, Yee KO, Lipman R, Bronson R, Weinreb P, Huang X, Sheppard D, Lawler J: **Characterization of integrin beta6 and thrombospondin-1 double-null mice.** *J Cell Mol Med* 2005, **9**(2):421–437.
39. Hogmalm A, Sheppard D, Lappalainen U, Bry K: **beta6 Integrin subunit deficiency alleviates lung injury in a mouse model of bronchopulmonary dysplasia.** *Am J Respir Cell Mol Biol* 2010, **43**(1):88–98.
40. Yoneyama M, Kikuchi M, Matsumoto K, Imaizumi T, Miyagishi M, Taira K, Foy E, Loo YM, Gale M Jr, Akira S, *et al*: **Shared and unique functions of the DExD/H-box helicases RIG-I, MDA5, and LGP2 in antiviral innate immunity.** *J Immunol* 2005, **175**(5):2851–2858.
41. Choi MK, Wang Z, Ban T, Yanai H, Lu Y, Koshiba R, Nakaima Y, Hangai S, Savitsky D, Nakasato M, *et al*: **A selective contribution of the RIG-I-like receptor pathway to type I interferon responses activated by cytosolic DNA.** *Proc Natl Acad Sci U S A* 2009, **106**(42):17870–17875.
42. Gitlin L, Benoit L, Song C, Cella M, Gilfillan S, Holtzman MJ, Colonna M: **Melanoma differentiation-associated gene 5 (MDA5) is involved in the innate immune response to Paramyxoviridae infection in vivo.** *PLoS Pathog* 2010, **6**(1):e1000734.
43. Gitlin L, Barchet W, Gilfillan S, Cella M, Beutler B, Flavell RA, Diamond MS, Colonna M: **Essential role of mda-5 in type I IFN responses to polyriboinosinic:polyribocytidylic acid and encephalomyocarditis picornavirus.** *Proc Natl Acad Sci U S A* 2006, **103**(22):8459–8464.
44. Kato H, Takeuchi O, Sato S, Yoneyama M, Yamamoto M, Matsui K,

Uematsu S, Jung A, Kawai T, Ishii KJ, *et al*: **Differential roles of MDA5 and RIG-I helicases in the recognition of RNA viruses.** *Nature* 2006, **441**(7089):101–105.
45. Andrews W, Barber M, Hernadez-Miranda LR, Xian J, Rakic S, Sundaresan V, Rabbitts TH, Pannell R, Rabbitts P, Thompson H, *et al*: **The role of Slit-Robo signaling in the generation, migration and morphological differentiation of cortical interneurons.** *Dev Biol* 2008, **313**(2):648–658.
46. Long H, Sabatier C, Ma L, Plump A, Yuan W, Ornitz DM, Tamada A, Murakami F, Goodman CS, Tessier-Lavigne M: **Conserved roles for Slit and Robo proteins in midline commissural axon guidance.** *Neuron* 2004, **42**(2):213–223.
47. Xian J, Clark KJ, Fordham R, Pannell R, Rabbitts TH, Rabbitts PH: **Inadequate lung development and bronchial hyperplasia in mice with a targeted deletion in the Dutt1/Robo1 gene.** *Proc Natl Acad Sci U S A* 2001, **98**(26):15062–15066.
48. Clark K, Hammond E, Rabbitts P: **Temporal and spatial expression of two isoforms of the Dutt1/Robo1 gene in mouse development.** *FEBS Lett* 2002, **523**(1–3):12–16.
49. Zschiedrich I, Hardeland U, Krones-Herzig A, Berriel Diaz M, Vegiopoulos A, Muggenburg J, Sombroek D, Hofmann TG, Zawatzky R, Yu X, *et al*: **Coactivator function of RIP140 for NFkappaB/RelA-dependent cytokine gene expression.** *Blood* 2008, **112**(2):264–276.
50. Ho PC, Chang KC, Chuang YS, Wei LN: **Cholesterol regulation of receptor-interacting protein 140 via microRNA-33 in inflammatory cytokine production.** *FASEB J* 2011, **25**(5):1758–1766.
51. Janeway CA, Travers P, Walport MJ, Shlomchik MJ: *Immunobiology: The Immune System in Health and Disease*. New York: Garland Science; 2005.
52. Ovsyannikova IG, Vierkant RA, Pankratz VS, Jacobson RM, Poland GA: **Extended LTA, TNF, LST1 and HLA gene haplotypes and their association with rubella vaccine-induced immunity.** *PLoS ONE* 2010, **5**(7):e11806.
53. Schiller C, Nitschke MJ, Seidl A, Kremmer E, Weiss EH: **Rat monoclonal antibodies specific for LST1 proteins.** *Hybridoma (Larchmt)* 2009, **28**(4):281–286.
54. Mulcahy H, O'Rourke KP, Adams C, Molloy MG, O'Gara F: **LST1 and NCR3 expression in autoimmune inflammation and in response to IFN-gamma, LPS and microbial infection.** *Immunogenetics* 2006, **57**(12):893–903.
55. Kilding R, Iles MM, Timms JM, Worthington J, Wilson AG: **Additional genetic susceptibility for rheumatoid arthritis telomeric of the DRB1 locus.** *Arthritis Rheum* 2004, **50**(3):763–769.
56. Lavi S, McConnell JP, Rihal CS, Prasad A, Mathew V, Lerman LO, Lerman A: **Local production of lipoprotein-associated phospholipase A2 and lysophosphatidylcholine in the coronary circulation: association with early coronary atherosclerosis and endothelial dysfunction in humans.** *Circulation* 2007, **115**(21):2715–2721.
57. Kim JY, Hyun YJ, Jang Y, Lee BK, Chae JS, Kim SE, Yeo HY, Jeong TS, Jeon DW, Lee JH: **Lipoprotein-associated phospholipase A2 activity is associated with coronary artery disease and markers of oxidative stress: a case–control study.** *Am J Clin Nutr* 2008, **88**(3):630–637.
58. Kostopanagiotou G, Avgerinos E, Costopanagiotou C, Arkadopoulos N, Andreadou I, Diamantopoulou K, Lekka M, Smyrniotis V, Nakos G: **Acute lung injury in a rat model of intestinal ischemia-reperfusion: the potential time depended role of phospholipases A(2).** *J Surg Res* 2008, **147**(1):108–116.
59. Sutton BS, Crosslin DR, Shah SH, Nelson SC, Bassil A, Hale AB, Haynes C, Goldschmidt-Clermont PJ, Vance JM, Seo D, *et al*: **Comprehensive genetic analysis of the platelet activating factor acetylhydrolase (PLA2G7) gene and cardiovascular disease in case–control and family datasets.** *Hum Mol Genet* 2008, **17**(9):1318–1328.
60. Wang Q, Hao Y, Mo X, Wang L, Lu X, Huang J, Cao J, Li H, Gu D: **PLA2G7 gene polymorphisms and coronary heart disease risk: a meta-analysis.** *Thromb Res* 2010, **126**(6):498–503.
61. Sadegh-Nasseri S, Chen M, Narayan K, Bouvier M: **The convergent roles of tapasin and HLA-DM in antigen presentation.** *Trends Immunol* 2008, **29**(3):141–147.
62. Turnquist HR, Petersen JL, Vargas SE, McIlhaney MM, Bedows E, Mayer WE, Grandea AG 3rd, Van Kaer L, Solheim JC: **The Ig-like domain of tapasin influences intermolecular interactions.** *J Immunol* 2004, **172**(5):2976–2984.
63. Garbi N, Tiwari N, Momburg F, Hammerling GJ: **A major role for tapasin as a stabilizer of the TAP peptide transporter and consequences for MHC class I expression.** *Eur J Immunol* 2003, **33**(1):264–273.
64. Williams AP, Peh CA, Purcell AW, McCluskey J, Elliott T: **Optimization of the MHC class I peptide cargo is dependent on tapasin.** *Immunity* 2002, **16**(4):509–520.
65. Raghuraman G, Lapinski PE, Raghavan M: **Tapasin interacts with the membrane-spanning domains of both TAP subunits and enhances the structural stability of TAP1 x TAP2 Complexes.** *J Biol Chem* 2002, **277**(44):41786–41794.
66. Rufer E, Leonhardt RM, Knittler MR: **Molecular architecture of the TAP-associated MHC class I peptide-loading complex.** *J Immunol* 2007, **179**(9):5717–5727.
67. Fukuda A, Tokonabe S, Hamada M, Matsumoto M, Tsukui T, Nogi Y, Hisatake K: **Alleviation of PC4-mediated transcriptional repression by the ERCC3 helicase activity of general transcription factor TFIIH.** *J Biol Chem* 2003, **278**(17):14827–14831.
68. Kim YK, Bourgeois CF, Pearson R, Tyagi M, West MJ, Wong J, Wu SY, Chiang CM, Karn J: **Recruitment of TFIIH to the HIV LTR is a rate-limiting step in the emergence of HIV from latency.** *EMBO J* 2006, **25**(15):3596–3604.
69. Briggs FB, Goldstein BA, McCauley JL, Zuvich RL, De Jager PL, Rioux JD, Ivinson AJ, Compston A, Hafler DA, Hauser SL, *et al*: **Variation within DNA repair pathway genes and risk of multiple sclerosis.** *Am J Epidemiol* 2010, **172**(2):217–224.
70. Young LR, Borchers MT, Allen HL, Gibbons RS, McCormack FX: **Lung-restricted macrophage activation in the pearl mouse model of Hermansky-Pudlak syndrome.** *J Immunol* 2006, **176**(7):4361–4368.
71. Sammon JW: **A nonlinear mapping for data structure analysis.** *IEEE Transactions on Computers* 1969, **18**:401–409.
72. Ljungberg K, Holmgren S, Carlborg O: **Simultaneous search for multiple QTL using the global optimization algorithm DIRECT.** *Bioinformatics* 2004, **20**(12):1887–1895.
73. Wang X, Agarwala R, Capra J, Chen Z, Church D, Ciobanu D, Li Z, Lu L, Mozhui K, Mulligan M, *et al*: **High-throughput sequencing of the DBA/2J mouse genome.** *BMC Bioinformatics* 2010, **11**(Suppl 4):O7. doi:10.1186/1471-2105-1111-S1184-O1187.

doi:10.1186/1471-2164-13-411
Cite this article as: Nedelko *et al.*: Distinct gene loci control the host response to influenza H1N1 virus infection in a time-dependent manner. *BMC Genomics* 2012 **13**:411.